

**The role of aggregation in the fate and transport of  
nanoparticles in the environment: building a robust  
continuum modelling platform**

**Thesis submitted in accordance with the requirements of the  
University of Liverpool and National Tsing Hua University for the  
degree of Doctor in Philosophy (Dual-PhD) by Peyman Babakhani**

**July 2018**

## Summary

Nanoparticles (NP) can be released into the environment either purposefully e.g., for groundwater remediation of hazardous contaminants such as radionuclide or inadvertently from various sources such as consumer products. Crucially, models are required that can predict the fate and transport of NP in the environment. Continuum models have been pioneering in describing most mechanisms for NP transport in porous media. This study aims at addressing challenges that hinder the efficient application of such models. These can be broken down into six main areas, diversity in basis, assumptions made, ability to predict, transport mechanisms included, the efficiency of models, and finally not taking all natural environmental conditions into account. Among transport mechanisms, aggregation phenomenon is the most important one while it has less been considered within continuum models. In this study, extensive literature data analysis has been conducted using artificial neural network (ANN), Monte Carlo, and a sensitivity analysis technique to develop empirical correlations for predicting five unknown continuum model parameters based on 20 experimental factors. Comprehensive experiments and modelling were performed on the aggregation of NP in quiescent aqueous environments to find the best modelling approaches describing NP aggregation and removal. The selected model set was combined with continuum models of NP transport in porous media to predict the transport and aggregation of NP at environmentally-relevant scales, i.e., aquifer. This, however, revealed a need for a more efficient aggregation model. Further work was committed to proposing an efficient mass-concentration-based aggregation model and to investigating the impacts of system dynamics on aggregation.

The results suggest that ANN can be a useful way of developing empirical correlations for predicting continuum model parameters, and many insights were obtained from its sensitivity analyses. For instance, porous media heterogeneity, which was considered as a parameter for the first time, showed sensitivities higher than those of dispersivity. Investigations in aqueous media showed that considering both early and late stages of aggregation and sedimentation in the model yielded highest sedimentation rate at an intermediate ionic strength rather than the highest ionic strength. A mass concentration-based chain-reaction model, which was more efficient than the standard population balance model with a comparable or better accuracy in describing NP aggregation was proposed for future combinations with continuum models. System dynamics can enhance aggregation rate and lead to relatively compact aggregates over different stages of aggregation, sedimentation, and resuspension.

Although several challenges for using continuum models were mitigated in this study, incorporating aggregation, which is the most important mechanism that triggers other transport mechanisms and controls the final fate of NP in the environment, remains an issue due to complications identified in this study. This issue is mainly brought about because of dynamics of porous media. Nevertheless, continuum models are currently pioneering among various modelling approaches for simulating the fate and transport of NP in subsurface environments.

## **Keywords**

Nanoparticle; continuum model; advection-dispersion equation (ADE); transport phenomena; attachment; aggregation; porous media; parameter prediction; artificial neural network (ANN); sensitivity analysis; model uncertainties; early and late stage aggregation; sedimentation; population balance modelling; estimating fractal dimension; settling velocity; Hydroxyapatite (HAp) nanoparticles; environmental fate and transport; parent-daughter chain reaction model; mass-concentration; derived count rate; solid-body rotator; shattered graphene oxide (SGO); natural environmental system dynamics; porous media dynamic; surface water resuspension; aggregate restructuring; attachment efficiency; concurrent aggregation and transport.

# Acknowledgments

First and foremost, I express my utmost gratitude to the Almighty God for bestowing upon me the ability to accomplish this research.

I sincerely thank Dr Jonathan Bridge, my initial primary supervisor at the University of Liverpool (UoL), for admitting me on this dual-degree program and encouraging me from the very beginning to take this opportunity and to carry on throughout the work. His broad knowledge and deep thinking upgraded the outputs of my work. I highly appreciate the help and support of Prof Reuy-an Doong, my primary supervisor at National Tsing Hua University (NTHU). On the chemistry aspect of my thesis, I learnt a great deal from his boundless knowledge in this field. I am very grateful to Prof Karl Whittle, my second primary supervisor at UoL during the last 1.5 years of my PhD, for frequent, fruitful discussions and for his valuable guidance in completing my thesis. I would like to express my deep gratitude to Dr Tanapon Phenrat who, though unofficially, was my main advisor during my MSc research, in the early stage of my PhD, when the things becoming convoluted in learning chemistry and nuclear science, appeared again like a *deus ex machina* and helped me to find my way again. I also benefited from cooperation with his collaborators, Dr Fritjof Fagerlund (Uppsala University) and Prof Greg Lowry (Carnegie Mellon University). My special thanks are extended to other professors who participated in my supervisory team or my viva at NTHU, Prof Chu-Fang Wang, Dr Chien-Hou Wu, Prof Yang-hsin Shih, Prof Chun-Nan Hsu and at UoL, Dr Ming Li, and Dr Maulik Patel. I especially thank Dr Chien-Hou Wu for giving me full-time access to the Zetasizer instrument in his lab, and Prof Chu-Fang Wang, Dr Yu-Fen Huang, and Dr Guenter Engling at NTHU and Dr Raechelle D'Sa at UoL for modestly welcoming me to their laboratories whenever the need arose.

I would also like to thank all my lab-mates at NTHU and my officemates at UoL for their friendly cooperation and for tolerating me during my stay. Among my labmates at NTHU, my special thanks go to Rama Shanker Sahu (the lab King!) for his friendship and for spending long hours to show me how to synthesis GO, Binh Nguyen (and his disciples!) for always being ready to help me and for their friendship, Samy and Dong Dong for help in manufacturing my reactor, Dr Kartick Bindumadhavan for constructive discussions on fighting with bacteria, Chung-Yi Wu, for his excellent management of the Zetasizer instrument, and Cheng-Kuo Tsai (Vicent) for being a great friend and for helping me to find many essential things in Taiwan. I am also grateful to my cousin, Payam Miri, for his help on sketching some of figures.

Last but not least, I wish to offer my very great appreciation to my parents and my siblings for their support, prayer, and patience during this long journey.

## List of publications arising from the thesis

1. “Babakhani, P.; Bridge, J.; Doong, R.-a.; Phenrat, T., Continuum-based models and concepts for the transport of nanoparticles in saturated porous media: A state-of-the-science review. *Advances in Colloid and Interface Science* 2017, 246, (Supplement C), 75-104.”
2. “Babakhani, P.; Bridge, J.; Doong, R.-a.; Phenrat, T., Parameterization and prediction of nanoparticle transport in porous media: A reanalysis using artificial neural network. *Water Resour. Res.* 2017, 53, 4564-4585.”
3. “Babakhani, P.; Doong, R.-a.; Bridge, J., The significance of early and late stages of coupled aggregation and sedimentation in the fate of nanoparticles: measurement and modelling. *Environmental Science & Technology*, 2018. DOI: 10.1021/acs.est.7b05236”
4. “Babakhani, P.; Bridge, J.; Fagerlund, F.; Doong, R.-a.; Whittle, K., Comparison of a new mass-concentration, chain-reaction model with the population-balance model for early- and late-stage aggregation of shattered graphene oxide nanoparticles. In Review.”
5. “Babakhani, P.; Bridge, J.; Phenrat, T.; Doong, R.-a.; Whittle, K., Aggregation and sedimentation of shattered graphene oxide nanoparticles in dynamic environments: a solid-body rotational approach. *Environmental Science: Nano*, 2018. DOI:10.1039/C8EN00443A”

## Copyright permission note

These papers have been adapted in this thesis with permission from their respective publishers, Elsevier, Wiley, American Chemical Society for paper #1-3, respectively, or with obtaining open access from Royal Society of Chemistry for paper #5. It should be noted that the materials within chapter 1 have mostly been taken from paper #1 and partly from the introductions of other papers. Chapters 2,3,5, and 6 are entirely reproductions of papers #2–5. Appendices A–D are from paper #1 and Appendices E–H are supporting information of papers #2–5.

## Co-authorship statement

This thesis has been written according to the University of Liverpool's *postgraduate research code of practice – appendix 7* in an integrated-article format. All works in this thesis including conceiving the study, literature review, designing the experiments and modelling processes, developing conceptual and numerical models, performing the experiments, analysing and interpreting the results, writing the manuscripts, reviewing/revising the manuscripts, coordinating with other authors, and responding to referees' comments have been carried out by the candidate. Other co-authors in the five papers presented in this thesis as published or in-review articles, including primary supervisors of the research (Dr Jonathan Bridge, Prof Karl Whittle, and Prof Ruey-an Doong) and international collaborators (Dr Tanapon Phenrat and Dr Fritjof Fagerlund), have reviewed and revised the manuscripts and have given many suggestions during the progress of the work.

# Table of Contents

Summary .....	i
Acknowledgments.....	iii
List of publications arising from the thesis .....	iv
Copyright permission note .....	iv
Co-authorship statement .....	v
List of Figures .....	xi
List of Tables .....	xv
Nomenclature .....	xviii
List of abbreviations.....	xxiii
Chapter 1 .....	1
1 Introduction and literature review .....	1
1.1 Chapter overview.....	1
1.2 Radionuclide contamination in the environment.....	2
1.3 The use of nanoparticles for environmental remediation of radionuclide .....	4
1.4 Nanoparticle transport phenomena in porous media and their continuum modelling approaches.....	7
1.4.1 Subsurface transport mechanisms and the status of continuum modelling .....	7
1.4.2 Advection and dispersion .....	14
1.4.3 Attachment and detachment .....	16
1.4.4 Aggregation in porous media and its interaction with other phenomena .....	28
1.5 Applicability of continuum models .....	33
1.5.1 Experimental validation of model concepts .....	33
1.5.2 Upscaling of continuum models for NP transport .....	34
1.6 Thesis structure and objectives.....	35
1.7 References .....	37
Chapter 2 .....	56
2 Parameterisation and Prediction of Nanoparticles Transport in Porous Media: a Reanalysis using Artificial Neural Network.....	56
2.1 Chapter overview.....	56
2.1.1 Scope .....	56
2.1.2 Abstract .....	57
2.2 Introduction .....	57
2.3 Dataset and parametrization .....	60
2.4 Artificial neural network modelling procedure .....	68
2.5 Results and discussion.....	69
2.5.1 General fitting results .....	70

2.5.2	Model parameter sensitivity results .....	73
2.5.3	Model validation.....	85
2.5.4	Model robustness .....	86
2.6	Conclusions .....	89
2.7	References .....	91
Chapter 3	.....	99
3	The significance of early and late stages of coupled aggregation and sedimentation in the fate of nanoparticles: measurement and modelling .....	99
3.1	Chapter overview.....	99
3.1.1	Scope .....	99
3.1.2	Abstract .....	100
3.2	Nomenclature .....	100
3.3	List of abbreviations.....	101
3.4	Introduction .....	102
3.5	Modelling .....	103
3.6	Materials and Methods .....	107
3.6.1	Numerical modelling.....	107
3.6.2	Experiment procedure .....	107
3.7	Results and discussion.....	108
3.7.1	Experimental results .....	108
3.7.2	Model screening .....	111
3.7.3	Aggregate structure and sedimentation velocity.....	112
3.7.4	Attachment efficiency and fractal dimension .....	115
3.7.5	Mass removal rates and measurement depth .....	118
3.7.6	Implications for the fate of NP in groundwater and aquatic environments .....	120
3.8	References .....	122
Chapter 4	.....	128
4	Combining population balance and continuum models for aggregation and transport of nanoparticles at 3-D scale .....	128
4.1	Chapter overview.....	128
4.2	Introduction .....	128
4.3	Combining a population balance model and a continuum model.....	129
4.3.1	Model combination.....	129
4.3.2	Model parameters .....	131
4.3.3	Simulation characteristics.....	133
4.3.4	Mathematical models.....	136
4.4	Model validation.....	140
4.5	Prediction performance of the model .....	142

4.6	Upscaling to 3-D domain.....	143
4.7	References .....	146
Chapter 5	.....	149
5	Comparison of a new mass-concentration, chain-reaction model with the population-balance model for early- and late-stage aggregation of shattered graphene oxide nanoparticles .....	149
5.1	Chapter overview.....	149
5.1.1	Scope .....	149
5.1.2	Abstract .....	150
5.2	Introduction .....	150
5.3	Model Development .....	154
5.4	Experimental.....	159
5.5	Results and discussion.....	160
5.5.1	Validation of the model against analytical solution .....	160
5.5.2	Experimental results .....	161
5.5.3	Model fit results.....	163
5.5.4	Estimated parameter trends .....	165
5.5.5	Comparison of model efficiency and accuracy .....	167
5.6	Conclusions .....	169
5.7	References .....	171
Chapter 6	.....	177
6	Aggregation and sedimentation of shattered graphene oxide nanoparticles (SGO) in dynamic environments: a solid-body rotational approach.....	177
6.1	Chapter overview.....	177
6.1.1	Scope .....	177
6.1.2	Abstract .....	178
6.2	Introduction .....	178
6.3	Materials and Methods .....	181
6.3.1	Rotating cylinder setup.....	181
6.3.2	SGO synthesis .....	182
6.3.3	Experimental procedure.....	183
6.4	Theory and modelling.....	184
6.4.1	Flow regime.....	184
6.4.2	Particle aggregation.....	185
6.5	Results and discussion.....	187
6.5.1	Flow regime and particle trajectory analysis .....	187
6.5.2	Aggregation experiment results .....	189
6.5.3	Aggregation modelling results.....	193

6.6	Conclusions .....	198
6.7	References .....	200
Chapter 7	.....	206
7	Conclusions .....	206
7.1	Key conclusions.....	206
7.2	Recommendations for future studies .....	208
Appendix A	.....	210
8	Other NP transport phenomena .....	210
8.1	Straining .....	210
8.1.1	Mechanism .....	210
8.1.2	Criteria and manifestation .....	210
8.1.3	Modelling approaches of straining .....	213
8.2	Site-blocking and ripening .....	215
8.2.1	Site-blocking mechanism and related modelling approaches.....	215
8.2.2	Ripening mechanism and related modelling approaches.....	217
8.3	Size exclusion.....	221
8.3.1	Significance for NP .....	221
8.3.2	Mechanism .....	222
8.3.3	Continuum modelling approaches of size exclusion .....	225
8.4	References .....	228
Appendix B	.....	240
9	Summary of transport column experiments and their continuum modelling approaches.....	240
9.1	References .....	253
Appendix C	.....	257
10	Equilibrium vs kinetic terms in continuum models.....	257
10.1	References .....	264
Appendix D	.....	267
11	Overview of the concurrent occurrence of multiple transport phenomena .....	267
11.1	Conceptual model of transport for stable monodisperse dispersions .....	267
11.2	Conceptual model of transport for stable poly-disperse dispersions .....	267
11.3	Conceptual model of transport for unstable poly-disperse dispersions .....	268
11.4	References .....	271
Appendix E	.....	273
12	Supporting information for Chapter 2 .....	273
12.1	Further details on ANN modelling procedure .....	273
12.2	Description of PaD method for analysis of the sensitivities.....	275
12.3	Validation of the developed MATLAB Code .....	276

12.4	Evaluating the possible effect of mean imputation for the missingness in the data .....	276
12.5	Figures .....	277
12.6	Tables .....	281
12.7	References .....	284
Appendix F	.....	287
13	Supporting information for Chapter 3 .....	287
13.1	Drag coefficient correction factor and fluid collection efficiency.....	287
13.2	Various sedimentation velocity models.....	288
13.3	Details of the MATLAB code for simulating the aggregation and sedimentation of nanoparticles .....	290
13.4	Variable attachment efficiency model with DLVO.....	295
13.5	Development of parameter estimation algorithm .....	296
13.6	Comparison between numerical and analytical solutions.....	298
13.7	Further investigations of sedimentation models combined with the MP approach .....	300
13.8	Assessing the impact of number of depth discretization intervals.....	301
13.9	Experimental versus modelling PSDs .....	301
13.10	Figures .....	303
13.11	Tables .....	316
13.12	References .....	321
Appendix G	.....	324
14	Supporting information for Chapter 5 .....	324
14.1	Figures .....	324
Appendix H	.....	327
15	Supporting information for chapter 6 .....	327
15.1	Figures .....	327
15.2	Tables .....	332
15.3	References .....	332

# List of Figures

<b>Figure 1.1</b>	Potential strategies for the emplacement of NP in remediation of the contaminated zone with radionuclide: (a) NP injection/deposition at the downgradient of the source zone (PRB concept); (b) NP injected at the source zone and extracting the plume from the downgradient; (c) NP injection at the upgradient and extracting the plume from the source or downgradient.....	6
<b>Figure 1.2</b>	The paradigm of various modelling approaches for simulating fate and transport of engineered nanomaterials (ENM) in the environment, showing the status of continuum-based models and their potential links with the available data sources and other modelling approaches.....	11
<b>Figure 1.3</b>	Literature survey of various phenomena operative in the transport of nanoparticles based on the number of studies found in the Web of Science database in December, 2015 [184].....	14
<b>Figure 1.4</b>	Breakthrough curves generated by numerical solution of model Types (i) with MT3DMS model code following [74] for various $Katt$ values ( $S^{-1}$ ). Other parameters of flow and porous media conditions were selected according to [73, 74] (or refer Table B1). .....	19
<b>Figure 1.5</b>	Breakthrough curves generated by numerical solution of (a) model Type (ii) from Table 1.1, for various $Kdet$ values ( $S^{-1}$ ) and a fixed $Katt = 0.001 S^{-1}$ and (b) model Type (v) from Table 1.1, for various retardation factors and a fixed $Katt = 0.001 S^{-1}$ with MT3DMS model code following [74]. Other parameters of flow and porous media conditions were selected according to [73, 74] (or refer Table B1).....	23
<b>Figure 2.1</b>	Ternary plot of heterogeneity parameter for the category of disturbed soils (range of 60 to 90% heterogeneity) based on different amounts of clay, silt and sand. The plot is overlain by the ‘USDA Soil Texture Triangle’. The colour bar represents the heterogeneity values which are determined by Eq. 2.1. ....	65
<b>Figure 3.1</b>	Evolution of averaged hydrodynamic diameter, $D_H$ , (a,b) and change in mean derived count rate (DCR) normalized to the initial derived count rate ( $DCR_0$ ) (c) for HAp NPs at the point of measurement at various IS with a fixed pH at 6 (a,c) and various pH with a fixed IS at 5 mM $CaCl_2$ (b). The model used here was FP with power law formulation and Brinkman collision model. The modelling approach includes a fixed initial PSD with considering the pre-early stage of aggregation and a constant attachment efficacy (approach B).....	110
<b>Figure 3.2</b>	Trends of settling velocity, $U$ , normalized to the settling velocity of primary particle, $U_0$ , versus particle radius of each size class, $a$ , normalized by the primary particle radius (smallest size class), $a_0$ , calculated by four different types of velocity models. Fractal dimension is set as 1.6, 2, and 2.3. The primary particle radius used in these models is 40 nm. ....	114
<b>Figure 3.3</b>	Modelled mass concentration, $C$ , profiles normalized by the initial mass concentration, $C_0$ , versus the water column depth at (a) 5 mM $CaCl_2$ and (b) 10 mM $CaCl_2$ after 50, 150, and 300 min. The continuous lines represent approach A (case-specific initial PSD) and dashed lines represent approach C (fixed initial PSD combined with variable $\alpha$ computed by DLVO).....	119
<b>Figure 5.1</b>	Evolutions of Size (a,b) and change in normalized derived count rate ( $DCR/DCR_0$ ), (c,d) for SGO NPs at various IS ( $NaClO_4$ and $CaCl_2$ ) with a fixed pH at 6 (a,c) and various pH with a fixed IS at 20 mM $NaClO_4$ (b,d). Continuous lines represent C-CRM; dash lines represent FP technique, and dot lines represent the S-CRM model outcomes.....	162

<b>Figure 5.2</b>	Estimated parameter trends for different models: aggregation rate constants ( $\alpha$ , $A_s$ , and $A_c$ for FP, S-CRM, and C-CRM approaches), vs electrolyte concentration (a,b), and vs pH (c), and fractal dimension, $D_f$ , vs electrolyte concentration (d,e) and vs pH (f).....	166
<b>Figure 6.1</b>	Particle trajectories resulted from Eqs. (6.1-6.8) with virtually varying $D_f$ and particle radii considering two scenarios: (1) for particle initially placed in the middle of the cylinder radius (left-hand side panels) and (2) particle initially placed near the wall of the cylinder (right-hand side panels). The rotational direction is counter clockwise. ....	189
<b>Figure 6.2</b>	Experimental and modelling results of SGO aggregation/sedimentation under two electrolyte concentrations of 0.5 (a,b) and 0.75 mM $\text{CaCl}_2$ (c,d) at a fixed pH of 6 within static and rotating cylinders, and the cuvette of the DLS instrument (control measurement). The position of sampling in the cylinder ( $a_{cyl}=2.5$ cm) was at the centre of the cross-section and the control measurement position was at 2.4 cm below water surface. Panels show averaged hydrodynamic size (a,c), and normalized concentration (b,d). The normalized mass concentrations for control cases are obtained from DLS derived count rate data while for other cases these are determined using UV-Vis. The average of the duplicate of control measurements are shown with standard deviation as error bars. The cases of 0.75 mM $\text{CaCl}_2$ were conducted in duplicate and the experimental data of duplicate experiments are superimposed while each set fitted with the model separately. The model set used includes FP population-balance technique with the power-law model for settling velocity and the Brinkman permeability model for collision frequencies.....	190
<b>Figure 6.3</b>	Experimental photos of SGO aggregates formed over longer times for the case of rotating cylinder filled with SGO NP in 0.75 mM $\text{CaCl}_2$ solution and pH 6. The full photographs of cylinder corresponding to each time is available in Fig. H5, Appendix H. The snapshots in this figure were obtained at the same scale from the bottom of the cylinder.....	193
<b>Figure 6.4</b>	Estimated attachment efficiency (a) and fractal dimension (b) for SGO aggregation/sedimentation experiments under two electrolyte concentrations of 0.5 and 0.75 mM $\text{CaCl}_2$ at fixed pH 6 within control, static, and rotating cylinders. The position of sampling in the cylinder was at the centre of the cross-section ( $a_{cyl}=2.5$ cm) and control measurement position was at 2.4 cm below water surface. In the control, the model was fitted to the average of the duplicated online measurements while in other cases the model was fitted to both duplicate experiment datasets (if available), and the mean and standard deviation of estimated values are reported. ....	195
<b>Figure A1</b>	Possible retention sites for straining from [33].....	211
<b>Figure A2</b>	Possible regimes of transport mechanisms: (a) when particle-surface attachment tendency is higher than particle-particle attachment tendency and (b) when particle-particle attachment tendency is higher than particle-surface attachment tendency. Mobile particle/aggregates are shown in green while retained particle/aggregates are shown in yellow.....	220
<b>Figure D1</b>	The proposed conceptual models (a) for coupled effects of straining and size exclusion causing hyper-exponential shaped retention profile in the case of injecting poly-disperse particle dispersion into the experimental packed column and (b) for concurrent effects of agglomeration, deposition/straining, and size exclusion forming non-monotonic retention profile. Mobile particle/aggregates are shown in green while retained particle/aggregates are shown in yellowish brown.....	270

<b>Figure E1</b>	Diagram of porous media heterogeneity ranges used in developing the heterogeneity parameter. ....	277
<b>Figure E2</b>	Schematic of the three-layer perceptron ANN structure used in this study. ....	277
<b>Figure E3</b>	The flow chart of code algorithm developed in MATLAB <sup>®</sup> for ANN modelling, analysis of sensitivity and uncertainties, as well as finding the best model for prediction. Equation S2 in the chart refers to Eq. (E1).....	278
<b>Figure E4</b>	Log linear regressions between the attachment rate and the pore water velocity for the raw experimental data.....	279
<b>Figure E5</b>	Relationship between <i>Katt</i> and the pH obtained from the present study, and Seetha et al. [20], as well as CFT, the collector efficiencies of which were obtained based on the correlations of Phenrat et al. [21] and Tufenkji and Elimelech [22]. The data were selected in the ranges of simulated values in Seetha et al. [20]. Most of experimental conditions used resembled those of [23]. The parameter values used in the model are: a free-polymer concentration of zero mg/L, a particle zeta potential of -30 mV, and a grain zeta potential of -30 mV, a particle diameter of 150 nm, a grain diameter of 0.15 mm, a NP density of 6.7 g/cm <sup>3</sup> , an input concentration of 200 mg/L, a column diameter (Inner) of 2.6 cm, a column length of 25.5 cm, a heterogeneity of 15 % (clean sand), porosities of 0.33 and 0.4, a dispersivity of 0.015 cm, a pore water velocity of 0.015 cm/min, an IS of 10 mM, an injection duration of 1 PVs, an aspect ratio of 1, an adsorbed coating concentration of 1 mg/L, saturation magnetizations of zero and 570 kA/m, an IEP pH at 6.3, and pH ranging from 3 to 10. Extra parameters assumed in the correlations of Seetha et al. [20] include a temperature of 298 °K, a dynamic viscosity of 0.89 mPa.S, and a cylindrical pore constriction radius of $6.2 \times 10^{-5}$ m calculated based on grain size following Phenrat et al. [21]. Single collector attachment efficiency in the equation of Tufenkji and Elimelech [22] was assumed equal to one. ....	280
<b>Figure F1</b>	The linear correlation between the derived count rate (kilo count per second) and the mass concentration (mg/L) of HAp NP for three different ranges of concentration: up to 500 mg/L (left panel), up to 250 mg/L (middle panel), and up to 100 mg/L (right panel). Standard deviations of duplicate experiments are shown as error bars which are barely visible. ....	303
<b>Figure F2</b>	Mass concentration-based particle size distribution in the beginning (a-c), middle (after 150 min, d-f), and the end of each aggregation experiment (300 min, g-i) at various IS and a fixed pH at 6. The model used here was FP approach with using power law velocity formulation and Brinkman collision model. The approaches are: case-specific initial PSD (a,d,g), fixed initial PSD in all cases (b,e,h), fixed initial PSD along with a variable attachment efficiency predicted by DLVO (c,f,i). It should be noted that size in the horizontal axis refers to diameters specified for bins. ....	304
<b>Figure F3</b>	Mass concentration-based particle size distribution in the beginning (a-c), middle (after 150 min, d-f), and the end of each aggregation experiment (300 min, g-i) at various pH and a fixed IS at 5 mM CaCl <sub>2</sub> . The model used here was FP approach with using power law velocity formulation and Brinkman collision model. The approaches are: case-specific initial PSD (a,d,g), fixed initial PSD in all cases (b,e,h), fixed initial PSD along with a variable attachment efficiency predicted by DLVO (c,f,i). It should be noted that size in the horizontal axis refers to diameters specified for bins. ....	305
<b>Figure F4</b>	Different modelling approaches to sedimentation velocity and collision frequency calculation using the FP (a,b) and MP (c,d) aggregation model. Hollow large red circles are the experimental data obtained at pH 10 and 5 mM CaCl <sub>2</sub> . ....	306

<b>Figure F5</b>	Evolutions of $D_H$ and DCR data modeled with MP models along with Brinkman permeability-based collision rates and different velocity models including: power Law (left), Brinkman permeability (middle), and size-distribution-based (right) models. The experimental data include three cases conducted under pH values of 7, 10, and 11, at 5 mM $\text{CaCl}_2$ .	307
<b>Figure F6</b>	Size distribution modeled with MP model along with Brinkman permeability-based collision rates and different velocity models including: power Law (left), Brinkman permeability (middle), and size-distribution-based (right) models. The experimental data include three cases conducted under pH values of 7, 10, and 11, at 5 mM $\text{CaCl}_2$ .	307
<b>Figure F7</b>	DLVO profiles for various concentrations of $\text{CaCl}_2$ and different particle radii.	308
<b>Figure F8</b>	Evolution of Size (a-d) and change in normalized derived count rate (e-h) for HAp NPs at the point of measurement at various IS with a fixed pH at 6 (a,c,e,g) and various pH with a fixed IS at 5 mM $\text{CaCl}_2$ (b,d,f,h). The model set used here includes the FP approach with power law velocity formulation and Brinkman collision model. The modelling approaches include using case-specific observed initial PSDs (approach A) (a,b,e,f) and using a fixed initial PSD with considering the pre-early stage of aggregation combined with a variable attachment efficiency predicted by DLVO (approach C) (c,d,g,h).	308
<b>Figure F9</b>	Zeta potential versus pH at 0 and 5 mM $\text{CaCl}_2$ (a) and versus various electrolyte concentration at pH 6 (b).	309
<b>Figure F10</b>	Evolution of Size (a) and change in normalized derived count rate (shown as $C/C_0$ ) (b) and PSDs at the start (c), the middle (d), and the end (e) of experiments for HAp NPs with different sample volumes, 1, 3, and 4 mL corresponding to different depths of measurements, 0.33, 2.33, and 3.33 cm, respectively. Experiments were conducted at pH=6 and an IS of 5 mM $\text{CaCl}_2$ . The models used here comprise of FP approach, power law settling velocity formulation, and Brinkman collision rate model	310
<b>Figure F11</b>	Set initial particle size distribution used in the fixed-initial-condition approach.	311
<b>Figure F12</b>	The outputs of FP numerical model compared with the analytical solution for pure aggregation. All the initial population of particles is placed in the first bin. Similar to the condition of the case at pH 6 and IS of 10 mM $\text{CaCl}_2$ , the primary particle size was assumed 800 nm. Attachment efficiency was assumed one and $D_f$ was assumed 3. The geometric discretization spacing factor, $q$ , varied between 1.1 and 3.	311
<b>Figure F13</b>	The outputs of MP numerical model compared with the analytical solution for pure aggregation. All the initial population of particles is placed in one bin. The rest of the condition were selected similar to the case at pH 6 and IS of 10 mM $\text{CaCl}_2$ . Attachment efficiency was assumed one and $D_f$ was assumed 3. The geometric discretization spacing factor, $q$ , varied between 1.1 and 3.	312
<b>Figure F14</b>	The outputs of FP numerical model compared with the analytical solution for pure aggregation with log-normal initial PSD. The rest of the condition were selected similar to the case at pH 6 and IS of 10 mM $\text{CaCl}_2$ . Attachment efficiency was assumed to be one and $D_f$ is 3 (a,b) or 1.8 (c,d). The geometric discretization spacing factor, $q$ , is 1 (a,c) or 3 (b,d).	313
<b>Figure F15</b>	The outputs of MP numerical model compared with the analytical solution for pure aggregation with log-normal initial PSD. The rest of the condition were selected similar to the case at pH 6 and IS of 10 mM $\text{CaCl}_2$ . Attachment efficiency	

	was assumed to be one and $D_f$ is 3 (a,b) or 1.8 (c,d). The geometric discretization spacing factor, $q$ is 1 (a,c) or 2 (b,d).....	314
<b>Figure F16</b>	Predicted mass concentration profiles with sedimentation depth, $Z$ , confirming that selection of the number of depth intervals chosen is not significant in the prediction of mass loss rates using the models described in this work. ....	315
<b>Figure G1</b>	Zeta potential of SGO nanoparticles at different electrolyte concentrations (mM) of $\text{NaClO}_4$ and $\text{CaCl}_2$ at pH 6 (a) and for different pH values at an electrolyte concentration of 20 mM $\text{NaClO}_4$ (b). ....	324
<b>Figure G2</b>	The correlation between different concentrations and their equivalent derived count rate (DCR). ....	325
<b>Figure G3</b>	Comparisons of PSD for SGO NPs at various $\text{CaCl}_2$ (panels a-c) and $\text{NaClO}_4$ (d-f) concentrations with a fixed pH at 6 and various pH (g-i) with a fixed IS at 20 mM $\text{NaClO}_4$ at the beginning ( $t=0$ , a,d,g), middle ( $t=150$ min, b,e,h), and the end of experiments ( $t=300$ min, c,f,i). Continuous lines represent C-CRM; dot lines represent FP technique, and hash lines represent the S-CRM model outcomes. ....	326
<b>Figure H1</b>	The experimental setup used in this work (a) and an enlarged photograph of the cylinder (b). The diameter of the cylinder shown in panel (a) is 8.2 cm which was manufactured for initial trials while the diameter of the cylinder shown in panel (b) is 5 cm which was used for the main experiments.....	327
<b>Figure H2</b>	Experimental photos of the cylinder ( $a_{\text{cyl}}=2.5$ cm) rotating at 4.71 rph corresponding to $Re=0.91$ after Methylene Blue injection.....	328
<b>Figure H3</b>	(a) The rotational component of velocity and (b) shear rate vs distance from the centre of the cylinder for the cylinder at different times. ....	329
<b>Figure H4</b>	Velocity vectors for various $D_f$ and particle radii.....	330
<b>Figure H5</b>	Experimental photos of SGO aggregation over longer times for the case of rotating cylinder filled with SGO NP in 0.75 mM $\text{CaCl}_2$ solution and pH 6.....	331
<b>Figure H6</b>	Variation of nondimensionalized collision frequency calculated for collision between particles/aggregates with radii 50 (a), 500 (b), or 2000 (c) nm with all other particle size classes for different fractal dimensions. Other input parameters of the aggregation model assumed as: attachment efficiency $\alpha=1$ , particle density 1800 $\text{Kg/m}^3$ , and shear rate $G=0$ . $\tau$ is the characteristic time of aggregation [1] and $n_0$ is the initial population of particles.....	331

## List of Tables

<b>Table 1.1</b>	List of continuum-based modelling types applied for the transport of nanoparticles in porous media to date. *	24
<b>Table 2.1</b>	List of the two groups of parameters, modelling parameters and experimental/environmental properties.*	65
<b>Table 2.2</b>	Fitting results and the number of optimum nodes obtained by ANN code for various continuum model parameters. ....	71
<b>Table 2.3</b>	Sensitivity analysis outcomes, RS (%).....	74
<b>Table 3.1</b>	Model parameters estimated by fitting FP models to both early and late stages of aggregation under different electrolyte concentrations (at fixed pH 6) and different pH (at fixed electrolyte concentration, 5 mM $\text{CaCl}_2$ ) over 5 h, based on three modelling approaches (A, B, C), and mass removal results estimated by the models for a sample volume of 3 mL (3 cm water depth) after 5 h. The power-law	

	model and Brinkman-based permeability model are used to calculate the sedimentation velocity and collision frequencies, respectively.....	112
<b>Table 4.1</b>	Parameters used in 1-D simulations following [10, 26]......	132
<b>Table 4.2</b>	Parameters used in 2-D simulations. ....	133
<b>Table 4.3</b>	Lower ( $I_A$ ) and upper ( $I_B$ ) integration limits in calculation of the probabilities of particle interaction with the primary ( $\varepsilon_1$ ) and secondary ( $\varepsilon_1$ ) minima of DLVO profile based on five classes of interaction energy profile illustrated in Fig. 4.4. ....	139
<b>Table 5.1</b>	Nash-Sutcliffe determination coefficient, $R^2_{NS}$ for fittings to hydrodynamic diameter data with different models across various solution chemistries. ....	164
<b>Table 5.2</b>	Comparison of the model run times and mass balance errors for different cases of model fittings.....	168
<b>Table 6.1</b>	Summary of modelling parameters and experimental characteristics. ....	187
<b>Table B1</b>	Summary of the NP transport studies experimental conditions and outcomes together with the major observed phenomena, the shapes of the breakthrough curve and residual concentration profile, and types of the applied continuum model. ....	240
<b>Table C1</b>	Parameter values and fitting results for cases of F3 at 30 mg/L and F1 at 6 g/L using non-equilibrium and equilibrium models. <sup>a</sup> .....	261
<b>Table C2</b>	Parameter values and fitting results for cases low concentration of 0.3 g/L and high concentration (washed-MRNIP2) of 6 g/L using non-equilibrium and equilibrium models. <sup>a</sup> .....	262
<b>Table E1</b>	The values of isoelectric point (IEP) or the point of zero charge (PZC) assumed for each NP type in the dataset.....	281
<b>Table E2</b>	Linear correlations between $K_{att}$ and ionic strength for the separated data of different ionic compositions.....	281
<b>Table E3</b>	Ranges of heterogeneity parameter ( $\Theta$ ) variation for different amounts of Clay, Silt, and Sand. ....	282
<b>Table E4</b>	Sensitivity analysis outcomes, RS (%). ....	283
<b>Table F1</b>	Fixed pivot fitting results with various sedimentation velocity and collision rate models. ....	316
<b>Table F2</b>	Moving pivot fitting results with various sedimentation velocity and collision rate models. ....	317
<b>Table F3</b>	Goodness-of-fit results for FP model fittings to various experimental cases under different pH, IS, over 5 h with three approaches, to consider the initial condition: (1) PSD obtained at the initial measurement of each case; (2) an identical PSD for all cases; (3) an identical PSD for all cases and considering variable $\alpha$ based on DLVO. The power-law model and Brinkman-based permeability model are used to calculate the sedimentation velocity and collision frequencies, respectively. Measured zeta potential are also compared with the adjusted zeta potential in fittings when approach 3 is used. ....	318
<b>Table F4</b>	The results of MP model in combination with three different sedimentation velocity models fit against experimental data of different pH. The Brinkman permeability model is used to calculate collision rates. ....	318
<b>Table F5</b>	Fixed pivot with the case-specific initial PSD approach fittings to early stage (the first 20 min) of various experimental cases under different cases of high pH, and IS. The power-law model and Brinkman-based permeability model are used to calculate the sedimentation velocity and collision frequencies, respectively...	319
<b>Table F6</b>	Fixed pivot with the case-specific initial PSD approach fittings to early and late stages at pH 6 and 5 mM $\text{CaCl}_2$ at different measurement depths. The power-law model and Brinkman-based permeability model are used to calculate the sedimentation velocity and collision frequencies, respectively.....	320

<b>Table H1</b>	Parameter values estimated in the fitting process together with Nash-Sutcliff goodness-of-fit criterion, $R^2_{NS}$ . .....	332
-----------------	---	-----

# Nomenclature

$a_0$	primary particle radius [L]
$a_{ave,t}$	the equivalent radius of the geometric mean size of PSD at time $t$
$A_{H\ 123}$	combined Hamaker constant [ $ML^2T^{-2}$ ] for the particle-water-surface system
$a_i$	aggregate radius in size class $i$ [L]
$a_k$	radius of size class $k$
$a_{max}$	radius of largest aggregate size class
$CI$	confidence interval
$C_k$	mass concentration [ $ML^{-3}$ ] of fluid-phase particles for size class $k$
$d_{50}$	median porous media grain size [L]
$d_{50\ agg}$	median size of particles within each aggregate
$D_f$	fractal dimension [–]
$D_H$	Hydrodynamic diameter
$d_i$	diameter of aggregate in size class $i$
$D_{i,j}$	dispersion coefficient tensor [ $L^2T^{-1}$ ]
$D_k$	diameters of primary particles (the smallest size class) $k$
$d_k$	diameters of the given size class $k$
$D_{sed}$	sedimentation exponent
$G$	shear rate [ $T^{-1}$ ]
$g$	gravitational acceleration
$h$	separation distance [L] between the colloid and the solid-water interface
$h_s$	distance between the surface of the charged particles and the slipping plane (usually taken as 5 Å)

$i, j$	subscripts used to indicate aggregates size class $i$ and $j$
$J_1, J_2$	Bessel functions of the first kind and orders 1 and 2
$k$	aggregate size class index
$K_{att\ k}$	attachment rate coefficient [ $T^{-1}$ ] for size class $k$
$k_b$	Boltzmann constant
$K_d$	distribution coefficient based on the equilibrium or linear isotherm model
$K_{det\ k}$	detachment rate coefficient for size class $k$ [ $T^{-1}$ ]
$k_{max}$	maximum number of classes considered in numerical models (<100)
$l_A$	lower integration limits
$l_B$	upper integration limits
$m_k$	mass of each aggregate in size class $k$
$n_0$	initial population of particles determined from the initial PSD
$n_k$	aggregate number concentration in size class $k$ [ $L^{-3}$ ]
$P_{Cl}$	percentage of clay in the soil
$P_{Sd}$	percentage of sand in the soil
$P_{St}$	percentage of silt in the soil
$q$	geometric factor
$r$	radial distance from the centre of the rotating cylinder
$r_0$	initial radial position of the particle in cylindrical coordinates
$r^2$	correlation coefficient
$R^2_{NS}$ or $R^2$	Nash–Sutcliffe model efficiency or coefficient of determination
$Re$	Reynolds number

$RS$	relative sensitivity
$S_k$	mass concentration of deposited phase particles of size class $k$ [ $MM^{-3}$ ]
$T$	temperature [ $K$ ]
$t$	time elapsed [ $T$ ]
$U_0$	sedimentation velocity of primary particles [ $LT^{-1}$ ]
$U_k$	aggregate sedimentation velocity in size class $k$ [ $LT^{-1}$ ]
$u_x, u_y$	horizontal and vertical rectangular components of velocity in the cylinder
$u_\theta$	angular component of the linear velocity in rotational system
$v_0$	solid volume of primary particles [ $L^3$ ]
$V_{ave}$	pore water velocity [ $L T^{-1}$ ] averaged over the spatial domain of the model
$V_i$	pore water velocity [ $L T^{-1}$ ]
$v_k$	volume of solids of each aggregate in size class $k$ [ $L^3$ ]
$x, y$	position of the particle in rectangular coordinates
$x_i, x_j$	distances [ $L$ ] along the respective Cartesian coordinate axis, $i$ and $j$ , in porous media
$Y_{k,k-1}$	yield coefficient [-] between species $k-1$ and $k$
$Z_s$	sedimentation depth [ $L$ ]

## Greek

$\alpha$	attachment efficiency for particle-particle aggregation [-]
$\alpha_{pc k}$	attachment efficiency for interactions between particles of size class $k$ and collectors (porous media grains)
$\beta_{1,1}$	the maximum of $\beta_{k,k}$ range
$\beta_{Diff}$	differential settling collision frequency [ $L^3T^{-1}$ ]
$\beta_{i,j}$	collision kernel or collision frequency between aggregates in size classes $i$ and $j$ [ $L^3T^{-1}$ ]

$\beta_k$	first-order mass transfer rate between the mobile and retained phases for species $k$
$\beta_{k,k}$	collision frequency between each class of aggregates and classes of the same size
$\beta_{k,kave}$	collision frequency between each class of aggregates and the class that has an equivalent size with the geometric average size of the PSD in each time step
$\beta_{kmax,kave}$	the maximum of $\beta_{k,kave}$ range
$\beta_{Orth}$	orthokinetic collision frequency [ $L^3T^{-1}$ ]
$\beta_{PrIk}$	perikinetic collision frequency [ $L^3T^{-1}$ ]
$\gamma$	shear rate [ $T^{-1}$ ]
$\gamma_1, \gamma_2$	parameters representing the role of applied hydrodynamic torque ( $T_H$ ) and adhesive torque ( $T_A$ )
$\delta_{i,j}$	Kronecker delta
$\varepsilon$	porosity of porous media [-]
$\varepsilon_0$	permittivity of a vacuum ( $8.854 \times 10^{-12} C/(V \cdot m)$ )
$\varepsilon_1$	probability of colloid interaction with the primary energy minima
$\varepsilon_2$	probability of colloid interaction with the secondary energy minima of DLVO, respectively
$\varepsilon_m$	dielectric constant of the medium (water) [-] taken as 78.5
$\zeta$	zeta potential (V)
$\eta_{\theta k}$	collision or contact efficiency of size class $k$ and collectors
$\eta_c$	fluid collection efficiency of an aggregate
$\Theta$	heterogeneity estimated for the disturbed soil category
$\theta_0$	initial angular position of the particle in cylindrical coordinates
$\theta_{sf}$	dimensionless particle-shape factor

$\kappa_{Deb}$	inverse of the Debye length (nm)
$\kappa_k$	permeability of aggregates in size class $k$ [ $L^2$ ]
$A_c$	aggregation constant of the collision-based chain reaction model (C-CRM)
$A_s$	aggregation constant of the size-based chain reaction model (S-CRM)
$\mu$	dynamic viscosity of the suspending medium [ $M T^{-1} L^{-1}$ ]
$\nu$	kinematic viscosity [ $L^2 T^{-1}$ ]
$\zeta$	non-dimensional permeability of the porous aggregate
$\rho_0$	density of primary particles, [ $ML^{-3}$ ]
$\rho_b$	porous medium bulk density [ $ML^{-3}$ ]
$\rho_w$	density of water [ $ML^{-3}$ ]
$\sigma_c$	collision diameter assumed as 0.26 nm
$\Phi$	mean value of the dimensionless total sphere-plate interaction energy
$\Phi^{Bron}$	Born repulsion for sphere-plate interactions
$\Phi_d$	total sphere-plate interaction energy [ $Kg m^2 S^{-2}$ ]
$\Phi^{el}$	electrostatic repulsion for sphere-plate interactions
$\varphi_k$	porosity of aggregates in size class $k$
$\varphi_{s1}, \varphi_{s2}$	surface potentials (mV) for the porous media grain and/or the interacting particles
$\Phi^{vdW}$	van der Waals attraction for sphere-plate interactions
$\omega$	angular velocity of the cylinder
$\Omega_i$	drag coefficient correction factor
$\lambda_k$	first-order reaction coefficient [ $T^{-1}$ ] in a classical chain reaction model or the rate of aggregation in the new paradigm for species or size class $k$
$\lambda_w$	characteristic wavelength assumed equal to 100 nm

## List of abbreviations

BTC	breakthrough curve
CCC	critical coagulation concentration
C-CRM	collision-frequency-based chain reaction model
CFT	colloid filtration theory
DCR	derived count rate
DI	deionized
DLA	diffusion limited aggregation
DLS	dynamic light scattering
DLVO	Derjaguin, Landau, Verwey, and Overbeek
FP	fixed pivot
GO	graphene oxide
GW	groundwater
HAp	hydroxyapatite
HPC	high performance cluster
HTC	high throughput computational
IEP	isoelectric point
IS	ionic strength
MP	moving pivot
NP	nanoparticles
PB	population balance
PBE	population balance equation

PSD	particle size distribution
RLA	reaction limited aggregation
S-CRM	size-based chain reaction model
SGO	shattered graphene oxide
SW	surface water

# Chapter 1

## 1 Introduction and literature review

### 1.1 Chapter overview

Engineered nanoparticles (NP) are now widespread in the environment. Often these are released accidentally or in waste streams. Various controlled applications have also been proposed. For example, when cleaning radioactively contaminated sites, facilities etc., NP show promise for *in situ* remediation. Continuum modelling methods are ideal for designing remediation strategies as they are scalable from laboratory-based column experiments to aquifer sized transport studies. They can also successfully describe the simultaneous occurrence of various transport phenomena of NP within porous media. However, there are still multiple obstacles to successful robust application of such models for describing or predicting NP transport phenomena.

In this chapter, the need for the remediation of radionuclides and the potential for using NP is outlined. The literature focusing on NP transport mechanisms and their respective continuum modelling approaches is then reviewed. Amongst common transport phenomena, aggregation (agglomeration) and deposition/detachment are fully discussed in this chapter whilst other transport mechanisms are described fully in Appendices A and B. Previously-developed models are utilized to explain the phenomena that can be simulated using continuum models (e.g., attachment/detachment using an equilibrium model as elaborated in Appendix C). Additionally, the concurrent occurrence of multiple phenomena is conceptualized with reference to the full discussion in Appendix D. The main challenges of continuum models are discussed further as they will be systematically addressed in the following chapters. The population balance models of aggregation in aqueous media are introduced and outlined. The challenges and necessities of combining population balance models and continuum models are also elaborated, and a new approach is proposed to address these challenges. Finally, the differences between the aggregation under quiescent condition and the dynamic condition are discussed too. These will be systematically investigated in the penultimate chapter of the thesis. A large part of this chapter together with Appendices A to D were published as the following critical

review paper on the transport mechanisms of NP along with their continuum modelling approaches, with the key points relevant to the work in this thesis:

“Babakhani, P.; Bridge, J.; Doong, R.-a.; Phenrat, T., Continuum-based models and concepts for the transport of nanoparticles in saturated porous media: A state-of-the-science review. *Advances in Colloid and Interface Science* 2017, 246, (Supplement C), 75-104.”

## 1.2 Radionuclide contamination in the environment

Radioactive contaminants have long been recognized as an environmental pollutant due to their radiotoxicity, chemical properties, and abundance. Depending on the type of radionuclide it can take thousands of years for radionuclide to become a non-hazardous material [1]. Thus, it is vital to remove these hazardous pollutants safely from the environment.

There are many medical, industrial and scientific applications of radionuclide such as the use of cesium-137 ( $^{137}\text{Cs}$ ) in food production industries and medical treatment and diagnosis or the use of strontium-90 ( $^{90}\text{Sr}$ ) in medical and agricultural studies [2]. Yet, the most important points of concern for emission of radioactive material into the environment were the Chernobyl catastrophe in April 1986 which resulted in extensive release of radioactive materials (totally 14 EBq<sup>1</sup>, including 1.8 EBq of  $^{131}\text{I}$ , 0.085 EBq of  $^{137}\text{Cs}$ , 0.01 EBq of  $^{90}\text{Sr}$  and 0.003 EBq of plutonium) [2, 3] and the Fukushima disaster in March 2011, resulting in release of a substantial amount of radionuclide into the environment, especially the marine environment [4]. At Fukushima a total of ~1 EBq of radionuclide was released into the atmosphere, and 10 PBq<sup>2</sup> was released into the sea. The majority of the released radioactive material (10 PBq) was isotopes of caesium (both  $^{134}\text{Cs}$  and  $^{137}\text{Cs}$  almost equally) as well as iodine,  $^{131}\text{I}$ ; and strontium,  $^{90}\text{Sr}$  [4].

Radionuclides released into the atmosphere often deposit onto topsoil, which can infiltrate into groundwater [3-5]. The horizontal movement of surface water in the catchments near Chernobyl was found to play an important role in the transport of deposited radionuclides within the root-region soil [3]. The surface water movement

---

<sup>1</sup> 1 EBq =  $10^{18}\text{Bq}$  (Exabecquerel)

<sup>2</sup> 1 PBq =  $10^{15}\text{Bq}$  (Petabecquerel)

eventually led to the transport of radionuclides into the oceans. Not only can the discharge flux of radionuclide-contaminated surface water contaminate the oceans, but they are also substantial sinks for radionuclides in the atmosphere via both dry and wet deposition [5]. For instance, it has been estimated that the entire quantity of  $^{137}\text{Cs}$  emitted to the atmosphere from the Fukushima Dai-ichi accident was 15 PBq while the released  $^{137}\text{Cs}$  to the ocean was from 3.5 to 16.2 PBq [5]. It is comparable with that of surface deposition of  $^{137}\text{Cs}$  following the Chernobyl accident onto the Black sea and Baltic sea as 2.8 PBq and 3.0 PBq, respectively [3].

Radionuclides such as Pu and Am can often be found in solute forms. However, when their concentration in water exceeds their solubility limits, they form colloids, which are defined as microscopically dispersed insoluble particles suspended in another substance which is typically water in the context of environmental science [6]. These colloids are called “true colloids”, whereas when natural colloidal particles uptake radionuclide they may be called “pseudo-colloids” [7]. The transport of aqueous radionuclides in the environment, by themselves, is not significant due to their high affinity for adsorption onto the surface of the soil grains or rock surfaces. However, in the presence of other colloidal particles such as natural particles ubiquitous in the environment, e.g., clay minerals, or in the presence of engineered nanoparticles (NP), radionuclides will readily be adsorbed and can be transported over large distances. This is because finer particles have a higher surface area and therefore higher potential, and capacity, for uptake of radionuclides than that of the subsurface matrix. Accordingly, the mobility of radionuclides is controlled by the mobility of these particles, which are carrying the radionuclides [8-10]. For instance, Kersting et al. [10] observed a migration distance of 1.3 km at Nevada test site for Pu which they attributed to subsurface colloidal transport.

The impact of colloidal particles in the migration of radionuclides can be so significant that part of the radionuclides, which have been attached onto the larger particles among the polydisperse population of particles, can be transported even faster than the average groundwater velocity. This phenomenon has been ascribed to the size exclusion effect, also known as hydrodynamic chromatography effect [6, 11-15]. This phenomenon is fully discussed in Appendices A and B along with other transport mechanisms of nanoparticles.

### **1.3 The use of nanoparticles for environmental remediation of radionuclide**

Nanoparticles are defined as materials with all three dimensions between 1 and 100 nm; in contrast to traditional colloidal particles which range in size from 1 nm to ~1  $\mu\text{m}$  (ISO/TS 27687:2008)[16]. Nanoparticles have shown significant potentials for environmental remediation [17]. The main characteristic of NP that gives them an edge over their traditional counterparts, is their high specific surface area [18]. Nowadays, NP such as nanoscale zerovalent iron (NZVI) have been used for *in situ* groundwater remediation at the field-scale in a number of projects around the world [19-21]. This technology shows promise for removal of the radionuclide at laboratory scales, e.g., using graphene oxide (GO) nanomaterials [22, 23], hydroxyapatite (HAp) NP [24-26], and iron NPs [27-32]. However, effective *in situ* field-scale applications of these NP for remediation of radionuclide contaminated sites are hindered by the lack of adequate modelling tools that can simulate NP behaviour and transport under realistic environmental conditions. Considering the long-established potential for colloids to enhance mobility in groundwater environments [8, 10] or to facilitate redistribution in surface water bodies [33-35], this lack of modelling capability is a critical concern. Such modelling tools are needed to design the remediation strategy in a way that potential off-site migration of both NP and the adsorbed radionuclide on their surface is prevented when the technology is used in the field or pilot scale.

The effectiveness of NP technology implementation relies upon the accurate design of the delivery system. The design of NP emplacement strategy is of crucial importance for performing a successful environmental remediation. The influential factors include the amount of required NP, injection flow rate, position of emplacement, the layout of injection/extraction wells etc. [21]. In addition, since one of the major expenses of remediation with NP is related to the well drilling and pumping [36, 37], pre-designing the NP emplacement technique optimises the remediation.

The initial focus for the use of NP in remediating contaminated groundwater and soil was based on their ability to disperse in porous media, due to their small size. Yet this was hindered by aggregation and substantial retention NP [38]. This obstacle was overcome by developing a variety of surface modification and functionalizing

techniques to increase their stability, mobility, and targetability [39-53]. Nonetheless, even with a large number of studies on functionalization of NP to target various contaminants better, its delivery method is still challenging [54-56]. Migration distances of up to 6 m have been observed for NZVI in field-scale projects using different delivery technologies such as pressure-activated injection probes [47, 57] vertical and 45°-oriented wells and applying a Sidewinder tool [58], pneumatic injection, direct injection [41], groundwater circulation from pumping well to injection well [59], and gravity injection well [43, 46, 60], suggesting that the general reliable migration distance of 1.5 m [54] has been met at field scale whereas assessing the risk of off-site migration needs serious attention.

Primarily, there were two views regarding the conception of NP application in subsurface remediation. The first was to use NP to treat the plume of mobile, dissolved contaminants, based on the former idea of permeable reactive barriers (PRB) [61-63]. The second was to target the source zone of contaminants, e.g., dense, non-aqueous phase liquid (DNAPL) [64]. The latter application of the technology is more important because it enables remediation of contamination zones where many other remediation technologies are inapplicable, e.g., when there is an aboveground structure that does not allow use of other technologies such as pump-and-treat or traditional PRBs [58, 65]. Figure 1.1 outlines the potential or rather ideal strategies that can be useful for consideration in the subsurface remediation of radionuclides using NP based on the aforementioned concepts and considering the possibility of using horizontal wells [66, 67] which may assist the emplacement and distribution of NP in the subsurface. Accordingly, NP can be either injected into subsurface at the downgradient of the source zone to act as a PRB as shown in Fig. 1.1a, or they can be injected at the source zone while extracting the plume from the downgradient as shown in Fig. 1.1b. Alternatively, NP can be injected at the upgradient while extracting the plume from the source or downgradient as shown in Fig. 1.1c.

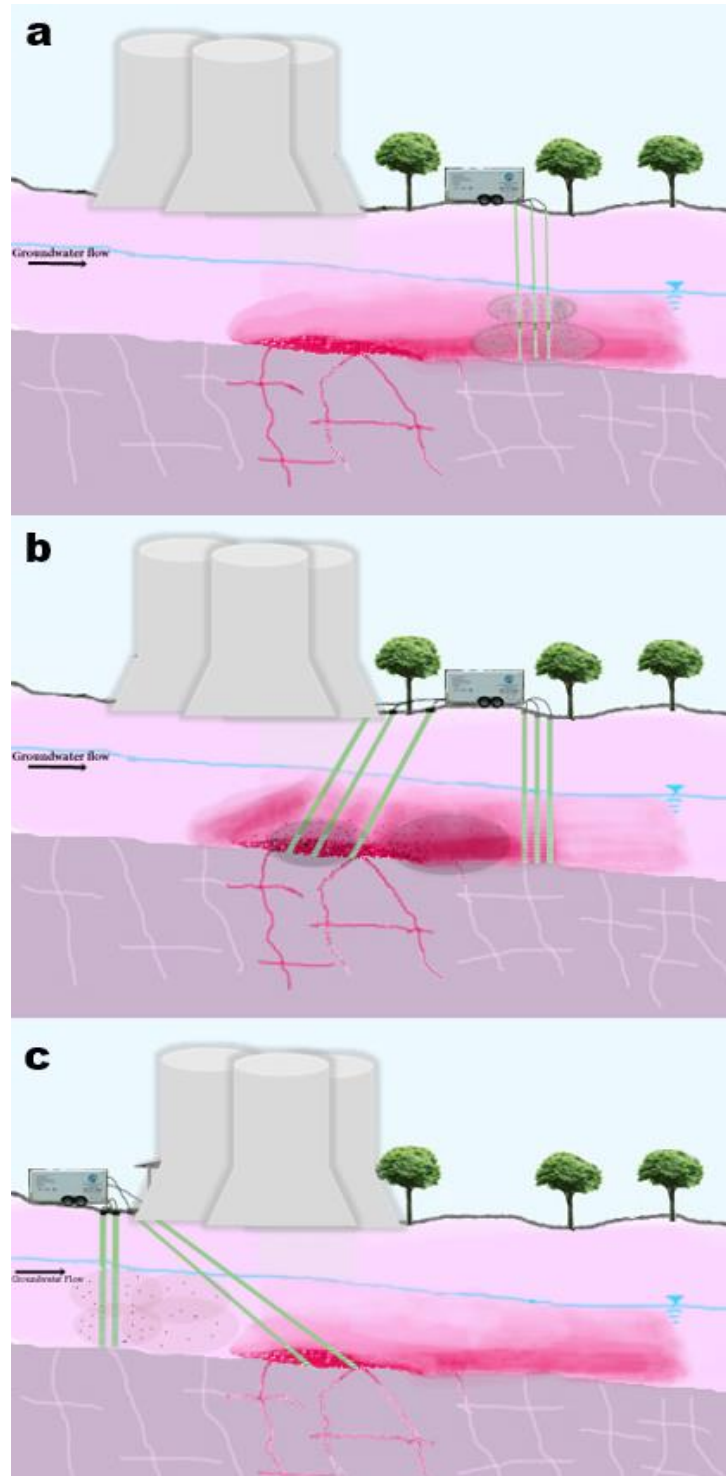


**Figure 1.1** Potential strategies for the emplacement of NP in remediation of the contaminated zone with radionuclide: (a) NP injection/deposition at the downgradient of the source zone (PRB concept); (b) NP injected at the source zone and extracting the plume from the downgradient; (c) NP injection at the upgradient and extracting the plume from the source or downgradient.

## **1.4 Nanoparticle transport phenomena in porous media and their continuum modelling approaches**

### **1.4.1 Subsurface transport mechanisms and the status of continuum modelling**

Nanoparticles (NP) possess unique properties in engineered and environmental systems when compared to their micron size counterparts [18, 68]. Such uniqueness leads to complications in predicting unintended exposure and risk of NP as well as their associated solute contaminants [69-73]. A wide range of physicochemical interactions impact NP transport in the subsurface. The relative significance of such processes for NP may differ from that of larger colloids. For instance, aggregation is potentially one of the most important phenomena that can occur for NP transported in porous media [73-75] while it may be less considerable for common colloids because of higher Brownian diffusion of NP in comparison to the larger-sized colloidal particles.

Depending on the scale of the assessment and the required resolution/precision of the outcomes, modelling tools deployed for assessing the behaviour of NP in porous media may be categorized in three major model groups: 1) abstract; 2) mechanistic; and 3) continuum [69, 76-78]. Selection of the most appropriate model for a given problem is a trade-off between simplicity and accuracy [79, 80]. Abstract models including material flow analysis (MFA) or multi-media models (MMM), are based on the principle of mass balance and assess the release and fate of NP in the environment from the global level, i.e., worldwide, down to the local levels, e.g., estuaries [e.g., 70, 78, 80, 81, 82-89]. Most of these models are based on simple algebraic equations and may not sufficiently capture the influential factors [90, 91], although attempts have been made to address this, e.g., by combining with Smoluchowski model for aggregation of NP or considering first-order rate constants for all processes including hetero-aggregation [90, 92-94]. These models typically take statistical and probabilistic approaches that incur unknown uncertainties in the total results or in the individual parameters which require rigorous uncertainty analysis [82, 83, 85]. MFA-based models are simplistically top-down models [89] with a lack of suitable analytical

methods for quantification, detection and analysis of environmentally relevant data of NP distribution at the relevant length scales [80, 88].

Mechanistic models focus on individual particles by considering the forces, torques, and energy of both the particle and interacting media [69, 77, 95-102]. Such forces are typically described using Derjaguin–Landau–Verwey–Overbeek (DLVO) theory for both interactions between particles and particles and interactions between particles and plate resembling porous media surface [95, 103]. The basic DLVO theory considers two forces of van der Waals attraction originated from electromagnetic interactions (range of influence 5-10 nm) and electrostatic repulsion arisen from adsorbed functional group or surface reaction (range of influence 1-20 nm) [104]. The extended DLVO (X-DLVO or E-DLVO) has been introduced when other non-DLVO forces are involved. These additional forces with their respective ranges of influence include: steric repulsion resulted from adsorbed polymers or surfactant on the surface of particles (1-5 nm), bridging attraction also resulted from adsorbed polymers or surfactant on the surface of particles (5-50 nm), Born repulsion arisen from interpenetrating electron cloud (0.3-2 nm), hydration repulsion emanated from surface/solvent interactions (1.5 nm), hydrophobic attraction from capillary pressure (20-60 nm), and magnetic attraction resulted from magnetic dipole (100 nm) [104]. Mechanistic models become increasingly complex to apply when several phenomena simultaneously occur during NP transport in porous media [12-15, 71, 73, 74, 96, 105-110]. Moreover, the intrinsic complexities and heterogeneities prevalent in real environmental conditions, such as surface roughness [111-114], natural organic matter (NOM) [72, 95, 115], iron oxyhydroxide coating [116-118], silylation [119], extracellular polymeric substance, and biofilm [120-122] make it unfeasible to use models such as classical colloid filtration theory (CFT) [111-114], DLVO theory [95, 103], and Maxwell model [123-125] which typically impose assumptions of uniformity in charge distribution, sphericity of interacting particles, dilute dispersion, additivity for only two forces, additivity of every molecule effect, point-charge ions, ideal distribution of ions, continuum medium, constant permittivity, uniform solvent, and larger thickness of diffuse layer than particle radius [126]. Detailed descriptions of the DLVO theory and the CFT with their governing equations are presented in Chapters 3 and 4 as well as Appendix F where these theories are used either for

qualitative assessment and interpretation of continuum model results or for quantitative combination with continuum or population balance models.

Continuum-based models are defined as partial-differential equations based on the continuity principle, either the mass conservation law (mass balance) or particle number/volume balance, over the bulk spatial and temporal domains of the system which are either continuous or numerically-discretized continuous domains [69, 76, 77, 127-129]. This definition contrasts with pore-scale models where the domain has a discrete configuration of solid and fluid [129]. In this chapter, I narrow down the scope of the continuum-based models to Eulerian techniques and thus exclude the particle tracking analysis (generally Lagrangian methods) [75, 107], since they consider particles separate from the fluid. It should be noted that commonly “continuum” terminology has been used to designate a range of larger spatial scales of the model domain ( $\gg 1$  cm) in contrast to micro/pore-scale models (1-100  $\mu\text{m}$ ) [129]. From this thesis’s viewpoint not only the spatial scalability of continuum models, but also their ability to provide information about the kinetics of phenomena, transient situations, and heterogeneities in the bulk spatial domain, are considered unique features of continuum-based models. The overarching goal of this thesis which is developing the models in realistic environmental scales, e.g., aquifers, necessitates the use of computationally affordable models such as continuum models. Thus, the use of Lagrangian approaches which are more computationally demanding than continuum models is not considered in this research.

Continuum models have previously been used widely for simulating miscible contaminants and classical colloid transport problems, and more recently they have been gaining popularity for modelling NP transport [80, 128, 130-132]. These models can be applied across various length scales such as pore scale [133], column experiments [e.g., 74, 134-136], bench-scale experiments [74], mesocosm experiments [87, 137], and field scale operations [138, 139]. This allows continuum-based models to be applied not only for delineating the risk of NP release and the design of remediation strategies in the local scale, but also for validating global assessment models of NP transport in the environment by applying them in tandem [76, 89]. In contrast to mechanistic approaches which deal with forces or energy, continuum models deal with rates. These models can accommodate different data such as number concentration [e.g., 74, 134, 140-142] or mass concentration [e.g., 142, 143, 144].

They can be modified to transform the data internally [74, 75], can therefore be calibrated and validated against a wide variety of available data types obtained from various laboratory experiments or realistic field measurements [74, 138, 139, 145]. More noteworthy, is their capability to describe several transport phenomena simultaneously [e.g., 74, 134, 144, 146-153].

No single fate and transport modelling approach precludes application in parallel with any other, as each offers different insights. Figure 1.2 illustrates the concept of a comprehensive, multi-model analysis of engineered nanomaterials in the environment. For instance, continuum models for groundwater can be integrated with MFA to track the fate of NP in the subsurface where the required data for MFA is less available [89]. This class of model can be used to average the results from pore scale mechanistic simulations to obtain the one-dimensional concentration field and consequently estimate the values of the average deposition rate coefficients [133].

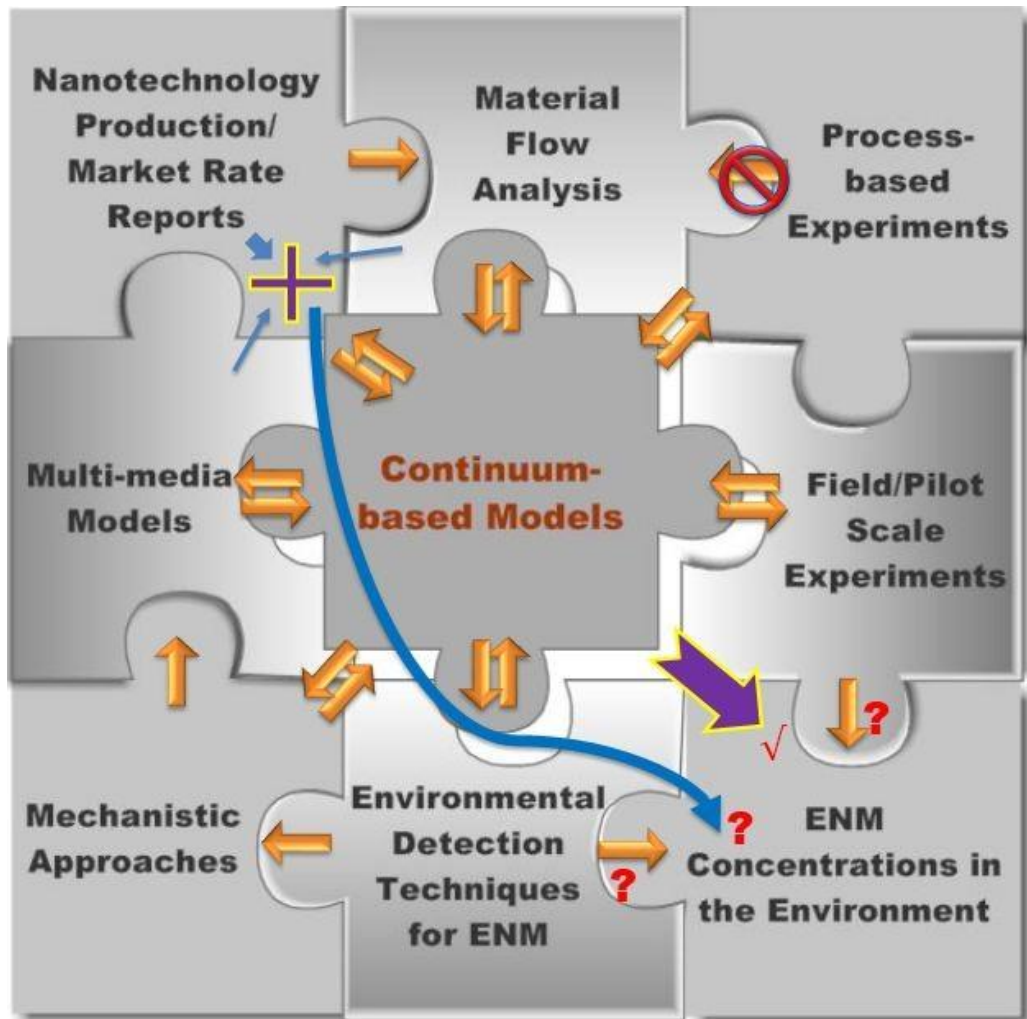


**Figure 1.2** The paradigm of various modelling approaches for simulating fate and transport of engineered nanomaterials (ENM) in the environment, showing the status of continuum-based models and their potential links with the available data sources and other modelling approaches.

To date, there have been several reviews on the transport behaviour of NP [e.g., 70, 80, 87, 95, 96, 130, 154-156] and other colloids [e.g., 69, 77, 101, 114, 140, 142, 157-163]. Nevertheless, most of these reviews commit to investigate mechanistic approaches such as CFT and/or DLVO theory. Thus far, from the continuum viewpoint, there is no comprehensive review on various phenomena taking place for NP in porous media, with an overview of the concurrent impacts of different transport mechanisms lacking. Therefore, in this research all possible transport mechanisms of NP in porous media are reviewed and their superposition within the context of continuum modelling is discussed. These mechanisms comprise advection, dispersion,

irreversible deposition, attachment, detachment, agglomeration, straining, blocking, ripening, and size exclusion. Since the focus of the thesis is on attachment and aggregation mechanisms, these mechanisms are described in detail in this chapter and the full discussions related to other transport phenomena including straining (physical trapping of particles in the pore throats narrower than the size of particles), site blocking (decreasing deposition due to filling of attachment sites), ripening (favourable attachment of arriving particles to previously deposited particles, opposite of the site blocking), and size exclusion (the exclusion of particles from pores and stagnant domains of the media that are smaller than the size of particles or are less accessible to them) are presented in Appendix A. I describe the basic conceptual model applied along with each mathematical model for these processes. The motives behind selecting the conceptual model and their limitations are also discussed. Further conceptual scenarios in which various transport mechanisms are acting together are proposed to resolve inconsistencies incurred in the interpretation of the experimental outcomes using one model only. The discussion related to this is available in Appendix D. Some issues of upscaling continuum models to multidimensional scales are briefly discussed as this will be addressed in following chapters.

It should be noted that to date 16 types of continuum-based models have been used for simulation of NP transport (Table 1.1). Here I have collected information from almost 50 papers on NP transport column experiments and continuum modelling and summarized them in Table B1 (Appendix B), which highlights underlying mechanisms of transport together with the respective types of the applied continuum model. Since the final goal of the present research is to propose continuum models as a robust tool of modelling NP transport, in the experiments, meta-analysis, and literature review performed in this thesis, I have used a broad range of environmentally-relevant NP. In the rest of the thesis, however, the focus is only on two types of NP, i.e., HAp and shattered graphene oxide (SGO) NP because of their importance in the remediation of radionuclide and a lack of investigation on their environmental behaviours in comparison to other NP such as NZVI. Within the context of the present thesis quantitative use of DLVO (or E-DLVO) has been only used for HAp NP, whereas qualitative use of DLVO has been used for shattered GO NP as well. It should be noted that the qualitative use of DLVO for GO is already common in the literature [120, 164, 165]. Quantitative application of DLVO or E-DLVO for HAp is believed not to

produce significant errors due to near spherical shape of HAp NP. Other limitations and potential uncertainties of the use of DLVO for HAp are described in Chapters 3 and 4.

In order to explain various deposition mechanisms, I used the MT3DMS [131] code to produce breakthrough curves for various combinations of attachment and detachment parameters. I also used this model following [74] in an assessment of the validity of assuming an equilibrium term to describe NP attachment/detachment and concurrent agglomeration/attachment in porous media, the discussion of which is available in Appendix C. This code, which is basically a solutal contaminant transport code, has already been used for simulating the transport of NP in porous media frequently [74, 166, 167]. Figure 1.3 shows the result of a preliminary survey of literature on the major processes considered in transport of various NP in porous media. Aggregation (or agglomeration) is the most frequently-reported process across all NP types followed by straining, blocking, ripening, size exclusion, reversible deposition, and irreversible deposition, respectively. Despite this, aggregation and size exclusion in porous media have been widely neglected in continuum modelling studies of NP transport [74, 75], at least in comparison with straining [117, 134, 152, 153, 165, 168-182], blocking [117, 144, 165, 169, 170, 173, 174, 176, 180, 183], and ripening [147-149, 152, 153] effects. The core focus of this research is on aggregation and developing a continuum modelling platform to accurately and efficiently consider this phenomenon.

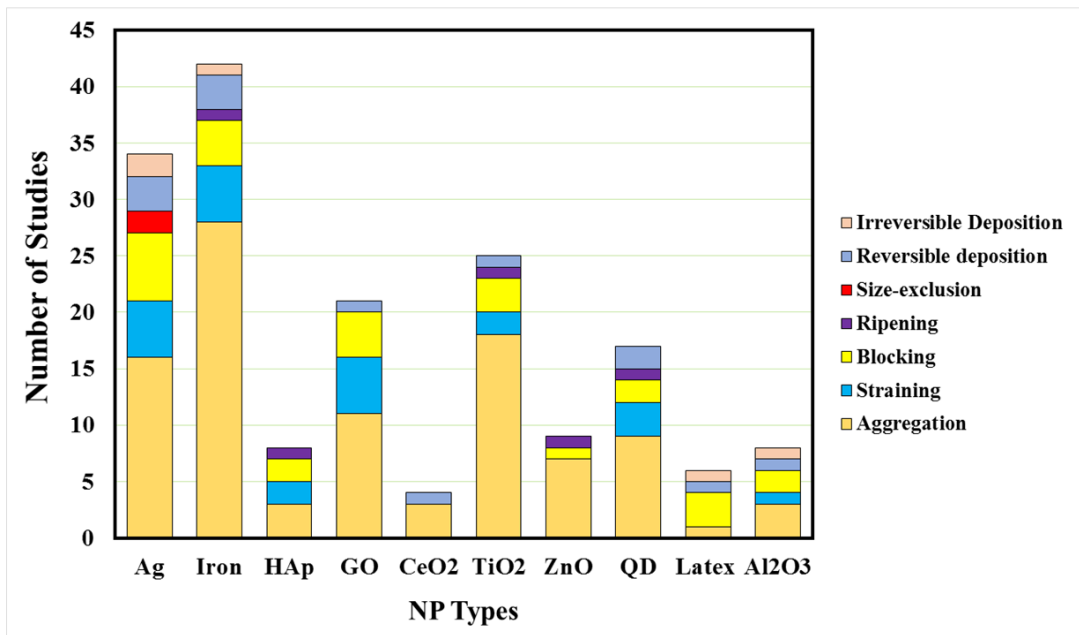


**Figure 1.3** Literature survey of various phenomena operative in the transport of nanoparticles based on the number of studies found in the Web of Science database in December, 2015 [184].

### 1.4.2 Advection and dispersion

Advection and dispersion mechanisms of colloids/NP are recognized to be broadly the same as those of solutes such as ionic species, organic compounds, radionuclides etc. [102, 157]. Advection is the mechanism of transport with the average velocity of flowing groundwater. Mechanical dispersion [131] spreads the solute or particle suspension both parallel with and normal to the direction of flow, due to the difference between the real velocity of the water inside the pores and the mean groundwater velocity, which arises from microscale velocity variation both within and between pores of different sizes [129, 131, 185-190]. Adding molecular diffusion to mechanical dispersion will result in hydrodynamic dispersion [131].

In case of slow groundwater velocity, such as flow through compacted porous media, dispersion is of low significance but, can nevertheless result from the molecular diffusion due to concentration gradients [191, 192]. Accordingly, the transport of solute and colloids/NP through porous media in the most simplified form might be

described by the following basic partial differential ‘advection-dispersion’ equation (ADE) [128, 161, 191-195]:

$$\frac{\partial C}{\partial t} + \frac{\rho_b}{\varepsilon} \frac{\partial S}{\partial t} = D \frac{\partial^2 C}{\partial x^2} - V \frac{\partial C}{\partial x} \quad (1.1)$$

where  $x$  is distance in the porous media [with the dimension of L];  $t$  is time elapsed [T];  $C$  [ $N L^{-3}$ ;  $N$  represents the particle number] and  $S$  [ $NM^{-1}$ ] are particle number concentrations of fluid-phase particles and deposited phase particles, respectively [e.g., 74, 134, 140-142], or alternatively  $C$  [ $ML^{-3}$ ] and  $S$  [ $MM^{-1}$ ] are particle mass concentrations of fluid-phase particles and deposited phase particles, respectively [e.g., 142, 143, 144];  $V$  [ $L T^{-1}$ ] is the pore water velocity (also known as real water velocity, linear groundwater flow velocity, seepage water velocity, interstitial velocity, or advection velocity). This is different from the Darcy velocity (also known as the superficial velocity or approach velocity) which is equal to the porosity times the pore water velocity [ $LT^{-1}$ ].  $D$  is the hydrodynamic dispersion or simply dispersion coefficient [ $L^2T^{-1}$ ];  $\varepsilon$  is the bed porosity [—]; and  $\rho_b$  is the porous medium bulk density [ $ML^{-3}$ ].

The dispersion in Eq. (1.1) is defined by analogy to Fick's law of diffusion and is linearly related to the pore water velocity. In a one-dimensional uniform flow field such as column experiments transverse dispersion is not considered and thus the dispersion coefficient has one longitudinal component related to pore water velocity [131, 196]:

$$D = \alpha_L V + D^* \quad (1.2)$$

where  $\alpha_L$  is longitudinal dispersivity [L] and  $D^*$  is the effective molecular diffusion coefficient [ $L^2T^{-1}$ ].  $\alpha_L$  is typically an intrinsic property of the porous medium as well as a function of scale [136, 196-198]. Thus, the common practice for both particle and reactive solute transport is to determine this coefficient based on the breakthrough curve (BTC) for nonreactive solute transport through any given porous media [136, 193, 196, 199]. However, in the case of particle transport, Chrysikopoulos and Katzourakis [136] in a meta-study of 48 different BTCs, found that dispersivity can exhibit a positive correlation with particle size and pore water velocity. They suggested that the dispersion coefficient should be obtained from the particle breakthrough data rather than nonreactive solute transport due to the potential for particulate-specific

dispersion mechanisms such as size exclusion and preferential flow (discussed in Appendix A) [134, 136, 187, 198]. Nonetheless, this approach can make the inverse modelling problematic when there are other parameters that must be estimated to represent other particle transport phenomena. Further research is needed to understand the uniqueness of estimated parameters based on fitting continuum model outputs to experimental data, particularly if dispersivity is considered along with other NP transport parameters in the inverse modelling process.

Molecular diffusion is commonly neglected in particle and solute transport studies with pore water velocities in the ranges of natural groundwater velocities [131, 198, 200]. However, it can become significant in very compact and fine porous media, fractured media with very low porewater velocities, or when there are other processes involved such as thermal or electrophoresis effects [131, 201-204]. The intrinsic diffusivity of colloidal particles decreases with increasing size according to the Stokes-Einstein equation and is typically more than three orders of magnitude lower than the molecular diffusion for common solutes [136, 205-207]. For instance, the diffusivity of water is around  $2.3 \times 10^{-9} \text{ m}^2\text{s}^{-1}$  at 25 °C while for spherical particles with a diameter of 100 nm it is around  $4.9 \times 10^{-12} \text{ m}^2\text{s}^{-1}$  according to Stokes-Einstein. Nevertheless, NP differ from larger colloids since diffusion may remain a significant mechanism in their transport behaviours. Molnar et al. [69] recently identified the high diffusivity of NP as a barrier toward developing mechanistic modelling approaches for NP transport as well as a reason for the lack of distinction between solute and NP mobility properties. To date, NP diffusion has been rarely considered as a distinct parameter in the continuum models—only one study [204] has considered its effect via Stokes-Einstein equation in the numerical transport model. Yet, frequently mechanistic modelling approaches have recognized its potential influence on the deposition behaviour of NP [71, 72, 113].

### **1.4.3 Attachment and detachment**

#### **1.4.3.1 Irreversible deposition**

Solute mass transfer from liquid to solid phases is generally dominated by sorption which is usually modelled as a reversible kinetic process [208]. However, colloids and NP interact with solid surfaces of porous media through a number of mechanisms

which may yield attachment that is practically irreversible. In other words, solute retention which appears irreversible at short timescales can be considered reversible at larger time scales under the same conditions [208], whereas irreversibly attached particles may not be detached unless a significant physical or chemical perturbation occurs in the conditions of the system [112]. Irreversible deposition or physicochemical filtration was well described by CFT. This was performed initially by drawing analogy to the transport in flocculation process [111], later by trajectory analysis [209], and by using filtration mass balance equations in a sphere around a single collector [210]. Filtration theory needs estimation of two parameters, the single-collector attachment efficiency,  $\alpha$ , and single-collector collision or contact efficiency,  $\eta_0$ . The first of these describes the probability of any collision between a particle and a collector resulting in attachment; the second describes the probability of that collision occurring in the first place.

Although there has been a marked advancement in predicting  $\eta_0$  through use of correlation equations with controllable parameters such as Péclet number, particle:grain size ratio, and so on [71, 72, 113, 211], the estimation of  $\alpha$  still requires either empirical derivations, which may not be generalizable, or laboratory-column experiments [71, 80, 113, 130, 155]. This limitation has caused researchers to go as far as eliminating  $\alpha$  — replaced by a parameter for fractioning reversibly and irreversibly deposited particles [212].

In continuum-based models, the definition of the attachment term depends upon the conceptualization of deposition. The simplified form of the governing ADE equation for NP transport in porous media can be written with a first-order irreversible attachment term as model type (i), Table 1.1 [161, 195]. In this model,  $K_{att}$  is attachment rate coefficient [ $T^{-1}$ ] which can be related to the parameters of CFT via the following equation [113, 114, 193, 213-215]:

$$K_{att} = \frac{3(1-\varepsilon)}{2d_{50}} \alpha \eta_0 V \quad (1.3)$$

where  $d_{50}$  is the median porous media grain size [L] and  $\varepsilon$  is the porosity of porous media [—]. Although the parameter  $K_{att}$  can be expressed via the theoretical relationship of Eq. (1.3), determination of  $\alpha$  may still require experimental data. On this basis, throughout this chapter I will deal directly with the parameter  $K_{att}$  instead

of  $\alpha$  [133, 135]. From a continuum modelling viewpoint, type (i) models only describe irreversible deposition and do not consider subsequent detachment. In experimental conditions where attachment is the only operative mechanism, increases in the value of  $K_{att}$  lead to a flat reduction of the BTC plateau as shown in Fig. 1.4. The curves in this figure are produced by numerical solution of type (i) model using the MT3DMS code [74].

Table B1 shows that 20% of NP continuum modelling studies use type (i) models. It is evident that most of these studies use very simplified experimental conditions, highlighting that this model and thereby CFT are strictly limited in scope of application to steady flow through idealized, uniform media. There have already been several review papers [69, 96, 99-102, 106, 154, 157, 162] discussing the deposition mechanisms of NP and colloids in porous media. From the perspective of continuum modelling, however, it is apparent that deposition cannot be considered in isolation except in the most artificial circumstances.

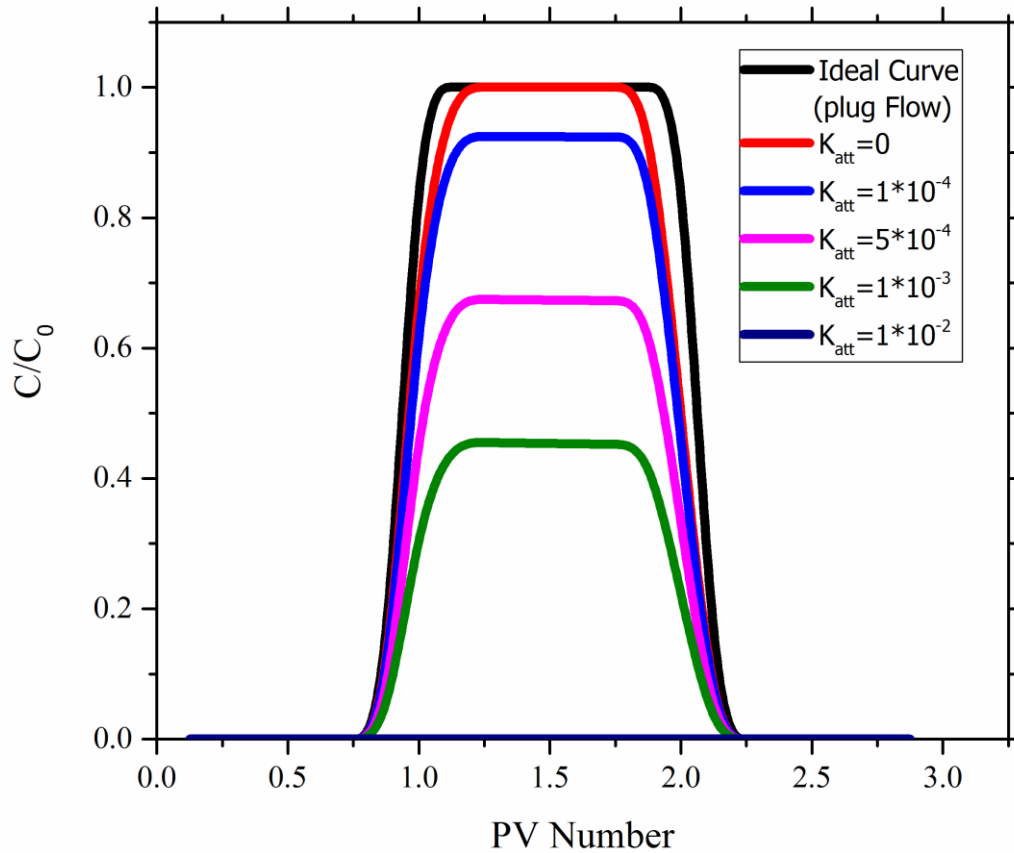


**Figure 1.4** Breakthrough curves generated by numerical solution of model Types (i) with MT3DMS model code following [74] for various  $K_{att}$  values ( $S^{-1}$ ). Other parameters of flow and porous media conditions were selected according to [73, 74] (or refer Table B1).

### 1.4.3.2 Detachment

When the particle association with the solid surface is not strong enough to be permanently retained, particles can be subject to reversible deposition and thereby detachment. Particles can be maintained temporary when they are trapped at a shallow DLVO secondary minimum [71, 73], or as recently found even at a shallow primary minimum resulting from nanoscale surface heterogeneities [216, 217], or held at the surface by hydrodynamic forces. Depending on how fast the diffusion is, the process of attachment-detachment can be considered in form of either fast forward—backward

interactions of particles or discrete retention—re-entrainment of particles [144, 212, 214, 218]. In other words, if particle detachment is so fast that the net result of particle interactions with the solid surface is dominated by attachment, it is only the attachment that can be perceptible. On the other hand, if the detachment rate is low, for example in slow-diffusion regimes experienced by larger ( $> 1 \mu\text{m}$ ) aggregate sizes then particles may be first deposited and then be subject to detachment in time; this case is commonly termed ‘re-entrainment’ [212, 214].

Commonly among literature studies, three forms of detachments are inferred: (1) detachment shown by tailing in the BTC; (2) detachment through retarded or delayed BTC; and (3) detachment or release in the form of separated peaks following the BTC. The first type of detachment typically emerges where the feeding solution into the column inlet is switched from the injecting particle dispersion to the particle-free solution with the same ionic strength and pH (two-phase injection experiments). This is the most common reference to ‘detachment’ and has been observed for various NP such as NZVI [147, 181], carbon nanotubes [219], silica [144], nanoporous silicate [220], and Ag NP [221-223] (Table B1). This is also known as re-entrainment and has been observed as dramatically extended BTC tailing which has been observed for a wide variety of particles [212, 214, 218, 224]. The underlying mechanism for this kind of detachment is commonly sought in the hydrodynamic forces [73, 146, 225, 226]. The governing set of transport equations considering kinetic detachment of this type is given as type (ii) models (Table 1.1) [142, 188], as well as types (iii) and (iv) models accounting for dual-site attachment/detachment. Using the MT3DMS code [131], I numerically solved type (ii) set of equations. The outcomes, by holding  $K_{att}$  constant while varying  $K_{det}$ , are presented in Fig. 1.5a. This figure shows that rising  $K_{det}$  not only causes the emergence of tailing in BTC, but also this leads to an asymmetric rise in the plateau of BTC which is higher at the side of the descending limb. The plateau elevates until finally it becomes flat at the largest value of  $K_{det}$  where BTC resembles the conservative transport behaviour.

In the second type of detachment, retardation appears as a horizontal shift in the NP BTC compared to conservative transport BTC (Fig. 1.5b). This has been observed for iron NP [227], Ag NP [183, 221, 222], carboxyl-modified latex NP [228], HAP NP [170], and QDs [229-231] (Table B1). The most pronounced occurrence of the retardation has been observed for NP with small sizes ( $<10 \text{ nm}$ ) such as QDs,

particularly at elevated IS, decreased pH, [230-232], smaller sizes of porous media grains [230, 233] or increased temperature [229]. It should be noted that although I categorize here retardation as a kind of detachment, in several studies which have observed retardation, ‘detachment’ has been ruled out through not observing the tailing in the BTC [228, 230-237]. Nevertheless, based on the sum of evidence it is believed that retardation results from reversible interaction of particles with the porous media surfaces – attachment and detachment, therefore — the net result of which will control the final transport of particles [74]. In the case of QDs, the delay in the BTC may arise from the fast diffusive mass transfer rate of QDs from bulk solution to the sand surface and slower mass transfer of QD from the solid phase to the bulk phase [230]. Retardation in its linear form is mathematically related to the most common parameter in the literature of reactive transport modelling in groundwater known as distribution coefficient or partition coefficient  $K_d$ . The use of  $K_d$ , however, requires applying an assumption of equilibrium between the dissolved and sorbed phases of solute contaminant (or attached and mobile phases of particles as discussed in Appendix C). The respective model of this parameter is given in Table 1.1, as type (v). The solution to this model using MT3DMS code is shown in Fig. 1.5b. This figure elucidates how retardation (and acceleration as described in Appendix A, under “Size exclusion”) of BTC can occur in combination with a significant amount of irreversible attachment ( $K_{att} = 1 \times 10^{-3} S^{-1}$ ).

The third type of detachment is related to the cases where after injection of the particle dispersion (first phase) and particle-free background solution (second phase), a solution with a lower IS or a different pH is flushed through the porous media container. The released mass can be seen in the BTC in form of separate peak(s) following the primary breakthrough [109, 110, 234, 236, 238-241]. The model for simulating the release is given as type (vi) model in Table 1.1 [110, 157, 234]. This equation assumes that remobilized particles do not reattach again, with the rationale that conditions following a perturbation that causes release are less favourable for reattachment than the original conditions [110].

Overall, for very small NP that display high diffusivity, thereby more collisions, detachment typically emerges in form of retardation of the BTC [144, 230], whereas for larger particles, due to hydrodynamics of the system, detachment may emerge in the form of tailing of the BTC [73, 146, 225, 226]. I suggest that in future studies

selecting an appropriate detachment model should be based on the aforementioned categorization. It should be mentioned, however, that the models listed in this study for every transport mechanism are not strictly the only available approach, and there might be other alternatives, particularly in the field of particle transport literature. For instance, there have been other modelling approaches to the release of attached particles under perturbation (third type of detachment) [242, 243]. There is clearly a need for further work to understand the thresholds or transitions between different detachment phenomena and relate these, if possible, to changes in the rates of competing underlying processes acting on particles.

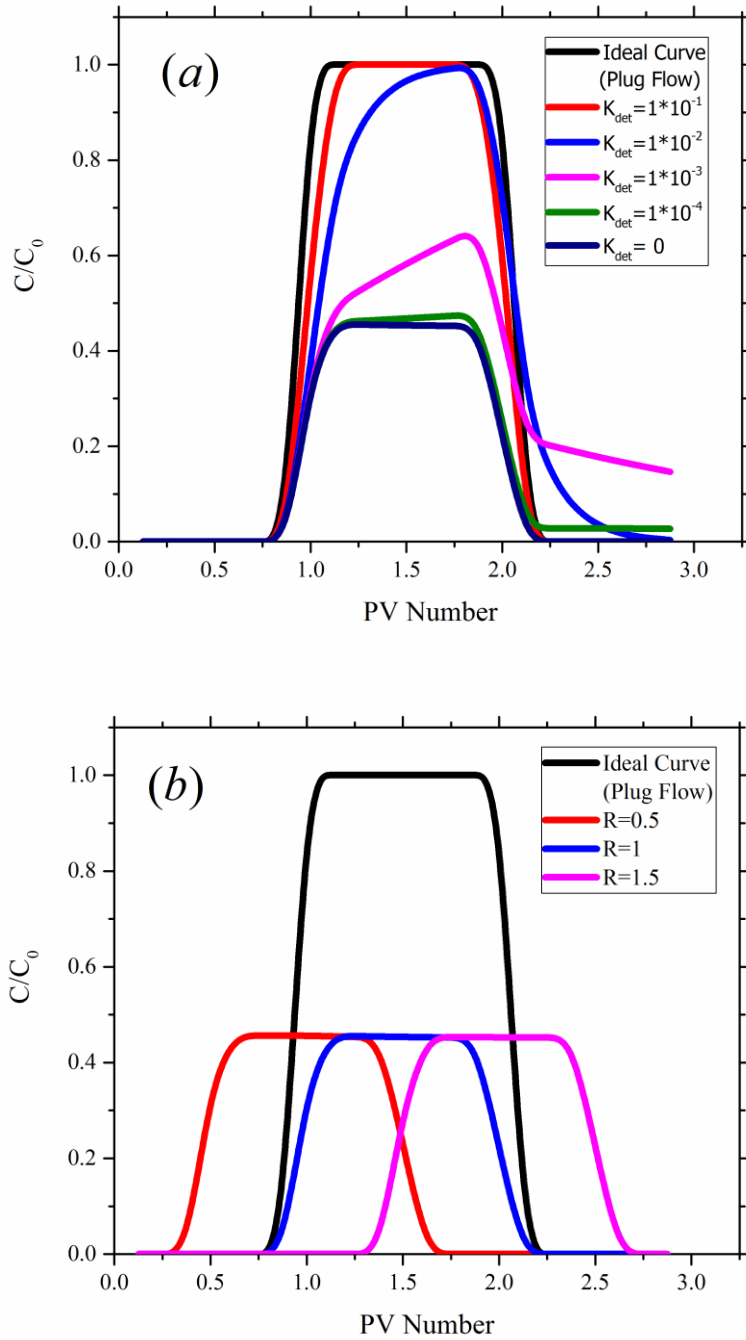


**Figure 1.5** Breakthrough curves generated by numerical solution of (a) model Type (ii) from Table 1.1, for various  $K_{det}$  values ( $S^{-1}$ ) and a fixed  $K_{att} = 0.001 S^{-1}$  and (b) model Type (v) from Table 1.1, for various retardation factors and a fixed  $K_{att} = 0.001 S^{-1}$  with MT3DMS model code following [74]. Other parameters of flow and porous media conditions were selected according to [73, 74] (or refer Table B1).

**Table 1.1** List of continuum-based modelling types applied for the transport of nanoparticles in porous media to date. \*

Model type No.	NP transport model equations	Modelled mechanisms in addition to advection and dispersion	Fitting parameters in addition to dispersion	Ref.
i	b) $\frac{\rho_b}{\varepsilon} \frac{\partial S}{\partial t} = K_{att} C$	attachment	$K_{att}$	[161, 195, 244]
ii	b) $\frac{\rho_b}{\varepsilon} \frac{\partial S}{\partial t} = K_{att} C - \frac{\rho_b}{\varepsilon} K_{det} S$	attachment/ detachment	$K_{att}, K_{det}$	[142, 188]
iii	b) $\frac{\rho_b}{\varepsilon} \frac{\partial S}{\partial t} = K_{att} C - \frac{\rho_b}{\varepsilon} f_r K_{det} S$	attachment and dual-site detachment	$K_{att}, K_{det}, f_r$	[245]
iv	b) $\frac{\partial S}{\partial t} = \frac{\partial S_1}{\partial t} + \frac{\partial S_2}{\partial t}$ c) $\frac{\rho_b}{\varepsilon} \frac{\partial S_1}{\partial t} = K_{att,1} C - \frac{\rho_b}{\varepsilon} K_{det,1} S_1$ d) $\frac{\rho_b}{\varepsilon} \frac{\partial S_2}{\partial t} = K_{att,2} C - \frac{\rho_b}{\varepsilon} K_{det,2} S_2$	dual-site attachment/ detachment	$K_{att,1}, K_{det,1},$ $K_{att,2}, K_{det,2}$	[246]
v	a) $\frac{\partial C}{\partial t} (1 + \frac{\rho_b}{\varepsilon} K_d) = D \frac{\partial^2 C}{\partial x^2} - V \frac{\partial C}{\partial x} - K_{att} C$	attachment, adsorption (retardation)	$K_{att}, K_d$	[193] [237]
vi	a) $\frac{\rho_b}{\varepsilon} \frac{\partial S}{\partial t} = K_{rel} \frac{\rho_b}{\varepsilon} (S - S_{eq}) H_0(S - S_{eq})$ b) $S_{eq} = f_{nr} S_i$	Release after perturbation	$K_{rel}, f_{nr}$	[110, 157, 234]
vii	a) $\frac{\partial C}{\partial t} + \frac{\rho_b}{\varepsilon} \frac{\partial S}{\partial t} = D \frac{\partial^2 C}{\partial x^2} - V \frac{\partial C}{\partial x} - \lambda_1 C - \lambda_2 \frac{\rho_b}{\varepsilon} S$ b) $\frac{\rho_b}{\varepsilon} \frac{\partial S}{\partial t} = K_{att} C - \frac{\rho_b}{\varepsilon} K_{det} S$ c) $C = \frac{\hat{C}}{\frac{4}{3}\pi r^3 \rho_p}$ d) $S = \frac{\hat{S}}{\frac{4}{3}\pi r^3 \rho_p}$ e) $r = r_0 e^{\frac{\lambda_1 t}{3}}$	agglomeration, attachment/ detachment, and irreversible deposition	$K_{att}, K_{det}, \lambda_1,$ $\lambda_2$	[74]

<b>viii</b>	b)	$\frac{\rho_b}{\varepsilon} \frac{\partial S}{\partial t} = K_{\text{att}} \psi_x C - \frac{\rho_b}{\varepsilon} K_{\text{det}} S$	depth-dependent (straining)	$K_{\text{att}}, K_{\text{det}}, \beta$	[134]
	c)	$\psi_x = \left(\frac{d_c+x}{d_c}\right)^{-\beta}$	attachment together with detachment		
<b>ix</b>	b)	$\frac{\rho_b}{\varepsilon} \frac{\partial S}{\partial t} = K_{\text{att}} \psi_b C - \frac{\rho_b}{\varepsilon} K_{\text{det}} S$	site-blocking	$K_{\text{att}}, K_{\text{det}}, S_m$	[144]
	c)	$\psi_b = \left(1 - \frac{S}{S_m}\right)$	attachment together with detachment		
<b>x</b>	b)	$\frac{\partial S}{\partial t} = \frac{\partial S_1}{\partial t} + \frac{\partial S_2}{\partial t}$	dual-site with site-	$K_{\text{att},1}, K_{\text{att},2},$	[228]
	c)	$\frac{\rho_b}{\varepsilon} \frac{\partial S_1}{\partial t} + \frac{\rho_b}{\varepsilon} \frac{\partial S_2}{\partial t} = K_{\text{att},1} \psi_{b,1} C + K_{\text{att},2} \psi_{b,2} C$	blocking kinetic attachment for available and not available	$S_{m,1}, S_{m,2}$	
	d)	$\psi_{b,1} = \left(1 - \frac{S_1}{S_{m,1}}\right)$	favourable sites		
	e)	$\psi_{b,2} = \left(1 - \frac{S_2}{S_{m,2}}\right)$			
<b>xi</b>	b)	$\frac{\partial S}{\partial t} = \frac{\partial S_1}{\partial t} + \frac{\partial S_2}{\partial t}$	dual-site with site-	$K_{\text{att},1}, K_{\text{det},1},$	[170]
	c)	$\frac{\rho_b}{\varepsilon} \frac{\partial S_1}{\partial t} = K_{\text{att},1} \psi_b C - \frac{\rho_b}{\varepsilon} K_{\text{det},1} S_1$	blocking attachment and depth-dependent	$K_{\text{att},2}, K_{\text{det},2},$ $S_m, \beta$	
	d)	$\frac{\rho_b}{\varepsilon} \frac{\partial S_2}{\partial t} = K_{\text{att},2} \psi_x C - \frac{\rho_b}{\varepsilon} K_{\text{det},2} S_2$	(straining), together with detachment		
	e)	$\psi_b = \left(1 - \frac{S_1}{S_m}\right)$			
	f)	$\psi_x = \left(\frac{d_c+x}{d_c}\right)^{-\beta}$			
<b>xii</b>	b)	$\frac{\rho_b}{\varepsilon} \frac{\partial S}{\partial t} = K_{\text{att}} \psi_b \psi_x C - \frac{\rho_b}{\varepsilon} K_{\text{det}} S$	site-blocking, depth-dependent	$K_{\text{att}}, K_{\text{det}}, S_m,$	[152]
	c)	$\psi_b = \left(1 - \frac{S}{S_m}\right)$	(straining)	$\beta$	
	d)	$\psi_x = \left(\frac{d_c+x}{d_c}\right)^{-\beta}$	attachment together with detachment		
<b>xiii</b>	b)	$\frac{\rho_b}{\varepsilon} \frac{\partial S}{\partial t} = K_{\text{att}} \psi_x C - \frac{\rho_b}{\varepsilon} K_{\text{det}} S + \rho_b K_{\text{rip}} S C$	ripening, depth- dependent (straining)	$K_{\text{att}}, K_{\text{det}},$ $K_{\text{rip}}, \beta$	[152, 153]
	c)	$\psi_x = \left(\frac{d_c+x}{d_c}\right)^{-\beta}$	attachment together with detachment		
<b>xiv</b>	a)	$\frac{\partial C_1}{\partial t} + \frac{\rho_b}{\varepsilon} \frac{\partial S_1}{\partial t} = D \frac{\partial^2 C_1}{\partial x^2} - V \frac{\partial C_1}{\partial x} - \frac{\rho_b}{\varepsilon} K_{12} F_p$	dual-species for transport of aggregated and non-aggregated	$K_{\text{att},1}, K_{\text{det},1},$ $K_{\text{att},2}, K_{\text{det},2},$ $S_m, \beta, K_{12},$ $S_{\text{crit}1},$	[151]

	b)	$\frac{\partial C_2}{\partial t} + \frac{\rho_b}{\varepsilon} \frac{\partial S_2}{\partial t} = D \frac{\partial^2 C_2}{\partial x^2} - V \frac{\partial C_2}{\partial x} + \frac{\rho_b}{\varepsilon} K_{12} F_p$	species with site-blocking attachment and		
	c)	$\frac{\rho_b}{\varepsilon} \frac{\partial S_1}{\partial t} = K_{att,1} \psi_b \psi_x C_1 - \frac{\rho_b}{\varepsilon} K_{det,1} S_1 - \frac{\rho_b}{\varepsilon} K_{12} F_p$	depth-dependent (straining), detachment		
	d)	$\frac{\rho_b}{\varepsilon} \frac{\partial S_2}{\partial t} = K_{att,2} C_2 - \frac{\rho_b}{\varepsilon} K_{det,2} S_2$			
	e)	$\psi_b = \left(1 - \frac{S_1}{S_m}\right)$			
	f)	$\psi_x = \left(\frac{d_c + x}{d_c}\right)^{-\beta}$			
	g)	$F_p = \max(S_1 - S_{crit1}, 0)$			
<b>xv</b>	b)	$\frac{\partial S}{\partial t} = \frac{\partial S_1}{\partial t} + \frac{\partial S_2}{\partial t}$	dual-site with site-blocking/ripening attachment and	$K_{att,1}, K_{det,1},$	[147,
	c)	$\frac{\rho_b}{\varepsilon} \frac{\partial S_1}{\partial t} = K_{att,1} \psi_1 C - \frac{\rho_b}{\varepsilon} K_{det,1} S_1$	depth-dependent (straining), detachment	$K_{att,2}, K_{det,2},$	148]
	d)	$\frac{\rho_b}{\varepsilon} \frac{\partial S_2}{\partial t} = K_{att,2} \psi_2 C - \frac{\rho_b}{\varepsilon} K_{det,2} S_2$		$A_1, \beta_1, \beta_2$	
	e)	$\psi_1 = (1 + A_1 S_1^{\beta_1})$			
	f)	$\psi_2 = \left(\frac{d_c + x}{d_c}\right)^{\beta_2}$			
<b>xvi</b>	b)	$\frac{\partial S}{\partial t} = \frac{\partial S_1}{\partial t} + \frac{\partial S_2}{\partial t}$	dual-site with site-blocking attachment and	$K_{att,1}, K_{det,1},$	[178]
	c)	$\frac{\rho_b}{\varepsilon} \frac{\partial S_1}{\partial t} = K_{att,1} \psi_b C$	straining at very high ionic strength	$K_{att,2}, K_{det,2},$	
	d)	$\frac{\rho_b}{\varepsilon} \frac{\partial S_2}{\partial t} = K_{att,2} \psi_x C$		$S_m, \beta$	
	e)	$\psi_b = \left(1 - \frac{S_1}{S_m}\right)$			
	f)	$\psi_x = \max(1, S_2^{S_m'})$			

\* Wherever Eq. (a) is not presented, it must be considered the same as Eq. (1.1)  $f_r$  is the fraction of reversibly retained particles [—];  $\psi_b$  is the Langmuirian blocking function related to the fraction of porous medium available for deposition [—];  $S_m$  is the maximum retained-particle phase concentration, i.e., particle retention capacity [ $\text{NM}^{-1}$  or  $\text{MM}^{-1}$ ];  $\psi_x$  is the depth-dependent retention function commonly used for hyper-exponential retention profile modelling [—];  $d_c$  is the granular media average diameter [L];  $\beta$  is the empirical depth-dependent retention parameter [—];  $K_{rip}$  is the particle-particle interaction rate coefficient between fluid-phase particles and deposited phase particles [ $\text{L}^3 \text{T}^{-1}$ ];  $F_p$  is the aggregated species production function [ $\text{NM}^{-1}$ ];  $S_{crit1}$  is the critical concentration of  $S_1$  when production starts [ $\text{NM}^{-1}$ ];  $K_{12}$  is the first-order production coefficient to account for the release rate of aggregated species [ $\text{T}^{-1}$ ];  $A_1$  and  $\beta_1$  are the multiplier and exponent coefficients, respectively [—], which define the interaction dynamics, i.e., ripening for  $A_1 > 0$  and  $\beta_1 > 0$  or blocking for  $\beta_1 = 1$  and  $A_1 = -1/S_m$ ;  $\psi_1$  is the expression for the effect of ripening or blocking which is equal to  $\psi_b$  when  $\beta_1 = 1$  and  $A_1 = -1/S_m$ ;  $\psi_2$  is the expression for the effect of straining, equal to  $\psi_x$  if assuming  $\beta_2 = -\beta$ ;  $\hat{C}$  is the mass concentration of fluid-phase particles [ $\text{ML}^{-3}$ ];

$\hat{S}$  is the mass concentration of deposited-phase particles [ $\text{MM}^{-1}$ ];  $r$  is the average radii of particles in the fluid phase and deposited phase [L];  $r_0$  is the average radius of particles (or agglomerates) at  $t = 0$  [L];  $\rho_p$  is the average density of the particles or aggregates [ $\text{ML}^{-3}$ ];  $\lambda_1$  is the pseudo-first-order reaction rate [ $\text{T}^{-1}$ ], which stands for the decay in population of particles due to agglomeration;  $\lambda_2$  is the pseudo-first-order reaction rate [ $\text{T}^{-1}$ ], which stands for the decay in the population of deposited, detachable particles and represents irreversible deposition;  $K_{rel}$  is the release rate constant,  $S_{eq}$  [ $\text{NM}^{-1}$  or  $\text{MM}^{-1}$ ] is the equilibrium value of  $S$  in the new steady state following perturbation;  $H_o(S-S_{eq})$  is the Heaviside function (acting as a cancelling function) which is equal to one when  $S > S_{eq}$  and zero when  $S \leq S_{eq}$ ;  $S_i$  [ $\text{NM}^{-1}$  or  $\text{MM}^{-1}$ ] is the value of  $S$  before the perturbation;  $f_{nr}$  [-] is the fraction of deposited particles that are not released with the perturbation in the system conditions; and indexes 1 and 2 in dual-sites models stand for sites 1 and 2 and in dual species model stand for species 1 and 2. The rest of parameters are presented in the Nomenclature.

### 1.4.3.3 Coexistence of both irreversible deposition and reversible attachment/detachment

In many practical cases both kinds of interaction can exist in the same system together, resulting in both reversible and irreversible depositions. This has been frequently observed in studies with dual deposition sites or polydisperse NP dispersions (containing fractions of small and large particles) [e.g., 71, 73, 74, 247, 248, 249]. In these cases, neither equilibrium sorption nor non-equilibrium kinetic attachment/detachment models alone can satisfactorily describe NP transport, as none of them take into account the absolute irreversible deposition by themselves. In the case of the equilibrium model, the irreversibility is not taken into account because a physical relationship between the mobile-phase concentration and the immobile-phase concentration (sorption isotherms) is imposed upon the governing equation for transport in porous media via the  $\partial S/\partial t$  term [208]. Regarding the non-equilibrium model, absolute irreversibility cannot be reached, unless the detachment rate in type (ii) model, (Table 1.1) is considered equal to zero—in which case the model reduces to type (i), Table 1.1. It was clearly illustrated in Fig. 1.5a that any increase in  $K_{det}$  value resulted in the emergence of tailing in BTC, as well as an asymmetric rise in the plateau of BTC, suggesting that absolute irreversibility cannot be achieved by model type (ii) alone. Therefore, both equilibrium and non-equilibrium attachment/detachment models are intrinsically reversible and cannot take into account the absolute irreversibility of particles in the transport problems.

Accordingly, there is need for an additional term to describe irreversible deposition. Commonly, if the  $K_d$  parameter can be used by invoking the equilibrium

assumption, then description of irreversible deposition is made by addition of a sink term to decay the concentration of the fluid phase—similar to the simple irreversible deposition model explained already (model type (i), Table 1.1). This combination results in model type (v), Table 1.1. The BTC produced by such a model is shown in Fig. 1.5b. However, should the equilibrium assumption not be invoked, then the kinetic model already has a term that decays the concentration of the fluid-phase, and no additional term can be added to decay the concentration of this phase. In this case a sink term that decays the concentration/population of the attached phase ( $-\lambda_2 \frac{\rho_b}{\epsilon} S$ ) may be added to the model in order to take account of irreversible deposition—as given in model type (vii), suggested by Babakhani et al. [74], Table 1.1. Thus, in future modelling practices, I propose using either of the aforementioned approaches whenever both reversible and irreversible attachments are suspected to be operative simultaneously, e.g., due to heterogeneity in the population of particles. For such cases, these approaches are believed to be more rigorous representations of real condition rather than dual-site deposition models, e.g., model types (iii) and (iv). Further research is required to test this assertion across a range of scales and systems.

## **1.4.4 Aggregation in porous media and its interaction with other phenomena**

### **1.4.4.1 Definitions and observations**

Homoaggregation or homoagglomeration of particles (herein simply called aggregation) during transport within porous media is one of the least understood phenomena relating to colloid or NP in the subsurface. It is of paramount importance as it causes change in the size and hence the transport characteristics as well as the size-dependent functionality of NP. Understanding aggregation within porous media is therefore crucial to a range of environmental applications of NP, as well as assessments of environmental hazard. The terms 'aggregation' and 'stability' have been used interchangeably but they are two distinct processes; aggregation only considers the attachment of particles to each other, while stability considers both their attachment and their subsequent sedimentation and removal from the aqueous media [250-255]. This difference is more pronounced in the context of porous media. In particular, the restricted length scales for sedimentation to take place in pores and that they are

advecting through the pores may distinguish the aggregation in porous media from that in bulk liquids.

To date, the most common model for simulating the aggregation of colloidal particles is the Smoluchowski model [75, 91, 114, 146, 256-258]. This model is based on the superposition of three mechanisms: perikinetic, orthokinetic, and differential sedimentation. The perikinetic mechanism of aggregation involves particle-particle collisions caused by the Brownian motion of particles. Orthokinetic aggregation involves collisions arising from any motion or flow in a fluid that can cause shear stress. Differential sedimentation occurs when the particle sizes are so different that larger particles settle faster than the smaller ones and collide with those in their paths [74, 114]. Detailed accounts of aggregation modelling, e.g., consideration of the fractal nature of aggregates or of gravitational sedimentation in aqueous media will be given later in this chapter. Aggregation of NP, in spite of being the focus of ongoing studies in aqueous media [91, 137, 257, 259-261] has been largely ignored by models of transport in porous media. Many modelling studies on NP transport reported to date have overlooked aggregation by assuming that in the selected experimental conditions aggregation might have not been operative. This rationale may be justified in several conditions: high experimental values of zeta potential or stability analysis based on critical coagulation concentration (CCC) or DLVO theory [229, 262, 263]; the lack of significant size change observed under equivalent conditions in batch experiments [116, 180, 228, 234, 239, 264-266]; or by observing no significant change in the concentration of suspended NP in such batch experiments, indicated the absence of sedimentation [e.g., 120]. Despite this, the formation of NP aggregates during transport in porous media has been experimentally demonstrated by a large number of studies for NP such as NZVI [59, 71, 73, 74, 96, 146, 155, 227, 267], HAP [153, 171, 172, 175], Graphene/GO [120, 164, 165, 176-178], Ag NP [262, 266, 268], CeO<sub>2</sub> [269], TiO<sub>2</sub> [179, 270-273], ZnO [121, 182, 245, 274, 275], and Al<sub>2</sub>O<sub>3</sub> NP [264, 265] (Table B1). The results from batch experiments may not be a real indicator of the particle conditions in porous media, because aggregation in batch experiment in absence of flow can lack at least one of the driving mechanisms of aggregation; that is orthokinetic aggregation, and they also ignore other impacts of dynamic conditions encountered in porous media [74, 91, 164, 245, 250]. For instance, enhanced local polydispersity in particle size distribution in pores can be responsible for accelerated agglomeration.

This local polydispersity in the population of particles may arise from the complex multi-cascade processes of advective and diffusive transport [136, 187, 276, 277], tortuosity in porous media [197], detached agglomerates with different sizes arriving from the up-gradient pores [151, 214], and size selective deposition/preferential retention [153, 171, 180]. It is also worth mentioning that observations in effluent samples that show no change in the size over time or as a function of the column length, should not be used as evidence for no aggregation, since aggregation tends to lead to large, more easily-deposited entities, it is preferentially the smaller, unaggregated particles which remain mobile as far as the column outlet [74, 153, 171, 180, 253, 254, 278].

Aggregation can affect the deposition of particles during their transport within porous media in a number of ways. Increase in size due to aggregation can reduce diffusivity thereby decreasing the frequency of collisions with pore surfaces [279]. The formation of porous aggregates can also alter their sedimentation velocity as well as collision rates with solid surfaces compared to those of impermeable spheres with equivalent mass and size [280]. The porosity and thus settling velocity of fractal aggregates can change with their growing in size because of the change in the fractal dimension, which is an indication of their density [281-284]. For particles which collide with surfaces, increase in size of aggregates can increase the magnitude of the DLVO interaction energy secondary minimum, thereby increasing attachment rates [71-73, 249]. These interconnected and dynamic effects of change in particle size which occur differentially across a particle population render it complicated to develop a mechanistic approach for simulating the concurrent aggregation and transport of NP [74, 75, 107].

#### **1.4.4.2 Modelling considerations**

Very few studies have attempted to develop a model for NP aggregation during transport in porous media in continuum framework [74, 107, 146]. These models were mostly developed specifically for NZVI because of its importance in remediation of groundwater contaminants and the need for designing field remediation strategies [73-75, 146, 249]. Phenrat et al. [71, 72] developed empirical attachment and contact efficiency relationships for predicting the sizes of aggregates and the subsequent deposition of formed aggregates based on a range of one-dimensional (1-D) column

transport data of polymer-modified NZVI particles. These empirical correlations can be used along with continuum model to simulate NP aggregation and transport in porous media. Raychoudhury et al. [146] combined the Smoluchowski model of aggregation with the CFT model within an advection-dispersion equation in order to simulate the aggregation and transport of polymer-modified NZVI. However, they did not explicitly obtain the particle-particle attachment efficiency within the porous media. Instead, they determined aggregation kinetic parameters from static batch experiments and used them for fitting the model against the breakthrough data. As noted above, there can be significant differences between static experiments with those conducted in a real dynamic environment of the porous media [130]. It was also not clear how the computational demand of using Smoluchowski model for NP was dealt with in that study, and whether particle size distribution dynamics were considered.

Taghavy et al. [75] used the Smoluchowski equation and CFT, all within a Lagrangian approach based on random-walk particle tracking to simulate the concurrent aggregation and transport of NZVI. Although they tackled the problem of binary collision in their probabilistic modelling approach, the aggregation model in that study was limited to considering only the perikinetic aggregation [91, 250]. Furthermore, the use of a Lagrangian approach limits the possibility of running a model in inverse mode because oscillations around the expected mean outcomes of Lagrangian methods such as random-walk particle-tracking hinder the optimization process in the inverse problem [107]. Lagrangian approach also comes with consequent computational expenses when up-scaled [107, 130, 154]. Both aforementioned studies were also limited to one dimensional transport of NP.

Babakhani et al. [74] modified a widely-used solute transport model, MT3DMS, in order to incorporate the influence of aggregation together with other transport phenomena including attachment, detachment, and subsequent irreversible deposition of aggregates. They used a simple pseudo first-order reaction model to represent homoaggregation (Model type (vii), Table 1.1). The basis of common aggregation models such as the Smoluchowski model is a second-order rate equation [114, 285-287] although there is a limited number of studies which have used a first-order formulation for aggregation [288-292]. Babakhani et al. showed that the use of a pseudo-first order model could describe the aggregation behaviour of NP in porous media conditions of homogenous one-dimensional and heterogeneous two-

dimensional domains successfully. Interestingly, in the experimental cases where the conditions were favourable for disaggregation of NZVI, the model was still applicable by showing negative rates for the aggregation parameter [74]. Nevertheless, in that study, the effect of particle size distribution in porous media was not taken into consideration.

Another approach to modelling aggregation was developed by Bradford et al. [151] that addressed hyper-exponential and non-monotonic trends of RCP. This was a dual-constituent model with the aim of capturing the transport and straining of pathogenic *E. coli*. The conceptual model assumed that *E. coli* could aggregate when a large number of mono-dispersed *E. coli* were deposited at straining sites. Then aggregates of *E. coli* which formed in the deposited phase could be released into the aqueous phase as a result of flow shear force after reaching a critical concentration. A two-constituent model (one constituent for the individual mono-disperse *E. coli*. and the other one for the released *E. coli*. aggregates) was developed. This model is presented as model type (xiv) in Table 1.1. The drawback of this model is the use of four extra parameters in comparison with a common model of straining and site-blocking, e.g., model type (xii), Table 1.1. Application of the Akaike information criterion (AIC) by Bradford et al. [151], described elsewhere in this chapter, showed the two-species straining model performed better than the well-known first-order attachment-detachment model (type (ii), Table 1.1). However, it was not investigated whether this model could have been better than the first-order attachment-detachment model with straining and blocking functions (model type (xii), Table 1.1). It should be noted that aggregation in the study of Bradford et al. was assumed to occur at the deposited-particle phase, opposed to common consideration of aggregation process which takes place in the fluid phase [114]. Although this model distinguished the aggregating from non-aggregating species, still it did not consider the particle size distribution within the pores.

Hyper-exponential RCPs are commonly attributed to a manifestation of straining mechanism as described in Appendix A. However, a substantial number of studies have attributed hyper-exponential RCPs to the aggregation process [121, 153, 245, 266, 274, 293-297]. Here, I suggest two arguments against this possibility. The first reason is that the aggregation process is a time-dependent mechanism [74, 291, 292] and thus increase in particle size should occur progressively over the course of migration through the porous media. Therefore, the average size of retained aggregates

should increase toward the outlet of the column; however, observations of hyper-exponential RCP indicate typically a decrease in the size of the retained particles along the column length [171, 172, 245, 274]. The second reason, derived from experimental observations [173, 219, 298, 299], is that a decrease in the influent concentration causes greater hyper-exponential behaviour. This is assumed to be because at low concentrations of NP the capacity for straining will be exceeded only at the vicinity of the column inlet causing hyper-exponential shape while at high concentration, the capacity for straining will be uniformly met over the whole column length. On the other hand, aggregation is well known to be a concentration-dependent phenomenon [71, 73, 74, 146, 291, 300, 301] which typically increases with the population of particles by a second-order rate [114, 256, 287]. If aggregation is the reason for the hyper-exponential behaviour, then the increase on the injecting concentration of NP must enhance the hyper-exponential pattern because of the ascended aggregation tendency. The outcomes of the aforementioned experimental studies show the opposite. One may attribute the hyper-exponential behaviour to aggregation in the feeding reservoir of the NP upon injecting into the column experiment. Nonetheless, in the studies which carried out the ultra-sonication of the stock dispersion [165, 171, 172, 297, 302], still a hyper-exponential distribution emerged as well as a decrease in the retained particle size along the column length [171, 172], suggesting that the aggregation in the stock dispersion container cannot be responsible for hyper-exponential behaviour.

Further carefully-designed experimental work is clearly required to better inform both conceptual and mathematical models of aggregation and its contribution to NP transport and fate in porous media. What is clear from the available evidence is that successful models must be validated against effluent breakthrough and perhaps retained mass profile data across a range of scales and physicochemical conditions [303]. Future studies must be also directed to develop both continuum models and experimental techniques that can capture the effects of particle size distribution dynamics resulting from aggregation processes within pores. This can obviously give valuable insights into the roles of concurrent transport mechanisms.

## **1.5 Applicability of continuum models**

### **1.5.1 Experimental validation of model concepts**

Here, recent developments in the experimental methods required to validate and test the models are briefly outlined. A crucial advance on standard column methods is represented by methods which ‘open the box’ on time-dependent changes within the porous medium. Recent advancement in real-time monitoring of transport in porous media include detecting solute transport by gamma imaging [304], colloid transport by fluorescence imaging [305-307], and NP transport by MRI [308]. X-ray computed tomography (XCT) has also been shown to have the potential for imaging the attached phase of NP, but its application at bulk scale is challenging due to interference at the grain/void interface and being limited to high electron density materials with high X-ray contrast [69]. Real-time monitoring of the attached phase of particles has been achieved by Roth et al. [309] via static light scattering (SLS) yielding important parameters such as permeability, the radius of gyration (analogous to the hydrodynamic radius), and the fractal dimension of deposited aggregates. Static light scattering can obtain very small length scales (voxel resolution as low as 50 nm) at significantly lower cost than alternatives such as X-ray microtomography. Nevertheless, this technique requires a refractive index matched porous media which limits its ability to probe realistic environmental conditions in key parameters such as viscosity and surface properties [310]. The dynamics of the concurrent agglomeration and transport of NP in real porous media has not been monitored by any experimental technique within the literature reviewed here. Developing robust experimental evidence for validating models such as those proposed here, in particular where multiple processes are postulated, and BTC/RCP interpretations are equivocal, remains a critical research priority.

### **1.5.2 Upscaling of continuum models for NP transport**

In spite of the large number of NP transport studies in 1-D column experiments, multidimensional transport reports are scarce [19, 41, 46, 57]. Likewise, multidimensional modelling tools are still undeveloped [74, 138, 139, 145, 166, 167, 311, 312]. At larger scales, the nature of underlying phenomena can change compared to 1-D transport, due to the introduction of new impacts from nonuniform flow field, e.g. radial flow around injection wells [79, 313]. It is likely that the patterns of the BTC and RCP discussed throughout the present chapter change significantly. In particular when the domain is heterogeneous, e.g. layered media [55, 249], multiple peaks can appear in the plateau of the BTC which cannot be modelled even when

considering heterogeneous zones as conducted in [74]. Substantial differences may exist regarding the amount of pore space or solid surfaces available in 3-D porous media domain compared to that of simple ideal 1-D column domain. This can cause further deviations of column experiment outcomes compared to realistic environmental conditions.

Well-known, 3-D groundwater modelling packages such as HYDRUS and MODFLOW have been modified to capture some of the transport mechanisms of NP. To date, HYDRUS [314] has been adapted to simulate most of the NP transport mechanisms discussed in this chapter, except aggregation [315]. A 2-D or 3-D application of HYDRUS for NP transport has not been reported thus far. In addition, capabilities of simulating variable density or variable viscosity characteristics of transport that can be influential in fate and transport of NP in porous media have not been reported for this package. On the other hand, the MODFLOW family of models, such as MT3DMS [131], SEAWAT [316], and RT3D [317] have been already applied for multidimensional transport simulations of NP with considering specific NP transport mechanisms including aggregation [74], density driven transport pattern [312], site blocking [166, 167], straining [47], and even reaction with groundwater contaminants [56]. Neither size exclusion as a specific phenomenon nor particle size distribution driven by aggregation, has been considered in these models yet.

A MATLAB-based software called MNM1D was developed for capturing NP transport mechanisms [147]. This model is mainly expressed as model type (xv) in Table 1.1. Recently, this was combined with RT3D to simulate micro and nanoparticles transport in 3-D porous media [311]. However, this model, too, has not considered aggregation and size exclusion mechanisms of NP aggregates within porous media. Therefore, there exists the need for development of new 3-D modelling tools or further adaptation of current groundwater modelling package to take more of the NP transport mechanisms into account.

## **1.6 Thesis structure and objectives**

In this thesis based on the research priorities that were identified in this chapter, I try to address the challenges of the use of continuum models for the transport of NP in aqueous and porous media. In doing so, I first classify and clarify a variety of continuum models and concepts that have been used for the transport of NP in porous

media as performed in this chapter and in appendices A-C. I then describe and conceptualize different scenarios that can be applied for simulating multiple phenomena of NP transport in subsurface environment (the discussion of which is available in Appendix D). The main challenges are the predictivity of continuum models as well as the need for a more efficient consideration of agglomeration. A method is proposed for forward application of the continuum models using artificial neural network (ANN). This also allows analysing the sensitivity of various environmental factors on continuum model parameters which has all been covered in chapter 2. In the next stage, I narrow down the focus on modelling the aggregation in aqueous media based on fitting against data obtained from long-term batch experiments on Hydroxyapatite (HAp) NP, which have application for radionuclide-contaminated site remediation [24-26]. This leads to finding the best current modelling set for being used with continuum models as elaborated in chapter 3. The best model set for aggregation is then combined with a 3-D continuum transport model code, MT3D-USGS with recently updated sophisticated capabilities presenting it as a tool for groundwater remediation design [318]. The model is validated against 1-D experimental data from literature and against the previous MATLAB code as presented in chapter 4. Performing aggregation and transport simulations at 3-D scale reveals the computational expenses as a barrier for efficient modelling. There are other factors such as system dynamics that have not been considered in the model. Thus, in the next stage a novel method is developed for modelling NP aggregation based on a classical parent-daughter chain reaction as covered in chapter 5. This is validated against experimental data of aggregation and sedimentation of shattered graphene oxide (SGO) NP which also have application for radionuclide adsorption [22, 23]. This approach is believed to be more compatible with continuum models due to being based on mass concentration. When compared with a standard population balance model, the new approach turned out to be more efficient. Finally, I investigate the possibility of additional impact that porous media, as a dynamic system, can have on the aggregation process compared to that of the quiescent condition of batch experiment. This, which is presented in chapter 6, is conducted through a solid-body rotational system to shed light on the trends of aggregate size and structure under dynamic condition.

The overarching objective of the thesis is to propose continuum modelling approach as a robust modelling tool for simulating the aggregation and transport of NP

in porous media environments. To achieve this major goal, step-by-step objectives are set, as listed below:

- Define and conceptualize continuum modelling approaches.
- Address the challenge of predictivity.
- Find a best modelling set based on current population-balance approach for aggregation based on experimental data in quiescent batch experiment.
- Combine the best aggregation model set with continuum model.
- Find a more efficient approach that can be used with continuum models.
- Investigate the impacts that porous media as a dynamics system can potentially have on aggregation compared to quiescent batch experiments.

## 1.7 References

1. Vesilind, P.A., J.J. Peirce, and R.F. Weiner, *Environmental Engineering*. 1994: Butterworth-Heinemann.
2. USEPA, *Common radionuclides found at superfund sites*. Office of Radiation and Indoor Air Office of Solid Waste and Emergency Response, Washington, DC 20460, 2002. **EPA 540/R-00-004**.
3. Anspaugh, L.R., *Environmental consequences of the Chernobyl accident and their remediation: Twenty years of experience*. Report of the Chernobyl Forum Expert Group 'Environment', 2005.
4. Kitamura, A., et al., *Mathematical modeling of radioactive contaminants in the Fukushima environment*. Nuclear Science and Engineering, 2015. **179**(1): p. 105-119.
5. Misumi, K., et al., *Factors controlling the spatiotemporal variation of <sup>137</sup>Cs in seabed sediment off the Fukushima coast: implications from numerical simulations*. Journal of environmental radioactivity, 2014. **136**: p. 218-228.
6. Kurosawa, S., et al., *Model analysis of the colloid and radionuclide retardation experiment at the Grimsel Test Site*. Journal of colloid and interface science, 2006. **298**(1): p. 467-475.
7. Buddemeier, R.W. and J.R. Hunt, *Transport of colloidal contaminants in groundwater: radionuclide migration at the Nevada Test Site*. Applied geochemistry, 1988. **3**(5): p. 535-548.
8. McCarthy, J.F. and J.M. Zachara, *Subsurface transport of contaminants*. Environmental Science & Technology, 1989. **23**(5): p. 496-502.
9. Smith, P.A. and C. Degueudre, *Colloid-facilitated transport of radionuclides through fractured media*. Journal of contaminant hydrology, 1993. **13**(1): p. 143-166.

10. Kersting, A.B., et al., *Migration of plutonium in ground water at the Nevada Test Site*. Nature, 1999. **397**(6714): p. 56-59.
11. Li, S.-H., H.-T. Yang, and C.-P. Jen, *Modeling of colloid transport mechanisms facilitating migration of radionuclides in fractured media*. Nuclear technology, 2004. **148**(3): p. 358-368.
12. Li, S.-H. and C.-P. Jen, *Modeling of hydrodynamic chromatography for colloid migration in fractured rock*. Nuclear technology, 2001. **133**(2): p. 253-263.
13. Jen, C.-P. and S.-H. Li, *Effects of hydrodynamic chromatography on colloid-facilitated migration of radionuclides in the fractured rock*. Waste Management, 2001. **21**(6): p. 499-509.
14. Albarran, N., et al., *Analysis of latex, gold and smectite colloid transport and retention in artificial fractures in crystalline rock*. Colloids and Surfaces A: Physicochemical and Engineering Aspects, 2013. **435**: p. 115-126.
15. Xie, J., et al., *Insights into transport velocity of colloid-associated plutonium relative to tritium in porous media*. Scientific reports, 2014. **4**.
16. Elimelech, M., J. Gregory, and X. Jia, *Particle deposition and aggregation: measurement, modelling and simulation*. 1998: Butterworth-Heinemann.
17. Patil, S.S., et al., *Nanoparticles for environmental clean-up: a review of potential risks and emerging solutions*. Environmental Technology & Innovation, 2016. **5**: p. 10-21.
18. Keane, E., *Fate, transport, and toxicity of nanoscale zero-valent iron (nZVI) used during superfund remediation*. US Environmental Protection Agency, 2009.
19. Johnson, R.L., et al., *Field-Scale Transport and Transformation of Carboxymethylcellulose-Stabilized Nano Zero-Valent Iron*. Environmental science & technology, 2013. **47**: p. 1573-1580.
20. Zhao, X., et al., *An overview of preparation and applications of stabilized zero-valent iron nanoparticles for soil and groundwater remediation*. Water research, 2016. **100**: p. 245-266.
21. Bardos, P., et al., *Taking Nanotechnological Remediation Processes from Lab Scale to End User Applications for the Restoration of a Clean Environment; A Risk/Benefit Appraisal for the Application of Nano-Scale Zero Valent Iron (nZVI) for the Remediation of Contaminated Sites*. NANOREM NZVI risk benefit issues paper, 2014. **Project Nr.: 309517, EU, 7th FP, NMP.2012.1.2**.
22. Yu, S., et al., *Sorption of radionuclides from aqueous systems onto graphene oxide-based materials: a review*. Inorganic Chemistry Frontiers, 2015.
23. Romanchuk, A.Y., et al., *Graphene oxide for effective radionuclide removal*. Physical Chemistry Chemical Physics, 2013. **15**(7): p. 2321-2327.
24. Wen, T., et al., *Efficient capture of strontium from aqueous solutions using graphene oxide-hydroxyapatite nanocomposites*. Dalton Transactions, 2014. **43**(20): p. 7464-7472.
25. Handley-Sidhu, S., et al., *Uptake of Sr<sup>2+</sup> and Co<sup>2+</sup> into biogenic hydroxyapatite: implications for biomineral ion exchange synthesis*. Environmental science & technology, 2011. **45**(16): p. 6985-6990.
26. Kanel, S.R., et al., *Nano-Scale Hydroxyapatite: Synthesis, Two-Dimensional Transport Experiments, and Application for Uranium Remediation*. Journal of Nanotechnology, 2011. **2011**: p. 1-5.
27. Ling, L. and W.-x. Zhang, *Enrichment and Encapsulation of Uranium with Iron Nanoparticle*. Journal of the American Chemical Society, 2015. **137**(8): p. 2788-2791.

28. Jing, C., et al., *Illite-supported nanoscale zero-valent iron for removal of <sup>238</sup>U from aqueous solution: characterization, reactivity and mechanism*. Journal of Radioanalytical and Nuclear Chemistry, 2015. **304**(2): p. 859-865.
29. Crane, R.A., et al., *Magnetite and zero-valent iron nanoparticles for the remediation of uranium contaminated environmental water*. Water research, 2011. **45**(9): p. 2931-2942.
30. Crane, R.A., M. Dickinson, and T.B. Scott, *Nanoscale zero-valent iron particles for the remediation of plutonium and uranium contaminated solutions*. Chemical Engineering Journal, 2015. **262**: p. 319-325.
31. Dickinson, M. and T.B. Scott, *The application of zero-valent iron nanoparticles for the remediation of a uranium-contaminated waste effluent*. Journal of Hazardous Materials, 2010. **178**(1-3): p. 171-179.
32. Burghardt, D. and A. Kassahun, *Development of a reactive zone technology for simultaneous in situ immobilisation of radium and uranium*. Environmental Geology, 2005. **49**(2): p. 314-320.
33. Kansanen, P.H., et al., *Sedimentation and distribution of gamma-emitting radionuclides in bottom sediments of southern Lake Päijänne, Finland, after the Chernobyl accident*. Hydrobiologia, 1991. **222**(2): p. 121-140.
34. Evangelidou, N. and H. Florou, *The dispersion of <sup>137</sup>Cs in a shallow Mediterranean embayment (Saronikos Gulf–Elefsis Bay), estimated inventories and residence times*. Journal of environmental radioactivity, 2012. **113**: p. 87-97.
35. Otosaka, S. and T. Kobayashi, *Sedimentation and remobilization of radiocesium in the coastal area of Ibaraki, 70 km south of the Fukushima Dai-ichi Nuclear Power Plant*. Environmental monitoring and assessment, 2013. **185**(7): p. 5419-5433.
36. Fan, X., et al., *Design of optimal groundwater remediation systems under flexible environmental-standard constraints*. Environmental Science and Pollution Research, 2014: p. 1-12.
37. Gavaskar, A., L. Tatar, and W. Condit, *Cost and performance report nanoscale zero-valent iron technologies for source remediation*. 2005, DTIC Document.
38. Elliott, D.W. and W.-X. Zhang, *Field assessment of nanoscale bimetallic particles for groundwater treatment*. Environmental Science & Technology, 2001. **35**(24): p. 4922-4926.
39. Quinn, J., et al., *Field demonstration of DNAPL dehalogenation using emulsified zero-valent iron*. Environmental Science & Technology, 2005. **39**(5): p. 1309-1318.
40. Su, C., et al., *A two and half-year-performance evaluation of a field test on treatment of source zone tetrachloroethene and its chlorinated daughter products using emulsified zero valent iron nanoparticles*. Water Research, 2012. **46**(16): p. 5071-5084.
41. Su, C., et al., *Travel distance and transformation of injected emulsified zerovalent iron nanoparticles in the subsurface during two and half years*. Water research, 2013. **47**(12): p. 4095-4106.
42. O'Hara, S.O., et al., *Field and laboratory evaluation of the treatment of DNAPL source zones using emulsified zero-valent iron*. Remediation Journal, 2006. **16**(2): p. 35-56.
43. He, F., D. Zhao, and C. Paul, *Field assessment of carboxymethyl cellulose stabilized iron nanoparticles for in situ destruction of chlorinated solvents in source zones*. Water Research, 2010. **44**(7): p. 2360-2370.
44. Bennett, P., et al., *In situ testing of metallic iron nanoparticle mobility and reactivity in a shallow granular aquifer*. Journal of contaminant hydrology, 2010. **116**(1): p. 35-46.

45. Johnson, R.L., et al., *Field-Scale Transport and Transformation of Carboxymethylcellulose-Stabilized Nano Zero-Valent Iron*. Environmental science & technology, 2013.
46. Kocur, C.M., et al., *Characterization of nZVI mobility in a field scale test*. Environmental Science & Technology, 2014. **48**(5): p. 2862-2869.
47. Köber, R., et al., *Nanoscale zero-valent iron flakes for groundwater treatment*. Environmental Earth Sciences, 2014. **72**(9): p. 3339-3352.
48. Henn, K.W. and D.W. Waddill, *Utilization of nanoscale zero-valent iron for source remediation—A case study*. Remediation Journal, 2006. **16**(2): p. 57-77.
49. Doong, R.-a., et al., *Mesoporous silica supported bimetallic Pd/Fe for enhanced dechlorination of tetrachloroethylene*. RSC Advances, 2015. **5**(110): p. 90797-90805.
50. Lin, F.-h. and R.-a. Doong, *Highly efficient reduction of 4-nitrophenol by heterostructured gold-magnetite nanocatalysts*. Applied Catalysis A: General, 2014. **486**: p. 32-41.
51. Doong, R.-a. and C.-Y. Liao, *Enhanced visible-light-responsive photodegradation of bisphenol A by Cu, N-codoped titanate nanotubes prepared by microwave-assisted hydrothermal method*. Journal of hazardous materials, 2016.
52. Li, M., et al., *Tuning the adsorption capability of multi-walled carbon nanotubes to polar and non-polar organic compounds by surface oxidation*. Separation and Purification Technology, 2013. **117**: p. 98-103.
53. Saleh, N., et al., *Adsorbed triblock copolymers deliver reactive iron nanoparticles to the oil/water interface*. Nano letters, 2005. **5**(12): p. 2489-2494.
54. Tratnyek, P.G., et al., *Chapter 10: IN SITU Chemical Reduction For Source Remediation In "Chlorinated Solvent Source Zone Remediation, in Chlorinated Solvent Source Zone Remediation*, B.H. Kueper, Editor. 2014, Springer New York, 2014. 307-351. . p. 307-351.
55. Phenrat, T., et al., *Polymer-Modified FeO Nanoparticles Target Entrapped NAPL in Two Dimensional Porous Media: Effect of Particle Concentration, NAPL Saturation, and Injection Strategy*. Environmental Science & Technology, 2011. **45**(14): p. 6102-6109.
56. Fagerlund, F., et al., *PCE dissolution and simultaneous dechlorination by nanoscale zero-valent iron particles in a DNAPL source zone*. Journal of Contaminant Hydrology, 2012. **131**(1-4): p. 9-28.
57. Edmiston, P.L., et al., *Pilot scale testing composite swellable organosilica nanoscale zero-valent iron—Iron-Osorb®—for in situ remediation of trichloroethylene*. Remediation Journal, 2011. **22**(1): p. 105-123.
58. Jordan, M., et al., *Remediation of a former dry cleaner using nanoscale zero valent iron*. Remediation Journal, 2013. **24**(1): p. 31-48.
59. Wei, Y.-T., et al., *Biodegradable surfactant stabilized nanoscale zero-valent iron for in situ treatment of vinyl chloride and 1, 2-dichloroethane*. Journal of hazardous materials, 2012. **211**: p. 373-380.
60. Wei, Y.-T., et al., *Influence of nanoscale zero-valent iron on geochemical properties of groundwater and vinyl chloride degradation: A field case study*. Water Research, 2010. **44**(1): p. 131-140.
61. Henderson, A.D. and A.H. Demond, *Long-term performance of zero-valent iron permeable reactive barriers: a critical review*. Environmental Engineering Science, 2007. **24**(4): p. 401-423.

62. Joo, S.H. and F. Cheng, *Nanotechnology for environmental remediation*. 2006: Springer Science & Business Media.
63. Tratnyek, P.G. and R.L. Johnson, *Nanotechnologies for environmental cleanup*. *Nano today*, 2006. **1**(2): p. 44-48.
64. Huling, S.G. and J.W. Weaver, *Dense nonaqueous phase liquids*. 1991: Superfund Technology Support Center for Ground Water, Robert S. Kerr Environmental Research Laboratory.
65. Grieger, K.D., et al., *Environmental benefits and risks of zero-valent iron nanoparticles (nZVI) for in situ remediation: Risk mitigation or trade-off?* *Journal of Contaminant Hydrology*, 2010. **118**(3): p. 165-183.
66. Rosansky, S., W. Condit, and R. Sirabian, *Best practices for injection and distribution of amendments*. 2013, Technical Report TR-NAVFAC-EXWC-EV.
67. Ralinda R. Miller, P.G., *Horizontal Wells*. Technology Overview Report; Ground-Water Remediation Technologies Analysis Center, 1996. **TO-96-02**.
68. Klaine, S.J., et al., *Nanomaterials in the environment: behavior, fate, bioavailability, and effects*. *Environmental Toxicology and Chemistry*, 2008. **27**(9): p. 1825-1851.
69. Molnar, I.L., et al., *Predicting colloid transport through saturated porous media: A critical review*. *Water Resources Research*, 2015.
70. Peijnenburg, W., et al., *Fate assessment of engineered nanoparticles in solids dominated media—Current insights and the way forward*. *Environmental Pollution*, 2016.
71. Phenrat, T., et al., *Empirical correlations to estimate agglomerate size and deposition during injection of a polyelectrolyte-modified Fe0 nanoparticle at high particle concentration in saturated sand*. *Journal of Contaminant Hydrology*, 2010. **118**(3-4): p. 152-164.
72. Phenrat, T., et al., *Estimating Attachment of Nano- and Submicrometer-particles Coated with Organic Macromolecules in Porous Media: Development of an Empirical Model*. *Environmental Science & Technology*, 2010. **44**(12): p. 4531-4538.
73. Phenrat, T., et al., *Particle size distribution, concentration, and magnetic attraction affect transport of polymer-modified Fe0 nanoparticles in sand columns*. *Environ. Sci. Technol.*, 2009. **43**(13): p. 5079-5085.
74. Babakhani, P., et al., *Modified MODFLOW-based model for simulating the agglomeration and transport of polymer-modified Fe nanoparticles in saturated porous media*. *Environ Sci Pollut Res*, 1-20, doi:10.1007/s11356-015-5193-0, 2015.
75. Taghavy, A., K.D. Pennell, and L.M. Abriola, *Modeling coupled nanoparticle aggregation and transport in porous media: A Lagrangian approach*. *Journal of Contaminant Hydrology*, 2015. **172**: p. 48-60.
76. Kelly, R.A., et al., *Selecting among five common modelling approaches for integrated environmental assessment and management*. *Environmental Modelling & Software*, 2013. **47**: p. 159-181.
77. Adamczyk, Z., et al., *Mechanisms of nanoparticle and bioparticle deposition—Kinetic aspects*. *Colloids and Surfaces A: Physicochemical and Engineering Aspects*, 2013. **439**: p. 3-22.
78. Mackay, D., et al., *An introduction to multimedia models*. CEMC Report, 2001(200102): p. 30.
79. Comba, S. and J. Braun, *A new physical model based on cascading column experiments to reproduce the radial flow and transport of micro-iron particles*. *Journal of contaminant hydrology*, 2012. **140**: p. 1-11.

80. Dale, A., et al., *Modeling nanomaterial environmental fate in aquatic systems*. Environmental Science & Technology, 2015.
81. Gottschalk, F., et al., *Modeled environmental concentrations of engineered nanomaterials (TiO<sub>2</sub>, ZnO, Ag, CNT, fullerenes) for different regions*. Environmental science & technology, 2009. **43**(24): p. 9216-9222.
82. Gottschalk, F., et al., *Possibilities and limitations of modeling environmental exposure to engineered nanomaterials by probabilistic material flow analysis*. Environmental Toxicology and Chemistry, 2010. **29**(5): p. 1036-1048.
83. Keller, A.A. and A. Lazareva, *Predicted releases of engineered nanomaterials: from global to regional to local*. Environmental Science & Technology Letters, 2013. **1**(1): p. 65-70.
84. Keller, A.A., et al., *Global life cycle releases of engineered nanomaterials*. Journal of Nanoparticle Research, 2013. **15**(6): p. 1-17.
85. Sun, T.Y., et al., *Comprehensive probabilistic modelling of environmental emissions of engineered nanomaterials*. Environmental Pollution, 2014. **185**: p. 69-76.
86. Mueller, N.C. and B. Nowack, *Exposure modeling of engineered nanoparticles in the environment*. Environmental science & technology, 2008. **42**(12): p. 4447-4453.
87. Baalousha, M., et al., *Modeling Nanomaterials Fate and Uptake in the Environment: Current Knowledge and Future Trends*. Environmental Science: Nano, 2016.
88. Gottschalk, F., T. Sun, and B. Nowack, *Environmental concentrations of engineered nanomaterials: review of modeling and analytical studies*. Environmental Pollution, 2013. **181**: p. 287-300.
89. Nowack, B., et al., *Progress towards the validation of modeled environmental concentrations of engineered nanomaterials by analytical measurements*. Environmental Science: Nano, 2015.
90. Meesters, J.A.J., et al., *Multimedia modeling of engineered nanoparticles with SimpleBox4nano: model definition and evaluation*. Environmental Science & Technology, 2014. **48**(10): p. 5726-5736.
91. Quik, J.T.K., D. van De Meent, and A.A. Koelmans, *Simplifying modeling of nanoparticle aggregation–sedimentation behavior in environmental systems: A theoretical analysis*. Water Research, 2014. **62**: p. 193-201.
92. Arvidsson, R., et al., *Challenges in exposure modeling of nanoparticles in aquatic environments*. Human and Ecological Risk Assessment, 2011. **17**(1): p. 245-262.
93. Praetorius, A., M. Scheringer, and K. Hungerbühler, *Development of environmental fate models for engineered nanoparticles – a case study of tio<sub>2</sub> nanoparticles in the rhine river*. Environmental Science & Technology, 2012. **46**(12): p. 6705-6713.
94. Liu, H.H. and Y. Cohen, *Multimedia environmental distribution of engineered nanomaterials*. Environmental science & technology, 2014. **48**(6): p. 3281-3292.
95. Hotze, E.M., T. Phenrat, and G.V. Lowry, *Nanoparticle Aggregation: Challenges to Understanding Transport and Reactivity in the Environment*. J. Environ. Qual. , 2010. **39**: p. 1909–1924.
96. Petosa, A.R., et al., *Aggregation and deposition of engineered nanomaterials in aquatic environments: role of physicochemical interactions*. Environmental Science & Technology, 2010. **44**(17): p. 6532-6549.
97. Adamczyk, Z. and P. Weroński, *Application of the DLVO theory for particle deposition problems*. Advances in Colloid and Interface Science, 1999. **83**(1): p. 137-226.

98. Grasso, D., et al., *A review of non-DLVO interactions in environmental colloidal systems*. *Reviews in Environmental Science and Biotechnology*, 2002. **1**(1): p. 17-38.
99. Bradford, S.A. and S. Torkzaban, *Colloid transport and retention in unsaturated porous media: A review of interface-, collector-, and pore-scale processes and models*. *Vadose Zone Journal*, 2008. **7**(2): p. 667-681.
100. Keir, G., V. Jegatheesan, and S. Vigneswaran, *Deep bed filtration: modeling theory and practice*. *Water and Wastewater Treatment Technologies*, V. Saravanamuthu, ed., Eolss Publishers, Oxford, UK, 2009: p. 263-307.
101. McDowell-Boyer, L.M., J.R. Hunt, and N. Sitar, *Particle transport through porous media*. *Water Resour. Res.*, 1986. **22**(13): p. 1901-1921.
102. Schijven, J.K. and S.M. Hassanizadeh, *Removal of viruses by soil passage: Overview of modeling, processes, and parameters*. *Crit. Rev. Environ. Sci. Technol.*, 2000. **30**: p. 49 – 127.
103. Phenrat, T., et al., *Stabilization of aqueous nanoscale zerovalent iron dispersions by anionic polyelectrolytes: adsorbed anionic polyelectrolyte layer properties and their effect on aggregation and sedimentation*. *Journal of Nanoparticle Research*, 2008. **10**(5): p. 795-814.
104. Saleh, N.B., et al., *Aggregation Kinetics and Fractal Dimensions of Nanomaterials in Environmental Systems*. *Engineered Nanoparticles and the Environment: Biophysicochemical Processes and Toxicity*, 2016. **4**.
105. Pan, B. and B. Xing, *Applications and implications of manufactured nanoparticles in soils: a review*. *European Journal of Soil Science*, 2012. **63**(4): p. 437-456.
106. Jegatheesan, V. and S. Vigneswaran, *Deep Bed Filtration: Mathematical Models and Observations*. *Critical Reviews in Environmental Science and Technology*, 2005. **35**(6): p. 515-569.
107. Taghavy, A., et al., *Mathematical modeling of the transport and dissolution of citrate-stabilized silver nanoparticles in porous media*. *Environmental Science & Technology*, 2013. **47**(15): p. 8499-8507.
108. Bradford, S.A., et al., *Physical factors affecting the transport and fate of colloids in saturated porous media*. *Water Resources Research*, 2002. **38**(12): p. 63-1.
109. Bradford, S.A., et al., *Equilibrium and kinetic models for colloid release under transient solution chemistry conditions*. *Journal of contaminant hydrology*, 2015.
110. Torkzaban, S., et al., *Colloid release and clogging in porous media: Effects of solution ionic strength and flow velocity*. *Journal of contaminant hydrology*, 2015.
111. Yao, K.-M., M.T. Habibian, and C.R. O'Melia, *Water and waste water filtration. Concepts and applications*. *Environmental Science & Technology*, 1971. **5**(11): p. 1105-1112.
112. Ryan, J.N. and M. Elimelech, *Colloid mobilization and transport in groundwater*. *Colloids and Surfaces A*, 1996. **107**: p. 1-56.
113. Tufenkji, N. and M. Elimelech, *Correlation equation for predicting single-collector efficiency in physicochemical filtration in saturated porous media*. *Environmental Science & Technology*, 2004. **38**(2): p. 529-536.
114. Elimelech, M., et al., *Particle deposition and aggregation: measurement, modelling and simulation*. 1998, Amsterdam: Elsevier.
115. Sirk, K.M., et al., *Effect of adsorbed polyelectrolytes on nanoscale zero valent iron particle attachment to soil surface models*. *Environmental science & technology*, 2009. **43**(10): p. 3803-3808.

116. Liu, L., et al., *Effects of pH and surface metal oxyhydroxides on deposition and transport of carboxyl-functionalized graphene in saturated porous media*. Journal of nanoparticle research, 2013. **15**(11): p. 1-8.
117. Wang, D., et al., *Humic acid facilitates the transport of ARS-labeled hydroxyapatite nanoparticles in iron oxyhydroxide-coated sand*. Environmental science & technology, 2012. **46**(5): p. 2738-2745.
118. Tian, Y., et al., *Deposition and transport of functionalized carbon nanotubes in water-saturated sand columns*. Journal of hazardous materials, 2012. **213**: p. 265-272.
119. Elimelech, M., et al., *Relative insignificance of mineral grain zeta potential to colloid transport in geochemically heterogeneous porous media*. Environmental science & technology, 2000. **34**(11): p. 2143-2148.
120. He, J.-Z., et al., *Biofilms and extracellular polymeric substances mediate the transport of graphene oxide nanoparticles in saturated porous media*. Journal of hazardous materials, 2015. **300**: p. 467-474.
121. Jiang, X., et al., *Initial transport and retention behaviors of ZnO nanoparticles in quartz sand porous media coated with Escherichia coli biofilm*. Environmental Pollution, 2013. **174**: p. 38-49.
122. Li, Z., et al., *Transport of nanoparticles with dispersant through biofilm coated drinking water sand filters*. Water research, 2013. **47**(17): p. 6457-6466.
123. Zhang, W., et al., *Attachment efficiency of nanoparticle aggregation in aqueous dispersions: modeling and experimental validation*. Environmental science & technology, 2012. **46**(13): p. 7054-7062.
124. Marmur, A., *A kinetic theory approach to primary and secondary minimum coagulations and their combination*. Journal of Colloid and Interface Science, 1979. **72**(1): p. 41-48.
125. Wu, L., et al., *Aggregation kinetics of graphene oxides in aqueous solutions: experiments, mechanisms, and modeling*. Langmuir, 2013. **29**(49): p. 15174-15181.
126. Baalousha, M., *Effect of nanomaterial and media physicochemical properties on nanomaterial aggregation kinetics*. NanoImpact, 2017. **6**: p. 55-68.
127. Jacobson, M.Z., *Fundamentals of atmospheric modeling*. 2005: Cambridge university press.
128. Van Genuchten, M.T. and P.J. Wierenga, *Mass transfer studies in sorbing porous media I. Analytical solutions*. Soil Science Society of America Journal, 1976. **40**(4): p. 473-480.
129. Mehmani, Y. and M.T. Balhoff, *Mesoscale and hybrid models of fluid flow and solute transport*. Rev Mineral Geochem, 2015. **80**: p. 433-459.
130. Dale, A.L., G.V. Lowry, and E.A. Casman, *Much ado about  $\alpha$ : reframing the debate over appropriate fate descriptors in nanoparticle environmental risk modeling*. Environmental Science: Nano, 2015.
131. Zheng, C. and P.P. Wang, *A modular three-dimensional multi-species transport model for simulation of advection, dispersion and chemical reactions of contaminants in groundwater systems; documentation and user's guide*. US Army Engineer Research and Development Center Contract Report SERDP-99-1, Vicksburg, Mississippi, USA, 1999.
132. Saiers, J.E. and G.M. Hornberger, *Migration of  $^{137}\text{Cs}$  through quartz sand: experimental results and modeling approaches*. Journal of Contaminant Hydrology, 1996. **22**(3-4): p. 255-270.

133. Seetha, N., et al., *Correlation equations for average deposition rate coefficients of nanoparticles in a cylindrical pore*. Water Resources Research, 2015. **51**(10): p. 8034-8059.
134. Bradford, S.A., et al., *Modeling colloid attachment, straining, and exclusion in saturated porous media*. Environmental science & technology, 2003. **37**(10): p. 2242-2250.
135. Bradford, S.A. and S. Torkzaban, *Determining parameters and mechanisms of colloid retention and release in porous media*. Langmuir, 2015. **31**(44): p. 12096-12105.
136. Chrysikopoulos, C.V. and V.E. Katzourakis, *Colloid particle size-dependent dispersivity*. Water Resources Research, 2015.
137. Therezien, M., A. Thill, and M.R. Wiesner, *Importance of heterogeneous aggregation for NP fate in natural and engineered systems*. Science of The Total Environment, 2014. **485**: p. 309-318.
138. Cullen, E., et al., *Simulation of the subsurface mobility of carbon nanoparticles at the field scale*. Advances in Water Resources, 2010. **33**(4): p. 361-371.
139. Krol, M.M., et al., *A field-validated model for in situ transport of polymer-stabilized nZVI and implications for subsurface injection*. Environmental science & technology, 2013. **47**(13): p. 7332-7340.
140. Bradford, S.A., et al., *Significance of straining in colloid deposition: Evidence and implications*. Water Resour. Res., 2006. **42**(12): p. W12S15.
141. Song, L. and M. Elimelech, *Dynamics of colloid deposition in porous media: modeling the role of retained particles*. Colloids and Surfaces A, 1993. **73**: p. 49-63.
142. Kretzschmar, R., et al., *Mobile subsurface colloids and their role in contaminant transport*. Advances in agronomy, 1999. **66**: p. 121-193.
143. Sun, N., et al., *A novel two-dimensional model for colloid transport in physically and geochemically heterogeneous porous media*. Journal of contaminant hydrology, 2001. **49**(3): p. 173-199.
144. Saiers, J.E., G.M. Hornberger, and L. Liang, *First-and second-order kinetics approaches for modeling the transport of colloidal particles in porous media*. Water Resources Research, 1994. **30**(9): p. 2499-2506.
145. Chowdhury, A.I.A., et al., *NZVI injection into variably saturated soils: Field and modeling study*. Journal of Contaminant Hydrology, 2015. **183**: p. 16-28.
146. Raychoudhury, T., N. Tufenkji, and S. Ghoshal, *Aggregation and deposition kinetics of carboxymethyl cellulose-modified zero-valent iron nanoparticles in porous media*. Water Research, 2012. **46**(6): p. 1735-1744.
147. Tosco, T. and R. Sethi, *Transport of non-Newtonian suspensions of highly concentrated micro-and nanoscale iron particles in porous media: a modeling approach*. Environmental Science & Technology, 2010. **44**(23): p. 9062-9068.
148. Hosseini, S.M. and T. Tosco, *Transport and retention of high concentrated nano-Fe/Cu particles through highly flow-rated packed sand column*. Water Research, 2013. **47**(1): p. 326-338.
149. Shen, C., et al., *Effects of solution chemistry on straining of colloids in porous media under unfavorable conditions*. Water resources research, 2008. **44**(5).
150. Scheibe, T.D. and B.D. Wood, *A particle-based model of size or anion exclusion with application to microbial transport in porous media*. Water resources research, 2003. **39**(4).

151. Bradford, S.A., J. Simunek, and S.L. Walker, *Transport and straining of E. coli O157: H7 in saturated porous media*. Water Resources Research, 2006. **42**(12).
152. Bradford, S.A. and M. Bettahar, *Concentration dependent transport of colloids in saturated porous media*. Journal of Contaminant Hydrology, 2006. **82**(1): p. 99-117.
153. Wang, D., et al., *Transport of fluorescently labeled hydroxyapatite nanoparticles in saturated granular media at environmentally relevant concentrations of surfactants*. Colloids and Surfaces A: Physicochemical and Engineering Aspects, 2014. **457**: p. 58-66.
154. Cornelis, G., *Fate descriptors for engineered nanoparticles: the good, the bad, and the ugly*. Environmental Science: Nano, 2015. **2**(1): p. 19-26.
155. O'Carroll, D., et al., *Nanoscale zero valent iron and bimetallic particles for contaminated site remediation*. Advances in Water Resources, 2013. **51**: p. 104-122.
156. Praetorius, A., et al., *The road to nowhere: equilibrium partition coefficients for nanoparticles*. Environmental Science: Nano, 2014. **1**(4): p. 317-323.
157. Bradford, S.A., et al., *Modeling microorganism transport and survival in the subsurface*. Journal of environmental quality, 2014. **43**(2): p. 421-440.
158. Ginn, T.R., *A brief review of bacterial transport in natural porous media*. 1995, Pacific Northwest Lab., Richland, WA (United States).
159. Keller, A.A. and M. Auset, *A review of visualization techniques of biocolloid transport processes at the pore scale under saturated and unsaturated conditions*. Advances in Water Resources, 2007. **30**(6): p. 1392-1407.
160. Massoudieh, A. and T.R. Ginn, *Colloid-facilitated contaminant transport in unsaturated porous media*. Modelling of pollutants in complex environmental systems, 2010. **2**: p. 263-286.
161. Herzig, J.P., D.M. Leclerc, and P.L. Goff, *Flow of Suspensions through Porous Media—Application to Deep Filtration*. Industrial & Engineering Chemistry, 1970. **62**(5): p. 8-35.
162. Ives, K.J., *Rapid filtration*. Water Research, 1970. **4**(3): p. 201-223.
163. Tufenkji, N., *Modeling microbial transport in porous media: Traditional approaches and recent developments*. Advances in Water Resources, 2007. **30**(6): p. 1455-1469.
164. Sun, Y., et al., *Transport, retention, and size perturbation of graphene oxide in saturated porous media: Effects of input concentration and grain size*. Water research, 2015. **68**: p. 24-33.
165. Fan, W., et al., *Transport of graphene oxide in saturated porous media: Effect of cation composition in mixed Na–Ca electrolyte systems*. Science of The Total Environment, 2015. **511**: p. 509-515.
166. Bai, C. and Y. Li, *Modeling the transport and retention of nC 60 nanoparticles in the subsurface under different release scenarios*. Journal of contaminant hydrology, 2012. **136**: p. 43-55.
167. Becker, M.D., et al., *In situ measurement and simulation of nano-magnetite mobility in porous media subject to transient salinity*. Nanoscale, 2015. **7**(3): p. 1047-1057.
168. Wang, D., et al., *Transport of ARS-labeled hydroxyapatite nanoparticles in saturated granular media is influenced by surface charge variability even in the presence of humic acid*. Journal of hazardous materials, 2012. **229**: p. 170-176.

169. Wang, D., et al., *Hyperexponential and nonmonotonic retention of polyvinylpyrrolidone-coated silver nanoparticles in an Ultisol*. Journal of contaminant hydrology, 2014. **164**: p. 35-48.
170. Wang, D., et al., *Facilitated transport of copper with hydroxyapatite nanoparticles in saturated sand*. Soil Science Society of America Journal, 2012. **76**(2): p. 375-388.
171. Wang, D., Y. Jin, and D.P. Jaisi, *Effect of Size-Selective Retention on the Cotransport of Hydroxyapatite and Goethite Nanoparticles in Saturated Porous Media*. Environmental science & technology, 2015. **49**(14): p. 8461-8470.
172. Wang, D., Y. Jin, and D. Jaisi, *Cotransport of Hydroxyapatite Nanoparticles and Hematite Colloids in Saturated Porous Media: Mechanistic Insights from Mathematical Modeling and Phosphate Oxygen Isotope Fractionation*. Journal of Contaminant Hydrology, 2015. **182**: p. 194-209.
173. Liang, Y., et al., *Sensitivity of the transport and retention of stabilized silver nanoparticles to physicochemical factors*. water research, 2013. **47**(7): p. 2572-2582.
174. Wang, D., et al., *Transport and Retention of Polyvinylpyrrolidone-Coated Silver Nanoparticles in Natural Soils*. Vadose Zone J., 2015.
175. Wang, D., et al., *Facilitated transport of Cu with hydroxyapatite nanoparticles in saturated sand: Effects of solution ionic strength and composition*. water research, 2011. **45**(18): p. 5905-5915.
176. Fan, W., et al., *Effects of surfactants on graphene oxide nanoparticles transport in saturated porous media*. Journal of Environmental Sciences, 2015.
177. Qi, Z., L. Zhang, and W. Chen, *Transport of graphene oxide nanoparticles in saturated sandy soil*. Environmental Science: Processes & Impacts, 2014. **16**(10): p. 2268-2277.
178. Qi, Z., et al., *Factors controlling transport of graphene oxide nanoparticles in saturated sand columns*. Environmental toxicology and chemistry, 2014. **33**(5): p. 998-1004.
179. Fang, J., et al., *Modeling the transport of TiO<sub>2</sub> nanoparticle aggregates in saturated and unsaturated granular media: effects of ionic strength and pH*. water research, 2013. **47**(3): p. 1399-1408.
180. Braun, A., et al., *Transport and deposition of stabilized engineered silver nanoparticles in water saturated loamy sand and silty loam*. Science of The Total Environment, 2014.
181. Raychoudhury, T., N. Tufenkji, and S. Ghoshal, *Straining of Polyelectrolyte-Stabilized Nanoscale Zero Valent Iron Particles during Transport through Granular Porous Media*. Water Research, 2014. **50**(0): p. 80-90.
182. Sun, P., et al., *Distinguishable Transport Behavior of Zinc Oxide Nanoparticles in Silica Sand and Soil Columns*. Science of The Total Environment, 2015. **505**: p. 189-198.
183. Liang, Y., et al., *Retention and remobilization of stabilized silver nanoparticles in an undisturbed loamy sand soil*. Environmental science & technology, 2013. **47**(21): p. 12229-12237.
184. Web of Science™, <http://apps.webofknowledge.com/>.
185. Prieve, D.C. and P.M. Hoysan, *Role of colloidal forces in hydrodynamic chromatography*. Journal of Colloid and Interface Science, 1978. **64**(2): p. 201-213.
186. Fallah, H., et al., *Size Exclusion Mechanism, Suspension Flow through Porous Medium*. International Journal of Modern Nonlinear Theory and Application, 2012. **1**(04): p. 113.
187. James, S.C. and C.V. Chrysikopoulos, *Effective velocity and effective dispersion coefficient for finite-sized particles flowing in a uniform fracture*. Journal of colloid and interface science, 2003. **263**(1): p. 288-295.

188. de Marsily, G., *Quantitative hydrogeology; groundwater hydrology for engineers*. Academic Press, New York, NY, 1986.
189. Howington, S.E., J.F. Peters, and T.H. Illangasekare, *Discrete network modeling for field-scale flow and transport through porous media*, in *Technical Report CHL-97-21*. 1997, Discretionary Research Program, US Army Corps of Engineers MD, US.
190. Mehmani, Y. and M.T. Balhoff, *Eulerian network modeling of longitudinal dispersion*. Water Resources Research, 2015. **51**(10): p. 8586-8606.
191. Zheng, C. and P. Wang, *MT3DMS, A modular three-dimensional multi-species transport model for simulation of advection, dispersion and chemical reactions of contaminants in groundwater systems; documentation and user's guide*. U.S. Army Corps Engineers, Engineer Research and Development Center, Contract Report SERDP-99-1, Vicksburg, MS, 1999: p. 202.
192. Huang, P.M., Y. Li, and M.E. Sumner, *Handbook of soil sciences: properties and processes*, ed. S. Edition. Vol. I. 2011, New York, US: CRC Press Taylor and Francis Group an informa business.
193. Harvey, R.W. and S.P. Garabedian, *Use of colloid filtration theory in modeling movement of bacteria through a contaminated sandy aquifer*. Environmental Science & Technology, 1991. **25**(1): p. 178-185.
194. Zhang, W., et al., *Transport and retention of biochar particles in porous media: effect of pH, ionic strength, and particle size*. Ecohydrology, 2010. **3**(4): p. 497–508.
195. Iwasaki, T., J.J. Slade, Jr., and W.E. Stanley, *SOME NOTES ON SAND FILTRATION [with Discussion]*. Journal (American Water Works Association), 1937. **29**(10): p. 1591-1602.
196. Wang, H.F. and M.P. Anderson, *Introduction to groundwater modeling: finite difference and finite element methods*. 1995: Academic Press.
197. Illangasekare, T.H., C.C. Frippiat, and R. Fućík, *Dispersion and Mass Transfer Coefficients in Groundwater of Near-Surface Geologic Formations*. Handbook of Chemical Mass Transport in the Environment, ed. L.J. Thibodeaux, B. Rouge, and D. Mackay. 2010: CRC Press/Taylor and Francis Group.
198. Keller, A.A., S. Sirivithayapakorn, and C.V. Chrysikopoulos, *Early breakthrough of colloids and bacteriophage MS2 in a water-saturated sand column*. Water Resources Research, 2004. **40**(8).
199. Parker, J.C., T. Van Genuchten, and S. Virginia Agricultural Experiment, *Determining Transport Parameters from Laboratory and Field Tracer Experiments*. Bulletin (Virginia Agricultural Experiment Station). 1984: Virginia Agricultural Experiment Station.
200. Sirivithayapakorn, S. and A. Keller, *Transport of colloids in saturated porous media: A pore-scale observation of the size exclusion effect and colloid acceleration*. Water Resources Research, 2003. **39**(4).
201. Chowdhury, A.I.A., et al., *Electrophoresis enhanced transport of nano-scale zero valent iron*. Advances in Water Resources, 2012. **40**(0): p. 71-82.
202. Darbha, G.K., et al., *Site-specific retention of colloids at rough rock surfaces*. Environmental science & technology, 2012. **46**(17): p. 9378-9387.
203. Reiche, T., U. Noseck, and T. Schäfer, *Migration of Contaminants in Fractured-Porous Media in the Presence of Colloids: Effects of Kinetic Interactions*. Transport in Porous Media, 2015: p. 1-28.

204. Salama, A., et al., *Numerical investigation of nanoparticles transport in anisotropic porous media*. Journal of contaminant hydrology, 2015. **181**: p. 114-130.
205. Batchelor, G.K., *Brownian diffusion of particles with hydrodynamic interaction*. Journal of Fluid Mechanics, 1976. **74**(01): p. 1-29.
206. Sharma, M. and S. Yashonath, *Size dependence of solute diffusivity and Stokes-Einstein relationship: Effect of van der Waals interaction*. Diffusion Fundamentals, 2007. **6**: p. 35-1.
207. Zheng, Q., S.E. Dickson, and Y. Guo, *Differential transport and dispersion of colloids relative to solutes in single fractures*. Journal of colloid and interface science, 2009. **339**(1): p. 140-151.
208. Limousin, G., et al., *Sorption isotherms: A review on physical bases, modeling and measurement*. Applied Geochemistry, 2007. **22**(2): p. 249-275.
209. Rajagopalan, R. and C. Tien, *Trajectory analysis of deep-bed filtration with the sphere-in-cell porous media model*. AIChE Journal, 1976. **22**(3): p. 523-533.
210. Logan, B.E., et al., *Clarification of clean-bed filtration models*. Journal of Environmental Engineering, 1995. **121**(12): p. 869-873.
211. Li, J., X. Xie, and S. Ghoshal, *Correlation Equation for Predicting the Single-Collector Contact Efficiency of Colloids in a Horizontal Flow*. Langmuir, 2015. **31**(26): p. 7210-7219.
212. Landkamer, L.L., et al., *Colloid transport in saturated porous media: Elimination of attachment efficiency in a new colloid transport model*. Water Resources Research, 2013. **49**(5): p. 2952-2965.
213. O'Carroll, D., et al., *Nanoscale zero valent iron and bimetallic particles for contaminated site remediation*. Advances in Water Resources, 2012(0): p. 1-19.
214. Johnson, W.P., X. Li, and S. Assemi, *Deposition and re-entrainment dynamics of microbes and non-biological colloids during non-perturbed transport in porous media in the presence of an energy barrier to deposition*. Advances in Water Resources, 2007. **30**(6): p. 1432-1454.
215. O'Carroll, D.M., S.A. Bradford, and L.M. Abriola, *Infiltration of PCE in a system containing spatial wettability variations*. Journal of Contaminant Hydrology, 2004. **73**(1-4): p. 39-63.
216. Torkzaban, S. and S.A. Bradford, *Critical role of surface roughness on colloid retention and release in porous media*. Water research, 2016. **88**: p. 274-284.
217. Wang, Z., et al., *Spontaneous Detachment of Colloids from Primary Energy Minima by Brownian Diffusion*. PloS one, 2016. **11**(1).
218. Zhang, P., et al., *Potential Artifacts in Interpretation of Differential Breakthrough of Colloids and Dissolved Tracers in the Context of Transport in a Zero-Valent Iron Permeable Reactive Barrier*. Groundwater, 2001. **39**(6): p. 831-840.
219. Kasel, D., et al., *Transport and retention of multi-walled carbon nanotubes in saturated porous media: Effects of input concentration and grain size*. water research, 2013. **47**(2): p. 933-944.
220. Shang, J., C. Liu, and Z. Wang, *Transport and retention of engineered nanoporous particles in porous media: effects of concentration and flow dynamics*. Colloids and Surfaces A: Physicochemical and Engineering Aspects, 2013. **417**: p. 89-98.
221. Flory, J., et al., *Influence of pH on the transport of silver nanoparticles in saturated porous media: laboratory experiments and modeling*. Journal of nanoparticle research, 2013. **15**(3): p. 1-11.

222. Kanel, S.R., et al., *Influence of natural organic matter on fate and transport of silver nanoparticles in saturated porous media: laboratory experiments and modeling*. Journal of Nanoparticle Research, 2013. **17**(3): p. 1-13.
223. Neukum, C., A. Braun, and R. Azzam, *Transport of engineered silver (Ag) nanoparticles through partially fractured sandstones*. Journal of contaminant hydrology, 2014. **164**: p. 181-192.
224. Zhang, P., et al., *Extended tailing of bacteria following breakthrough at the Narrow Channel Focus Area, Oyster, Virginia*. Water Resources Research, 2001. **37**(11): p. 2687-2698.
225. Bergendahl, J. and D. Grasso, *Prediction of colloid detachment in a model porous media: hydrodynamics*. Chemical Engineering Science, 2000. **55**(9): p. 1523-1532.
226. Torkzaban, S., S.A. Bradford, and S.L. Walker, *Resolving the Coupled Effects of Hydrodynamics and DLVO Forces on Colloid Attachment in Porous Media*. Langmuir, 2007. **23**(19): p. 9652-9660.
227. Harendra, S. and C. Vipulanandan, *Fe/Ni bimetallic particles transport in columns packed with sandy clay soil*. Industrial & Engineering Chemistry Research, 2010. **50**(1): p. 404-411.
228. Sasidharan, S., et al., *Coupled effects of hydrodynamic and solution chemistry on long-term nanoparticle transport and deposition in saturated porous media*. Colloids and Surfaces A: Physicochemical and Engineering Aspects, 2014. **457**: p. 169-179.
229. Kini, G.C., et al., *Salt-and temperature-stable quantum dot nanoparticles for porous media flow*. Colloids and Surfaces A: Physicochemical and Engineering Aspects, 2014. **443**: p. 492-500.
230. Torkzaban, S., et al., *Transport and deposition of functionalized CdTe nanoparticles in saturated porous media*. Journal of contaminant hydrology, 2010. **118**(3): p. 208-217.
231. Wang, Y., et al., *Effect of surface coating composition on quantum dot mobility in porous media*. Journal of nanoparticle research, 2013. **15**(8): p. 1-16.
232. Torkzaban, S., et al., *Impacts of bridging complexation on the transport of surface-modified nanoparticles in saturated sand*. Journal of contaminant hydrology, 2012. **136**: p. 86-95.
233. Wang, Y., et al., *Influence of Residual Polymer on Nanoparticle Deposition in Porous Media*. Environmental Science & Technology, 2014. **48**(18): p. 10664-10671.
234. Torkzaban, S., et al., *Release of Quantum Dot Nanoparticles in Porous Media: Role of Cation Exchange and Aging Time*. Environmental Science & Technology, 2013. **47**(20): p. 11528-11536.
235. Treumann, S., et al., *An explanation for differences in the process of colloid adsorption in batch and column studies*. Journal of contaminant hydrology, 2014. **164**: p. 219-229.
236. Torkzaban, S., et al., *Hysteresis of colloid retention and release in saturated porous media during transients in solution chemistry*. Environmental science & technology, 2010. **44**(5): p. 1662-1669.
237. He, F., et al., *Transport of carboxymethyl cellulose stabilized iron nanoparticles in porous media: Column experiments and modeling*. Journal of Colloid and Interface Science, 2009. **334**(1): p. 96-102.
238. Lanphere, J.D., C.J. Luth, and S.L. Walker, *Effects of solution chemistry on the transport of graphene oxide in saturated porous media*. Environmental science & technology, 2013. **47**(9): p. 4255-4261.

239. Li, Z., et al., *Transport and deposition of CeO<sub>2</sub> nanoparticles in water-saturated porous media*. Water research, 2011. **45**(15): p. 4409-4418.
240. Godinez, I.G. and C.J.G. Darnault, *Aggregation and transport of nano-TiO<sub>2</sub> in saturated porous media: effects of pH, surfactants and flow velocity*. Water research, 2011. **45**(2): p. 839-851.
241. Jones, E.H. and C. Su, *Fate and transport of elemental copper (Cu<sup>0</sup>) nanoparticles through saturated porous media in the presence of organic materials*. water research, 2012. **46**(7): p. 2445-2456.
242. Grolimund, D. and M. Borkovec, *Release of colloidal particles in natural porous media by monovalent and divalent cations*. Journal of Contaminant Hydrology, 2006. **87**(3): p. 155-175.
243. Tiraferri, A., R. Sethi, and T.A.E. Tosco, *Ionic Strength Dependent Transport of Microparticles in Saturated Porous Media: Modeling Mobilization and Immobilization Phenomena under Transient Chemical Conditions*. 2009.
244. Tufenkji, N. and M. Elimelech, *Deviation from the Classical Colloid Filtration Theory in the Presence of Repulsive DLVO Interactions*. Langmuir, 2004. **20**(25): p. 10818-10828.
245. Jiang, X., M. Tong, and H. Kim, *Influence of natural organic matter on the transport and deposition of zinc oxide nanoparticles in saturated porous media*. Journal of colloid and interface science, 2012. **386**(1): p. 34-43.
246. Schijven, J.F., S.M. Hassanizadeh, and R.H.A.M. de Bruin, *Two-site kinetic modeling of bacteriophages transport through columns of saturated dune sand*. Journal of Contaminant Hydrology, 2002. **57**(3): p. 259-279.
247. Tufenkji, N., *Application of a dual deposition mode model to evaluate transport of Escherichia coli D21 in porous media*. Water resources research, 2006. **42**(12).
248. Zhang, W., et al., *Transport and retention of biochar particles in porous media: effect of pH, ionic strength, and particle size*. Ecohydrology, 2010. **3**(4): p. 497-508.
249. Phenrat, T., et al., *Transport and deposition of polymer-modified FeO nanoparticles in 2-D heterogeneous porous media: Effects of particle concentration, FeO content, and coatings*. Environmental Science & Technology, 2010. **44**(23): p. 9086-9093.
250. Risovic, D. and M. Martinis, *The role of coagulation and sedimentation mechanisms in the two-component model of sea-particle size distribution*. Fizika, 1994. **3**(2): p. 103-118.
251. Tang, P. and J.A. Raper, *Modelling the settling behaviour of fractal aggregates—a review*. Powder technology, 2002. **123**(2): p. 114-125.
252. Friedlander, S.K., *On the particle-size spectrum of atmospheric aerosols*. Journal of Meteorology, 1960. **17**(3): p. 373-374.
253. Friedlander, S.K., *Similarity considerations for the particle-size spectrum of a coagulating, sedimenting aerosol*. Journal of Meteorology, 1960. **17**(5): p. 479-483.
254. Jeffrey, D.J., *Quasi-stationary approximations for the size distribution of aerosols*. Journal of the Atmospheric Sciences, 1981. **38**(11): p. 2440-2443.
255. Abel, J.S., et al., *Sedimentation in flocculating colloidal suspensions*. Journal of materials research, 1994. **9**(02): p. 451-461.
256. Smoluchowski, M., *Versuch einer mathematischen Theorie der Koagulationskinetik kolloider Lösungen*. Zeitschrift fuer Physikalische Chemie. 92., 1917. **129-68**.

257. Quik, J.T.K., et al., *Heteroaggregation and sedimentation rates for nanomaterials in natural waters*. Water research, 2014. **48**: p. 269-279.
258. Hunt, J.R., *Self-similar particle-size distributions during coagulation: theory and experimental verification*. Journal of Fluid Mechanics, 1982. **122**: p. 169-185.
259. Liu, H.H., et al., *Analysis of nanoparticle agglomeration in aqueous suspensions via constant-number Monte Carlo simulation*. Environmental Science & Technology, 2011. **45**(21): p. 9284-9292.
260. Yu, H., et al., *Prediction of the Particle Size Distribution Parameters in a High Shear Granulation Process Using a Key Parameter Definition Combined Artificial Neural Network Model*. Industrial & Engineering Chemistry Research, 2015. **54**(43): p. 10825-10834.
261. Goudeli, E., M.L. Eggersdorfer, and S.E. Pratsinis, *Coagulation–Agglomeration of fractal-like particles: Structure and self-preserving size distribution*. Langmuir, 2015. **31**(4): p. 1320-1327.
262. El Badawy, A.M., et al., *Key factors controlling the transport of silver nanoparticles in porous media*. Environmental science & technology, 2013. **47**(9): p. 4039-4045.
263. Toloni, I., F. Lehmann, and P. Ackerer, *Modeling the effects of water velocity on TiO<sub>2</sub> nanoparticles transport in saturated porous media*. Journal of contaminant hydrology, 2014. **171**: p. 42-48.
264. Rahman, T., J. George, and H.J. Shipley, *Transport of aluminum oxide nanoparticles in saturated sand: Effects of ionic strength, flow rate, and nanoparticle concentration*. Science of The Total Environment, 2013. **463–464**: p. 565-571.
265. Rahman, T., H. Millwater, and H.J. Shipley, *Modeling and sensitivity analysis on the transport of aluminum oxide nanoparticles in saturated sand: Effects of ionic strength, flow rate, and nanoparticle concentration*. Science of The Total Environment, 2014. **499**: p. 402-412.
266. Neukum, C., A. Braun, and R. Azzam, *Transport of stabilized engineered silver (Ag) nanoparticles through porous sandstones*. Journal of contaminant hydrology, 2014. **158**: p. 1-13.
267. Wang, Q., et al., *Mobilization and deposition of iron nano and sub-micrometer particles in porous media: A glass micromodel study*. Journal of hazardous materials, 2011. **192**(3): p. 1466-1475.
268. Cornelis, G., et al., *Transport of silver nanoparticles in saturated columns of natural soils*. Science of the Total Environment, 2013. **463**: p. 120-130.
269. Lv, X., et al., *Effects of Humic Acid and Solution Chemistry on the Retention and Transport of Cerium Dioxide Nanoparticles in Saturated Porous Media*. Water, Air, & Soil Pollution, 2014. **225**(10): p. 1-9.
270. Choy, C.C., M. Wazne, and X. Meng, *Application of an empirical transport model to simulate retention of nanocrystalline titanium dioxide in sand columns*. Chemosphere, 2008. **71**(9): p. 1794-1801.
271. Dunphy Guzman, K.A., M.P. Finnegan, and J.F. Banfield, *Influence of surface potential on aggregation and transport of titania nanoparticles*. Environmental Science & Technology, 2006. **40**(24): p. 7688-7693.
272. Fang, J., et al., *Stability of titania nanoparticles in soil suspensions and transport in saturated homogeneous soil columns*. Environmental pollution, 2009. **157**(4): p. 1101-1109.

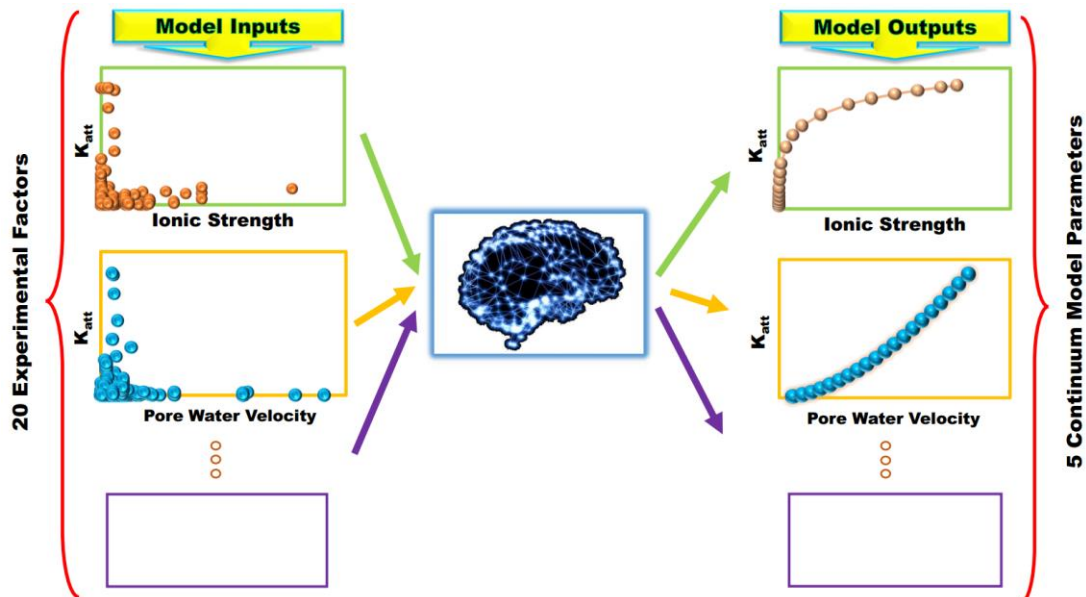
273. Solovitch, N., et al., *Concurrent aggregation and deposition of TiO<sub>2</sub> nanoparticles in a sandy porous media*. Environmental science & technology, 2010. **44**(13): p. 4897-4902.
274. Jiang, X., et al., *Transport and deposition of ZnO nanoparticles in saturated porous media*. Colloids and Surfaces A: Physicochemical and Engineering Aspects, 2012. **401**: p. 29-37.
275. Kurlanda-Witek, H., B.T. Ngwenya, and I.B. Butler, *Transport of bare and capped zinc oxide nanoparticles is dependent on porous medium composition*. Journal of contaminant hydrology, 2014. **162**: p. 17-26.
276. Klimentko, A.Y., et al., *Conditional model for sorption in porous media with fractal properties*. Transport in porous media, 2012. **92**(3): p. 745-765.
277. Shapiro, A.A. and P.G. Bedrikovetsky, *A stochastic theory for deep bed filtration accounting for dispersion and size distributions*. Physica A: Statistical Mechanics and its Applications, 2010. **389**(13): p. 2473-2494.
278. Phenrat, T., et al., *Supporting Information for "Particle size distribution, concentration, and magnetic attraction affect transport of polymer-modified Fe<sub>0</sub> nanoparticles in sand columns"*. Environ. Sci. Technol., 2009. **43**(13): p. 5079-5085.
279. Lin, S. and M.R. Wiesner, *Deposition of Aggregated Nanoparticles □ A Theoretical and Experimental Study on the Effect of Aggregation State on the Affinity between Nanoparticles and a Collector Surface*. Environmental science & technology, 2012. **46**(24): p. 13270-13277.
280. Li, X. and B.E. Logan, *Collision frequencies of fractal aggregates with small particles by differential sedimentation*. Environmental science & technology, 1997. **31**(4): p. 1229-1236.
281. Li, X.-Y. and B.E. Logan, *Permeability of fractal aggregates*. Water research, 2001. **35**(14): p. 3373-3380.
282. Meng, Z., S.M. Hashmi, and M. Elimelech, *Aggregation rate and fractal dimension of fullerene nanoparticles via simultaneous multiangle static and dynamic light scattering measurement*. Journal of colloid and interface science, 2013. **392**: p. 27-33.
283. Chakraborti, R.K., et al., *Changes in fractal dimension during aggregation*. Water Research, 2003. **37**(4): p. 873-883.
284. Johnson, C.P., X. Li, and B.E. Logan, *Settling Velocities of Fractal Aggregates*. Environmental Science & Technology, 1996. **30**(6): p. 1911-1918.
285. Holthoff, H., et al., *Coagulation rate measurements of colloidal particles by simultaneous static and dynamic light scattering*. Langmuir, 1996. **12**(23): p. 5541-5549.
286. Holthoff, H., et al., *Measurement of absolute coagulation rate constants for colloidal particles: comparison of single and multiparticle light scattering techniques*. Journal of colloid and interface science, 1997. **192**(2): p. 463-470.
287. Szilagy, I., et al., *Particle aggregation mechanisms in ionic liquids*. Physical Chemistry Chemical Physics, 2014. **16**(20): p. 9515-9524.
288. Birkner, F.B. and J.J. Morgan, *Polymer flocculation kinetics of dilute colloidal suspensions*. Journal (American Water Works Association), 1968: p. 175-191.
289. Swift, D.L. and S.K. Friedlander, *The coagulation of hydrosols by Brownian motion and laminar shear flow*. Journal of colloid science, 1964. **19**(7): p. 621-647.
290. Logan, B.E., et al., *Rapid formation and sedimentation of large aggregates is predictable from coagulation rates (half-lives) of transparent exopolymer particles (TEP)*. Deep Sea Research Part II: Topical Studies in Oceanography, 1995. **42**(1): p. 203-214.

291. Baalousha, M., *Aggregation and disaggregation of iron oxide nanoparticles: Influence of particle concentration, pH and natural organic matter*. Science of The Total Environment, 2009. **407**(6): p. 2093-2101.
292. Kocur, C.M., D.M. O'Carroll, and B.E. Sleep, *Impact of nZVI stability on mobility in porous media*. Journal of Contaminant Hydrology, 2013. **145**(0): p. 17-25.
293. Chatterjee, J., S. Abdulkareem, and S.K. Gupta, *Estimation of colloidal deposition from heterogeneous populations*. water research, 2010. **44**(11): p. 3365-3374.
294. Chatterjee, J. and S.K. Gupta, *An agglomeration-based model for colloid filtration*. Environmental Science & Technology, 2009. **43**(10): p. 3694-3699.
295. Chen, K.L. and M. Elimelech, *Aggregation and deposition kinetics of fullerene (C60) nanoparticles*. Langmuir, 2006. **22**(26): p. 10994-11001.
296. Chen, K.L. and M. Elimelech, *Influence of humic acid on the aggregation kinetics of fullerene (C 60) nanoparticles in monovalent and divalent electrolyte solutions*. Journal of Colloid and Interface Science, 2007. **309**(1): p. 126-134.
297. Wang, X., et al., *Cotransport of multi-walled carbon nanotubes and titanium dioxide nanoparticles in saturated porous media*. Environmental Pollution, 2014. **195**: p. 31-38.
298. Xu, S., B. Gao, and J.E. Saiers, *Straining of colloidal particles in saturated porous media*. Water Resources Research, 2006. **42**(12).
299. Bradford, S.A., S. Torkzaban, and J. Simunek, *Modeling colloid transport and retention in saturated porous media under unfavorable attachment conditions*. Water Resources Research, 2011. **47**(10).
300. Phenrat, T., et al., *Aggregation and sedimentation of aqueous nanoscale zerovalent iron dispersions*. Environmental Science & Technology, 2007. **41**(1): p. 284-290.
301. Baalousha, M., et al., *The concentration-dependent behaviour of nanoparticles*. Environmental Chemistry, 2015. **13**(1): p. 1-3.
302. Han, Y., et al., *Transport, retention, and long-term release behavior of ZnO nanoparticle aggregates in saturated quartz sand: Role of solution pH and biofilm coating*. Water research, 2016. **90**: p. 247-257.
303. Goldberg, E., et al., *Critical assessment of models for transport of engineered nanoparticles in saturated porous media*. Environmental science & technology, 2014. **48**(21): p. 12732-12741.
304. Corkhill, C.L., et al., *Real-Time Gamma Imaging of Technetium Transport through Natural and Engineered Porous Materials for Radioactive Waste Disposal*. Environmental science & technology, 2013. **47**(23): p. 13857-13864.
305. Bridge, J.W., S.A. Banwart, and A.L. Heathwaite, *Noninvasive quantitative measurement of colloid transport in mesoscale porous media using time lapse fluorescence imaging*. Environmental science & technology, 2006. **40**(19): p. 5930-5936.
306. Bridge, J.W., S.A. Banwart, and A.L. Heathwaite, *High-resolution measurement of pore saturation and colloid removal efficiency in quartz sand using fluorescence imaging*. Environmental science & technology, 2007. **41**(24): p. 8288-8294.
307. Bridge, J.W., A.L. Heathwaite, and S.A. Banwart, *Measurement of colloid mobilization and redeposition during drainage in quartz sand*. Environmental science & technology, 2009. **43**(15): p. 5769-5775.
308. Ramanan, B., et al., *Investigation of nanoparticle transport inside coarse-grained geological media using magnetic resonance imaging*. Environmental science & technology, 2011. **46**(1): p. 360-366.

309. Roth, E.J., B. Gilbert, and D.C. Mays, *Colloid deposit morphology and clogging in porous media: Fundamental insights through investigation of deposit fractal dimension*. Environmental science & technology, 2015. **49**(20): p. 12263-12270.
310. Byron, M.L. and E.A. Variano, *Refractive-index-matched hydrogel materials for measuring flow-structure interactions*. Experiments in fluids, 2013. **54**(2): p. 1-6.
311. Bianco, C., T. Tosco, and R. Sethi, *A 3-dimensional micro-and nanoparticle transport and filtration model (MNM3D) applied to the migration of carbon-based nanomaterials in porous media*. Journal of Contaminant Hydrology, 2016. **193**: p. 10-20.
312. Kanel, S.R., et al., *Two dimensional transport characteristics of surface stabilized zero-valent iron nanoparticles in porous media*. Environmental Science & Technology, 2007. **42**(3): p. 896-900.
313. Comba, S. and J. Braun, *An empirical model to predict the distribution of iron micro-particles around an injection well in a sandy aquifer*. Journal of Contaminant Hydrology, 2012. **132**(0): p. 1-11.
314. Šimunek, J., et al., *The HYDRUS-1D software package for simulating the one-dimensional movement of water, heat, and multiple solutes in variably-saturated media, version 4.08*. University of California, Riverside, Dept. of Environmental Sciences HYDRUS Software Series, 2009. **3**: p. 330.
315. Šimunek, J., M.T. van Genuchten, and M. Šejna, *Recent Developments and Applications of the HYDRUS Computer Software Packages*. Vadose Zone Journal, 2016. **15**(7).
316. Langevin, C.D., et al., *SEAWAT Version 4: A computer program for simulation of multi-species solute and heat transport*. 2008, (No. 6-A22) Geological Survey (US).
317. Clement, T.P., *A Modular Computer Code for Simulating Reactive Multispecies Transport in 3-Dimensional Groundwater Systems*. The U.S. Department of Energy, 1997: p. 1-59.
318. Bedekar, V., et al., *MT3D-USGS version 1: A US Geological Survey release of MT3DMS updated with new and expanded transport capabilities for use with MODFLOW*. 2016, US Geological Survey.

## Chapter 2

# 2 Parameterisation and Prediction of Nanoparticles Transport in Porous Media: a Reanalysis using Artificial Neural Network



### 2.1 Chapter overview

#### 2.1.1 Scope

In addressing one of the main challenges for effective use of continuum models, i.e., predictivity, this chapter establishes a way for predicting continuum model parameters, and also tries to identify important experimental factors through extensive sensitivity analysis. This chapter has been published as the following paper and is reproduced with permission from Wiley:

“Babakhani, P.; Bridge, J.; Doong, R.-a.; Phenrat, T., Parameterization and prediction of nanoparticle transport in porous media: A reanalysis using artificial neural network. *Water Resour. Res.* 2017, 53, 4564-4585.”

### **2.1.2 Abstract**

The continuing rapid expansion of industrial and consumer processes based on nanoparticles (NP) necessitates a robust model for delineating their fate and transport in groundwater. An ability to reliably specify the full parameter set for prediction of NP transport using continuum models is crucial. In this chapter a reanalysis is performed on a dataset of 493 published column experiment outcomes together with their continuum modelling results. Experimental properties were parametrized into 20 factors which are commonly available. They were then used to predict 5 key continuum model parameters as well as the effluent concentration via artificial neural network (ANN)-based correlations. The Partial Derivatives (PaD) technique and Monte Carlo method were used for the analysis of sensitivities and model-produced uncertainties, respectively. The outcomes shed light on several controversial relationships between the parameters, e.g., it was revealed that the trend of  $K_{att}$  with average pore water velocity was positive. The resulting correlations, despite being developed based on a ‘black-box’ technique, (ANN), were able to explain the effects of theoretical parameters such as critical deposition concentration (CDC), even though these parameters were not explicitly considered in the model. Porous media heterogeneity was considered as a parameter for the first time, and showed sensitivities higher than those of dispersivity. The model performance was validated well against subsets of the experimental data and was compared with current models. The robustness of the correlation matrices was not completely satisfactory, since they failed to predict the experimental breakthrough curves (BTCs) at extreme values of ionic strengths.

## **2.2 Introduction**

The rapid development of nanotechnology is identified as sufficiently remarkable as to be comparable with the industrial revolution [1]. A comprehensive evaluation of the fate and transport of engineered nanoparticles (NP) is pivotal to enable robust prediction and management of nanoparticulate materials in environmental matrices.

One of the endpoints of the NP life cycle is the subsurface soil and thereby groundwater [2]. Nanoparticles can be introduced into groundwater unintentionally from various sources during manufacturing/application/disposal stages; or they may be injected intentionally in applications such as *in situ* groundwater remediation or recovery enhancement of oil and gas reservoirs [3-5].

Diversity of the subsurface conditions on the one hand and variations in the characteristics of NP on the other limits the success of many current models in predicting the transport of NP. The ongoing development of hybrid NP with various architectures and coatings makes it inefficient to develop a specific model for each individual type of NP, suggesting the need for developing a robust model that can capture the transport behaviour of as many types of NP as possible [6-9]. To date, the most widely-used theory to predict the transport of NP and colloids has been the clean-bed (or classical) colloid filtration theory (CFT) [10-13]. However, models based on CFT still find it challenging to take into account the physical retention (straining) of colloid [14-16], heterogeneity in the colloid population [17, 18], and heterogeneity in the surface chemistry [19-21]. Its application when several transport phenomena occur simultaneously is under question.

Continuum-based models can describe the transport of NP in porous media when various mechanisms are involved concurrently and across various scales, provided that conceptual models of various transport phenomena can be defined and validated properly in the mathematical framework [13, 22, 23]. These models are construed as partial-differential equations developed based on the mass or particle number balance [13, 23]. The drawback in using continuum models is that the model parameters cannot be simply estimated and necessitate the output data of continuum models to be fitted against a set of experimental or field data which may not be available [13, 24, 25]. Efforts to predict individual parameters of continuum model via regression analysis and/or mechanistic approaches, e.g., estimating attachment rate coefficient [26], site-blocking or straining parameters, have been very limited [14, 27-31]. Furthermore, the effects of many experimental and environmental factors such as soil heterogeneity and dispersivity on the continuum model parameters are still unknown.

Recently, Goldberg et al. [24] used a machine learning technique known as ‘random forest ensemble’ to find the most important environmental parameters in

retention of NP transport. Although the outcomes of their paper provide very useful insights into the retention behaviour of NP in porous media, they are limited to regression analysis of retained fraction and retained mass profiles of NP in porous media. The artificial neural network (ANN) is a powerful algorithm which emulates the processing system of the human brain in terms of the structure and interactions of neurons with the information signals [32-36]. This concept, which was originally proposed in 1940s by McCulloch and Pitts [37], has been introduced as a versatile and universal tool for function approximation problems, especially in non-linear systems, where other mathematical/mechanistic techniques are difficult to implement [32, 38, 39]. In spite of extensive applications in the fields of environmental, hydrology, and civil engineering over several decades [32, 34], ANN is still relatively untested in colloidal transport problems. Particularly, a direct application of ANN to simulate or analyse data related to the transport of NP in porous media has not been reported thus far, although it has been applied for the transport of other contaminants such as nitrate [40]. ANN is categorized as a ‘black-box’ model because it is difficult to draw any conceptual relationship between the mathematics of the model and the underlying physical phenomena. Nevertheless, various sensitivity analysis techniques have been developed in order to gain insight into the influence of input variables on the ANN outputs [34, 35, 41, 42]. For instance, Gevrey et al. [41] assessed seven methods for the sensitivity analysis of ANN in ecological systems and found that the ‘Partial Derivatives’ technique (PaD) is the most useful and stable method [34, 35, 41].

The goal of the present study is two-fold. First, an ANN-based code is developed comprising PaD and Monte Carlo methods to analyse continuum-model parameter sensitivities and uncertainties in respect of 20 experimental or environmental factors that may influence the transport of NP in porous media in 493 separate experiments published in more than 50 peer-reviewed studies. Second, the ability of the ANN-based correlation matrices to independently predict the continuum-model parameters is investigated. If the final correlation matrices are successful in predicting model parameters, they can be easily used to estimate the major parameters of continuum models based on NP characteristics and transport conditions that are known or simply measurable. This would mitigate the need for parameter calibration of the continuum model in future column transport studies. To the best of the authors’ knowledge, this is the first time such a thorough modelling, sensitivity, and uncertainty analysis has

been conducted on the continuum-model parameters associated with a wide variety of environmental/experimental factors.

### 2.3 Dataset and parametrization

Data for NP extracted for comprising silver (AgNP), nanoscale zero valent iron (NZVI), Fe<sub>3</sub>O<sub>4</sub>, hydroxyapatite (HAp), graphene and graphene oxide (GO), cerium dioxide (CeO<sub>2</sub>), TiO<sub>2</sub>, zinc oxide (ZnO), quantum dots (QDs), latex, silica, aluminium oxide (Al<sub>2</sub>O<sub>3</sub>), and boehmite NP. All the parameters together with their statistics, and ranges are given in Table 2.1. The parameters for which the data were collected were in two groups: 1) modelling parameters that result from fitting the continuum model to experimental breakthrough and/or retention profile data; and 2) all the possible factors that could be feasibly measured from the experimental or real environmental properties without relying on current theories and without the need for performing any major experiment.

The required data for the first group of parameters, i.e., modelling parameters, were gathered for the attachment rate constant,  $K_{att}$ , (1/h) was common among all of these models. Other most common parameters were the detachment rate constant,  $K_{det}$ , (1/h), the maximum retained-particle phase concentration or colloidal retention capacity,  $S_m$ , (mg/g), and the empirical depth-dependent retention parameter,  $\beta$ , [—]. Investigations were also extended to the second attachment rate constant,  $K_{att_2}$  (1/h), representing the second site attachment rate. The second group of parameters - hereafter termed 'factors' - includes aqueous phase ionic strength (IS), pH, zeta-potential of particle and porous media surfaces, NP coating and free-polymer concentrations, input NP concentration, dimensions of the porous medium (column length and diameter), average pore water velocity, grain diameter, porosity, dispersivity, heterogeneity, number of injected pore volumes (PV), particle diameter, particle density, aspect ratio of NP, the pH of isoelectric point (or point of zero charge pH), and saturation magnetization. Note that in order to consider both negative and positive values of zeta potential, in a consistent trend, zeta potential data were normalized by the minimum of their range, as explained in Table 2.1.

The dataset mostly included saturated porous media — only in one paper the porous media was unsaturated [43] which involved undisturbed soil with ~90%

saturation degree. The temperature of experiments had to be close to 25 °C. A criterion was applied that the fitting  $R^2$  for continuum modelling parameters had to be at least 0.7 in order to incorporate the data of that modelling study. The isoelectric pH (IEP) or the pH of zero charge (PZC) were rarely reported in the given papers and therefore the same value was assumed for all data of each type of NP according to other literature sources given in Table E1. It is difficult to put the data of ionic strength (IS) from various studies together into the model as a single parameter because of the diversity in the ionic compositions. In this study, IS data were synchronized for various ionic species by drawing linear correlations between various ionic species. For this purpose, the dataset was first divided based on the different ionic compositions and tried to seek linear correlations between IS data of each ionic species with  $K_{att}$  as the most representative parameter of NP transport. In this way, linear correlations were achieved for the data of NaCl, CaCl<sub>2</sub>, NaHCO<sub>3</sub>, KNO<sub>3</sub>, and MgSO<sub>4</sub>, with correlation coefficients ranging from 0.42 to 0.93 (Table E2). Although these linear correlations were not very strong, they could be useful for pre-treatment of IS data since they were also statistically significant based on Fisher F test (Table E2) [44]. Eventually, based on these linear correlations, the IS values of CaCl<sub>2</sub>, NaHCO<sub>3</sub>, KNO<sub>3</sub>, and MgSO<sub>4</sub> were scaled to the IS values of NaCl which was afterwards used as input to the ANN modelling and extended to other model parameters as well. Other ionic compositions which did not show a linear relationship with  $K_{att}$  were involved in the IS data without any specific treatment. These species were NaNO<sub>3</sub>, Ca(NO<sub>3</sub>)<sub>2</sub>, NaClO<sub>4</sub>, and KCl which comprised less than 13 % of the dataset.

The outliers in the dataset were identified via statistical techniques such as box plot and the Grubbs test [45, 46]. However, in order to prevent the loss of important data only certain outliers were removed or replaced that could be evidently true anomalies, e.g., a case that had been measured with a completely different technique than others in that family [47, 48]. After this stage, the percentage of missing data compared to the whole dataset of input variables was 6.5 %. This missingness mostly involved the dispersivity parameter — 3.0 % of the whole dataset or 60 % of the expected data for this parameter (Table 2.1). Therefore, a separate ANN network was developed to predict the missing data of dispersivity and also for future modelling purposes via the available data. This was accomplished by assuming dispersivity to be dependent on six factors including (1) column length, (2) column diameter, (3) average pore water

velocity, (4) heterogeneity, (5) porosity, and (6) grain diameter [49-52]. In order to avoid losing the effective dataset, the rest of gaps in the data for experimental conditions parameters were imputed with the average of the available data for each parameter. This may not affect the overall result of ANN modelling significantly, because the total percentage of missing data was low (3.5 %). Among these data gaps, the maximum missing rate was 31 % associated with the grain zeta-potential, followed by 12 % for particle zeta-potential, and 10 % for adsorbed coating concentration (Table 2.1). These missingness rates might not be significant because a missingness rate of 73 % or more for each parameter has been common in the literature [53]. It should be noted that there were also missingness in the data of predicted parameters, including  $K_{det}$ ,  $S_m$ ,  $\beta$ , and  $K_{att_2}$ . However, eliminating these gaps did not lead to significant loss in the dataset. Finally, the used dataset for  $K_{att}$  and  $C/C_0$  was 493 cases while for  $K_{det}$ ,  $S_m$ ,  $\beta$ , and  $K_{att_2}$  it was reduced to 200, 286, 214, and 186 cases, respectively.

The heterogeneity of the soil texture is an important factor in the transport of NP in porous media [54]. Nevertheless, there has not been any simple robust systematic definition of porous media heterogeneity in the context of particle transport so that it can be considered as a parameter in continuum models. Parameters such as permeability or tortuosity which have not been considered in this study, due to the lack of sufficient data in the literature, and parameters like porosity and grain size which have already been included as independent experimental factors altogether cannot take into account the impact of variations in the soil texture and surface properties on NP interactions with porous media. Thus, in the scope of this study it is necessary to develop a stand-alone parameter to represent media heterogeneity. Given the available information in the literature about the effective heterogeneities that affect the transport of NP at the continuum scale, and considering the practical purpose of current modelling study, a rough categorization of porous media types is assumed in order to define a unified heterogeneity parameter. This conceptualization of the unified heterogeneity parameter and the resultant formula are merely simplifications based on a rationale that mainly considers the spatial variability of the porous media surface properties as opposed to the heterogeneity of the hydraulic conductivity (flow). This is based upon a series of intuitive assumptions imposed by the type of porous media, e.g., the nature of the soil sample (clean or treated laboratory porous media, disturbed, and undisturbed), grain coating, and grain size distribution. In doing so, porous media

containing only glass beads was assumed to have the minimum heterogeneity (0.0 %) compared to other possible types of porous media and the porous media consisting of undisturbed natural soil was assumed to have the highest heterogeneity (100 %). Then three categories were considered between 0.0 % and 100 % heterogeneity.

The first category, clean sand, was considered in the range of 10 % to 20 % heterogeneity, attributing the heterogeneity for typically-washed sand as 15 %. The second class was assumed for coated sand in the range of 20 % to 60 % heterogeneity, depending on the concentration of porous media coating or the proportion of coated sand to uncoated sand, compared to the case of typical clean sand. The third class of heterogeneity, i.e., disturbed soil samples, was considered in the range of 60 % to 90 % depending on clay, silt and sand contents of the soil. The degree of the heterogeneity in the latter category was considered based on the following assumptions. First, a uniform soil consisting of similar proportions of the sand, clay and silt contents was considered with a heterogeneity degree close to the middle of this category, i.e., 75 %. Second, increase in the amount of the clay was considered to enhance the degree of heterogeneity because of the high surface area and highly asymmetric clay platelet, and amphoteric behaviour of the edges, i.e., having both positive and negative charges for the same geochemical conditions, which leads to ambivalent interactions with nanoparticles at the same time [55-60]. Furthermore, the greater the differences in the boundaries of the size range, the higher the heterogeneity. As such, a soil consisting of 50 % clay and 50 % sand should be considered more heterogeneous than a soil containing 50 % silt and 50 % sand. These equivocal impacts need to be expressed using a simple formulation to estimate the heterogeneity factor for the soil category so that it can be useable to estimate the heterogeneity consistently within large datasets such as that used in the present study. Considering aforementioned assumptions and using data for  $K_{att}$ , the following formula was developed to estimate the degree of heterogeneity in the disturbed soil category which is within the range of 60 % to 90 %:

$$\Theta = 60 + 6 \left( \frac{1}{2} \frac{P_{Cl}}{P_{St} + P_{Cl}} + \frac{1}{2} \frac{P_{Cl}}{P_{Cl} + P_{St} + P_{Sd}} + \frac{1}{2} \frac{P_{St}}{P_{Sd} + P_{St}} + 3 \frac{P_{Cl} + P_{St}}{P_{Cl} + P_{St} + P_{Sd}} + \frac{P_{Cl} \times P_{Sd}}{(P_{Cl} + P_{St}) \times (P_{St} + P_{Sd})} \right) \quad (2.1)$$

where  $\Theta$  is the estimated heterogeneity in this range (%),  $P_{Cl}$ ,  $P_{St}$ , and  $P_{Sd}$  are the percentages of clay, silt, and sand in the soil, respectively. The ternary plot of the heterogeneity parameter in the soil subcategory is sketched in Fig. 2.1, and for practical

purposes and comparison, it is overlain by the "USDA Soil Texture Triangle", a classification which has been used for soil texture in other contexts [61-63]. Table E3 shows the variations of  $\theta$  or heterogeneity in the range of 60-90 % for different amounts of clay, silt and sand. According to this relationship, the maximum possible heterogeneity for disturbed soil (90 %) will be obtained for a soil with 99.9 % clay and 0.1 % sand and the minimum heterogeneity of the soil category, 60.0 %, is obtained for a soil with 99.9 % sand and 0.1 % silt. This minimum value of heterogeneity increases to 64.5% when the proportions of clay and silt change to 0.05 % and 0.05 %, respectively, and further increases to 69.0 % when clay and silt contents are 0.1 % and 0.0 %, respectively. The diagram of this categorization of heterogeneous porous media is given in Fig. E1 in the Appendix E. It should be noted that there are other types of heterogeneities such as micro- and nano-surface roughness heterogeneities [13, 64, 65] as well as other similar concepts such as immobile zone [13, 65] that might be counted as heterogeneity. These are not considered here due to the lack of sufficient information in the current literature. It is believed that a unifying approach for conceptualization of the heterogeneity parameter in sequential ranges is more efficient and flexible than considering different types of heterogeneities, each as an individual parameter, and it is also potentially more powerful when it comes to the comparison of sensitivities among 20 experimental factors.

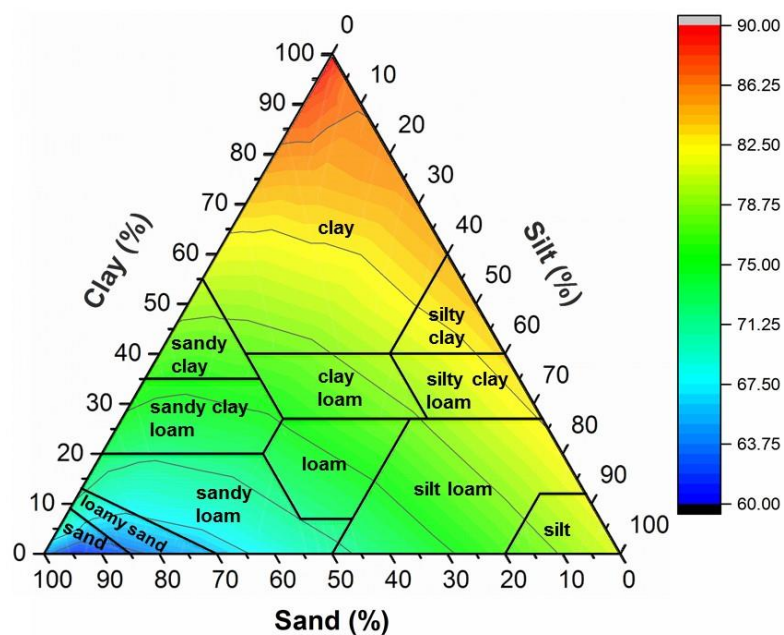


**Figure 2.1** Ternary plot of heterogeneity parameter for the category of disturbed soils (range of 60 to 90% heterogeneity) based on different amounts of clay, silt and sand. The plot is overlain by the ‘USDA Soil Texture Triangle’. The colour bar represents the heterogeneity values which are determined by Eq. 2.1.

**Table 2.1** List of the two groups of parameters, modelling parameters and experimental/environmental properties.\*

Abbr.	Description and unit	Min	Max	Mean	Missing Rate (%)	Note
<b>Free Pol. Conc.</b>	Free-polymer conc. (mg/L) if cotransport	$1 \times 10^{-7}$	$1 \times 10^4$	97	7.3	The concentration of various polymers (e.g., NOM, surfactant, protein) in the stock dispersion of nanoparticles
<b>Zeta_ NP</b>	Zeta potential of nanoparticles (mV)	$1 \times 10^{-2}$	$1.1 \times 10^2$	44	11.6	All values are offset (added) by the absolute min of data, -72 mV.
<b>d<sub>p</sub></b>	Hydrodynamic diameter of nanoparticles (average) (nm)	97	$3.9 \times 10^3$	$3.4 \times 10^2$	0.6	Mostly measured by Dynamic Light Scattering (DLS) or nanoparticle tracking analysis (NTA).

<b>Abbr.</b>	<b>Description and unit</b>	<b>Min</b>	<b>Max</b>	<b>Mean</b>	<b>Missing Rate (%)</b>	<b>Note</b>
<b>NP Dens.</b>	Density of nanoparticles (g/cm <sup>3</sup> )	1.1	10	5.6	0.0	Density of the bulk material of NP.
<b>C<sub>0</sub></b>	Injected concentration of NP slurry (mg/L)	1.6×10 <sup>-3</sup>	2.0×10 <sup>4</sup>	3.4×10 <sup>2</sup>	0.0	
<b>Col. Diam.</b>	Packed column diameter (cm)	6.6×10 <sup>-1</sup>	8.0	2.4	0.6	Inner diameter
<b>Col. Leng.</b>	Packed column length (cm)	3.0	50	15	0.0	
<b>Heterogen.</b>	Heterogeneity parameter (%)	1	1×10 <sup>2</sup>	32	0.0	Categorization soil heterogeneity for this parameter is thoroughly described in the text.
<b>d<sub>g</sub></b>	Size of porous media grains (average diameter) (mm)	8.7×10 <sup>-2</sup>	1.8	4.7×10 <sup>-1</sup>	0.0	Average grain size of natural soils was obtained by considering the size of clay, 0.002 mm, silt 0.002-0.064 mm and sand 0.064-2 mm.
<b>Zeta_Grain</b>	Zeta potential of porous media grains (mV)	1×10 <sup>-2</sup>	1.4×10 <sup>2</sup>	48	30.6	All values are offset (added) by the absolute min of data, -87 mV.
<b>Porosity</b>	Porosity of packed porous media	1.9×10 <sup>-1</sup>	5.7×10 <sup>-1</sup>	4.0×10 <sup>-1</sup>	2.8	
<b>Veloc.</b>	Pore water velocity (cm/min)	2.2×10 <sup>-3</sup>	18	1.4	0.0	
<b>Disp.</b>	Dispersivity (cm)	1.2×10 <sup>-3</sup>	1.6	2.8×10 <sup>-1</sup>	59.6	
<b>pH</b>	Acidity	3.0	11	6.8	3.9	
<b>IS</b>	Ionic strength (mM)	1×10 <sup>-2</sup>	7.9×10 <sup>2</sup>	29	2.6	The treatment of data is described in the text.
<b>PV No.</b>	Number of injected pore volumes into porous media [—]	1	1.2×10 <sup>2</sup>	11	0.0	In several studies it was estimated from the BTC. In cases where the injection was continuous the maximum number of PV used in the simulation (shown in the graph) was used.
<b>Aspect rati.</b>	Particle shape aspect ratio	1	3.8×10 <sup>3</sup>	1.5×10 <sup>2</sup>	0.6	Mostly calculated as the ratio of the hydrodynamic size to the

<b>Abbr.</b>	<b>Description and unit</b>	<b>Min</b>	<b>Max</b>	<b>Mean</b>	<b>Missing Rate (%)</b>	<b>Note</b>
						smallest reported dimension of the particles.
<b>Coat. Conc.</b>	Total average adsorbed coating concentration in the dispersion (mg/L)	$1 \times 10^{-7}$	$1.9 \times 10^2$	7.3	10.3	Mostly various polymers or in few cases Cu (in three of papers: Hosseini and Tosco, 2013; Wang et al., 2011; 2012). If the amount of adsorbed polymer was not clear, then half the total initial polymer concentration was assumed as free-polymer concentration and half as coating concentration.
<b>Sat. Magnet. et.</b>	Saturation magnetization (kA/m)	$1 \times 10^{-7}$	$5.7 \times 10^2$	73	0.0	It was assumed according to [66] as 570 kA/m for NZVI and 330 kA/m for $\text{Fe}_3\text{O}_4$ and for other NPs as zero.
<b>IEP</b>	Isoelectric point pH or alternatively point of zero charge (PZC)	1.9	9.4	6.0	0.0	Mostly obtained from other literatures as listed in Table E1.
<b>K<sub>att</sub></b>	Attachment rate constant parameter (1/h)	$1.3 \times 10^{-5}$	$2.1 \times 10^3$	76	NA	Only in one study it was assumed zero [67] because the applied model involved using the partition coefficient parameter.
<b>K<sub>det</sub></b>	Detachment rate constant parameter (1/h)	$1 \times 10^{-9}$	$3.7 \times 10^4$	$1 \times 10^2$	NA	
<b>S<sub>m</sub></b>	Maximum retained-particle phase concentration (mg/g)	$2.6 \times 10^{-8}$	$1 \times 10^9$	$4.1 \times 10^8$	NA	
<b>β</b>	Empirical depth-dependent retention parameter [—].	$1 \times 10^{-9}$	1.5	$2.0 \times 10^{-1}$	NA	
<b>K<sub>att2</sub></b>	Attachment rate constant parameter for the second attachment sites or the second	$1 \times 10^{-9}$	$3.8 \times 10^3$	76	NA	

Abbr.	Description and unit	Min	Max	Mean	Missing Rate (%)	Note
	transporting species (1/h)					
C/C <sub>0</sub>	Eluted mass (concentration) per injected mass (concentration) (%)	1×10 <sup>-1</sup>	1×10 <sup>2</sup>	58	NA	In general, the height of the BTC plateau at the middle of its width or the peak.

\* NA: not applicable

## 2.4 Artificial neural network modelling procedure

A three-layer configuration for the ANN model was adopted as it is commonly used in the literature [33, 35, 42]. These layers comprise an input layer, a hidden layer, and an output layer. Each of these layers is composed of a series of nodes (neurons) as illustrated in Fig. E2. Each node in the hidden layer receives signals (its input information) from all nodes of the input layer and each node in the output layer receives signals from all nodes of the hidden layer. These signals depend upon the strength of connections which are defined as weights and biases. These weight and biases are also known as the network structure and their values are initially unknown. They can be determined by fitting the network against any known dataset of interest which have both input and outputs sets. In this study, the inputs are defined as the 20 common factors identified within the literature data and the outputs against which the model is tested are the 5 key continuum model parameters plus the normalised effluent concentration. The model therefore operates by optimising hidden layer node weight-bias combinations against the input-output data of all the literature datasets consisting of up to 493 column experiment records. This procedure is called training of the network. Once these weights and biases are estimated, the network can be used for prediction of unknown outputs of a new dataset [33].

The number of nodes in the input layer and in the output layer are the same as the number of input and output variables in the dataset, respectively. The number of hidden-layer nodes, however, should be selected by trial-and-error in which the best fit in the training process is achieved while the number of hidden-layer nodes is kept

minimum [33, 38]. The training is performed with the Levenberg–Marquardt back-propagation learning algorithm for optimization of the weights and biases. Levenberg–Marquardt is a well-known, generic and efficient algorithm that is widely used for non-linear curve-fitting problems to minimize the errors between the given data and model-generated data in order to ascertain the parameters of the model [33, 35, 68]. Back-propagation is the way of calculating the propagation of errors from the output layer toward the input layer and forward the information from input layer toward the output layer [33, 38, 69]. This approach has been proved to be efficient and fast enough for most of the problems [32, 34, 35, 70, 71]. A thorough introduction to ANN was recently given by Yu et al. [33].

A potential defect in ANN analysis of sensitivity is the possibility of significant variation in the structure (weights and biases) of the trained network in different training times [34]. Furthermore, the optimum number of nodes in the hidden layer may change upon selecting various initial weights and biases. Although these variations may not affect the outputs of an established network, this hinders a deterministic analysis of sensitivity procedure [34]. Therefore, in this work the uncertainties imposed by the variation in the structure of the network on the outcomes of the sensitivity analysis are assessed through a Monte Carlo approach [72]. This was conducted using a MATLAB<sup>®</sup> (Mathworks, USA) code that (1) finds the optimum number of hidden layer neurons (in a range of 5 to 35 nodes) by iterating the training process in an inner loop, (2) conducts the analysis of sensitivity method of PaD on the optimized model as described in the Appendix E, (3) iterates all this procedure for 1000 times in an outer loop so that the average result of the sensitivities can be ascertained together with the relevant uncertainty statistics, and (4) finds the network with the best generalization to be presented in a spreadsheet for future predictions. The result of this uncertainty analysis performed on the sensitivity analysis approach is presented by calculating the 95 % confidence interval (CI) according to the 2.5<sup>th</sup> and 97.5<sup>th</sup> percentiles of the Student's t-distribution [72-74]. The details of the PaD method used for ANN sensitivity analysis along with further description of the uncertainty analysis and the validation of the code against artificial data are available in the Appendix E (Figs. E3).

## **2.5 Results and discussion**

### 2.5.1 General fitting results

Over 1000 iterations, the ANN was able to successfully find the relationships between the inputs and the outputs for each of five continuum model parameters with an average Nash-Sutcliffe goodness-of-fit  $R^2_{NS}$  ranging from 0.884 to 0.967— mean overall  $R^2_{NS}$  of 0.930 (Table 2.2). The standard deviations of these  $R^2_{NS}$  values were relatively low ( $< 0.03$ , Table 2.2), suggesting the uncertainties that can result from poor fitting in certain iterations of the sensitivity analysis runs are minor. The goodness of fitting, however, was not as high when  $C/C_0$  was considered as a direct predictable parameter from experimental factors (mean  $R^2_{NS} = 0.778$ , Table 2.2). Overall, these goodness-of-fit ranges are comparable with Nourani and Sayyah-Fard [35] carrying out ANN sensitivity analysis on daily evaporation data, where  $R^2_{NS}$  values were less than 0.9.

The numbers of optimum nodes which give the best fitting via the inner loop of the code were averaged over 1000 outer iterations. These figures were between 16 and 22 for different continuum parameters as well as  $C/C_0$  (Table 2.2). Standard deviations for these values, however, were between 5 to 6 (Table 2.2), indicating the change in the structure of the network may be significant and might therefore diversify the results of the sensitivity analysis even though the model is able to gain a consistent goodness-of-fit to the experimental data as mentioned above. Therefore, as noted in Section 3.1 the Monte Carlo approach was used to assess the uncertainties related to variable trained model structure. The outcomes, shown as error bars in Figs. 2.2 and 2.3, indicate that the ranges of variations in the sensitivity outcomes with 95 % CI are relatively small and do not preclude ranking of parameter sensitivities from high to low.

In the following sensitivity analysis results, since a series of 20 experimental/environmental factors are involved in the analysis, one may expect that if all factors were equally significant (a null hypothesis for this work), then each would have a relative sensitivity ( $RS$ ) of 5%. To generalise, if the number of input factors varies, then the baseline value and hence the ‘cut-off’ value for significance, would vary accordingly. For example, if 10 input factors were considered in an ANN model, then within this framework, the baseline significance is at 10%. Since the objective of this study is to identify the relative sensitivities, the omission of relatively low sensitive

factors in future modelling studies is not recommend. Yet, one may consider factors with  $RS$  below 2.5 % (50% of the baseline sensitivity) as insignificant. Further targeted work is required to establish the practical interpretation of such a threshold.

**Table 2.2** Fitting results and the number of optimum nodes obtained by ANN code for various continuum model parameters.

	$K_{att}$	$K_{det}$	$S_m$	$\beta$	$K_{att2}$	$C/C_0$
<b>Average <math>R^2_{NS}</math> (1000 simulations)</b>	0.884	0.886	0.967	0.954	0.958	0.778
<b>Standard deviations of <math>R^2_{NS}</math> (1000 simulations)</b>	0.03	0.03	0.01	0.02	0.03	0.03
<b>average optimum nodes (1000 simulations)</b>	21	17	16	19	18	22
<b>standard deviation of optimum node (1000 simulations)</b>	6	6	5	6	6	6
<b>best <math>R^2_{NS}</math> among 1000 simulations</b>	0.947	0.950	0.983	0.992	1.000	0.875
<b>corresponding node to the best <math>R^2_{NS}</math></b>	21	17	19	11	12	11
<b>best Generalization Efficiency (GE)</b>	0.93	0.96	0.98	1.01	1.02	0.89
<b>corresponding node to best GE</b>	25	13	14	10	18	24
<b>corresponding <math>R^2_{NS}</math> to the best GE</b>	0.913	0.902	0.971	0.950	0.967	0.830

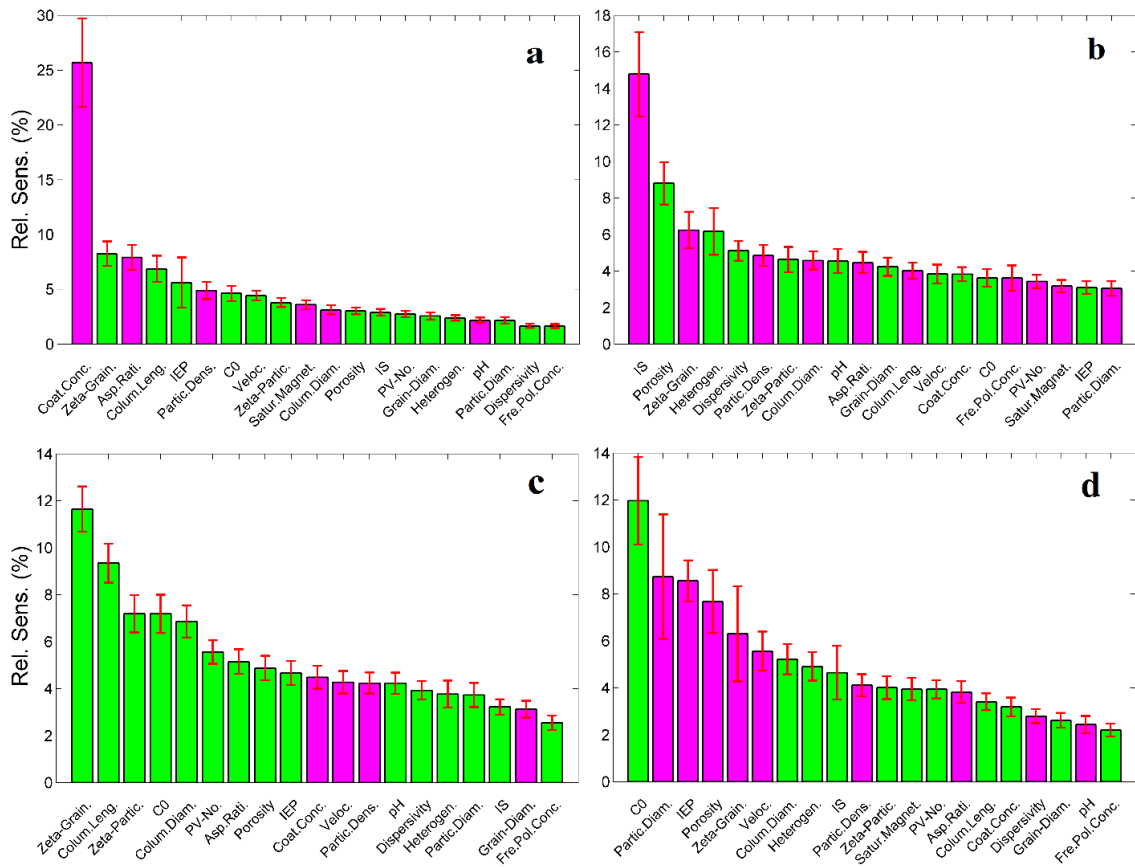


**Figure 2.2** Relative sensitivity outcomes for (a)  $K_{att}$ , (b)  $K_{det}$ , (c)  $S_m$ , and (d)  $\beta$ , with respect to experimental factors. In the case of  $S_m$ , saturation magnetization is excluded due to having no variation in the available data. Green-colored bars indicate positive correlation between input and output while magenta-colored bars indicate negative correlation. Error bars represent 95% confidence intervals on each sensitivity value over 1000 independent ANN model runs. The abbreviations are provided in Table 2.1.

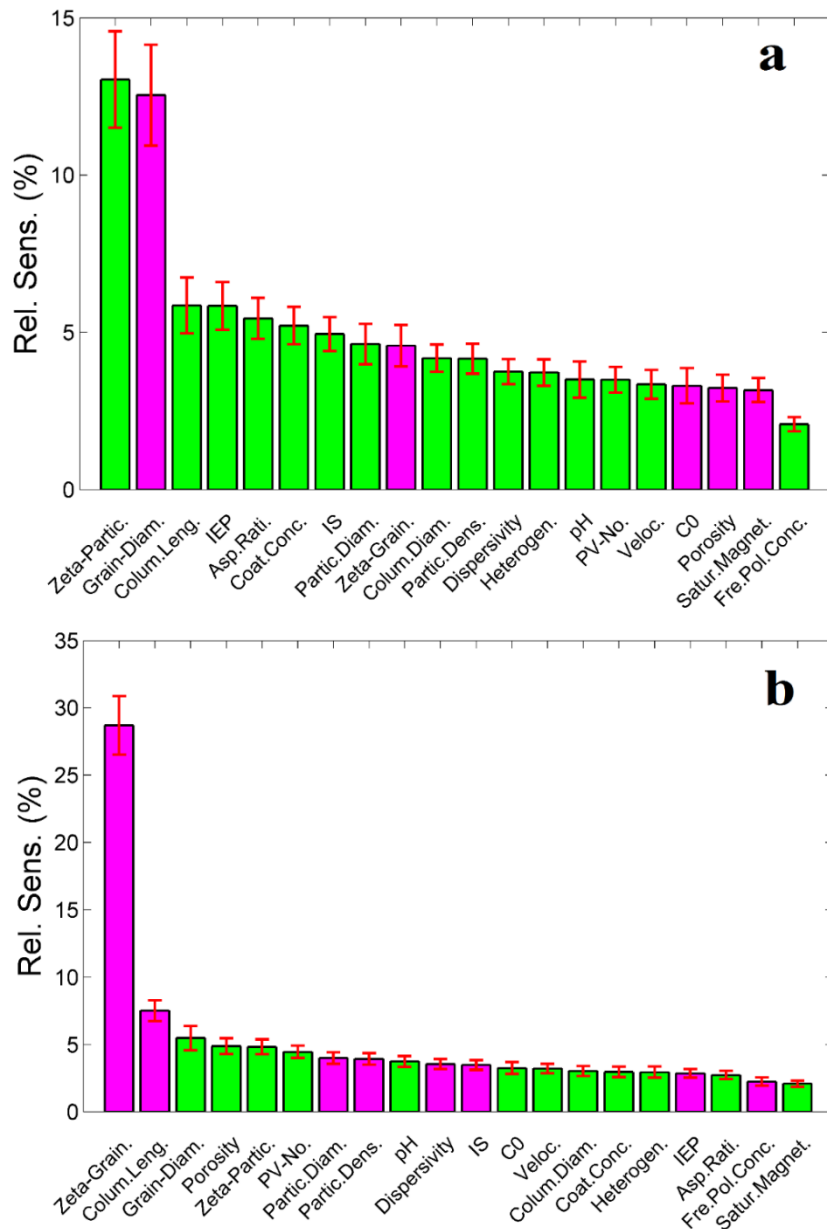


**Figure 2.3** Relative sensitivity outcomes for (a)  $K_{att2}$  and (b)  $C/C_0$  with respect to 20 experimental factors. Green-colored bars indicate positive correlation between input and output while magenta-coloured bars indicate negative correlation. Error bars represent 95 % confidence intervals. The abbreviations are provided in Table 2.1.

## 2.5.2 Model parameter sensitivity results

### 2.5.2.1 Sensitivity results for $K_{att}$

Figure 2.2a shows that  $K_{att}$  is more sensitive to surface -related factors, such as the coating concentration ( $RS = 25.7 \%$ ), grain zeta-potential ( $RS = 8.3 \%$ ), aspect ratio

of NP ( $RS = 7.9\%$ ), and isoelectric point (IEP) of NP ( $RS = 5.6\%$ ), rather than pore-scale factors, such as dispersivity ( $RS = 1.7\%$ ), heterogeneity ( $RS = 2.4\%$ ), and porosity ( $RS = 3.0\%$ ) (Table 2.3). The very high sensitivity of  $K_{att}$  to coating concentration, which is over three times higher than that of the next important factor, the grain zeta-potential, is in agreement with a large number of experimental studies emphasizing the crucial role of NP surface coating, which can be various polymers (e.g., NOM, surfactant, protein) or metal dopants such as Cu, in modifying the attachment of NP [75-80].

**Table 2.3** Sensitivity analysis outcomes, RS (%).

	$C/C_0$	$K_{att}$	$K_{det}$	$S_m$	$\beta$	$K_{att2}$
<b>Asp.Rati.</b>	2.7	-7.9	-4.5	5.2	-3.8	5.4
<b><math>C_0</math></b>	3.3	4.6	3.6	7.2	12.0	-3.3
<b>Coat.Conc.</b>	3.0	-25.7	3.8	-4.5	3.2	5.2
<b>Colum.Diam.</b>	3.0	-3.1	-4.6	6.9	5.2	4.2
<b>Colum.Leng.</b>	-7.5	6.9	-4.0	9.3	3.4	5.9
<b>Dispersivity</b>	-3.6	1.7	5.1	3.9	-2.8	3.8
<b>Fre.Pol.Conc.</b>	-2.2	1.6	-3.6	2.5	2.2	2.1
<b>Grain-Diam.</b>	5.5	2.6	4.2	-3.1	2.6	-12.5
<b>Heterogen.</b>	3.0	2.4	6.2	3.8	4.9	3.7
<b>IEP</b>	-2.9	5.6	3.1	4.7	-8.6	5.8
<b>IS</b>	-3.5	2.9	-14.8	3.2	4.6	4.9
<b>Partic.Dens.</b>	-3.9	-4.9	-4.8	-4.2	-4.1	4.2
<b>Partic.Diam.</b>	-4.0	2.2	3.0	3.7	-8.7	4.6
<b>pH</b>	3.7	-2.2	4.5	4.2	-2.4	3.5
<b>Porosity</b>	4.9	3.0	8.8	4.9	-7.7	-3.2
<b>PV-No.</b>	4.5	2.7	-3.4	5.6	3.9	3.5
<b>Satur.Magnet.</b>	2.1	-3.6	-3.2	NA	3.9	-3.2
<b>Veloc.</b>	3.2	4.4	3.8	-4.3	-5.6	3.3
<b>Zeta-Grain.</b>	-28.7	8.3	-6.2	11.6	-6.3	-4.6
<b>Zeta-Partic.</b>	4.8	3.8	4.6	7.2	4.0	13.0

NA: not applicable.

In contrast, the free-polymer concentration appeared to have the least contribution to the attachment rate of NP ( $RS = 1.6 \%$ , Table 2.3). Free polymer is known to affect the attachment rates in several potentially conflicting ways. Higher concentration of free polymer can elevate the viscosity of the fluid [81]; it can block the attachment surfaces in competition with NP [81, 82]; it can slow down the agglomeration process [75]; on the other hand, in the presence of divalent cations polymer bridging can bring about a substantial level of agglomeration and deposition [83-85]. The present result, which is obtained for a broad range of NP and polymer types, e.g., NOM, surfactant, and protein, with a mean concentration of  $\sim 100$  mg/L (Table 2.1), suggests that these four effects counterbalance each other over a range of conditions. However, the bridging mechanism influence appears still to be the dominant process, because based on this investigation the trend between free-polymer concentration and the attachment rate is positive rather than negative (Fig. 2.2a).

The aspect ratio of NP has a notable influence on the attachment rate ( $RS = 7.9 \%$ ) with a negative correlation. Thus far, only few studies have addressed the effect of aspect ratio on the transport behaviour of NP in porous media. It should be noted that here the aspect ratio is defined as the ratio of the major dimension length to the minor dimension length of the particle, or plate diameter to plate thickness [28] which is different from the use of this terminology in colloid filtration theory literature [e.g., 86] where it is interpreted as the ratio of particle to collector sizes. The reported trends for  $K_{att}$  with aspect ratio include a rising trend for latex microsphere (aspect ratio range of 1:1 to 3:1) [87], a decreasing trend for carboxylate-modified fluorescent polystyrene NP (aspect ratio range of 1:1 to 4:1) under the favourable attachment conditions, and an increasing trend under the unfavourable conditions [88]. Recently, [89] compared the retention of cylindrical NP (multiwalled carbon nanotubes) with spherical NP ( $C_{60}$ ) and observed that at low IS values ( $< 11$  mM) the spherical NP displayed a greater mobility than the cylindrical NP whereas at a higher IS (60 mM) the mobility of cylindrical NP was considerably higher than the spherical NP. In the present study which encompasses a broad range of aspect ratios from 1:1 to 1:3800 and also comprises the two-dimensional GO nanosheets, it appears that generally a higher aspect ratio results in a reduced attachment rate. This might be because of the reduced translational diffusion resulted from the higher aspect ratios of particles [90]. This can in turn decrease the mass transfer rate to the collector surface and thereby

reducing the attachment rate. Initial particle size, however, is far less sensitive ( $RS = 2.2\%$ ). This might be because of the fact that the real size of the NP aggregates that controls the attachment rate is different from the initial size because of the occurrence of agglomeration within porous media as discussed below.

Column length affected the attachment rate with  $RS = 6.9\%$ , and with a positive correlation. It is complicated to draw any conclusion about this relationship since a variety of retention behaviours might occur along the length of the porous media which may not only involve the attachment process but also involve other phenomena, such as straining, site blocking, size exclusion and agglomeration [14, 43, 64, 82, 91-100]. Agglomeration of NP in porous media has been widely neglected in modelling studies. However, assuming that the agglomeration of NP is significant, the longer length of the column may allow particles to agglomerate in sufficient time during their migration along the column length. This can in turn intensify their consequent retention rates since the larger sizes of NP come with deeper energy minimum wells and therefore higher retention rates [75, 101, 102] as well as higher chance for straining as described in detail in Chapter 1.

An increase in average pore water velocity causes a rise in  $K_{att}$  ( $RS = 4.4\%$ ). This agrees well with CFT which suggests an increase in velocity promotes the mass transfer rate between the aqueous and attached phases whereby enhancing the attachment rate [10, 12, 64]. This trend, however, contradicts with the study of Seetha et al. [26]. In the broad experimental data of NP transport used in this study, it is hard to figure out a linear or log linear model fit between velocity and  $K_{att}$  data. A log linear fit between the logarithm transformed data of pore water velocity and  $\text{Log } K_{att}$  shows a poor correlation coefficient of 0.2 (Fig. E4). This line still demonstrates a positive slope (0.72) between the two variables. Therefore, here it is interesting to use the final ANN-based correlations, which will be discussed later, in order to compare the trend of predicted  $K_{att}$  versus pore water velocity with correlations of other studies. The empirical correlations of Seetha et al. [26] were used for  $K_{att}$  and collector efficiencies of [75] and [86] to calculate  $K_{att}$  based on CFT. As shown in Fig. 2.4, in the empirical model of Seetha et al. [26],  $K_{att}$  decreases with velocity by a slope of -272. However, according to the correlations of the present study,  $K_{att}$  increases with the velocity with a slope of 106.7. This is in agreement with the trend based on the correlations of [86]

yielding a positive slope of 440.0 and is also consistent with that of [75] which yields a low positive slope of 0.76.

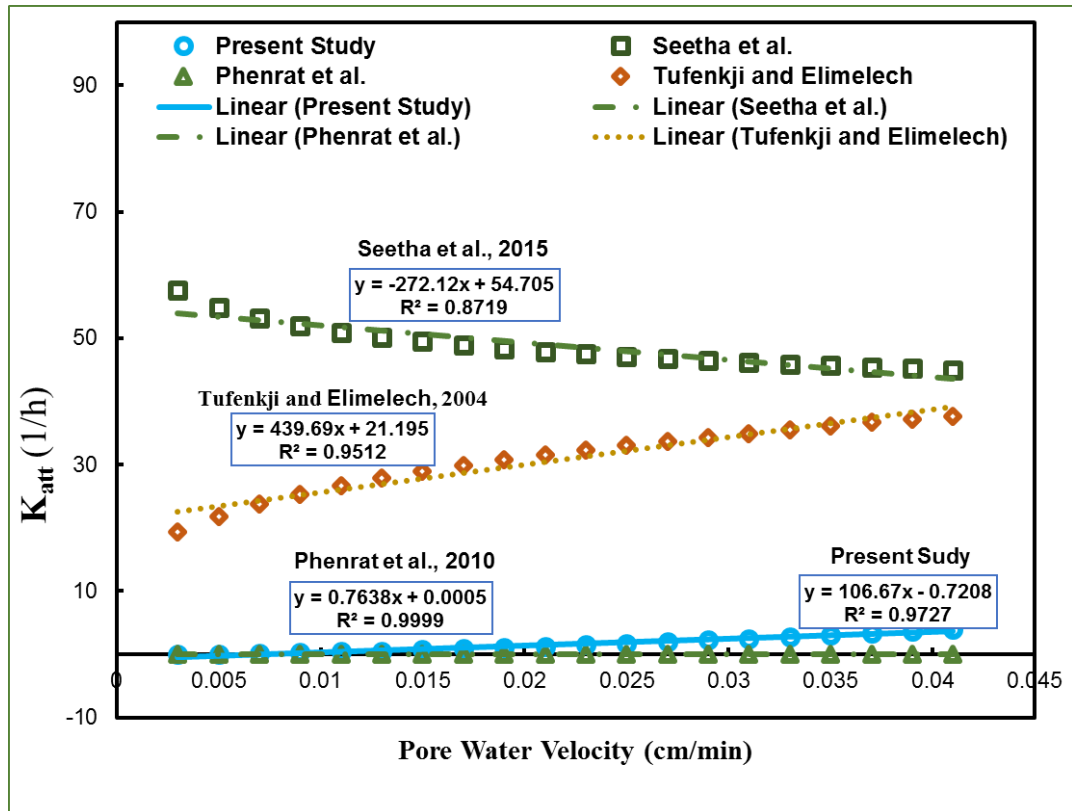


**Figure 2.4** Relationship between  $K_{att}$  and the pore water velocity obtained from the final model of the present study, Seetha et al. [26], and CFT, the collector efficiencies of which were obtained based on the correlations of [75] or [86]. The input data for the pore water velocity were artificially generated in regular intervals and the rest of the input data were mostly selected similar to [102]. These data were mostly in the ranges of simulated values in Seetha et al. [26], except for Peclet number range which was extended to values above 50 when the velocity increased to more than 0.015 cm/min. The parameter values used here are: free-polymer concentration 0 mg/L, particle zeta potential -30 mV, and grain zeta potential -50 mV, particle diameter 150 nm, grain diameter 0.15 mm, NP density 6.7 g/cm<sup>3</sup>, input concentration 200 mg/L, column diameter (Inner) 2 cm, column length 25.5 cm, heterogeneity 15 % (clean sand), porosity 0.33, dispersivity 0.015 cm, pH 5, IS 10 mM, injection duration 1 PVs, aspect ratio 1, adsorbed coating concentration 1 mg/L, saturation magnetization 570 kA/m (assuming NZVI), IEP pH 6.3, and pore water velocity ranging from 0.003 to 0.039 cm/min. Extra parameters assumed in the correlations of Seetha et al. [26] include temperature 298 K, dynamic viscosity 0.89 mPa.S, and cylindrical pore constriction radius  $6.2 \times 10^{-5}$  m calculated based on grain size following [75]. Single collector attachment efficiency in the equation of [86] was assumed equal to one. The linear fittings are only for identifying whether the trends are increasing or decreasing.

Ionic strength and pH have been among the most well-studied parameters in the context of NP transport because of their significant impacts revealed under individual experimental outcomes [e.g., 64, 100, 103, 104]. However, the present analysis results shown in Figs. 2.2 and 2.3 indicate they are not among the most crucial factors controlling the attachment rate as the most important parameter of the continuum models. Figure 2.5 shows modelling trends of  $K_{att}$  versus IS determined by the ANN-based correlation of this study and by the correlations of Seetha et al. [26] and [86]. It is evident that the impacts of the critical deposition concentration (CDC) and probably the critical coagulation concentration (CCC) [105] are reflected in the modelled curves of this study and those of Seetha et al. [26]. The decrease in the slope of the curve is slightly less in the present correlation compared to that of Seetha et al. [26] and CDC might not be clearly distinguishable in the current study's results. It is reasonable because the current study's model considers multiple NP types which may display various CCC and/or CDC. This comparison further shows that considering IS versus  $K_{att}$ , a satisfactory overall agreement between the performances of this study's model with others is obtained in the ranges of parameters used in this figure (given in the caption of Fig. 2.5).

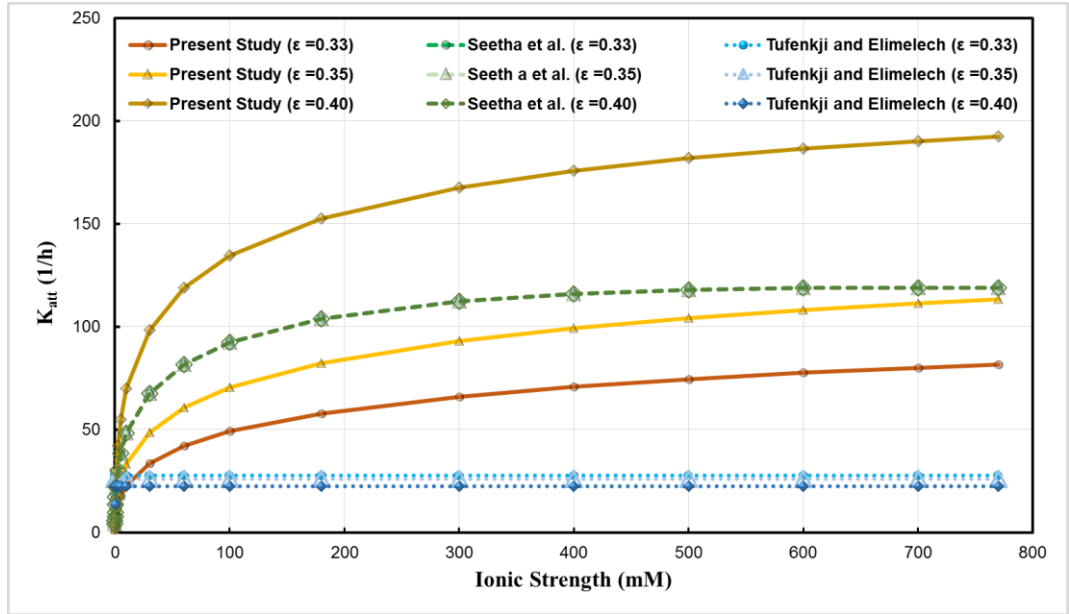


**Figure 2.5** Relationship between  $K_{att}$  and the IS obtained from the present study, and Seetha et al. [26], as well as CFT, the collector efficiencies of which were obtained based on the correlation of Tufenkji and Elimelech [86]. The data were selected in the ranges of simulated values in Seetha et al. [26], except for  $N_{E1}$  and  $N_{DL}$  that were partly out of range. Most of experimental conditions used resembled those of [103]. The parameter values are: free-polymer concentration of zero mg/L, particle zeta potential of -40 mV, and grain zeta potential -50 mV, particle diameter 150 nm, grain diameter 0.15 mm, NP density 3.2 g/cm<sup>3</sup>, input concentration 200 mg/L, column diameter (Inner) 2.6 cm, column length 20.2 cm, heterogeneity 15 % (clean sand), porosities 0.33, 0.35, and 0.4, pore water velocity 0.015 cm/min, dispersivity 0.02 cm, pH at 5, injection duration for 5 PVs, aspect ratio 5, adsorbed coating concentration 1 mg/L, saturation magnetization zero (kA/m), IEP pH 6.7, and IS values in range of 0.01 to 770 mM. Extra parameters assumed in the correlations of Seetha et al. [26] include temperature 298 K, dynamic viscosity 0.89 mPa.S, and cylindrical pore constriction radius  $6.2 \times 10^{-5}$  m calculated based on grain size following Phenrat et al. [75]. Single collector attachment efficiency in the equation of Tufenkji and Elimelech [86] was assumed equal to one. Lines in figure are plotted to guide eyes.

It should be noted that the low sensitivity of IS appears at odds with intuition based on major current concepts in colloid science, such as DVLO theory. One interpretation of the low sensitivity of  $K_{att}$  to IS is that the ranges of IS in the training dataset are dominated by values above the CCC and CDC values of major NP, after which attachment is less dependent or not dependent on the IS. Another possible interpretation is that the rate of attachment is more controlled by diffusion in the aqueous phase rather than the interaction energy minimum depth (controlled by IS),

because once NP arrive in the vicinity of the surface of the collector, they can be retained no matter how deep the secondary minimum depth is. On the other hand, the effects of detachment processes ( $K_{det}$ ) may mask the role of IS in attachment of NP, resulting in a less overall sensitivity for this factor in controlling  $K_{att}$  as appeared in the result of the present study.

In terms of pH, it appears that the point of zero charge (PZC) or IEP, which is also taken into consideration as a factor in the model, is  $\sim 2.5$  times more sensitive than pH (Table 2.3). Furthermore, from the experimental viewpoint change in the pH may correspond to a simultaneous change in the zeta potential. Therefore, it is possible that the effective role of pH in attachment rate is manifested in the model sensitivity results through IEP and zeta-potential rather than the pH itself. The ANN-based correlation trends, shown in Fig. E5 reveal that present correlation predictions for  $K_{att}$  is close to those of Phenrat et al. [75] when the saturation magnetization feature is considered non-zero, whereas they tend towards Tufenkji and Elimelech [86] predictions when the saturation magnetization is assumed zero. The correlations of Phenrat et al. [75] also consider the effect of particle magnetization while other current models do not. It might also suggest that when the particles are magnetic then the effect of solution chemistry on the attachment rate is less pronounced because magnetic forces overshadow the solution chemistry [75].

### 2.5.2.2 Sensitivity results for $K_{det}$

Figure 2.2b shows that the most important experimental factor in controlling the detachment rate is IS with  $RS = 14.8 \%$  and with a negative correlation, which is in agreement with other studies (Table 2.3) [e.g., 106, 107]. Detachment of the attached particles should be mostly controlled by the strength of the forces between attached particle and the solid surface. This strength is related to depth of the DLVO minimum energy well which is in turn associated with IS [108, 109]. This is consistent with previous results that IS has a significant impact on detachment even though it was not highly sensitive for  $K_{att}$ , since the depth of the DLVO energy minimum, is less important in determining the probability of entering it than of leaving it.

In contrast to the relatively low sensitivities obtained for factors representing the pore scale in the case of  $K_{att}$ , for  $K_{det}$  these factors, i.e., porosity ( $RS = 8.8 \%$ ), heterogeneity ( $RS = 6.2 \%$ ), and dispersivity ( $RS = 5.1 \%$ ), turned out to be among

the most sensitive parameters, all showing a positive correlation. For particles which are already immobilized on the surface of grains, these factors may be more important, because they represent variation in the number and accessibility of low shear, low flow and high-retention pore surface sites from which removal of particles by hydrodynamic forces may be difficult. [75, 110].

Grain zeta-potential is also one of most important factors ( $RS = 6.2\%$ ) contributing to detachment rate as was also the case for  $K_{att}$ . The sensitivities to other factors are rather similar, and are ranging from slightly below the baseline, i.e.,  $RS = 4.6\%$  for particle zeta-potential down to  $RS = 3\%$  for particle diameter.

### 2.5.2.3 Sensitivity results for $S_m$

$S_m$  represents the capacity of the porous media for retention of particles [98, 111]. Similar to the sensitivity results of  $K_{att}$  and  $K_{det}$ , here the grain zeta-potential ( $RS = 11.6\%$ ) is among the most sensitive factors along with the particle zeta-potential, ( $RS = 7.2\%$ ) (Fig. 2.2c and Table 2.3). According to this result when the zeta-potential increases (less negative), the capacity of the porous media to retain particles increases. High sensitivities are determined for factors related to the load of particles in porous media such as input concentration ( $RS = 7.2\%$ ) and the number of injecting PVs ( $RS = 5.6\%$ ) with a positive correlation—in agreement with elsewhere [64, 112]. The factors representing the available surface area such as column length, column diameter, aspect ratio, and porosity are also highly sensitive ( $RS$  ranging from  $4.9\%$  to  $9.3\%$ ) and show a direct relationship, which is in accordance with the underlying concept of  $S_m$  describing its capacity for retaining particles and also in agreement with Saiers et al. [98], mentioning a close correlation between the surface area and  $S_m$ .

Similar to the sensitivity results of  $K_{att}$ , here IS and pH are not among the most sensitive factors for  $S_m$  —  $RS$  is  $3.2\%$  and  $4.2\%$  for IS and pH, respectively. Elevated  $S_m$  with the IS has been attributed to microscopic or nanoscale surface heterogeneities since rising IS can screen the double layer and may therefore reduce the long range influence of these forces to below the influence range of microscopic heterogeneities [64, 65]. In the light of the present modelling results for  $S_m$ , which shows the highest sensitivities for the factors related to the mean surface electrostatic charge, i.e., grain and particle zeta-potentials, while demonstrating two- to four-folds lower sensitivity

for the IS, it is revealed that surface microscopic heterogeneities, even if important in triggering the IS-related influence on the  $S_m$ , are still far less relevant than the mean surface characteristics, such as zeta-potential, in controlling the capacity of the retention sites. This is also in line with the results of previous sections where  $K_{att}$  was moderately sensitive to IS whereas  $K_{det}$  was most sensitive to IS among all the experimental features, suggesting that this is the ionic strength and thereby the depth of the DLVO minimum that control the strength of the interfacial forces standing against the detachment of attached particles and not nano- and micro-scale surface heterogeneities. Furthermore, according to the present results, the sensitivity of  $S_m$  to velocity is slightly below the expected baseline sensitivity ( $RS = 4.3\%$ ) and velocity has an inverse relationship with  $S_m$  (Fig. 2.2c). This negative correlation is in complete agreement with the hypothesis that larger torques resulting from fluid shear can reduce the quantity of retention sites with interactions at the secondary minimum [26, 64, 102, 110], also indicating against the domination of microscopic heterogeneity over the secondary minimum interactions [64].

#### 2.5.2.4 Sensitivity results for $\beta$

The exponent of the depth-dependent retention model,  $\beta$ , determines the shape of particle spatial distribution in the packed column [14]. The depth-dependent shape of the residual concentration profile (RCP) has been the focus of many investigations relating the hyper-exponential behaviour of RCP to straining [e.g., 113, 114] or a non-monotonic behaviour of RCP to agglomeration [114]. For  $\beta = 0$  an exponential RCP is expected whereas for  $\beta > 0$  one expects either a hyper-exponential or uniform RCP shape.

Sensitivity analysis results for  $\beta$  (Fig. 2.2d and Table 2.3) show that the most sensitive factor affecting the retention behaviour of the NP is the influent concentration with  $RS = 12.0\%$  and a direct relationship. This opposes the outcomes of Raychoudhury et al. [97] reporting a minor influence of influent CMC-NZVI concentration (ranging from 1.085 to 1.7 g/L) on the retention via straining, whereas this agrees with several other studies [64, 113, 115, 116] highlighting the effect of injected concentration on the depth-dependent behaviour. Particle diameter is the second most important factor ( $RS = 8.7\%$ ) with a reverse association. This indicates the logic behind the use of particle-size to the grain-size ratio as a criterion for

identifying whether or not straining is an underlying phenomenon in transport of particles [16, 100, 117]. However, the trend of  $\beta$  with particle size does not match that developed for traditional colloids, the reason for which is not clear. Recently, the use of this criteria in NP transport studies was criticized due to the potential role of agglomeration in altering the particle size during the transport in porous media [118].

Porous media heterogeneity showed a direct relationship ( $RS = 4.9\%$ ) whilst dispersivity revealed a negative correlation ( $RS = 2.8\%$ ). These trends perhaps suggest that higher heterogeneity, e.g., with more angular retention sites, can induce hyper-exponential behaviour or straining whereas a flow regime with higher dispersivity gives more chance for detouring when the particles are going to be trapped in the contact angles in straining process.

### 2.5.2.5 Sensitivity results for $K_{att2}$

The results for the second site attachment rate are shown in Fig. 2.3a and Table 2.3. The sensitivity of  $K_{att2}$  to particle zeta potential and grain diameter was surprisingly high with  $RS = 13.0\%$  (positive correlation) and  $RS = 12.5\%$  (negative correlation), respectively. In contradiction to the results of previous modelling parameters, particularly those of  $K_{att}$ , where grain zeta-potential was mainly among the most important factors, here it is the particle zeta-potential that is the most sensitive one, the increase of which promotes attachment in second sites. In spite of the fact that the aim of incorporating  $K_{att2}$  in the continuum model is to capture the effect of secondary attachment sites, the conceptual model for using this parameter in the context of NP transport is not clear. Reinvestigating the relevant literature studies revealed that the common underlying phenomena reported by almost all of these papers [82, 83, 92, 116, 119-125] is agglomeration, although ripening and clogging have been reported as well [126, 127]. The current result clearly shows a high sensitivity to particle zeta-potential, the increase of which (less negative) causes higher degree of agglomeration [128, 129]. Interestingly, it matches the recently proposed model [101] in which the agglomeration model was linked with the continuum model through an additional first-order sink term which is mathematically similar to  $K_{att2}$ . Therefore, opposed to the proposed conceptual model for deploying  $K_{att2}$ , that is capturing the effect of secondary deposition sites, here it is evident that this factor had to be incorporated in models in order to represent the agglomeration effect on the transport of NP in porous

media. The underlying reason for the high influence of grain diameter in curbing  $K_{att2}$  is not clear. Yet, if the aforementioned conceptual model of agglomeration coexistence holds true, it suggests that agglomeration is more crucial for smaller grain diameters and thereby for narrower pore spaces than larger pore spaces. Future experimental studies are needed to confirm this hypothesis.

#### **2.5.2.6 Sensitivity results for $C/C_0$**

The sensitivity outcomes for normalized effluent concentration in respect of experimental factors are shown in Fig. 2.3b and Table 2.3. In this section the crucial role of grain zeta-potential in the fate and transport of NP become clearer since it displays the highest sensitivity ( $RS = 28.7\%$ ) among all the experimental factors. This sensitivity is around four times higher than the next-most important factor which is the filtration (column) length ( $RS = 7.5\%$ ). This is in line with the study of Goldberg et al. [24] which demonstrated by machine learning that there is a strong contribution of the zeta-potential in controlling the retained fraction of NP in porous media. Although for continuum model parameters the grain size was not among the most important factors, for  $C/C_0$  it turned out to be the third most sensitive factor ( $RS = 5.5\%$ ) with a positive correlation. The situation is similar for the porosity with  $RS = 4.9\%$  and a direct relationship with  $C/C_0$ , suggesting that after the surface charge and the filtration length, the dominant factors in controlling the transport of NP is the size of the pore space geometry. This is also in agreement with the study of Goldberg et al. [24] who found these factors moderately important. The load of particles, i.e., PV number and injecting concentration are also moderately important predictors of  $C/C_0$  with  $RS = 4.5\%$  and  $RS = 3.3\%$ , respectively, with positive correlations. Goldberg et al. [24] found these features even more important than the pore space geometry (porosity and grain diameter). Particle diameter is moderately sensitive ( $RS = 4.0\%$ ) and exhibits a negative correlation which is consistent with the current theories stating that larger deposition energy minima resulted from larger size cause less mobility. This is also in harmony with the concept of straining that larger particles have more chance of entrapment in grain-grain contact angles resulting in less mobility [14, 86, 101, 102].

The rest of parameters have relatively similar contribution to  $C/C_0$  with  $RS$  ranging from  $3.9\%$  down to  $2.7\%$ , except saturation magnetization with  $RS = 2.1\%$  and free-polymer concentration with  $RS = 2.2\%$ . The low sensitivity of free-polymer

concentration, which was also the case in the results of continuum modelling parameters discussed previously, suggests that the net contribution of this factor might not be significant in the fate and transport of NP in the environment, since it causes equivocal influences on the transport phenomena as described previously. These results opposes those of Goldberg et al. [24] reporting the highest importance for the NOM concentration while the lowest importance for coating.

### 2.5.3 Model validation

In this section I try to systematically validate the model predictions by comparing the performance of  $K_{att}$  predictions obtained via ANN with those resulted from [26] and CFT, the collector efficiencies of which was determined after [86] or [75]. In doing so, the data of polymer-modified NZVI transport in saturated column experiments were used from [101, 102] for which the parameters of all four empirical models, namely, the present study, [26], [86], and [75], were available. For this purpose, instead of randomly dividing the dataset into three categories of training, validation, and testing sets in the ANN modelling procedure I designated the data from [101, 102] as the validation set and the rest of the dataset as the training set (472 cases).

The results for this simulation are presented in Fig. 2.6, which shows that none of the current models are able to predict  $K_{att}$  in the range of parameters used here. In sharp contrast, the ANN derived model parameterisation can very closely predict the  $K_{att}$  values obtained from calibration of the continuum model. It should be mentioned that the best network matrices chosen among 1000 iterations of the sensitivity analysis procedure were incorporated in a spreadsheet which can be easily used as empirical model for future predictions of a wide range of the continuum transport parameters or  $C/C_0$  at the scale of column experiment. The dimensions of the coefficient matrices in this model are comparable with those of Seetha et al. [26]. This spreadsheet is presented as electronic supplementary materials along with the version of this chapter which is published as a paper in *Water Resources Research*, and is freely available from the journal's website.

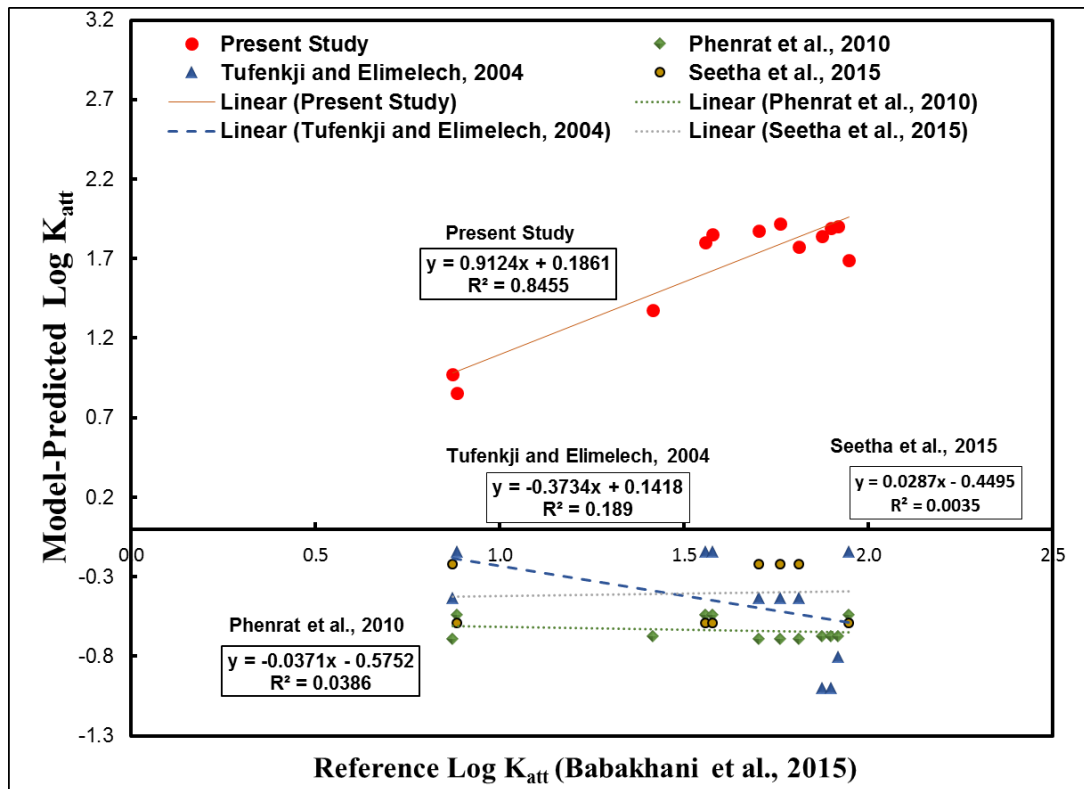


**Figure 2.6** Comparison between the predictions of  $K_{att}$  obtained based on ANN as the validation set with those resulted from [26] and CFT combined with empirical models of [86] or [75]. The reference dataset used is taken from the experimental report of [102] and continuum modelling of [101].

## 2.5.4 Model robustness

In the previous section an agreement was achieved between the predicted parameters by the ANN-based model and those determined by continuum model calibration in the literature. As a slight change in the values of continuum model parameters can significantly change the shape and/or position of the BTC, here it is worth to practically compare experimental BTCs with those generated using a continuum model based on the parameters predicted by this study's correlations. To the best of authors' knowledge, only one study [130] has thus far performed this type of comparison, which was in a limited range of experimental parameters. For this section, I use MT3DMS code [101, 131] to generate the BTCs based on the prediction of the ANN-based model for either sets of  $K_{att}$  and  $K_{det}$ , or  $K_{att}$  alone. The experimental BTC data of hydroxyapatite NP transport in porous media were used from Wang et al. [103] which comprise transport in presence of humic acid together with either KCl or  $\text{CaCl}_2$  as

electrolyte or dissolved Cu as contaminant. Since the behaviour of  $\text{Cu}^{2+}$  is deemed to be similar to that of  $\text{Ca}^{2+}$ , here I added the concentration of  $\text{Cu}^{2+}$  as IS of the solution similar to that of  $\text{Ca}^{2+}$ .

As shown in Fig. 2.7, the performance of the model with only one parameter,  $K_{att}$ , in reproducing BTCs at middle concentrations of KCl seems better ( $R^2 = 0.53$  and  $R^2 = 0.43$  for 10 mM and 50 mM KCl, respectively) than that at low concentration of 1 mM ( $R^2 = 0.22$ ) and high concentration of 100 mM KCl ( $R^2 < 0$ ). Likewise, at high concentration of divalent electrolyte (1 mM  $\text{CaCl}_2$ ),  $R^2$  was less than zero, while at lower concentrations of 0.1 mM, 0.3 mM, and 0.5 mM  $\text{CaCl}_2$ ,  $R^2$  values were 0.88, 0.30, and 0.74, respectively. Interestingly, the model was able to capture the BTC at low concentrations of Cu even though such a dataset, i.e., transport in presence of external contaminant, had not been incorporated in the training phase of the ANN model. In these cases,  $R^2$  values for  $1 \times 10^{-3}$  mM,  $1 \times 10^{-2}$  mM, and  $1 \times 10^{-1}$  mM Cu were 0.92, 0.92, and 0.89, respectively. Yet, similar to previous ionic species, at high concentration of Cu ( $5 \times 10^{-1}$  mM), the model failed to predict experimental BTC ( $R^2 < 0$ ). The use of parameter set of  $K_{att}$  and  $K_{det}$  did not change the result substantially—the differences of positive  $R^2$  values between the two-parameter set and one-parameter set varied in the range of -0.09 to 0.02.

The correlations proposed in this study overall show better performance than previous correlations in reproducing experimental BTCs based on mere experimental characteristics. However, still there are several cases where the model fails to predict the experimental BTC such as very high or low IS values. Although I used ‘early stopping’ technique [69, 72, 132, 133] along with a generalization efficiency criteria that selected the network with the best prediction performance in the iteration loops, there are other techniques that can be tried for improving the generalization of the model in future studies, e.g., Bayesian regularization.

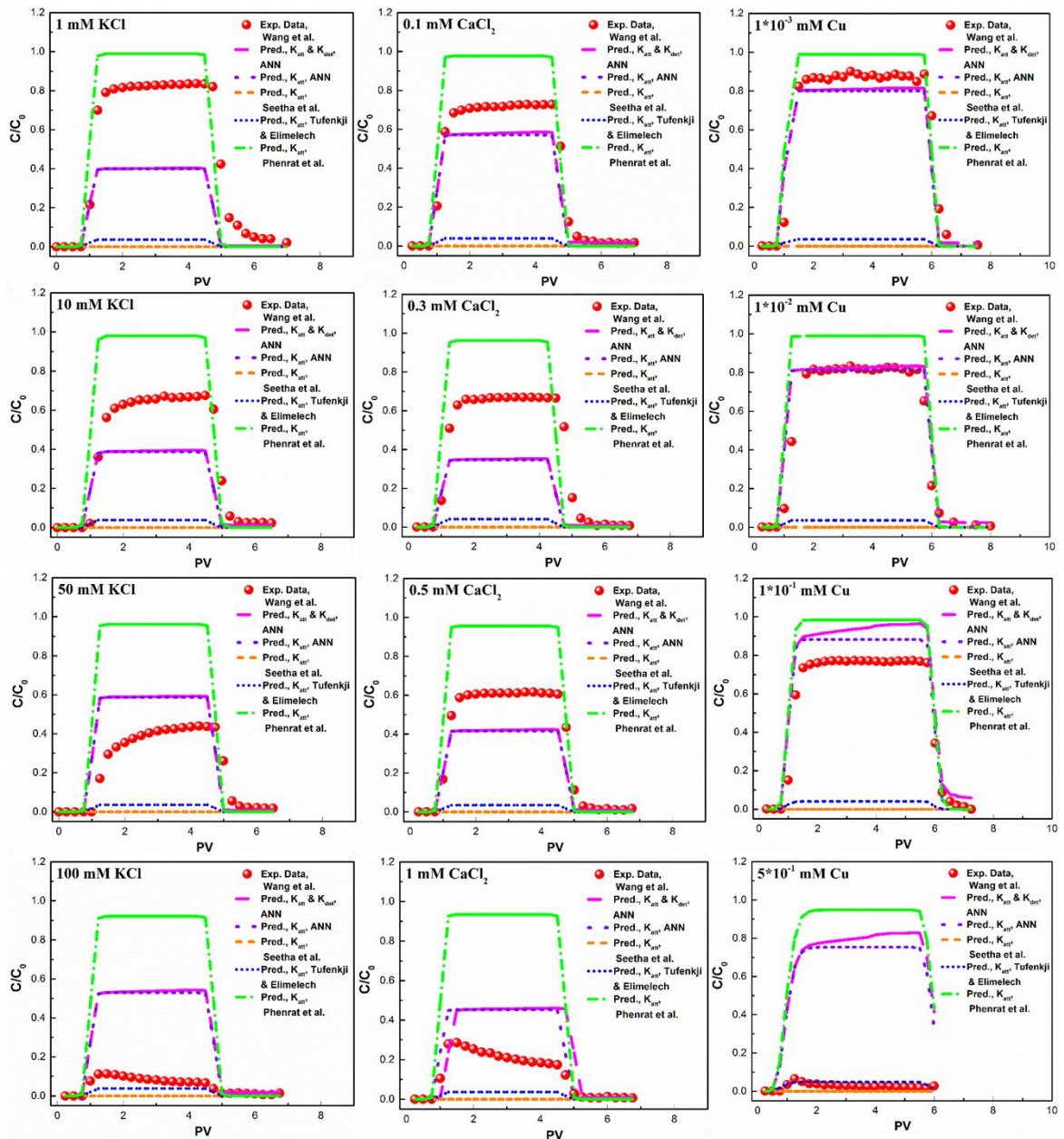


**Figure 2.7** Testing the model predictions against experimental data of Wang et al. [103] (with permission from Elsevier) for various concentrations of KCl, CaCl<sub>2</sub>, and Cu as solution ionic strength. The BTCs have been produced with MT3DMS model using either set of  $K_{att}$  and  $K_{det}$  or  $K_{att}$  alone, predicted from the ANN-based correlations. Dispersivity parameter was obtained via a separated ANN-based empirical model in all cases. Other modelled BTCs are determined by only  $K_{att}$  from [26, 75, 86]. For magnification or color interpretation of the figure, the reader is referred to the web version of paper published on this chapter.

## 2.6 Conclusions

This study used an artificial neural network to reanalyse a large dataset of NP transport in porous media and develop nonlinear empirical correlations for predicting the continuum model parameters as well as  $C/C_0$ . The sensitivities of each continuum model parameter to experimental factors were analysed and the predominant and general trends between these parameters were determined. Many interesting insights are gained from sensitivity analysis which can guide the future development of mechanistic models for predicting the fate and transport of NP as well as selections of influential factors for future modelling and experimental studies.

For instance, IS and pH were not as sensitive as coating concentration in determining  $K_{att}$ . In contrast to the current ambiguity regarding the trend of attachment rate with pore water velocity, ANN showed a clear positive correlation.  $K_{att}$  was more sensitive to the surface-related factors, than flow-regime-related factors whereas  $K_{det}$  was more sensitive to the flow-regime-related factors. The most sensitive factor in determining  $K_{det}$  was the IS of the solution. In the case of  $S_m$ , the factors relevant to the surface area, including column length, column diameter, aspect ratio, and porosity were moderately to highly sensitive ( $RS$  ranging from 4.9 % to 9.3 %). The most important feature in curbing the depth-dependent behaviour of RCP was the influent concentration with a positive correlation. The pattern of sensitive factors around  $K_{att_2}$  indicate towards the influence of agglomeration on the NP transport rather than its commonly proposed conceptual model as the attachment rate of secondary sites.

The high sensitivity to grain zeta-potential was evident in almost all cases—ranging from 4.6 % to 28.7 %. This might oppose the important role of microscopic surface heterogeneities in transport of NP in porous media. Particle zeta-potential was mostly sensitive for  $S_m$  and  $K_{att_2}$ . One of the most well-studied factors in the literature, IS, showed a sensitivity in range of 2.9 % to 14.8 %. For the first time a simple unified parameter is considered for the porous media heterogeneity. i.e., heterogeneity imposed by the nature of the soil sample (clean or treated laboratory porous media, disturbed, and undisturbed), grain coating, and grain size distribution. Although the conceptualization approach of this parameter was based on a series of simplifying rationale, its sensitivity turned out to be in range of 2.4 % to 6.2 %, suggesting that

considering the porous media heterogeneity in continuum modelling is even more important than dispersivity ( $RS = 1.7\%$  to  $5.1\%$ ) which has long been recognized as one of the most influential parameters affecting the transport of materials in porous media. Yet, the development of the heterogeneity as a unified parameter from several relevant influences in this study is still in an infancy level and mainly aimed at satisfying the needs of the present study. Future studies are necessary to establish a more rigorous definition of heterogeneity as a unified parameter to be considered in continuum modelling of NP transport, as even a rough representation of this factor turned out to be significant. Here, the highest sensitivity to heterogeneity was revealed for the  $K_{det}$ .

The developed ANN-based correlations in this study performed very well in predicting the continuum model parameters, such as  $K_{att}$  and turned out to be superior to current empirical correlation methods available in the literature of colloid and NP transport. Finally, the experimental breakthrough curves were tried to be reproduced by continuum model based on the parameters fully predicted from empirical correlations. From 12 cases of investigated BTCs, in three cases the model totally failed to predict BTCs ( $R^2 < 0$ ) which all involved very high IS values. Yet, the model was able to predict other nine experimental BTCs with a mean  $R^2$  of  $0.65 \pm 0.26$ . The empirical correlations obtained in this study are formulated in a spreadsheet file so that they can be easily tested against other datasets and used for future pre-estimation of continuum model parameters as well as  $C/C_0$ .

## 2.7 References

1. Lanphere, J.D., C.J. Luth, and S.L. Walker, *Effects of solution chemistry on the transport of graphene oxide in saturated porous media*. Environmental science & technology, 2013. **47**(9): p. 4255-4261.
2. Keller, A.A., et al., *Global life cycle releases of engineered nanomaterials*. Journal of Nanoparticle Research, 2013. **15**(6): p. 1-17.
3. Yu, H., et al., *Flow enhancement of water-based nanoparticle dispersion through microscale sedimentary rocks*. Scientific reports, 2015. **5**.
4. Tratnyek, P.G. and R.L. Johnson, *Nanotechnologies for environmental cleanup*. Nano today, 2006. **1**(2): p. 44-48.
5. Ehtesabi, H., et al., *Enhanced heavy oil recovery in sandstone cores using tio2 nanofluids*. Energy & Fuels, 2013. **28**(1): p. 423-430.
6. Saleh, N.B., et al., *Research strategy to determine when novel nanohybrids pose unique environmental risks*. Environmental Science: Nano, 2015. **2**(1): p. 11-18.
7. Huang, C.H., et al., *Three-Dimensional Hierarchically Ordered Porous Carbons with Partially Graphitic Nanostructures for Electrochemical Capacitive Energy Storage*. ChemSusChem, 2012. **5**(3): p. 563-571.
8. Chou, T.-c., et al., *Architectural design of hierarchically ordered porous carbons for high-rate electrochemical capacitors*. Journal of Materials Chemistry A, 2013. **1**(8): p. 2886-2895.
9. Huang, C.-H., et al., *Direct synthesis of controllable microstructures of thermally stable and ordered mesoporous crystalline titanium oxides and carbide/carbon composites*. Chemistry of Materials, 2010. **22**(5): p. 1760-1767.
10. Yao, K.-M., M.T. Habibian, and C.R. O'Melia, *Water and waste water filtration. Concepts and applications*. Environmental Science & Technology, 1971. **5**(11): p. 1105-1112.
11. Rajagopalan, R. and C. Tien, *Trajectory analysis of deep-bed filtration with the sphere-in-cell porous media model*. AIChE Journal, 1976. **22**(3): p. 523-533.
12. Logan, B.E., et al., *Clarification of clean-bed filtration models*. Journal of Environmental Engineering, 1995. **121**(12): p. 869-873.
13. Molnar, I.L., et al., *Predicting colloid transport through saturated porous media: A critical review*. Water Resources Research, 2015.
14. Bradford, S.A., et al., *Modeling colloid attachment, straining, and exclusion in saturated porous media*. Environmental science & technology, 2003. **37**(10): p. 2242-2250.
15. Bradford, S.A., et al., *Significance of straining in colloid deposition: Evidence and implications*. Water Resour. Res., 2006. **42**(12): p. W12S15.
16. Bradford, S.A., et al., *Physical factors affecting the transport and fate of colloids in saturated porous media*. Water Resources Research, 2002. **38**(12): p. 63-1.
17. Tong, M. and W.P. Johnson, *Colloid population heterogeneity drives hyperexponential deviation from classic filtration theory*. Environmental science & technology, 2007. **41**(2): p. 493-499.
18. Jones, E.H. and C. Su, *Fate and transport of elemental copper (Cu 0) nanoparticles through saturated porous media in the presence of organic materials*. water research, 2012. **46**(7): p. 2445-2456.

19. Bolster, C.H., et al., *Spatial distribution of deposited bacteria following miscible displacement experiments in intact cores*. Water Resources Research, 1999. **35**(6): p. 1797-1807.
20. Li, X., T.D. Scheibe, and W.P. Johnson, *Apparent decreases in colloid deposition rate coefficients with distance of transport under unfavorable deposition conditions: A general phenomenon*. Environmental Science & Technology, 2004. **38**(21): p. 5616-5625.
21. Tufenkji, N. and M. Elimelech, *Spatial distributions of Cryptosporidium oocysts in porous media: Evidence for dual mode deposition*. Environmental science & technology, 2005. **39**(10): p. 3620-3629.
22. Nowack, B., et al., *Progress towards the validation of modeled environmental concentrations of engineered nanomaterials by analytical measurements*. Environmental Science: Nano, 2015.
23. Babakhani, P., et al., *Continuum-Based Models and Concepts for the Transport of Nanoparticles in Saturated Porous Media: A State-of-the-Science Review*. In Review, Advance in Colloid and Interface Science, In Review.
24. Goldberg, E., et al., *Prediction of nanoparticle transport behavior from physicochemical properties: machine learning provides insights to guide the next generation of transport models*. Environmental Science: Nano, 2015. **2**(4): p. 352-360.
25. Peijnenburg, W., et al., *Fate assessment of engineered nanoparticles in solids dominated media—Current insights and the way forward*. Environmental Pollution, 2016.
26. Seetha, N., et al., *Correlation equations for average deposition rate coefficients of nanoparticles in a cylindrical pore*. Water Resources Research, 2015. **51**(10): p. 8034-8059.
27. Xu, S., B. Gao, and J.E. Saiers, *Straining of colloidal particles in saturated porous media*. Water Resources Research, 2006. **42**(12).
28. Xu, S., Q. Liao, and J.E. Saiers, *Straining of nonspherical colloids in saturated porous media*. Environmental science & technology, 2008. **42**(3): p. 771-778.
29. Porubcan, A.A. and S. Xu, *Colloid straining within saturated heterogeneous porous media*. Water research, 2011. **45**(4): p. 1796-1806.
30. Xu, S. and J.E. Saiers, *Colloid straining within water-saturated porous media: Effects of colloid size nonuniformity*. Water resources research, 2009. **45**(5).
31. Hassan, A.A., et al., *Computational fluid dynamics simulation of transport and retention of nanoparticle in saturated sand filters*. Journal of hazardous materials, 2013. **244**: p. 251-258.
32. Morshed, J. and J.J. Kaluarachchi, *Application of artificial neural network and genetic algorithm in flow and transport simulations*. Advances in Water Resources, 1998. **22**(2): p. 145-158.
33. Yu, H., et al., *Prediction of the Particle Size Distribution Parameters in a High Shear Granulation Process Using a Key Parameter Definition Combined Artificial Neural Network Model*. Industrial & Engineering Chemistry Research, 2015. **54**(43): p. 10825-10834.
34. Lu, M., S.M. AbouRizk, and U.H. Hermann, *Sensitivity analysis of neural networks in spool fabrication productivity studies*. Journal of Computing in Civil Engineering, 2001. **15**(4): p. 299-308.

35. Nourani, V. and M. Sayyah-Fard, *Sensitivity analysis of the artificial neural network outputs in simulation of the evaporation process at different climatologic regimes*. Advances in Engineering Software, 2012. **47**(1): p. 127-146.
36. Maier, H.R. and G.C. Dandy, *The use of artificial neural networks for the prediction of water quality parameters*. Water Resour Res, 1996. **32**(4): p. 1013-1022.
37. McCulloch, W.S. and W. Pitts, *A logical calculus of the ideas immanent in nervous activity*. The bulletin of mathematical biophysics, 1943. **5**(4): p. 115-133.
38. Yerramareddy, S., S.C.Y. Lu, and K.F. Arnold, *Developing empirical models from observational data using artificial neural networks*. Journal of Intelligent Manufacturing, 1993. **4**(1): p. 33-41.
39. Nourani, V., A.H. Baghanam, and M. Gebremichael, *Investigating the Ability of Artificial Neural Network (ANN) Models to Estimate Missing Rain-gauge Data*. Journal of Environmental Informatics, 2012. **19**(1).
40. Hosseini, S.M., M. Kholghi, and H. Vagharfard, *Numerical and meta-modeling of nitrate transport reduced by nano-Fe/Cu particles in packed sand column*. Transport in porous media, 2012. **94**(1): p. 149-174.
41. Gevrey, M., I. Dimopoulos, and S. Lek, *Review and comparison of methods to study the contribution of variables in artificial neural network models*. Ecological modelling, 2003. **160**(3): p. 249-264.
42. Gevrey, M., I. Dimopoulos, and S. Lek, *Two-way interaction of input variables in the sensitivity analysis of neural network models*. Ecological modelling, 2006. **195**(1): p. 43-50.
43. Liang, Y., et al., *Retention and remobilization of stabilized silver nanoparticles in an undisturbed loamy sand soil*. Environmental science & technology, 2013. **47**(21): p. 12229-12237.
44. Donaldson, T.S., *Power of the F-test for nonnormal distributions and unequal error variances*. 1966: Rand Corporation New york.
45. Grubbs, F.E., *Procedures for detecting outlying observations in samples*. Technometrics, 1969. **11**(1): p. 1-21.
46. Chambers, J.M., *Graphical methods for data analysis*. 1983.
47. Aggarwal, C.C., *OUTLIER ANALYSIS*. Springer New York, 2013. **9781461463962 • 9781461463955**: p. 1-446.
48. Yang, H., *The case for being automatic: introducing the automatic linear modeling (LINEAR) procedure in SPSS statistics*. Multiple Linear Regression Viewpoints, 2013. **39**(2): p. 27-37.
49. Chrysikopoulos, C.V. and V.E. Katzourakis, *Colloid particle size-dependent dispersivity*. Water Resources Research, 2015.
50. Howington, S.E., J.F. Peters, and T.H. Illangasekare, *Discrete network modeling for field-scale flow and transport through porous media*, in *Technical Report CHL-97-21*. 1997, Discretionary Research Program, US Army Corps of Engineers MD, US.
51. Illangasekare, T.H., C.C. Frippiat, and R. Fućík, *Dispersion and Mass Transfer Coefficients in Groundwater of Near-Surface Geologic Formations*. Handbook of Chemical Mass Transport in the Environment, ed. L.J. Thibodeaux, B. Rouge, and D. Mackay. 2010: CRC Press/Taylor and Francis Group.
52. James, S.C. and C.V. Chrysikopoulos, *Effective velocity and effective dispersion coefficient for finite-sized particles flowing in a uniform fracture*. Journal of colloid and interface science, 2003. **263**(1): p. 288-295.

53. Schafer, J.L. and J.W. Graham, *Missing data: our view of the state of the art*. Psychological methods, 2002. **7**(2): p. 147.
54. Cullen, E., et al., *Simulation of the subsurface mobility of carbon nanoparticles at the field scale*. Advances in Water Resources, 2010. **33**(4): p. 361-371.
55. Kim, H.-J., et al., *Effect of kaolinite, silica fines and pH on transport of polymer-modified zero valent iron nano-particles in heterogeneous porous media*. Journal of Colloid and Interface Science, 2012. **370**(1): p. 1-10.
56. Tombacz, E. and M. Szekeres, *Colloidal behavior of aqueous montmorillonite suspensions: the specific role of pH in the presence of indifferent electrolytes*. Applied Clay Science, 2004. **27**(1): p. 75-94.
57. Chowdhury, A.I.A., et al., *Electrophoresis enhanced transport of nano-scale zero valent iron*. Advances in Water Resources, 2012. **40**(0): p. 71-82.
58. Tsujimoto, Y., C. Chassagne, and Y. Adachi, *Dielectric and electrophoretic response of montmorillonite particles as function of ionic strength*. Journal of colloid and interface science, 2013. **404**: p. 72-79.
59. Holmboe, M., et al., *Effects of  $\gamma$ -irradiation on the stability of colloidal Na<sup>+</sup>-Montmorillonite dispersions*. Applied Clay Science, 2009. **43**(1): p. 86-90.
60. Amorós, J.L., et al., *Electrokinetic and rheological properties of highly concentrated kaolin dispersions: Influence of particle volume fraction and dispersant concentration*. Applied Clay Science, 2010. **49**(1): p. 33-43.
61. Jaisi, D.P. and M. Elimelech, *Single-Walled Carbon Nanotubes Exhibit Limited Transport in Soil Columns*. Environmental Science & Technology, 2009. **43**(24): p. 9161-9166.
62. Plaster, E.J., *Soil science and management*, ed. 3rd. 1997: Delmar Publishers.
63. Saey, T., et al., *A pedotransfer function to evaluate the soil profile textural heterogeneity using proximally sensed apparent electrical conductivity*. Geoderma, 2009. **150**(3-4): p. 389-395.
64. Liang, Y., et al., *Sensitivity of the transport and retention of stabilized silver nanoparticles to physicochemical factors*. water research, 2013. **47**(7): p. 2572-2582.
65. Torkzaban, S., et al., *Transport and fate of bacteria in porous media: Coupled effects of chemical conditions and pore space geometry*. Water Resources Research, 2008. **44**(4).
66. Phenrat, T., et al., *Aggregation and sedimentation of aqueous nanoscale zerovalent iron dispersions*. Environmental Science & Technology, 2007. **41**(1): p. 284-290.
67. Kini, G.C., et al., *Salt-and temperature-stable quantum dot nanoparticles for porous media flow*. Colloids and Surfaces A: Physicochemical and Engineering Aspects, 2014. **443**: p. 492-500.
68. Doherty, J., *Pest, Model-Independent Parameter Estimation User Manual: 5th Edition*. 2004: Watermark Numerical Computing.
69. Coulibaly, P., F. Anctil, and B. Bobee, *Daily reservoir inflow forecasting using artificial neural networks with stopped training approach*. Journal of Hydrology, 2000. **230**(3): p. 244-257.
70. Noori, R., et al., *How Reliable Are ANN, ANFIS, and SVM Techniques for Predicting Longitudinal Dispersion Coefficient in Natural Rivers?* Journal of Hydraulic Engineering, 2015. **142**(1): p. 04015039.
71. Hagan, M.T. and M.B. Menhaj, *Training feedforward networks with the Marquardt algorithm*. Neural Networks, IEEE Transactions on, 1994. **5**(6): p. 989-993.

72. Dehghani, M., et al., *Uncertainty analysis of streamflow drought forecast using artificial neural networks and Monte-Carlo simulation*. International Journal of Climatology, 2014. **34**(4): p. 1169-1180.
73. Castrup, S. *Comparison of methods for establishing confidence limits and expanded uncertainties*. 2010.
74. Couto, P.R.G., J.C. Damasceno, and S.P. de Oliveira, *Monte Carlo simulations applied to uncertainty in measurement*. 2013: INTECH Open Access Publisher.
75. Phenrat, T., et al., *Empirical correlations to estimate agglomerate size and deposition during injection of a polyelectrolyte-modified Fe<sub>0</sub> nanoparticle at high particle concentration in saturated sand*. Journal of Contaminant Hydrology, 2010. **118**(3-4): p. 152-164.
76. Phenrat, T., et al., *Partial Oxidation ("Aging") and Surface Modification Decrease the Toxicity of Nanosized Zerovalent Iron*. Environmental Science & Technology, 2008. **43**(1): p. 195-200.
77. Phenrat, T. and G.V. Lowry, *Chapter 18 - Physicochemistry of Polyelectrolyte Coatings that Increase Stability, Mobility, and Contaminant Specificity of Reactive Nanoparticles Used for Groundwater Remediation*, in *Nanotechnology Applications for Clean Water*, S. Nora, et al., Editors. 2009, William Andrew Publishing: Boston. p. 249-267.
78. Phenrat, T., et al., *Stabilization of aqueous nanoscale zerovalent iron dispersions by anionic polyelectrolytes: adsorbed anionic polyelectrolyte layer properties and their effect on aggregation and sedimentation*. Journal of Nanoparticle Research, 2008. **10**(5): p. 795-814.
79. Phenrat, T., et al., *Estimating Attachment of Nano- and Submicrometer-particles Coated with Organic Macromolecules in Porous Media: Development of an Empirical Model*. Environmental Science & Technology, 2010. **44**(12): p. 4531-4538.
80. Wang, Y., et al., *Effect of surface coating composition on quantum dot mobility in porous media*. Journal of nanoparticle research, 2013. **15**(8): p. 1-16.
81. Becker, M.D., et al., *A multi-constituent site blocking model for nanoparticle and stabilizing agent transport in porous media*. Environmental Science: Nano, 2015.
82. Wang, D., et al., *Hyperexponential and nonmonotonic retention of polyvinylpyrrolidone-coated silver nanoparticles in an Ultisol*. Journal of contaminant hydrology, 2014. **164**: p. 35-48.
83. Wang, D., et al., *Facilitated transport of Cu with hydroxyapatite nanoparticles in saturated sand: Effects of solution ionic strength and composition*. water research, 2011. **45**(18): p. 5905-5915.
84. Chen, K.L. and M. Elimelech, *Aggregation and deposition kinetics of fullerene (C<sub>60</sub>) nanoparticles*. Langmuir, 2006. **22**(26): p. 10994-11001.
85. Torkzaban, S., et al., *Impacts of bridging complexation on the transport of surface-modified nanoparticles in saturated sand*. Journal of contaminant hydrology, 2012. **136**: p. 86-95.
86. Tufenkji, N. and M. Elimelech, *Correlation equation for predicting single-collector efficiency in physicochemical filtration in saturated porous media*. Environmental Science & Technology, 2004. **38**(2): p. 529-536.
87. Salerno, M.B., et al., *Transport of rodlike colloids through packed beds*. Environmental science & technology, 2006. **40**(20): p. 6336-6340.

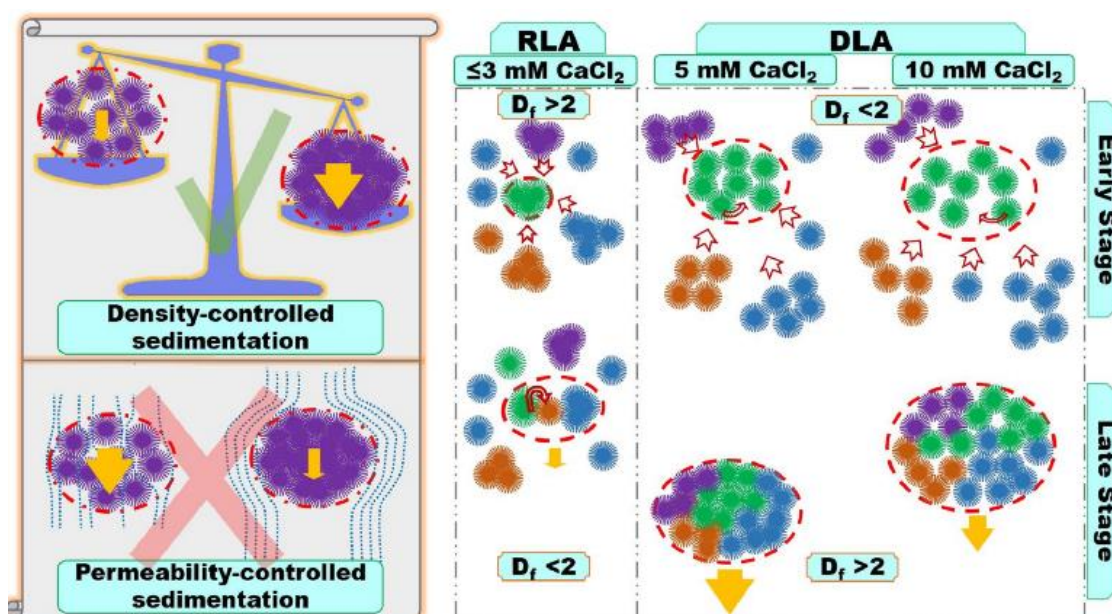
88. Seymour, M.B., et al., *Transport and Retention of Colloids in Porous Media: Does Shape Really Matter?* Environmental Science & Technology, 2013. **47**(15): p. 8391-8398.
89. Hedayati, M., et al., *Transport and retention of carbon-based engineered and natural nanoparticles through saturated porous media.* Journal of Nanoparticle Research, 2016. **18**(3): p. 1-11.
90. Ortega, A. and J.G. de la Torre, *Hydrodynamic properties of rodlike and disklike particles in dilute solution.* The Journal of chemical physics, 2003. **119**(18): p. 9914-9919.
91. Wang, D., et al., *Transport of fluorescently labeled hydroxyapatite nanoparticles in saturated granular media at environmentally relevant concentrations of surfactants.* Colloids and Surfaces A: Physicochemical and Engineering Aspects, 2014. **457**: p. 58-66.
92. Wang, D., et al., *Transport of ARS-labeled hydroxyapatite nanoparticles in saturated granular media is influenced by surface charge variability even in the presence of humic acid.* Journal of hazardous materials, 2012. **229**: p. 170-176.
93. Wang, D., Y. Jin, and D.P. Jaisi, *Effect of Size-Selective Retention on the Cotransport of Hydroxyapatite and Goethite Nanoparticles in Saturated Porous Media.* Environmental science & technology, 2015. **49**(14): p. 8461-8470.
94. Wang, D., Y. Jin, and D. Jaisi, *Cotransport of Hydroxyapatite Nanoparticles and Hematite Colloids in Saturated Porous Media: Mechanistic Insights from Mathematical Modeling and Phosphate Oxygen Isotope Fractionation.* Journal of Contaminant Hydrology, 2015. **182**: p. 194-209.
95. Wang, D., et al., *Transport and Retention of Polyvinylpyrrolidone-Coated Silver Nanoparticles in Natural Soils.* Vadose Zone J., 2015.
96. Braun, A., et al., *Transport and deposition of stabilized engineered silver nanoparticles in water saturated loamy sand and silty loam.* Science of The Total Environment, 2014.
97. Raychoudhury, T., N. Tufenkji, and S. Ghoshal, *Straining of Polyelectrolyte-Stabilized Nanoscale Zero Valent Iron Particles during Transport through Granular Porous Media.* Water Research, 2014. **50**(0): p. 80-90.
98. Saiers, J.E., G.M. Hornberger, and L. Liang, *First-and second-order kinetics approaches for modeling the transport of colloidal particles in porous media.* Water Resources Research, 1994. **30**(9): p. 2499-2506.
99. Wang, D., et al., *Facilitated transport of copper with hydroxyapatite nanoparticles in saturated sand.* Soil Science Society of America Journal, 2012. **76**(2): p. 375-388.
100. Shen, C., et al., *Effects of solution chemistry on straining of colloids in porous media under unfavorable conditions.* Water resources research, 2008. **44**(5).
101. Babakhani, P., et al., *Modified MODFLOW-based model for simulating the agglomeration and transport of polymer-modified Fe nanoparticles in saturated porous media.* Environ Sci Pollut Res, 1-20, doi:10.1007/s11356-015-5193-0, 2015.
102. Phenrat, T., et al., *Particle size distribution, concentration, and magnetic attraction affect transport of polymer-modified Fe<sub>0</sub> nanoparticles in sand columns.* Environ. Sci. Technol., 2009. **43**(13): p. 5079-5085.
103. Wang, D., et al., *Transport behavior of humic acid-modified nano-hydroxyapatite in saturated packed column: effects of Cu, ionic strength, and ionic composition.* Journal of colloid and interface science, 2011. **360**(2): p. 398-407.

104. Saleh, N., et al., *Ionic Strength and Composition Affect the Mobility of Surface-Modified Fe<sub>0</sub> Nanoparticles in Water-Saturated Sand Columns*. Environmental Science & Technology, 2008. **42**(9): p. 3349-3355.
105. Grolimund, D., M. Elimelech, and M. Borkovec, *Aggregation and deposition kinetics of mobile colloidal particles in natural porous media*. Colloids and Surfaces A: Physicochemical and Engineering Aspects, 2001. **191**(1–2): p. 179-188.
106. Bradford, S.A., et al., *Equilibrium and kinetic models for colloid release under transient solution chemistry conditions*. Journal of contaminant hydrology, 2015.
107. Torkzaban, S., et al., *Colloid release and clogging in porous media: Effects of solution ionic strength and flow velocity*. Journal of contaminant hydrology, 2015.
108. Bergendahl, J. and D. Grasso, *Prediction of colloid detachment in a model porous media: hydrodynamics*. Chemical Engineering Science, 2000. **55**(9): p. 1523-1532.
109. Bergendahl, J. and D. Grasso, *Prediction of colloid detachment in a model porous media: Thermodynamics*. AIChE Journal, 1999. **45**(3): p. 475-484.
110. Torkzaban, S., S.A. Bradford, and S.L. Walker, *Resolving the Coupled Effects of Hydrodynamics and DLVO Forces on Colloid Attachment in Porous Media*. Langmuir, 2007. **23**(19): p. 9652-9660.
111. Adamczyk, Z., et al., *Kinetics of localized adsorption of colloid particles*. Advances in Colloid and Interface Science, 1994. **48**: p. 151-280.
112. Sun, Y., et al., *Transport, retention, and size perturbation of graphene oxide in saturated porous media: Effects of input concentration and grain size*. Water research, 2015. **68**: p. 24-33.
113. Kasel, D., et al., *Transport and retention of multi-walled carbon nanotubes in saturated porous media: Effects of input concentration and grain size*. water research, 2013. **47**(2): p. 933-944.
114. Bradford, S.A., J. Simunek, and S.L. Walker, *Transport and straining of E. coli O157: H7 in saturated porous media*. Water Resources Research, 2006. **42**(12).
115. Bradford, S.A., et al., *Coupled Factors Influencing Concentration-Dependent Colloid Transport and Retention in Saturated Porous Media*. Environmental Science & Technology, 2009. **43**(18): p. 6996-7002.
116. Sun, P., et al., *Distinguishable Transport Behavior of Zinc Oxide Nanoparticles in Silica Sand and Soil Columns*. Science of The Total Environment, 2015. **505**: p. 189-198.
117. Herzig, J.P., D.M. Leclerc, and P.L. Goff, *Flow of Suspensions through Porous Media—Application to Deep Filtration*. Industrial & Engineering Chemistry, 1970. **62**(5): p. 8-35.
118. Johnson, W.P., H. Ma, and E. Pazmino, *Straining credibility: a general comment regarding common arguments used to infer straining as the mechanism of colloid retention in porous media*. Environmental science & technology, 2011. **45**(9): p. 3831-3832.
119. Cornelis, G., et al., *Transport of silver nanoparticles in saturated columns of natural soils*. Science of the Total Environment, 2013. **463**: p. 120-130.
120. Qi, Z., et al., *Factors controlling transport of graphene oxide nanoparticles in saturated sand columns*. Environmental toxicology and chemistry, 2014. **33**(5): p. 998-1004.
121. Qi, Z., L. Zhang, and W. Chen, *Transport of graphene oxide nanoparticles in saturated sandy soil*. Environmental Science: Processes & Impacts, 2014. **16**(10): p. 2268-2277.

122. Fang, J., et al., *Modeling the transport of TiO<sub>2</sub> nanoparticle aggregates in saturated and unsaturated granular media: effects of ionic strength and pH*. *Water Research*, 2013. **47**(3): p. 1399-1408.
123. He, J.-Z., et al., *Biofilms and extracellular polymeric substances mediate the transport of graphene oxide nanoparticles in saturated porous media*. *Journal of Hazardous Materials*, 2015. **300**: p. 467-474.
124. Rahman, T., J. George, and H.J. Shipley, *Transport of aluminum oxide nanoparticles in saturated sand: Effects of ionic strength, flow rate, and nanoparticle concentration*. *Science of The Total Environment*, 2013. **463–464**: p. 565-571.
125. Rahman, T., H. Millwater, and H.J. Shipley, *Modeling and sensitivity analysis on the transport of aluminum oxide nanoparticles in saturated sand: Effects of ionic strength, flow rate, and nanoparticle concentration*. *Science of The Total Environment*, 2014. **499**: p. 402-412.
126. Tosco, T. and R. Sethi, *Transport of non-Newtonian suspensions of highly concentrated micro-and nanoscale iron particles in porous media: a modeling approach*. *Environmental Science & Technology*, 2010. **44**(23): p. 9062-9068.
127. Hosseini, S.M. and T. Tosco, *Transport and retention of high concentrated nano-Fe/Cu particles through highly flow-rated packed sand column*. *Water Research*, 2013. **47**(1): p. 326-338.
128. Fan, W., et al., *Effects of surfactants on graphene oxide nanoparticles transport in saturated porous media*. *Journal of Environmental Sciences*, 2015.
129. Fan, W., et al., *Transport of graphene oxide in saturated porous media: Effect of cation composition in mixed Na–Ca electrolyte systems*. *Science of The Total Environment*, 2015. **511**: p. 509-515.
130. Landkamer, L.L., et al., *Colloid transport in saturated porous media: Elimination of attachment efficiency in a new colloid transport model*. *Water Resources Research*, 2013. **49**(5): p. 2952-2965.
131. Zheng, C. and P.P. Wang, *A modular three-dimensional multi-species transport model for simulation of advection, dispersion and chemical reactions of contaminants in groundwater systems; documentation and user's guide*. US Army Engineer Research and Development Center Contract Report SERDP-99-1, Vicksburg, Mississippi, USA, 1999.
132. Beale, M.H., M.T. Hagan, and H.B. Demuth. *Neural network toolbox™ user's guide*. 2015. The MathWorks, Inc. 3 Apple Hill Drive Natick, MA 01760-2098 [www.mathworks.com](http://www.mathworks.com).
133. Bishop, C.M., *Regularization and complexity control in feed-forward networks*. 1995.

## Chapter 3

### 3 The significance of early and late stages of coupled aggregation and sedimentation in the fate of nanoparticles: measurement and modelling



#### 3.1 Chapter overview

##### 3.1.1 Scope

This chapter is essential in the context of the thesis since the best modelling approaches found in this chapter are extensively used in the following chapters for describing the aggregation process in aquatic environments and in porous media. This chapter has been published as the following paper and has been reproduced with permission from American Chemical Society (ACS):

“Babakhani, P.; Doong, R.-a.; Bridge, J., The significance of early and late stages of coupled aggregation and sedimentation in the fate of nanoparticles: measurement and modelling. *Environmental Science & Technology*, 2018. DOI: 10.1021/acs.est.7b05236”

### 3.1.2 Abstract

Despite aggregation’s crucial role in controlling the environmental fate of nanoparticles (NP), the extent to which current models can describe the progressive stages of NP aggregation/sedimentation is still unclear. In this study, 24 model combinations of two population-balance models (PBMs) and various collision frequency and settling velocity models are used to analyse spatiotemporal variations in the size and concentration of hydroxyapatite (HAp) NP. The impact of initial conditions and variability in attachment efficiency,  $\alpha$ , with aggregate size are investigated. Although permeability models perform well in calculating collision frequencies, they are not appropriate for describing settling velocity because of their negative correlation or insensitivity in respect to fractal dimension. Considering both early and late stages of aggregation, both experimental and model data indicate overall mass removal peaks at an intermediate ionic strength (5 mM CaCl<sub>2</sub>) even though the mean aggregate size continued to increase through higher ionic strengths (to 10 mM CaCl<sub>2</sub>). This trend was consistent when different approaches to the initial particle size distribution (PSD) were used and when a variable or constant  $\alpha$  was used. These results point to the importance of accurately considering different stages of aggregation in modelling NP fate within various environmental conditions.

### 3.2 Nomenclature

$a_0$	primary particle radius or particle radius in the smallest size class [L]
$a_k$	aggregate radius in size class $k$ [L]
$D_f$	fractal dimension [-]
$D_H$	hydrodynamic diameter
$G$	shear rate [T <sup>-1</sup> ]
$i, j$	subscripts used to indicate aggregates size class $i$ and $j$

$k_b$	Boltzmann constant
$k_{max}$	maximum number of classes considered in the numerical model (<100)
$n_k$	aggregate number concentration in size class $k$ [ $L^{-3}$ ]
$q$	geometric factor
$T$	temperature [ $K$ ]
$U_k$	aggregate sedimentation velocity in size class $k$ [ $LT^{-1}$ ]
$U_0$	sedimentation velocity of primary particles [ $LT^{-1}$ ]
$v_k$	volume of solids of each aggregate in size class $k$ [ $L^3$ ]
$v_0$	volume of primary particles [ $L^3$ ]
$Z_s$	sedimentation depth [ $L$ ]
$\alpha$	attachment efficiency [-]
$\beta_{i,j}$	aggregate collision frequency in size class $i$ and $j$ [ $L^3T^{-1}$ ]
$\beta_{Diff}$	differential settling collision frequency [ $L^3T^{-1}$ ]
$\beta_{Orth}$	orthokinetic collision frequency [ $L^3T^{-1}$ ]
$\beta_{Prik}$	perikinetic collision frequency [ $L^3T^{-1}$ ]
$\delta_{j,i}$	Kronecker delta
$\mu$	dynamic viscosity of the suspending medium [ $M T^{-1} L^{-1}$ ]

### 3.3 List of abbreviations.

CCC	critical coagulation concentration
DCR	derived count rate
DI	deionized
DLA	diffusion limited aggregation
DLS	dynamic light scattering
DLVO	Derjaguin, Landau, Verwey, and Overbeek
FP	fixed pivot

HAp	hydroxyapatite
IS	ionic strength
MP	moving pivot
NP	nanoparticles
PB	population balance
PSD	particle size distribution
RLA	reaction limited aggregation

### 3.4 Introduction

Nanoparticles, often unintentionally released into the environment, have also shown promise in remediation of hazardous contaminants such as radionuclides [1-3]. Effective *in situ* field-scale management of NP is hindered by the lack of adequate models to simulate NP fate and transport in realistic environmental compartments [4, 5]. Considering the long-established potential for colloids to enhance the mobility of contaminants in groundwater environments [6, 7] or facilitate their redistribution in surface water bodies [8-10], this lack of predictive capability is a critical concern. Aggregation of NP is important because progressive increase in particle size can substantially affect NP mobility, reactivity and hence potential contribution to mobilization of other solute contaminants [4, 11-13]. Aggregation has complex interactions with other NP transport mechanisms such as sedimentation [4, 5, 14, 15]. This leads to distinct changes in trends of particle concentration or size over time [14, 16]. The early stage of aggregation, in which the slope of mean particle size versus time is typically linear, is the subject of many studies [15, 17, 18]. However, the late stage of aggregation, more common in environmentally-relevant conditions where phenomena such as aggregation and sedimentation occur over longer periods with no clear initial condition, has received relatively little attention to date [14, 16].

In late-stage conditions, NP aggregate sizes increase sufficiently to induce sedimentation and removal from suspension. This may lead to decreasing concentration of NP dispersion and consequently reduction in aggregation rates.

Conversely, differentially-settling aggregates may collect smaller particles more easily during late-stage. Sedimentation-induced movement of aggregates may bring about aggregate restructuring [19]. This may affect the number of collisions among aggregates thereby changing their consequent aggregation rates and settling velocity [19, 20]. These complex interacting phenomena may drive localised nonlinearities in slope of mean particle size or concentration versus time. Many established theories and concepts, such as CCC, are invalidated during late-stage aggregation since they are based upon the linear slope of size or concentration versus time at the early stage [21, 22].

The ability of PB models to account for both stages in tandem while retaining meaningful description of the system in terms of parameters such as attachment efficiency,  $\alpha$ , and fractal dimension,  $D_f$ , is still unclear but is important if PB approaches are to be used to provide description of aggregation processes within larger-scale models of NP fate and transport [20, 23]. In this study, the quiescent aggregation and sedimentation of HAp NP is measured and modeled across a range of solution chemistries and at different measurement depths over a period of at least five hours—sufficient in most of the cases for systems to develop late stage conditions. Two numerical approaches to aggregation combined with different settling velocity and collision frequency terms are systematically investigated to find the models which best describe observed mean particle size, averaged concentration, and PSD. Using the best-performing model set, it is then investigated how the trends of parameters change from early-stage to early-late-stage cases across a range of solution chemistries and at different positions within a short column. The initial PSD is a critical variable in aggregation modelling. Models with three approaches were applied: initial PSD observed in each experiment as the initial condition in each model (A); constant initial condition for all experiments/models (B); and the latter approach with variable- $\alpha$  across different size classes, accounting for aggregate size-driven variations in surface interaction energy profiles according to the DLVO theory (C) [24]. This comprehensive experimental and numerical study yields new insights into both the changing dynamics of aggregation as NP systems evolve over time, and the applicability of model concepts used to describe them.

### **3.5 Modelling**

Population balance models such as the Smoluchowski model [25, 26] are the most widely-used methods for predicting aggregation-driven PSD of colloidal suspensions [27-29]. However, the basic discretised form of these models applies only when each aggregate size class volume is considered the arithmetic sum of volumes of smaller classes. To span the size range that can result from early and late stages of aggregation, e.g., 40 nm to 10  $\mu\text{m}$ , over  $10^5$  size classes are required, for each of which the PB equation should be solved. This is computationally impractical, particularly when other transport phenomena are modelled or for iterative calibration of parameters against experimental data. A geometric size discretization technique proposed [30, 31] to mitigate this issue was recently used by Dale et al. [32] to simulate aggregation and dissolution of environmentally-relevant NP. A geometric series of aggregate volumes is given as  $v_{i+1}/v_i = 2^{1/q}$ , where  $q$  is an integer greater than or equal to one. However, values of  $q$  derived from PSD obtained from experimental techniques such as DLS are typically non-integer, e.g., considering the size discretization approach used by Malvern Zetasizer instrument (Nano ZS, UK) on its output data and using the aforementioned formula for  $q$  along with Eq. F24 (Appendix F)  $q$  may vary by  $D_f$  from  $q = 1.574$  for  $D_f = 3$  to  $q = 2.63$  for  $D_f = 1.8$ .

More flexible approaches include FP and MP techniques [33, 34]. Fixed-pivot maintains a minimum number of size classes (bins) via selective refinement of a coarse discretization of the particle volume dimension. This approach can consider binary or multiple collisions. Ignoring terms for breakage and adding a sedimentation term, the FP model conserving two properties of mass and number can be expressed as [33]:

$$\begin{aligned} \frac{dn_k}{dt} = & \sum_{\substack{j,i \\ v_{k-1} \leq (v_j+v_i) \leq v_{k+1}}}^{j \geq i} \left[ 1 - \frac{1}{2} \delta_{j,i} \right] \eta_k \alpha_{j,i} \beta_{j,i} n_j n_i \\ & - n_k \sum_{i=1}^{k_{max}} \alpha_{k,i} \beta_{k,i} n_i - \frac{U_k}{Z_s} n_k \end{aligned} \quad (3.1)$$

where  $\eta_k$  is given as:

$$\eta_k = \begin{cases} \frac{v_{k+1} - (v_j + v_i)}{v_{k+1} - v_k}, & v_k \leq (v_j + v_i) \leq v_{k+1} \\ \frac{(v_j + v_i) - v_{k-1}}{v_k - v_{k-1}}, & v_{k-1} \leq (v_j + v_i) \leq v_k \end{cases} \quad (3.2)$$

The MP model [34] assumes that when the particle number concentration in a size class changes from sharp-decreasing gradients toward near-uniformity, the 'pivot' (the representative point of each size class in the particle size distribution) moves from the lower end of that class toward the middle. Two differential equations need to be solved over time. Omitting the breakage-relevant terms and considering the sedimentation term, the governing equations for the MP model become:

$$\frac{dn_k}{dt} = \sum_{\substack{j \geq i \\ v_k \leq (v_j + v_i) \leq v_{k+1}}} \left[ 1 - \frac{1}{2} \delta_{j,i} \right] \alpha_{j,i} \beta_{j,i} n_j n_i - n_k \sum_{i=1}^{k_{max}} \alpha_{k,i} \beta_{k,i} n_i - \frac{U_k}{Z_s} n_k \quad (3.3)$$

$$\frac{dv_k}{dt} = \frac{1}{n_k} \sum_{\substack{j \geq i \\ v_k \leq (v_j + v_i) \leq v_{k+1}}} \left[ 1 - \frac{1}{2} \delta_{j,i} \right] [(v_j + v_i) - v_k] \alpha_{j,i} \beta_{j,i} n_j n_i \quad (3.4)$$

Equations (3.1-3.4) can be solved for a given initial PSD, to yield PSDs resulting from aggregation and sedimentation at any time for a specified sedimentation depth  $Z_s$ . From the PSD, other quantities such as mean  $D_H$  and mass concentration can be determined as described in the Appendix F. Note that, following common practice in this area [35-37], sedimentation is not modelled as a mass transfer process but as a net mass loss rate for each size class which scales linearly with  $Z_s$ .

The collision frequency for environmental colloids is commonly given as the sum of three mechanisms: perikinetic collisions (Brownian), orthokinetic collisions (shear-induced aggregation under fluid motion), and differential settling (collection of smaller

aggregates by the larger ones during sedimentation) [17]. Expressing collision frequencies based on the volume (or mass) of aggregates as a representative variable [32, 38], using fractal dimension relationships and considering permeability drag effects [39], the following relationships yield:

$$\beta_{PrIk_{i,j}} = \frac{2k_b T}{3\mu} \left( v_i^{\left(\frac{1}{D_f}\right)} + v_j^{\left(\frac{1}{D_f}\right)} \right) \left( \frac{1}{\Omega_i} v_i^{-\left(\frac{1}{D_f}\right)} + \frac{1}{\Omega_j} v_j^{-\left(\frac{1}{D_f}\right)} \right) \quad (3.5)$$

$$\beta_{Orth_{i,j}} = \frac{c}{\pi} v_0^{\left(1-\frac{3}{D_f}\right)} \left( \eta_{c_i}^{\left(\frac{1}{2}\right)} v_i^{\left(\frac{1}{D_f}\right)} + \eta_{c_j}^{\left(\frac{1}{2}\right)} v_j^{\left(\frac{1}{D_f}\right)} \right)^3 \quad (3.6)$$

$$\beta_{Diff_{i,j}} = \frac{3}{2} \left( \frac{\pi}{6} \right)^{\frac{1}{3}} v_0^{\left(\frac{2}{3}-\frac{2}{D_f}\right)} \left( \eta_{c_i}^{\left(\frac{1}{2}\right)} v_i^{\left(\frac{1}{D_f}\right)} + \eta_{c_j}^{\left(\frac{1}{2}\right)} v_j^{\left(\frac{1}{D_f}\right)} \right)^2 |U_i - U_j| \quad (3.7)$$

The superposition of the three rates gives the total rate of collisions,  $\beta(i, j)$ :

$$\beta_{i,j} = \beta_{PrIk_{i,j}} + \beta_{Orth_{i,j}} + \beta_{Diff_{i,j}} \quad (3.8)$$

where  $\Omega$  is the drag coefficient correction factor defined as the ratio of drag force exerted on a permeable aggregate to drag force exerted on an impervious aggregate with the same size [35, 40], and  $\eta_c$  is the fluid collection efficiency of an aggregate, defined as the ratio of flow through an aggregate to total flow approaching the aggregate [35, 41]. To calculate collision frequencies, two permeability models are used: the Brinkman permeability model [35, 42] and the Davies permeability model [43]. Additionally, the use of collision frequencies calculated based only on fractal relationships without permeability consideration is investigated [44, 45]. Four types of settling velocity models were investigated for NP aggregates of fractal nature. These include an empirical power-law equation [46, 47], a permeability model based on the Davies correlation [43, 48], a permeability model based on the Brinkman model [35, 40, 41], and a fractal model which considers the effect of the size distribution of primary particles forming each aggregate [49, 50]. Finally, in the variable  $\alpha$  approach,  $\alpha$  was calculated based on DLVO theory considering only van der Waals attraction and electrostatic repulsion interaction energies. The Hamaker constant for HAP-water-

HAp system was calculated as  $2.77 \times 10^{-21}$  J [51]. All models and their related equations are thoroughly introduced in the Appendix F.

## **3.6 Materials and Methods**

### **3.6.1 Numerical modelling**

Details of MATLAB (Mathworks, USA) codes for all models used in this study are available in the Appendix F. In brief, an explicit forward Euler scheme was used for the time derivative. The explicit approach was chosen due to potential inaccuracy and computational problems of using an iterative implicit approach [52]. A simple forward Euler approach was selected since higher-order schemes, such as fourth-order Runge-Kutta, were previously found ineffective in solving PB models, which are examples of “stiff” problems [32, 53]. Potential numerical instability in certain ranges of parameters within the explicit model was mitigated by an adjustable time step and a novel optimization algorithm based on a heuristic approach which, by incrementing a parameter at a time within set ranges, enhanced the fit between observations and model outputs using a parallel processing approach. An automatic increase of initial time step of the ‘slave’ numerical model by the ‘master’ optimization algorithm helped prevent unstable runs affecting the optimization process.

Parameter calibration was conducted on the Chadwick high performance cluster and the Condor high throughput computational systems at the University of Liverpool. Comparison of numerical model performance with analytical solutions of the Smoluchowski model for both monodisperse [17] and log-normal-distributed initial conditions [54] is demonstrated in the Appendix F. The Nash–Sutcliffe determination coefficient (a conservative  $R^2$ ) [55] was used to assess goodness of fit. In this study, the parameters are calibrated based on the hydrodynamic size as an objective function and investigate how well the fitted model describes concentration variation over time and PSD at certain times.

### **3.6.2 Experiment procedure**

Hydroxyapatite (particle density =  $3.16 \text{ g/cm}^3$ ) was obtained from Alfa Aesar, UK. Evolution of aggregate mean size, PSD and concentration over time were measured by

DLS (Malvern Zetasizer Nano ZS, UK). The valid measurement size range reported by the manufacturer is from 1 nm to  $10^4$  nm. Measurements were carried out with an interval of  $\sim 3.37$  min. For all measurements, the number of runs was 5 (duration 10 s), beam attenuator index was 11, position of measurement was 6.5 mm following pre-tests to establish the least noise and highest reproducibility in the count rate as well as the Z-average data (hydrodynamic diameter,  $D_H$ ). Zeta potential was measured with the same instrument with an automatic adjustment. To prevent the growth of bacteria in samples during the course of the experiment, 10 mM sodium azide was added. This was also beneficial due to its buffering capability to ensure a stable pH, although corollary measurements indicated a potential variation of  $\pm 0.52$  at pH 7-10 over 24 h.

All experiments were conducted for at least 5 hours and in duplicate according to this procedure: (1) prepare particle dispersion in DI water with a final particle concentration 50 mg/L, and sodium azide concentration 10 mM; (2) adjust pH at 6, 7, 10, or  $11 \pm 0.05$  with NaOH/HCl (100 mM); (3) ultrasonicate 5 min, add electrolyte ( $\text{CaCl}_2$ ) to reach concentrations of 0, 1, 2.5, 3, 5, 7.5, 10 mM, immediately vortex 5 sec, transfer to a disposable cuvette and immediately start the DLS measurement. The whole process duration, from ultrasonication until the start of the first measurement, was  $70 \pm 20$  sec. Standard sample volume of 3 mL resulted in a measurement depth of  $\sim 2.33$  cm. The impact of the measurement depth was also investigated by varying the sample volume as 1 mL, 3 mL, and 4 mL, corresponding to approximate measurement depths of 0.33 cm, 2.33 cm, and 3.33 cm, respectively. The DCR, which is the measured DLS count rate divided by the attenuation factor was extracted from the DLS data and used as an indicator of mass concentration [56-58]. To assess the significance of the relationship between DCR and the mass concentration, DCR was measured at different concentrations (1, 5, 10, 50, 100, 250, and 500 mg/L) of HAp NP.

## **3.7 Results and discussion**

### **3.7.1 Experimental results**

Figure 3.1 shows averaged  $D_H$  and DCR for HAp at various solution chemistries over 5 hours. Dynamic light scattering measurements of aggregate  $D_H$  evolution showed low noise and good reproducibility as indicated by small standard deviations of

duplicate experiments (error bars, Fig. 3.1). However, stability of DCR measurements tended to decrease over time. At constant pH 6, below 3 mM CaCl<sub>2</sub> the slope of  $D_H$  versus time is near linear on a semi-log plot throughout the experiment; above 3 mM the slope asymptotes from a steep slope at < 40 min to a gentle slope at greater times, revealing both early and late stages of aggregation/sedimentation (Fig. 3.1a). This also suggests that the CCC lies between 3 and 5 mM CaCl<sub>2</sub>. Similar behaviour is observed for various pH when the ionic strength is held at 5 mM CaCl<sub>2</sub> (Fig. 3.1b). Figures 3.1c,d illustrate DCR data normalized to the initial DCR value of each experiment. This quantity drops below 0.5 by the end of the experiments in most cases under the DLA regime (>4 mM CaCl<sub>2</sub>). However, normalized DCR increases over time for RLA regime (CaCl<sub>2</sub> concentrations < 4 mM). This increasing trend might be interpreted as settling, slow-aggregating particles arriving at the point of measurement from further up the water column, causing increase of mass concentration in this point to above the initial uniform concentration in the sample. Such an increased concentration in the lower positions of the water column has been already reported [59-61]. Although DCR data have been used as proxy for particle mass concentration in multiple studies [57, 58, 62, 63], its application in NP studies is less common [56], and there have been indications that DCR can be affected by size [64] or the number of particles [61] in addition to the mass. The relationship between the DCR and HAp concentration was already presented in Appendix F (Fig. F1) with a linear correlation ( $r^2 > 0.98$  and  $P \gg 0.05$ ) between these two factors. It should be noted that the use of DLS data like any experimental technique has inherent measurement uncertainties, e.g., mean hydrodynamic size might be affected by the larger fraction of PSD [65]. However, as shown in PSD results (Figs. F2 and F3) developing a monodisperse PSD toward later times suggests that this impact might not be significant here.

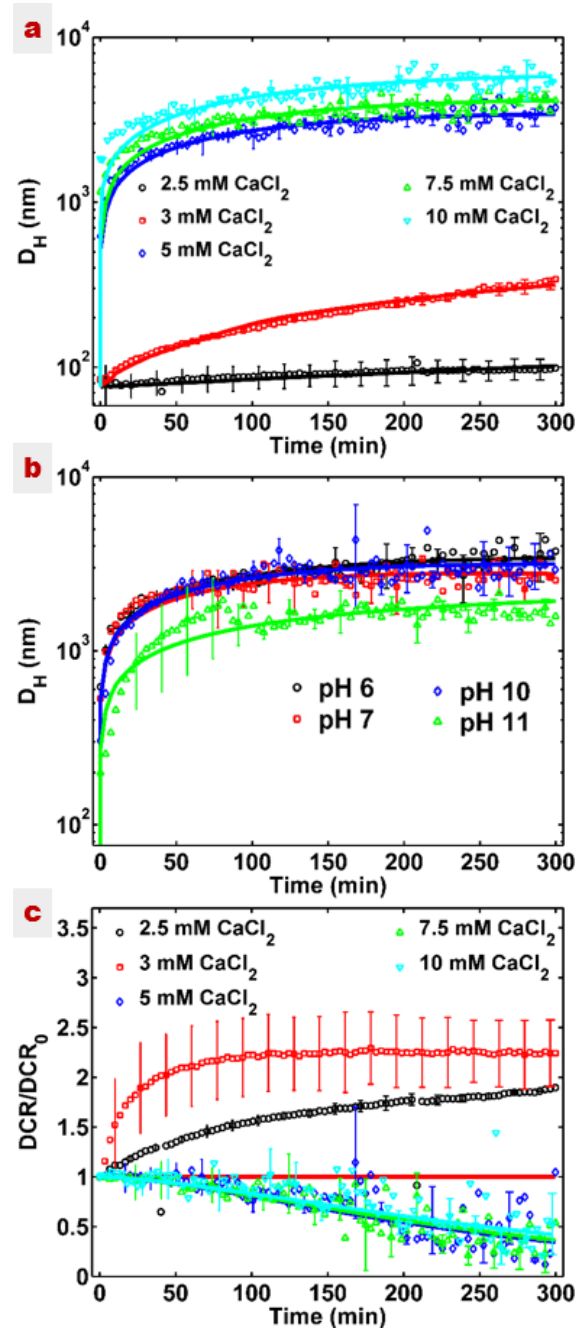


**Figure 3.1** Evolution of averaged hydrodynamic diameter,  $D_H$ , (a,b) and change in mean derived count rate (DCR) normalized to the initial derived count rate ( $\text{DCR}_0$ ) (c) for HAp NPs at the point of measurement at various IS with a fixed pH at 6 (a,c) and various pH with a fixed IS at 5 mM  $\text{CaCl}_2$  (b). The model used here was FP with power law formulation and Brinkman collision model. The modelling approach includes a fixed initial PSD with considering the pre-early stage of aggregation and a constant attachment efficacy (approach B).

### 3.7.2 Model screening

A detailed discussion of the screening of the 24 model combinations is provided in Appendix F (Figs. F4-F6 and Tables F11-F44). Briefly, for both FP and MP models, calculation of collision frequencies using the simple fractal approach or Davies permeability correlation led to poorer matches between the experimental and modelled  $D_H$  values (Fig. F4) than when permeability collision frequencies were based on the Brinkman model. In the two former collision models,  $R^2_{NS}$  of  $D_H$  data was below 0.5, whereas for the Brinkman permeability model  $R^2_{NS}$  increased up to 0.71 (Tables F1 and F2). Fits to DCR data were relatively insensitive to model type (Table F3). The simple fractal and Davies permeability correlation approaches led to  $D_H$  curve shapes inconsistent with the experimental data. Therefore, these two collision frequency models were discarded. The best among the settling velocity models, using the FP numerical approach, was the power-law formulation in terms of fitting for  $D_H$  data ( $R^2_{NS} = 0.71$ ). Using the MP scheme, the power law, Brinkman permeability, and size distribution models gave close fitting results with  $R^2_{NS}$  equal to 0.68, 0.71, and 0.70, respectively, against  $D_H$  data and 0.62, 0.58, and 0.87, respectively against DCR data (Table F2).

The FP model performs much faster than the MP method in simulating both early and late stages of aggregation. In fact, once the initial stage of the aggregation is passed, a significant increase (e.g., 500 times) in the time step length can be adopted for the FP model without affecting model stability. The MP method, in spite of being originally faster than FP [53], is not as flexible as FP in reducing the number of time steps in the late stage, potentially because of sharp gradients at longer times caused by the additional volume-based equation in the MP model. The final selected model set (FP, Brinkman-permeability-based collision frequency, and power-law settling velocity) based on a case-specific initial PSD (approach A, Table 3.1) fit the experimental data with mean  $R^2_{NS}$  of 0.795 ( $D_H$ ) and 0.670 (DCR) for all cases with various pH and IS except the cases under the RLA regime (Fig. 3.1, Table F3). The model matched to  $D_H$  data could well describe normalized DCR trends under the DLA condition, suggesting that in this regime DCR is an appropriate representative of mass concentration.

**Table 3.1** Model parameters estimated by fitting FP models to both early and late stages of aggregation under different electrolyte concentrations (at fixed pH 6) and different pH (at fixed electrolyte concentration, 5 mM CaCl<sub>2</sub>) over 5 h, based on three modelling approaches (A, B, C), and mass removal results estimated by the models for a sample volume of 3 mL (3 cm water depth) after 5 h. The power-law model and Brinkman-based permeability model are used to calculate the sedimentation velocity and collision frequencies, respectively.

Param.	Model. approac h	Electrolyte Concentration (mM)					pH		
		2.5	3	5	7.5	10	7	10	11
$\alpha$	A	$1.1 \times 10^{-4}$	$7.1 \times 10^{-3}$	11.60	8.10	1.10	15.4	6.33	1.59
	B	$2.0 \times 10^{-6}$	$1.0 \times 10^{-5}$	1.13	1.13	1.23	1.65	1.37	0.21
	C	NA	NA	NA	NA	NA	NA	NA	NA
$D_f$	A	1.53	1.48	2.03	2.12	2.27	2.26	2.32	2.70
	B	1.71	1.38	2.53	2.53	2.45	2.69	2.63	2.66
	C	1.50	1.50	2.50	2.42	2.25	2.60	2.61	2.70
Remov. %	A	0.4	1.0	86.1	86.9	70.0	94.9	88.8	84.7
	B	0.1	0.1	77.5	75.8	71.8	86.3	81.6	50.9
	C	0.1	0.1	75.0	72.2	65.0	78.0	76.8	55.1

A: initial PSD; B: identical PSD; C: identical PSD, DLVO; NA: not applicable

### 3.7.3 Aggregate structure and sedimentation velocity

The model fit results indicate that models assuming bulk density-controlled sedimentation tend to outperform models assuming permeability-controlled sedimentation. The impact of aggregate structure on settling velocity is a disputed subject [66]. Enhanced sedimentation velocities compared to Stokes' law based on hydrodynamic size have been reported and interpreted as flow through the aggregates

reducing the aggregate drag [40, 42, 43, 67]. Other studies [47, 68, 69] point to the overestimation of Stokes' law for floc sedimentation velocity. I compared trends in terminal settling velocity versus the size of aggregates resulted from each sedimentation model used in the present study.

Figure 3.2 illustrates, for three values of  $D_f$  (1.6, 2.0, and 2.3), that the highest sedimentation velocity is predicted by the Davies permeability model, followed by the Brinkman, size-distribution-based and power-law models, respectively. The Davies permeability model predicts an increase in sedimentation velocity with decrease of  $D_f$  in agreement with other studies [40, 43, 67]. However, this model yields an estimate of settling velocity that is much higher than all the other models [70]. The Brinkman model exhibits a slight increase of velocity with  $D_f$  which is only discernible for particles of less than  $1 \mu m$  in size—not considerable in the sedimentation process [17, 71]. This low sensitivity of settling velocity to the aggregate structure contradicts experimental observations [40, 42, 43, 47, 67, 68]. However, both power-law and size-distribution-based models predict increased velocity with  $D_f$  due to the greater bulk density of aggregates (Fig. 3.2). This variation is more significant for the power-law model compared to the size-distribution-based model, suggesting that the power-law expression is more sensitive to  $D_f$ . Overall, simulations incorporating these bulk density-controlled sedimentation terms yielded the best fits against experimental data.

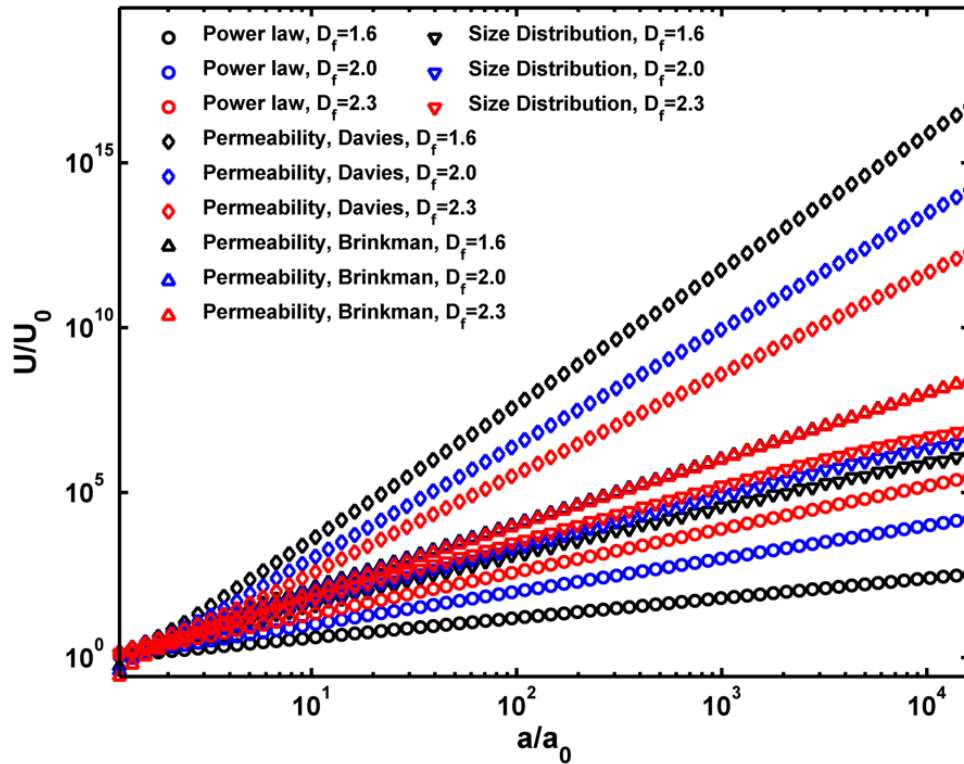


**Figure 3.2** Trends of settling velocity,  $U$ , normalized to the settling velocity of primary particle,  $U_0$ , versus particle radius of each size class,  $a$ , normalized by the primary particle radius (smallest size class),  $a_0$ , calculated by four different types of velocity models. Fractal dimension is set as 1.6, 2, and 2.3. The primary particle radius used in these models is 40 nm.

Figure 3.2 shows that for particles of the same matter and with constant diameter, reducing  $D_f$  (i.e. increasing porosity and decreasing mass) results in considerable reduction in the settling velocity according to power-law and size-distribution-based models. Recently, in an insightful study, Emadzadeh and Chiew [72] showed that for large synthetic particles ( $> 1$  cm in size and density  $\gg 1$  g cm $^{-3}$ ) with identical matter and diameter, increasing porosity corresponding to a decreased mass caused reduction of the terminal settling velocity. However, when particles of different matter were used to maintain the mass constant too, the particles with higher porosity exhibited higher settling velocity. This implies for homogeneous NP aggregates with density of primary particles  $\gg 1$  g cm $^{-3}$ , the impact of the bulk density of aggregates far outweighs permeability or drag effects, in agreement with the analysis based on best fits to early and late stage HAp aggregation data and in contrast to Johnson et al. [43].

### 3.7.4 Attachment efficiency and fractal dimension

Table 3.1 shows the parameters determined from the fitting (optimisation) procedure, demonstrating that with the increase of  $\text{CaCl}_2$  concentration above 5 mM the model parameter  $\alpha$  increases above one. Classical theories of aggregation [18, 22] prescribe that attachment efficiency increases until the double layer repulsion is completely screened, where the CCC is met and  $\alpha$  is equal to one. Calculation of DLVO profiles, shown in Fig. F7, confirms that at  $[\text{CaCl}_2] \geq 5$  mM there is no energy barrier against aggregation. Values greater than one in this model parameter are interpreted as indicating a mechanism associated with the late-stage aggregation which enhances the *effective* attachment efficiency above its classical limit. Although there have been cases in the literature reporting  $\alpha$  above unity [67, 73-76], to investigate this further, the model was fitted to  $D_H$  data only at the early stage (first 20 min) of the processes. Since including  $D_f$  as an estimating parameter was found not to be necessary for early-stage fitting, this was fixed at 1.6 (close to the common DLA range) for all cases of pH and high IS. Results, presented in Table F5, reveal that for most of the cases  $\alpha$  reduces to below one. The only remaining case with  $\alpha > 1$  also reduces to below one if  $D_f$  is considered as a free parameter in the optimization process.

To scrutinize this issue further, the initial PSD was fixed in all cases based on a single-peaked PSD extracted from the experimental case with no aggregation (approach B, Table 3.1). In this approach, the very first moments of the aggregation ( $\sim 70$  s), which are not captured in experiments, are considered by the model with shear coagulation operating, and the sedimentation process turned off as described in the Appendix F. This approach yields slightly poorer goodness-of-fit (mean  $R^2_{NS}$  0.736 for  $D_H$  and 0.513 for DCR) than approach A (mean  $R^2_{NS}$  0.763 for  $D_H$  and 0.64 for DCR) for cases of  $\text{IS} > 5$  mM and various pH (Figs. 3.1, F8 and Table F3). In contrast to approach A, approach B yields  $\alpha$  closer to one in all cases of high IS (maximum  $\alpha$  is 1.65 which occurs at pH 7, Table 3.1). Furthermore, the condition in which  $\alpha$  varies from 0 to 1 with particle/aggregate size according to varying DLVO interaction energies, was investigated using a fixed-PSD initial condition (approach C, Table 3.1). The results (Fig. F8 and Table F3) show that for cases of IS higher than 5 mM and for various pH, mean model fit  $R^2_{NS}$  is rather lower than that of previous approaches—0.687 and 0.429 for  $D_H$  and DCR, respectively. Although this approach could fit

experimental data cases at 5, 7.5, and 10 mM CaCl<sub>2</sub>, with only one adjustable parameter ( $D_f$ ), there was a need for adding another adjustable parameter in other cases, due probably to uncertainties in measurement of factors like zeta potential (with common accuracy on the order of  $\pm 10\%$ ) [77] as reported in Fig. F9 and Table F3. Even considering two adjustable parameters ( $D_f$  and zeta potential), approach C was still unable to fit the case at 3 mM CaCl<sub>2</sub>. Other non-DLVO factors such as specific-ion effects [78] which have not been considered in this study or some basic assumptions of the DLVO such as perfect sphere [79] ignored for nonuniform-shaped porous aggregates might be reasons for the discrepancies.

Conventionally, open aggregate structures ( $D_f$  tends to 1.8) are formed in DLA regime where every contact results in attachment, while more compacted structures ( $D_f$  tends to 2.1) are formed under the more selective RLA condition [17, 80]. As shown in Table 3.1, models fitted across both early and late stage data indicate that at CaCl<sub>2</sub> concentrations  $\leq 3$  mM (RLA)  $D_f$  is lower than 1.8 while at  $\geq 5$  mM (DLA)  $D_f$  ranges is higher than 2.03 and further increases with pH (up to 2.7 at pH 11). Approach B yielded even larger  $D_f$  on average by 11% compared to approach A. This difference was 8% for approach C. Strongly overlapping ranges of  $D_f$  for RLA and DLA regimes have been frequently reported in the literature [47, 81-85], especially for particles subject to mechanisms other than Brownian diffusion, such as ‘ballistic’ aggregation [17], orthokinetic aggregation [81, 86], and differential sedimentation [19]. These can be the result of linear trajectories [17] or restructuring [19, 41]. It has also been indicated in the literature [87, 88] that rapid particle-cluster aggregation leads to a denser aggregate ( $D_f=2.5$ ) than cluster-cluster aggregation ( $D_f=1.8$ ). Allain et al. [19] reported a  $D_f$  value of 2.2 for calcium carbonate colloids within the DLA regime under quiescent sedimentation, and others [86] reported  $D_f$  in range of 2.3 to 2.8 for calcium phosphate in a system with settling and shear. Experimentally-measured  $D_f$  reported in the literature are typically limited to the early stage of aggregation or lower aggregation rates than those investigated in the present study.

Fitting the model to only the early stage of experiments showed ranges of  $D_f$  consistent with conventional expectations (Table F5) under the DLA regime. The contrasting trends obtained when fitting to both stages together suggests the crucial role of late-stage aggregation process in modifying this parameter. The observation of

an increase in the DCR curves under the RLA regime versus decreasing DCR in the DLA regime indicates that sedimentation under the RLA regime is slower than that under the DLA regime (Fig. 3.1c). This implies that the bulk density and therefore  $D_f$  of aggregates in the RLA regime should be lower than that under the DLA condition.

It is deduced that in the late stage, evolved aggregates formed from mixed particle-cluster populations under the RLA condition are less compact than early-stage aggregates, potentially as a result of irregular packing geometries and inaccessibility of internal pore spaces to incident particles in unfavourable interaction conditions [89]. Decreasing  $D_f$  over the course of experiments has been observed already for fullerene NP under both DLA and RLA regimes [90]. However, due to uncertainties associated with the DCR data obtained under the RLA regime (discussed below), further experimental/modelling investigations are required to confirm this explanation. Conversely, aggregates formed in late-stage DLA conditions may have higher  $D_f$  (compared to less-compact early stage aggregates) as a result of internal reorganisation of particles within each aggregate, aggregate-aggregate collisions, and trapping individual particles in voids of large, open clusters during their downward sedimentation [19, 89]. It should be mentioned that model-fit parameter values might bear both experimental and model uncertainties. Direct experimental measurement of  $D_f$  under the late-stage conditions used in this research is a priority for future work to confirm the model predictions reported here.

Although all three modelling approaches are reasonably successful in fitting the experimental data, none of final models does so while maintaining all parameter values simultaneously within the ranges expected from previous literature. The model formulation applied in the present study is not able to reproduce the experimentally observed rise in DCR data under the RLA regime, because the sedimentation term used in these models is a simple decay term (last term in Eqs. 3.1 and 3.3) which avoids the computational expense and potential numerical dispersion problems of solving a spatio-temporal partial-differential equation [91]. Although it was shown that DCR is an appropriate indicator of the mass concentration under DLA, it remains for future studies to validate this conclusion under the RLA regime. The modelled PSDs are shown in Figs. F2 and F3 and discussed in detail in the Appendix E. Overall, approach

B demonstrates the best overall match between observed PSD and modelled PSD through late-stage conditions.

### **3.7.5 Mass removal rates and measurement depth**

Table 3.1 shows the predicted mean percentage mass removal after 5 h within a 3 cm modelled water column for different pH and IS, using parameter values estimated in both early and late stages. Under the RLA regime (2.5 and 3 mM CaCl<sub>2</sub>) a negligible ( $\leq 0.5\%$ ) decrease in mass concentration indicates that sedimentation is minimal, in agreement with experimental observations (Fig 3.1c). Under the DLA regime (5-10 mM CaCl<sub>2</sub>) and at various pH, for the three approaches A, B and C predicted mass removal reaches 85.4%, 74.5%, and 71.0%, respectively. Figure 3.3 shows that predicted mass removal is greater in the upper part of the water column. Removal percentage is maximum at pH 7 (86.4%, average of the three modelling approaches, Table 3.1). With increasing pH above pH 7, mass removal decreases (down to 63.6% on average), consistent with the decrease of  $\alpha$  and increase of  $D_f$  (Table 3.1). Surprisingly, as illustrated in Fig. 3.3 under the DLA condition, the percentage mass removal consistently (under almost all modelling approaches) decreases with increase in the IS from on average 79.5% at 5 mM CaCl<sub>2</sub> to 78.3% and 68.9% at 7.5 and 10 mM CaCl<sub>2</sub>, respectively (Table 3.1, Fig. 3.3).

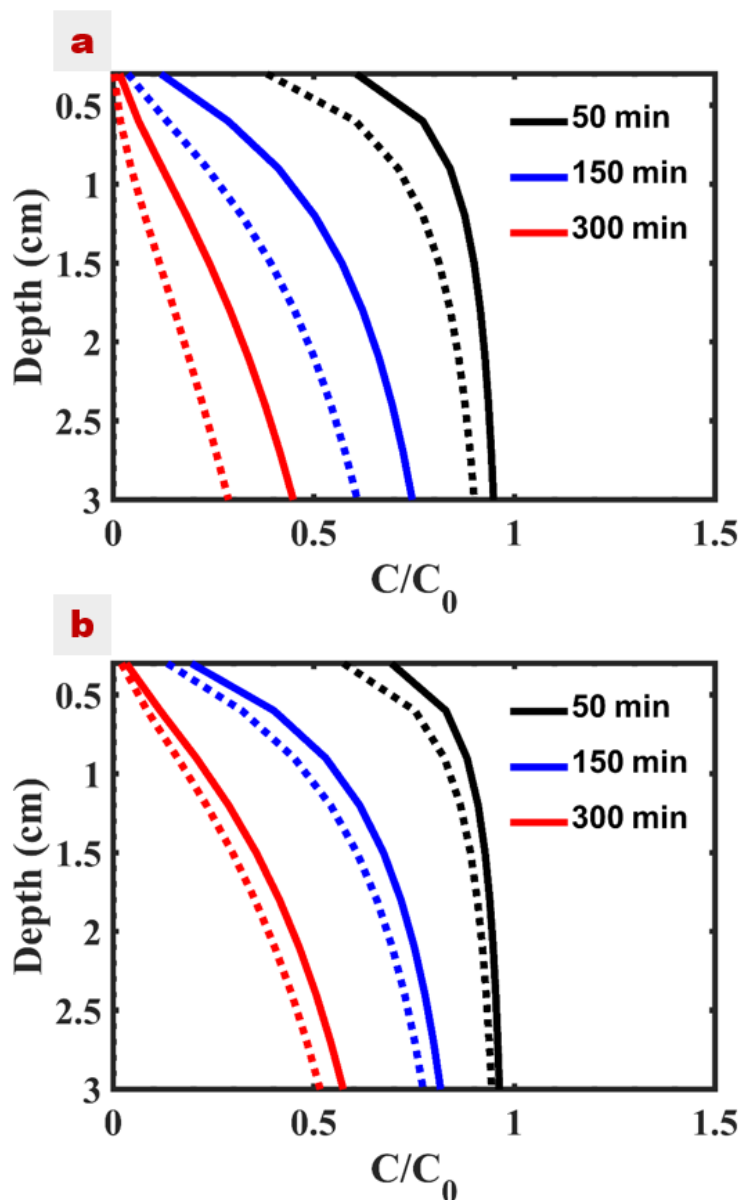


**Figure 3.3** Modelled mass concentration,  $C$ , profiles normalized by the initial mass concentration,  $C_0$ , versus the water column depth at (a) 5 mM  $\text{CaCl}_2$  and (b) 10 mM  $\text{CaCl}_2$  after 50, 150, and 300 min. The continuous lines represent approach A (case-specific initial PSD) and dashed lines represent approach C (fixed initial PSD combined with variable  $\alpha$  computed by DLVO).

It was examined experimentally how the depth of measurement from the surface of the liquid affects the parameter values obtained using approach A. The results for depths of 0.33, 2.33, and 3.33 cm are presented in Table F6 and Fig. F10. For measurements at short distance below the water surface (0.33 cm), the aggregation is

significantly lower than when measured at greater depths (2.33 and 3.33 cm). This might indicate the significance of differential sedimentation in aggregation of HAp NP. This also indicates that the late stage of coupled aggregation-sedimentation processes is less noticeable in the regions just below the surface of water. The model fit results (Table F6) confirm that late-stage influences on both  $\alpha$  and  $D_f$  increase with the measurement depth. Crucially,  $\alpha$  determined for the smallest depth (0.33 cm) assumes a value lower than one and  $D_f$  is relatively closer to the common threshold of DLA regime which agrees with fit result of early stage alone (Table F5). This strongly associates parameter values  $\alpha > 1$  and  $D_f$  outside expected ranges of DLA regime, with the complications of interacting late-stage processes during coupled aggregation and sedimentation.

### **3.7.6 Implications for the fate of NP in groundwater and aquatic environments**

The combination of experiment and modelling approaches presented here has enabled the complex interactions between aggregation and sedimentation to be investigated in NP systems well inside the late-stage at which the particle-aggregate population has evolved significantly from its initial PSD. These conditions are likely to be the norm in most environmental systems in which NP have been resident for any length of time. It is demonstrated that population balance models can be applied to systems at both stages of aggregate evolution. Although the best-performing model suite included permeability-based models for describing collision frequencies, the empirical, density-controlled descriptions for settling velocity were able to better describe the observed trends in experimental data over 5 h of coupled aggregation and sedimentation. Allowing the attachment efficiency to vary with aggregate size did not significantly alter model outcomes compared to assumption of a constant attachment efficiency, but fitted parameters were much more sensitive to the specification of the initial PSD. In terms of reduction in computational effort over the late-stage of the processes, the FP aggregation model was found to have a greater capability than the MP technique. These results have significance in developing practical, computationally-efficient models for the fate and transport of NP in the environment.

While models fitted to only early stage data showed trends in attachment efficiency and fractal dimension consistent with classical theory, these trends varied as the systems evolved. The results demonstrate that at lower IS (RLA), aggregation is slow, and sedimentation is negligible in the timescales considered here. At intermediate IS (5 mM CaCl<sub>2</sub>) near the CCC, a moderate-rate DLA develops a population of NP clusters which are optimally more efficient at collecting (by aggregation) and removing (by sedimentation) large numbers of smaller particles and aggregates than that at higher IS (7.5 and 10 mM CaCl<sub>2</sub>) where the system moves rapidly to fewer, larger, but less-compact aggregates, and overall mass removal rates are reduced due to slower sedimentation. These lower removal rates within high-IS solutions may bring about lifetimes and potential transport distances of NP aggregates in aqueous suspension in settings such as marine environments, coastal aquifers, or in soil pore microenvironments that are longer than expected based on conventional models or extrapolations from experimental data obtained only in early-stage conditions. Although the population balance techniques applied in the present study alleviate computational expenses of using an arithmetic particle size discretization well with a geometric discretization when applied to small-scale laboratory conditions, it remains a question whether such models are efficient when coupled to fate and transport models at larger environmental scales, e.g., aquifer and watershed. These issues are tried to be addressed in the following chapters.

## 3.8 References

1. Wang, D., Y. Jin, and D. Jaisi, *Cotransport of Hydroxyapatite Nanoparticles and Hematite Colloids in Saturated Porous Media: Mechanistic Insights from Mathematical Modeling and Phosphate Oxygen Isotope Fractionation*. Journal of Contaminant Hydrology, 2015. **182**: p. 194-209.
2. Fuller, C., et al., *Mechanisms of uranium interactions with hydroxyapatite: Implications for groundwater remediation*. Environmental Science & Technology, 2002. **36**(2): p. 158-165.
3. Kanel, S.R., et al., *Nano-Scale Hydroxyapatite: Synthesis, Two-Dimensional Transport Experiments, and Application for Uranium Remediation*. Journal of Nanotechnology, 2011. **2011**: p. 1-5.
4. Babakhani, P., et al., *Continuum-based models and concepts for the transport of nanoparticles in saturated porous media: A state-of-the-science review*. Advances in Colloid and Interface Science, 2017. **246**(Supplement C): p. 75-104.
5. Babakhani, P., et al., *Parameterization and prediction of nanoparticle transport in porous media: A reanalysis using artificial neural network*. Water Resources Research, 2017. **53**: p. 4564-4585.
6. McCarthy, J.F. and J.M. Zachara, *Subsurface transport of contaminants*. Environmental Science & Technology, 1989. **23**(5): p. 496-502.
7. Kersting, A.B., et al., *Migration of plutonium in ground water at the Nevada Test Site*. Nature, 1999. **397**(6714): p. 56-59.
8. Kansanen, P.H., et al., *Sedimentation and distribution of gamma-emitting radionuclides in bottom sediments of southern Lake Päijänne, Finland, after the Chernobyl accident*. Hydrobiologia, 1991. **222**(2): p. 121-140.
9. Evangelidou, N. and H. Florou, *The dispersion of <sup>137</sup>Cs in a shallow Mediterranean embayment (Saronikos Gulf–Elefsis Bay), estimated inventories and residence times*. Journal of environmental radioactivity, 2012. **113**: p. 87-97.
10. Otosaka, S. and T. Kobayashi, *Sedimentation and remobilization of radiocesium in the coastal area of Ibaraki, 70 km south of the Fukushima Dai-ichi Nuclear Power Plant*. Environmental monitoring and assessment, 2013. **185**(7): p. 5419-5433.
11. Babakhani, P., et al., *Modified MODFLOW-based model for simulating the agglomeration and transport of polymer-modified Fe nanoparticles in saturated porous media*. Environ Sci Pollut Res, 1-20, doi:10.1007/s11356-015-5193-0, 2015.
12. Phenrat, T., et al., *Particle size distribution, concentration, and magnetic attraction affect transport of polymer-modified Fe<sub>0</sub> nanoparticles in sand columns*. Environ. Sci. Technol., 2009. **43**(13): p. 5079-5085.
13. Keller, A.A., et al., *Stability and aggregation of metal oxide nanoparticles in natural aqueous matrices*. Environmental science & technology, 2010. **44**(6): p. 1962-1967.
14. Phenrat, T., et al., *Aggregation and sedimentation of aqueous nanoscale zerovalent iron dispersions*. Environmental Science & Technology, 2007. **41**(1): p. 284-290.
15. Gambinossi, F., S.E. Mylon, and J.K. Ferri, *Aggregation kinetics and colloidal stability of functionalized nanoparticles*. Advances in colloid and interface science, 2015. **222**: p. 332-349.
16. Szilagyi, I., et al., *Particle aggregation mechanisms in ionic liquids*. Physical Chemistry Chemical Physics, 2014. **16**(20): p. 9515-9524.

17. Elimelech, M., J. Gregory, and X. Jia, *Particle deposition and aggregation: measurement, modelling and simulation*. 1998: Butterworth-Heinemann.
18. Afshinnia, K., et al., *Effect of nanomaterial and media physicochemical properties on Ag NM aggregation kinetics*. Journal of Colloid and Interface Science, 2017. **487**: p. 192-200.
19. Allain, C., M. Cloitre, and F. Parisse, *Settling by cluster deposition in aggregating colloidal suspensions*. Journal of colloid and interface science, 1996. **178**(2): p. 411-416.
20. Lin, S. and M.R. Wiesner, *Deposition of Aggregated Nanoparticles—A Theoretical and Experimental Study on the Effect of Aggregation State on the Affinity between Nanoparticles and a Collector Surface*. Environmental science & technology, 2012. **46**(24): p. 13270-13277.
21. Afshinnia, K., et al., *The concentration-dependent aggregation of Ag NPs induced by cystine*. Science of the Total Environment, 2016. **557**: p. 395-403.
22. Grolimund, D., M. Elimelech, and M. Borkovec, *Aggregation and deposition kinetics of mobile colloidal particles in natural porous media*. Colloids and Surfaces A: Physicochemical and Engineering Aspects, 2001. **191**(1–2): p. 179-188.
23. Westerhoff, P. and B. Nowack, *Searching for global descriptors of engineered nanomaterial fate and transport in the environment*. Accounts of chemical research, 2012. **46**(3): p. 844-853.
24. Zhang, W., *Nanoparticle aggregation: principles and modeling*, in *Nanomaterial Impacts on Cell Biology and Medicine*, Y.C. David G. Capco, Editor. 2014, Springer. p. 19-43.
25. Smoluchowski, M., *Versuch einer mathematischen Theorie der Koagulationskinetik kolloider Lösungen*. Zeitschrift fuer Physikalische Chemie. 92., 1917. **129-68**.
26. Chandrasekhar, S., *Stochastic problems in physics and astronomy*. Reviews of modern physics, 1943. **15**(1): p. 1.
27. Rigopoulos, S., *Population balance modelling of polydispersed particles in reactive flows*. Progress in Energy and Combustion Science, 2010. **36**(4): p. 412-443.
28. Ramkrishna, D., *Population balances: Theory and applications to particulate systems in engineering*. 2000: Academic press.
29. Ramkrishna, D. and M.R. Singh, *Population balance modeling: current status and future prospects*. Annual review of chemical and biomolecular engineering, 2014. **5**: p. 123-146.
30. Hounslow, M.J., R.L. Ryall, and V.R. Marshall, *A discretized population balance for nucleation, growth, and aggregation*. AIChE Journal, 1988. **34**(11): p. 1821-1832.
31. Lister, J., D. Smit, and M. Hounslow, *Adjustable discretized population balance for growth and aggregation*. AIChE Journal, 1995. **41**(3): p. 591-603.
32. Dale, A.L., G.V. Lowry, and E.A. Casman, *Accurate and fast numerical algorithms for tracking particle size distributions during nanoparticle aggregation and dissolution*. Environmental Science: Nano, 2017. **4**(1): p. 89-104.
33. Kumar, S. and D. Ramkrishna, *On the solution of population balance equations by discretization—I. A fixed pivot technique*. Chemical Engineering Science, 1996. **51**(8): p. 1311-1332.
34. Kumar, S. and D. Ramkrishna, *On the solution of population balance equations by discretization—II. A moving pivot technique*. Chemical Engineering Science, 1996. **51**(8): p. 1333-1342.

35. Thill, A., et al., *Flocs restructuring during aggregation: experimental evidence and numerical simulation*. Journal of Colloid and Interface Science, 2001. **243**(1): p. 171-182.
36. Quik, J.T.K., et al., *Heteroaggregation and sedimentation rates for nanomaterials in natural waters*. Water research, 2014. **48**: p. 269-279.
37. Markus, A.A., et al., *Modeling aggregation and sedimentation of nanoparticles in the aquatic environment*. Science of The Total Environment, 2015. **506**: p. 323-329.
38. Hunt, J.R., *Self-similar particle-size distributions during coagulation: theory and experimental verification*. Journal of Fluid Mechanics, 1982. **122**: p. 169-185.
39. Veerapaneni, S. and M.R. Wiesner, *Hydrodynamics of fractal aggregates with radially varying permeability*. Journal of Colloid and Interface Science, 1996. **177**(1): p. 45-57.
40. Vikesland, P.J., et al., *Aggregation and sedimentation of magnetite nanoparticle clusters*. Environmental Science: Nano, 2016. **3**(3): p. 567-577.
41. Jeldres, R.I., F. Concha, and P.G. Toledo, *Population balance modelling of particle flocculation with attention to aggregate restructuring and permeability*. Advances in colloid and interface science, 2015. **224**: p. 62-71.
42. Li, X.-Y. and B.E. Logan, *Permeability of fractal aggregates*. Water research, 2001. **35**(14): p. 3373-3380.
43. Johnson, C.P., X. Li, and B.E. Logan, *Settling Velocities of Fractal Aggregates*. Environmental Science & Technology, 1996. **30**(6): p. 1911-1918.
44. Aziz, J.J., C.A. Serra, and M.R. Wiesner, *Hydrodynamics of permeable aggregates in differential sedimentation*. Environmental engineering science, 2003. **20**(1): p. 21-31.
45. Therezien, M., A. Thill, and M.R. Wiesner, *Importance of heterogeneous aggregation for NP fate in natural and engineered systems*. Science of The Total Environment, 2014. **485**: p. 309-318.
46. Li, D.H. and J. Ganczarczyk, *Fractal geometry of particle aggregates generated in water and wastewater treatment processes*. Environmental Science & Technology, 1989. **23**(11): p. 1385-1389.
47. Sterling, M.C., et al., *Application of fractal flocculation and vertical transport model to aquatic sol-sediment systems*. Water research, 2005. **39**(9): p. 1818-1830.
48. Logan, B.E. and J.R. Hunt, *Advantages to microbes of growth in permeable aggregates in marine systems*. Limnol. Oceanogr, 1987. **32**(5): p. 1034-1048.
49. Vahedi, A. and B. Gorczyca, *Settling velocities of multifractal flocs formed in chemical coagulation process*. Water research, 2014. **53**: p. 322-328.
50. Khelifa, A. and P.S. Hill, *Models for effective density and settling velocity of flocs*. Journal of Hydraulic Research, 2006. **44**(3): p. 390-401.
51. Wang, D., et al., *Humic acid facilitates the transport of ARS-labeled hydroxyapatite nanoparticles in iron oxyhydroxide-coated sand*. Environmental science & technology, 2012. **46**(5): p. 2738-2745.
52. Jacobson, M.Z., *Fundamentals of atmospheric modeling*. 2005: Cambridge university press.
53. Nopens, I., D. Beheydt, and P.A. Vanrolleghem, *Comparison and pitfalls of different discretised solution methods for population balance models: a simulation study*. Computers & chemical engineering, 2005. **29**(2): p. 367-377.

54. Lee, K.W., Y.J. Lee, and D.S. Han, *The log-normal size distribution theory for Brownian coagulation in the low Knudsen number regime*. Journal of Colloid and Interface Science, 1997. **188**(2): p. 486-492.
55. Nash, J.E. and J.V. Sutcliffe, *River flow forecasting through conceptual models part I — A discussion of principles*. Journal of Hydrology, 1970. **10**(3): p. 282-290.
56. Wallace, S.J., et al., *Drug release from nanomedicines: selection of appropriate encapsulation and release methodology*. Drug delivery and translational research, 2012. **2**(4): p. 284-292.
57. Missana, T., et al., *Analysis of colloids erosion from the bentonite barrier of a high level radioactive waste repository and implications in safety assessment*. Physics and Chemistry of the Earth, Parts A/B/C, 2011. **36**(17): p. 1607-1615.
58. Holmboe, M., et al., *Effects of  $\gamma$ -irradiation on the stability of colloidal Na<sup>+</sup>-Montmorillonite dispersions*. Applied Clay Science, 2009. **43**(1): p. 86-90.
59. Song, D., et al., *Sedimentation of particles and aggregates in colloids considering both streaming and seepage*. Journal of Physics D: Applied Physics, 2016. **49**(42): p. 425303.
60. Byun, J., et al., *Volumetric concentration maximum of cohesive sediment in waters: A numerical study*. Water, 2014. **7**(1): p. 81-98.
61. Brom, v.d., *Aggregation of gold clusters by complementary hydrogen bonding*. 2006, University of Groningen.
62. García-García, S., S. Wold, and M. Jonsson, *Kinetic determination of critical coagulation concentrations for sodium-and calcium-montmorillonite colloids in NaCl and CaCl<sub>2</sub> aqueous solutions*. Journal of colloid and interface science, 2007. **315**(2): p. 512-519.
63. García-García, S., M. Jonsson, and S. Wold, *Temperature effect on the stability of bentonite colloids in water*. Journal of colloid and interface science, 2006. **298**(2): p. 694-705.
64. Baalousha, M., et al., *Effect of monovalent and divalent cations, anions and fulvic acid on aggregation of citrate-coated silver nanoparticles*. Science of the Total Environment, 2013. **454**: p. 119-131.
65. Tomaszewska, E., et al., *Detection limits of DLS and UV-Vis spectroscopy in characterization of polydisperse nanoparticles colloids*. Journal of Nanomaterials, 2013. **2013**: p. 60.
66. Bushell, G.C., et al., *On techniques for the measurement of the mass fractal dimension of aggregates*. Advances in Colloid and Interface Science, 2002. **95**(1): p. 1-50.
67. Li, X. and B.E. Logan, *Collision frequencies of fractal aggregates with small particles by differential sedimentation*. Environmental science & technology, 1997. **31**(4): p. 1229-1236.
68. Vahedi, A. and B. Gorczyca, *Predicting the settling velocity of flocs formed in water treatment using multiple fractal dimensions*. Water research, 2012. **46**(13): p. 4188-4194.
69. Jin, B., B.-M. Wilén, and P. Lant, *A comprehensive insight into floc characteristics and their impact on compressibility and settleability of activated sludge*. Chemical Engineering Journal, 2003. **95**(1): p. 221-234.
70. Lee, D.J., et al., *On the free-settling test for estimating activated sludge floc density*. Water Research, 1996. **30**(3): p. 541-550.

71. Risovic, D. and M. Martinis, *The role of coagulation and sedimentation mechanisms in the two-component model of sea-particle size distribution*. *Fizika*, 1994. **3**(2): p. 103-118.
72. Emadzadeh, A. and Y.M. Chiew, *Settling velocity of a porous sphere*, in *River Flow 2016*. 2016, CRC Press. p. 555-562.
73. Metreveli, G., et al., *Impact of chemical composition of ecotoxicological test media on the stability and aggregation status of silver nanoparticles*. *Environmental Science: Nano*, 2016. **3**(2): p. 418-433.
74. Zhang, W., et al., *Attachment efficiency of nanoparticle aggregation in aqueous dispersions: modeling and experimental validation*. *Environmental science & technology*, 2012. **46**(13): p. 7054-7062.
75. Logan, B.E., et al., *Clarification of clean-bed filtration models*. *Journal of Environmental Engineering*, 1995. **121**(12): p. 869-873.
76. Martin, M.J., et al., *Scaling bacterial filtration rates in different sized porous media*. *Journal of Environmental Engineering*, 1996. **122**(5): p. 407-415.
77. Lowry, G.V., et al., *Guidance to improve the scientific value of zeta-potential measurements in nanoEHS*. *Environmental Science: Nano*, 2016. **3**(5): p. 953-965.
78. Oncsik, T., et al., *Specific ion effects on particle aggregation induced by monovalent salts within the Hofmeister series*. *Langmuir*, 2015. **31**(13): p. 3799-3807.
79. Baalousha, M., *Effect of nanomaterial and media physicochemical properties on nanomaterial aggregation kinetics*. *NanoImpact*, 2017. **6**: p. 55-68.
80. Chowdhury, I., S.L. Walker, and S.E. Mylon, *Aggregate morphology of nano-TiO<sub>2</sub>: role of primary particle size, solution chemistry, and organic matter*. *Environmental Science: Processes & Impacts*, 2013. **15**(1): p. 275-282.
81. Jiang, Q. and B.E. Logan, *Fractal dimensions of aggregates determined from steady-state size distributions*. *Environmental Science & Technology*, 1991. **25**(12): p. 2031-2038.
82. Potenza, M.A.C., et al., *Dynamics of colloidal aggregation in microgravity by critical Casimir forces*. *EPL (Europhysics Letters)*, 2014. **106**(6): p. 68005.
83. Schaefer, D.W., et al., *Fractal geometry of colloidal aggregates*. *Physical Review Letters*, 1984. **52**(26): p. 2371.
84. Zhang, J.j. and X.y. Li, *Modeling particle-size distribution dynamics in a flocculation system*. *AIChE Journal*, 2003. **49**(7): p. 1870-1882.
85. Lee, B.J. and F. Molz, *Numerical simulation of turbulence-induced flocculation and sedimentation in a flocculant-aided sediment retention pond*. *Environmental Engineering Research*, 2014. **19**(2): p. 165-174.
86. Tang, P., J. Greenwood, and J.A. Raper, *A model to describe the settling behavior of fractal aggregates*. *Journal of colloid and interface science*, 2002. **247**(1): p. 210-219.
87. Hanus, L.H., R.U. Hartzler, and N.J. Wagner, *Electrolyte-induced aggregation of acrylic latex. 1. Dilute particle concentrations*. *Langmuir*, 2001. **17**(11): p. 3136-3147.
88. Russel, W.B., D.A. Saville, and W.R. Schowalter, *Colloidal dispersions*. 1989: Cambridge university press.
89. González, A.E., *Colloidal Aggregation Coupled with Sedimentation: A Comprehensive Overview*, in *Advances in Colloid Science*. 2016, InTech.

90. Meng, Z., S.M. Hashmi, and M. Elimelech, *Aggregation rate and fractal dimension of fullerene nanoparticles via simultaneous multiangle static and dynamic light scattering measurement*. Journal of colloid and interface science, 2013. **392**: p. 27-33.
91. Zheng, C. and P.P. Wang, *A modular three-dimensional multi-species transport model for simulation of advection, dispersion and chemical reactions of contaminants in groundwater systems; documentation and user's guide*. US Army Engineer Research and Development Center Contract Report SERDP-99-1, Vicksburg, Mississippi, USA, 1999.

## Chapter 4

# 4 Combining population balance and continuum models for aggregation and transport of nanoparticles at 3-D scale

### 4.1 Chapter overview

This chapter investigates whether the accurate population balance model, fixed pivot (FP), validated in previous chapter for nanoparticle (NP) aggregation modelling in aqueous media, can be combined with a three-dimensional (3-D) continuum modelling code, MT3D-USGS, in a forward prediction mode by incorporating other particle transport theories and/or previously-developed artificial neural network correlations (in chapter 2) to elucidate concurrent NP aggregation and transport at laboratory (1-D) and pilot (3-D) scales.

Incorporating aggregation into the model improves substantially the prediction ability of current theoretical and empirical approaches for NP deposition in porous media. However, running the model at 3-D scale leads to long CPU runtimes indicating the need for developing more efficient aggregation models for future effective modelling of aggregation and transport at environmentally-relevant scales. Addressing the need for a more efficient modelling approach to aggregation will be addressed in chapter 5. Additionally, aggregation behaviours within porous media may be different from that in aquatic media studied to date due to dynamic nature of cascading pores as will be scrutinized in chapter 6.

### 4.2 Introduction

A large number of studies have shown that under environmental conditions NP can grow in size due to aggregation, especially within porous media [1-3]. This can reduce NP mobility in porous media through the mechanisms of attachment, straining, and ripening [4-7]. In this part of the thesis an accurate population balance model for nanoparticle aggregation, i.e., the fixed pivot (FP) technique [8], is combined with a

3-D continuum model for NP transport, MT3D-USGS [9], to investigate the impact of NP aggregation during transport in a 1-D laboratory-scale domain and within a 3-D pilot-scale domain. After model validation against previous aggregation codes [2] and against 1-D experimental data from literature [10], the model is used at 1-D and 3-D scales. In this part of the thesis Hydroxyapatite (HAp) NP is used as the model NP due to their promising application in remediation of groundwater contaminated with radionuclide [11-14], and their potentials for being used as agricultural fertilizer [15-17].

## **4.3 Combining a population balance model and a continuum model**

### **4.3.1 Model combination**

For combination with the continuum model, the FP modelling approach to aggregation was chosen due to its flexibility in selecting the particle volume/size discretization, potential computational efficiency, and conservation of mass and number of particles.[2, 8, 18]The Brinkman permeability model for collision frequencies, and a power-law expression for settling velocity inducing differential sedimentation collisions were also selected based on a recent model screening study [2].

The recent release of the public-domain MT3DMS code (US Geological Survey), the MT3D-USGS [9, 19], was modified in the present study to incorporate the FP population balance technique. This code was recently upgraded extensively for incorporating water treatment scenarios by Bedekar et al. [9]. The subroutines of the MT3D-USGS were modified to integrate the FP model as illustrated in the flowcharts of the model algorithms in Fig. 4.1. In doing so, the FP model equations are solved based on number concentration in the most inner loop of the code following a conversion of mass concentration to number concentration for each size class (MT3D species) within each time step. The calculated increment in number concentration is then converted back to mass concentration which is exerted on the transport equation solution for each size class within each transport time step. A MATLAB code was developed for calculating the required inputs for the modified MT3D-USGS code, e.g., collision frequencies and transport parameters as shown in Fig. 4.1. The model equations are presented in Section 4.3.4.

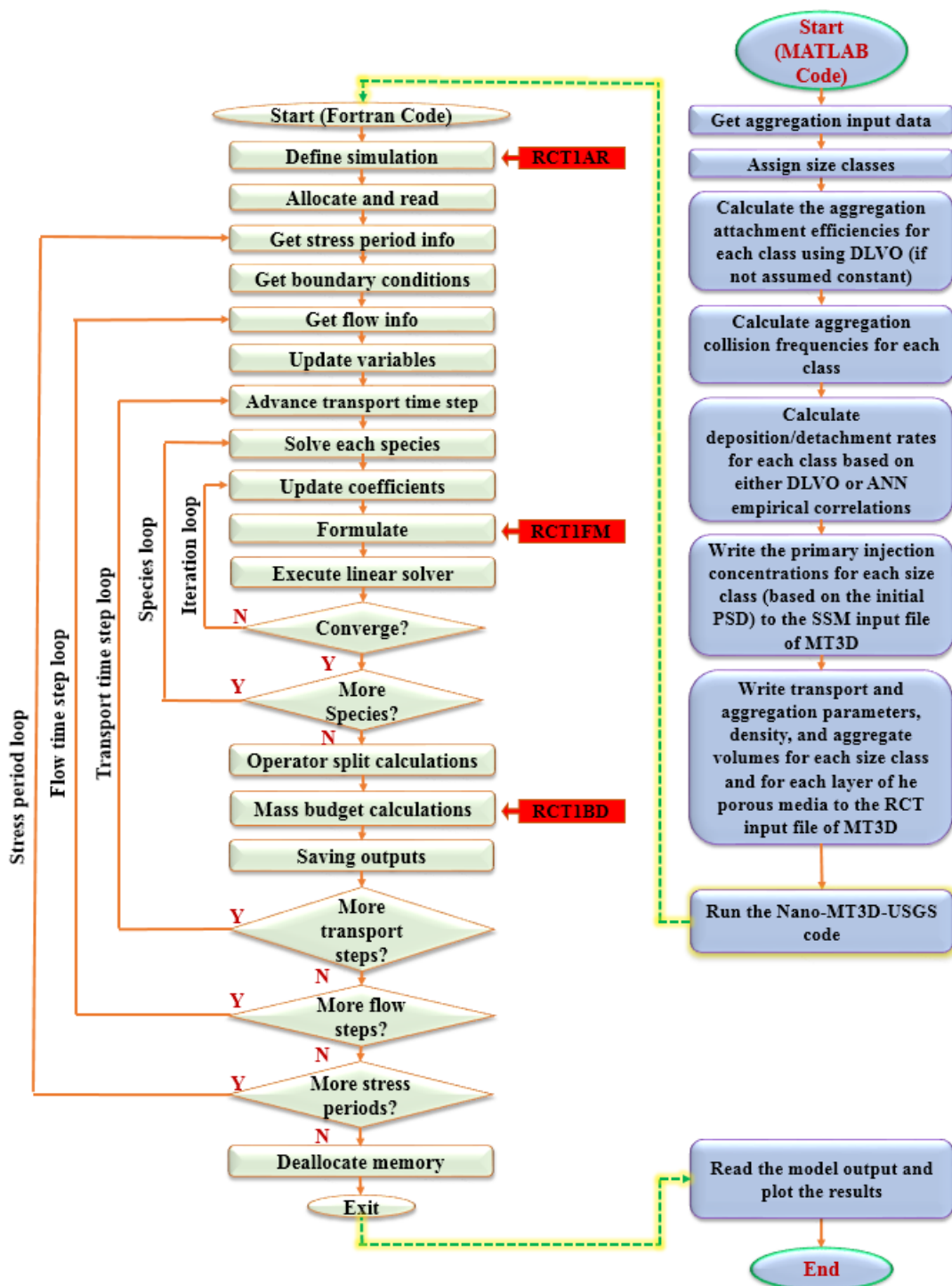


**Figure 4.1** The flowcharts of the integrated FP technique in the USGS-MT3D code which is controlled by a MATLAB code. The subroutine names shown in red boxes are those which are modified in the original MT3D-UGS code. Blue charts are related to the MATLAB code while green charts belong to the Fortran code.

### 4.3.2 Model parameters

In this section, it is assumed that the NP deposition is described only by an attachment rate term; ignoring other possible deposition mechanisms, i.e., straining, ripening, and site blocking. The attachment rate coefficient,  $K_{att}$ , for each size class was calculated according to colloid filtration theory (CFT) [20, 21] combined with Derjaguin, Landau, Verwey, and Overbeek (DLVO) theory [22-24] designated herein as CFT-DLVO as described later. The interaction energy forces included in the extended DLVO calculations of the present study were van der Waals attraction, electrostatic repulsion, and Born repulsion [24, 25]. Alternatively, recently developed, ANN-based empirical correlations [26] were used to calculate  $K_{att}$ . Using the latter approach, the detachment rate coefficient,  $K_{det}$ , was also incorporated into the model. However, the use of ANN-based empirical correlations is currently limited to the 1-D scale.

Although a variable particle-particle attachment efficiency,  $\alpha_{agg}$ , with size, predicted using DLVO theory [2, 27], was also incorporated into the model, herein a constant  $\alpha_{agg}$  is used for the sake of simplicity and since current theories may not be able to fully describe aggregation mechanisms in porous media systems due to complex interacting influences of pore tortuosity and the arrival of aggregates from up-gradient pores causing heterogeneous mixing of aggregate populations [28]. Considering  $\alpha_{agg}$  as an unknown constant parameter allows for the circumvention of such complex impacts. Model parameters have been assumed spatially constant. Hence, the calculation of  $K_{att}$  was performed using a constant velocity averaged over the entire model domain (Tables 4.1 and 4.2).

**Table 4.1** Parameters used in 1-D simulations following [10, 26].

<b>Parameter</b>	<b>50 mM KCl dataset</b>	<b>0.5 mM CaCl<sub>2</sub> dataset</b>
<b>Free polymer concentration (mg/L)</b>	10, Humic acid	10, Humic acid
<b>NP zeta potential (mV)</b>	-28.8	-31.4
<b>NP average diameter (nm)</b>	100	100
<b>NP density (g/cm<sup>3</sup>)</b>	3.16	3.2
<b>NP Concentration (mg/L)</b>	200	200
<b>Column diameter (cm)</b>	2.6	2.6
<b>Column length (cm)</b>	20.2	20.2
<b>Heterogeneity (%)</b>	15	15
<b>Grain size, d (mm)</b>	0.6	0.6
<b>Grain Zeta potential (mV)</b>	-40.2	-34.4
<b>Porosity</b>	0.39	0.39
<b>Pore water velocity (cm/min)</b>	1.12	1.11
<b>Dispersivity (cm)</b>	$4.8 \times 10^{-3}$	$6.6 \times 10^{-3}$
<b>pH</b>	5.7	5.7
<b>Electrolyte concentration (mM)</b>	50	0.5
<b>Number of PVs</b>	3.75	3.75
<b>Particle aspect ratio</b>	5	5
<b>Adsorbed coating concentration (mg/L)</b>	0	0
<b>Saturation magnetization (kA/m)</b>	0	0
<b>IEP pH</b>	6.7	6.7
<b>PSD size range (nm)</b>	18.2 to $2.41 \times 10^4$	18.2 to $2.41 \times 10^4$
<b>Number of size classes</b>	50	50
<b>Soil bulk density (kg/m<sup>3</sup>)</b>	1590	1590
<b>Dispersivity (cm)</b>	0.048	0.048
<b>Hamaker constant (<math>A_{H123}</math>) (J)</b>	$2.94 \times 10^{-21}$	$2.94 \times 10^{-21}$
<b>Fractal dimension</b>	2.0	2.0

**Table 4.2** Parameters used in 2-D simulations.

<b>Parameter</b>	<b>Assumed Values</b>
<b>NP zeta potential (mV)</b>	-28.8
<b>NP average diameter (nm)</b>	100
<b>NP density (g/cm<sup>3</sup>)</b>	3.16
<b>NP Concentration (mg/L)</b>	900 and 4500
<b>Test dimensions (m)</b>	3.6(L)×3(W)×2.4(H)
<b>Grain size, d (mm)</b>	0.6
<b>Grain Zeta potential (mV)</b>	-40.2
<b>Porosity</b>	0.35
<b>Pore water velocity (averaged) (cm/min)</b>	2.4
<b>Dispersivity (cm)</b>	1
<b>Ionic strength (mM)</b>	50
<b>Injection duration (min)</b>	~67
<b>PSD size range (nm)</b>	18.2 to $2.67 \times 10^3$
<b>Number of size classes</b>	35
<b>Soil bulk density (kg/m<sup>3</sup>)</b>	1400
<b>Longitudinal dispersivity (cm)</b>	1
<b>Horizontal to longitudinal dispersivity</b>	1/10
<b>Vertical to longitudinal dispersivity</b>	1/100
<b>Hamaker constant (<math>A_{H123}</math>) (J)</b>	$2.94 \times 10^{-21}$
<b>Fractal dimension</b>	2.0

### 4.3.3 Simulation characteristics

The modified MT3D-USGS code was validated against previous MATLAB code [2] for the case of pure aggregation. The predictive model performance was assessed against 1-D experimental data from Wang et al. [10]. Such data include hydroxyapatite (HAp) NP transport BTCs, the details of which have been summarized in Table 4.1.

Three-dimensional simulations were conducted based on a pilot-scale experiment of Johnson et al. [5] on the transport of nanoscale zero valent iron (NZVI) in a confined aquifer. Only the experiment domain and flow regime characteristics were considered in present simulations. The injected particles were assumed to be HAp NP, with the same properties as those in 1-D simulations. The simulation characteristics are listed

in Table 4.2. The model domain is shown in Fig. 4.2 and space discretization is shown in Figs. 4.3a,b. In brief, the active part of the domain consists of a sand layer confined by silica flour layer at the top and a sandy/clay layer at the bottom which is underlain by a clay layer [5]. Three injection wells and six extraction wells are used to circulate the groundwater in the main confined layer. The NP dispersion is injected only through the middle injection well. The transport of NP is monitored using a row of observation wells at the centreline of the model domain plan (wells #1-6) following Johnson et al. , and as illustrated in Fig. 4.2. Fifty size classes were considered in the 1-D simulation and 35 classes were considered in the 3-D modelling.

The initial PSD was assumed monodisperse [2] yielding an average initial hydrodynamic diameter,  $D_H$ , of  $\sim 80$  nm which is similar to HAp NP dimensions, 20 nm in width and 100 nm in length, reported by Wang et al. [10]. The size varied geometrically [2] from 18.2 nm to  $2.41 \times 10^4$  nm in the 1-D model and to  $2.67 \times 10^3$  in the 3-D model.

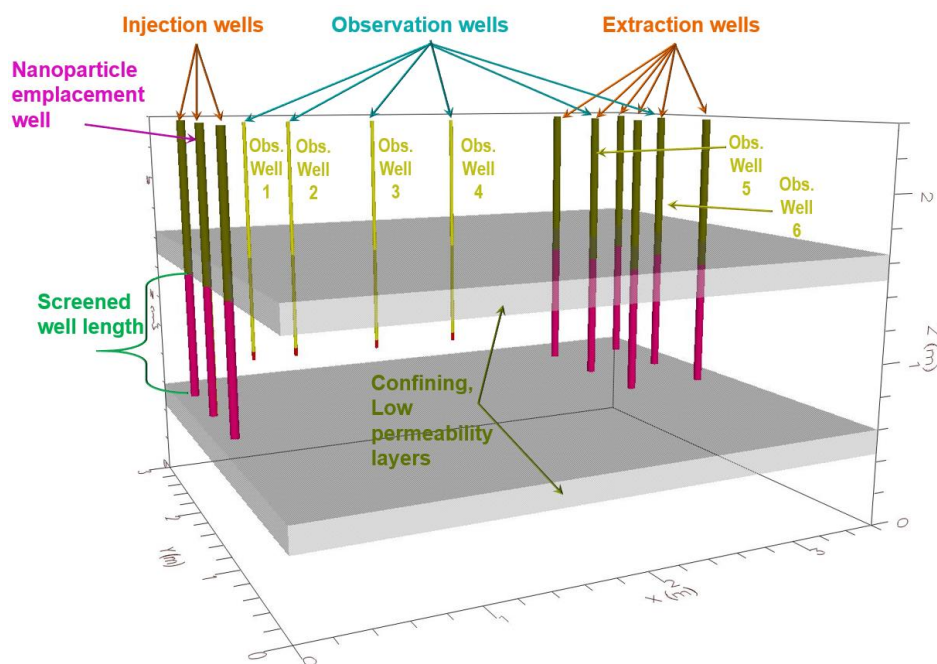


**Figure 4.2** Three-dimensional model domain used for simulations.

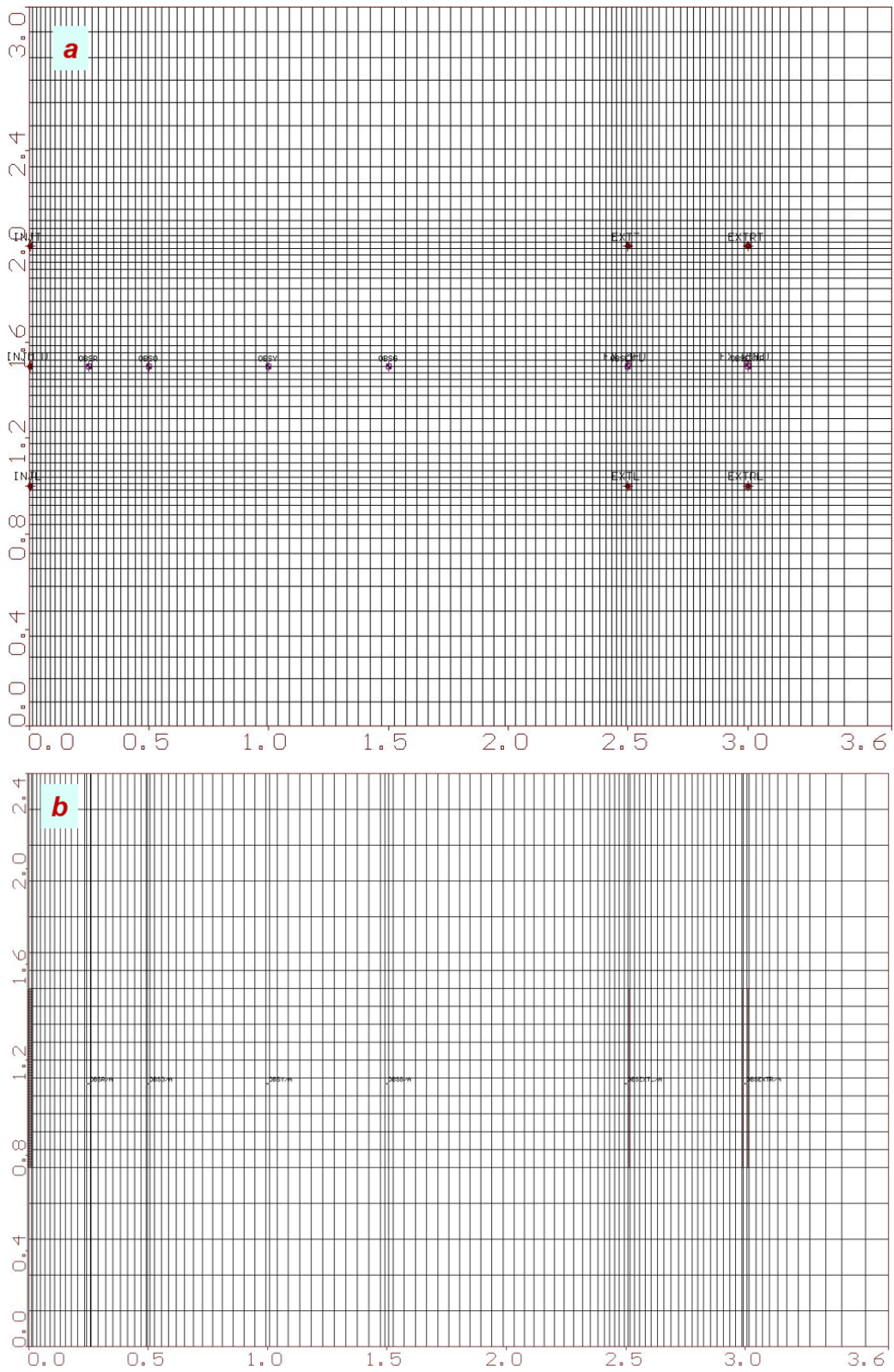


**Figure 4.3** Space discretization of the 3-D model domain simulation for finite difference solution of the coupled aggregation and transport problem. (a) plan view of the domain; (b) side view of the domain in a cross section along the row of observation wells.

#### 4.3.4 Mathematical models

The governing equation (continuum model) of nanoparticle transport in porous medium for size class  $k$  in a 3-D transient flow may be written as follows [1, 19]:

$$\varepsilon \frac{\partial C_k}{\partial t} + \rho_b \frac{\partial S_k}{\partial t} = \frac{\partial}{\partial x_i} \left( \varepsilon D_{i,j} \frac{\partial C_k}{\partial x_j} \right) - \frac{\partial (\varepsilon V_i C_k)}{\partial x_i} \quad (4.1)$$

$$\rho_b \frac{\partial S_k}{\partial t} = \varepsilon K_{att_k} C_k - \rho_b K_{det_k} S_k \quad (4.2)$$

These equations can be solved using the MT3D code when a non-equilibrium sorption model is considered. In doing so, model parameters for each size class can be converted as:  $K_{att_k} = \beta_k / \varepsilon$  and  $K_{det_k} = \beta_k / (\rho_b K_{d_k})$ . In MT3D documentation [19],  $\beta_k$  is the first-order mass transfer rate between the mobile and retained phases for species  $k$ . It should be noted that detachment can be excluded from this model formulation of the MT3D code by assigning a large value to  $K_{d_k}$  [29, 30].

The fixed pivot (FP) [8] population balance model equations accounting for the dynamics of the particle size distribution (PSD) resulted from aggregation based on conserving two properties of mass and number were described in previous sections.

The volume of each size class  $v_k$  can be calculated from Eq. (F24) and the mass of each bin can be calculated from Eq. (F25) [31]. The conversion between the mass concentration  $C_k$ , and the number concentration  $n_k$ , is then performed via:

$$C_k = m_k n_k \quad (4.3)$$

Equations for the collision frequencies were given in previous sections [2].

Two approaches were used to calculate the attachment rate coefficient,  $K_{att_k}$ : First using a combination of colloid filtration theory (CFT) [20, 21] and Derjaguin, Landau, Verwey, and Overbeek (DLVO) theory [24] (CFT-DLVO); Second based on ANN-based empirical correlations recently developed [26]. Using the latter approach, the detachment rate coefficient,  $K_{det}$ , is also incorporated in the model. However, ANN-based empirical correlations are currently limited to predictions in 1-D scale and thus these are not used in 3-D simulations of the present study.

Attachment rate coefficient using CFT-DLVO can be calculated as follows [21]:

$$K_{att_k} = \frac{3(1-\varepsilon)}{2d_{50}} \alpha_{pc_k} \eta_{0_k} V_{ave} \quad (4.4)$$

Collision efficiency, which is related the flux of particles approaching the surface of a porous media grain, can be calculated using the well-established correlation equation of Tufenkji and Elimelech [21]. Despite the existence of several empirical correlations developed for calculating  $\alpha_{pc_k}$  [32, 33], here a theoretical approach based on the extended DLVO theory is used following Bradford and Torkzaban [24]:

$$\alpha_{pc} = \varepsilon_1 \gamma_1 + \varepsilon_2 \gamma_2 \quad (4.5)$$

where  $\gamma_1$  and  $\gamma_2$  are parameters representing the role of applied hydrodynamic torque ( $T_H$ ) and adhesive torque ( $T_A$ ) in the above equation—equal one when  $T_H \leq T_A$  and zero when  $T_H > T_A$ . Here since I assume only irreversible deposition in the CFT-DLVO approach,  $\gamma_1$  and  $\gamma_2$  are assumed to be one. Based on energy balance,  $\varepsilon_j$  ( $j = 1$  or  $2$ ) can be calculated [24]:

$$\varepsilon_j = \int_{l_A}^{l_B} \frac{2\sqrt{\Phi}}{\pi} \exp(-\Phi) d\Phi = \left( \operatorname{erf}(\sqrt{l_B}) - \sqrt{\frac{4l_B}{\pi}} \exp(-l_B) \right) - \left( \operatorname{erf}(\sqrt{l_A}) - \sqrt{\frac{4l_A}{\pi}} \exp(-l_A) \right) \quad (4.6)$$

The total interaction energy [Kg m<sup>2</sup> S<sup>-2</sup>],  $\Phi_d$ , is calculated as a sum of three interaction energies, i.e., van der Waals attraction,  $\Phi^{vdW}$ , electrostatic repulsion,  $\Phi^{el}$ , and Born repulsion,  $\Phi^{Born}$ :

$$\Phi_d(h) = \Phi^{vdW}(h) + \Phi^{el}(h) + \Phi^{Born}(h) \quad (4.7)$$

The sphere-plate van der Waals interaction energy can be calculated using the expression of Gregory [34]:

$$\Phi^{vdW}(h) = -\frac{A_{H123} a_k}{6h} \left[ 1 + \frac{14h}{\lambda_w} \right]^{-1} \quad (4.8)$$

The combined Hamaker constant,  $A_{H123}$ , for hydroxyapatite NP interacting with water-quartz interface is given as  $2.94 \times 10^{-21}$  J [35]. The electrostatic repulsion energy for a sphere-plate interaction is determined from [36]:

$$\begin{aligned} \Phi^{el}(h) = \pi \varepsilon_m \varepsilon_0 a_k \left\{ 2\varphi_1 \varphi_2 \ln \left[ \frac{1 + \exp(-\kappa_{Deb} h)}{1 - \exp(-\kappa_{Deb} h)} \right] + (\varphi_1^2 \right. \\ \left. + \varphi_2^2) \ln[1 - \exp(-2\kappa_{Deb} h)] \right\} \end{aligned} \quad (4.9)$$

where  $\varphi_1$  and  $\varphi_2$  are usually assumed approximately equal to the zeta potential of the porous media grain and/or the interacting particle surfaces [27]. In a more accurate way they can be determined from Eq. (F38) [37-39].

Born repulsion can be calculated as follows [24]:

$$\Phi^{Born}(h) = -\frac{A_{H123} \sigma_c^6}{7560} \left[ \frac{8a_k + h}{(2a_k + 7)^7} + \frac{6a_k - h}{h^7} \right] \quad (4.10)$$

The collision diameter,  $\sigma_c$ , is assumed as 0.26 nm in order to achieve a primary minimum depth at 0.157 nm following [24], a commonly accepted distance of closest approach. The values of  $l_A$  and  $l_B$  in Eq. (4.6) are determined following [24]. In brief, five types of the interaction energy profile are considered, ranging from favourable to unfavourable interaction condition evaluated using  $\Phi_{1min}$ ,  $\Phi_{2min}$ , and  $\Phi_{max}$  standing for primary minimum, secondary minimum, and the energy barrier in the total interaction energy profile as shown in Fig. 4.4. Based on these classes and ignoring the detachment, the values of  $l_A$  and  $l_B$  can be determined from Table 4.3 [24].

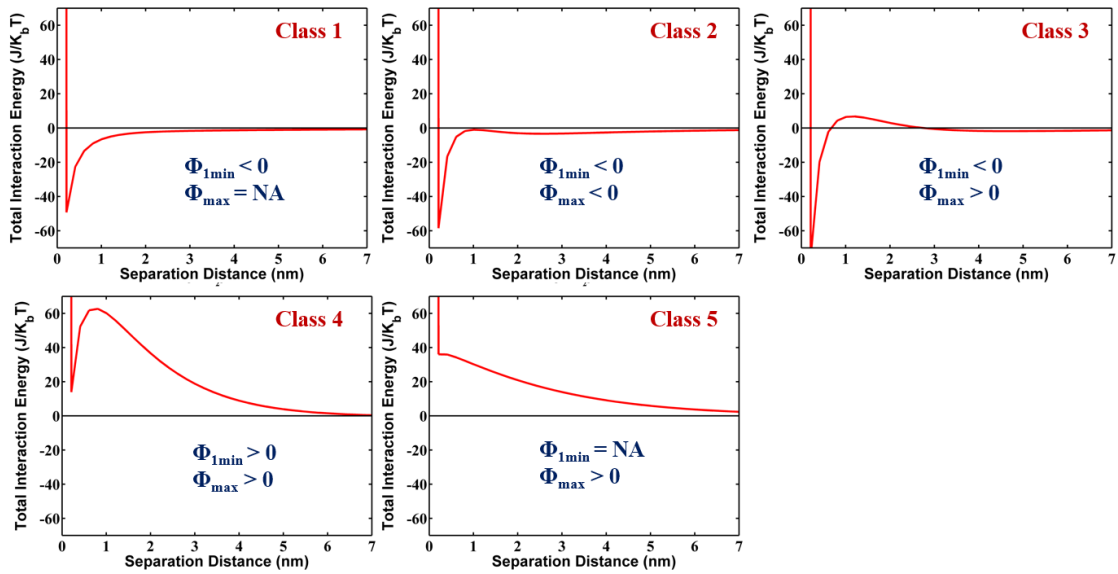


**Figure 4.4** Five classes of possible interaction energy profile that can happen for favorable and unfavorable interaction conditions evaluated using primary minimum,  $\Phi_{1min}$ , secondary minimum,  $\Phi_{2min}$ , and the energy barrier,  $\Phi_{max}$ . The profiles have been generated using a MATLAB code developed for plotting the interaction energy profiles of extended DLVO by arbitrarily varying zeta potentials, particle radius, and ionic strength to produce similar figures with those of Bradford and Torkzaban [24].

**Table 4.3** Lower ( $l_A$ ) and upper ( $l_B$ ) integration limits in calculation of the probabilities of particle interaction with the primary ( $\varepsilon_1$ ) and secondary ( $\varepsilon_2$ ) minima of DLVO profile based on five classes of interaction energy profile illustrated in Fig. 4.4.

Class no.	$\varepsilon_1$	$\varepsilon_1$	$\varepsilon_2$	$\varepsilon_2$
	$l_A$	$l_B$	$l_A$	$l_B$
1	0	$ \Phi_{1min} $	NA*	NA
2	$ \Phi_{2min} - \Phi_{max} $	$ \Phi_{1min} - \Phi_{max} $	0	$ \Phi_{2min} - \Phi_{max} $
3	$ \Phi_{2min}  + \Phi_{max}$	$ \Phi_{1min}  + \Phi_{max}$	0	$ \Phi_{2min} $
4	$ \Phi_{2min}  + \Phi_{max}$	$\Phi_{max} - \Phi_{1min}$	0	$ \Phi_{2min} $
5	NA	NA	0	-0.119

\*NA: not applicable

In the alternative approach, i.e., calculation of the attachment rate coefficient based on the ANN-based empirical correlations developed in [26], simply the neural network

empirical matrices in MATLAB format were used in the main MATLAB code developed in this study for performing the simulations. The main MATLAB code utilizes these networks to calculate both attachment and detachment rate coefficients for each size class using 20 experimental characteristics listed in Table 4.3. It should be noted that these correlation networks are exerted in an MS Excel spreadsheet (available online as electronic supporting information of [26]).

Although a variable particle-particle attachment efficiency,  $\alpha_{agg}$ , with size, predicted using DLVO theory [2, 27], was also incorporated in the modified MT3D model, herein I only use a constant  $\alpha_{agg}$  for the sake of simplicity. The parameters of the model have been assumed spatially constant. Thus, the calculation of the  $K_{att}$  was performed based on an average constant velocity in the whole model domain.

#### **4.4 Model validation**

The modified MT3D-USGS was validated for pure aggregation by comparing its results with those of the MATLAB code validated in the previous study [2]. Here the comparison of the two codes was carried out by turning off reaction terms in the governing equation of the modified MT3D-USGS code [40], allowing only the transport (advection/dispersion) and the aggregation mechanisms to be operative within a 1-D domain. For a synchronized duration, the aggregation results for the quiescent (static) condition, calculated by the MATLAB code, should be able to match the modified MT3D-USGS code outputs in the porous media domain at the beginning of the BTC plateau. The results, shown in Fig. 4.5, demonstrate that PSDs computed by the two codes agree well for various ranges of attachment efficiencies and fractal dimensions. Slight discrepancies between the two codes observed in peaks of PSDs may relate to the interference of the dispersion mechanism in the transport model results. The average hydrodynamic diameter,  $D_H$ , trends over time at the outlet calculated by the modified MT3D-USGS are compared with results of MATLAB codes in Fig. 4.6. According to these results the two curves meet at the beginning of the BTC plateau in all cases. After this stage,  $D_H$  curves for static condition keep growing while those of the transport model remain constant due to the same aggregation time (residence time) for all aggregates transported through the porous media system. The mass balance errors calculated by the modified MT3D-USGS was

less than 0.1% in all simulations. These results demonstrate the validity of the modified MT3D-USGS.

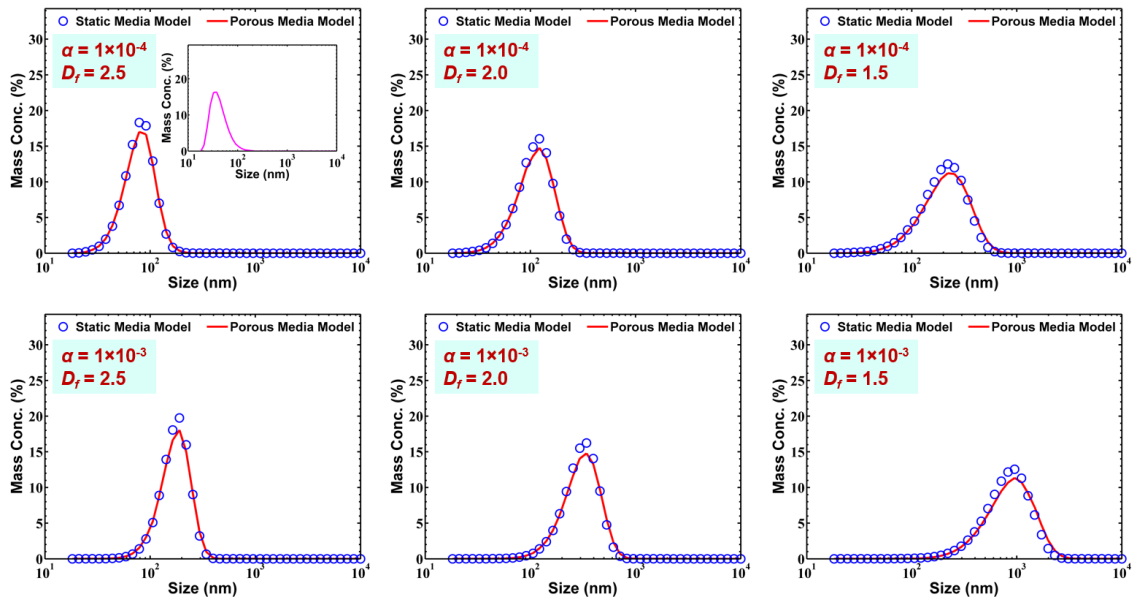


**Figure 4.5** Comparison of the PSDs produced by modified MT3D-USGS model and a previously develop MATLAB code for aggregation in no-flow condition for the case of pure aggregation with different values of attachment efficiency and fractal dimension. The inset illustrates the initial PSD.

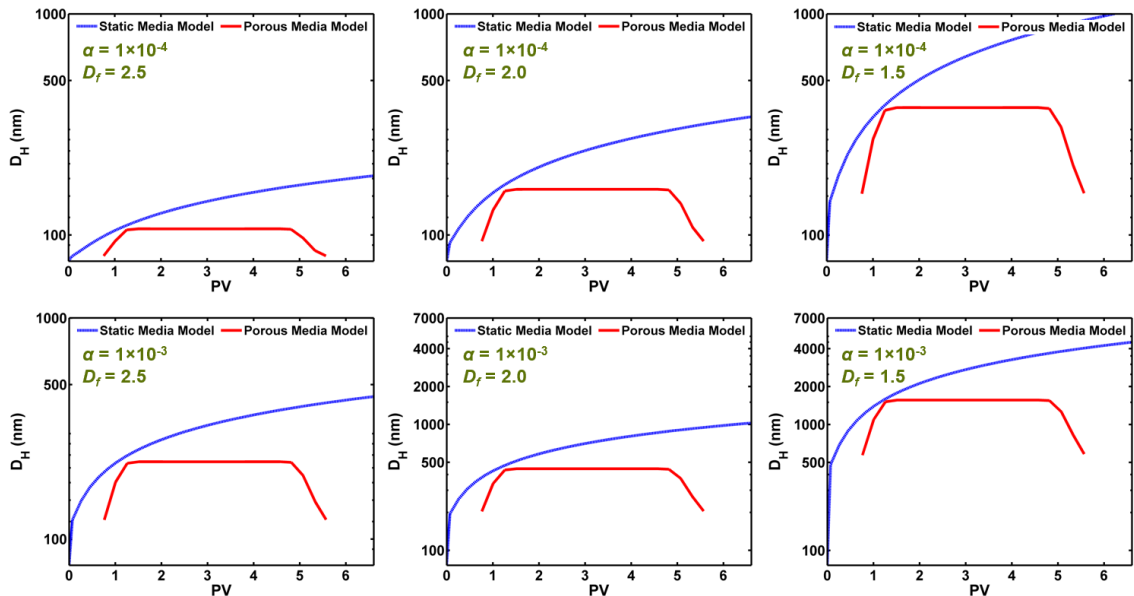


**Figure 4.6** Comparison of the mean hydrodynamic diameter  $D_H$  produced by modified MT3D-USGS model and a previously develop MATLAB code for aggregation in no-flow condition for the case of pure aggregation with different values of attachment efficiency and fractal dimension.

## 4.5 Prediction performance of the model

Column experiment data of [10] at two electrolyte concentrations of 50 mM KCl and 0.5 mM CaCl<sub>2</sub> were used to assess the predictivity of the model when combined with two approaches of CFT-DLVO [24] and ANN-based correlations [26]. The results, shown in Fig. 4.7, reveal that incorporating the aggregation into the model by increasing  $\alpha_{agg}$  from zero to  $1 \times 10^{-3}$  to  $4 \times 10^{-3}$  results in better predictions by approaches incorporating CFT-DLVO and ANN correlations. Babakhani et al. [26] using ANN overpredicted the same experimental BTC plateau height at 50 mM KCl ( $R^2=0.432$ ) and underpredicted that at 0.5 mM CaCl<sub>2</sub> ( $R^2=0.738$ ) using a constant attachment coefficient with size and without considering the aggregation. Considering a variable attachment efficiency with size classes, the use of the ANN-based correlations in the present investigation, under-predicts the BTC plateau in both cases more noticeably ( $R^2 < 0$ ) than the previous study (Fig. 4.7a,b). However, when the aggregation was included in the model, the experimental BTC plateau heights were reproduced well at both 50 mM KCl ( $R^2=0.900$ ) and 0.5 mM CaCl<sub>2</sub> ( $R^2=0.985$ ).

In opposite to ANN correlations, CFT-DLVO without considering the aggregation in the model overpredicts the height of BTC plateau ( $R^2 < 0$ ). This discrepancy may not be because of ignoring the electrosteric repulsion interaction energy emanated from the presence of humic acid (10 mg/L) within experimental HAp dispersions, since considering such a repulsive force in the model is expected to reduce NP attachment, and thus tends to elevate the BTC height [41]. When aggregation is incorporated, the model predicts the height of the BTC well at 50 mM KCl ( $R^2=0.889$ ), whereas at 0.5 mM CaCl<sub>2</sub> it does not show a discernible impact on the modelled BTC probably due to ignoring the role of bridging interactions in the presence of divalent cation (CaCl<sub>2</sub>) and polymer (humic acid) in the present extended DLVO calculation [26, 42-44]. Overall, these results suggest that including the aggregation in NP transport continuum models can substantially improve the predictivity of current approaches, such as the DLVO theory and ANN empirical correlations.

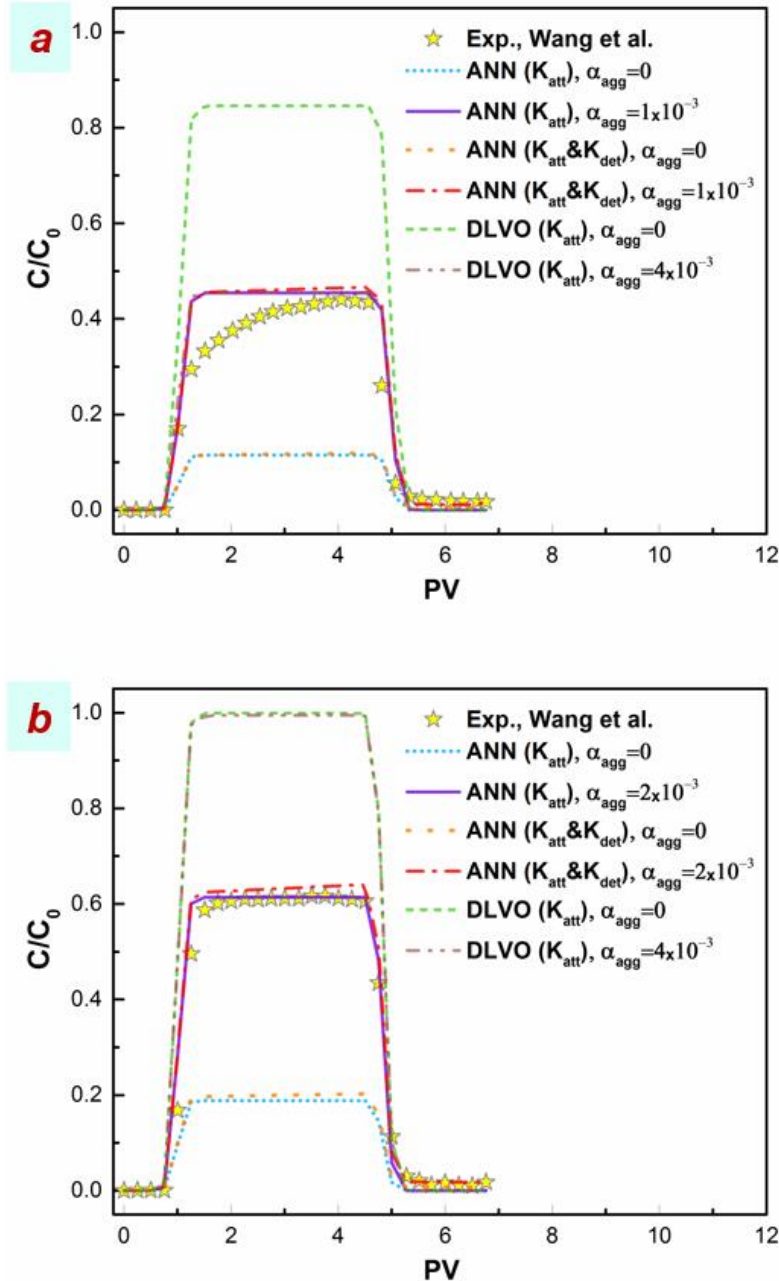


**Figure 4.7** Comparison of the modified MT3D-USGS model outcomes with experimental data of Wang et al. [10] at two chemical conditions: (a) 50 mM KCl (b) 0.5 mM CaCl<sub>2</sub>. The full experimental details are summarized in Table 4.1. The modelling approaches include the use of CFT-DLVO and ANN based correlations for predicting attachment ( $K_{att}$ ) and detachment ( $K_{det}$ ) rate coefficients.

## 4.6 Upscaling to 3-D domain

The transport of HAp NP in a 3-D model domain generally shows a high mobility (Fig. 4.8a,d). The extent of aggregation within the 3-D porous media domain even with

considering  $\alpha_{agg}=1$  is far lower than that in 1-D simulations with  $\alpha_{agg}=4.2\times 10^{-3}$ . In 1-D modelling results (Fig. 4.6), the mean hydrodynamic diameter,  $D_H$ , grows above 1200 nm whereas within the 3-D model results, shown in Fig. 4.8b,e,  $D_H$  increases to a maximum of 373 nm. This may be due to large volume of pore spaces collectively within the 3-D model domain leading to a radial dilution of the NP dispersion thereby reducing their aggregation even though the injected NP concentration in the 3-D dispersion is 22.5 times higher than that of the 1-D domain (Tables 4.1 and 4.2).

When aggregation is included, the change in mean  $D_H$  is not considerable at wells #1 and #2 whereas it becomes significant at well #3 to #6, where the trends exhibit a peak corresponding to the centre of the BTC but with a more gradual rise and fall compared to BTCs (Fig. 4.8b,e). It should be noted that calculating the mean hydrodynamic size based on size class concentrations in porous media system can be complex as such concentrations are affected by aggregation and other transport mechanisms simultaneously. In line with  $D_H$  trends, time-dependent PSDs, shown in Fig. 4.8c,f for well #4, demonstrate considerable aggregation and evolution of PSD when aggregation is included. This is in spite of the fact that BTCs in Fig. 4.8,d which are resulted from the sum of concentrations in all size classes did not show a substantial change with including aggregation. This can be due to physicochemical conditions considered in this investigation which exhibits considerable aggregation but slight deposition.

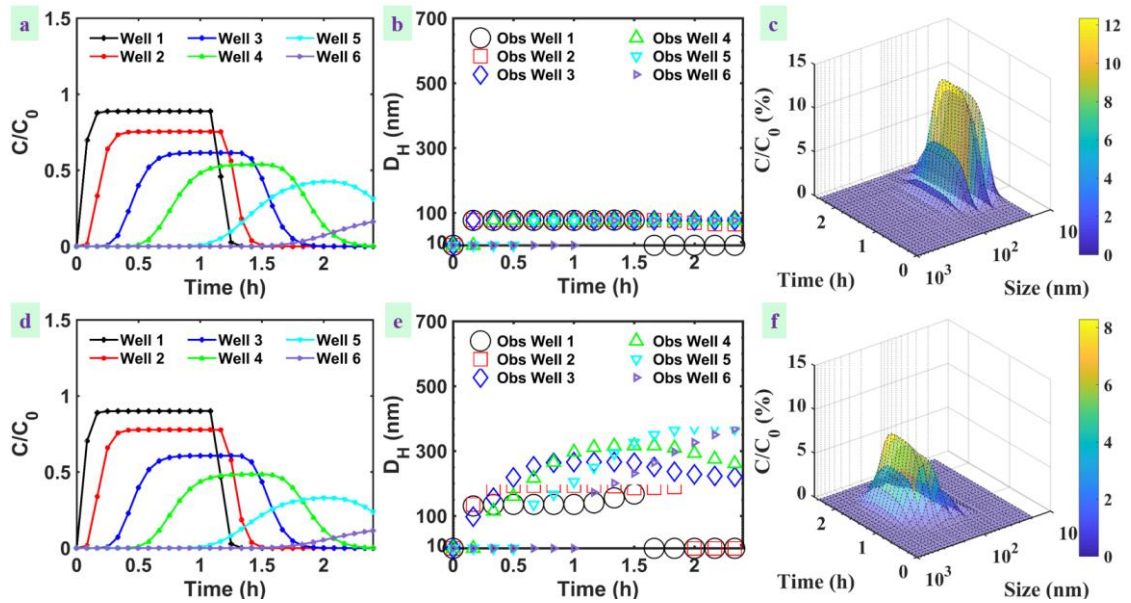


**Figure 4.8** Three-dimensional simulation results with aggregation not included ( $\alpha_{agg}=0$ , a,b,c) and included ( $\alpha_{agg}=1$ , d,e,f) for breakthrough curves (a,d), average hydrodynamic diameter  $D_H$  (b,e), and time resolved-PSD at well #4 (c,f) In panels c,f size refers to particle diameter.

The model runtime of 3-D simulations was 66.5 h on a 64-bit Operating System with 3.5 GHz Intel® Xeon® CPU and 32 GB RAM. Parallelizing the code using OpenMP capability in Fortran [45] and using the same number of nodes as the number of size classes did not help reducing the runtime due probably to communication time between the cluster nodes and the head node. Although running the modified model in this study was feasible for forward-modelling of a relatively simple 3-D domain, it can be inefficient to perform the simulation for larger domains and may not be practical when inverse modelling is required too. Therefore, further work is needed to develop more efficient modelling approaches for combination with continuum models.

## 4.7 References

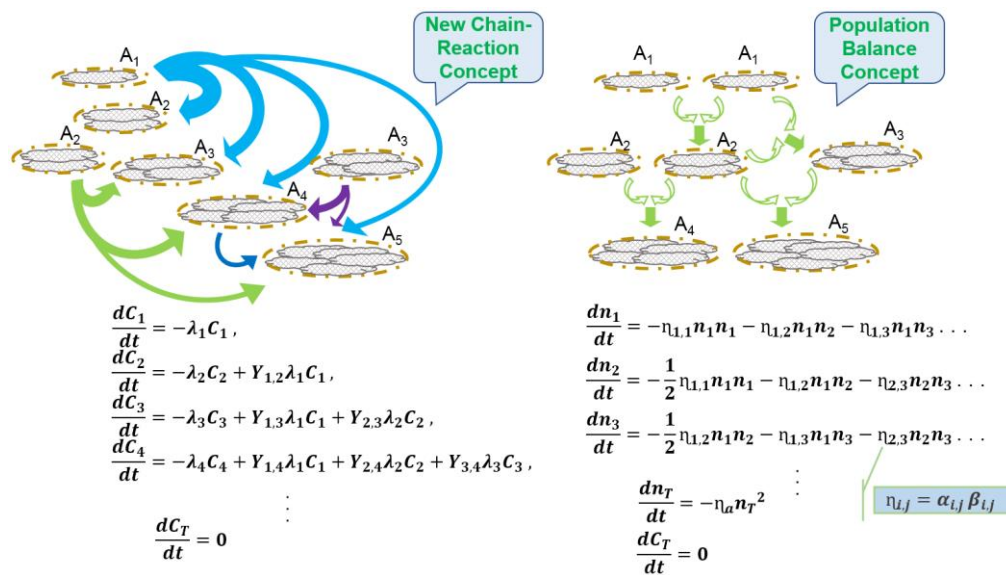
1. Babakhani, P., et al., *Continuum-based models and concepts for the transport of nanoparticles in saturated porous media: A state-of-the-science review*. Advances in Colloid and Interface Science, 2017. **246**(Supplement C): p. 75-104.
2. Babakhani, P., R.-a. Doong, and J. Bridge, *Significance of early and late stages of coupled aggregation and sedimentation in the fate of nanoparticles: measurement and modelling*. Environmental science & technology, 2018. doi: **10.1021/acs.est.7b05236**.
3. Wang, M., et al., *Concurrent aggregation and transport of graphene oxide in saturated porous media: Roles of temperature, cation type, and electrolyte concentration*. Environmental Pollution, 2018. **235**: p. 350-357.
4. Phenrat, T., et al., *Particle size distribution, concentration, and magnetic attraction affect transport of polymer-modified FeO nanoparticles in sand columns*. Environ. Sci. Technol., 2009. **43**(13): p. 5079-5085.
5. Johnson, R.L., et al., *Field-Scale Transport and Transformation of Carboxymethylcellulose-Stabilized Nano Zero-Valent Iron*. Environmental science & technology, 2013. **47**: p. 1573-1580.
6. El Badawy, A.M., et al., *Key factors controlling the transport of silver nanoparticles in porous media*. Environmental science & technology, 2013. **47**(9): p. 4039-4045.
7. Fan, W., et al., *Transport of graphene oxide in saturated porous media: Effect of cation composition in mixed Na–Ca electrolyte systems*. Science of The Total Environment, 2015. **511**: p. 509-515.
8. Kumar, S. and D. Ramkrishna, *On the solution of population balance equations by discretization—I. A fixed pivot technique*. Chemical Engineering Science, 1996. **51**(8): p. 1311-1332.
9. Bedekar, V., et al., *MT3D-USGS version 1: A US Geological Survey release of MT3DMS updated with new and expanded transport capabilities for use with MODFLOW*. 2016, US Geological Survey.
10. Wang, D., et al., *Transport behavior of humic acid-modified nano-hydroxyapatite in saturated packed column: effects of Cu, ionic strength, and ionic composition*. Journal of colloid and interface science, 2011. **360**(2): p. 398-407.
11. Vermeul, V.R., et al., *An injectable apatite permeable reactive barrier for in situ <sup>90</sup>Sr immobilization*. Groundwater Monitoring & Remediation, 2014. **34**(2): p. 28-41.
12. Wen, T., et al., *Efficient capture of strontium from aqueous solutions using graphene oxide–hydroxyapatite nanocomposites*. Dalton Transactions, 2014. **43**(20): p. 7464-7472.
13. Handley-Sidhu, S., et al., *Uptake of Sr<sup>2+</sup> and Co<sup>2+</sup> into biogenic hydroxyapatite: implications for biomineral ion exchange synthesis*. Environmental science & technology, 2011. **45**(16): p. 6985-6990.
14. Kanel, S.R., et al., *Nano-Scale Hydroxyapatite: Synthesis, Two-Dimensional Transport Experiments, and Application for Uranium Remediation*. Journal of Nanotechnology, 2011. **2011**: p. 1-5.
15. Wang, D., Y. Jin, and D.P. Jaisi, *Effect of Size-Selective Retention on the Cotransport of Hydroxyapatite and Goethite Nanoparticles in Saturated Porous Media*. Environmental science & technology, 2015. **49**(14): p. 8461-8470.
16. Dimkpa, C.O. and P.S. Bindraban, *Nanofertilizers: New products for the industry?* Journal of agricultural and food chemistry, 2017.

17. Wang, D., Y. Jin, and D. Jaisi, *Cotransport of Hydroxyapatite Nanoparticles and Hematite Colloids in Saturated Porous Media: Mechanistic Insights from Mathematical Modeling and Phosphate Oxygen Isotope Fractionation*. Journal of Contaminant Hydrology, 2015. **182**: p. 194-209.
18. Dale, A.L., G.V. Lowry, and E.A. Casman, *Accurate and fast numerical algorithms for tracking particle size distributions during nanoparticle aggregation and dissolution*. Environmental Science: Nano, 2017. **4**(1): p. 89-104.
19. Zheng, C. and P.P. Wang, *A modular three-dimensional multi-species transport model for simulation of advection, dispersion and chemical reactions of contaminants in groundwater systems; documentation and user's guide*. US Army Engineer Research and Development Center Contract Report SERDP-99-1, Vicksburg, Mississippi, USA, 1999.
20. Yao, K.-M., M.T. Habibian, and C.R. O'Melia, *Water and waste water filtration. Concepts and applications*. Environmental Science & Technology, 1971. **5**(11): p. 1105-1112.
21. Tufenkji, N. and M. Elimelech, *Correlation equation for predicting single-collector efficiency in physicochemical filtration in saturated porous media*. Environmental Science & Technology, 2004. **38**(2): p. 529-536.
22. Adamczyk, Z. and P. Weroński, *Application of the DLVO theory for particle deposition problems*. Advances in Colloid and Interface Science, 1999. **83**(1): p. 137-226.
23. Van Oss, C.J., R.F. Giese, and P.M. Costanzo, *DLVO and non-DLVO interactions in Hectorite*. Clays Clay Miner, 1990. **38**(2): p. 151-159.
24. Bradford, S.A. and S. Torkzaban, *Determining parameters and mechanisms of colloid retention and release in porous media*. Langmuir, 2015. **31**(44): p. 12096-12105.
25. Ruckenstein, E. and D.C. Prieve, *Adsorption and desorption of particles and their chromatographic separation*. AIChE Journal, 1976. **22**(2): p. 276-283.
26. Babakhani, P., et al., *Parameterization and prediction of nanoparticle transport in porous media: A reanalysis using artificial neural network*. Water Resources Research, 2017. **53**: p. 4564-4585.
27. Zhang, W., *Nanoparticle aggregation: principles and modeling*, in *Nanomaterial Impacts on Cell Biology and Medicine*, Y.C. David G. Capco, Editor. 2014, Springer. p. 19-43.
28. Babakhani, P., et al., *Aggregation and sedimentation of shattered graphene oxide nanoparticles in dynamic environments: a solid-body rotational approach*. Environmental Science: Nano, 2018. doi: **10.1039/C8EN00443A**.
29. Becker, M.D., et al., *In situ measurement and simulation of nano-magnetite mobility in porous media subject to transient salinity*. Nanoscale, 2015. **7**(3): p. 1047-1057.
30. Bai, C. and Y. Li, *Modeling the transport and retention of nC 60 nanoparticles in the subsurface under different release scenarios*. Journal of contaminant hydrology, 2012. **136**: p. 43-55.
31. Sterling, M.C., et al., *Application of fractal flocculation and vertical transport model to aquatic sol-sediment systems*. Water research, 2005. **39**(9): p. 1818-1830.
32. Li, J., X. Xie, and S. Ghoshal, *Correlation Equation for Predicting the Single-Collector Contact Efficiency of Colloids in a Horizontal Flow*. Langmuir, 2015. **31**(26): p. 7210-7219.
33. Phenrat, T., et al., *Empirical correlations to estimate agglomerate size and deposition during injection of a polyelectrolyte-modified Fe0 nanoparticle at high particle*

- concentration in saturated sand*. Journal of Contaminant Hydrology, 2010. **118**(3–4): p. 152-164.
34. Gregory, J., *Approximate expressions for retarded van der Waals interaction*. Journal of Colloid and Interface Science, 1981. **83**(1): p. 138-145.
  35. Wang, D., et al., *Humic acid facilitates the transport of ARS-labeled hydroxyapatite nanoparticles in iron oxyhydroxide-coated sand*. Environmental science & technology, 2012. **46**(5): p. 2738-2745.
  36. Hogg, R., T.W. Healy, and D.W. Fuerstenau, *Mutual coagulation of colloidal dispersions*. Transactions of the Faraday Society, 1966. **62**: p. 1638-1651.
  37. Inyang, M., et al., *Filtration of engineered nanoparticles in carbon-based fixed bed columns*. Chemical engineering journal, 2013. **220**: p. 221-227.
  38. Tian, Y., et al., *Transport of engineered nanoparticles in saturated porous media*. Journal of Nanoparticle Research, 2010. **12**(7): p. 2371-2380.
  39. Li, K. and Y. Chen, *Effect of natural organic matter on the aggregation kinetics of CeO<sub>2</sub> nanoparticles in KCl and CaCl<sub>2</sub> solutions: measurements and modeling*. Journal of hazardous materials, 2012. **209**: p. 264-270.
  40. Babakhani, P., et al., *Modified MODFLOW-based model for simulating the agglomeration and transport of polymer-modified Fe nanoparticles in saturated porous media*. Environ Sci Pollut Res, 1-20, doi:10.1007/s11356-015-5193-0, 2015.
  41. Phenrat, T., et al., *Estimating Attachment of Nano- and Submicrometer-particles Coated with Organic Macromolecules in Porous Media: Development of an Empirical Model*. Environmental Science & Technology, 2010. **44**(12): p. 4531-4538.
  42. Wang, D., et al., *Facilitated transport of Cu with hydroxyapatite nanoparticles in saturated sand: Effects of solution ionic strength and composition*. water research, 2011. **45**(18): p. 5905-5915.
  43. Chen, K.L. and M. Elimelech, *Aggregation and deposition kinetics of fullerene (C<sub>60</sub>) nanoparticles*. Langmuir, 2006. **22**(26): p. 10994-11001.
  44. Torkzaban, S., et al., *Impacts of bridging complexation on the transport of surface-modified nanoparticles in saturated sand*. Journal of contaminant hydrology, 2012. **136**: p. 86-95.
  45. Hermanns, M., *Parallel programming in Fortran 95 using OpenMP*. Universidad Politecnica de Madrid, Spain, 2002.

# Chapter 5

## 5 Comparison of a new mass-concentration, chain-reaction model with the population-balance model for early- and late-stage aggregation of shattered graphene oxide nanoparticles



### 5.1 Chapter overview

#### 5.1.1 Scope

This chapter addresses one of the research priorities indicated in the previous chapter, that was a need for a more efficient aggregation model. Thus, a new modelling framework is proposed for efficient and accurate description of aggregation phenomenon. This approach is based on mass-concentration which is more relevant to environmental problems and is compatible with other fate and transport models. This chapter has been submitted as the following manuscript:

“Babakhani, P.; Bridge, J.; Fagerlund, F.; Doong, R.-a.; Whittle, K., Comparison of a new mass-concentration, chain-reaction model with the population-balance model

for early- and late-stage aggregation of shattered graphene oxide nanoparticles, In Review.”

### **5.1.2 Abstract**

Integrated modelling of multiple, interacting transport mechanisms of nanoparticles (NP), including aggregation as an essential phenomenon, is imperative to mitigate and manage NP in the environment. Aggregation as an essential mechanism impacting NP functionality and fate and transport in the environment is currently modelled accurately using population balance equation (PBE) models which are computationally expensive when combined with other NP fate and transport models. A new mass-concentration-based, chain-reaction modelling (CRM) framework is proposed to alleviate computational expenses of PBE and to facilitate combination with other fate and transport models, especially when they are based on mass concentration. Model performance is compared with analytical PBE solution and a standard numerical PBE technique (fixed pivot, FP) by fitting against experimental data (hydrodynamic diameter and derived count rate of dynamic light scattering used as representative of mass concentration) for early- and late-stage, aggregation of shattered graphene oxide (SGO) NP across a broad range of solution chemistries. The CRM demonstrates slightly better fit to the data (mean  $R^2_{NS}$  0.36 and 0.33) than the FP model ( $R^2_{NS}$  0.29). Similar trends or ranges are obtained for model parameters, namely aggregation rate constant and fractal dimension, between CRM and FP approaches. Computationally, the CRM is an order-of-magnitude faster than the FP technique, suggesting that it can be a promising modelling framework for efficient and accurate modelling of NP aggregation.

## **5.2 Introduction**

Production of nanomaterials is now a mainstream commercial industry. For example, graphene oxide (GO) nanosheets with 12 morphologies are routinely manufactured across 40 countries, within 15 industries, and 585 applications [1, 2]. Commercial waste streams can lead to uncontrolled spread of nanomaterials in the environment [3, 4], however, there is also a range of opportunities for use of nanomaterials in environmental systems, e.g., environmental applications such as clean-up of radionuclide contaminated sites [5-7], agronomic applications such as the

use as nano-fertilizers and nano-pesticides [8, 9], and petroleum applications such as oil/gas reservoir recovery enhancement [10, 11]. Emissions of nanomaterials used in research and development activities have been already detected in river water and sediments [12]. Particularly, graphene-based nanomaterials are effectively insoluble in water [13], and therefore they may be subject to prolonged lifetimes within aquatic environments. Therefore, it is of paramount importance to predict and control the transport and fate of these materials, especially in form of nanoparticles (NP), within surface water and groundwater environments, a task which is already a key challenge for water and environmental engineers.

Continuum models are considered as the most appropriate and efficient means of tackling this challenge for real-world or site-scale problems [14]. Such models are most simply known as the advection-dispersion equations describing bulk mass transport over continuous spatial domains [14]. One of the critical phenomena that controls NP fate and transport in the environment [14, 15] as well as their functionality in environmental and engineering systems [11, 16, 17] is aggregation. Efficient integration of aggregation models with other NP fate and transport models, particularly continuum models, is of paramount importance to enable the estimation of NP release into aquatic environments and designing NP application strategies.

Current modelling approaches to NP aggregation can be categorized as: (i) explicit physical representation of the early stage of aggregation only [18-20] and (ii) population-balance-equation (PBE) numerical schemes [21-25]. The significance of the late stage of aggregation along with broad and diverse ranges of conditions encountered in the natural environment make current theories and concepts of early-stage aggregation less applicable in environmentally-relevant conditions [24, 26]. Besides, efficient and accurate combination of PBE with Eulerian-based continuum models can be challenging due to computational expenses in numerical approaches or due to the incompatibility of the main variable of PBE (particle number concentration) with that typically used in continuum model equations (mass concentration) when the use of analytical solution is desirable.

Despite considerable advancements in predicting continuum model parameters by incorporating current theories, such as colloid filtration theory (CFT) and Derjaguin, Landau, Verwey, and Overbeek (DLVO) theory [27-29], or by utilizing techniques

such as artificial neural network (ANN) and Monte Carlo [30], the broad spectrum of environmental conditions and varied characteristics of emerging single, hybrid, or coated NP [31, 32] eventually make the use of inverse modelling in estimating model parameters unavoidable. Particularly, further development of predictive models requires data obtained from inverse modelling [30]. The computational expense of inverse modelling makes the use of an integrated PBE-continuum model even more challenging, if possible at all using non-specialist computing resources.

Recent investigation of the NP aggregation within dynamic environments revealed the need for further development of aggregation models to take realistic environmental conditions into account [33]. Such consideration, however, may require integration of aggregation model with other computation tools, such as computational fluid dynamics (CFD), or other fate models which might be still hindered by computational demands.

Several simplifying approaches for considering aggregation in fate and transport models of NP have been already validated against experimental or field data [15, 34-36]. However, these approaches rely on simplifying assumptions which either do not account for particle size distribution (PSD) [15] or may use five or fewer size classes [34, 35, 37] which have been criticized for not being accurate [25, 38]. Several accurate binning approaches to the solution of PBE still require an ideal grid discretization for the particle size dimension [38, 39] which is typically not readily available from experimental measurement data [24]. Although this problem has been partially resolved in more flexible schemes such as fixed pivot (FP) and moving pivot (MP) [40, 41], complexity and conditionality (e.g., summations, if-commands, or coupled equations) in these model algorithms still reduce their efficiency when being implemented in larger modelling frameworks of the fate and transport of NP in the environment. There are other numerical approaches [42, 43] which mostly use different collision kernels, e.g., sum or product kernels, than those used for the aggregation of colloidal particles in environmental condition, i.e., a sum of Brownian, differential sedimentation, and orthokinetic collision frequencies [18]. Besides, the potential dependency of these models on their numerical schemes, e.g., finite volume, might make it complex to combine them with other NP fate models with a different numerical scheme, e.g., finite element [44]. Finally, although moment-based methods such as direct quadrature method of moments may be more efficient for modelling aggregation than aforementioned techniques, they use a limited number ( $< 6$ ) of

quadrature points which might not give sufficient resolution to satisfy the needs for other fate and transport models being combined with them [25]. Furthermore, these methods were also found not to be appropriate for other NP fate phenomena like dissolution [25]. Although selection of the best model is a trade-off between simplicity and accuracy and may finally be controlled by the scale of the problem [14, 45, 46], developing more efficient and accurate modelling approaches to aggregation is necessary as there is no upper limit on the scalability of environmental problems.

Since the seminal work of Marian Smoluchowski in 1917 [47], PBEs have been extensively modified and used for modelling aggregation phenomena while less attention has been paid to developing aggregation models based on mass balance. In this study, a simple mass-concentration-based approach is presented to model aggregation more efficiently than common PBE and with an improved or similar accuracy. A parent-daughter chain reaction model (CRM) which is based on the mass concentration, may be capable of accounting for dynamics of the aggregate populations by resembling each particle size class as a species of the reaction. Fundamentally, an aggregation model generally follows a second order expression if described in terms of particle number concentration [18, 48, 49]. For pure aggregation, this expression leads to a decay in the number concentration of primary particles and the total number concentration over time while the total mass concentration is preserved. Conversely, a mass concentration-based model should be able to describe mass transfer among classes of the aggregates while maintaining the total mass constant.

The CRM is based on a series of first-order decay expressions maintaining the total mass in the system constant. Although not a physico-chemically exact description of aggregating particles, it is hypothesised that the dynamics of a cascading system of multiple, kinetically-interacting species such as described by the CRM concept may be an efficient model for an evolving system of aggregating NP. The use of first-order expressions in this approach may reduce the computational expenses of the second-order terms used in population balance models since typically a first-order expression can be solved numerically with less computation efforts than a second-order expression [50]. Such a model may also offer a simpler way of considering NP reaction with other environmental contaminants within the aggregation model as currently considering simple adsorption of solute onto aggregates with varying size classes

requires complex formulations [51]. In this study, it is investigated whether this approach, after being validated against analytical solution of the PBE [52, 53], can describe the change in mean particle size, PSD, and concentration of shattered graphene oxide (SGO) NP under quiescent conditions of aggregation and sedimentation. The model performance is also compared with a typical PBE, i.e., the FP technique [40] which has been widely used as a standard approach for comparison with other models [42, 54, 55]. To the best of authors' knowledge this is the first time that a mass-concentration-based CRM formulation is used for modelling the aggregation of colloidal particles. The previous use of the terminology 'parallel parent and daughter' in the literature of particle aggregation [56] was associated with the discretization of the PBE model.

### 5.3 Model Development

The basic CRM model which has long been used in the context of contaminant transport with groundwater is as follows [57-59]:

$$\frac{dC_k}{dt} = L(C_k) - \lambda_k C_k + Y_{k-1,k} \lambda_{k-1} C_{k-1} \quad (5.1)$$

If  $k = 1$ :

$$\frac{dC_1}{dt} = L(C_1) - \lambda_1 C_1 \quad (5.2)$$

where  $C_k$  is mass concentration [ $\text{ML}^{-3}$ ] of species  $k$ ,  $L(C_k)$  stands for the non-reaction terms including other transport mechanisms such as advection, dispersion, fluid sinks/sources, and/or sedimentation;  $\lambda_k$  is the first-order reaction coefficient [ $\text{T}^{-1}$ ] for species  $k$ , and  $Y_{k-1,k}$  is the yield coefficient [-] between species  $k-1$  and  $k$ , which for physical chain-reaction models can be calculated from the stoichiometric relationship between the two species [58].

Applying this concept to aggregation mechanisms and considering a sectional approach in which size class  $k$  can have multiple additional primary particles compared to size class  $k-1$ , means that when particles of size class  $k-1$  aggregate with each other, the mass concentration of their class decays and the mass concentration of one size class larger,  $k$ , increases. Based on this concept and disregarding the term,  $L(C_k)$  in Eq. (5.1), i.e., considering pure aggregation, one needs to assume  $Y_{k-1,k} = 1$ , in order to maintain the total mass of all size classes constant. This model, however, may only

consider the aggregation of size class  $k-1$  resulting in creation of mass in class  $k$ . In order to consider aggregations between a range of size classes resulting in redistribution of mass from class  $k-1$  among several larger classes, the basic form of the CRM model was modified to allow aggregation reactions of size class  $k$  with all other smaller size classes as follows:

$$\frac{dC_k}{dt} = L(C_k) - \lambda_k C_k + \sum_{i=1}^{k-1} Y_{i,k} \lambda_i C_i \quad (5.3)$$

where  $k$  is the aggregate class size for which Eq. (5.3) is being solved. Since in the aggregation process first smaller aggregates are formed and then larger ones after collisions of the formers, the probability for transformation into larger classes should decrease with the increase in size class. As a first study developing this modelling framework for aggregation, a rough assumption is taken that  $Y_{i,k}$  can be expressed as a linear probability distribution in proportion to the volume of each size class and with a total sum equal to one:

$$Y_{i,k} = \frac{v_{k_{max}-k+i+1}}{\sum_{j=i+1}^{k_{max}} v_j} \quad (5.4)$$

where  $k_{max}$  is the maximum number of classes considered in the model, and  $v$  is the volume of each class. For instance, assuming  $k_{max} = 5$  and combining both Eqs. (5.3) and (5.4) yields:

$$\frac{dC_1}{dt} = -\lambda_1 C_1, \quad k=1$$

$$\frac{dC_2}{dt} = -\lambda_2 C_2 + \frac{v_5}{v_2 + v_3 + v_4 + v_5} \lambda_1 C_1, \quad k=2$$

$$\frac{dC_3}{dt} = -\lambda_3 C_3 + \frac{v_4}{v_2 + v_3 + v_4 + v_5} \lambda_1 C_1 + \frac{v_5}{v_3 + v_4 + v_5} \lambda_2 C_2, \quad k=3$$

$$\begin{aligned} \frac{dC_4}{dt} = & -\lambda_4 C_4 + \frac{v_3}{v_2 + v_3 + v_4 + v_5} \lambda_1 C_1 + \frac{v_4}{v_3 + v_4 + v_5} \lambda_2 C_2 \\ & + \frac{v_5}{v_4 + v_5} \lambda_3 C_3, \quad k=4 \end{aligned}$$

$$\begin{aligned} \frac{dC_5}{dt} = & \frac{v_2}{v_2 + v_3 + v_4 + v_5} \lambda_1 C_1 + \frac{v_3}{v_3 + v_4 + v_5} \lambda_2 C_2 \\ & + \frac{v_4}{v_4 + v_5} \lambda_3 C_3 + \frac{v_5}{v_5} \lambda_4 C_4, \quad k=5 \end{aligned}$$

Since the present study only considers sedimentation along with aggregation,  $L(C_k)$  is considered as [24, 60]:

$$L(C_k) = -\frac{U_k}{Z_s} C_k \quad (5.5)$$

where  $U_k$  is the sedimentation velocity of aggregates in class  $k$  [ $\text{LT}^{-1}$ ] and  $Z_s$  is the sedimentation depth [L]. As  $\lambda_k$  may vary in each size class, an additional expression is needed to describe these variations. In the present study, two relationships with semi-empirical nature are proposed that might best describe these changes. First, the size of each bin is directly considered as the main variable. This size-based semi-empirical equation, hereafter designated as S-CRM, is as follows:

$$\lambda_k = \frac{A_S}{\tau} \left( \frac{|a_{k_{max}-k+1} - a_{ave,t}|}{a_k} \right)^{1/2}, \quad 2 \leq k \leq k_{max} \quad (5.6)$$

where  $A_S$  is the aggregation constant of the S-CRM  $a_{ave,t}$  is the equivalent radius of the geometric mean size of PSD at time  $t$ , and  $\tau$  is the characteristic time [T] of aggregation (coagulation time or aggregation half-life) given as follows [18]:

$$\tau = \frac{3\mu}{4k_b T n_0} \quad (5.7)$$

where  $k_b$  is the Boltzmann constant,  $\mu$  is the viscosity of the suspending medium [ $\text{M T}^{-1} \text{L}^{-1}$ ],  $T$  is temperature [K],  $n_0$  is the initial population of particles which can be determined from the initial PSD. Equation (5.6) is based on this concept that the rate of aggregation,  $\lambda_k$ , may vary with the size of class in respect to the geometric-average size of the PSD [24]. When the geometric mean size of the aggregates grows during the aggregation process, the rates may also change for each class of particle over time. Therefore, the rates are updated in every time steps of the numerical solution. It should be noted that this model considers the Brownian motion through  $\tau$ , and it may also consider the differential sedimentation mechanism of aggregation through dynamics of  $a_{ave,t}$  over time.

Alternatively, the concept of collision frequencies from the Smoluchowski model [47, 61] is utilized to account for variations in  $\lambda_k$  across size classes. However, instead of taking all possible collisions into account, it is assumed that two types of collisions are dominant among all possible collisions. These include collisions between particles of similar size [62, 63] and collisions between any given particles and a particle with

a representative mean size of PSD [62, 63]. By adding these two types of collision frequencies and nondimensionalizing each term by the maximum of their range, the following expression is resulted which is hereafter designated as C-CRM:

$$\lambda_k = \frac{A_C}{\tau} \left( \frac{\beta_{k,k}}{\beta_{1,1}} + \frac{\beta_{k,k_{ave}}}{\beta_{k_{max},k_{ave}}} \right) \quad (5.8)$$

where  $A_C$  is the aggregation constant of the C-CRM,  $\beta_{k,k}$  is the collision frequency between each class of aggregates and classes of the same size;  $\beta_{k,k_{ave}}$  is the collision frequency between each class of aggregates and the class that has an equivalent size with the geometric average size of the PSD in each time step;  $\beta_{1,1}$  and  $\beta_{k_{max},k_{ave}}$  are the maximum of  $\beta_{k,k}$  and  $\beta_{k,k_{ave}}$  ranges, respectively, for all size classes. Calculations of these collision frequencies with considering all three aggregation mechanisms (Brownian, differential sedimentation, and orthokinetic aggregations) are presented previously [18, 24] and are also available in Chapter 3 as Eqs. (3.5-3.7) .

The performances of the models are compared with an accurate population balance model solution known as the FP scheme [40] given as:

$$\begin{aligned} \frac{dn_k}{dt} = & \sum_{\substack{j \geq i \\ v_{k-1} \leq (v_j + v_i) \leq v_{k+1}}} \left[ 1 - \frac{1}{2} \delta_{j,i} \right] \eta_k \alpha \beta_{j,i} n_j n_i \\ & - n_k \sum_{i=1}^{k_{max}} \alpha \beta_{k,i} n_i - \frac{U_k}{Z_s} n_k \end{aligned} \quad (5.9)$$

where  $\eta_k$  is:

$$\eta_k = \begin{cases} \frac{v_{k+1} - (v_j + v_i)}{v_{k+1} - v_k}, & v_k \leq (v_j + v_i) \leq v_{k+1} \\ \frac{(v_j + v_i) - v_{k-1}}{v_k - v_{k-1}}, & v_{k-1} \leq (v_j + v_i) \leq v_k \end{cases} \quad (5.10)$$

where  $n_k$  is particle number concentration of aggregates consisting of  $k$  primary particles [ $L^{-3}$ ],  $v_i$  is the volume of solids in each aggregate in size class  $i$ ,  $\delta$  is Kronecker delta, and  $\alpha$  is the attachment efficiency which is typically estimated as an aggregation constant through model fitting to experimental data. A code written in

MATLAB<sup>®</sup> (Mathworks, USA) was used and modified for solving this study's models, the details of which are summarised in the Appendix F and detailed in Babakhani et al. [24]. Briefly, an explicit forward Euler scheme was used for the time discretization of Eqs. (5.3) and (5.9) with an adjustable time-step. A power-law model [64-66] was used for settling velocity and the Brinkman permeability-based model [67-69] was used for collision frequencies. This model set was already found to best describe early and late stages of aggregation and sedimentation of HAp NP among 24 model combinations [24]. The initially observed PSD was used as the initial condition in of the aggregation model. The optimization algorithm code developed in the former study [24] was also used here for calibration of parameters including aggregation constant ( $A$  in CRM or  $\alpha$  in PBE) and fractal dimension ( $D_f$ ). This algorithm was aimed at using parallel processing of the MATLAB efficiently and avoid unstable runs of the aggregation model in certain ranges of parameters affecting the optimization process by automatic reduction of the time step length. All simulation characteristics were the same for different modelling approaches.

The analytical solution used for comparison with the CRM was based on a log-normal distribution initial PSD. This solution which yields the total number of suspended aggregates at time  $t$ ,  $N_t$ , is founded on only a Brownian kernel [52, 53]:

$$N_t = \frac{n_0}{1 + A\beta_0 n_0 t} \quad (5.11)$$

where

$$A = 1 + \exp(Z_0) \quad (5.12)$$

$$Z_0 = \ln^2(\sigma_0) \quad (5.13)$$

$$\beta_0 = \alpha_{smol} \frac{2k_B T}{3\mu} \quad (5.14)$$

where  $\sigma_0$  is the geometric standard deviation of the initial PSD and  $\alpha_{smol}$  is the attachment efficiency assumed within the analytical solution. The result of the analytical solution was compared with that of CRM for the same condition and with turning off the sedimentation mechanism by assuming identical density of particles with that of water over a broad range of input parameters such as initial concentration, primary particle size of PSD, and fractal dimension. The binning approach for solving

the analytical solution includes an arithmetic series of aggregate volumes while for the CRM and FP approaches the binning approach is a geometrical series ( $v_{i+1}/v_i = 2^{1/q}$ , where  $q$  is the geometric factor). The number of size bins in the analytical solution was selected as 200 and in the numerical solution was selected as 49. When fitting to experimental data, the number of size classes was variable between 64-76 bins depending on the initial PSD broadness.

The Nash–Sutcliffe determination coefficient,  $R^2_{NS}$ , is used as a goodness-of-fit criterion and as objective function in the fitting process, given as follows [70-73]:

$$R^2_{NS} = 1 - \frac{\sum_{j=1}^{J^o} (X_j^o - X_j^m)^2}{\sum_{j=1}^{J^o} (X_j^o - \bar{X}^o)^2} \quad (5.15)$$

where  $X_j^o$  is the  $j^{\text{th}}$  record of the quantity being measured or observed,  $J^o$  is the total number of records,  $X_j^m$  is the  $j^{\text{th}}$  record of the quantity being modeled or computed,  $\bar{X}^o$  is average of the observation data.  $R^2_{NS}$  ranges between  $-\infty$  and 1 with values between 0 and 1 showing acceptable and excellent matches, respectively [72]. In order to compare the CPU runtimes for different models, the models were run on a 64-bit Operating System with 3.5 GHz Intel® Xeon® CPU and 32 GB RAM.

## 5.4 Experimental

Graphene oxide (particle density 1.8 g/cm<sup>3</sup>) was obtained from Siniocarbon, China, in powder form and dispersed in deionized (DI) water at 2 g/L. Shattered graphene oxide was then produced via intensive ultra-sonication of the GO dispersion to achieve initial uniform hydrodynamic diameter (90 nm). This was accomplished using a probe sonication at an amplitude of 30 and power of 40 W for 2 h with 30-second stop following each 30 s sonication. The dispersion was then centrifuged for 30 min at 19500 ± 500 rpm to remove the larger fraction of particles. Finally, the dispersion was passed through a 0.45 μm syringe filter and the filtrate was kept in dark at 4 °C as the stock dispersion.

The evolution of aggregate size over time along with particle size distribution and concentration change were measured by Dynamic Light Scattering (DLS) (Malvern Zetasizer Nano ZS, UK) assuming its capability for characterizing non-spherical particles/aggregates following previous studies [74-76]. The valid measurement size

range reported using the manufacturer is 1 nm to  $10^4$  nm. The same instrument was used for measuring the zeta potential. Dynamic light scattering measurements were carried out with an interval of  $\sim 3.4$  min. The instrument settings for size measurement were adapted and fixed for all measurements following Babakhani et al. [24]. In this protocol the number of runs is set at 5, each with a duration of 10 s. The beam attenuator is set at a unit of 11. The position of measurement is placed at the farthest possible distance from the opposite wall of the cuvette to the beam source, i.e., 6.5 mm in order to gain a better sampling of all size ranges across the cuvette. All experiments were conducted in duplicate for a duration  $>5$  h. The standard deviations of the duplicate tests are reported as error bars in the final plots. A sample volume of 3 mL was used inside the cuvette for all cases, corresponding to the measurement depth of  $\sim 2.3$  cm. The derived count rate (DCR) data from DLS measurements were used as an indicator of mass concentration [24, 77-79]. Derived count rate was measured at different concentrations (5, 50, 500, and 1000 mg/L) of SGO to examine the correlation between the two quantities.

All experiments were conducted according to the following procedure: (1) prepare the particle dispersion in DI water for a final particle concentration of 50 mg/L; (2) adjust the pH at  $6 \pm 0.05$  (or alternatively at 2.5, 4, 7.5, or 10) with NaOH/HCl (100 mM); (3) ultrasonication for 5 min, add the electrolyte (either  $\text{NaClO}_4$ , or  $\text{CaCl}_2$ ), immediately vortex for 5 s, transform to a disposable cuvette, and immediately start the measurement. The whole process after taking from ultrasonicator until the start of the first measurement was around  $70 \pm 20$  s.

## 5.5 Results and discussion

### 5.5.1 Validation of the model against analytical solution

Since the aggregation rate constants of S-CRM and C-CRM,  $A_S$  and  $A_C$ , are not expected to scale with the attachment efficiency,  $\alpha_{Smol}$ , in the analytical solution of the Smoluchowski model, CRMs were tried to fit to the analytical solution by adjusting  $A_S$  and  $A_C$  as free parameters. Over 100 min aggregation, within a fairly broad range of conditions, i.e., varying  $q$  within 1-3,  $D_f$  within 1.5-2.5, primary particle size,  $a_0$ , between 200 and 300 nm, and initial concentration,  $C_0$ , between 10 and 50 mg/L, which were totally 99 cases, the S-CRM was able to fit the total number of particles

over time produced by the analytical solution (assuming  $\alpha_{Smol} = 1$ ) very well with a mean  $R^2_{NS}$  of  $0.990 \pm 0.01$ . In a similar condition, but with  $a_0$  range of 300 and 400 nm, and  $C_0$  range of 1 and 10 mg/L (99 cases), the C-CRM was able to fit the analytical solution (assuming  $\alpha_{Smol} = 1$ ) with a lower mean  $R^2_{NS}$   $0.804 \pm 0.230$  compared to that of S-CRM. These results suggest that overall the CRM is able to describe the aggregation phenomena although the performance of the model varies with semi-empirical approaches developed for estimating aggregation rate constants.

### 5.5.2 Experimental results

The results of hydrodynamic size evolution and DCR are presented in Fig. 5.1. The DLS measurement settings [24] was promising for SGO NP aggregation with low levels of noise in most datasets and fair reproducibility indicated by small standard deviations of duplicate experiments. The late stage of aggregation/sedimentation does not appear within 5 h for electrolyte concentrations  $\leq 0.5$  mM  $\text{CaCl}_2$  and  $\leq 20$  mM  $\text{NaClO}_4$  at pH 6 (reaction limited regime, RLA) whereas above these thresholds the late stage appears as a significant reduction in the slope of the  $D_H$  curve versus time. Likewise, at pH  $< 6$  and 20 mM  $\text{NaClO}_4$ , the late stage of aggregation appears in  $D_H$  curves. These are in general agreement with aggregation trends of HAp observed in the previous study [24]. It appears that critical coagulation concentration (CCC) [19] above which the system is considered under the diffusion limited regime (DLA), is between 0.5-1 mM for  $\text{CaCl}_2$  and between 30-50 mM for  $\text{NaClO}_4$ . Considering matched  $D_H$  curves for SGO aggregation at 0.5  $\text{CaCl}_2$  and 30 mM  $\text{NaClO}_4$ , CCC ration of monovalent to divalent electrolyte is estimated to be 40 which is in accordance with the Schulze-Hardy rule [19] and in close agreement with ratios measured for GO elsewhere [80]. Likewise, around three times lower absolute zeta potential has been measured for SGO in  $\text{CaCl}_2$  solution (-7.1 mV) than that in  $\text{NaClO}_4$  solution (-22.3 mV, Fig. G1).

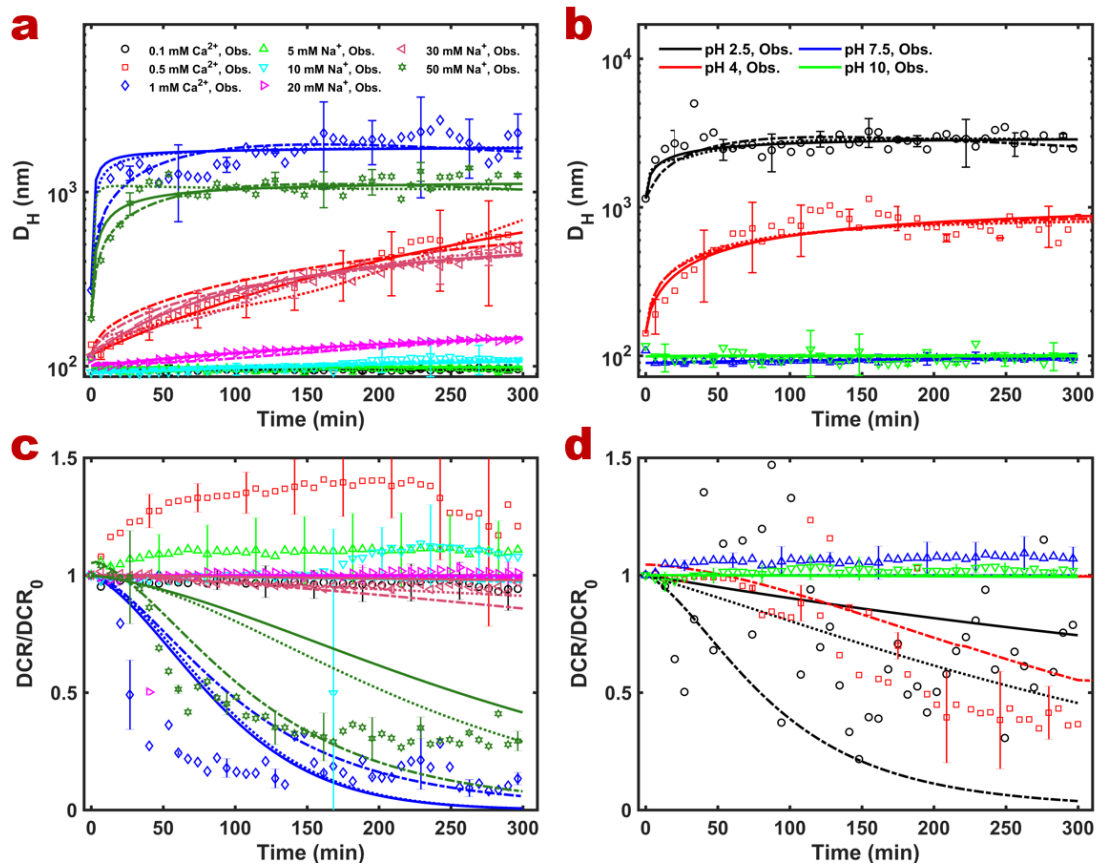


**Figure 5.1** Evolutions of Size (a,b) and change in normalized derived count rate ( $DCR/DCR_0$ ), (c,d) for SGO NPs at various IS ( $NaClO_4$  and  $CaCl_2$ ) with a fixed pH at 6 (a,c) and various pH with a fixed IS at 20 mM  $NaClO_4$  (b,d). Continuous lines represent C-CRM; dash lines represent FP technique, and dot lines represent the S-CRM model outcomes.

At moderate concentration of  $CaCl_2$  (0.5 mM),  $DCR/DCR_0$  demonstrates significant increase over time whereas at 30 mM  $NaClO_4$ ,  $DCR/DCR_0$  tends to show a mild decreasing trend. The increase in  $DCR/DCR_0$  is similar to the previous observations of Babakhani et al., [24] for HAp NP in presence of 0.3 mM  $CaCl_2$  at pH 6 (RLA regime). In the mentioned reference, this behaviour was attributed to faster sedimentation rate of HAp NP than their aggregation rate under the RLA regime giving rise to early arrival of aggregates from the upper part of water column to the measurement depth and increasing the local concentration at this point. Nevertheless, here this behaviour seems to be specific to the presence of  $CaCl_2$  since this is not noticeable at 30 mM  $NaClO_4$  although a slight rise in  $DCR/DCR_0$  is observed for lower

NaClO<sub>4</sub> concentrations—5 and 10 mM (Fig. 5.1c). While the reason for such behaviour is not clear, previous model prediction of DCR/DCR<sub>0</sub> [24] under DLA and a linear correlation obtained between SGO mass concentration and DCR data with correlation coefficient  $r^2 = 0.952$  and  $P$  value  $\gg 0.05$  (Fig. G2) suggest that under the DLA regime the use of DCR/DCR<sub>0</sub> as a representation of normalized mass concentration is valid in all cases. Furthermore, Babakhani et al. [33] verified the use DCR/DCR<sub>0</sub> under the RLA regime at 0.5 and 0.75 mM CaCl<sub>2</sub> solutions, as the rising trend for normalized mass concentration of synthesized SGO over time was consistently observed for normalized mass concentration measured by UV-Vis spectroscopy. Nonetheless, results under the RLA still remain unverified using a model.

### 5.5.3 Model fit results

Nash–Sutcliffe determination coefficients for different model fits to  $D_H$  data are shown in Table 5.1 and simulated curves vs observations of  $D_H$  and DCR are illustrated in Fig. 5.1. On average, FP, S-CRM, and C-CRM, show similar goodness-of-fit to  $D_H$  curves with mean  $R^2_{NS}$ , 0.29, 0.33, and 0.36, respectively. The performance of S-CRM method is slightly poorer than other methods in terms of reproducing the sudden change in  $D_H$  gradient between early and late stages of aggregation under the DLA regime (1 mM CaCl<sub>2</sub> and 50 mM NaClO<sub>4</sub>, Fig. 5.1a). It seems S-CRM and FP are less capable of mimicking the straight log linear curve of  $D_H$  under the RLA regime (0.5 mM CaCl<sub>2</sub> and 30 mM NaClO<sub>4</sub>) than C-CRM method which also reproduces well the change of  $D_H$  slope under the DLA regime. This is consistent with the maximum mean  $R^2_{NS}$  obtained for the C-CRM.

**Table 5.1** Nash-Sutcliff determination coefficient,  $R^2_{NS}$  for fittings to hydrodynamic diameter data with different models across various solution chemistries.

pH	Electrolyte concentration	FP	C-CRM	S-CRM
6	0.1 mM CaCl <sub>2</sub>	-0.093	-0.092	-0.092
	0.5 mM CaCl <sub>2</sub>	0.862	0.947	0.830
	1 mM CaCl <sub>2</sub>	0.505	0.340	0.422
	5 mM NaClO <sub>4</sub>	-1.141	-0.826	-0.843
	10 mM NaClO <sub>4</sub>	0.683	0.694	0.842
	20 mM NaClO <sub>4</sub>	0.827	0.978	0.971
	30 mM NaClO <sub>4</sub>	0.923	0.940	0.912
	50 mM NaClO <sub>4</sub>	0.447	0.587	0.178
2.5	20 mM NaClO <sub>4</sub>	-0.245	0.067	-0.072
4		0.492	0.488	0.537
7.5		0.257	0.256	0.255
10		0.000	-0.033	0.000

It should be noted that  $R^2_{NS}$  might not perform robustly as an objective function in cases where the mean distance of the data points with the horizontal axis is small, i.e., at low aggregation rates such as cases at low electrolyte concentrations of 0.1 mM CaCl<sub>2</sub> and 5 mM NaClO<sub>4</sub> or at high pH of 10, since even though visually a good match is obtained between the two graphs of the observation and modelled data,  $R^2_{NS}$  is not reaching a value close to one as expected. This can cause difficulty for the optimization code to find the best set of parameters in such cases. Although reducing the criteria of  $R^2_{NS}$  difference in two successive iterations (e.g., from 0.1 to 0.001 in the first loop) could to some extent help finding the best parameter values in such cases, still  $R^2_{NS}$  value as a goodness-of-fit criterion remained low.

Considering the DCR data (Fig. 5.1c,d), none of models reproduces the rising behaviour of DCR curves at intermediate IS because the simple explicit decay sedimentation term employed in this study is not expected to reproduce increase in the concentration. Within the DLA regime, however, all models can, to some extent,

reproduce the nonlinear reduction in normalized DCR. In describing DCR trends within this regime, FP technique appeared to perform best followed by S-CRM and C-CRM (Fig. 5.1c,d).

The model-produced PSDs based on  $D_H$  and DCR-matched models are shown in Fig. G3. It appears that none of the models can reproduce the PSD in all cases. In most of the cases, both CRM approaches tend to preserve the initial position of the PSD over time, although the heights of the peaks are changing. This is more noticeable for the C-CRM than S-CRM. The fixed pivot approach exhibits considerable movement of the PSD position, appears to overestimate the experimental PSD, and cannot reproduce the stationary stage of the PSD, especially toward the late stage of aggregation. It is possible that in the case of CRM the mass gradually moves to larger size classes and becomes subject to sedimentation before it appears as movement of the PSD. Such a steady-state or equilibrium condition of the PSD has frequently been used as a basic assumption in model developments [15, 81-83]. Fixed pivot can reproduce the overall shape of the observed PSD generally better than other methods. On average, in terms of reproducing PSD, the size-based CRM performs relatively better than the other two methods because it produces PSDs with closer position to observed PSD, than that produced by FP and with a closer shape to observed PSD than that resulted by C-CRM (Fig. G3).

#### 5.5.4 Estimated parameter trends

The trends of estimated parameters including aggregation rate constants ( $A_S$ ,  $A_C$ , or  $\alpha$ ) and fractal dimension,  $D_f$ , are shown in Fig. 5.2 for different solution chemistries. According to this figure the trends of aggregation rate constants, are consistent among all cases. Unlike HAp NPs in a previous study [24], which exhibited multimodal trends of  $\alpha$  estimated using the FP method with IS, here FP-estimated values of  $\alpha$  for SGO show a positive semi-log linear trend with IS with a correlation coefficient,  $r^2 > 0.8$  (Fig. 5.2a,b) and a negative semi-log linear trend with pH with  $r^2 = 0.98$  (Fig. 5.2c). Interestingly, consistent with the trends of  $\alpha$ , the CRM-estimated aggregation constants  $A_S$  and  $A_C$  display a positive semi-log linear trend with IS ( $r^2 > 0.88$ ) and a negative semi-log linear trend with pH ( $r^2 = 0.73$  for C-CRM and  $r^2 = 0.86$  for S-CRM). The gradients of the lines fitted to  $A_S$  and  $A_C$  versus IS and pH match very well with that of  $\alpha$  ( $P = 0.44$  and  $0.49 \gg 0.05$ ) (Fig. 5.2a-c).

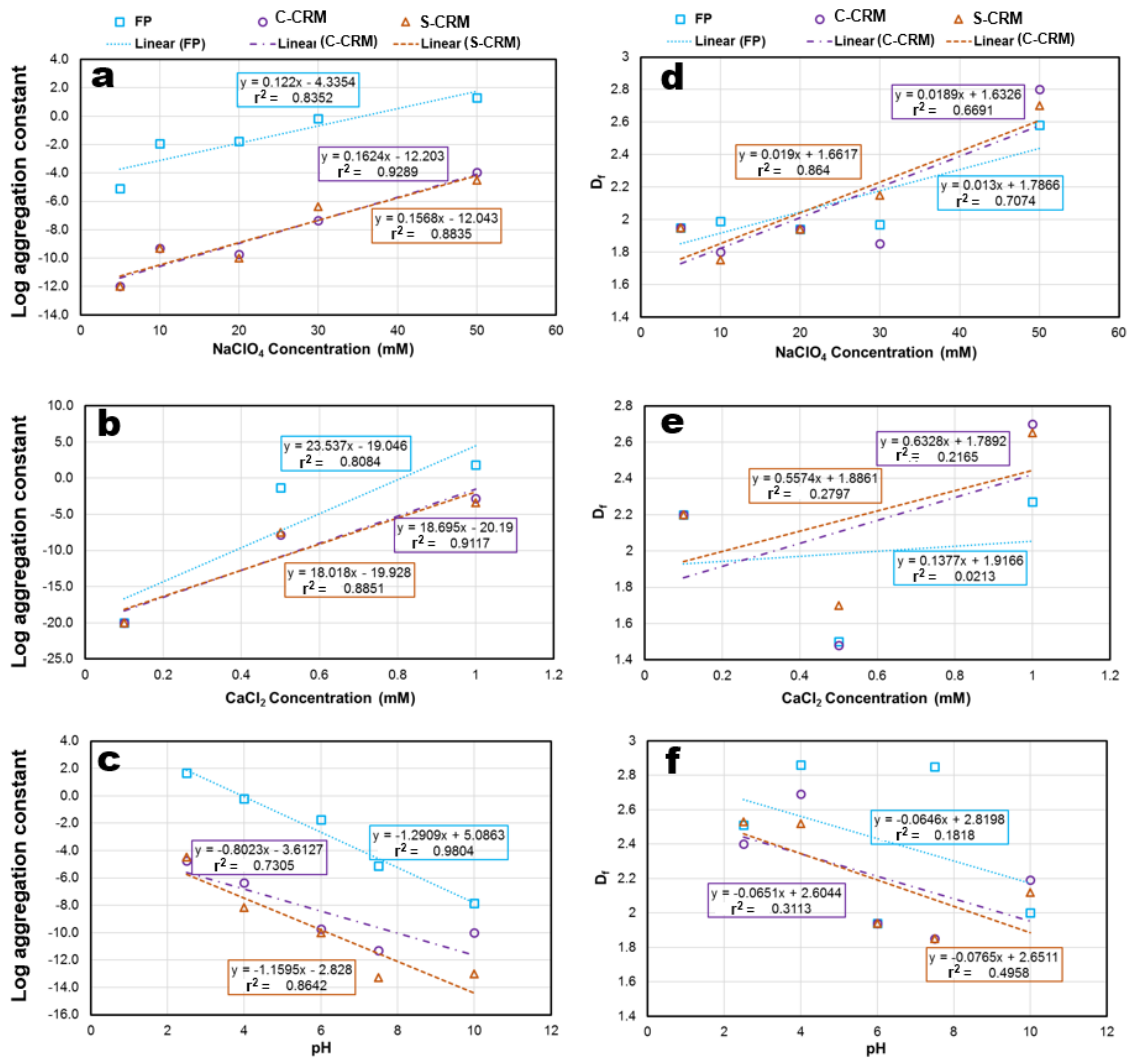


**Figure 5.2** Estimated parameter trends for different models: aggregation rate constants ( $\alpha$ ,  $A_S$ , and  $A_C$  for FP, S-CRM, and C-CRM approaches), vs electrolyte concentration (a,b), and vs pH (c), and fractal dimension,  $D_f$ , vs electrolyte concentration (d,e) and vs pH (f).

Fractal dimension generally increases with IS (Fig. 5.2d,e) and decreases with pH (Fig. 5.2f), which is in agreement with Chowdhury et al. [84] measuring  $D_f$  for TiO<sub>2</sub> NP using static light scattering (SLS). Yet, unlike aggregation constant patterns,  $D_f$  trends are not effectively linear as indicated by low  $r^2$  values shown in Fig. 5.2d-f. This is mostly because of large  $D_f$  determined at lowest IS which emanates from the fact that in the lowest IS, the aggregation is not operative and therefore particles remain in their primary size which should have a geometry close to Euclidian thereby having a  $D_f$  close to 3 [24]. Estimated  $D_f$  in the present study yields close ranges for the three

models, namely, from 1.50 to 2.86 for the FP model, from 1.48 to 2.80 for C-CRM and from 1.70 to 2.70 for S-CRM. High values of  $D_f$  (2.27-2.8) were commonly determined at high IS (DLA regime) while low  $D_f$  values (1.48-1.99) were estimated at intermediate IS (RLA regime). Although similar ranges for  $D_f$  under DLA have been frequently reported [66, 82, 85-90], this is opposite to common ranges of  $D_f$ , reported for aggregates formed in controlled condition where they are not subject to restructuring, i.e.,  $D_f$  close to 2.2 within RLA regime and close to 1.7 within the DLA regime [18, 69, 84, 91]. The underlying reason for  $D_f$  values of differing from common ranges is attributed to restructuring of aggregates at greater depths during the late stage of aggregation in quiescent condition [24] as the typical trends and ranges of  $D_f$  were achieved when the FP model was fitted only to the early stage of aggregation, or when the measurement depth was reduced to just below the surface of the water column. Overall, the general consistency of parameter trends confirms the validation of modelling and parameter estimation processes.

### **5.5.5 Comparison of model efficiency and accuracy**

The results of model run time and mass balance error for every case of simulation for experimental duration of 18000 s are reported in Table 5.2. Based on these results the computational times widely vary with experimental cases due to different aggregation rates, initial PSDs, etc. The mean runtime for the FP technique is  $6.14 \pm 8.9$  min which is comparable or less than computational runtimes in simulations of pure aggregation elsewhere [25, 54, 55]. Using the FP for pure aggregation Nopen et al. [54] showed that the computational time significantly increased, e.g., from 4 to 174 s, with the number of size classes, 25 to 46. Scaling these reported computational times from simulation durations of  $10^3$ - $10^9$  s [54] to that of the present study (18000 s) yields a mean runtime of  $9.06 \pm 16.3$  min which is comparable with that of the present study with 64-76 size classes, suggesting that the FP has been implemented effectively in the present study.

**Table 5.2** Comparison of the model run times and mass balance errors for different cases of model fittings.

pH	Electrolyte concentration	Model	Mass	Model	Mass	Model	Mass
		Run Time (min)	balance error (%)	Run Time (min)	balance error (%)	Run Time (min)	balance error (%)
		FP	C-CRM		S-CRM		
6	0.1 mM CaCl <sub>2</sub>	3.77	-7.1E-14	0.06	-2.8E-14	0.04	-2.8E-14
	0.5 mM CaCl <sub>2</sub>	0.60	-2.1E-04	0.28	5.3E-10	0.04	9.4E-11
	1 mM CaCl <sub>2</sub>	1.23	-4.1E-01	2.22	-9.5E-06	1.48	-9.1E-05
	5 mM NaClO <sub>4</sub>	30.06	1.1E-08	0.13	-2.8E-14	0.09	1.4E-14
	10 mM NaClO <sub>4</sub>	0.94	-2.9E-05	0.29	-1.0E-08	0.20	-1.5E-08
	20 mM NaClO <sub>4</sub>	5.99	-3.8E-05	0.66	2.1E-11	0.47	8.4E-13
	30 mM NaClO <sub>4</sub>	1.32	-2.4E-05	0.27	-4.7E-06	0.18	-5.0E-06
	50 mM NaClO <sub>4</sub>	4.73	-5.1E-02	2.08	-3.6E-05	1.34	-3.8E-05
2.5	20 mM NaClO <sub>4</sub>	2.59	4.4E-07	1.03	1.9E-08	0.70	2.5E-09
4		18.17	-3.9E-07	3.67	1.1E-13	1.10	2.8E-14
7.5		0.46	3.1E-12	0.07	-2.7E-08	0.05	-1.0E-08
10		3.87	4.0E-12	0.22	3.0E-13	0.12	-1.4E-14

Interestingly, the CRMs turn out to be on average about one order-of-magnitude faster than the FP method with mean runtimes  $0.92 \pm 1.15$  for C-CRM and  $0.49 \pm 0.53$  min, for S-CRM. The FP technique is a widely-accepted population-balance model [54, 92], with an ability to preserve the two properties, population and mass. The MATLAB code for solving this model was already validated against analytical solutions of the population balance given for different initial conditions [24]. Here the FP method which is inherently a PBM yields a fairly low average absolute mass balance error ( $3.9 \times 10^{-2}$  %). However, the proposed models of the present study which are inherently mass-balance models show even lower absolute mass balance errors;  $4.2 \times 10^{-6}$  % and  $1.1 \times 10^{-5}$  %, for C-CRM and S-CRM models, respectively, suggesting that the use of mass balance in modelling aggregation not only leads to a more efficient simulation but also enhances the accuracy.

## 5.6 Conclusions

In this study a new modelling framework is proposed based on a mass-balance parent-daughter chain reaction formulation. This includes a series of first-order decay reaction expressions with mass concentration as the main variable. Two semi-empirical approaches based on size (S-CRM) or collision frequencies (C-CRM) were proposed for considering variations in the decay-reaction rates in terms of aggregate size classes. In fitting to analytical solutions of the aggregation model with a log normal initial PSD within a range of conditions S-CRM outperforms C-CRM in terms of goodness-of-fit criterion. When fitting to a range of experimental data for early and late aggregation and sedimentation of SGO, the performances of both approaches were generally similar to or better than that of the standard PBE model. The new models were found averagely one order-of-magnitude faster than the FP method while yielding a lower average mass balance error. However, in contrast to FP, CRM approaches tended to show a quasi-stationary state for the shape of the PSD at moderate or low aggregation rates. Similar trends for aggregation rate constants, estimated from model fitting to experimental data, are obtained for all models, and close ranges are obtained for fractal dimensions, suggesting that model parameters for the proposed CRM are meaningful and may follow conventional models. However, the PBE-estimated aggregation rate constants may not scale with those of the CRM as it is not expected to do necessarily.

Based on the overall agreement between the CRM and analytical/numerical solutions of PBE as well as experimental data of SGO aggregation for hydrodynamic diameter and dimensionless DCR, it is concluded that a CRM formulation is able to describe NP aggregation phenomena under a broad range of conditions. This approach is promising approach for more-efficient modelling of particle aggregation phenomena in various environmental transport and fate problems, particularly in combination with Eulerian approaches with mass-concentration as state variable, where the use of PBE may come with high computational expenses [23, 93] or where higher accuracy than that achieved by current simplifying approaches is required [25, 36]. Further work may address the applicability of the CRM in the various specific conditions of

environmental and engineering systems, e.g., dynamic environments or and porous media, and to improve its description of the PSD by CRM.

## 5.7 References

1. Zurutuza, A. and C. Marinelli, *Challenges and opportunities in graphene commercialization*. Nature nanotechnology, 2014. **9**(10): p. 730.
2. Nanotechnology-Products-Database. 2017.
3. Keller, A.A., et al., *Global life cycle releases of engineered nanomaterials*. Journal of Nanoparticle Research, 2013. **15**(6): p. 1-17.
4. Zhao, J., et al., *Graphene in the aquatic environment: adsorption, dispersion, toxicity and transformation*. Environmental science & technology, 2014. **48**(17): p. 9995-10009.
5. Romanchuk, A.Y., et al., *Graphene oxide for effective radionuclide removal*. Physical Chemistry Chemical Physics, 2013. **15**(7): p. 2321-2327.
6. Yu, S., et al., *Sorption of radionuclides from aqueous systems onto graphene oxide-based materials: a review*. Inorganic Chemistry Frontiers, 2015.
7. Patil, S.S., et al., *Nanoparticles for environmental clean-up: a review of potential risks and emerging solutions*. Environmental Technology & Innovation, 2016. **5**: p. 10-21.
8. Kah, M., et al., *A critical evaluation of nanopesticides and nanofertilizers against their conventional analogues*. Nature nanotechnology, 2018: p. 1.
9. Dimkpa, C.O. and P.S. Bindraban, *Nanofertilizers: New products for the industry?* Journal of agricultural and food chemistry, 2017.
10. Ehtesabi, H., et al., *Enhanced heavy oil recovery in sandstone cores using tio2 nanofluids*. Energy & Fuels, 2013. **28**(1): p. 423-430.
11. Pham, N.H. and D.V. Papavassiliou, *Hydrodynamic effects on the aggregation of nanoparticles in porous media*. International Journal of Heat and Mass Transfer, 2018. **121**: p. 477-487.
12. Sanchís, J., et al., *Occurrence of C60 and related fullerenes in the Sava River under different hydrologic conditions*. Science of The Total Environment, 2018. **643**: p. 1108-1116.
13. Farré, M., J. Sanchís, and D. Barceló, *Adsorption and desorption properties of carbon nanomaterials, the potential for water treatments and associated risks*, in *Nanotechnologies for Environmental Remediation*. 2017, Springer. p. 137-182.
14. Babakhani, P., et al., *Continuum-based models and concepts for the transport of nanoparticles in saturated porous media: A state-of-the-science review*. Advances in Colloid and Interface Science, 2017. **246**(Supplement C): p. 75-104.
15. Babakhani, P., et al., *Modified MODFLOW-based model for simulating the agglomeration and transport of polymer-modified Fe nanoparticles in saturated porous media*. Environ Sci Pollut Res, 1-20, doi:10.1007/s11356-015-5193-0, 2015.
16. Abraham, P.M., et al., *Sorption of silver nanoparticles to environmental and model surfaces*. Environmental science & technology, 2013. **47**(10): p. 5083-5091.
17. Nickel, C., et al., *Mobility of coated and uncoated TiO<sub>2</sub> nanomaterials in soil columns—Applicability of the tests methods of OECD TG 312 and 106 for nanomaterials*. Journal of environmental management, 2015. **157**: p. 230-237.
18. Elimelech, M., J. Gregory, and X. Jia, *Particle deposition and aggregation: measurement, modelling and simulation*. 1998: Butterworth-Heinemann.

19. Afshinnia, K., et al., *Effect of nanomaterial and media physicochemical properties on Ag NM aggregation kinetics*. Journal of Colloid and Interface Science, 2017. **487**: p. 192-200.
20. Gambinossi, F., S.E. Mylon, and J.K. Ferri, *Aggregation kinetics and colloidal stability of functionalized nanoparticles*. Advances in colloid and interface science, 2015. **222**: p. 332-349.
21. Ramkrishna, D. and M.R. Singh, *Population balance modeling: current status and future prospects*. Annual review of chemical and biomolecular engineering, 2014. **5**: p. 123-146.
22. Ramkrishna, D., *Population balances: Theory and applications to particulate systems in engineering*. 2000: Academic press.
23. Rigopoulos, S., *Population balance modelling of polydispersed particles in reactive flows*. Progress in Energy and Combustion Science, 2010. **36**(4): p. 412-443.
24. Babakhani, P., R.-a. Doong, and J. Bridge, *Significance of early and late stages of coupled aggregation and sedimentation in the fate of nanoparticles: measurement and modelling*. Environmental science & technology, 2018. doi: **10.1021/acs.est.7b05236**.
25. Dale, A.L., G.V. Lowry, and E.A. Casman, *Accurate and fast numerical algorithms for tracking particle size distributions during nanoparticle aggregation and dissolution*. Environmental Science: Nano, 2017. **4**(1): p. 89-104.
26. Baalousha, M., *Effect of nanomaterial and media physicochemical properties on nanomaterial aggregation kinetics*. NanoImpact, 2017. **6**: p. 55-68.
27. Bradford, S.A. and S. Torkzaban, *Determining parameters and mechanisms of colloid retention and release in porous media*. Langmuir, 2015. **31**(44): p. 12096-12105.
28. Bradford, S.A., et al., *Contributions of nanoscale roughness to anomalous colloid retention and stability behavior*. Langmuir, 2017. **33**(38): p. 10094-10105.
29. Abdelfatah, E., et al., *Mechanistic study of nanoparticles deposition and release in porous media*. Journal of Petroleum Science and Engineering, 2017. **157**: p. 816-832.
30. Babakhani, P., et al., *Parameterization and prediction of nanoparticle transport in porous media: A reanalysis using artificial neural network*. Water Resources Research, 2017. **53**: p. 4564-4585.
31. Wang, D., et al., *Modeling the Transport of the "New-Horizon" Reduced Graphene Oxide—Metal Oxide Nanohybrids in Water-Saturated Porous Media*. Environmental science & technology, 2018. **52**(8): p. 4610-4622.
32. Saleh, N.B., et al., *Research strategy to determine when novel nanohybrids pose unique environmental risks*. Environmental Science: Nano, 2015. **2**(1): p. 11-18.
33. Babakhani, P., et al., *Aggregation and sedimentation of shattered graphene oxide nanoparticles in dynamic environments: a solid-body rotational approach*. Environmental Science: Nano, 2018. doi: **10.1039/C8EN00443A**.
34. de Klein, J.J.M., et al., *Towards validation of the NanoDUFLOW nanoparticle fate model for the river Dommel, The Netherlands*. Environmental Science: Nano, 2016. **3**(2): p. 434-441.
35. Praetorius, A., M. Scheringer, and K. Hungerbühler, *Development of environmental fate models for engineered nanoparticles— a case study of tio2 nanoparticles in the rhine river*. Environmental Science & Technology, 2012. **46**(12): p. 6705-6713.
36. Quik, J.T.K., D. van De Meent, and A.A. Koelmans, *Simplifying modeling of nanoparticle aggregation—sedimentation behavior in environmental systems: A theoretical analysis*. Water Research, 2014. **62**: p. 193-201.

37. Sani-Kast, N., et al., *Addressing the complexity of water chemistry in environmental fate modeling for engineered nanoparticles*. Science of the Total Environment, 2015. **535**: p. 150-159.
38. Lister, J., D. Smit, and M. Hounslow, *Adjustable discretized population balance for growth and aggregation*. AIChE Journal, 1995. **41**(3): p. 591-603.
39. Hounslow, M.J., R.L. Ryall, and V.R. Marshall, *A discretized population balance for nucleation, growth, and aggregation*. AIChE Journal, 1988. **34**(11): p. 1821-1832.
40. Kumar, S. and D. Ramkrishna, *On the solution of population balance equations by discretization—I. A fixed pivot technique*. Chemical Engineering Science, 1996. **51**(8): p. 1311-1332.
41. Kumar, S. and D. Ramkrishna, *On the solution of population balance equations by discretization—II. A moving pivot technique*. Chemical Engineering Science, 1996. **51**(8): p. 1333-1342.
42. Kumar, J., et al., *An efficient numerical technique for solving population balance equation involving aggregation, breakage, growth and nucleation*. Powder Technology, 2008. **182**(1): p. 81-104.
43. Singh, M., J. Kumar, and A. Bück, *A volume conserving discrete formulation of aggregation population balance equations on non-uniform meshes*. IFAC-PapersOnLine, 2015. **48**(1): p. 192-197.
44. Šimunek, J., et al., *The HYDRUS-1D software package for simulating the one-dimensional movement of water, heat, and multiple solutes in variably-saturated media, version 4.08*. University of California, Riverside, Dept. of Environmental Sciences HYDRUS Software Series, 2009. **3**: p. 330.
45. Comba, S. and J. Braun, *A new physical model based on cascading column experiments to reproduce the radial flow and transport of micro-iron particles*. Journal of contaminant hydrology, 2012. **140**: p. 1-11.
46. Dale, A., et al., *Modeling nanomaterial environmental fate in aquatic systems*. Environmental Science & Technology, 2015.
47. Smoluchowski, M., *Versuch einer mathematischen Theorie der Koagulationskinetik kolloider Lösungen*. Zeitschrift fuer Physikalische Chemie. 92., 1917. **129-68**.
48. Szilagyi, I., et al., *Particle aggregation mechanisms in ionic liquids*. Physical Chemistry Chemical Physics, 2014. **16**(20): p. 9515-9524.
49. Han, M. and D.F. Lawler, *The (relative) insignificance of G in flocculation*. Journal (American Water Works Association), 1992: p. 79-91.
50. LeVeque, R.J., *Finite difference methods for differential equations*. Draft version for use in AMath, 1998. **585**(6).
51. Burd, A.B., S.B. Moran, and G.A. Jackson, *A coupled adsorption–aggregation model of the POC/234Th ratio of marine particles*. Deep Sea Research Part I: Oceanographic Research Papers, 2000. **47**(1): p. 103-120.
52. Lee, K.W., Y.J. Lee, and D.S. Han, *The log-normal size distribution theory for Brownian coagulation in the low Knudsen number regime*. Journal of Colloid and Interface Science, 1997. **188**(2): p. 486-492.
53. Tourbin, M. and C. Frances, *Experimental characterization and population balance modelling of the dense silica suspensions aggregation process*. Chemical Engineering Science, 2008. **63**(21): p. 5239-5251.

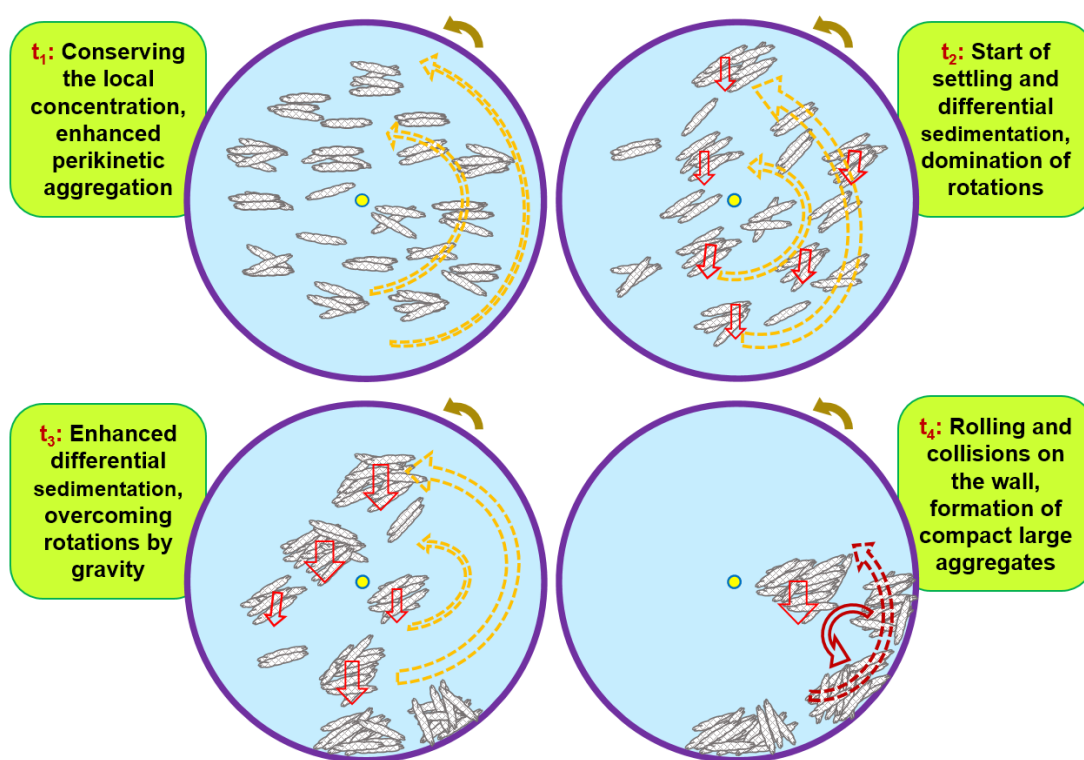
54. Nopens, I., D. Beheydt, and P.A. Vanrolleghem, *Comparison and pitfalls of different discretised solution methods for population balance models: a simulation study*. Computers & chemical engineering, 2005. **29**(2): p. 367-377.
55. Majumder, A., et al., *Lattice Boltzmann method for population balance equations with simultaneous growth, nucleation, aggregation and breakage*. Chemical engineering science, 2012. **69**(1): p. 316-328.
56. Bove, S., T. Solberg, and B.H. Hjertager, *A novel algorithm for solving population balance equations: the parallel parent and daughter classes. Derivation, analysis and testing*. Chemical Engineering Science, 2005. **60**(5): p. 1449-1464.
57. Bedekar, V., et al., *MT3D-USGS version 1: A US Geological Survey release of MT3DMS updated with new and expanded transport capabilities for use with MODFLOW*. 2016, US Geological Survey.
58. Clement, T.P., *A Modular Computer Code for Simulating Reactive Multispecies Transport in 3-Dimensional Groundwater Systems*. The U.S. Department of Energy, 1997: p. 1-59.
59. Zheng, C., *MT3D99, A Modular 3D Multispecies Transport Simulator User's Guide*. SS Papadopulos & Associates Inc, 2000.
60. Markus, A.A., et al., *Modeling aggregation and sedimentation of nanoparticles in the aquatic environment*. Science of The Total Environment, 2015. **506**: p. 323-329.
61. Chandrasekhar, S., *Stochastic problems in physics and astronomy*. Reviews of modern physics, 1943. **15**(1): p. 1.
62. Hunt, J.R., *Self-similar particle-size distributions during coagulation: theory and experimental verification*. Journal of Fluid Mechanics, 1982. **122**: p. 169-185.
63. Hunt, J.R., *Particle aggregate breakup by fluid shear*, in *Estuarine cohesive sediment dynamics*. 1986, Springer. p. 85-109.
64. Li, D.H. and J. Ganczarczyk, *Fractal geometry of particle aggregates generated in water and wastewater treatment processes*. Environmental Science & Technology, 1989. **23**(11): p. 1385-1389.
65. Dolgonosov, B.M., *Kinetics of sedimentation of a coagulating suspension*. Theoretical Foundations of Chemical Engineering, 2005. **39**(6): p. 635-642.
66. Sterling, M.C., et al., *Application of fractal flocculation and vertical transport model to aquatic sol-sediment systems*. Water research, 2005. **39**(9): p. 1818-1830.
67. Veerapaneni, S. and M.R. Wiesner, *Hydrodynamics of fractal aggregates with radially varying permeability*. Journal of Colloid and Interface Science, 1996. **177**(1): p. 45-57.
68. Li, X.-Y. and B.E. Logan, *Permeability of fractal aggregates*. Water research, 2001. **35**(14): p. 3373-3380.
69. Vikesland, P.J., et al., *Aggregation and sedimentation of magnetite nanoparticle clusters*. Environmental Science: Nano, 2016. **3**(3): p. 567-577.
70. Nash, J.E. and J.V. Sutcliffe, *River flow forecasting through conceptual models part I — A discussion of principles*. Journal of Hydrology, 1970. **10**(3): p. 282-290.
71. Babakhani, P., et al., *Supplementary Material for "Modified MODFLOW-based model for simulating the agglomeration and transport of polymer-modified Fe nanoparticles in saturated porous media"*. Environ Sci Pollut Res, 1-20, doi:10.1007/s11356-015-5193-0, 2015.

72. Nourani, V. and M. Sayyah-Fard, *Sensitivity analysis of the artificial neural network outputs in simulation of the evaporation process at different climatologic regimes*. Advances in Engineering Software, 2012. **47**(1): p. 127-146.
73. Aqil, M., et al., *Analysis and prediction of flow from local source in a river basin using a Neuro-fuzzy modeling tool*. Journal of environmental management, 2007. **85**(1): p. 215-223.
74. Sun, Y., et al., *Transport, retention, and size perturbation of graphene oxide in saturated porous media: Effects of input concentration and grain size*. Water research, 2015. **68**: p. 24-33.
75. Liu, L., et al., *Effects of surfactant type and concentration on graphene retention and transport in saturated porous media*. Chemical Engineering Journal, 2015. **262**: p. 1187-1191.
76. Liu, L., et al., *Effects of pH and surface metal oxyhydroxides on deposition and transport of carboxyl-functionalized graphene in saturated porous media*. Journal of nanoparticle research, 2013. **15**(11): p. 1-8.
77. Wallace, S.J., et al., *Drug release from nanomedicines: selection of appropriate encapsulation and release methodology*. Drug delivery and translational research, 2012. **2**(4): p. 284-292.
78. Missana, T., et al., *Analysis of colloids erosion from the bentonite barrier of a high level radioactive waste repository and implications in safety assessment*. Physics and Chemistry of the Earth, Parts A/B/C, 2011. **36**(17): p. 1607-1615.
79. Holmboe, M., et al., *Effects of  $\gamma$ -irradiation on the stability of colloidal Na<sup>+</sup>-Montmorillonite dispersions*. Applied Clay Science, 2009. **43**(1): p. 86-90.
80. Jiang, Y., et al., *Graphene oxides in water: correlating morphology and surface chemistry with aggregation behavior*. Environmental science & technology, 2016. **50**(13): p. 6964-6973.
81. Friedlander, S.K., *Similarity considerations for the particle-size spectrum of a coagulating, sedimenting aerosol*. Journal of Meteorology, 1960. **17**(5): p. 479-483.
82. Zhang, J.j. and X.y. Li, *Modeling particle-size distribution dynamics in a flocculation system*. AIChE Journal, 2003. **49**(7): p. 1870-1882.
83. Jeffrey, D.J., *Quasi-stationary approximations for the size distribution of aerosols*. Journal of the Atmospheric Sciences, 1981. **38**(11): p. 2440-2443.
84. Chowdhury, I., S.L. Walker, and S.E. Mylon, *Aggregate morphology of nano-TiO<sub>2</sub>: role of primary particle size, solution chemistry, and organic matter*. Environmental Science: Processes & Impacts, 2013. **15**(1): p. 275-282.
85. Schaefer, D.W., et al., *Fractal geometry of colloidal aggregates*. Physical Review Letters, 1984. **52**(26): p. 2371.
86. Hanus, L.H., R.U. Hartzler, and N.J. Wagner, *Electrolyte-induced aggregation of acrylic latex. 1. Dilute particle concentrations*. Langmuir, 2001. **17**(11): p. 3136-3147.
87. Russel, W.B., D.A. Saville, and W.R. Schowalter, *Colloidal dispersions*. 1989: Cambridge university press.
88. Allain, C., M. Cloitre, and F. Parisse, *Settling by cluster deposition in aggregating colloidal suspensions*. Journal of colloid and interface science, 1996. **178**(2): p. 411-416.
89. González, A.E., *Colloidal Aggregation Coupled with Sedimentation: A Comprehensive Overview*, in *Advances in Colloid Science*. 2016, InTech.

90. Tang, P., J. Greenwood, and J.A. Raper, *A model to describe the settling behavior of fractal aggregates*. Journal of colloid and interface science, 2002. **247**(1): p. 210-219.
91. Zhang, J. and J. Buffle, *Multi-method determination of the fractal dimension of hematite aggregates*. Colloids and Surfaces A: Physicochemical and Engineering Aspects, 1996. **107**: p. 175-187.
92. Nopens, I. and P.A. Vanrolleghem, *Comparison of discretization methods to solve a population balance model of activated sludge flocculation including aggregation and breakage*. Mathematical and Computer Modelling of Dynamical Systems, 2006. **12**(5): p. 441-454.
93. Drumm, C., et al., *One-group reduced population balance model for CFD simulation of a pilot-plant extraction column*. Industrial & Engineering Chemistry Research, 2010. **49**(7): p. 3442-3451.

## Chapter 6

### 6 Aggregation and sedimentation of shattered graphene oxide nanoparticles (SGO) in dynamic environments: a solid-body rotational approach



#### 6.1 Chapter overview

##### 6.1.1 Scope

This chapter aims at taking a realistic look at aggregation of NP in porous media and surface waters with focus on the role of environmental dynamics. The outcomes are important for future model development of aggregation in such environments. The result of this chapter has been published as the following paper which has been made open access with support from the University of Liverpool:

“Babakhani, P.; Bridge, J.; Phenrat, T.; Doong, R.-a.; Whittle, K., Aggregation and sedimentation of shattered graphene oxide nanoparticles in dynamic environments: a solid-body rotational approach. *Environmental Science: Nano*, 2018. DOI:10.1039/C8EN00443A”

### **6.1.2 Abstract**

Nanoparticle (NP) aggregation is typically investigated in either quiescent or turbulent mixing conditions; neither is fully representative of dynamic natural environments. In groundwater, complex interacting influences of advective-diffusive transport, pore tortuosity, and the arrival of aggregates from up-gradient pores impacts the aggregation behaviour of NPs, whereas in surface waters, continuous mixing of fresh particle and aged aggregate populations amends aggregation rates. To mimic such conditions, a cylinder reactor containing shattered graphene oxide NP (<100 nm) suspension was set to rotate with a Reynolds Number ( $Re$ ) in the range of natural systems and with zero shear. Two main aggregation phases were then observed. Up to 250-350 min, NP remained near the rotational axis longer than in static conditions, giving rise to higher aggregation rates interpreted as an enhanced perikinetic aggregation and differential sedimentation due to mixing with resuspending aggregates. In this phase, a population-balance model estimated an attachment efficiency >5 times in the rotating system than in the static system. Later (5-13 h) aggregates collided with extensively each other, broke, and reformed on the rotating cylinder wall giving rise to larger, denser aggregates (>1  $\mu$ m). These results thus shed new light on the differences in aggregation behaviour between porous media and other natural environmental systems compared to quiescent batch experiments.

## **6.2 Introduction**

With the increasing global proliferation of commercial applications for nanomaterials, they are becoming increasingly released into the natural environment either accidentally in waste streams or deliberately within environmental clean-up, agronomy, and petroleum reservoir recovery applications [1]. Among various nanomaterials, the use of graphene nanomaterials is rapidly growing due to their broad constructional, industrial, environmental, and medical applications and arising from their use with other nanomaterials as nanohybrids [2-7]. Graphene nanosheets may end

up in the environment in various forms of particulate matter such as crumpled graphene [8-10], multilayer graphene [4, 5, 11], shattered nanosheets [12], and fractal aggregates/hetero-aggregates [13, 14]. Once they have entered aquatic environments, aggregation of such particles can significantly affect their functionality and transport behaviour, particularly in aqueous and porous media [4, 5, 15]. Despite the existence of many studies on homo- and hetero-aggregation of various nanoparticles (NP) [14, 16-21], and abundant reports on the impacts of various factors on the aggregation behaviour of these NP [22-26], it still remains a problem of how system dynamics modify aggregation. It is particularly of paramount importance in groundwater (GW) transport to understand how such complex multi-cascade processes of advective and diffusive transport [27-30], tortuosity in porous media [31], and the arrival of aggregates from up-gradient pores [32, 33] impact the aggregation behaviour of NP. Additionally, it is critical to investigate how resuspension phenomenon occurring within surface water (SW) bodies, such as lakes, river, and sea at various scales, influences the aggregation of NP in these environments [34-37].

Typically, current experimental techniques investigating NP aggregation dynamics are limited to simple quiescent or turbulent mixing batch experiments which may not adequately capture aggregation conditions in real systems [38, 39]. Whilst research into incorporating aggregation models within porous media transport models continues [38, 40, 41], steps must be taken to validate the individual aspects of aggregation models in dynamic media. One of these impacts can be the heterogeneous or anisotropic mixing in the population of nanoaggregates induced by the environmental dynamics such as cascading/cycling conditions within GW and SW systems [27-30, 32, 33, 36, 37, 42-44] that can modify the particle size distribution (PSD) evolution trends under aggregation/sedimentation conditions. To investigate such systems, a slow rotating cylinder is used in which these impacts are simulated by slow continuous revolutions of the cylinder. This simple apparatus allows monitoring the particle size dynamics during aggregation which is cumbersome or impossible in other experimental approaches used for studying the NP fate, such as packed column experiments [45] or mesocosm tests [46].

Rolling cylinders have been used extensively in marine science to mimic the natural condition of marine snow aggregate formation [47]. This system consists of a cylinder which is saturated with water and is placed horizontally to rotate around its

axis slowly so that no significant shear is induced in the fluid inside. Since the initial condition is static, i.e., the cylinder is initially at rest at zero time, the initial rotations can cause shear in the fluid. Once this has passed, the system rotates as a solid body [48, 49]. This technique [50, 51], has been also utilized to study the interactions of bacteria [52], organic carbon accumulation in marine sediments [53], aggregation of diatom [54], and their interactions with resuspended sediments [55], larvae interactions with anisotropic fluid motions [56], and interactions of microplastic with phytoplankton aggregates [57]. However, to the best of authors' knowledge there has not been any systematic application of rolling cylinders to determine the aggregation of engineered NP in aqueous environmental systems to date. To mimic the condition of porous media, the system was designed with a Reynolds number ( $Re$ ) within the range encountered in natural systems, i.e., from less than one to 10 [58, 59]. The main objective of using such a system was to investigate how NP aggregation behaviour changes over time when the local mass concentration is kept constant, a phenomenon that can occur in pores of subsurface porous media and in resuspending surface waters. Using such a rotating cylinder, the angle between NP displacement directions and the gravity or removal direction is continuously changing without significant mechanical shear, thus preventing particle removal via settling within the axial area of the cylinder. This allows aggregates to develop to very large dimensions until gravity forces impacting on large grown aggregates which are probably more compact than initial aggregates overcome rotational displacements, and the system enters an unstable situation where aggregates tend to settle. The primary aim therefore is to shed light on unexpected higher aggregation rates of NP in GW systems when compared with many standard experimental and modelling results, and on how NP aggregation can be influenced by resuspension and population mixing in SW systems [34, 38, 60, 61]. This may underpin development of new mathematical descriptions of aggregation mechanism for a more accurate consideration of these mechanism in models of NP fate and transport in the environment which take other complex concurrent transport/transformation mechanisms into account [38, 41, 62].

Since the largest use of graphene nanomaterials may result from their high strength and flexibility (~100 stronger than steel) [4], it is possible that they release into the environment as shattered graphene because they may undergo extreme physical or chemical stresses during the usage or upon entering waste streams. Therefore, in this

study shattered graphene oxide (SGO) particles with a primary hydrodynamic size ( $D_H$ ) of 90 nm is used. In the scope of this study, which lumps the impact of particle surface characteristics and interactions in one free parameter, i.e., attachment efficiency, within the fitting process, SGO may also act as a representative for other NP types due to their small hydrodynamic size ( $D_H < 100$  nm) and since in terms of general aggregation behaviour, e.g., hydrodynamic size and mass concentration trends over time, they exhibit similar patterns to other NP, such as hydroxyapatite (HAp) NP [40]. It should be mentioned that the original GO sheets may not represent NP due to their large aspect ratio and being considered as a 2-D material.

## **6.3 Materials and Methods**

### **6.3.1 Rotating cylinder setup**

Acrylic cylinders were manufactured with inner diameters of 5 cm and length of 19.1 cm to rotate at 4.71 rotations per hour (rph) to yield a low Reynolds number, 5.7, mimicking environmental condition within GW system (Reynolds number ranging from below one to 10) as well as resuspending SW system (Reynolds number in range of 0.1 to 16) [58, 59]. Methylene blue was used to investigate both the dispersion of matter inside the cylinder and the flow regime as a solid-body rotation. In this case the dye was injected through a needle as an instant point source into the cylinder to see how its diffusion/dispersion is affected by the rotations. A belt-pulley was set to reduce, by >200 times, the rotational velocity of a laboratory stirrer (Eyela NZ, Japan) with an adjustable revolution rate as illustrated in Figs. 6.1, H1. The connection of cylinder to the rotational apparatus was filled with soft plastic, preventing any transfer of shaking from the apparatus to the cylinder. The prepared NP dispersions were poured into the cylinder in the beginning of each experiment to set up each case with an initially homogeneous dispersion. Sampling for particle size measurement was challenging due to the possibility of aggregate breakage resulting from any shear force. To alleviate this, all the channels through which the samples had to pass including syringe tips and a glass pipe inside the cylinder, were selected with an inner diameter larger than ~2 mm. Sampling was performed by syringe removal (without needle) with a minor flow rate to minimize the impact of shear force on aggregates. With great care they were then directly transferred to the Dynamic Light Scattering (DLS) cuvette for size measurement. Samples were taken using a straight glass pipe centred on one side

of the cylinder up to approximately one-third of the length (Fig. 6.1). In order to keep the reactor saturated at all times during the experiment and to prevent bubble formation, a syringe with a long needle was used to inject the stock dispersion into the cylinder simultaneous with sampling, with the needle leaned towards the wall of the cylinder and entered up to approximately two-third of the length of the cylinder, to be far enough from the sampling point in the middle (see Fig. 6.1). The volume of each sample was <1.5 mL and an average of 16 samples were taken in each experimental setup. Therefore, the total volume of reactor exchanged with the initially provided stock dispersion was around 24 mL which is less than 10% when compared with the total volume of the cylinder (~375 mL). After obtaining, the samples were immediately analysed for size and PSD using DLS (Malvern Zetasizer, Nano ZS model, UK) selecting the number of runs to 5 each with a duration of 10 s and adjusting the beam attenuator to 11 and the position of measurement at 6.5 mm. The refractive index of graphene oxide (GO) used in the calculation of volume-based PSD was assumed as 1.333 and the absorption as 0.01. It should be noted that the sensitivity of volume-based PSD to these factors was minor despite their being expected to be influential. Based on preliminary batch experiment, ionic strength (IS) was selected at 0.5 and 0.75 mM CaCl<sub>2</sub> with a pH of 6. These IS values are less than or close to the critical coagulation concentration (CCC) (based on experimental results from previous section).

The derived count rate (DCR) of DLS output has been used as a measure of mass concentration [63-65]. However, since DCR significance under the reaction limited aggregation (RLA) remains unvalidated, the mass concentration in each sample was also determined using UV-Vis spectroscopy (Hitachi, U-4100 model, Japan) at a wavelength of 230 nm, with a calibrated absorption curve. With such a curve (intercept = 0) measured absorbance normalized by the initial absorbance in each experiment was used as representative of normalized mass concentrations.

### **6.3.2 SGO synthesis**

Graphene oxide was synthesized by the chemical exfoliation of natural graphite flakes using a modified Hummers method following Sahu et al. [66]. This was conducted through the constant stirring of graphite (2.0 g) in a solution of 225 mL sulfuric acid and 50 mL phosphoric acid, followed by gradual addition of 5 g potassium

permanganate at a constant temperature of 35 °C and continuous stirring, which was maintained for 10 h. The mixture was then diluted with 225 mL of DI water and kept in an ice bath, subsequently, 3mL of H<sub>2</sub>O<sub>2</sub> was added for permanganate residual removal, with the mixture centrifuged and washed with 1 M hydrochloric acid. This was followed by washing with phosphate buffer (pH 11). Finally, the synthesized GO was washed with DI water repeatedly to reach the neutral pH. Shattered GO was prepared via intensive ultra-sonication of a GO dispersion (2 g/L) to achieve initial uniform hydrodynamic size below 100 nm. This was conducted using a probe sonication at a power of 40 W for 2 h with 30-second stops following 30-second sonication intervals. This dispersion was then centrifuged for 30 min at 19500 ± 500 rpm to remove the larger fraction of particles. Finally, the dispersion was passed through a 0.45- $\mu$ m syringe filter, and the filtrate kept in the dark at 4 °C as the stock dispersion. Sodium azide was added (10 mM) to each experimental dispersion to prevent the growth of bacteria during analysis and due to its buffering ability in maintaining a constant pH during the course of experiments [40].

### 6.3.3 Experimental procedure

The cylinder tests were performed as follows: (1) prepare particle dispersions in deionized (DI) water with a final SGO concentration 50 mg/L, and sodium azide concentration 10 mM; (2) adjust pH at 6±0.05 with NaOH/HCl (100 mM) while stirring with a magnet stirrer; (3) ultrasonicate for 5 min in sonication bath, add electrolyte, (CaCl<sub>2</sub>) to reach final concentrations 0.5 and 0.75 mM, stop stirring 5 s after adding the electrolyte, and take the first sample; (4) fill the cylinder with the prepared dispersion, emplace the syringe and the sampling pipe, seal, and leave at rest for static cases or on the rotating mode for dynamic cases (in total taking ~10-15 min from the time of stopping the stirrer until the complete setup of the cylinder); and (5) take samples (<1.5 mL) at certain times to be analysed immediately by DLS. After obtaining each sample the glass pipe was evacuated using a syringe to prevent interference of the solution inside the pipe with the next sampling. After analysis by DLS, the same samples were carefully preserved at 4 °C for analysis using UV-Vis, which were carried out following dilution by 7.5 times and sonication for 5 min to obtain a uniform dispersion. Selected experiments which could have been prone to uncertainties (e.g., due to higher IS) were carried out in duplicate. Control experiments

were undertaken in a similar condition to cylinder experiment but inside 3-mL DLS cuvettes with time resolved online measurement. In these experiments after ultrasonication of the suspension for 5 min, the electrolyte was added, and the sample was immediately vortexed for 5 s. Then it was transferred to a disposable cuvette, after which time-resolved DLS measurement was started immediately. The whole process duration, from ultrasonication until the start of the first measurement, was  $70 \pm 20$  s. The sample volume of 3 mL corresponds to a measurement depth of  $\sim 23.3$  mm which is close to the radius of the cylinder. In control experiments, time-resolved DCR data normalized to the initially observed DCR was used as an indicator of mass concentration [40, 63-65].

## 6.4 Theory and modelling

### 6.4.1 Flow regime

A simplified form of Navier-Stokes equation in cylindrical coordinate can be expressed as [48]:

$$\frac{du_\theta}{dt} = \nu \left[ \frac{\partial^2 u_\theta}{\partial r^2} + \frac{1}{r} \frac{\partial u_\theta}{\partial r} - \frac{u_\theta}{r^2} \right] \quad (6.1)$$

where  $u_\theta$  is the angular component of the linear velocity,  $r$  is the radial distance from the centre of the cylinder, and  $\nu$  is the kinematic viscosity [ $L^2T^{-1}$ ]. For the initial condition,  $u_\theta = 0$ , and boundary condition,  $u_\theta = \omega a_{cyl}$  at  $r = a_{cyl}$ , where  $a_{cyl}$  is the radius of the cylinder and  $\omega$  is the angular velocity of the cylinder. The analytical solution of Eq. (6.1) is [48, 67]:

$$u_\theta = \omega r - \sum_{i=1}^{\infty} A_i J_1(\lambda_i r) e^{-\lambda_i^2 \nu t} \quad (6.2)$$

where  $A_i = 2\omega(\lambda_i J_2(\lambda_i a_{cyl}))^{-1}$ ,  $J_1$  and  $J_2$  are Bessel functions of the first kind and orders 1 and 2, respectively, and  $\lambda_i \approx i\pi a_{cyl}^{-1}$ . The horizontal and vertical rectangular components of velocity,  $u_x$  and  $u_y$  are:

$$u_x = -u_\theta \sin \theta \quad (6.3)$$

$$u_y = u_\theta \cos \theta - U_k \quad (6.4)$$

where  $U_k$  is settling velocity of aggregates in size class  $k$  [L T<sup>-1</sup>]. Among various approaches to settling velocity [68-71], a power-law model can best describe the settling velocity of NP aggregates as derived in the Appendix F [40, 68-71]:

$$U_k = \frac{g}{18\mu} (\rho_0 - \rho_w)(2a_0)^{3-D_f}(2a_k)^{D_f-1} \quad (6.5)$$

where  $a_0$  is the radius of the primary particles,  $a_k$  is the radius of aggregates,  $D_f$  is the fractal dimension of aggregates,  $g$  is the gravitational acceleration,  $\mu$  is the viscosity of fluid,  $\rho_0$  is the density of primary particles [ML<sup>-3</sup>], and  $\rho_w$  is the density of water [ML<sup>-3</sup>].

Once the system reaches the equilibrium conditions, i.e. solid-body rotation, particle trajectories can be calculated as [48]:

$$x = -r_0 \sin(\omega t - \theta_0) + \frac{U_k}{\omega} \quad (6.6)$$

$$y = r_0 \cos(\omega t - \theta_0) \quad (6.7)$$

where  $r_0$  and  $\theta_0$  represent initial position of the particle in cylindrical coordinates and  $x$  and  $y$  are positions of the particle in rectangular coordinates at time  $t$ .

The shear rate,  $\gamma$ , resulted from the gradient of velocity across the cylinder radius is given as [48]:

$$\gamma = \sum_{i=1}^{\infty} A_i e^{-\lambda_i^2 \nu t} \left( -\frac{\lambda_i}{2} J_0(\lambda_i r) + \frac{1}{r} J_1(\lambda_i r) + \frac{\lambda_i}{2} J_2(\lambda_i r) \right) \quad (6.8)$$

## 6.4.2 Particle aggregation

A flexible population-balance model known as fixed pivot (FP) [72], capable of considering initial particle size distribution (PSD) and consequent evolution of PSD in early and late stages of aggregation is used to model the dynamic behaviour of hydrodynamic diameter, overall mass concentration, and PSD for SGO aggregation experiments. Conserving two properties of mass and number, the model equation for aggregation combined with sedimentation term is as follows [72]:

$$\frac{dn_k}{dt} = \sum_{\substack{j \geq i \\ v_{k-1} \leq (v_j + v_i) \leq v_{k+1}}} \left[ 1 - \frac{1}{2} \delta_{j,i} \right] \eta_k \alpha \beta_{j,i} n_j n_i - n_k \sum_i \alpha \beta_{k,i} n_i - \frac{U_k}{Z_s} n_k \quad (6.9)$$

where  $n_k$  is the particle number concentration of aggregates in size class  $k$  [ $L^{-3}$ ],  $\beta$  is the collision frequency,  $\alpha$  is the attachment efficiency factor,  $v$  is the representative volume of each size class in the grid,  $\delta$  is Kronecker's delta,  $Z_s$  is sedimentation depth or measurement depth [L], and  $\eta_k$  is:

$$\eta_k = \begin{cases} \frac{v_{k+1} - (v_j + v_i)}{v_{k+1} - v_k}, & v_k \leq (v_j + v_i) \leq v_{k+1} \\ \frac{(v_j + v_i) - v_{k-1}}{v_k - v_{k-1}}, & v_{k-1} \leq (v_j + v_i) \leq v_k \end{cases} \quad (6.10)$$

An explicit forward Euler scheme was used for the time discretization of Eq. (6.9) with an adjustable time-step, as this can be more efficient than higher-order schemes for solving “stiff” problems such as population balance models [73, 74]. Since the Brinkman permeability-based model [75-77] performs best for modelling collision frequencies, this approach was used in the present study. All collision kernels were expressed based on aggregate volume so that the impact of aggregate shapes which are unknown will interfere less in the model results. The measured initial PSD was directly used as the initial condition. A new optimization algorithm code [40] was also used here to estimate the parameter values ( $\alpha$  and  $D_f$ ) by matching the modelled with experimental data for mean hydrodynamic diameter ( $D_H$ ) and normalized concentration data ( $C/C_0$ ). In these fittings, the contribution weight of the  $D_H$  was assumed to be twice  $C/C_0$ . Aggregation modelling was performed only at a single spatial point, i.e., the centre of the cylinder cross-section, corresponding to the point of measurement and considering the sedimentation depth in Eq. (6.9),  $Z_s$ , as the radius of the cylinder. Full model equations together with details of extensive model testing and the MATLAB codes and optimization algorithm are available in Appendix F and in Babakhani et al. [40]. A summary of the model parameters and experimental characteristics are provided in Table 6.1.

**Table 6.1** Summary of modelling parameters and experimental characteristics.

Parameter	Symbol	Value
Shear rate ( $s^{-1}$ )	$G$	0
Dynamic viscosity of fluid (water) (Pa.s)	$\mu$	0.00089
Temperature (K)	T	298
Density of primary particle ( $kg.m^{-3}$ )	$\rho_0$	1800
Density of the medium (water) ( $kg.m^{-3}$ )	$\rho_w$	1000
Initial NP concentration ( $mg.L^{-1}$ )	$C_0$	50
Cylinder radius (cm)	$a_{cyl}$	2.5
Cylinder length (cm)	$L_{cyl}$	19.1
Sedimentation depth (cm)	$Z_s$	2.33, 2.5
angular velocity (rph)	$\omega$	4.71
Radius of the primary particles (nm), variable depending on the first non-zero bin of initial PSD	$a_0$	6.75-45
Ionic strength (mM $CaCl_2$ ) (mM)		0.5, 0.75
pH		6.0
Number of size classes, variable depending on broadness of the initial PSD		63-86
Attachment efficiency	$\alpha$	Fitting parameter
Fractal dimension	$D_f$	Fitting parameter

## 6.5 Results and discussion

### 6.5.1 Flow regime and particle trajectory analysis

The experimental results of the cylinder with a drop of dye injected in the beginning of the experiment (Fig. H2) shows that generally within the first ~10-20 min a thin layer of dye forms at the rotating wall. After ~60 min, however, this thin layer is still noticeable, but begins to slowly diffuse into the bulk solution and after ~90-100 min it is barely visible. These results suggest that the rotational regime can be considered as solid-body and the diffusion of dye is the only mechanism of mixing in the cylinder after ~10-20 min. Consistent with these outcomes, the calculations of rotation velocity and shear rate for the cylinder, shown in Fig. H3, demonstrate that within 10 min rotational velocity reaches a steady-state (solid-body rotation) and the shear stress produced in cylinder fluid totally disappears (blue lines). This duration is negligible compared to the total course of experiment > 5 h and is not captured in the sampling

intervals when NP dispersions are used in the cylinder. Both experimental and modelling results confirm the validity of assuming steady-state and zero-shear conditions in the system.

Figure 6.1 shows results of particle trajectory analysis modelled using Eqs. (6.1-6.8) with varying fractal dimension and particle radius for two scenarios: (1) particle is initially placed in the middle of the cylinder radius and (2) particle initially placed near the wall of the cylinder. Based on this analysis, the movement of NP and their aggregates ranging in radius from 20 nm to 100  $\mu\text{m}$  depends significantly on the fractal dimension. For aggregates up to a radius of  $\sim 1 \mu\text{m}$  and for fractal dimension up to 2.5, their trajectories follow the “fixed” solid-body rotation regime as illustrated by Tagawa et al. [78]. However, for aggregate radii in range of 10-100  $\mu\text{m}$  with  $D_f \geq 2.5$ , trajectories start to deviate from this regime and show a tendency towards the so-called “cascading” or “suspending” regimes [78]. Sedimentation velocity is so rapid for aggregates of radius  $>100 \mu\text{m}$  and  $D_f = 2.9$  that they interact with the cylinder wall instead of rotating with the solid body. In agreement with these results, Fig H4 shows that velocity vectors exhibit a nonuniform distribution for aggregates with 10  $\mu\text{m}$  radius and  $D_f = 2.9$ , highlighting the importance of aggregate fractal dimensionality and size in controlling particle trajectories.

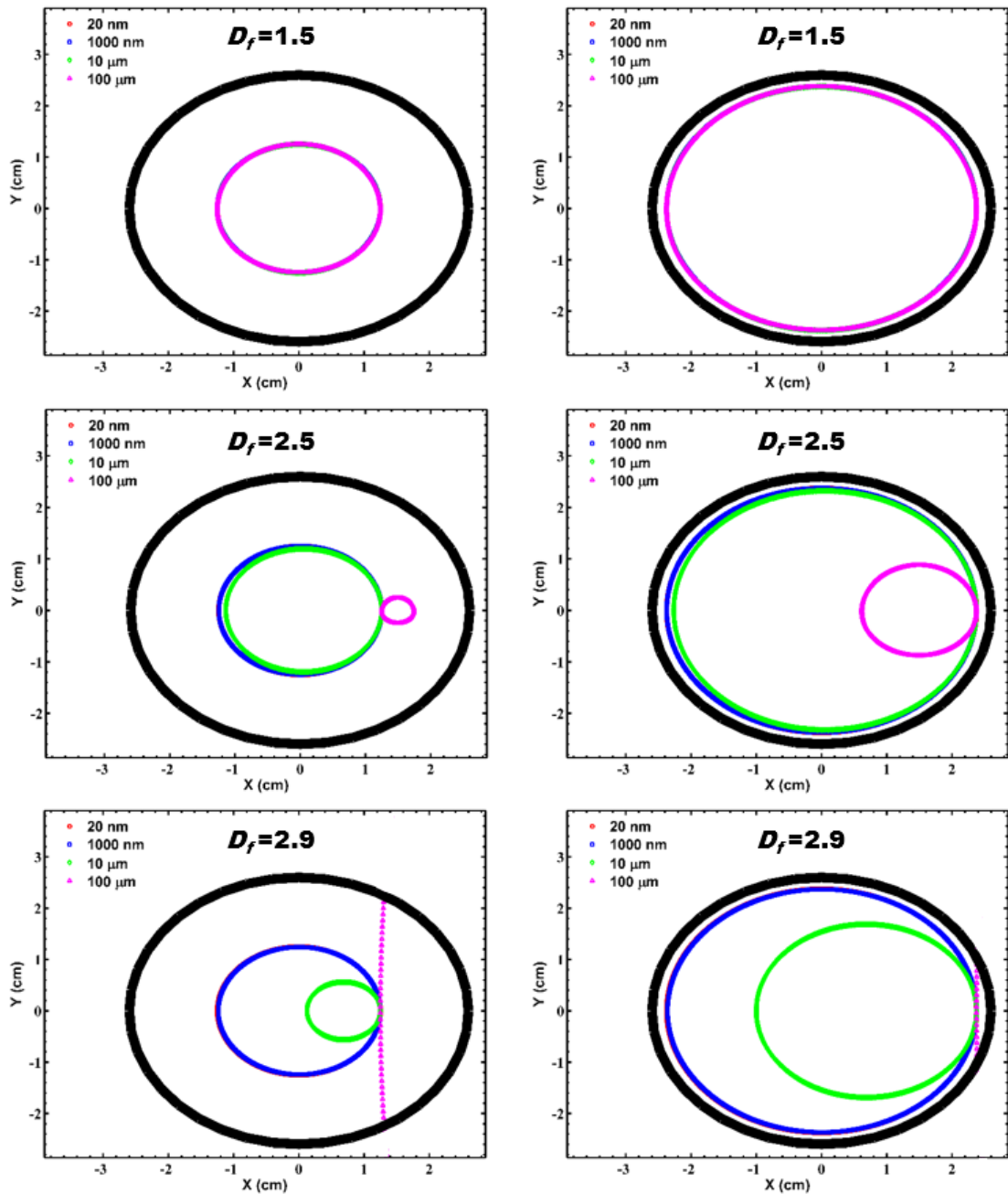


**Figure 6.1** Particle trajectories resulted from Eqs. (6.1-6.8) with virtually varying  $D_f$  and particle radii considering two scenarios: (1) for particle initially placed in the middle of the cylinder radius (left-hand side panels) and (2) particle initially placed near the wall of the cylinder (right-hand side panels). The rotational direction is counter clockwise.

## 6.5.2 Aggregation experiment results

Experiments were undertaken in the cylinder under both rotating and static (non-rotating) conditions, and as a control within a cuvette under static conditions with

continuous monitoring using dynamic light scattering (DLS). Figure 6.2a shows that the averaged hydrodynamic diameter ( $D_H$ ) follows a log-linear trend with time at 0.5 mM  $\text{CaCl}_2$  in all experiments. However, at 0.75 mM  $\text{CaCl}_2$  (Fig. 6.2c) the gradient decreases over time after a rapid initial rise, which is interpreted as a transition from early (fresh, monodisperse particle population) to late (aged, polydisperse particle population) stage conditions within a coupled aggregation/sedimentation system.

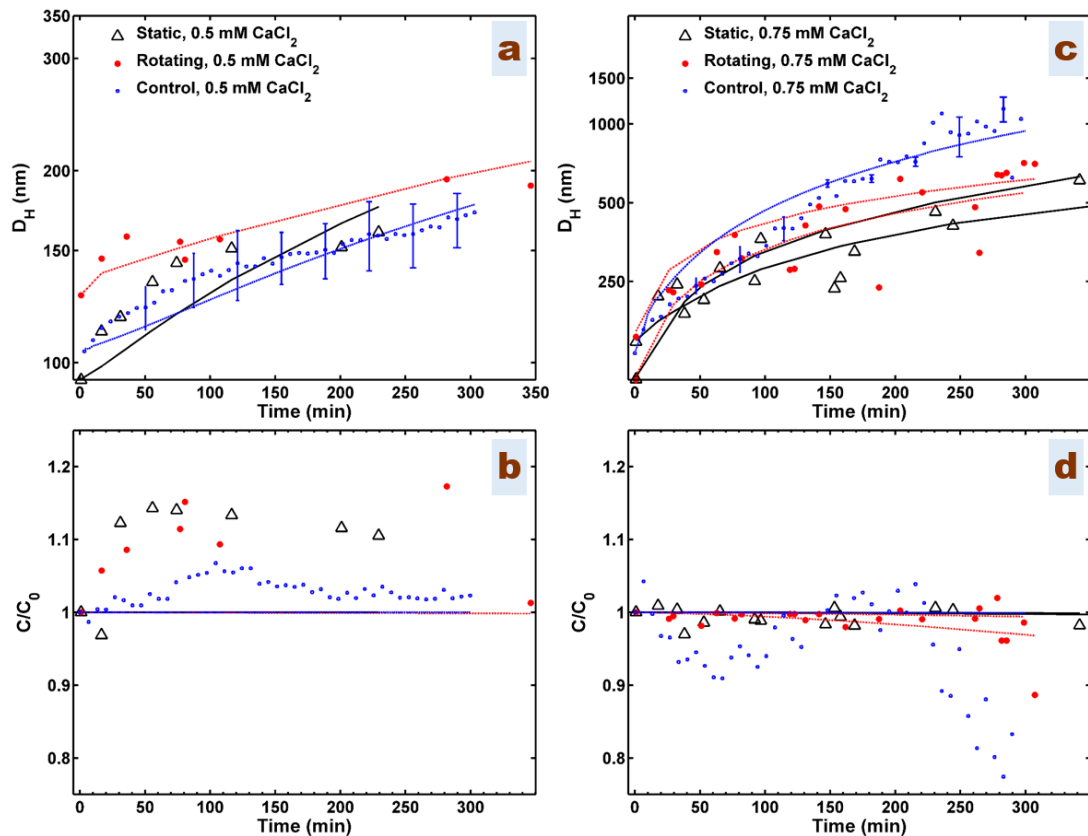


**Figure 6.2** Experimental and modelling results of SGO aggregation/sedimentation under two electrolyte concentrations of 0.5 (a,b) and 0.75 mM  $\text{CaCl}_2$  (c,d) at a fixed pH of 6 within static and rotating cylinders, and the cuvette of the DLS instrument (control measurement). The position of sampling in the cylinder ( $a_{cyl}=2.5$  cm) was at the centre of the cross-section and the control measurement position was at 2.4 cm below water surface. Panels show averaged hydrodynamic size (a,c), and normalized concentration (b,d). The normalized mass concentrations for control cases are obtained from DLS derived count rate data while for other cases these are determined using UV-Vis. The average of the duplicate of control measurements are shown with standard deviation as error bars. The cases of 0.75 mM  $\text{CaCl}_2$  were conducted in duplicate and the experimental data of duplicate experiments are superimposed while each set fitted with the model separately. The model set used includes FP population-balance technique with the power-law model for settling velocity and the Brinkman permeability model for collision frequencies.

Under the solutions present and within the selected periods for size measurement (up to 300-350 min), the sedimentation is not generally significant (Fig. 6.2b,d). The trend of  $D_H$  measurement at 0.5 mM CaCl<sub>2</sub> within the static cylinder closely matches that in the control, demonstrating the validity of the design of sampling in the cylinder experiments. This was also the case at 0.75 mM CaCl<sub>2</sub> but only in the early stages <120 min, as shown in Fig 6.2c after this time  $D_H$  in the control continues to rise, whereas  $D_H$  in the static cylinder tends towards an asymptote over time. The reason for this behaviour is not clear, it could be due to minor differences in the conditions between the two experiments, such as variation in temperature or dimensionality between the cylinder and the cuvette. One might attribute this behaviour to the breakage of aggregates larger than ~500 nm during sampling from the cylinder experiments. However, this is less likely to be a reason for the observed lower growth of aggregates in the static cylinder compared to the control system, because the control experiment shows a level of sedimentation which is not observed for the static case (Fig. 6.2d) whereas sedimentation measurement is not expected to be affected by the breakage. This suggests that in this case there might be a level of uncertainty for the control test rather than the occurrence of breakage in the cylinder samples as also indicated by the larger standard deviations in the control after ~230 min.

Generally, the experimental observations using the rotating cylinder initially show higher aggregation rates than that of the static cylinder (Fig. 6.2a,c). In the case of 0.5 mM CaCl<sub>2</sub>, normalized mass concentration curves show increases in concentration to above the initial uniform concentration at the point of measurement (Fig. 6.2b). Interestingly, these results are consistent for both measurement techniques, i.e., UV-Vis used for the cylinder samples and DLS derived count rate used for the control data, and are also in agreement with previous measurements of DCR for HAp NP aggregation at IS below CCC [40]. Babakhani et al. [40] used the FP model already to validate the use of DCR data as representative of mass concentration during NP aggregation at IS above CCC leading to a decline in mass over time. The present study's results tend to agree with the use of DCR data as representative of mass concentration at IS below CCC as well.

The experimental photos of the rotating cylinder at 0.75 mM CaCl<sub>2</sub> at different times are shown in Fig. H5 and the magnified images of aggregates formed at each time are shown in Fig. 6.3. It appears that visible aggregates form on the wall after

~290 min, corresponding to the start of removal in the sedimentation curve after 250-300 min (Fig. 6.2d). Large networks of gel-like aggregates form at the bottom after ~315 min which as a result of extensive sliding on the wall and consequent collisions, breakage, and reforming, become denser over time until finally they form larger (>1 cm) granular dense aggregates as indicated by their darker colour compared to those formed at earlier times (s. 8.3, H5) [79, 80]. When finally, the sizes of aggregates grow larger and their structure become more compact to induce their higher settling velocity due to their higher bulk density, the settling velocity overcomes the resuspension due to the cylinder rotation. This results in millimetre-sized aggregates appear immediately on the cylinder wall sliding and colliding consequently producing compact centimetre-sized SGO granules appear on the wall of the rotating cylinder in longer time (5-13 h), and the suspension becomes clear of the SGO NP.

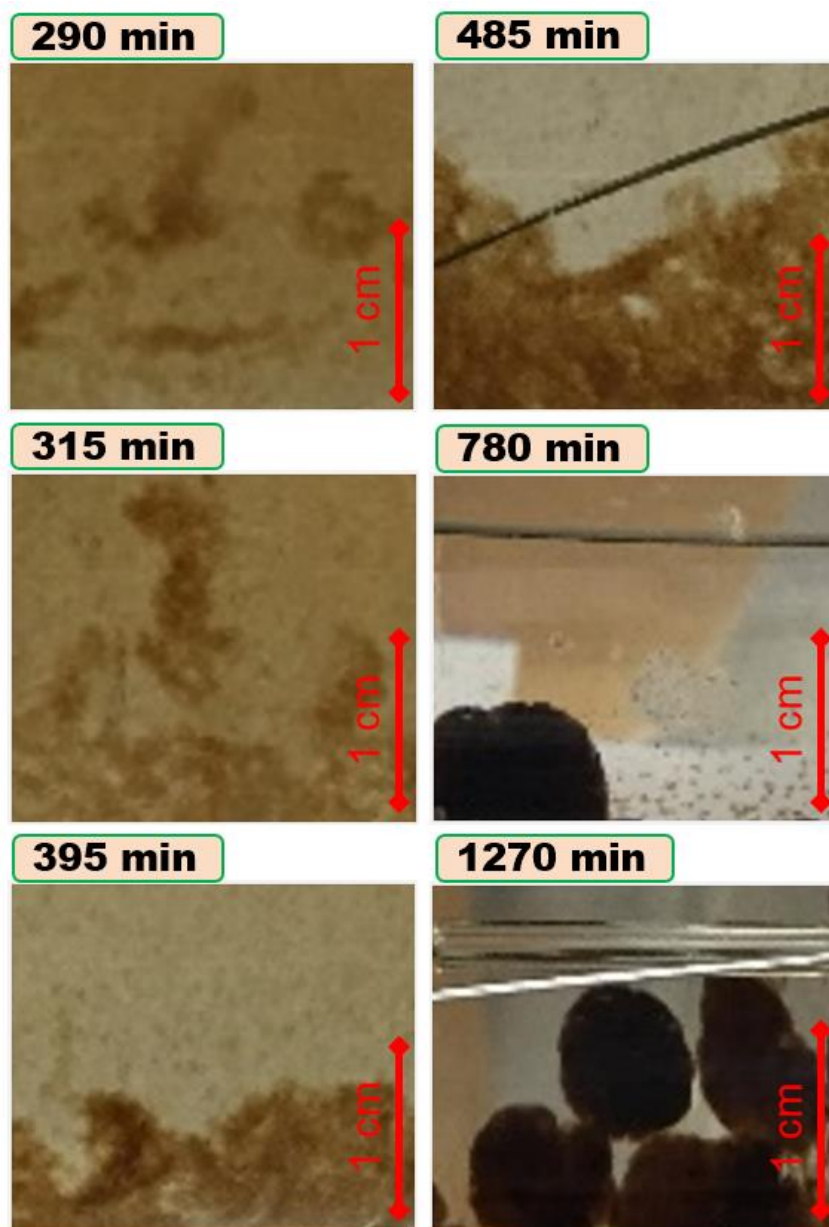


**Figure 6.3** Experimental photos of SGO aggregates formed over longer times for the case of rotating cylinder filled with SGO NP in 0.75 mM CaCl<sub>2</sub> solution and pH 6. The full photographs of cylinder corresponding to each time is available in Fig. H5, Appendix H. The snapshots in this figure were obtained at the same scale from the bottom of the cylinder.

### 6.5.3 Aggregation modelling results

Data from the first 250-350 min of experiments (before the evolution of larger, settling macro-aggregates) were used to fit models of the aggregation in the suspended phase. The estimated parameter values are shown in Fig. 6.4 and are also available in Table

H1 along with Nash-Sutcliffe [15]  $R^2_{NS}$  values used as a goodness-of-fit criterion. The model set used in this study (FP population-balance technique with the power-law model for settling velocity and the Brinkman permeability model for collision frequencies) can fit both  $D_H$  and normalized concentration ( $C/C_0$ ) well with an average  $R^2_{NS}$   $0.758 \pm 0.18$  for  $D_H$  data. Parameter values estimated for the model matched to the control data agree well with those of static cylinder measurements at electrolyte concentrations of 0.5 mM  $\text{CaCl}_2$  and 0.75 mM  $\text{CaCl}_2$  (<29% difference). The rolling cylinder experiment shows 5 and 7 times greater attachment efficiency (Fig. 6.4a) than that of the static system at 0.5 and 0.75 mM  $\text{CaCl}_2$ , respectively. Likewise,  $D_f$  estimated in the rolling cylinder experiment is on average 10% and 31% larger than that of the static cylinder at 0.5 and 0.75 mM  $\text{CaCl}_2$ , respectively (Fig. 6.4b).

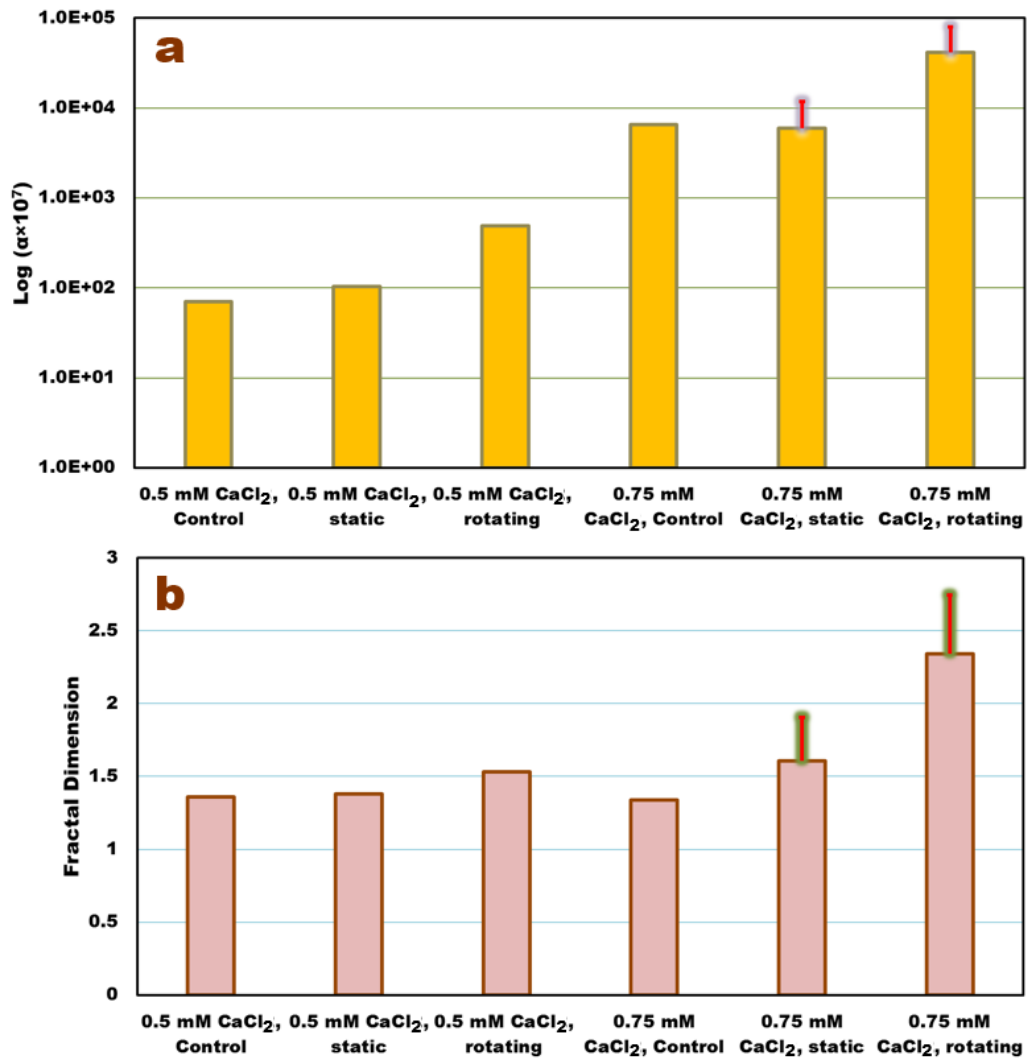


**Figure 6.4** Estimated attachment efficiency (a) and fractal dimension (b) for SGO aggregation/sedimentation experiments under two electrolyte concentrations of 0.5 and 0.75 mM CaCl<sub>2</sub> at fixed pH 6 within control, static, and rotating cylinders. The position of sampling in the cylinder was at the centre of the cross-section ( $a_{cyl}=2.5$  cm) and control measurement position was at 2.4 cm below water surface. In the control, the model was fitted to the average of the duplicated online measurements while in other cases the model was fitted to both duplicate experiment datasets (if available), and the mean and standard deviation of estimated values are reported.

The results clearly indicate that conditions within the rotating cylinder enhance aggregation rate and leads to aggregates with more compact structures (via increasing  $D_f$ ). For higher IS than those of the present research's experimental conditions and longer times than those of the aggregation simulations, the impact of system dynamics may well be higher (Fig. 6.3, H5). Although the process of the aggregation at longer

times (sliding on the wall) is different from that at early stages (aggregation of suspended particles/aggregates), occurrence of both phases is relevant to the natural environment. In GW system, large aggregates attached to porous medium solid surfaces can be translated, rolled over and collide with each other, thereby aggregating in the retained phase [32, 38]. They can also be detached and transported to a new pore where they can interact with new NP or aggregates [32, 38], whether in the suspended phase or in the retained phase. Likewise, in a SW system the aggregates which have already settled onto deeper depths, can be transported with sediments or be resuspended where they could encounter new particles. It should be noted that in both modes, aggregates become more compact, shown either by enhanced  $D_f$  resulted from the model or by change in colour of aggregates to a darker colour observed in the cylinder [79, 80]. The current cylinder condition ignores many aspects of convoluted groundwater pores, such the constricted geometry of pores, shear effect, nonuniform flow regime, and dynamic interactions between suspended particles and solid surfaces [81-84]. Nevertheless, ignoring such aspects may allow a better understanding of the dynamic impacts on the individual aggregation/sedimentation mechanisms. For instance, including shear stress in the system [39, 84, 85] can overshadow the impact of system dynamics due to addition of other complexities such as break-up of aggregates [86]. This cylinder can be further modified in future studies, e.g., by modifying the wall surface roughness or adding short edges/partitions on the inner wall in order to consider more complexities of natural conditions.

The system developed different stages in respect to the interplay between aggregation and sedimentation mechanisms within the rotating cylinder. Up to 250-350 min, where the sliding of aggregates on the wall is still not significant, the maximum  $D_f$  obtained in the present study is 2.34 (at 0.75 mM CaCl<sub>2</sub> within the rotational cylinder) and the maximum aggregate  $D_H$  is below 1  $\mu\text{m}$  (Fig. 6.2a,c). According to the particle tracking analysis results (Figs. 6.1 and H4), for these values of  $D_f$  and  $D_H$ , the effect of gravity on aggregates may not be strong enough to deviate aggregate trajectories from a uniform solid-body regime. In agreement with this, the results from sedimentation over time (Fig. 6.2b) show minor or no removal of NP over the periods up to 250 or 350 min. Hence, within these periods the only difference between the static and rotating systems is seemingly that particle orientations with respect to the gravitational force vector are continuously changing for aggregates in

the rotational system while they remain constant within the static system. This might maintain the local particle concentration within the axial area high at initial stages and therefore enhance the number of collisions resulting from Brownian motion, thereby increasing the overall rate of aggregation. At 0.75 mM CaCl<sub>2</sub>, at times <150 min normalized mass concentration data shows a slight decrease in the suspended mass in both the control and static cylinder experiments which is not noticeable in the case of rotational cylinder (Fig. 6.2d). However, after 250-300 min mass removal in the rotating cylinder becomes increasingly significant as the aggregates become large and dense enough for the gravity force on them to overcome the rotational force leading to their settlement on the cylinder wall. Enhanced aggregation and removal within the rotating cylinder compared to the static cylinder emanates also from differential sedimentation mechanism [87] of aggregation.

In fact, attachment efficiency is generally expected to be a function of NP surface characteristics [88]. However, the present study indicates that system dynamics increase the effective attachment efficiency, even though chemical conditions controlling surface properties were consistent between rotating, static and control experiments. To investigate this behaviour, the collision frequencies were calculated between particles with radii of 50, 500, and 5000 nm and particles with all other size classes up to a radius of 15  $\mu\text{m}$  and for various  $D_f$  (1.5-2.9) as illustrated in Fig. H6. Based on collision frequency formulations used in the present study, representing the state-of-art equations for environmentally-relevant NP [40, 74, 89], the impact of differential sedimentation mechanism of aggregation, which is notably affected by the structure of aggregates ( $D_f$ ), is around 3-5 orders-of-magnitude lower than that of perikinetic aggregation across the range of aggregate sizes, which is impacted less by the structure of aggregates ( $D_f$ ), for the range of aggregate sizes observed in this study in early stages of aggregation. Experimental photos (at 0.75 mM CaCl<sub>2</sub>, Fig. 6.3, H5) suggest that at 290 min aggregates are sufficiently large (>10  $\mu\text{m}$ , based on Fig. 6.1) and/or compact enough ( $D_f > 2.5$ , based on Fig. 6.1) for the trajectories to deviate from solid body rotation and to settle on the wall, suggesting that in this condition sedimentation and therefore differential settling mechanism of aggregation is significant. However, the current collision frequency formulation may not be able to take this effect into account because for a similar range of aggregate size/fractal dimension they predict negligible contribution for differential sedimentation. This

deviation may also arise from restructuring or change in the fractal dimension over the course of the experiment increases its significance in the later stages of aggregation [40, 70, 90]. Taking such a transient change in the fractal dimension, which causes a variation in the particle volume discretization, into account needs special computational consideration. Modelling the whole rotating cylinder domain for aggregation may shed light on the complex interactions of resuspending aggregates and the reasons for the observed differences in the attachment efficiency between the two systems of dynamic and static. Furthermore, additional experimental analysis on the structure of aggregates is needed to verify the estimated fractal dimension values, e.g., using static light scattering (SLS) [90] to monitor the dynamics of the aggregate structure online during the test. The impact of system dynamics can be even more crucial where the existence of natural colloids induces hetero-aggregation with NP [16]. In such systems, the initial diversities in density, size, and interactions of particles may affect both the initial availability of surfaces for Brownian-driven aggregation and differential settling aggregation. These are beyond the scope of current study and may be subject of future studies.

## **6.6 Conclusions**

In the early stage of experiments reported here, whilst the majority of particles remain suspended, maintenance of mass concentration in the axial area of the rotating cylinder increased the number of collisions induced by Brownian motion and arising from differential sedimentation collisions with resuspending larger aggregates. This enhanced the aggregation rate which emerged relating to the attachment efficiency estimated based on model fit to experimental data. As the system evolves and aggregates grow sufficiently to show significant sedimentation, resuspension of settling aggregates in the rotating cylinder increased differential sedimentation, further enhancing the aggregation rate. This consequently leads to an immediate formation of aggregates on the cylinder wall that afterwards start rolling and sliding on the wall. These processes give rise to the formation of more compact aggregates, leading to an increase in fractal dimension in all stages as revealed by greater fractal dimension in the rotating system compared to that of static system and control and indicated by dark colour of aggregate formed on the cylinder wall at the end of experiments.

Numerous studies have reported higher aggregation rates in groundwater, surface-water and other natural environmental systems when compared to quiescent batch experiments [34, 38, 60, 61]. The results from this study demonstrate that this effect can be understood in terms of systems where, even in the absence of hydrodynamic shear, particle suspensions are to some extent prevented from sedimentation. Such effects are simulated here by continuous rotation in a slow-moving cylinder, which models slow flow through tortuous pore networks in natural systems which are characteristic of changing flow directions and mixing of old and new particle populations. It should be noted that considering the importance of hetero-aggregation (aggregation of NP with natural colloids) in the fate of NP in natural waters [16, 91-93], the present study serves as a first stage to investigate hetero-aggregation in more realistic conditions. The system used in this study has also important applications for water treatment, e.g., as a settling unit that can be optimized through adjustment of the fractal dimension and aggregation rate where the adsorption of contaminants to NP is maximised whilst the NP removal due to settling is minimised. Further studies are required to consider a variable fractal dimension in the model for taking reorganization of aggregates into account and to investigate the spatial variations of aggregate sizes in both phases of suspended and settled particles. It also remains for future studies to experimentally verify the model estimated fractal dimension values through direct, online measurements.

## 6.7 References

1. Patil, S.S., et al., *Nanoparticles for environmental clean-up: a review of potential risks and emerging solutions*. Environmental Technology & Innovation, 2016. **5**: p. 10-21.
2. Wang, D., et al., *Investigating and Modeling the Transport of the 'New-Horizon' Reduced Graphene Oxide—Metal Oxide Nanohybrids in Water-Saturated Porous Media*. Environmental science & technology, 2018.
3. Ren, W. and H.-M. Cheng, *The global growth of graphene*. Nature nanotechnology, 2014. **9**(10): p. 726.
4. Park, M.V.D.Z., et al., *Considerations for safe innovation: the case of Graphene*. ACS nano, 2017. **11**(10): p. 9574-9593.
5. Zhao, J., et al., *Graphene in the aquatic environment: adsorption, dispersion, toxicity and transformation*. Environmental science & technology, 2014. **48**(17): p. 9995-10009.
6. Romanchuk, A.Y., et al., *Graphene oxide for effective radionuclide removal*. Physical Chemistry Chemical Physics, 2013. **15**(7): p. 2321-2327.
7. Yu, S., et al., *Sorption of radionuclides from aqueous systems onto graphene oxide-based materials: a review*. Inorganic Chemistry Frontiers, 2015.
8. Ma, X., M.R. Zachariah, and C.D. Zangmeister, *Crumpled nanopaper from graphene oxide*. Nano letters, 2011. **12**(1): p. 486-489.
9. Gudarzi, M.M., *Colloidal stability of graphene oxide: aggregation in two dimensions*. Langmuir, 2016. **32**(20): p. 5058-5068.
10. Spector, M.S., et al., *Conformations of a tethered membrane: Crumpling in graphitic oxide?* Physical review letters, 1994. **73**(21): p. 2867.
11. Kamrani, S., et al., *Transport and retention of carbon dots (CDs) in saturated and unsaturated porous media: Role of ionic strength, pH, and collector grain size*. Water research, 2017.
12. Yang, H.W., et al., *Non-Invasive Synergistic Treatment of Brain Tumors by Targeted Chemotherapeutic Delivery and Amplified Focused Ultrasound-Hyperthermia Using Magnetic Nanographene Oxide*. Advanced materials, 2013. **25**(26): p. 3605-3611.
13. Hua, Z., et al., *Aggregation and resuspension of graphene oxide in simulated natural surface aquatic environments*. Environmental pollution, 2015. **205**: p. 161-169.
14. Wang, H., et al., *Heteroaggregation of engineered nanoparticles and kaolin clays in aqueous environments*. Water research, 2015. **80**: p. 130-138.
15. Babakhani, P., et al., *Parameterization and prediction of nanoparticle transport in porous media: A reanalysis using artificial neural network*. Water Resources Research, 2017. **53**: p. 4564-4585.
16. Hotze, E.M., T. Phenrat, and G.V. Lowry, *Nanoparticle Aggregation: Challenges to Understanding Transport and Reactivity in the Environment*. J. Environ. Qual. , 2010. **39**: p. 1909–1924.
17. Phenrat, T., et al., *Aggregation and sedimentation of aqueous nanoscale zerovalent iron dispersions*. Environmental Science & Technology, 2007. **41**(1): p. 284-290.
18. Sotirelis, N.P. and C.V. Chrysikopoulos, *Heteroaggregation of graphene oxide nanoparticles and kaolinite colloids*. Science of the Total Environment, 2017. **579**: p. 736-744.

19. Kim, H.-J., et al., *Effect of kaolinite, silica fines and pH on transport of polymer-modified zero valent iron nano-particles in heterogeneous porous media*. Journal of Colloid and Interface Science, 2012. **370**(1): p. 1-10.
20. Therezien, M., A. Thill, and M.R. Wiesner, *Importance of heterogeneous aggregation for NP fate in natural and engineered systems*. Science of The Total Environment, 2014. **485**: p. 309-318.
21. Zhao, J., et al., *Heteroaggregation of graphene oxide with minerals in aqueous phase*. Environmental science & technology, 2015. **49**(5): p. 2849-2857.
22. Afshinnia, K., et al., *The concentration-dependent aggregation of Ag NPs induced by cystine*. Science of the Total Environment, 2016. **557**: p. 395-403.
23. Afshinnia, K., et al., *Effect of nanomaterial and media physicochemical properties on Ag NM aggregation kinetics*. Journal of Colloid and Interface Science, 2017. **487**: p. 192-200.
24. Baalousha, M., *Aggregation and disaggregation of iron oxide nanoparticles: Influence of particle concentration, pH and natural organic matter*. Science of The Total Environment, 2009. **407**(6): p. 2093-2101.
25. Baalousha, M., *Effect of nanomaterial and media physicochemical properties on nanomaterial aggregation kinetics*. NanoImpact, 2017. **6**: p. 55-68.
26. Baalousha, M., et al., *Effect of monovalent and divalent cations, anions and fulvic acid on aggregation of citrate-coated silver nanoparticles*. Science of the Total Environment, 2013. **454**: p. 119-131.
27. Shapiro, A.A. and P.G. Bedrikovetsky, *A stochastic theory for deep bed filtration accounting for dispersion and size distributions*. Physica A: Statistical Mechanics and its Applications, 2010. **389**(13): p. 2473-2494.
28. Chrysikopoulos, C.V. and V.E. Katzourakis, *Colloid particle size-dependent dispersivity*. Water Resources Research, 2015.
29. Soltanian, M.R., et al., *Relating reactive solute transport to hierarchical and multiscale sedimentary architecture in a Lagrangian-based transport model: 2. Particle displacement variance*. Water Resources Research, 2015. **51**(3): p. 1601-1618.
30. Soltanian, M.R., et al., *A note on upscaling retardation factor in hierarchical porous media with multimodal reactive mineral facies*. Transport in Porous Media, 2014. **108**(2): p. 355-366.
31. Illangasekare, T.H., C.C. Frippiat, and R. Fućik, *Dispersion and Mass Transfer Coefficients in Groundwater of Near-Surface Geologic Formations*. Handbook of Chemical Mass Transport in the Environment, ed. L.J. Thibodeaux, B. Rouge, and D. Mackay. 2010: CRC Press/Taylor and Francis Group.
32. Bradford, S.A., J. Simunek, and S.L. Walker, *Transport and straining of E. coli O157: H7 in saturated porous media*. Water Resources Research, 2006. **42**(12).
33. Johnson, W.P., X. Li, and S. Assemi, *Deposition and re-entrainment dynamics of microbes and non-biological colloids during non-perturbed transport in porous media in the presence of an energy barrier to deposition*. Advances in Water Resources, 2007. **30**(6): p. 1432-1454.
34. Velzeboer, I., et al., *Rapid settling of nanoparticles due to heteroaggregation with suspended sediment*. Environmental Toxicology and Chemistry, 2014. **33**(8): p. 1766-1773.
35. Markus, A.A., et al., *Modeling aggregation and sedimentation of nanoparticles in the aquatic environment*. Science of The Total Environment, 2015. **506**: p. 323-329.

36. Wang, Y.P., et al., *Sediment resuspension, flocculation, and settling in a macrotidal estuary*. Journal of Geophysical Research: Oceans, 2013. **118**(10): p. 5591-5608.
37. Diercks, A.-R., et al., *Scales of seafloor sediment resuspension in the northern Gulf of Mexico*. Elem Sci Anth, 2018. **6**(1).
38. Babakhani, P., et al., *Continuum-based models and concepts for the transport of nanoparticles in saturated porous media: A state-of-the-science review*. Advances in Colloid and Interface Science, 2017. **246**(Supplement C): p. 75-104.
39. Zahnw, J.C., et al., *Coagulation and fragmentation dynamics of inertial particles*. Physical Review E, 2009. **80**(2): p. 026311.
40. Babakhani, P., R.-a. Doong, and J. Bridge, *Significance of early and late stages of coupled aggregation and sedimentation in the fate of nanoparticles: measurement and modelling*. Environmental science & technology, 2018. doi: **10.1021/acs.est.7b05236**.
41. Babakhani, P., et al., *Modified MODFLOW-based model for simulating the agglomeration and transport of polymer-modified Fe nanoparticles in saturated porous media*. Environ Sci Pollut Res, 1-20, doi:10.1007/s11356-015-5193-0, 2015.
42. Bradford, S.A., S. Torkzaban, and J. Simunek, *Modeling colloid transport and retention in saturated porous media under unfavorable attachment conditions*. Water Resources Research, 2011. **47**(10).
43. Phenrat, T., et al., *Transport and deposition of polymer-modified FeO nanoparticles in 2-D heterogeneous porous media: Effects of particle concentration, FeO content, and coatings*. Environmental Science & Technology, 2010. **44**(23): p. 9086-9093.
44. Torkzaban, S., S.A. Bradford, and S.L. Walker, *Resolving the Coupled Effects of Hydrodynamics and DLVO Forces on Colloid Attachment in Porous Media*. Langmuir, 2007. **23**(19): p. 9652-9660.
45. Roth, E.J., B. Gilbert, and D.C. Mays, *Colloid deposit morphology and clogging in porous media: Fundamental insights through investigation of deposit fractal dimension*. Environmental science & technology, 2015. **49**(20): p. 12263-12270.
46. Lowry, G.V., et al., *Long-term transformation and fate of manufactured Ag nanoparticles in a simulated large scale freshwater emergent wetland*. Environmental science & technology, 2012. **46**(13): p. 7027-7036.
47. Logan, B.E. and J.R. Kilps, *Fractal dimensions of aggregates formed in different fluid mechanical environments*. Water Research, 1995. **29**(2): p. 443-453.
48. Jackson, G.A., *Particle trajectories in a rotating cylinder: implications for aggregation incubations*. Deep Sea Research Part I: Oceanographic Research Papers, 1994. **41**(3): p. 429-437.
49. Jackson, G.A., *Coagulation in a rotating cylinder*. Limnology and Oceanography: Methods, 2015. **13**(4): p. 194-201.
50. Grossart, H.P., M. Simon, and B.E. Logan, *Formation of macroscopic organic aggregates (lake snow) in a large lake: The significance of transparent exopolymer particles, plankton, and zooplankton*. Limnology and Oceanography, 1997. **42**(8): p. 1651-1659.
51. Prairie, J.C., et al., *Delayed settling of marine snow at sharp density transitions driven by fluid entrainment and diffusion-limited retention*. Marine Ecology Progress Series, 2013. **487**: p. 185-200.
52. Ionescu, D., et al., *A new tool for long-term studies of POM-bacteria interactions: overcoming the century-old Bottle Effect*. Scientific reports, 2015. **5**.

53. Passow, U. and C.L. De La Rocha, *Accumulation of mineral ballast on organic aggregates*. *Global Biogeochemical Cycles*, 2006. **20**(1).
54. Crocker, K.M. and U. Passow, *Differential aggregation of diatoms*. *Marine ecology progress series*. Oldendorf, 1995. **117**(1): p. 249-257.
55. Ziervogel, K. and S. Forster, *Aggregation and sinking behaviour of resuspended fluffy layer material*. *Continental shelf research*, 2005. **25**(15): p. 1853-1863.
56. Fuchs, H.L., et al., *Directional flow sensing by passively stable larvae*. *Journal of Experimental Biology*, 2015. **218**(17): p. 2782-2792.
57. Long, M., et al., *Interactions between microplastics and phytoplankton aggregates: Impact on their respective fates*. *Marine Chemistry*, 2015. **175**: p. 39-46.
58. Sheng, Y.P. and W. Lick, *The transport and resuspension of sediments in a shallow lake*. *Journal of Geophysical Research: Oceans*, 1979. **84**(C4): p. 1809-1826.
59. Bear, J., *Dynamics of fluids in porous media*. 1972, New York.: American Elsevier.
60. Jones, S.E., et al., *Aggregation and resuspension of suspended particulate matter at a seasonally stratified site in the southern North Sea: physical and biological controls*. *Continental Shelf Research*, 1998. **18**(11): p. 1283-1309.
61. Cross, J., et al., *Biological controls on resuspension and the relationship between particle size and the Kolmogorov length scale in a shallow coastal sea*. *Marine Geology*, 2013. **343**: p. 29-38.
62. de Klein, J.J.M., et al., *Towards validation of the NanoDUFLOW nanoparticle fate model for the river Dommel, The Netherlands*. *Environmental Science: Nano*, 2016. **3**(2): p. 434-441.
63. Wallace, S.J., et al., *Drug release from nanomedicines: selection of appropriate encapsulation and release methodology*. *Drug delivery and translational research*, 2012. **2**(4): p. 284-292.
64. Missana, T., et al., *Analysis of colloids erosion from the bentonite barrier of a high level radioactive waste repository and implications in safety assessment*. *Physics and Chemistry of the Earth, Parts A/B/C*, 2011. **36**(17): p. 1607-1615.
65. Holmboe, M., et al., *Effects of  $\gamma$ -irradiation on the stability of colloidal Na<sup>+</sup>-Montmorillonite dispersions*. *Applied Clay Science*, 2009. **43**(1): p. 86-90.
66. Sahu, R.S., K. Bindumadhavan, and R.-a. Doong, *Boron-doped reduced graphene oxide-based bimetallic Ni/Fe nanohybrids for the rapid dechlorination of trichloroethylene*. *Environmental Science: Nano*, 2017.
67. Blyth, M., *Fluid Mechanics*. Personal Communication 2015. <https://archive.uea.ac.uk/~h007/notes/index.html>.
68. Li, D.H. and J. Ganczarzyk, *Fractal geometry of particle aggregates generated in water and wastewater treatment processes*. *Environmental Science & Technology*, 1989. **23**(11): p. 1385-1389.
69. Dolgonosov, B.M., *Kinetics of sedimentation of a coagulating suspension*. *Theoretical Foundations of Chemical Engineering*, 2005. **39**(6): p. 635-642.
70. Allain, C., M. Cloitre, and F. Parisse, *Settling by cluster deposition in aggregating colloidal suspensions*. *Journal of colloid and interface science*, 1996. **178**(2): p. 411-416.
71. Sterling, M.C., et al., *Application of fractal flocculation and vertical transport model to aquatic sol-sediment systems*. *Water research*, 2005. **39**(9): p. 1818-1830.

72. Kumar, S. and D. Ramkrishna, *On the solution of population balance equations by discretization—I. A fixed pivot technique*. Chemical Engineering Science, 1996. **51**(8): p. 1311-1332.
73. Nopens, I., D. Beheydt, and P.A. Vanrolleghem, *Comparison and pitfalls of different discretised solution methods for population balance models: a simulation study*. Computers & chemical engineering, 2005. **29**(2): p. 367-377.
74. Dale, A.L., G.V. Lowry, and E.A. Casman, *Accurate and fast numerical algorithms for tracking particle size distributions during nanoparticle aggregation and dissolution*. Environmental Science: Nano, 2017. **4**(1): p. 89-104.
75. Thill, A., et al., *Flocs restructuring during aggregation: experimental evidence and numerical simulation*. Journal of Colloid and Interface Science, 2001. **243**(1): p. 171-182.
76. Veerapaneni, S. and M.R. Wiesner, *Hydrodynamics of fractal aggregates with radially varying permeability*. Journal of Colloid and Interface Science, 1996. **177**(1): p. 45-57.
77. Li, X.-Y. and B.E. Logan, *Permeability of fractal aggregates*. Water research, 2001. **35**(14): p. 3373-3380.
78. Tagawa, Y., et al., *Wall forces on a sphere in a rotating liquid-filled cylinder*. Physics of Fluids, 2013. **25**(6): p. 063302.
79. Chakraborti, R.K., et al., *Changes in fractal dimension during aggregation*. Water Research, 2003. **37**(4): p. 873-883.
80. Bushell, G.C., et al., *On techniques for the measurement of the mass fractal dimension of aggregates*. Advances in Colloid and Interface Science, 2002. **95**(1): p. 1-50.
81. Abdel-Salam, A. and C.V. Chrysikopoulos, *Modeling of colloid and colloid-facilitated contaminant transport in a two-dimensional fracture with spatially variable aperture*. Transport in porous media, 1995. **20**(3): p. 197-221.
82. James, S.C. and C.V. Chrysikopoulos, *Effective velocity and effective dispersion coefficient for finite-sized particles flowing in a uniform fracture*. Journal of colloid and interface science, 2003. **263**(1): p. 288-295.
83. Pham, N.H. and D.V. Papavassiliou, *Hydrodynamic effects on the aggregation of nanoparticles in porous media*. International Journal of Heat and Mass Transfer, 2018. **121**: p. 477-487.
84. Phenrat, T., et al., *Particle size distribution, concentration, and magnetic attraction affect transport of polymer-modified Fe0 nanoparticles in sand columns*. Environ. Sci. Technol., 2009. **43**(13): p. 5079-5085.
85. Elimelech, M., J. Gregory, and X. Jia, *Particle deposition and aggregation: measurement, modelling and simulation*. 1998: Butterworth-Heinemann.
86. Higashitani, K., K. Iimura, and H. Sanda, *Simulation of deformation and breakup of large aggregates in flows of viscous fluids*. Chemical Engineering Science, 2001. **56**(9): p. 2927-2938.
87. Risovic, D. and M. Martinis, *The role of coagulation and sedimentation mechanisms in the two-component model of sea-particle size distribution*. Fizika, 1994. **3**(2): p. 103-118.
88. Phenrat, T., et al., *Empirical correlations to estimate agglomerate size and deposition during injection of a polyelectrolyte-modified Fe0 nanoparticle at high particle concentration in saturated sand*. Journal of Contaminant Hydrology, 2010. **118**(3-4): p. 152-164.

89. Jeldres, R.I., F. Concha, and P.G. Toledo, *Population balance modelling of particle flocculation with attention to aggregate restructuring and permeability*. *Advances in colloid and interface science*, 2015. **224**: p. 62-71.
90. Meng, Z., S.M. Hashmi, and M. Elimelech, *Aggregation rate and fractal dimension of fullerene nanoparticles via simultaneous multiangle static and dynamic light scattering measurement*. *Journal of colloid and interface science*, 2013. **392**: p. 27-33.
91. Praetorius, A., et al., *Heteroaggregation of titanium dioxide nanoparticles with model natural colloids under environmentally relevant conditions*. *Environmental science & technology*, 2014. **48**(18): p. 10690-10698.
92. Quik, J.T.K., et al., *Heteroaggregation and sedimentation rates for nanomaterials in natural waters*. *Water research*, 2014. **48**: p. 269-279.
93. Praetorius, A., et al., *Facing complexity through informed simplifications: a research agenda for aquatic exposure assessment of nanoparticles*. *Environmental Science: Processes & Impacts*, 2013. **15**(1): p. 161-168.

# Chapter 7

## 7 Conclusions

### 7.1 Key conclusions

Continuum models can successfully describe a variety of nanoparticles (NP) transport phenomena and their concomitant effects and are able to work at various scales ranging from column experiments to aquifer and watershed. Its importance among other modelling approaches therefore lies in part in its ability to link with other modelling techniques to bridge the gaps across temporal and spatial scales and to be used as means of validation for those models.

This research has highlighted a number of challenges, hindering the efficient application of such models. These can be broken down into six main areas: (i) diversity in basis; (ii) assumptions made; (iii) ability to predict; (iv) transport mechanisms included; (v) the efficiency of models; and finally (vi) not considering other possible important factors imposed by natural environmental conditions such as system dynamics. In this thesis, these challenges are addressed to present continuum models as a platform to find insight into the fate and transport of nanoparticles in the environment. The key conclusions are as follows:

- Through an extensive literature review it was concluded that hyper-exponential residual concentration profiles (RCP) is a sign of straining; ascending-plateau breakthrough curve (BTC) indicate blocking; descending-plateau BTC implies ripening, early-BTC is consistent with size exclusion, and non-monotonic RCP results from agglomeration of NP.
- Depending on the scale of the problem, equilibrium sorption may be applicable for NP transport as it turned out to be more efficient than kinetic model in terms of the number of fit parameters and goodness-of-fit criteria when the scale of the model and the level of complicity were augmented.
- In addressing the main challenges of the use of continuum models, i.e., forward modelling, nonlinear empirical correlations resulted from artificial neural network

(ANN) can be useful for estimation of continuum model parameters as well as  $C/C_0$ .

- ANN combined with Monte Carlo and a sensitivity analysis technique provided many interesting insights into the NP transport. For instance,  $K_{att}$  was more sensitive to the surface-related factors, than flow-regime-related factors whereas  $K_{det}$  was more sensitive to the flow-regime-related factors. A simplifying unified parameter considered for the heterogeneity in porous media turned out to be more sensitive than the dispersivity parameter.
- In finding appropriate population-balance models for early and late stages of NP aggregation/sedimentation in aquatic environments, it was revealed that the empirical, density-controlled descriptions for settling velocity were able to better describe NP aggregation and sedimentation than permeability-based models. Allowing the attachment efficiency to vary with aggregate size did not significantly alter model outcomes compared to the assumption of constant attachment efficiency, but fitted parameters were much more sensitive to the specification of the initial particle size distribution (PSD). Fitting to only early-stage data showed trends in attachment efficiency and fractal dimension consistent with classical theory, whereas these trends varied as the systems evolved to late stage. Lower removal rates were observed within high-IS than intermediate IS solutions as NP clusters were optimally more efficient at collecting (by aggregation) and removing (by sedimentation) large numbers of smaller particles and aggregates at intermediate IS than that at higher IS.
- The best model set for aggregation and sedimentation, i.e., FP with the power-law sedimentation velocity model and Brinkman-permeability collision frequency model, was combined with a 3-D continuum modelling code to accurately simulate concurrent aggregation and transport of NP within 3-D porous media. Incorporating the aggregation process into the model improved the predictivity of the current theoretical and empirical approaches for NP deposition. The model runtime for 3-D simulations was 66.5 h on 3.50-GHz CPU, hindering the simulation for larger domains and preventing inverse modelling
- A new modelling framework based on a mass-balance parent-daughter chain reaction formulation was proposed for more efficient modelling of aggregation. In fitting to analytical solutions CRM turned out promising with  $R^2_{NS} > 0.804$ . Fitting

to early and late aggregation and sedimentation of SGO, the performances of CRM was generally similar to or better than that of the FP method, and the new model was averagely one order-of-magnitude faster than the FP.

- Finally, a solid-body rotational system used to investigate the impact of environmental system dynamics on aggregation mechanisms showed that in the early stage of experiments, whilst most particles remained suspended, maintenance of mass concentration in the axial area of the rotating cylinder increased the number of collisions induced by Brownian motion and arising from differential sedimentation collisions with resuspending larger aggregates. This enhanced the aggregation and sedimentation rates, with subsequent increase in differential-sedimentation aggregation, further enhancing the aggregation rate. This led to an immediate formation of large and compact aggregates on the cylinder wall. Thus, higher aggregation rates observed in groundwater, surface-water and other natural environmental systems compared to quiescent batch experiments can be because of environmental dynamics which need to be considered in models
- Overall, in this thesis although multiple challenges in using continuum models were addressed, incorporating aggregation, which is one of the most important mechanisms in determining the final fate of NP in the environment, remains an issue due to the dynamics of porous media. Even with this, continuum models are currently pioneering among various modelling approaches for simulating the fate and transport of NP in subsurface environments.

## **7.2 Recommendations for future studies**

- Three-dimensional field-scale NP transport experiments should be conducted to obtain sufficient data to enable developing empirical correlations at environmentally-relevant scales for forward modelling of NP transport, such as those developed in this research at one-dimensional scale using ANN. This can also aid validating the conceptual ground of continuum models for NP transport in realistic conditions.
- The generalization and robustness of ANN predictions may still need improvement. It should be noted that a better generalization might not necessarily be achieved using more complex machine learning approaches.

- Further work is required to establish the heterogeneity as a parameter to be considered in modelling environmentally-relevant problems.
- Monitoring the dynamics of the aggregate structures at early and late stages processes using online techniques may lead to better understanding about the reality of restructuring during different stages of aggregation and sedimentation.
- Further work is needed to improve the basic assumptions of chain-reaction model, to validate it against other environmental conditions, to improve its description of the PSD, and to combine this model with NP fate and transport models.
- The use of solid-body rotator in the present research serves as a first step to investigate hetero-aggregation in future studies in realistic conditions.

In conclusion, while steps must be taken to enhance continuum model accuracy in description and prediction of NP fate and transport, the upscaling ability of models should be assessed simultaneously in order for continuum models to serve as the most accurate and efficient modelling platform with potential interactions with other modelling approaches and compatibility with relevant field and experimental data, to produce reliably informative outputs useful for decision making, regulatory demands, NP fate management, remediation strategy design etc. The work presented here is a comprehensive exploration of parameter sensitivities, model formulations and efficient computational approaches for the development of continuum models of NP fate and transport in the environment. It, therefore, represents a major step towards that goal.

# Appendix A

## 8 Other NP transport phenomena

### 8.1 Straining

#### 8.1.1 Mechanism

In addition to the filtration mechanisms which are driven by the interfacial forces between particles and the porous media surfaces, retention of particles in porous media can be driven by physical straining [1, 2]. Since straining has been identified recently as a key process of retention in the transport of NP in porous media [e.g., 3, 4-18], in this section this phenomenon is reviewed from the very fundamental concepts.

Straining is defined as the process of physical trapping of particles in the pore throats which are narrower than the size of particles. In the case of high concentration of particles, straining is deemed to occur as a result of concurrent arrival of many particles at a pore opening. This can result in “jamming” and “arching”, and eventually lead to “clogging” of the filtration surface [19, 20]. In engineered filtration systems such physical straining results in a continuous compressible cake [21, 22] or a mat with holes on it [22]. But although observed in experimental micromodel by the aid of pore visualization [23] this is not considered common in natural aquifers unless it is encountered at the upper area of porous media [24, 25] or in the case of injecting engineered NP into subsurface media, in the near vicinity of the injection well [e.g., 26, 27-29]. Occasionally straining has been further subdivided into two mechanisms of wedging and bridging. Wedging is the trapping of particles at two bounding surfaces without interference of particles while bridging is the simultaneous arriving and accumulation of particles at the pore constriction [30-32].

#### 8.1.2 Criteria and manifestation

In reality, even for ideal spherical and uniform grains and NP, the pores are not ideal flow channels for the transport of NP because of the existence of narrow spaces at the contact angle of the spheres. These angular spaces bring about a potential of straining

for different sizes of NP. Herzig et al. [33] illustrated different retention sites for straining as (Fig. A1): (1) surface sites; (2) crevice sites; (3) constriction sites; and (4) cavern sites. This initiated the development and the use of a criterion for straining model selection by the ratio of particle diameter to grain diameter ( $dp/dg$ ) [2, 34, 35]. This critical ratio for straining as obtained from experimental results simultaneously under the influence of physicochemical filtration and straining retention was found to be 0.0017 [1, 36-39]. The idea of a critical straining threshold is important in developing the conceptual model of NP transport in regards to straining, since many papers have attributed [3-18, 40, 41] or rejected [42-45] the influence of straining based on this criteria.

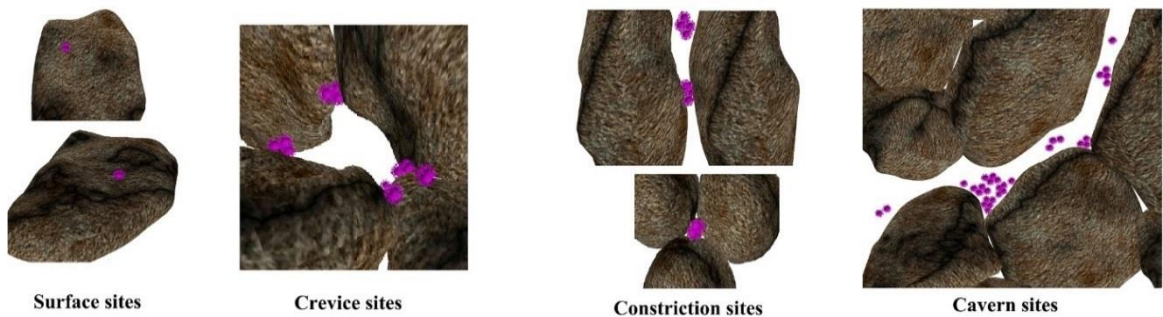


**Figure A1** Possible retention sites for straining from [33].

Physical straining has been recognized to contribute: (1) to the removal of  $\text{CeO}_2$  NP, (with  $dp/dg$  of 0.0002) ascribed to the angular shape of the porous media grains (industrial mineral silica) [3]; (2) to the removal of Ag NP following aggregation (with initial  $dp/dg = 3 \times 10^{-5}$ ) [4], or heteroaggregation (with initial  $dp/dg$  ranging from 0.0001 to 0.0004) [5], or due to the existence of a portion of pores smaller than the particle size (with overall  $dp/dg = 3 \times 10^{-4}$ ) [6]; (3) to removal of GO at high IS due to concurrent agglomeration in porous media with initial  $dp/dg$  in range of 0.003-0.009 [7, 8], or with initial  $dp/dg$  in range of 0.001-0.002 [40], or elevated  $dp/dg$  of 0.005 [9], and/or ascribed to increased surface roughness because of the biofilm-coated sand with initial  $dp/dg$  of 0.0005-0.0007 [41]; (4) to removal of  $\text{TiO}_2$  NP because of straining caused by aggregation during flow in porous media (initial  $dp/dg$  ranging from 0.001 to 0.010) [10] or due to presence of initial aggregates since suspended aggregates are more prone to encountering smaller pore throat (initial  $dp/dg =$

0.0005) [11], or because of the smaller pores resulted from the clay content in the soil (initial  $dp/dg$  in range of 0.0003 to 0.001) [12]; (5) to removal of ZnO NP at the high IS (50 mM NaNO<sub>3</sub>) due to heteroaggregation with soil particles, due to the presence of surface charge heterogeneities (resulting in subsequent clogging of the pores) (initial  $dp/dg$  in range of 0.001 to 0.009) [13], or due to the concurrent aggregation [14-16] with initial  $dp/dg$  in range of 0.0006 to 0.0012. Straining has also been recognized to contribute to the removal of HAP NP and goethite particles when co-transported and heteroaggregated, with maximum  $dp/dg$  of 0.0046 [17] or for HAP NP and hematite particles with maximum  $dp/dg$  of 0.0027 [18] being larger than the literature threshold value (0.002). These figures show that the criteria of 0.0017 cannot be valid for NP mainly due to the interference of other mechanisms.

In addition to this criterion, another sign for identifying the straining is the shape of the retained particle mass profile as function of distance from inlet (RCP). As such, a number of authors [45-53] attributed the retention behaviour to straining whenever they observed a hyper-exponential profile for the RCP; that is a marked decreasing rate of deposition with distance from inlet according to an inverse power law. This is in spite of the fact that hyper-exponential behaviour of the RCP can also be attributed to other factors and mechanisms such as surface roughness [1, 39, 54, 55], concurrent aggregation [56-59], particle population heterogeneity [60, 61], variations in the pore-scale velocity [62-64], and chemical heterogeneity [37, 65, 66]. Nevertheless, monotonic and/or non-monotonic RCPs can be observed when the straining is considered the dominant mechanism of retention [2, 48, 67, 68]. Non-monotonic RCP demonstrates a peak of concentration somewhere between the inlet and the outlet of the porous media domain [48]. Therefore, hyper-exponential behaviour of RCP may not be a deterministic sign of the straining phenomenon.

Despite extensive allusions to the reflection of transport and deposition mechanisms in the RCP shape among literature studies [e.g., 45, 46, 47-52], there have been fewer attempts to evaluate the slope of the BTC plateau in regard to the underlying mechanisms of transport. In this study, the information about various BTC plateau shapes including flat, ascending, and descending in both forms of limited duration of particle injection and continuous injection (experiments without post-flush of particle-free dispersion) were collected in Table B1. Straining has been reported along with a flat shaped plateau of BTC for AgNP following aggregation [4], GO at

intermediate IS [40], and ZnO in presence of biofilm or NOM [14, 16] and with an ascending-shaped plateau of BTC for HAP NP [69], GO at high IS [40], and ZnO [14, 15]. More frequently, however, straining has evidently come with an ascending-BTC plateau, e.g., for AgNP [70, 71]. NZVI [72], GO [7-9, 41], CeO<sub>2</sub> [3], TiO<sub>2</sub> [10], and ZnO [13]. This suggests that potential sites for straining mostly have a limited capacity. Once this capacity is met, a decrease in the retention rate results, that appears as an ascending-BTC plateau. Hence, straining is a phenomenon that should commonly occur along with other transport mechanisms, such as blocking.

### 8.1.3 Modelling approaches of straining

Generally, straining has been described either with a depth-dependent decaying exponential function [39] or with a concentration-dependent decaying exponential function [2, 35, 68] in the continuum-based modelling framework. The former includes one empirical parameter,  $\beta$ , standing for the shape of the particle spatial distribution and one extra variable of  $x$  standing for the distance from the inlet. This function, given below, is in fact able to predict the depth dependent RCP [39]:

$$\Psi_x = \left(\frac{d_c+x}{d_c}\right)^{-\beta} \quad (\text{A1})$$

where  $d_c$  is size of grains (collector) representing the pore length which is oftentimes considered as  $d_{50}$ , the median size of the porous media grains. The implementation of this function in the advection-dispersion model is its multiplication in the term for attachment (in  $K_{att}$ ) as given in model types (viii), (xi), (xii), (xiii), (xiv), and (xv) in Table 1.1. When  $\beta$  is equal to zero ( $\psi_x = 1$ ), the decrease of retained concentration with distance is exponential which is the case for clean bed filtration theory [46].

On the other hand, the concentration-dependent decaying exponential expression includes two parameters, a rate coefficient parameter,  $k_0$ , standing for straining kinetic rate coefficient [ $T^{-1}$ ] and the coefficient for the exponential decline in straining rates,  $\lambda$ , with the same unit as retained concentration variable,  $S$ , [ $NM^{-1}$  or  $MM^{-1}$ ] [2]:

$$\frac{\rho_b}{\varepsilon} \frac{\partial S}{\partial t} = k_0 C e^{-S/\lambda} \quad (\text{A2})$$

This equation is solved with the advection-dispersion equation. When  $S \approx 0$ , the equation becomes the same as that for clean bed colloid filtration theory.

The depth-dependent expression of Bradford et al. [39] has become more popular for simulation of colloid and NP straining to the extent that most of the recent literature studies on NP transport have utilized this expression to fit the BTC/ RCP of NP transport through column experiments, e.g., for hydroxyapatite NP [17, 18, 51, 69, 73-75] and silver NP [64, 74]. This expression only uses one parameter ( $\beta$ ) which can be estimated based on the observed shape of the RCP. In some studies a fixed value of 0.432 [7-10, 39, 40, 45, 46, 51, 64, 69, 73-76] or 1.532 [e.g., 77] has been used. In most studies, however, this parameter has been considered as a free parameter to be estimated in the inverse modelling and the values obtained are highly variable: 0.302 and 1.234 for Ag NP [78], 0.609 for CMC-NZVI [72], in range of 0.02 to 0.33 for ZnO NP [13], ranges of 0.659–2.28 and 0.764–1.69 in co-transport of HAP NP and hematite particles, respectively [18], or ranges of 0.432–1.85 and 0.432–1.57 in co-transport of HAP NP and goethite particles, respectively [17].

The depth-dependent model of Bradford et al. [39] considers a decaying attachment rate with distance which is favourable for capturing the hyper-exponential behaviour of RCP, frequently witnessed in the transport of colloid and NP subjected to concurrent physicochemical filtration and straining. On the other hand, in studies which have used the concentration-dependent model, the effect of physicochemical filtration had been turned off, by thoroughly cleaning of the sand and the use of deionized water (DI) as the dispersant solution, in order to maximize electrostatic repulsion between particles and sand surface thereby to expect the mere influence of straining unambiguously [2, 35, 67, 68, 79]. This brought about nearly a monotonic shaped RCP in those studies. It is still not clear whether this model can fit the BTCs and RCPs for the conditions where concurrent influences of physicochemical filtration and straining exist. It should be noted that the straining model of Bradford et al. has been criticized for not having enough power to describe the real straining phenomenon [80]. In other words, whenever the depth-dependent model has been fitted to the experimental data with hyper-exponential RCP, it is obscured, recalling the ambiguities of the relevancy of straining to the RCP behaviour, whether in reality the model describes the straining phenomena or it just captures the depth-dependent behaviour [80]. One key drawback of the depth-dependent model of Bradford et al. is that it is still unknown how the variable of depth or length should be treated when it comes to application of the model in two- and three-dimensional simulations [81].

Although recently Köber et al. [27] employed this model for field-scale simulations, the treatment of the variable,  $x$ , was not clarified by these authors. In addition to this difficulty in upscaling the depth-dependent model of Bradford et al., it is also unclear whether this model can be valid in the real condition of flow in larger scales where the effect of preferential flow paths is considerable [23, 82-85]. To date, relatively very few studies have discussed the occurrence of straining, clogging or pore plugging in the porous medium during NP transport in multi-dimensional domains [27, 28, 86, 87], some of which even tried to rule out these phenomena. Therefore, there is a crucial need to develop more rigorous conceptual models that can consider the concurrent effect of various phenomena occurring with straining of NP during transport in porous media. This may help providing insight into the role of each underlying mechanism. The problem becomes even more convoluted when other phenomena such as blocking/ripening and size exclusion are also involved as addressed in the next sections.

## 8.2 Site-blocking and ripening

### 8.2.1 Site-blocking mechanism and related modelling approaches

The surface of porous materials may have a limited capacity for the adsorption/attachment of solute/particles and once this capacity is filled, the adsorption/attachment of further solute/particles is hindered by the presence of previously sorbed/attached materials. The most well-known approach for modelling this quality, which is called site-blocking effect, is to use the Langmuir approach for solute/gas [88] and for particle [89] adsorption onto solid surfaces. This is used to model the site-blocking effect of colloidal particle attachment during transport in porous media via the following relationship [90]:

$$\psi_b = \left(1 - \frac{S}{S_m}\right) \quad (\text{A3})$$

where  $\psi_b$  is the Langmuirian blocking function related to the fraction of porous medium available for deposition [—] and  $S_m$  is the maximum retained-particle phase concentration, i.e., particle retention capacity [ $\text{NM}^{-1}$  or  $\text{MM}^{-1}$ ]. When used in the advection-dispersion model, this expression will result in a second-order particle deposition kinetics limited by aqueous phase as well as the solid phase concentrations

[90, 91]. The BTC produced by this model does not maintain a plateau but instead gradually climbs toward the peak (ascending plateau). This gradual rising plateau is a sign of decline in the deposition rate with increasing the amount of attached phase particles, i.e., the blocking effect [90]. Accordingly, many papers by observing the gradual increasing plateau of the BTC, applied the Langmuirian approach into the continuum model (model types (ix), (x), (xi), (xii), (xiv), and (xv), Table 1.1) in order to simulate the transport of NP such as Ag NP [6, 78], GO [92-94], CeO<sub>2</sub> NP [3], TiO<sub>2</sub> NP [42, 90], QD [79, 95-97], and CML [79]. Based on the satisfactory model fitting results, these studies proposed the blocking of the physicochemical attachment sites as an underlying phenomenon for transport of NP in porous media. However, the application of this model has not been only limited to the blocking due to physicochemical deposition but also has been widely applied for describing the depleting capacity of the straining sites over time via model types (xi) and (xii), Table 1.1, e.g., for AG NP [64, 74, 76-78], GO [7, 8], and several other colloids [e.g., 46]. In addition, in a few studies [73, 75], the Langmuirian type site-blocking function was combined with the depth-dependent model of straining in form of dual-deposition sites (model type (xi), Table 1.1)—one for time-dependent retention and another for depth-dependent deposition, without any mention of straining or blocking explicitly.

It is very important to note that a rising plateau of the BTC should not be always taken as a sign of site-blocking phenomenon. Recalling the BTC generated by using the simple non-equilibrium attachment/detachment model (model type (ii), Table 1.1) in Fig. 1.5a, ascending BTC plateaus can also emerge with increasing  $K_{det}$  values as described in Section 1.4.3. Nevertheless, these shapes of BTC, which result from simple attachment/detachment model, come with tailing which may not be the case when the underlying transport process is site blocking [e.g., 6, 9, 40, 42, 92, 93, 96-98] unless they occur simultaneously. In the latter case, both  $K_{det}$  and Langmuirian function should be included in the model at the same time [7, 41, 99] (Table B1).

From a mechanistic standpoint, the Langmuir function can be criticized for being a linear function of the surface coverage [100]. Therefore, a dynamic blocking function based on the non-equilibrium model of random sequential adsorption (RSA) mechanics as a nonlinear power-law function of surface coverage was developed in order to account for the real surface exclusion effects introduced by larger particles [100, 101]. Being a sort of mechanistic approach, this model obviated the need for

parameter estimation. This model was even employed to simulate the transport of colloid in heterogeneous porous media [102]. Nevertheless, this type of modelling approach generally comes with the disadvantages of ignoring the specific interactions of attaching particles with interfaces and with previously deposited particles, as well as inefficiency of their application for non-spherical particles [103]. Furthermore, they have the limitation of being strictly valid for just the irreversible deposition [103]. Detailed discussion of this model can be found in [103]. Overall, the identification of blocking phenomena is clearer than other transport mechanisms, such as straining and agglomeration, e.g., a rising-plateau BTC without tailing appears to be a clear sign of blocking mechanism in the system. A Langmuir type model, in spite of emanating from solute transport literature, has generally been found effective for modelling the site-blocking aspect of NP transport in porous media across different scales [104, 105].

### 8.2.2 Ripening mechanism and related modelling approaches

Ripening is the opposite of the blocking phenomenon, i.e. it is expected to occur when the particle-particle interactions/associations on the surface of porous media are stronger than the particle-surface interactions/associations. Also, in contrast to the blocking mechanism, in which the deposition rate decreases with time, ripening causes an increase in the deposition rate with time. This leads to a dropping plateau of the BTC in the case of ripening [18, 30, 34, 39, 59, 69, 106-115]. Ripening has been observed for NP such as NZVI [99, 110, 112, 113, 116, 117], HAP NP [17, 18, 69, 73], TiO<sub>2</sub> [106, 118, 119], nano- C<sub>60</sub> [120], CeO<sub>2</sub> NP [121], and ZnO NP [14, 15] typically at IS in the range 10–20 mM NaCl or 1 mM CaCl<sub>2</sub> [e.g., 15, 106, 119]. Increase in the inflow concentration of NP strongly affects the ripening and can result in clogging of porous media [99, 112].

In the context of continuum-based modelling of NP, two modelling approaches have generally been applied for ripening. First, a more robust form of Eq. (A3), already capable of modelling the blocking effect, was introduced to model the ripening phenomenon alternatively, given as Eq. (e) in model type (xv), Table 1.1 [34, 99, 112]. This equation represents ripening when  $\beta_1 > 0$  and  $A_1 > 0$  or blocking when  $\beta_1 = 1$  and  $A_1 = -1/S_m$ . Second, ripening has been modeled by adding a second-order term between aqueous phase and the attached phase to the mass balance equation of the attached phase as given in Eq. (b) in model type (xiii), Table 1.1 [46, 69].

The complexity of concurrent occurrence of various transport phenomena, namely, site-blocking and ripening along with aggregation, straining, and size exclusion, aggravated by the lack of proper experimental detection techniques, has not only caused problematic selection and application of various types of modelling approaches but also has been extended to the applied terminology in the literature of the subject [81, 122, 123]. Since ripening takes place in physicochemical conditions also favourable for aggregation, these terms sometimes have been used alternatively, or in other words, aggregation in porous media has been alluded to as ripening [34, 118, 124]. Yet, it should be clarified that aggregation, by itself, can occur both in the aqueous phase and the attached or immobilized phase separately. In aqueous phase, aggregation results from three mechanisms: perikinetic aggregation, differential sedimentation, and orthokinetic aggregation [125, 126] whilst in the attached phase, aggregation can result from the movement and/or rolling of the particles weakly attached on the secondary minimum of the collector surface and translating along the surface due to hydrodynamic drag forces and eventually their accumulation near the rear of the collector or at grain-to-grain contact areas [48, 63, 92, 127]. On the other hand, ripening arises from the interactions of depositing particles, still in the aqueous phase, with previously deposited particles, in the retained phase, leading to multilayer accumulation of particles on the surface of the collector [18, 69, 106, 114-116]. This also gives physical meaning to the second type of ripening model outlined above in which ripening is described by a second-order term standing for the interactions between the fluid phase and the attached phase.

Chen et al. [106] provided an alternative explanation for the increased NP retention during transport. They indicated that enhancement in deposition rate can be also due to the appearance of more favourable surfaces for further deposition resulting from the alteration of the media surface charge distribution. Those authors, furthermore, proposed that collision of NP aggregates with sand surface can reconstruct the aggregates, i.e., change the particle arrangement in the structure of aggregates. This amounts to a consequent reduction in the sand-NP aggregate repulsion forces thereby enhancing the deposition rate [106]. Nevertheless, this observation was based upon detecting a decrease in the particle size of the effluent samples, and no rigorous experimental evidence was provided. Countering this argument, similar behaviour would be expected via the concurrent agglomeration of NP similar to the conceptual

model proposed by [128] and numerically confirmed by [125]. In this interpretation, due to polydispersity of the injecting TiO<sub>2</sub> dispersion in the study of Chen et al., concurrent agglomeration of the middle and larger fractions of the particles during transport, resulted from their deeper energy wells [82, 128, 129], could cause the removal of the middle and larger fractions of particles via agglomeration and subsequent ripening. In this way, the average size of particles which could reach the outlet of the porous media was reduced [69, 125, 130]. This process has more recently been described as size selective retention. Future experimental studies with measurement of particle size distribution inside the pore spaces and pore solid surfaces are required to find a better distinction among these phenomena and, therefore, verify the continuum model conceptual ground.

It should be mentioned that blocking and ripening are two mutually exclusive phenomena, i.e., when physicochemical conditions are favourable for one, the other one should not take place. However, in practice they can still occur simultaneously within the continuum domain because of spatial heterogeneity in the porous media [114, 131]. In addition to concomitant blocking and ripening behaviours, transition from blocking phenomenon to ripening phenomenon has also been observed [17, 18, 106, 118, 119, 132]. Such shifts in the conditions of experiment that brings about a switching of the transport behaviour from blocking to ripening is important because this can also alter most of the other underlying transport phenomena and thus provide insights into the role of each individual phenomena when several mechanisms of NP transport are operating concomitantly (see Fig. A2a,b).

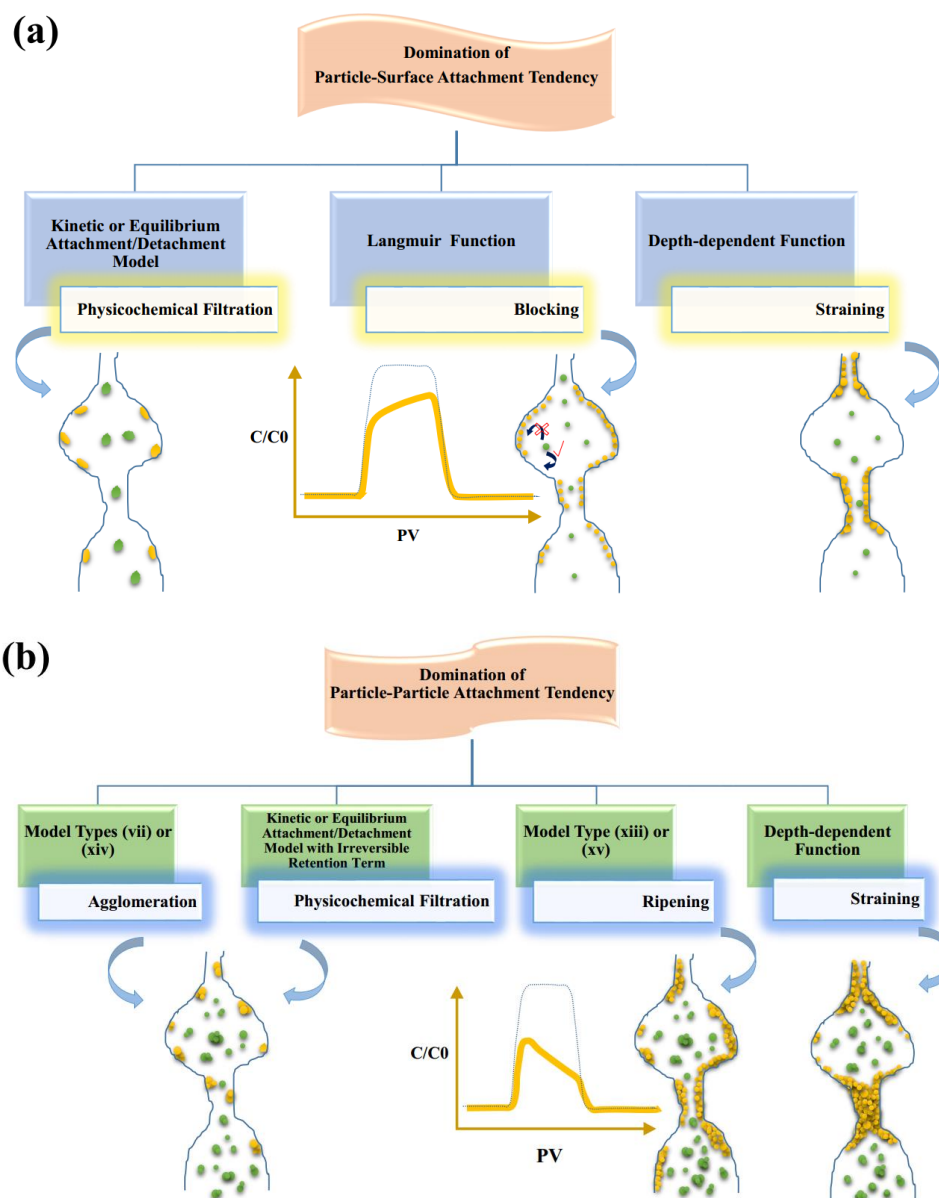


**Figure A2** Possible regimes of transport mechanisms: (a) when particle-surface attachment tendency is higher than particle-particle attachment tendency and (b) when particle-particle attachment tendency is higher than particle-surface attachment tendency. Mobile particle/aggregates are shown in green while retained particle/aggregates are shown in yellow.

Overall, two transport regimes can be encountered in the transport of NP in porous media. In the first regime, i.e., higher particle-surface attachment affinity than particle-particle attachment affinity, the major transport mechanisms are physicochemical filtration (describable by either kinetic or equilibrium attachment/detachment model), blocking (describable by Langmuir function), and perhaps together with physical

retention, i.e., straining (describable with depth-dependent function). This regime can produce ascending BTC plateaus (Fig. A2a). In practice, this condition may bring about a considerable mobility of NP which needs careful assessment of NP transport in order to prevent unwanted subsurface migration. The second regime is when the particle-particle attachment tendency becomes dominant. In this regime although physicochemical filtration as well as straining may still be operative, ripening is predominant together with agglomeration and further subsequent retention. This regime may create descending BTC plateaus (Fig. A2b). If the conditions of the experiment shift the transport behaviour from blocking to ripening, then hazardous aspects of unwanted NP migration might be relieved to some extent because of the substantial amount of the retention resulted from ripening. However, it may also be possible that in this regime even with significant agglomeration of NP in the mobile phase, ripening would not be the case. For instance, due to the lower input concentration ripening might not be significant. According to Table B1 ripening has been mostly the case when injection concentration ranged from 100 mg/L to 20000 mg/L while the typical injection concentration of studies reviewed here was  $27.5 \pm 11.5$  mg/L. If ripening does not occur in this regime, agglomeration might promote size exclusion, which will be described next, thereby results in great migration distances. Should it be the case, the hazardous aspect of NP transport within subsurface will be much more serious than what has been hitherto believed.

## **8.3 Size exclusion**

### **8.3.1 Significance for NP**

The importance of size exclusion was elucidated in considering the reasons for unexpected large migration distances of solute contaminants, such as radionuclides, in the subsurface because of their association with groundwater colloids, [133-142]. Size exclusion, also known in the more general concept as hydrodynamic chromatography, has been recognized as an underlying phenomenon for faster migration of particles compared to non-reactive solute in porous or fractured media [83, 115, 137, 140, 141, 143-152]. Due to this mechanism, up to 5.5 times enhancement in colloid velocity compared to mean pore water velocity has been observed in micro-models [83, 150].

Recently, the number of studies identifying size exclusion as an underlying transport phenomenon of various NP has increased. These NP thus far include AgNP [5, 78, 153, 154], TiO<sub>2</sub> [118, 155], NZVI [156], and carbon nanotubes [157]. Particularly, size exclusion is noticeable in two areas of NP transport research, namely biofilm coated porous media [153, 158] and co-transport/hetero-aggregation of NP [118, 132] even though these research areas are still at a relatively early stage. For example, studies on the co-transport of Au NP with SWNT [132] or TiO<sub>2</sub> with multi-walled carbon nanotubes (MWCNT) [118] showed that heteroaggregation of these NP can facilitate their transport in porous media [159-161]. Intuitively, it is easy to dismiss size exclusion for NP relative to larger colloids for the simple reason of their small size. However, notwithstanding the scientific necessity of obtaining robust proof of any such assertion, the potential for NP aggregation into particles large enough to experience size exclusion (section 10.3) provides a strong rationale for consideration of size exclusion in the context of NP fate and transport modelling.

### **8.3.2 Mechanism**

Detection of size exclusion based on BTC and RCP data is challenging when several transport mechanisms act together. In many modelling studies of colloid and NP transport in porous media this mechanism has been neglected because of not observing the early BTC [e.g., 7, 8, 162]. However, even though early BTC may not be observed, size exclusion can still be influential because its reflection in the BTC might be counterbalanced by other transport processes [34, 39, 147]. Size exclusion was suggested by Bradford et al. [39] to be influential in the depth-dependent behaviour of colloid retention. Agglomeration of NP can promote particle size growth which may in turn enhance the chance of size exclusion whilst it can also elevate physicochemical retention or retention via straining [39, 82, 128, 129, 163]. Although a satisfactory quantitative analysis of these effects acting simultaneously is still lacking [5, 125, 128, 142, 164], in this section the potential conceptual models of NP and colloid transport are elucidated when several transport processes operate concomitantly.

It should be clarified that herein size exclusion is considered as a mechanism of enhancing the transport of larger colloidal particles compared to smaller ones and nonreactive solute. This should be distinguished from some applications of the 'exclusion' terminology with the meaning of excluding particles from all of pores

(clogging) [1] or as a capture mechanism of particle deposition [97, 165-167]. Size exclusion has been generally referenced in the context of colloid transport on two different scales [146, 147, 152]. Firstly on a larger scale, i.e., bulk scale, the size exclusion concept has been referred to as the exclusion of particles larger than a portion of the pores that can be passed through by solute but not by the particles [30, 39, 46, 107, 108, 115, 146, 152, 168-174]. Secondly, at the pore scale size exclusion has been attributed to migration of particles on flow paths which are close to the centre of the pore channels where the velocity is theoretically 1.5 times larger than the mean pore water velocity—similar to the phenomena in solute transport context called “charge” or “anion exclusion”, but with different underlying forces [83, 145-147, 163, 175].

On the larger scale, the concept of inaccessibility of pores to particle rather than solute, which has also been termed as “pore exclusion” [176], in order to be significant, requires the threshold ratio of the pore throat to particle diameter to be larger than 1.5, suggesting for many environmental porous media that the size of the particles must be larger than 1–2  $\mu\text{m}$  [83]. Grolimund et al. [177] showed that the inaccessibility of small pores in the soil texture to colloidal particles did not change with variations of the pore water velocity and therefore exclusion of particles from the margins of the pore throats was the main cause of the breakthrough acceleration. The observation of 4–5.5 times enhancement in the particle velocity in a micromodel by Sirivithayapakorn and Keller [83], which was attributed to the preferential paths resulted from the selectivity of the pores, i.e., inaccessibility of the small pore to larger particles, as well as observation of detours in a micromodel by Auset and Keller [146] suggest that this type of size exclusion might be still considerable.

At the smaller scale, the velocity profile in an individual pore section, approximated as a cylinder, is expected to adopt a parabolic shape according to the Poiseuille flow profile, i.e., the velocity is zero at the wall and the maximum at the centre [144, 146, 149, 163, 178, 179]. Part of mass that resides at the centre of these pipes will arrive at the end of the pipes sooner than the mean velocity of the flow. This part of mass may contain the larger size fraction of the particles with lower Brownian diffusion compared to small particles or solute. Since materials with lower diffusion may be less distributed over the pore (or fracture) cross-section area and are less likely to reach areas near the pore (or fracture) walls, they are conceptually less prone to the movement with the sluggish velocities at the vicinity of the walls. This part of mass is

also less likely to move with retardation or attachment/detachment that occur in the area near pore channel walls. As a result, larger particles according to this conceptual model can migrate faster than average pore water velocity.

The underlying reasons presented in the current literature regarding why the particles tend to keep far from pore channel walls are neither satisfactory nor generic. For instance, it has been mentioned that the large size of particles prevent their centres of mass from sampling the areas very close to the pore (or fracture) walls, and/or that the surface-charge-induced repulsion of particles prevents them from entering certain pore regions close to walls [39, 83, 108, 115, 137, 139-141, 143, 145-152, 158, 170, 175, 177-182]. It has also been mentioned in co-transport of TiO<sub>2</sub> with MWCNT, that the long arm of MWCNT impede the heteroaggregates to reach the vicinity of the porous media solid surfaces where they can be deposited [118]. These reasons, however, may not be sufficient to describe the significant acceleration of migration velocity observed for particles compared to conservative solute, e.g., 1.45 times velocity enhancement observed by Grolimund et al. [177], because such velocities necessitates the majority of particles travel at an area very close to the centreline of the pore channels while in addition to diffusion several other mechanisms/forces such as gravitational sedimentation, interception, inertia, and momentum may tend to bring the particles to the surface of the pore (or fracture) wall or at least redistribute them across the pore space [20, 128, 129, 183, 184]. In addition, the limited influential distance range of repulsive forces to the vicinity of the pore walls as well as the change in the charge sign due to heterogeneity of the geological medium can downgrade the mere role of repulsion forces in keeping the particles far from the pore walls [142]. This lack of recognition about the underlying mechanism of size exclusion might be a reason for the complexity in identifying the size exclusion when several other transport mechanisms are also engaged. This is also the case even in the mechanistic modelling framework in which very few papers thus far have attempted to capture the effect of size exclusion phenomenon [141, 143, 144, 178].

In a study by Malkovsky and Pek [142], it was suggested that a substantial enhancement in the particle velocity relative to the average groundwater velocity can only result from drift forces created by the “Magnus effect” (the hydrodynamic force resulting on a rotating sphere in a heterogeneous flow field). This force causes the translation of particles toward the centreline [144, 163]. Essential conditions for the

Magnus effect to be functional are the rotation of colloidal particles and unequal velocities of particle and local groundwater streamlines [142]. However, it has been indicated that rotational component of particle is negligible for a range of ratios of particle diameter to pore throat (or aperture) width lower than 0.4 while typical ratios has been reported to be far lower — $10^{-4}$  to  $10^{-2}$  [144, 148, 185, 186]. Nevertheless, Malkovsky and Pek asserted that the Magnus effect was still considerable for relatively small particles due to significant oscillation resulting from Brownian motion. Other authors attributed the reason for cross-stream displacement of particles near a wall to the inertia in laminar flow [144, 187-190]. Based on this analysis, Segre and Silberberg [188, 190] found that particles close to the centreline tended to drift toward the wall of the tube and particles at the vicinity of the wall tended to drift toward the centre. This tendency led to an equilibrium position at a distance about 0.6 times of the tube radii from the centreline.

### **8.3.3 Continuum modelling approaches of size exclusion**

To date, no specific parameter has been added to the advection-dispersion model to represent size exclusion. However, several different approaches have been applied in the continuum modelling framework to capture the impact of size exclusion by adapting the basic flow and transport parameters including partition coefficient ( $K_d$ ), pore water velocity, volumetric water content (or porosity), and dispersivity [39, 151, 171, 179, 191-193]. In the simple linear adsorption model, anion exclusion was taken into account by allowing the partition coefficient to become negative in the parameter estimation process [192]. This is equivalent to letting the retardation factor in the parameter estimation process go lower than unity, that is then called "acceleration factor" [83] as was shown in Fig. 1.5b. For a non-equilibrium adsorption model, exclusion was incorporated by considering an equivalent exclusion distance from the pore wall where the concentration is effectively zero [191, 192]. Subsequently, an exclusion volume could be estimated by multiplying the exclusion distance in the specific surface area ( $L^2 M^{-1}$ ). This exclusion volume times the soil bulk density yielded an equivalent porosity that could be subtracted from the porosity of the immobile domain used in the non-equilibrium dual domain model [191, 192]. Likewise, Bradford et al. [39] in order to model size/charge exclusion, altered both

porosity, based on the water content accessible to particles, and Darcy velocity, based on the relative water permeability accessible to particles.

Some continuum approaches to size exclusion have been based on a known spatial distribution of pore/aperture width which was mainly obtained by a stochastic approach [171, 193]. The influence of size exclusion was then assimilated in the model by eliminating both advection and dispersion fluxes into the fracture elements of the numerical grid which had an aperture thickness smaller than  $15 \mu m$  [171] or 12 times the particle diameter [193]. In effect, this type of model considered the size exclusion at the larger scale, i.e., bulk scale size exclusion or pore rather than pore scale type. James and Chrysikopoulos [179] modified the Taylor dispersion coefficient, originally developed for dissolved matter, to account for the finite size of the colloidal particles. This way, they demonstrated that size exclusion from the slowest moving portion of the velocity profile increased the effective particle velocity whereby decreasing the overall particle dispersion. Scheibe and Wood [151] argued that increasing the velocity as a parameter for simulating size exclusion can result in altering dispersion (assuming no change in dispersivity), which is not conceptually consistent with the fact that the overall variance of the pore-scale velocity in respect to the size exclusion phenomenon should be decreased due to a lower chance of particles accessing certain regions of low velocity. Therefore, they proposed truncating the lower velocities from the velocity distribution profile to take account of the very low velocities adjacent to the pore walls that were not experienced by the particles. The advantage of their method was that the velocity field for particles was statistically similar to that of the pore water velocity distribution but slightly modified as a result of the truncation [151].

Overall, most of these modelling techniques are either based on a known (or a stochastically estimated) pore/aperture thickness distribution over the spatial domain [171, 193], or rely on modification of the other parameters and/or variables of the model such as velocity or dispersion [151, 179]. These issues can make the predictive power of the model less plausible when applied in larger scales. For instance, models which rely on the modification of the velocity field whereby estimating the parameters of model may not be applicable to real large-scale environmental problems in which the velocity field with its spatial and temporal variations in bulk scale is already unknown and might be affected by other factors as well when various phenomena such as straining and size exclusion coexist [34, 39]. This is also the case for the dispersivity

parameter, which should be estimated based on the tracer breakthrough data in order to be determined as a property of the porous media and independent from the phenomenological mechanisms of particle transport [146]. Once dispersivity is estimated from tracer BTC, the total number of parameters required to be determined in the procedure of particle transport model calibration are reduced. Yet, recent findings of Chrysikopoulos and Katzourakis [170] on showing the dependency of dispersivity on particle size shows that there is the need for reformulation of the continuum-based models in order to take account of the particle size distribution and its dynamics resulted from size exclusion, agglomeration and other transport phenomena. Such a modelling approach may be accomplished if a multi-species model formulation can be adapted for different particle size classes in terms of mass concentration [194]. The potential of heterogeneous particle populations to complicate transport models, even when the initial input population is uniform, has been well documented. However, the mechanisms which underpin such effects – homo- and hetero-aggregation simultaneous with particle transport and deposition – have been remarkably little studied in comparison to ‘static’ systems of flocculation and sedimentation.

## 8.4 References

1. Bradford, S.A., et al., *Physical factors affecting the transport and fate of colloids in saturated porous media*. Water Resources Research, 2002. **38**(12): p. 63-1.
2. Xu, S., B. Gao, and J.E. Saiers, *Straining of colloidal particles in saturated porous media*. Water Resources Research, 2006. **42**(12).
3. Li, Z., et al., *Transport and deposition of CeO<sub>2</sub> nanoparticles in water-saturated porous media*. Water research, 2011. **45**(15): p. 4409-4418.
4. El Badawy, A.M., et al., *Key factors controlling the transport of silver nanoparticles in porous media*. Environmental science & technology, 2013. **47**(9): p. 4039-4045.
5. Cornelis, G., et al., *Transport of silver nanoparticles in saturated columns of natural soils*. Science of the Total Environment, 2013. **463**: p. 120-130.
6. Neukum, C., A. Braun, and R. Azzam, *Transport of stabilized engineered silver (Ag) nanoparticles through porous sandstones*. Journal of contaminant hydrology, 2014. **158**: p. 1-13.
7. Fan, W., et al., *Effects of surfactants on graphene oxide nanoparticles transport in saturated porous media*. Journal of Environmental Sciences, 2015.
8. Fan, W., et al., *Transport of graphene oxide in saturated porous media: Effect of cation composition in mixed Na–Ca electrolyte systems*. Science of The Total Environment, 2015. **511**: p. 509-515.
9. Qi, Z., L. Zhang, and W. Chen, *Transport of graphene oxide nanoparticles in saturated sandy soil*. Environmental Science: Processes & Impacts, 2014. **16**(10): p. 2268-2277.
10. Fang, J., et al., *Modeling the transport of TiO<sub>2</sub> nanoparticle aggregates in saturated and unsaturated granular media: effects of ionic strength and pH*. water research, 2013. **47**(3): p. 1399-1408.
11. Choy, C.C., M. Wazne, and X. Meng, *Application of an empirical transport model to simulate retention of nanocrystalline titanium dioxide in sand columns*. Chemosphere, 2008. **71**(9): p. 1794-1801.
12. Fang, J., et al., *Stability of titania nanoparticles in soil suspensions and transport in saturated homogeneous soil columns*. Environmental pollution, 2009. **157**(4): p. 1101-1109.
13. Sun, P., et al., *Distinguishable Transport Behavior of Zinc Oxide Nanoparticles in Silica Sand and Soil Columns*. Science of The Total Environment, 2015. **505**: p. 189-198.
14. Jiang, X., M. Tong, and H. Kim, *Influence of natural organic matter on the transport and deposition of zinc oxide nanoparticles in saturated porous media*. Journal of colloid and interface science, 2012. **386**(1): p. 34-43.
15. Jiang, X., et al., *Transport and deposition of ZnO nanoparticles in saturated porous media*. Colloids and Surfaces A: Physicochemical and Engineering Aspects, 2012. **401**: p. 29-37.
16. Jiang, X., et al., *Initial transport and retention behaviors of ZnO nanoparticles in quartz sand porous media coated with Escherichia coli biofilm*. Environmental Pollution, 2013. **174**: p. 38-49.
17. Wang, D., Y. Jin, and D.P. Jaisi, *Effect of Size-Selective Retention on the Cotransport of Hydroxyapatite and Goethite Nanoparticles in Saturated Porous Media*. Environmental science & technology, 2015. **49**(14): p. 8461-8470.

18. Wang, D., Y. Jin, and D. Jaisi, *Cotransport of Hydroxyapatite Nanoparticles and Hematite Colloids in Saturated Porous Media: Mechanistic Insights from Mathematical Modeling and Phosphate Oxygen Isotope Fractionation*. Journal of Contaminant Hydrology, 2015. **182**: p. 194-209.
19. Jegatheesan, V. and S. Vigneswaran, *Deep Bed Filtration: Mathematical Models and Observations*. Critical Reviews in Environmental Science and Technology, 2005. **35**(6): p. 515-569.
20. Ives, K.J., *Rapid filtration*. Water Research, 1970. **4**(3): p. 201-223.
21. Cleasby, J.L. and E.R. Baumann, *Selection of sand filtration rates*. Journal (American Water Works Association), 1962: p. 579-602.
22. Ives, K.J. *Simplified Rational Analysis of Filter Behaviour*. in *ICE Proceedings*. 1963. Thomas Telford.
23. Auset, M. and A.A. Keller, *Pore-scale visualization of colloid straining and filtration in saturated porous media using micromodels*. Water resources research, 2006. **42**(12).
24. McDowell-Boyer, L.M., J.R. Hunt, and N. Sitar, *Particle transport through porous media*. Water Resour. Res, 1986. **22**(13): p. 1901-1921.
25. Wei, Y.-T., et al., *Influence of nanoscale zero-valent iron on geochemical properties of groundwater and vinyl chloride degradation: A field case study*. Water Research, 2010. **44**(1): p. 131-140.
26. Elliott, D.W. and W.-X. Zhang, *Field assessment of nanoscale bimetallic particles for groundwater treatment*. Environmental Science & Technology, 2001. **35**(24): p. 4922-4926.
27. Köber, R., et al., *Nanoscale zero-valent iron flakes for groundwater treatment*. Environmental Earth Sciences, 2014. **72**(9): p. 3339-3352.
28. Edmiston, P.L., et al., *Pilot scale testing composite swellable organosilica nanoscale zero-valent iron—Iron-Osorb®—for in situ remediation of trichloroethylene*. Remediation Journal, 2011. **22**(1): p. 105-123.
29. Rosansky, S., W. Condit, and R. Sirabian, *Best practices for injection and distribution of amendments*. 2013, Technical Report TR-NAVFAC-EXWC-EV.
30. Bradford, S.A. and S. Torkzaban, *Colloid transport and retention in unsaturated porous media: A review of interface-, collector-, and pore-scale processes and models*. Vadose Zone Journal, 2008. **7**(2): p. 667-681.
31. Zhang, L., et al., *Transport of fullerene nanoparticles (n C60) in saturated sand and sandy soil: controlling factors and modeling*. Environmental science & technology, 2012. **46**(13): p. 7230-7238.
32. Dong, H., et al., *Interaction between Cu 2+ and different types of surface-modified nanoscale zero-valent iron during their transport in porous media*. Journal of Environmental Sciences, 2015. **32**: p. 180-188.
33. Herzig, J.P., D.M. Leclerc, and P.L. Goff, *Flow of Suspensions through Porous Media—Application to Deep Filtration*. Industrial & Engineering Chemistry, 1970. **62**(5): p. 8-35.
34. Shen, C., et al., *Effects of solution chemistry on straining of colloids in porous media under unfavorable conditions*. Water resources research, 2008. **44**(5).
35. Xu, S., Q. Liao, and J.E. Saiers, *Straining of nonspherical colloids in saturated porous media*. Environmental science & technology, 2008. **42**(3): p. 771-778.

36. Foppen, J.W.A., A. Mporokoso, and J.F. Schijven, *Determining straining of Escherichia coli from breakthrough curves*. Journal of contaminant hydrology, 2005. **76**(3): p. 191-210.
37. Li, X., T.D. Scheibe, and W.P. Johnson, *Apparent decreases in colloid deposition rate coefficients with distance of transport under unfavorable deposition conditions: A general phenomenon*. Environmental Science & Technology, 2004. **38**(21): p. 5616-5625.
38. Tan, Y., et al., *Transport of bacteria in an aquifer sand: Experiments and model simulations*. Water resources research, 1994. **30**(12): p. 3243-3252.
39. Bradford, S.A., et al., *Modeling colloid attachment, straining, and exclusion in saturated porous media*. Environmental science & technology, 2003. **37**(10): p. 2242-2250.
40. Qi, Z., et al., *Factors controlling transport of graphene oxide nanoparticles in saturated sand columns*. Environmental toxicology and chemistry, 2014. **33**(5): p. 998-1004.
41. He, J.-Z., et al., *Biofilms and extracellular polymeric substances mediate the transport of graphene oxide nanoparticles in saturated porous media*. Journal of hazardous materials, 2015. **300**: p. 467-474.
42. Toloni, I., F. Lehmann, and P. Ackerer, *Modeling the effects of water velocity on TiO<sub>2</sub> nanoparticles transport in saturated porous media*. Journal of contaminant hydrology, 2014. **171**: p. 42-48.
43. Jones, E.H. and C. Su, *Transport and retention of zinc oxide nanoparticles in porous media: Effects of natural organic matter versus natural organic ligands at circumneutral pH*. Journal of hazardous materials, 2014. **275**: p. 79-88.
44. Kurlanda-Witek, H., B.T. Ngwenya, and I.B. Butler, *Transport of bare and capped zinc oxide nanoparticles is dependent on porous medium composition*. Journal of contaminant hydrology, 2014. **162**: p. 17-26.
45. Wang, D., et al., *Facilitated transport of Cu with hydroxyapatite nanoparticles in saturated sand: Effects of solution ionic strength and composition*. water research, 2011. **45**(18): p. 5905-5915.
46. Bradford, S.A. and M. Bettahar, *Concentration dependent transport of colloids in saturated porous media*. Journal of Contaminant Hydrology, 2006. **82**(1): p. 99-117.
47. Bradford, S.A. and N. Toride, *A stochastic model for colloid transport and deposition*. Journal of environmental quality, 2007. **36**(5): p. 1346-1356.
48. Bradford, S.A., J. Simunek, and S.L. Walker, *Transport and straining of E. coli O157:H7 in saturated porous media*. Water Resources Research, 2006. **42**(12).
49. Gargiulo, G., et al., *Bacteria transport and deposition under unsaturated conditions: The role of the matrix grain size and the bacteria surface protein*. Journal of contaminant hydrology, 2007. **92**(3): p. 255-273.
50. Gargiulo, G., et al., *Bacteria transport and deposition under unsaturated flow conditions: The role of water content and bacteria surface hydrophobicity*. Vadose Zone Journal, 2008. **7**(2): p. 406-419.
51. Wang, D., et al., *Transport of ARS-labeled hydroxyapatite nanoparticles in saturated granular media is influenced by surface charge variability even in the presence of humic acid*. Journal of hazardous materials, 2012. **229**: p. 170-176.
52. Kasel, D., et al., *Transport and retention of multi-walled carbon nanotubes in saturated porous media: Effects of input concentration and grain size*. water research, 2013. **47**(2): p. 933-944.

53. Ben-Moshe, T., I. Dror, and B. Berkowitz, *Transport of metal oxide nanoparticles in saturated porous media*. Chemosphere, 2010. **81**(3): p. 387-393.
54. Shellenberger, K. and B.E. Logan, *Effect of molecular scale roughness of glass beads on colloidal and bacterial deposition*. Environmental science & technology, 2002. **36**(2): p. 184-189.
55. Yoon, J.S., J.T. Germaine, and P.J. Culligan, *Visualization of particle behavior within a porous medium: Mechanisms for particle filtration and retardation during downward transport*. Water Resources Research, 2006. **42**(6).
56. Chen, K.L. and M. Elimelech, *Aggregation and deposition kinetics of fullerene (C60) nanoparticles*. Langmuir, 2006. **22**(26): p. 10994-11001.
57. Chen, K.L. and M. Elimelech, *Influence of humic acid on the aggregation kinetics of fullerene (C 60) nanoparticles in monovalent and divalent electrolyte solutions*. Journal of Colloid and Interface Science, 2007. **309**(1): p. 126-134.
58. Chatterjee, J. and S.K. Gupta, *An agglomeration-based model for colloid filtration*. Environmental Science & Technology, 2009. **43**(10): p. 3694-3699.
59. Chatterjee, J., S. Abdulkareem, and S.K. Gupta, *Estimation of colloidal deposition from heterogeneous populations*. water research, 2010. **44**(11): p. 3365-3374.
60. Tong, M. and W.P. Johnson, *Colloid population heterogeneity drives hyperexponential deviation from classic filtration theory*. Environmental science & technology, 2007. **41**(2): p. 493-499.
61. Jones, E.H. and C. Su, *Fate and transport of elemental copper (Cu 0) nanoparticles through saturated porous media in the presence of organic materials*. water research, 2012. **46**(7): p. 2445-2456.
62. Bradford, S.A., S. Torkzaban, and J. Simunek, *Modeling colloid transport and retention in saturated porous media under unfavorable attachment conditions*. Water Resources Research, 2011. **47**(10).
63. Bradford, S.A., S. Torkzaban, and A. Wiegmann, *Pore-scale simulations to determine the applied hydrodynamic torque and colloid immobilization*. Vadose Zone Journal, 2011. **10**(1): p. 252-261.
64. Liang, Y., et al., *Sensitivity of the transport and retention of stabilized silver nanoparticles to physicochemical factors*. water research, 2013. **47**(7): p. 2572-2582.
65. Bolster, C.H., et al., *Spatial distribution of deposited bacteria following miscible displacement experiments in intact cores*. Water Resources Research, 1999. **35**(6): p. 1797-1807.
66. Tufenkji, N. and M. Elimelech, *Spatial distributions of Cryptosporidium oocysts in porous media: Evidence for dual mode deposition*. Environmental science & technology, 2005. **39**(10): p. 3620-3629.
67. Porubcan, A.A. and S. Xu, *Colloid straining within saturated heterogeneous porous media*. Water research, 2011. **45**(4): p. 1796-1806.
68. Xu, S. and J.E. Saiers, *Colloid straining within water-saturated porous media: Effects of colloid size nonuniformity*. Water resources research, 2009. **45**(5).
69. Wang, D., et al., *Transport of fluorescently labeled hydroxyapatite nanoparticles in saturated granular media at environmentally relevant concentrations of surfactants*. Colloids and Surfaces A: Physicochemical and Engineering Aspects, 2014. **457**: p. 58-66.
70. Ren, D. and J.A. Smith, *Protein-capped silver nanoparticle transport in water-saturated sand*. Journal of Environmental Engineering, 2012. **139**(6): p. 781-787.

71. Neukum, C., A. Braun, and R. Azzam, *Transport of engineered silver (Ag) nanoparticles through partially fractured sandstones*. Journal of contaminant hydrology, 2014. **164**: p. 181-192.
72. Raychoudhury, T., N. Tufenkji, and S. Ghoshal, *Straining of Polyelectrolyte-Stabilized Nanoscale Zero Valent Iron Particles during Transport through Granular Porous Media*. Water Research, 2014. **50**(0): p. 80-90.
73. Wang, D., et al., *Humic acid facilitates the transport of ARS-labeled hydroxyapatite nanoparticles in iron oxyhydroxide-coated sand*. Environmental science & technology, 2012. **46**(5): p. 2738-2745.
74. Wang, D., et al., *Hyperexponential and nonmonotonic retention of polyvinylpyrrolidone-coated silver nanoparticles in an Ultisol*. Journal of contaminant hydrology, 2014. **164**: p. 35-48.
75. Wang, D., et al., *Facilitated transport of copper with hydroxyapatite nanoparticles in saturated sand*. Soil Science Society of America Journal, 2012. **76**(2): p. 375-388.
76. Wang, D., et al., *Transport and Retention of Polyvinylpyrrolidone-Coated Silver Nanoparticles in Natural Soils*. Vadose Zone J., 2015.
77. Liang, Y., et al., *Retention and remobilization of stabilized silver nanoparticles in an undisturbed loamy sand soil*. Environmental science & technology, 2013. **47**(21): p. 12229-12237.
78. Braun, A., et al., *Transport and deposition of stabilized engineered silver nanoparticles in water saturated loamy sand and silty loam*. Science of The Total Environment, 2014.
79. Torkzaban, S., et al., *Impacts of bridging complexation on the transport of surface-modified nanoparticles in saturated sand*. Journal of contaminant hydrology, 2012. **136**: p. 86-95.
80. Johnson, W.P., H. Ma, and E. Pazmino, *Straining credibility: a general comment regarding common arguments used to infer straining as the mechanism of colloid retention in porous media*. Environmental science & technology, 2011. **45**(9): p. 3831-3832.
81. Massoudieh, A. and T.R. Ginn, *Colloid-facilitated contaminant transport in unsaturated porous media*. Modelling of pollutants in complex environmental systems, 2010. **2**: p. 263-286.
82. Phenrat, T., et al., *Transport and deposition of polymer-modified Fe<sub>0</sub> nanoparticles in 2-D heterogeneous porous media: Effects of particle concentration, Fe<sub>0</sub> content, and coatings*. Environmental Science & Technology, 2010. **44**(23): p. 9086-9093.
83. Sirivithayapakorn, S. and A. Keller, *Transport of colloids in saturated porous media: A pore-scale observation of the size exclusion effect and colloid acceleration*. Water Resources Research, 2003. **39**(4).
84. Johnson, R.L., et al., *Field-Scale Transport and Transformation of Carboxymethylcellulose-Stabilized Nano Zero-Valent Iron*. Environmental science & technology, 2013. **47**: p. 1573-1580.
85. Kocur, C.M., et al., *Characterization of nZVI mobility in a field scale test*. Environmental Science & Technology, 2014. **48**(5): p. 2862-2869.
86. Salama, A., et al., *Numerical investigation of nanoparticles transport in anisotropic porous media*. Journal of contaminant hydrology, 2015. **181**: p. 114-130.
87. Cullen, E., et al., *Simulation of the subsurface mobility of carbon nanoparticles at the field scale*. Advances in Water Resources, 2010. **33**(4): p. 361-371.

88. Langmuir, I., *THE ADSORPTION OF GASES ON PLANE SURFACES OF GLASS, MICA AND PLATINUM*. Journal of the American Chemical Society, 1918. **40**(9): p. 1361-1403.
89. Adamczyk, Z., et al., *Kinetics of localized adsorption of colloid particles*. Advances in Colloid and Interface Science, 1994. **48**: p. 151-280.
90. Saiers, J.E., G.M. Hornberger, and L. Liang, *First-and second-order kinetics approaches for modeling the transport of colloidal particles in porous media*. Water Resources Research, 1994. **30**(9): p. 2499-2506.
91. Skopp, J., *Analysis of time-dependent chemical processes in soils*. Journal of environmental quality, 1986. **15**(3): p. 205-213.
92. Sun, Y., et al., *Transport, retention, and size perturbation of graphene oxide in saturated porous media: Effects of input concentration and grain size*. Water research, 2015. **68**: p. 24-33.
93. Feriencikova, L. and S. Xu, *Deposition and remobilization of graphene oxide within saturated sand packs*. Journal of hazardous materials, 2012. **235**: p. 194-200.
94. Liu, L., et al., *Effects of surfactant type and concentration on graphene retention and transport in saturated porous media*. Chemical Engineering Journal, 2015. **262**: p. 1187-1191.
95. Wang, Y., et al., *Effect of surface coating composition on quantum dot mobility in porous media*. Journal of nanoparticle research, 2013. **15**(8): p. 1-16.
96. Wang, Y., et al., *Influence of Residual Polymer on Nanoparticle Deposition in Porous Media*. Environmental Science & Technology, 2014. **48**(18): p. 10664-10671.
97. Torkzaban, S., et al., *Release of Quantum Dot Nanoparticles in Porous Media: Role of Cation Exchange and Aging Time*. Environmental Science & Technology, 2013. **47**(20): p. 11528-11536.
98. Sasidharan, S., et al., *Coupled effects of hydrodynamic and solution chemistry on long-term nanoparticle transport and deposition in saturated porous media*. Colloids and Surfaces A: Physicochemical and Engineering Aspects, 2014. **457**: p. 169-179.
99. Tosco, T. and R. Sethi, *Transport of non-Newtonian suspensions of highly concentrated micro-and nanoscale iron particles in porous media: a modeling approach*. Environmental Science & Technology, 2010. **44**(23): p. 9062-9068.
100. Johnson, P.R. and M. Elimelech, *Dynamics of colloid deposition in porous media: Blocking based on random sequential adsorption*. Langmuir, 1995. **11**(3): p. 801-812.
101. Schaaf, P. and J. Talbot, *Surface exclusion effects in adsorption processes*. The Journal of chemical physics, 1989. **91**(7): p. 4401-4409.
102. Sun, N., et al., *A novel two-dimensional model for colloid transport in physically and geochemically heterogeneous porous media*. Journal of contaminant hydrology, 2001. **49**(3): p. 173-199.
103. Adamczyk, Z., et al., *Mechanisms of nanoparticle and bioparticle deposition—Kinetic aspects*. Colloids and Surfaces A: Physicochemical and Engineering Aspects, 2013. **439**: p. 3-22.
104. Becker, M.D., et al., *In situ measurement and simulation of nano-magnetite mobility in porous media subject to transient salinity*. Nanoscale, 2015. **7**(3): p. 1047-1057.
105. Bai, C. and Y. Li, *Modeling the transport and retention of nC 60 nanoparticles in the subsurface under different release scenarios*. Journal of contaminant hydrology, 2012. **136**: p. 43-55.

106. Chen, G., X. Liu, and C. Su, *Transport and retention of TiO<sub>2</sub> rutile nanoparticles in saturated porous media under low-ionic-strength conditions: measurements and mechanisms*. Langmuir, 2011. **27**(9): p. 5393-5402.
107. Bradford, S.A., et al., *Significance of straining in colloid deposition: Evidence and implications*. Water Resour. Res., 2006. **42**(12): p. W12S15.
108. Bradford, S.A., et al., *Modeling microorganism transport and survival in the subsurface*. Journal of environmental quality, 2014. **43**(2): p. 421-440.
109. Deshpande, P.A. and D.R. Shonnard, *Modeling the effects of systematic variation in ionic strength on the attachment kinetics of Pseudomonas fluorescens UPER-1 in saturated sand columns*. Water resources research, 1999. **35**(5): p. 1619-1627.
110. Basnet, M., et al., *Reduced transport potential of a palladium-doped zero valent iron nanoparticle in a water saturated loamy sand*. Water research, 2015. **68**: p. 354-363.
111. Gastone, F., T. Tosco, and R. Sethi, *Guar gum solutions for improved delivery of iron particles in porous media (Part 1): Porous medium rheology and guar gum-induced clogging*. Journal of contaminant hydrology, 2014. **166**: p. 23-33.
112. Hosseini, S.M. and T. Tosco, *Transport and retention of high concentrated nano-Fe/Cu particles through highly flow-rated packed sand column*. Water Research, 2013. **47**(1): p. 326-338.
113. Tosco, T., F. Gastone, and R. Sethi, *Guar gum solutions for improved delivery of iron particles in porous media (Part 2): Iron transport tests and modeling in radial geometry*. Journal of contaminant hydrology, 2014. **166**: p. 34-51.
114. Nascimento, A.G., et al., *Temporal and spatial dynamics of blocking and ripening effects on bacterial transport through a porous system: A possible explanation for CFT deviation*. Colloids and Surfaces B: Biointerfaces, 2006. **53**(2): p. 241-244.
115. Kretzschmar, R., et al., *Mobile subsurface colloids and their role in contaminant transport*. Advances in agronomy, 1999. **66**: p. 121-193.
116. Basnet, M., S. Ghoshal, and N. Tufenkji, *Rhamnolipid biosurfactant and soy protein act as effective stabilizers in the aggregation and transport of palladium-doped zerovalent iron nanoparticles in saturated porous media*. Environmental science & technology, 2013. **47**(23): p. 13355-13364.
117. Tiraferri, A. and R. Sethi, *Enhanced transport of zerovalent iron nanoparticles in saturated porous media by guar gum*. Journal of Nanoparticle Research, 2009. **11**(3): p. 635-645.
118. Wang, X., et al., *Cotransport of multi-walled carbon nanotubes and titanium dioxide nanoparticles in saturated porous media*. Environmental Pollution, 2014. **195**: p. 31-38.
119. Chen, G., X. Liu, and C. Su, *Distinct effects of humic acid on transport and retention of tio<sub>2</sub> rutile nanoparticles in saturated sand columns*. Environmental Science & Technology, 2012. **46**(13): p. 7142-7150.
120. Cheng, X., A.T. Kan, and M.B. Tomson, *Study of C 60 transport in porous media and the effect of sorbed C 60 on naphthalene transport*. Journal of Materials Research, 2005. **20**(12): p. 3244-3254.
121. Lv, X., et al., *Effects of Humic Acid and Solution Chemistry on the Retention and Transport of Cerium Dioxide Nanoparticles in Saturated Porous Media*. Water, Air, & Soil Pollution, 2014. **225**(10): p. 1-9.
122. Molnar, I.L., et al., *Predicting colloid transport through saturated porous media: A critical review*. Water Resources Research, 2015.

123. Howington, S.E., J.F. Peters, and T.H. Illangasekare, *Discrete network modeling for field-scale flow and transport through porous media*, in *Technical Report CHL-97-21*. 1997, Discretionary Research Program, US Army Corps of Engineers MD, US.
124. Tong, M., H. Ma, and W.P. Johnson, *Funneling of flow into grain-to-grain contacts drives colloid–colloid aggregation in the presence of an energy barrier*. *Environmental science & technology*, 2008. **42**(8): p. 2826-2832.
125. Babakhani, P., et al., *Modified MODFLOW-based model for simulating the agglomeration and transport of polymer-modified Fe nanoparticles in saturated porous media*. *Environ Sci Pollut Res*, 1-20, doi:10.1007/s11356-015-5193-0, 2015.
126. Elimelech, M., et al., *Particle deposition and aggregation: measurement, modelling and simulation*. 1998, Amsterdam: Elsevier.
127. Kuznar, Z.A. and M. Elimelech, *Direct microscopic observation of particle deposition in porous media: Role of the secondary energy minimum*. *Colloids and Surfaces A: Physicochemical and Engineering Aspects*, 2007. **294**(1): p. 156-162.
128. Phenrat, T., et al., *Particle size distribution, concentration, and magnetic attraction affect transport of polymer-modified Fe<sub>0</sub> nanoparticles in sand columns*. *Environ. Sci. Technol.*, 2009. **43**(13): p. 5079-5085.
129. Phenrat, T., et al., *Empirical correlations to estimate agglomerate size and deposition during injection of a polyelectrolyte-modified Fe<sub>0</sub> nanoparticle at high particle concentration in saturated sand*. *Journal of Contaminant Hydrology*, 2010. **118**(3–4): p. 152-164.
130. Babakhani, P., et al., *Supplementary Material for "Modified MODFLOW-based model for simulating the agglomeration and transport of polymer-modified Fe nanoparticles in saturated porous media"*. *Environ Sci Pollut Res*, 1-20, doi:10.1007/s11356-015-5193-0, 2015.
131. Camesano, T.A., K.M. Unice, and B.E. Logan, *Blocking and ripening of colloids in porous media and their implications for bacterial transport*. *Colloids and Surfaces A: Physicochemical and Engineering Aspects*, 1999. **160**(3): p. 291-307.
132. Afrooz, A.R.M.N., et al., *Co-transport of gold nanospheres with single-walled carbon nanotubes in saturated porous media*. *Water research*, 2016. **99**: p. 7-15.
133. McCarthy, J.F. and J.M. Zachara, *Subsurface transport of contaminants*. *Environmental Science & Technology*, 1989. **23**(5): p. 496-502.
134. Smith, P.A. and C. Degueldre, *Colloid-facilitated transport of radionuclides through fractured media*. *Journal of contaminant hydrology*, 1993. **13**(1): p. 143-166.
135. Kersting, A.B., et al., *Migration of plutonium in ground water at the Nevada Test Site*. *Nature*, 1999. **397**(6714): p. 56-59.
136. Xie, J., et al., *Colloid-associated plutonium aged at room temperature: evaluating its transport velocity in saturated coarse-grained granites*. *Journal of contaminant hydrology*, 2015. **172**: p. 24-32.
137. Xie, J., et al., *Insights into transport velocity of colloid-associated plutonium relative to tritium in porous media*. *Scientific reports*, 2014. **4**.
138. Xie, J., et al., *Trace-level plutonium (IV) polymer stability and its transport in coarse-grained granites*. *Chemical Geology*, 2015. **398**: p. 1-10.
139. Grindrod, P., *The impact of colloids on the migration and dispersal of radionuclides within fractured rock*. *Journal of contaminant hydrology*, 1993. **13**(1): p. 167-181.

140. Kurosawa, S., et al., *Model analysis of the colloid and radionuclide retardation experiment at the Grimsel Test Site*. Journal of colloid and interface science, 2006. **298**(1): p. 467-475.
141. Jen, C.-P. and S.-H. Li, *Effects of hydrodynamic chromatography on colloid-facilitated migration of radionuclides in the fractured rock*. Waste Management, 2001. **21**(6): p. 499-509.
142. Malkovsky, V.I. and A.A. Pek, *Effect of elevated velocity of particles in groundwater flow and its role in colloid-facilitated transport of radionuclides in underground medium*. Transport in porous media, 2009. **78**(2): p. 277-294.
143. Li, S.-H., H.-T. Yang, and C.-P. Jen, *Modeling of colloid transport mechanisms facilitating migration of radionuclides in fractured media*. Nuclear technology, 2004. **148**(3): p. 358-368.
144. Li, S.-H. and C.-P. Jen, *Modeling of hydrodynamic chromatography for colloid migration in fractured rock*. Nuclear technology, 2001. **133**(2): p. 253-263.
145. Albarran, N., et al., *Analysis of latex, gold and smectite colloid transport and retention in artificial fractures in crystalline rock*. Colloids and Surfaces A: Physicochemical and Engineering Aspects, 2013. **435**: p. 115-126.
146. Auset, M. and A.A. Keller, *Pore-scale processes that control dispersion of colloids in saturated porous media*. Water Resources Research, 2004. **40**(3).
147. Keller, A.A., S. Sirivithayapakorn, and C.V. Chrysikopoulos, *Early breakthrough of colloids and bacteriophage MS2 in a water-saturated sand column*. Water Resources Research, 2004. **40**(8).
148. Small, H., F.L. Saunders, and J. Solc, *Hydrodynamic chromatography a new approach to particle size analysis*. Advances in Colloid and Interface Science, 1976. **6**(4): p. 237-266.
149. de Marsily, G., *Quantitative hydrogeology; groundwater hydrology for engineers*. Academic Press, New York, NY, 1986.
150. Keller, A.A. and M. Auset, *A review of visualization techniques of biocolloid transport processes at the pore scale under saturated and unsaturated conditions*. Advances in Water Resources, 2007. **30**(6): p. 1392-1407.
151. Scheibe, T.D. and B.D. Wood, *A particle-based model of size or anion exclusion with application to microbial transport in porous media*. Water resources research, 2003. **39**(4).
152. Dong, H., et al., *Relative dominance of physical versus chemical effects on the transport of adhesion-deficient bacteria in intact cores from South Oyster, Virginia*. Environmental science & technology, 2002. **36**(5): p. 891-900.
153. Mitzel, M.R. and N. Tufenkji, *Transport of industrial PVP-stabilized silver nanoparticles in saturated quartz sand coated with Pseudomonas aeruginosa PAO1 biofilm of variable age*. Environmental science & technology, 2014. **48**(5): p. 2715-2723.
154. Sagee, O., I. Dror, and B. Berkowitz, *Transport of silver nanoparticles (AgNPs) in soil*. Chemosphere, 2012. **88**(5): p. 670-675.
155. Solovitch, N., et al., *Concurrent aggregation and deposition of TiO<sub>2</sub> nanoparticles in a sandy porous media*. Environmental science & technology, 2010. **44**(13): p. 4897-4902.
156. Laumann, S., et al., *Carbonate minerals in porous media decrease mobility of polyacrylic acid modified zero-valent iron nanoparticles used for groundwater remediation*. Environmental Pollution, 2013. **179**: p. 53-60.

157. Jaisi, D.P. and M. Elimelech, *Single-Walled Carbon Nanotubes Exhibit Limited Transport in Soil Columns*. Environmental Science & Technology, 2009. **43**(24): p. 9161-9166.
158. Golmohamadi, M., et al., *The role of charge on the diffusion of solutes and nanoparticles (silicon nanocrystals, nTiO<sub>2</sub>, nAu) in a biofilm*. Environmental Chemistry, 2013. **10**(1): p. 34-41.
159. Therezien, M., A. Thill, and M.R. Wiesner, *Importance of heterogeneous aggregation for NP fate in natural and engineered systems*. Science of The Total Environment, 2014. **485**: p. 309-318.
160. Hotze, E.M., T. Phenrat, and G.V. Lowry, *Nanoparticle Aggregation: Challenges to Understanding Transport and Reactivity in the Environment*. J. Environ. Qual. , 2010. **39**: p. 1909–1924.
161. Kim, H.-J., et al., *Effect of kaolinite, silica fines and pH on transport of polymer-modified zero valent iron nano-particles in heterogeneous porous media*. Journal of Colloid and Interface Science, 2012. **370**(1): p. 1-10.
162. He, F., et al., *Transport of carboxymethyl cellulose stabilized iron nanoparticles in porous media: Column experiments and modeling*. Journal of Colloid and Interface Science, 2009. **334**(1): p. 96-102.
163. Prieve, D.C. and P.M. Hoysan, *Role of colloidal forces in hydrodynamic chromatography*. Journal of Colloid and Interface Science, 1978. **64**(2): p. 201-213.
164. Goldberg, E., et al., *Critical assessment of models for transport of engineered nanoparticles in saturated porous media*. Environmental science & technology, 2014. **48**(21): p. 12732-12741.
165. Torkzaban, S., et al., *Colloid release and clogging in porous media: Effects of solution ionic strength and flow velocity*. Journal of contaminant hydrology, 2015. **181**: p. 161-171.
166. Shapiro, A.A. and P.G. Bedrikovetsky, *A stochastic theory for deep bed filtration accounting for dispersion and size distributions*. Physica A: Statistical Mechanics and its Applications, 2010. **389**(13): p. 2473-2494.
167. You, Z., P. Bedrikovetsky, and L. Kuzmina. *Exact solution for long-term size exclusion suspension-colloidal transport in porous media*. 2013. Hindawi Publishing Corporation.
168. Sen, T.K. and K.C. Khilar, *Review on subsurface colloids and colloid-associated contaminant transport in saturated porous media*. Advances in colloid and interface science, 2006. **119**(2): p. 71-96.
169. Harter, T., S. Wagner, and E.R. Atwill, *Colloid transport and filtration of Cryptosporidium parvum in sandy soils and aquifer sediments*. Environmental science & technology, 2000. **34**(1): p. 62-70.
170. Chrysikopoulos, C.V. and V.E. Katzourakis, *Colloid particle size-dependent dispersivity*. Water Resources Research, 2015.
171. Abdel-Salam, A. and C.V. Chrysikopoulos, *Modeling of colloid and colloid-facilitated contaminant transport in a two-dimensional fracture with spatially variable aperture*. Transport in porous media, 1995. **20**(3): p. 197-221.
172. Schijven, J.K. and S.M. Hassanizadeh, *Removal of viruses by soil passage: Overview of modeling, processes, and parameters*. Crit. Rev. Environ. Sci. Technol., 2000. **30**: p. 49 – 127.

173. Wang, Y., S.A. Bradford, and J. Šimůnek, *Transport and fate of microorganisms in soils with preferential flow under different solution chemistry conditions*. Water Resources Research, 2013. **49**(5): p. 2424-2436.
174. Ryan, J.N. and M. Elimelech, *Colloid mobilization and transport in groundwater*. Colloids and Surfaces A, 1996. **107**: p. 1-56.
175. Ginn, T.R., *A brief review of bacterial transport in natural porous media*. 1995, Pacific Northwest Lab., Richland, WA (United States).
176. Ginn, T.R., *A travel time approach to exclusion on transport in porous media*. Water resources research, 2002. **38**(4): p. 12-1.
177. Grolimund, D., et al., *Transport of in Situ Mobilized Colloidal Particles in Packed Soil Columns*. Environmental Science & Technology, 1998. **32**(22): p. 3562-3569.
178. Fallah, H., et al., *Size Exclusion Mechanism, Suspension Flow through Porous Medium*. International Journal of Modern Nonlinear Theory and Application, 2012. **1**(04): p. 113.
179. James, S.C. and C.V. Chrysikopoulos, *Effective velocity and effective dispersion coefficient for finite-sized particles flowing in a uniform fracture*. Journal of colloid and interface science, 2003. **263**(1): p. 288-295.
180. Ginn, T.R., *Comment on "Stochastic analysis of virus transport in aquifers," by Linda L. Campbell Rehmann, Claire Welty, and Ronald W. Harvey*. Water Resources Research, 2000. **36**(7): p. 1981-1982.
181. Zheng, Q., S.E. Dickson, and Y. Guo, *Differential transport and dispersion of colloids relative to solutes in single fractures*. Journal of colloid and interface science, 2009. **339**(1): p. 140-151.
182. Weisbrod, N., et al., *Virus transport in a discrete fracture*. Water research, 2013. **47**(5): p. 1888-1898.
183. Tufenkji, N. and M. Elimelech, *Correlation equation for predicting single-collector efficiency in physicochemical filtration in saturated porous media*. Environmental Science & Technology, 2004. **38**(2): p. 529-536.
184. Chrysikopoulos, C.V. and V.I. Syngouna, *Effect of gravity on colloid transport through water-saturated columns packed with glass beads: Modeling and experiments*. Environmental science & technology, 2014. **48**(12): p. 6805-6813.
185. DiMarzio, E.A. and C.M. Guttman, *Separation by flow*. Journal of Polymer Science Part B: Polymer Letters, 1969. **7**(4): p. 267-272.
186. DiMarzio, E.A. and C.M. Guttman, *Separation by Flow*. Macromolecules, 1970. **3**(2): p. 131-146.
187. Cox, R.G. and S.K. Hsu, *The lateral migration of solid particles in a laminar flow near a plane*. International journal of multiphase flow, 1977. **3**(3): p. 201-222.
188. Segre, G. and A. Silberberg, *Behaviour of macroscopic rigid spheres in Poiseuille flow Part 2. Experimental results and interpretation*. Journal of fluid mechanics, 1962. **14**(01): p. 136-157.
189. Cox, R.G. and H. Brenner, *The lateral migration of solid particles in Poiseuille flow—I Theory*. Chemical Engineering Science, 1968. **23**(2): p. 147-173.
190. Segre, G. and A. Silberberg, *Behaviour of macroscopic rigid spheres in Poiseuille flow Part 1. Determination of local concentration by statistical analysis of particle passages through crossed light beams*. Journal of Fluid Mechanics, 1962. **14**(01): p. 115-135.
191. Krupp, H.K., J.W. Biggar, and D.R. Nielsen, *Relative flow rates of salt and water in soil*. Soil Science Society of America Journal, 1972. **36**(3): p. 412-417.

192. Van Genuchten, M.T., *Non-equilibrium transport parameters from miscible displacement experiments*. 1981.
193. Chrysikopoulos, C.V. and A. Abdel-Salam, *Modeling colloid transport and deposition in saturated fractures*. *Colloids and Surfaces A: Physicochemical and Engineering Aspects*, 1997. **121**(2): p. 189-202.
194. Jacobson, M.Z., *Fundamentals of atmospheric modeling*. 2005: Cambridge university press.

## Appendix B

### 9 Summary of transport column experiments and their continuum modelling approaches

**Table B1** Summary of the NP transport studies experimental conditions and outcomes together with the major observed phenomena, the shapes of the breakthrough curve and residual concentration profile, and types of the applied continuum model.

No.	NP Type	Coating and free polymer	Ionic strength (IS) species	pH	IS (mM)	C <sub>0</sub> (mg/L)	dp/dg* — —	C/C <sub>0</sub> (%)	BTC plateau shape**	RP shape	Major underlying phenomena	Model Type(s) used	Ref.
1	AgNP	citrate; polyvinylpyrrolidone; branched polyethyleneimine	NaNO <sub>3</sub>	7	5	10	2.7E-05 3.4E-05	20 — 100	flat	NM	physicochemical filtration; straining following aggregation	ix without the term K <sub>det</sub>	El Badawy et al. [1]
2	AgNP	proteinate capping with bovine serum albumin	MgSO <sub>4</sub>	6.7	0—50	50	9.1E-05 2.8E-04	0 75.7	ascending	NM	straining	ix	Ren and Smith [2]

No.	NP Type	Coating and free polymer	Ionic strength (IS) species	pH	IS (mM)	C <sub>0</sub> (mg/L)	dp/dg <sup>*</sup>	C/C <sub>0</sub> (%)	BTC plateau shape <sup>**</sup>	RP shape	Major underlying phenomena	Model Type(s) used	Ref.
3	AgNP	two nonionic surfactants: polyoxyethylene glycerol trioleate and polyoxyethylene (20) sorbitan mono-laurate	KNO <sub>3</sub>	6.5	1—10	1—10	8.6E-05	3.4 — 64.3	ascending	hyper-exponential	significant retardation	xii without the term K <sub>det</sub>	Liang et al. [3]
4	AgNP	Polyoxyethylene Glycerol Trioleate and Polyoxyethylene (20) Sorbitan mono-Laurat (Tween 20)	KNO <sub>3</sub>	6.5	1—5	1—10	7.4E-05— 1.9E-04	4.5 — 45.6	ascending	uniform, hyper-exponential or non-monotonic shapes	irreversible interactions in a primary minimum due to microscopic heterogeneity	xii without the term K <sub>det</sub>	Liang et al. [4]
5	AgNP	surfactant, polyoxyethylene glycerol trioleate and polyoxyethylene (20) sorbitan mono-laurat (Tween 20)	NaNO <sub>3</sub> ; Ca(NO <sub>3</sub> ) <sub>2</sub> ; H <sub>2</sub> O	5.9— 6.5	0—50	60	7E-05— 5.8E-04	0— 100	ascending	non-monotonic	size selective filtration; reversible deposition of the AgNP due to secondary minimum interactions.	ix; ix without K <sub>det</sub> ; xii; i	Braun et al. [5]

No.	NP Type	Coating and free polymer	Ionic strength (IS) species	pH	IS (mM)	C <sub>0</sub> (mg/L)	dp/dg <sup>*</sup>	C/C <sub>0</sub> (%)	BTC plateau shape <sup>**</sup>	RP shape	Major underlying phenomena	Model Type(s) used	Ref.
6	AgNP	coating: PVP; free polymer: HA	KNO <sub>3</sub> ; Ca(NO <sub>3</sub> ) <sub>2</sub>	5.8	0.5—100	10	5E-05—4.3E-03	0—88.3	ascending	non-monotonic	Increased aggregation of PVP- AgNP in presence of Ca <sup>2+</sup>	xii without the term K <sub>det</sub>	Wang et al. [6]
7	AgNP	PVP	KNO <sub>3</sub> ; Ca(NO <sub>3</sub> ) <sub>2</sub>	5.4—6.1	0.1—10	10	4.5E-05—2.5E-04	0.4—36.5	ascending	hyper-exponential or non-monotonic	significant retardation, aggregation, irreversible deposition	xii without the term K <sub>det</sub> ; xiv without the term K <sub>det1</sub> ; xiv without the term K <sub>det1</sub> and K <sub>det2</sub>	Wang et al. [7]
8	AgNP	PVP	KNO <sub>3</sub>	4.5—7.7	0.9—2.6	1.7	1.3E-04—3.6E-04	0.16—8.84	NC	depth-dependent	straining following heteroaggregation, size-exclusion	iv without the term K <sub>det2</sub>	Cornelis et al. [8]
9	AgNP	polyoxyethylene glycerol triolate and polyoxyethylene (20) sorbitan mono-laurat, 4%	H <sub>2</sub> O; NaNO <sub>3</sub> ; Ca(NO <sub>3</sub> ) <sub>2</sub>	7.3	0—10	474—800	2.3E-04—2.8E-04	43—100	ascending and rather flat	NM	blocking; physicochemical retention; aggregation; and probably straining	ix without the term K <sub>det</sub> ; i; ii;	Neukum et al. [9]

No.	NP Type	Coating and free polymer	Ionic strength (IS) species	pH	IS (mM)	C <sub>0</sub> (mg/L)	dp/dg* —	C/C <sub>0</sub> (%)	BTC plateau shape**	RP shape	Major underlying phenomena	Model Type(s) used	Ref.
10	NZVI	PAA	NaClO <sub>4</sub>	8.6	1	200	3.1E-04— 3.5E-04	18 —	continuous; flat	NM	aggregation; irreversible deposition	i	Laumann et al. [10]
11	Iron oxide NP	PAA	NC	NC	NC	20— 500	2.7E-05— 4.7E-05	88 —	continuous; flat	NM	irreversible deposition	i	Golzar et al., [11]
12	NZVI	CMC	NC	8.5	30— 160	100— 2500	5.4E-05— 1.3E-04	80	continuous; descending at low velocity	NM	aggregation and settling in the feeding stock dispersion	i with modified boundary condition	Kocur et al., [12]
13	NZVI	Pure PAA-nZVI; NOM; Lignin sulfonate; CMC; HA	NaHCO <sub>3</sub>	7.9— 8.3	1	200	1.6E-03— 1.9E-03	22 —	continuous; flat	NM	irreversible deposition	i	Laumann et al. [13]
14	NZVI	CMC	KCl	8.1	15	200	1.6E-05— 5.8E-05	69 —	symmetric, flat	NM	filtration due to Brownian diffusion and gravitational sedimentation	v	He et al. [14]

No.	NP Type	Coating and free polymer	Ionic strength (IS) species	pH	IS (mM)	C <sub>0</sub> (mg/L)	dp/dg* — —	C/C <sub>0</sub> (%)	BTC plateau shape**	RP shape	Major underlying phenomena	Model Type(s) used	Ref.
15	NZVI	CMC	NaHCO <sub>3</sub>	7.4	0.1	85— 1700	2.2E-04— 1.2E-03	55 — 97	predominately ascending	hyper-exponential	Straining; detachment	xi without $\psi_b$ and $K_{det2}$	Raychou dhury et al. [15]
16	NZVI	dispersed in xanthan solution	NC	NC	0—13	20000	1.0E-04	86 — 90	flat	hyper-exponential	attachment, detachment (tailing), blocking, ripening, and clogging	xv	Tosco et al. [16]
17	NZVI	Cu	Natural groundwater	7.2	40	8000	8.4E-05— 8.7E-05	61 — 90	ascending at low concentration (2 g/L), descending at middle concentration (5 g/L), and multiple peaks and tailing at very high concentrations (8 and 12 g/L)	NC	clogging after ripening	xv	Hosseini and Tosco [17]

No.	NP Type	Coating and free polymer	Ionic strength (IS) species	pH	IS (mM)	C <sub>0</sub> (mg/L)	dp/dg <sup>*</sup>	C/C <sub>0</sub> (%)	BTC plateau shape <sup>**</sup>	RP shape	Major underlying phenomena	Model Type(s) used	Ref.
18	NZVI	poly(styrene sulfonate) (PSS)	5 mM NaCl 5 mM NaHCO <sub>3</sub>	8	10	30—6000	1.6E-04—2.1E-3	61.5—97	flat	NM	agglomeration and subsequent irreversible deposition of agglomerates; disaggregation identified by the model.	ii; vii	Babakha ni et al. [18] and Phenrat et al. [19]
19	NZVI	CMC	NaHCO <sub>3</sub>	7.4	0.1	70—725	5.1E-04	55—72	continuous; ascending	NM	aggregation, detachment	vii	Babakha ni et al. [18] and Raychou dhury et al. [20]
20	HAP	Cu coated and humic acid as free polymer	NaCl; CaCl <sub>2</sub>	5.7—5.9	0—100	200	1.7E-04—2.3E-04	11—89	rather flat and ascending at the highest IS	hyper-exponential	aggregation	xi without considering $\psi_b$ and $K_{det2}$	Wang et al. [21]
21	HAP	Cu	NaCl	6.2—9	0.1	200	1.7E-04	32—90	flat at various pH and water velocity but	hyper-exponential	retardation; blocking	xi without $\psi_b$ ; xi	Wang et al. [22]

No.	NP Type	Coating and free polymer	Ionic strength (IS) species	pH	IS (mM)	C <sub>0</sub> (mg/L)	dp/dg*	C/C <sub>0</sub> (%)	BTC plateau shape**	RP shape	Major underlying phenomena	Model Type(s) used	Ref.
									ascending by increasing the amount of Fe coating on the sand.			without K <sub>det</sub>	
22	HAP	Alizarin red S (ARS)-labelled (coated) NP with humic acid as free polymer	NaCl	6—10.5	0.1	100	5E-04—6E-04	30.5—78.8	flat at various concentrations of HA, but descending at zero concentration of HA	hyper-exponential	blocking	xi without $\psi_b$ ; xi without K <sub>det</sub>	Wang et al. [23]
23	HAP	Alizarin red S (ARS)-labelled (coated) NP with humic acid as free polymer	NaCl	7.2	0.1—50	100	4E-04—1.1E-03	7.8—78.8	flat	hyper-exponential	aggregation	xi without $\psi_b$ and K <sub>det2</sub>	Wang et al. [24]
24	HAP	Alizarin red S (ARS)-labelled (coated) NP: in presence of SDBS and CTAB	NaCl	7	0.1	100	2.2E-04	0.8—78.6	descending	hyper-exponential	aggregation; ripening; straining; and size selective retention	xiii	Wang et al. [25]

No.	NP Type	Coating and free polymer	Ionic strength (IS) species	pH	IS (mM)	C <sub>0</sub> (mg/L)	dp/dg*	C/C <sub>0</sub> (%)	BTC plateau shape**	RP shape	Major underlying phenomena	Model Type(s) used	Ref.
25	GO	NA	NaCl	5.1	20—28	5—25	6E-04— 3.9E-03	0.2 — 56.9	ascending	exponential to uniform	aggregation; blocking	ix without K <sub>det</sub>	Sun et al. [26]
26	GO	NA	NaCl	6	1—100	5	1.3E-03	3.4 — 93.5	ascending	NM	blocking	ix without K <sub>det</sub>	Feriancikova and Xu [27]
27	GO	NA	NaCl	NC	1—100	12	5.5E-03	3— 99.4	ascending	NM	aggregation; blocking	i; ix without K <sub>det</sub>	Liu et al. [28]
28	graphene	SDBS and CTAB surfactants	DI water	NC	0.01	14— 16.5	9.1E-04— 9.9E-04	4.1 — 90.6	flat	NM	attachment	i	Liu et al. [29]
29	GO	NA	NaCl	7.1	50— 200	20	3E-03— 8.2E-3	22 — 75	ascending	NM	straining due to concurrent agglomeration; blocking	xii	Fan et al. [30]
30	graphene	Carboxyl-functionalized	NC	5.6— 8.3	NC	12	1.1E-03	88.4 — 99.8	flat to slightly ascending	NM	attachment	i	Liu et al. [31]

No.	NP Type	Coating and free polymer	Ionic strength (IS) species	pH	IS (mM)	C <sub>0</sub> (mg/L)	dp/dg <sup>*</sup>	C/C <sub>0</sub> (%)	BTC plateau shape <sup>**</sup>	RP shape	Major underlying phenomena	Model Type(s) used	Ref.
31	GO	NA	various Ca <sup>2+</sup> /N <sup>+</sup> ratios: 0; 0.15; 0.3; 0.6; 1; ∞	7	1—10	20	2.6E-03— 8.7E-03	1.8 — 80	ascending	NM	straining following agglomeration; blocking	xii	Fan et al. [32]
32	GO	NA	DI water; NaCl	4.8— 9	0—50	19.2— 21.7	9E-04— 2.5E-03	10.7 — 95.9	flat at intermediate IS and descending at high IS	Relative flat low and moderate IS, elevated from inlet point at high IS (50 mM)	clogging and straining following agglomeration; blocking	xi without K <sub>det</sub>	Qi et al. [33]
33	GO	NA	NaCl	7.2	1—50	20	5.1E-04— 6.6E-04	24 — 99.9	ascending	NC	aggregation; straining; blocking	xi with ψ <sub>x</sub> =1, without K <sub>det2</sub> , and	He et al. [34]

No.	NP Type	Coating and free polymer	Ionic strength (IS) species	pH	IS (mM)	C <sub>0</sub> (mg/L)	dp/dg *	C/C <sub>0</sub> (%)	BTC plateau shape **	RP shape	Major underlying phenomena	Model Type(s) used	Ref.
												by shifting the indexes 1 and 2	
34	GO	NA	DI water; NaCl; CaCl <sub>2</sub>	4—9	0—50	19.4—21.4	7.7E-04—3.8E-03	20.8—100	flat (in sand) or ascending (in soil) at high NaCl concentration, descending at high CaCl <sub>2</sub> concentration in soil	NM	aggregation; straining; blocking	xi without K <sub>det</sub> ; xvi	Qi et al. [35]
35	CeO <sub>2</sub>	HA	NaCl	7—10	1—100	200	6E-04—1.4E-03	9.9—74.8	flat	NM	Ripening in absence of HA due to aggregation	i	Lv et al. [36]
36	CeO <sub>2</sub>	NA	NaCl	3—9	1—100	10—50	2.1E-04	1.3—96.9	ascending	NM	aggregation; straining; blocking	ix	Li et al. [37]
37	TiO <sub>2</sub> , rutile	NA	KCl and KOH	10	5	50	1.7E-04	5—87	ascending	NM	blocking	ix without K <sub>det</sub>	Toloni et al. [38]

No.	NP Type	Coating and free polymer	Ionic strength (IS) species	pH	IS (mM)	C <sub>0</sub> (mg/L)	dp/dg*	C/C <sub>0</sub> (%)	BTC plateau shape**	RP shape	Major underlying phenomena	Model Type(s) used	Ref.
38	TiO <sub>2</sub> , anatase	NA	NaCl	2.6—9.6	0.1—50	35	1.2E-03—9.8E-03	0—94.1	continuous, flat at intermediate IS, ascending at high IS	NM	straining; aggregation; detachment	xi with $\psi_b=1$ and without $K_{det2}$	Fang et al. [39]
39	ZnO	NA	NaNO <sub>3</sub>	8.5	1—50	34—430	1.3E-03—9E-03	2.1—81.2	continuous, ascending	hyper-exponential	clogging; straining; aggregation; detachment; blocking; irreversible attachment	xi with $\psi_x$ , $\psi_{b1} = \psi_x$ ; and without $K_{det2}$	Sun et al. [40]
40, 41	ZnO	NA	NaCl; CaCl <sub>2</sub>	8	0.1—20	5	6E-04—1.2E-03	14.6—82.7	flat at low IS, descending at high IS; flat in presence of NOM, descending in absence of NOM at high IS	hyper-exponential	pore plugging; straining following the concurrent aggregation; detachment; blocking; irreversible attachment; and ripening	ii	Jiang et al. [41] and Jiang et al. [42]

No.	NP Type	Coating and free polymer	Ionic strength (IS) species	pH	IS (mM)	C <sub>0</sub> (mg/L)	dp/dg <sup>*</sup>	C/C <sub>0</sub> (%)	BTC plateau shape <sup>**</sup>	RP shape	Major underlying phenomena	Model Type(s) used	Ref.
42	ZnO	NA	NaCl; CaCl <sub>2</sub>	8	0.1—5	5	6E-04— 9E-04	11.3 — 79	flat in all cases	hyper-exponential	straining following the concurrent aggregation	ii	Jiang et al. [43]
43	QD-CdSe/ZnS	COOHP; PAA-octylamine (PAA-OA); linoleic acid (LA)	NaCl	5— 9.5	0—30	1.6E-03— 2.3E-03	5e-05— 2E-04	5.9 — 100	flat or spike like with retardation	NM	retardation	ix without K <sub>det</sub>	Wang et al. [44]
44	QD, CdSe/CdZnS	amphiphilic polymer, PAA-OA	NaCl	7	3	0.0016	8.7E-05— 2.5E-04	0.4 — 75.3	flat to ascending and spike like	non-monotonic	blocking by polymer	ix without K <sub>det</sub>	Wang et al. [45]
45	CdSe QDs	nonionic ethoxylated alcohol surfactant-Neodol	synthetic seawater	8.5	550— 1000	0.86	6.2E-05	91 — 96	flat	NM	retardation at elevated temperatures	v without K <sub>att</sub>	Kini et al. [46]
46	CdTe QDs	NA	NaCl; CaCl <sub>2</sub>	8	2—100	44.7	2E-04— 3E-04	5— 98	flat in NaCl solution and ascending in CaCl <sub>2</sub> solution	NM	blocking; release	ix without K <sub>det</sub>	Torkzaban et al. [47]
47	CML	NA	NaCl; CaCl <sub>2</sub>	7	0.5— 60	3.13— 25.0	2E-04— 4E-04	30 — 100	ascending, delayed	NM	blocking; delay	x	Sasidharan et al. [48]

No.	NP Type	Coating and free polymer	Ionic strength (IS) species	pH	IS (mM)	C <sub>0</sub> (mg/L)	d <sub>p</sub> /d <sub>g</sub> <sup>*</sup>	C/C <sub>0</sub> (%)	BTC plateau shape <sup>**</sup>	RP shape	Major underlying phenomena	Model Type(s) used	Ref.
48	Al <sub>2</sub> O <sub>3</sub>	NA	NaCl	4.8	0—100	50— 400	3E-04— 1.3E-03	52.5 — 95.9	flat	NM	aggregation; blocking	x with ψ <sub>b2</sub> =1	Rahman et al. [49] and Rahman et al. [50]
49	TiO <sub>2</sub> , anatase	NA	NaCl	4	1.1	100— 1000	8E-05— 7E-04	96.1 — 98.7	ascending	NM	irreversible deposition; blocking	ix without K <sub>det</sub>	Saiers et al. [51]
50	CdTe QDs and CML	NA	NaCl; CaCl <sub>2</sub>	8	0.5— 100	40.2— 250	2E-04— 7E-04	1— 99	ascending	NM	blocking	ix without detachment	Torkzaba n et al. [52]

<sup>\*</sup>d<sub>p</sub>/d<sub>g</sub> is calculated based on the ratio of the average hydrodynamic diameter to the average grain size which might not be according to the what the authors reported, i.e., they might have calculated d<sub>p</sub>/d<sub>g</sub> based on other types of size measurement techniques than hydrodynamic diameter used here; <sup>\*\*</sup>BTC plateau shape mostly considered at intermediate or favourable retention condition.. NM: not measured; NA: not applicable; NC: not clear; PVP: polyvinylpyrrolidone; CMC: carboxy-methyl-cellulose; PAA: Polyacrylic acid; SDBS: anionic sodium dodecyl benzene sulfonate; CTAB: cationic cetyltrimethylammonium bromide; COOHP: carboxyl derivatized polymer.

## 9.1 References

1. El Badawy, A.M., et al., *Key factors controlling the transport of silver nanoparticles in porous media*. Environmental science & technology, 2013. **47**(9): p. 4039-4045.
2. Ren, D. and J.A. Smith, *Protein-capped silver nanoparticle transport in water-saturated sand*. Journal of Environmental Engineering, 2012. **139**(6): p. 781-787.
3. Liang, Y., et al., *Retention and remobilization of stabilized silver nanoparticles in an undisturbed loamy sand soil*. Environmental science & technology, 2013. **47**(21): p. 12229-12237.
4. Liang, Y., et al., *Sensitivity of the transport and retention of stabilized silver nanoparticles to physicochemical factors*. water research, 2013. **47**(7): p. 2572-2582.
5. Braun, A., et al., *Transport and deposition of stabilized engineered silver nanoparticles in water saturated loamy sand and silty loam*. Science of The Total Environment, 2014.
6. Wang, D., et al., *Transport and Retention of Polyvinylpyrrolidone-Coated Silver Nanoparticles in Natural Soils*. Vadose Zone J., 2015.
7. Wang, D., et al., *Hyperexponential and nonmonotonic retention of polyvinylpyrrolidone-coated silver nanoparticles in an Ultisol*. Journal of contaminant hydrology, 2014. **164**: p. 35-48.
8. Cornelis, G., et al., *Transport of silver nanoparticles in saturated columns of natural soils*. Science of the Total Environment, 2013. **463**: p. 120-130.
9. Neukum, C., A. Braun, and R. Azzam, *Transport of engineered silver (Ag) nanoparticles through partially fractured sandstones*. Journal of contaminant hydrology, 2014. **164**: p. 181-192.
10. Laumann, S., et al., *Carbonate minerals in porous media decrease mobility of polyacrylic acid modified zero-valent iron nanoparticles used for groundwater remediation*. Environmental Pollution, 2013. **179**: p. 53-60.
11. Golzar, M., S.F. Saghavani, and M. Azhdari Moghaddam, *Experimental Study and Numerical Solution of Poly Acrylic Acid Supported Magnetite Nanoparticles Transport in a One-Dimensional Porous Media*. Advances in Materials Science and Engineering, 2014. **2014**.
12. Kocur, C.M., D.M. O'Carroll, and B.E. Sleep, *Impact of nZVI stability on mobility in porous media*. Journal of Contaminant Hydrology, 2013. **145**(0): p. 17-25.
13. Laumann, S., V. Micić, and T. Hofmann, *Mobility enhancement of nanoscale zero-valent iron in carbonate porous media through co-injection of polyelectrolytes*. Water research, 2014. **50**: p. 70-79.

14. He, F., et al., *Transport of carboxymethyl cellulose stabilized iron nanoparticles in porous media: Column experiments and modeling*. Journal of Colloid and Interface Science, 2009. **334**(1): p. 96-102.
15. Raychoudhury, T., N. Tufenkji, and S. Ghoshal, *Straining of Polyelectrolyte-Stabilized Nanoscale Zero Valent Iron Particles during Transport through Granular Porous Media*. Water Research, 2014. **50**(0): p. 80-90.
16. Tosco, T. and R. Sethi, *Transport of non-Newtonian suspensions of highly concentrated micro-and nanoscale iron particles in porous media: a modeling approach*. Environmental Science & Technology, 2010. **44**(23): p. 9062-9068.
17. Hosseini, S.M. and T. Tosco, *Transport and retention of high concentrated nano-Fe/Cu particles through highly flow-rated packed sand column*. Water Research, 2013. **47**(1): p. 326-338.
18. Babakhani, P., et al., *Modified MODFLOW-based model for simulating the agglomeration and transport of polymer-modified Fe nanoparticles in saturated porous media*. Environ Sci Pollut Res, 1-20, doi:10.1007/s11356-015-5193-0, 2015.
19. Phenrat, T., et al., *Particle size distribution, concentration, and magnetic attraction affect transport of polymer-modified FeO nanoparticles in sand columns*. Environ. Sci. Technol., 2009. **43**(13): p. 5079-5085.
20. Raychoudhury, T., N. Tufenkji, and S. Ghoshal, *Aggregation and deposition kinetics of carboxymethyl cellulose-modified zero-valent iron nanoparticles in porous media*. Water Research, 2012. **46**(6): p. 1735-1744.
21. Wang, D., et al., *Facilitated transport of Cu with hydroxyapatite nanoparticles in saturated sand: Effects of solution ionic strength and composition*. water research, 2011. **45**(18): p. 5905-5915.
22. Wang, D., et al., *Facilitated transport of copper with hydroxyapatite nanoparticles in saturated sand*. Soil Science Society of America Journal, 2012. **76**(2): p. 375-388.
23. Wang, D., et al., *Humic acid facilitates the transport of ARS-labeled hydroxyapatite nanoparticles in iron oxyhydroxide-coated sand*. Environmental science & technology, 2012. **46**(5): p. 2738-2745.
24. Wang, D., et al., *Transport of ARS-labeled hydroxyapatite nanoparticles in saturated granular media is influenced by surface charge variability even in the presence of humic acid*. Journal of hazardous materials, 2012. **229**: p. 170-176.
25. Wang, D., et al., *Transport of fluorescently labeled hydroxyapatite nanoparticles in saturated granular media at environmentally relevant concentrations of surfactants*. Colloids and Surfaces A: Physicochemical and Engineering Aspects, 2014. **457**: p. 58-66.
26. Sun, Y., et al., *Transport, retention, and size perturbation of graphene oxide in saturated porous media: Effects of input concentration and grain size*. Water research, 2015. **68**: p. 24-33.

27. Feriancikova, L. and S. Xu, *Deposition and remobilization of graphene oxide within saturated sand packs*. Journal of hazardous materials, 2012. **235**: p. 194-200.
28. Liu, L., et al., *Deposition and transport of graphene oxide in saturated and unsaturated porous media*. Chemical Engineering Journal, 2013. **229**: p. 444-449.
29. Liu, L., et al., *Effects of surfactant type and concentration on graphene retention and transport in saturated porous media*. Chemical Engineering Journal, 2015. **262**: p. 1187-1191.
30. Fan, W., et al., *Effects of surfactants on graphene oxide nanoparticles transport in saturated porous media*. Journal of Environmental Sciences, 2015.
31. Liu, L., et al., *Effects of pH and surface metal oxyhydroxides on deposition and transport of carboxyl-functionalized graphene in saturated porous media*. Journal of nanoparticle research, 2013. **15**(11): p. 1-8.
32. Fan, W., et al., *Transport of graphene oxide in saturated porous media: Effect of cation composition in mixed Na–Ca electrolyte systems*. Science of The Total Environment, 2015. **511**: p. 509-515.
33. Qi, Z., et al., *Factors controlling transport of graphene oxide nanoparticles in saturated sand columns*. Environmental toxicology and chemistry, 2014. **33**(5): p. 998-1004.
34. He, J.-Z., et al., *Biofilms and extracellular polymeric substances mediate the transport of graphene oxide nanoparticles in saturated porous media*. Journal of hazardous materials, 2015. **300**: p. 467-474.
35. Qi, Z., L. Zhang, and W. Chen, *Transport of graphene oxide nanoparticles in saturated sandy soil*. Environmental Science: Processes & Impacts, 2014. **16**(10): p. 2268-2277.
36. Lv, X., et al., *Effects of Humic Acid and Solution Chemistry on the Retention and Transport of Cerium Dioxide Nanoparticles in Saturated Porous Media*. Water, Air, & Soil Pollution, 2014. **225**(10): p. 1-9.
37. Li, Z., et al., *Transport and deposition of CeO<sub>2</sub> nanoparticles in water-saturated porous media*. Water research, 2011. **45**(15): p. 4409-4418.
38. Toloni, I., F. Lehmann, and P. Ackerer, *Modeling the effects of water velocity on TiO<sub>2</sub> nanoparticles transport in saturated porous media*. Journal of contaminant hydrology, 2014. **171**: p. 42-48.
39. Fang, J., et al., *Modeling the transport of TiO<sub>2</sub> nanoparticle aggregates in saturated and unsaturated granular media: effects of ionic strength and pH*. water research, 2013. **47**(3): p. 1399-1408.
40. Sun, P., et al., *Distinguishable Transport Behavior of Zinc Oxide Nanoparticles in Silica Sand and Soil Columns*. Science of The Total Environment, 2015. **505**: p. 189-198.

41. Jiang, X., M. Tong, and H. Kim, *Influence of natural organic matter on the transport and deposition of zinc oxide nanoparticles in saturated porous media*. Journal of colloid and interface science, 2012. **386**(1): p. 34-43.
42. Jiang, X., et al., *Transport and deposition of ZnO nanoparticles in saturated porous media*. Colloids and Surfaces A: Physicochemical and Engineering Aspects, 2012. **401**: p. 29-37.
43. Jiang, X., et al., *Initial transport and retention behaviors of ZnO nanoparticles in quartz sand porous media coated with Escherichia coli biofilm*. Environmental Pollution, 2013. **174**: p. 38-49.
44. Wang, Y., et al., *Effect of surface coating composition on quantum dot mobility in porous media*. Journal of nanoparticle research, 2013. **15**(8): p. 1-16.
45. Wang, Y., et al., *Influence of Residual Polymer on Nanoparticle Deposition in Porous Media*. Environmental Science & Technology, 2014. **48**(18): p. 10664-10671.
46. Kini, G.C., et al., *Salt-and temperature-stable quantum dot nanoparticles for porous media flow*. Colloids and Surfaces A: Physicochemical and Engineering Aspects, 2014. **443**: p. 492-500.
47. Torkzaban, S., et al., *Release of Quantum Dot Nanoparticles in Porous Media: Role of Cation Exchange and Aging Time*. Environmental Science & Technology, 2013. **47**(20): p. 11528-11536.
48. Sasidharan, S., et al., *Coupled effects of hydrodynamic and solution chemistry on long-term nanoparticle transport and deposition in saturated porous media*. Colloids and Surfaces A: Physicochemical and Engineering Aspects, 2014. **457**: p. 169-179.
49. Rahman, T., J. George, and H.J. Shipley, *Transport of aluminum oxide nanoparticles in saturated sand: Effects of ionic strength, flow rate, and nanoparticle concentration*. Science of The Total Environment, 2013. **463–464**: p. 565-571.
50. Rahman, T., H. Millwater, and H.J. Shipley, *Modeling and sensitivity analysis on the transport of aluminum oxide nanoparticles in saturated sand: Effects of ionic strength, flow rate, and nanoparticle concentration*. Science of The Total Environment, 2014. **499**: p. 402-412.
51. Saiers, J.E., G.M. Hornberger, and L. Liang, *First-and second-order kinetics approaches for modeling the transport of colloidal particles in porous media*. Water Resources Research, 1994. **30**(9): p. 2499-2506.
52. Torkzaban, S., et al., *Impacts of bridging complexation on the transport of surface-modified nanoparticles in saturated sand*. Journal of contaminant hydrology, 2012. **136**: p. 86-95.

## Appendix C

### 10 Equilibrium vs kinetic terms in continuum models

Incorporation of multiple transport mechanisms in continuum models and their application in complex, realistic domains and scales is not computationally efficient. The use of a partitioning (distribution) coefficient  $K_d$  in NP transport modelling is desirable because it reduces the number of parameters in the attachment/detachment process from two ( $K_{att}$  and  $K_{det}$ ) to one ( $K_d$ ), and more importantly facilitates the application of many analytical solutions and numerical tools for the governing equation [1-4]. However, the use of  $K_d$  nominally requires the assumption of an equilibrium state between the suspended and attached phases which has been recently debated in the context of NP fate and transport [1, 5-7]. Conceptually the equilibrium assumption is invalid since  $K_d$  is physically based on the Gibb's energy and thermodynamic equilibrium assumption, while NP suspensions are thermodynamically unstable [5]. On the other hand, several authors have successfully utilized the concept of  $K_d$  in modelling NP transport, mostly in form of type (v) models (Tables 1.1 and B1) [3, 8-13]. This is also in accordance with numerous experimental studies observing retarded BTCs [11, 14-20]. Retardation factor is related to  $K_d$  as  $R = 1 + \rho_b K_d / \varepsilon$ .

The equilibrium concept is increasingly popular in the context of NP adsorption to other surfaces in quiescent batch experiments [e.g., 21, 22-25]. Petersen et al. [23] obtained linear and nonlinear isotherms, respectively, for the sorption of regular and modified  $^{14}\text{C}$ -labeled multiwalled carbon nanotubes (MWCNTs) onto soil surfaces. Zhao et al. [13] found a linear adsorption isotherm fitted the attachment of GO NP saturated with Na and Ca ions onto the surface of goethite particles. Julich and Gäth [21] compared the sorption of copper oxide (CuO) NP with copper ions ( $\text{Cu}^{2+}$ ) onto soil and found out that the sorptivity of both of them followed the Freundlich isotherm with much stronger sorption obtained for CuO NP compared to  $\text{Cu}^{2+}$ . Abraham et al. [22] investigated the sorptivity of Ag NP onto model and environmental surfaces in

stable and unstable systems and found that the sorption in the stable system followed the nonlinear Langmuir isotherm; however in the unstable system Ag NP sorption did not follow any classical models, suggesting NP aggregation plays a key role in modifying sorption phenomena. Nickel et al. [26] tested whether the international standard guideline, OECD TG 106, for testing of nanomaterials adsorption/desorption, could be applicable for TiO<sub>2</sub> NP or not. The authors found that the guideline was not applicable because concurrent occurrence of agglomeration and adsorption was not accounted for.

While some, like Praetorius et al. [5] and subsequently Cornelis [7] have maintained criticism of the use of  $K_d$  in NP transport studies others (e.g. Dale et al. [1, 6]) suggest that although a theoretically-robust, mechanistic-based approach may perform better for controlled experimental conditions, when the complexity of the model domain and scale increases (i.e. in all environmentally-relevant conditions), more pragmatic approaches which ‘borrow’ entities such as  $K_d$  often turn out to be the more practical, and sometimes the only feasible solution. A fundamental part of the issue regarding the applicability of the equilibrium assumption must be related to the interference caused by co-acting aggregation phenomena in NP attachment to other surfaces. In this section, the application of a type (vii) continuum model [27] is demonstrated to practically test the assumption of linear adsorption (equilibrium), by replacing the first-order, reversible, kinetic-reaction equation (non-equilibrium) attachment/detachment expression with linear adsorption partitioning. Can a one-parameter adsorption model ( $K_d$ ) be a surrogate for the two-parameter attachment/detachment deposition model across a range of scales and system conditions? The type (vii) model separately accounts for: (1) the attachment/detachment process; (2) the agglomeration of particles in the suspended phase; and (3) the irreversible deposition of aggregates. This model is described in detail in [27].

An iteration procedure was developed to optimize the transport parameters related to deposition and agglomeration ( $K_{att}$ ,  $K_{det}$ ,  $\lambda_1$  and  $\lambda_2$ ) against the observed concentration data presented in [27]. In summary, experimentally-observed BTCs which were available in mass concentration were fitted by using WinPEST model [28] in order to estimate model parameters. Internally, the mass concentration is converted to particle number concentration for agglomerating particles while the obtained

parameters, are updated in the iterative procedure. Therefore, Eq. (e) in model type (vii), Table 1.1, is used to calculate the size of aggregates and, subsequently, Eq. (c) is used to calculate the population of aggregates (transformation of the mass concentration to the number particle concentration). Then, these transformed observation data are employed to recalibrate  $\lambda_1$  again. This procedure is iterated until the difference in  $\lambda_1$  values between two successive iterations is negligible ( $< 1\%$ ). Here, in order to test the hypothesis of the linear adsorption isotherm (equilibrium), Eqs. (a) and (b) in model type (vii) were substituted by the following single equation which is the standard equilibrium transport equation widely applied for the simulation of solute contaminants in the subsurface [8, 10, 29-32]:

$$\frac{\partial C}{\partial t} \left(1 + \frac{\rho_b}{\epsilon} K_d\right) = D \frac{\partial^2 C}{\partial x^2} - V \frac{\partial C}{\partial x} - \lambda_1 C - \lambda_2 \frac{\rho_b}{\epsilon} S \quad (C1)$$

where  $K_d$  is the partitioning or distribution coefficient between the aqueous and solid phases [ $L^3T^{-1}$ ] [4]. The MT3DMS code was used to solve the equations and one- and two-dimensional breakthrough data of polymer-modified NZVI [33, 34] were used for fittings as described previously [27]. Briefly, one dimensional transport data used here comprise a case of monodisperse suspension of polymer-modified NZVI (F3) at low concentration (30 mg/L) which was not an aggregating system as well as a polydisperse suspension (F1) at high concentration (6000 mg/L) which showed the highest aggregation according to the DLVO analysis reported in [34]. In addition, data of polymer-modified NZVI at high concentration (6000 mg/L) with removed excess polymer (washed-MRNIP2) and polymer-modified NZVI at low concentration (300 mg/L) (unwashed) from two dimensional (2-D) experiments were used from [33]. The 2-D experiments comprise a cell ( $30 \times 18 \times 2.5$  cm) containing three active layers: fine sand ( $d_{50} = 99 \mu\text{m}$ ), medium sand ( $d_{50} = 300 \mu\text{m}$ ), and coarse sand ( $d_{50} = 880 \mu\text{m}$ ). The NP dispersion was injected through the fine sand layer which was the middle one while a background groundwater flow had been set up through three side ports [33].

The results for 1-D simulations (Table C1) showed that incorporating  $K_d$  at low concentration (30 mg/L) in the case of F3 dispersion resulted in a just slightly poorer fit ( $R^2 = 0.977$ ,  $p = 0.59$ ) than the two-parameter kinetic model ( $R^2 = 0.987$ ,  $p = 0.43$ ). In the case of high concentration (6000 mg/L) for the F1 dispersion, however, the difference between the equilibrium and kinetic models was more pronounced. Final fitting statistics for the  $K_d$  model were  $R^2 = 0.971$ ,  $p = 0.18$ , while those of the 2-

parameter approach were  $R^2 = 0.996$ ,  $p = 0.87$  (Table C1). The parameter values resulted from the equilibrium model simulation after 1% convergence of  $\lambda_I$  in the iteration procedure were  $4.75 \times 10^{-5}$  L/g,  $1.5 \times 10^{-3}$  s<sup>-1</sup>, and  $2.69 \times 10^{-3}$  s<sup>-1</sup> for  $K_d$ ,  $\lambda_I$ , and  $\lambda_2$ , respectively (Table C1). The obtained values for  $K_d$  in this study are comparable to those of He et al., [8], which ranged from  $1.9 \times 10^{-5}$  to  $7.1 \times 10^{-5}$  L/g. When the simulations were up-scaled to 2-D domains, the equilibrium model resulted in poorer performance, compared to the non-equilibrium model, at low concentration than at high concentration.  $R^2$  for the case at low concentration (unwashed) with non-equilibrium and equilibrium model fittings was 0.787 and 0.636, respectively, whereas for the case at high concentration (washed MRNIP2)  $R^2$  was 0.951 and 0.948 (Table C2). Yet,  $p$  values at both low and high concentrations increased when the non-equilibrium model was substituted by the equilibrium model, from 0.61 to 0.79 and from 0.58 to 0.92 at low and high concentrations, respectively. In [27], the reason for poorer model performance at low concentration than that at high concentration transport in 2-D domain was attributed to the existence of excess polymer in the dispersion of NZVI at low concentration which was not taken into account directly by the applied non-equilibrium model. Here, this deviation is even more obvious when a simpler model, i.e., equilibrium, is used.

In order to determine which model performs better, the Akaike information criterion (AIC) was calculated [35], which is commonly used as a model selection criteria in colloid and NP transport studies [36-40]. This criterion prefers the model with the best goodness-of-fit measure and at the same time with the least number of fitting parameters, corresponding to the lowest AIC value. This can be calculated as [38]:

$$AIC = n_{obs} \log(\sigma^2) + 2k_{par} + \frac{2k_{par}(k_{par} + 1)}{n_{obs} - k_{par} - 1} \quad (C2)$$

where  $n_{obs}$  is the number of observation data,  $\sigma^2$  is the sum of squared residuals divided by  $n_{obs}$ , and  $k_{par}$  is the number of parameters estimated in the inverse modelling process.

**Table C1** Parameter values and fitting results for cases of F3 at 30 mg/L and F1 at 6 g/L using non-equilibrium and equilibrium models.<sup>a</sup>

	<b>F3-0.03 g/L- Non- equilibrium<sup>b</sup></b>	<b>F3-0.03 g/L- Equilibrium<sup>b</sup></b>	<b>F1-6 g/L- Non- equilibrium<sup>c</sup></b>	<b>F1-6 g/L - Equilibrium<sup>c</sup></b>
<b><math>K_d</math> or <math>K_{att}</math></b>	7.21E-03 <sup>d</sup>	4.99E-05 <sup>e</sup>	1.05E-02 <sup>d</sup>	4.75e-5 <sup>e</sup>
<b><math>K_{det}</math></b>	2.61E-02	NA	3.61E-02	NA
<b><math>\lambda_1</math></b>	NA	NA	8.89E-04	1.50e-3
<b><math>\lambda_2</math></b>	NA	NA	2.27E-03	2.69e-3
<b><math>r^2</math></b>	0.987	0.977	0.996	0.971
<b><math>P</math>-Value</b>	0.43	0.59	0.87	0.18
<b>AIC</b>	-97.8	-94.2	634	642

<sup>a</sup>The unit of  $K_d$  is  $m^3/Kg$  and the units of other parameters are  $s^{-1}$ . <sup>b</sup>Based on simple finite difference (FD) method. <sup>c</sup>Based on the total variation diminishing (TVD) method. <sup>d</sup> $K_{att}$ . <sup>e</sup> $K_d$ . NA: not applicable.

**Table C2** Parameter values and fitting results for cases low concentration of 0.3 g/L and high concentration (washed-MRNIP2) of 6 g/L using non-equilibrium and equilibrium models.<sup>a</sup>

	0.3 g/L- Non- equilibrium	0.3 g/L- Equilibrium	6 g/L- Non- equilibrium	6 g/L- Equilibrium
<b><math>K_d</math> or <math>K_{att}</math> fine</b>	6.82E-03 <sup>b</sup>	1.15E-05 <sup>c</sup>	2.34E-02 <sup>b</sup>	7.04E-05 <sup>c</sup>
<b><math>K_d</math> or <math>K_{att}</math> medium</b>	2.78E-03 <sup>b</sup>	2.02E-03 <sup>c</sup>	3.67E-03 <sup>b</sup>	4.27E-04 <sup>c</sup>
<b><math>K_d</math> or <math>K_{att}</math> coarse</b>	3.90E-03 <sup>b</sup>	8.00E-04 <sup>c</sup>	1.49E-01 <sup>b</sup>	1.08E-03 <sup>c</sup>
<b><math>K_{det}</math> fine</b>	4.88E-03	NA	5.02E-02	NA
<b><math>K_{det}</math> medium</b>	1.69E-05	NA	1.75E-04	NA
<b><math>K_{det}</math> coarse</b>	1.23E-03	NA	2.83E-02	NA
<b><math>\lambda_1</math> fine</b>	NA	NA	1.46E-04	7.04E-06
<b><math>\lambda_1</math> medium</b>	NA	NA	2.27E-03	1.32E-03
<b><math>\lambda_1</math> coarse</b>	NA	NA	9.87E-05	8.83E-05
<b><math>\lambda_2</math> fine</b>	NA	NA	2.48E-04	1.44E-04
<b><math>\lambda_2</math> medium</b>	NA	NA	3.08E-04	1.52E-03
<b><math>\lambda_2</math> coarse</b>	NA	NA	1.27E-04	1.55E-04
<b><math>R^2</math></b>	0.787	0.639	0.951	0.948
<b><math>P</math>-Value</b>	0.61	0.79	0.58	0.92
<b>AIC</b>	-37.4	-42.2	609	582

<sup>a</sup>The unit of  $K_d$  is  $m^3/Kg$  and the units of other parameters are  $s^{-1}$ . <sup>b</sup> $K_{att}$ . <sup>c</sup> $K_d$ . NA: not applicable.

The results of these calculations for both of the investigated cases in one dimensional domain showed that the lower AIC value was obtained when the non-equilibrium attachment/detachment model was applied—AIC values with non-equilibrium and equilibrium models for F3 at 0.03 g/L (no aggregation) were -97.8

and  $-94.2$ , respectively, and for F1 at 6 g/L (with aggregation) were 634 and 642, respectively (Table C1). This suggests that in one-dimensional simulations the kinetic attachment/detachment model is preferred rather than the linear adsorption partitioning model. Surprisingly, in two-dimensional simulations the equilibrium model was preferred by AIC instead of the non-equilibrium model—AIC values for non-equilibrium and equilibrium models at low concentration (0.3 g/L with free polymer) were  $-37.4$  and  $-42.2$ , respectively, and at high concentration (6 g/L, without free polymer) were 609 and 582, respectively (Table C1). It should be noted that since AIC is a statistical model identification test, it is the final differences that matters not the magnitude. Both Praetorius et al. [5] and Cornelis [7] compare  $K_d$  with  $\alpha$ ,  $\eta_0$ , or  $K_{att}$ . However,  $K_d$  which considers the exchange between the two phases of suspended and attached mass, neither can be compared with  $\alpha$ , individually, which determines what portion of collisions leads to attachment, nor with  $\eta_0$ , individually, which ascertains what flux of particles are colliding with the collector, nor with  $K_{att}$ , individually, which determines the rate of permanent removal without detachment. In practice,  $K_d$  might be only comparable with both  $K_{att}$  and  $K_{det}$  together, in a range that both equilibrium and kinetic model perform similarly [41]. If for a specific temporal and spatial scale the assumption of instantaneous reaction (local equilibrium) can be used [41], the concept of  $K_d$  can be defended, regardless of whether the system contains particles or solute, provided that the interfering role of other phenomena such as aggregation and subsequent irreversible removal will be accounted for by other terms in the model.

In other words, while strictly unjustifiable as a physical process for particle deposition in mechanistic models, nevertheless the equilibrium assumption may be an effective descriptor of reversible deposition behaviour by concurrent attachment and detachment processes within a continuum modelling framework. Overall, in the experimental conditions simulated here, fairly similar model performance was obtained between the two modelling approaches in 1-D simulations. When the model was up-scaled to a 2-D stratigraphic, heterogeneous, experimental domain, the higher efficiency in terms of the number of model fitting parameter suggested that the equilibrium model is preferable in comparison to the kinetic model. This confirms the potential for use of the equilibrium assumption as a justified simplification for modelling NP in more complex porous media.

## 10.1 References

1. Dale, A.L., G.V. Lowry, and E.A. Casman, *Much ado about  $\alpha$ : reframing the debate over appropriate fate descriptors in nanoparticle environmental risk modeling*. Environmental Science: Nano, 2015.
2. Weerts, A.H., et al., *Analytical models for contaminant transport in soils and groundwater*. Personal Communication, 1995.
3. Zhang, P., et al., *Synthesis of crystalline-phase silica-based calcium phosphonate nanomaterials and their transport in carbonate and sandstone porous media*. Industrial & Engineering Chemistry Research, 2011. **50**(4): p. 1819-1830.
4. EPA, U., *Understanding variation in partition coefficient,  $K_d$ , values*. Office of Air and Radiation, United States Environmental Protection Agency, , 1999. **EPA 402-R-99-004B**: p. 1-341.
5. Praetorius, A., et al., *The road to nowhere: equilibrium partition coefficients for nanoparticles*. Environmental Science: Nano, 2014. **1**(4): p. 317-323.
6. Dale, A., et al., *Modeling nanomaterial environmental fate in aquatic systems*. Environmental Science & Technology, 2015.
7. Cornelis, G., *Fate descriptors for engineered nanoparticles: the good, the bad, and the ugly*. Environmental Science: Nano, 2015. **2**(1): p. 19-26.
8. He, F., et al., *Transport of carboxymethyl cellulose stabilized iron nanoparticles in porous media: Column experiments and modeling*. Journal of Colloid and Interface Science, 2009. **334**(1): p. 96-102.
9. Zhang, W., et al., *Transport and retention of biochar particles in porous media: effect of pH, ionic strength, and particle size*. Ecohydrology, 2010. **3**(4): p. 497-508.
10. Harvey, R.W. and S.P. Garabedian, *Use of colloid filtration theory in modeling movement of bacteria through a contaminated sandy aquifer*. Environmental Science & Technology, 1991. **25**(1): p. 178-185.
11. Kini, G.C., et al., *Salt-and temperature-stable quantum dot nanoparticles for porous media flow*. Colloids and Surfaces A: Physicochemical and Engineering Aspects, 2014. **443**: p. 492-500.
12. Harendra, S. and C. Vipulanandan, *Fe/Ni bimetallic particles transport in columns packed with sandy clay soil*. Industrial & Engineering Chemistry Research, 2010. **50**(1): p. 404-411.
13. Zhao, J., et al., *Heteroaggregation of graphene oxide with minerals in aqueous phase*. Environmental science & technology, 2015. **49**(5): p. 2849-2857.
14. Liang, Y., et al., *Retention and remobilization of stabilized silver nanoparticles in an undisturbed loamy sand soil*. Environmental science & technology, 2013. **47**(21): p. 12229-12237.
15. Sasidharan, S., et al., *Coupled effects of hydrodynamic and solution chemistry on long-term nanoparticle transport and deposition in saturated porous media*. Colloids and Surfaces A: Physicochemical and Engineering Aspects, 2014. **457**: p. 169-179.
16. Wang, D., et al., *Facilitated transport of copper with hydroxyapatite nanoparticles in saturated sand*. Soil Science Society of America Journal, 2012. **76**(2): p. 375-388.
17. Torkzaban, S., et al., *Transport and deposition of functionalized CdTe nanoparticles in saturated porous media*. Journal of contaminant hydrology, 2010. **118**(3): p. 208-217.

18. Wang, Y., et al., *Effect of surface coating composition on quantum dot mobility in porous media*. Journal of nanoparticle research, 2013. **15**(8): p. 1-16.
19. Flory, J., et al., *Influence of pH on the transport of silver nanoparticles in saturated porous media: laboratory experiments and modeling*. Journal of nanoparticle research, 2013. **15**(3): p. 1-11.
20. Kanel, S.R., et al., *Influence of natural organic matter on fate and transport of silver nanoparticles in saturated porous media: laboratory experiments and modeling*. Journal of Nanoparticle Research, 2013. **17**(3): p. 1-13.
21. Julich, D. and S. Gäth, *Sorption behavior of copper nanoparticles in soils compared to copper ions*. Geoderma, 2014. **235**: p. 127-132.
22. Abraham, P.M., et al., *Sorption of silver nanoparticles to environmental and model surfaces*. Environmental science & technology, 2013. **47**(10): p. 5083-5091.
23. Petersen, E.J., et al., *Effects of polyethyleneimine-mediated functionalization of multi-walled carbon nanotubes on earthworm bioaccumulation and sorption by soils*. Environmental science & technology, 2011. **45**(8): p. 3718-3724.
24. Zhang, L., E.J. Petersen, and Q. Huang, *Phase distribution of 14C-labeled multiwalled carbon nanotubes in aqueous systems containing model solids: Peat*. Environmental science & technology, 2011. **45**(4): p. 1356-1362.
25. Forouzanoghar, M. and R.S. Kookana, *Sorption of nano-C 60 clusters in soil: hydrophilic or hydrophobic interactions?* Journal of Environmental Monitoring, 2011. **13**(5): p. 1190-1194.
26. Nickel, C., et al., *Mobility of coated and uncoated TiO<sub>2</sub> nanomaterials in soil columns—Applicability of the tests methods of OECD TG 312 and 106 for nanomaterials*. Journal of environmental management, 2015. **157**: p. 230-237.
27. Babakhani, P., et al., *Modified MODFLOW-based model for simulating the agglomeration and transport of polymer-modified Fe nanoparticles in saturated porous media*. Environ Sci Pollut Res, 1-20, doi:10.1007/s11356-015-5193-0, 2015.
28. Watermark Numerical Computing & Waterloo Hydrogeologic, I., *WinPEST User's Manual: Non-linear Parameter Estimation and Predictive Analysis Program*. 1999.
29. Zheng, C. and P.P. Wang, *A modular three-dimensional multi-species transport model for simulation of advection, dispersion and chemical reactions of contaminants in groundwater systems; documentation and user's guide*. US Army Engineer Research and Development Center Contract Report SERDP-99-1, Vicksburg, Mississippi, USA, 1999.
30. Schijven, J.K. and S.M. Hassanizadeh, *Removal of viruses by soil passage: Overview of modeling, processes, and parameters*. Crit. Rev. Environ. Sci. Technol., 2000. **30**: p. 49 – 127.
31. Zhang, W., et al., *Transport and retention of biochar particles in porous media: effect of pH, ionic strength, and particle size*. Ecohydrology, 2010. **3**(4): p. 497-508.
32. Saiers, J.E. and G.M. Hornberger, *Migration of 137Cs through quartz sand: experimental results and modeling approaches*. Journal of Contaminant Hydrology, 1996. **22**(3-4): p. 255-270.
33. Phenrat, T., et al., *Transport and deposition of polymer-modified FeO nanoparticles in 2-D heterogeneous porous media: Effects of particle concentration, FeO content, and coatings*. Environmental Science & Technology, 2010. **44**(23): p. 9086-9093.
34. Phenrat, T., et al., *Particle size distribution, concentration, and magnetic attraction affect transport of polymer-modified FeO nanoparticles in sand columns*. Environ. Sci. Technol., 2009. **43**(13): p. 5079-5085.

35. Akaike, H., *A new look at the statistical model identification*. Automatic Control, IEEE Transactions on, 1974. **19**(6): p. 716-723.
36. Bradford, S.A., J. Simunek, and S.L. Walker, *Transport and straining of E. coli O157: H7 in saturated porous media*. Water Resources Research, 2006. **42**(12).
37. Kasel, D., et al., *Transport and retention of multi-walled carbon nanotubes in saturated porous media: Effects of input concentration and grain size*. water research, 2013. **47**(2): p. 933-944.
38. Bradford, S.A., et al., *Equilibrium and kinetic models for colloid release under transient solution chemistry conditions*. Journal of contaminant hydrology, 2015.
39. Goldberg, E., et al., *Critical assessment of models for transport of engineered nanoparticles in saturated porous media*. Environmental science & technology, 2014. **48**(21): p. 12732-12741.
40. Bai, C. and Y. Li, *Time series analysis of contaminant transport in the subsurface: Applications to conservative tracer and engineered nanomaterials*. Journal of contaminant hydrology, 2014. **164**: p. 153-162.
41. Limousin, G., et al., *Sorption isotherms: A review on physical bases, modeling and measurement*. Applied Geochemistry, 2007. **22**(2): p. 249-275.

## **Appendix D**

### **11 Overview of the concurrent occurrence of multiple transport phenomena**

#### **11.1 Conceptual model of transport for stable monodisperse dispersions**

For stable monodisperse suspensions of larger sized NP, the conceptual model of Bradford et al. [1], may best describe the transport phenomena in porous media. In this model it was hypothesized that straining caused filling of the pores at contact areas of grains and caused those small pores to become dead-end at the near vicinity of the column inlet thereby constraining NP aggregates to sample only the continuous pore channels. After passing this region of the porous media in the experimental packed column, particles would be mounted on the fast-central streamlines of the pore channels with less interactions with the grain walls and narrow restrictions of pores at the grain-grain contacts due to the exclusion phenomena and thus the number of dead-end pores experienced by particles reduces with distance from the inlet of the column. In this way, the concentration of the RCP reduces significantly along the column length [1]. This must be the most plausible explanation regarding the hyper-exponential behaviour of the RCP for stable monodisperse dispersions.

#### **11.2 Conceptual model of transport for stable poly-disperse dispersions**

When the particle population is poly-disperse but stable, the case which is more pronounced for NP dispersions [2], the hyper-exponential RCP as depicted in Fig. (D1a) can still be developed as for monodisperse suspensions. At the entrance of the column all the particle size fractions have interactions with the surfaces of the porous media with higher chance of trapping larger particles due to the physical straining [1, 3] and/or physicochemical deposition resulted from their relatively deeper surface interaction energy minima [2, 4, 5]. As a proportion of large particles is irreversibly

retained near the areas of the wall surfaces or grain-grain contacts at the entrance of the packed column, other survived large particles would less meet the close-to-wall regions during their travel through the rest of the column length thanks to the size exclusion. On the other hand, the particles from the smaller fraction of the size distribution spectrum can still have interaction with the wall. Yet, they exhibit shallow secondary minima [2, 4-7] and thus are less subject to permanent deposition and also owing to their smaller size, they are less prone to straining all over the column length [1, 3, 5, 8]. Accordingly, neither significant deposition of small particles nor large particles can take place at the down-gradient of the column, in contrast to the entrance area. This concept is also compatible with blocking and ripening behaviours if one of them also occur. They can coincide with hyper-exponential shaped RCPs, because the retention process at the vicinity of the column entrance can be either straining or physicochemical filtration, regardless of whether the condition is favourable for blocking or ripening.

### **11.3 Conceptual model of transport for unstable poly-disperse dispersions**

One of the most complicated transport behaviours, observed more commonly in studies of NP than those of larger colloids, is non-monotonic retention [9-11]. Previous reports have ascribed the reason for this non-monotonic shape of the RCPs to a variety of phenomena such as the release of the attached particles from the region close to the column inlet and their re-entrapment in the down-gradient regions of the column or their translation, flowing, or funnelling in the attached phase as a third phase [12-16], presence of polymer competing with the NP for the adsorption sites at the inlet vicinity [17-19], surface heterogeneity [20, 21], and other system conditions such as grain types and size [12, 22]. Furthermore, ripening [23] and blocking are pointed out to be influential in causing non-monotonic shaped RCPs [18, 24]. Blocking can promote non-monotonic behaviour via filling of  $S_m$  sites at higher loading concentrations, coarser sand grains, lower velocity, and higher IS [12, 18]. It has also been indicated that non-monotonic RCPs can also occur as a consequence of straining [12] and agglomeration [19, 25]. Dual-species [12], dual-permeability [13], dual-domain [15], and stochastic models [10] have been deployed successfully in reproducing the non-monotonic shape of the RCP

Considering the widespread evidence for the significance of aggregation processes in NP suspensions and during transport [12, 13, 15], it is proposed that agglomeration plays a key role in producing the non-monotonic shaped RCP. In contrast to the translation of attached mass of particles or aggregates on the surface of the grains [12-16], it is asserted agglomeration in the fluid phase likely has the main contribution to bring about non-monotonic retention behaviour in unstable suspensions, as illustrated in Fig. D1b (adapted from [2, 26, 27]). Essentially, at the immediate vicinity of the packed column entrance, the average size of particles is so small that they can neither be subject to irreversible deposition nor to size exclusion although there might be a delay in this area because of higher interaction of NP with walls due to their higher diffusion. Then all the particles, in this way, are transported toward the down-gradient of the column during which they are also agglomerating within the aqueous phase of the pores, as the condition is favourable for agglomeration. When the agglomerates are sufficiently grown in size their fate might be determined in two possible ways. First, those agglomerates closer to pore walls could be subject to straining and/or irreversible retention somewhere in the midst of the column length. This retention would potentially appear to be more pronounced as a result of ripening. Second, those agglomerates which are farther from pore walls by this time would be mounted on the faster central streamlines of the pores because of size exclusion. In this way they can potentially travel all the rest of the route to the column outlet and survive from retention although still their size may keep growing in this way and still be vulnerable to the first possibility for retention as well. In combination, this aggregation-driven suite of processes leads to the appearance of a peak or a hotspot in the middle area of RCP. Clearly, assuming other factors to be held constant, the rate of aggregation should be a significant factor in determining the position of the non-monotonic peak as a function of distance from source.

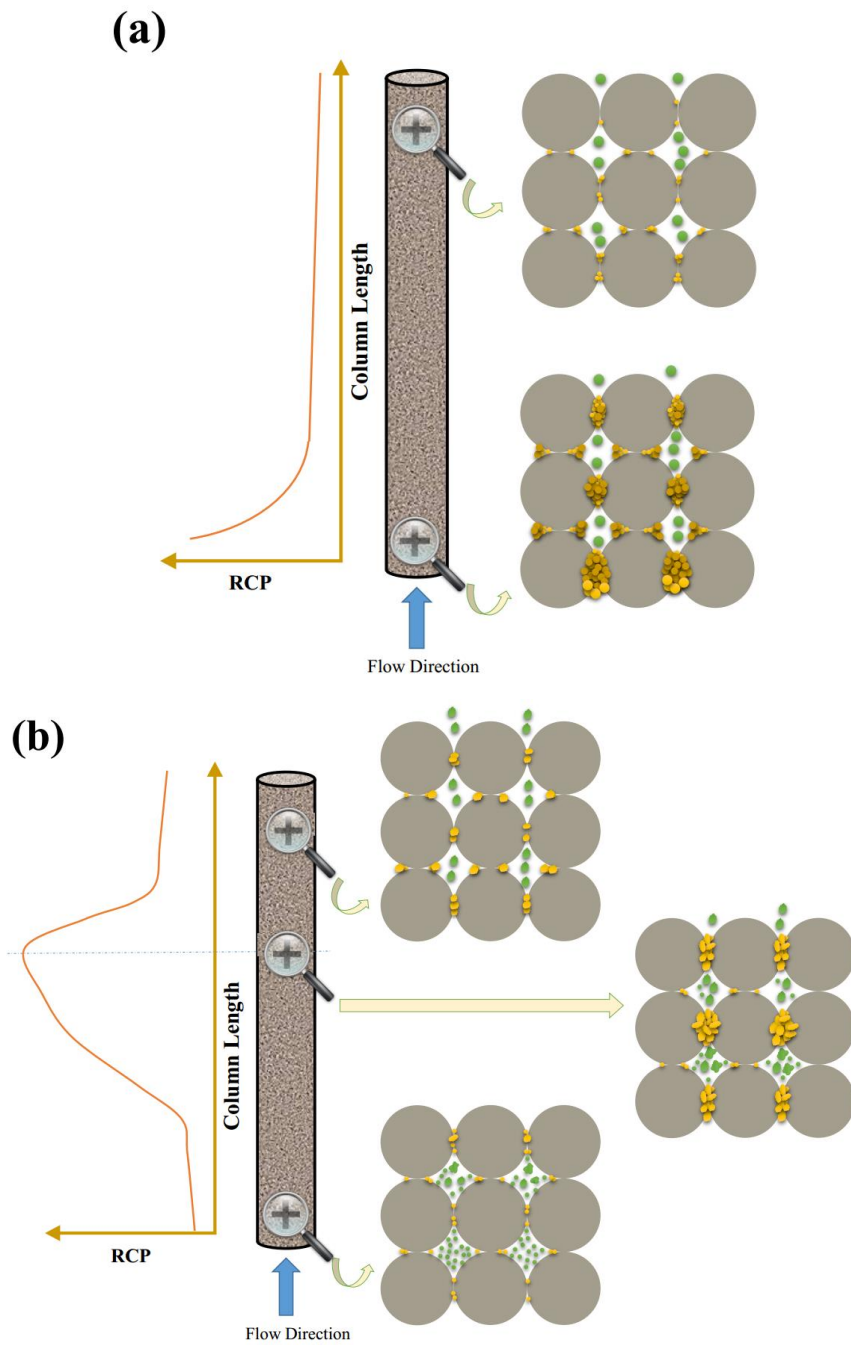


**Figure D1** The proposed conceptual models (a) for coupled effects of straining and size exclusion causing hyper-exponential shaped retention profile in the case of injecting poly-disperse particle dispersion into the experimental packed column and (b) for concurrent effects of agglomeration, deposition/straining, and size exclusion forming non-monotonic retention profile. Mobile particle/aggregates are shown in green while retained particle/aggregates are shown in yellowish brown.

## 11.4 References

1. Bradford, S.A., et al., *Modeling colloid attachment, straining, and exclusion in saturated porous media*. Environmental science & technology, 2003. **37**(10): p. 2242-2250.
2. Phenrat, T., et al., *Particle size distribution, concentration, and magnetic attraction affect transport of polymer-modified Fe0 nanoparticles in sand columns*. Environ. Sci. Technol., 2009. **43**(13): p. 5079-5085.
3. Bradford, S.A., et al., *Physical factors affecting the transport and fate of colloids in saturated porous media*. Water Resources Research, 2002. **38**(12): p. 63-1.
4. Phenrat, T., et al., *Empirical correlations to estimate agglomerate size and deposition during injection of a polyelectrolyte-modified Fe0 nanoparticle at high particle concentration in saturated sand*. Journal of Contaminant Hydrology, 2010. **118**(3-4): p. 152-164.
5. Shen, C., et al., *Effects of solution chemistry on straining of colloids in porous media under unfavorable conditions*. Water resources research, 2008. **44**(5).
6. Prieve, D.C. and P.M. Hoysan, *Role of colloidal forces in hydrodynamic chromatography*. Journal of Colloid and Interface Science, 1978. **64**(2): p. 201-213.
7. Phenrat, T., et al., *Transport and deposition of polymer-modified Fe0 nanoparticles in 2-D heterogeneous porous media: Effects of particle concentration, Fe0 content, and coatings*. Environmental Science & Technology, 2010. **44**(23): p. 9086-9093.
8. Auset, M. and A.A. Keller, *Pore-scale visualization of colloid straining and filtration in saturated porous media using micromodels*. Water resources research, 2006. **42**(12).
9. Wang, D., et al., *Hyperexponential and nonmonotonic retention of polyvinylpyrrolidone-coated silver nanoparticles in an Ultisol*. Journal of contaminant hydrology, 2014. **164**: p. 35-48.
10. Bradford, S.A. and N. Toride, *A stochastic model for colloid transport and deposition*. Journal of environmental quality, 2007. **36**(5): p. 1346-1356.
11. Goldberg, E., et al., *Critical assessment of models for transport of engineered nanoparticles in saturated porous media*. Environmental science & technology, 2014. **48**(21): p. 12732-12741.
12. Bradford, S.A., J. Simunek, and S.L. Walker, *Transport and straining of E. coli O157:H7 in saturated porous media*. Water Resources Research, 2006. **42**(12).
13. Yuan, H. and A.A. Shapiro, *A mathematical model for non-monotonic deposition profiles in deep bed filtration systems*. Chemical Engineering Journal, 2011. **166**(1): p. 105-115.
14. Li, X., et al., *Role of grain-to-grain contacts on profiles of retained colloids in porous media in the presence of an energy barrier to deposition*. Environmental science & technology, 2006. **40**(12): p. 3769-3774.
15. Bradford, S.A., S. Torkzaban, and J. Simunek, *Modeling colloid transport and retention in saturated porous media under unfavorable attachment conditions*. Water Resources Research, 2011. **47**(10).
16. Tong, M., H. Ma, and W.P. Johnson, *Funneling of flow into grain-to-grain contacts drives colloid-colloid aggregation in the presence of an energy barrier*. Environmental science & technology, 2008. **42**(8): p. 2826-2832.
17. Wang, Y., et al., *Influence of Residual Polymer on Nanoparticle Deposition in Porous Media*. Environmental Science & Technology, 2014. **48**(18): p. 10664-10671.

18. Liang, Y., et al., *Sensitivity of the transport and retention of stabilized silver nanoparticles to physicochemical factors*. *Water Research*, 2013. **47**(7): p. 2572-2582.
19. Chen, G., X. Liu, and C. Su, *Distinct effects of humic acid on transport and retention of TiO<sub>2</sub> rutile nanoparticles in saturated sand columns*. *Environmental Science & Technology*, 2012. **46**(13): p. 7142-7150.
20. Choy, C.C., M. Wazne, and X. Meng, *Application of an empirical transport model to simulate retention of nanocrystalline titanium dioxide in sand columns*. *Chemosphere*, 2008. **71**(9): p. 1794-1801.
21. Li, Y., et al., *Investigation of the transport and deposition of fullerene (C<sub>60</sub>) nanoparticles in quartz sands under varying flow conditions*. *Environmental Science & Technology*, 2008. **42**(19): p. 7174-7180.
22. Tong, M., T.A. Camesano, and W.P. Johnson, *Spatial variation in deposition rate coefficients of an adhesion-deficient bacterial strain in quartz sand*. *Environmental Science & Technology*, 2005. **39**(10): p. 3679-3687.
23. Wang, Y., et al., *Enhanced mobility of fullerene (C<sub>60</sub>) nanoparticles in the presence of stabilizing agents*. *Environmental Science & Technology*, 2012. **46**(21): p. 11761-11769.
24. Liang, Y., et al., *Retention and remobilization of stabilized silver nanoparticles in an undisturbed loamy sand soil*. *Environmental Science & Technology*, 2013. **47**(21): p. 12229-12237.
25. Chen, G., X. Liu, and C. Su, *Transport and retention of TiO<sub>2</sub> rutile nanoparticles in saturated porous media under low-ionic-strength conditions: measurements and mechanisms*. *Langmuir*, 2011. **27**(9): p. 5393-5402.
26. Babakhani, P., et al., *Modified MODFLOW-based model for simulating the agglomeration and transport of polymer-modified Fe nanoparticles in saturated porous media*. *Environ Sci Pollut Res*, 1-20, doi:10.1007/s11356-015-5193-0, 2015.
27. Babakhani, P., et al., *Supplementary Material for "Modified MODFLOW-based model for simulating the agglomeration and transport of polymer-modified Fe nanoparticles in saturated porous media"*. *Environ Sci Pollut Res*, 1-20, doi:10.1007/s11356-015-5193-0, 2015.

# Appendix E

## 12 Supporting information for Chapter 2

### 12.1 Further details on ANN modelling procedure

In order to be able to find the optimum hidden layer structure, all the random functions in the inner loop were tied to the status outside the inner loop so that the initial conditions (initial weights and biases) could be kept constant in the inner loop in finding the optimum hidden layer structure. Obviously, this status could change in various iterations of the outer loop in order to achieve the uncertainties produced by many model trainings with various initial number of optimum nodes, various weights and biases and various random selections of the dataset for training, test, and validation—as will be discussed later. Following the Monte Carlo analysis we assigned the status of the tied random function in each iteration of the outer loop based a normally distributed random matrix of 1000 elements containing natural numbers between 1 and  $10^4$ . The flow chart of this algorithm is shown in Fig. E3.

In order to improve the computational performance in the training process and as a standard pre-processing practice, ANN requires the raw input and output data to be normalized in a specific range, e.g., [-1, 1] or [0, 1] [1, 2]. Here we used a linear scaling function to distribute the data between the interval of [-1, 1] as described elsewhere [1, 2]. In addition, before this normalization all the data were log transformed following [3] so that the training procedure would be facilitated.

To obtain a better generalization of the network predictions and avoid overfitting issue, we used the “early stopping” strategy in MATLAB<sup>®</sup> [4-7]. This method divides the datasets into three subsets for training, validation and test. The validation subset is used to check when the maximum generalization of the network is gained, i.e., at the point when the mean square error (MSE) of the validation subset is beginning to increase and diverge from that of training subset. The test subset is used to verify whether the data division is performed appropriately [4, 8]. Therefore, it is important to divide the dataset randomly as has been performed in this study [8]. Although it might be advisable to employ the early stopping strategy with a slow training algorithms [4], it has been proposed to be used with Levenberg–Marquardt back-propagation learning algorithm in hydrology engineering [6, 7]. Thus, here we use these techniques together in order to increase the converging time while maximize the generalization.

Furthermore, to select the model with the best fitting result in the inner loop and with highest generalization among 1000 iterations of the outer loop, the following criteria were incorporated. These criteria were rested on the Nash–Sutcliffe determination coefficient (a conservative  $R^2$ ) [1, 3, 9, 10]. In the inner loop, simply the iteration at which yielded the maximum  $R^2$  (close to one) was selected as the network with the best number of the hidden layer nodes. In the outer loop the outcomes of the iteration at which the following function was maximum was selected. This function was considered based upon the fact that the higher the goodness-of-fit ration for the validation and test set to the training set is, the better the generalization. This is because if a model which is trained based on the training dataset can predict new test and validation datasets with a goodness-of-fit close to that of the training set, then that model performs well in fitting to any new datasets. Besides, an overall high ration of goodness-of-fit to the maximum possible goodness-of-fit for the training set is appreciated for a model to be able to fit any data. Thus, an average of these three ratios may be considered as the generalization efficiency of the model:

$$\text{Generalization Efficiency} = \frac{1}{3} \left( \frac{R^2_{\text{Val}}}{R^2_{\text{Train}}} + \frac{R^2_{\text{Test}}}{R^2_{\text{Train}}} + R^2_{\text{Train}} \right) \quad (\text{E1})$$

where,  $R^2_{\text{Train}}$ ,  $R^2_{\text{Val}}$ , and  $R^2_{\text{Test}}$  are the Nash–Sutcliffe deterministic coefficient for the training, validation and test data subsets, respectively. Maximizing this function results in selecting a model which not only has a proper fit but also performs better with new data. Finally, the structure, weights and biases of the selected model are proposed in a spreadsheet format for future predictions of continuum-based model parameters (i.e.,  $K_{att}$ ,  $K_{det}$ ,  $S_m$ ) based on the experimental/environmental conditions (pore water velocity, IS, pH, etc.).

In addition to “early stopping”, another strategy known as “Bayesian regularization” is available in Neural Network Toolbox of MATLAB which engages the determination of the optimum number of hidden layer nodes inside the training process algorithm, but requires longer run times. Herein, we used the “early stopping” method as it has been more frequently used in the fields of hydrology and environmental engineering and there are indications of the superiority of this technique over the Bayesian regularization in these fields [6, 11].

It should be noted that each parameter of the continuum-based model as well as  $C/C_0$  were considered as a single output of the ANN model rather than putting all the parameters together as output, because it allows finding insights into the phenomenological influence of various experimental conditions on each continuum-model parameter separately [12].

The uncertainties of the model was assessed through calculation of the 95 % confidence interval (CI) according to the 2.5<sup>th</sup> and 97.5<sup>th</sup> percentiles of the Student’s t-distribution as [7, 13, 14]:

$$CI = \frac{1.9623 \times \text{STDV}}{\sqrt{N_R}} \quad (\text{E2})$$

where STDV is the standard deviation of the sensitivities and  $N_R$  is the number of Monte Carlo realizations—or iterations of the outer loop.

## 12.2 Description of PaD method for analysis of the sensitivities

Using a simple three-layer configuration described in Chapter 2 (Section 2.4) and a hyperbolic tangent sigmoid function (tansig function of MATLAB) as the transfer (activation) function for the hidden layer and a linear transfer function (purelin function of MATLAB) for the output layer, we can derive the following relationship to calculate the partial derivatives of the output variable,  $N_o$ , in relation to the input variable,  $X_p$  [1]:

$$\frac{\partial N_o}{\partial X_p} = \sum_{h=1}^{n_h} W_{oh} (1 - N_h^2) W_{hp} \quad (\text{E3})$$

where subscripts  $h$  and  $o$  stand for hidden, and output layer, respectively, and subscript  $p$  is the specific node at the input layer, the derivative of which is being calculated.  $n_h$  is the optimized number of hidden layer nodes (neurons).  $W_{hp}$  and  $W_{oh}$  are the connection weight matrices between the hidden-to-input layers and output-to-hidden layers, respectively.  $N_h$  is the resulted signal obtained from exerting the transfer function on the processed signal from the hidden layer,  $S_h$  given as [1, 15]:

$$S_h = W_{hp} N_p + \sum_{i \neq p} W_{hi} N_i \quad (\text{E4})$$

where subscript  $i$  is the node index at the input layer. By applying the hyperbolic tangent sigmoid (tansig) transfer function deployed in this study,  $N_h$  can be obtained [1]:

$$N_h = \frac{2}{1 + e^{-2S_h}} - 1 \quad (\text{E5})$$

Finally, the relative contribution of each output to each input variable (parameter) can be accounted for by the sum of square partial derivatives for all the samples as follows [1]:

$$SSD = \sum_{d=1}^n \left( \frac{\partial N_o}{\partial X_p} \right)^2 \quad (\text{E6})$$

where  $SSD$  is the sum of square partial derivatives for an input variable and  $n$  is the number of samples or available data for each input variable. Herein, we used the relative square partial derivatives that is the ratio of  $SSD$  for each input variable to the sum of  $SSD$  for all input variables times 100. This is reported herein as the relative sensitivity (RS) which represents

the relative contribution of each input variable, e.g., experimental/environmental factors, to the output variable, e.g., continuum model parameters, in percentage. The code was validated against artificial data following Gevrey et al. [16] as depicted in the following section.

### 12.3 Validation of the developed MATLAB Code

In order to validate the data we generated 6 sets of random data ( $x_1$  to  $x_6$ ) with “randperm” function of MATLAB as the input for modelling. Then we used the flowing function to produce the output ( $y$ ) similar to Gevrey et al. [16]:

$$y = x_1 + x_2 - 10x_3 - 10x_4 + 20x_5 + 20x_6 \quad (\text{E7})$$

Here each input variable is inserted in a pair to be able to check the performance of the code. We simulated this artificial dataset by the code with 100 iterations of the outer loop, i.e., Monte Carlo runs.

The sensitivities obtained for  $x_1$  to  $x_6$  were 40.7, 38.9, 10.4, 9.9, 0.1, and 0.1, respectively (Fig. E4). The differences between  $x_1$ ,  $x_3$ , and  $x_5$  set with  $x_2$ ,  $x_4$ , and  $x_6$  set were not statistically significant ( $P$  value  $> 0.05$ ) [10]. The result showed that the sensitivity increases with the coefficients of the variables in Eq. (E7). Negative correlations between  $x_4$  and  $x_5$  parameters with  $y$  in Eq. (E7) was well produced (results not shown). The resulted sensitivities from this technique are not exactly the same as the real sensitivities values—the slopes or coefficients in Eq. (E7). It might be because of the complex structure of the ANN which makes it capable of simulating non-linear problem [17-19]. Overall, these results show that the developed code can describe the strengths and the signs of parameter relationships in an arbitrary model.

### 12.4 Evaluating the possible effect of mean imputation for the missingness in the data

In order to verify that the outcomes of the sensitivity analysis have not been biased by the mean imputation for the missing data, we repeated the modelling of cases of  $C/C_0$  by removing all the cases which contained missingness in the data of grain zeta-potential. This operation reduced the dataset from 493 cases to 342 cases. The result showed the sensitivity for the grain zeta-potential was still highest with  $RS = 28.6\%$ — less than 1 % difference with previous results. Furthermore, the sensitivity to the rest of parameters matched very well ( $R^2 = 0.981$  and  $P$  value = 1.00), with those of the data with imputed mean for the missingnesses, suggesting that this study’s results are not affected by the mean imputation in the dataset.

## 12.5 Figures

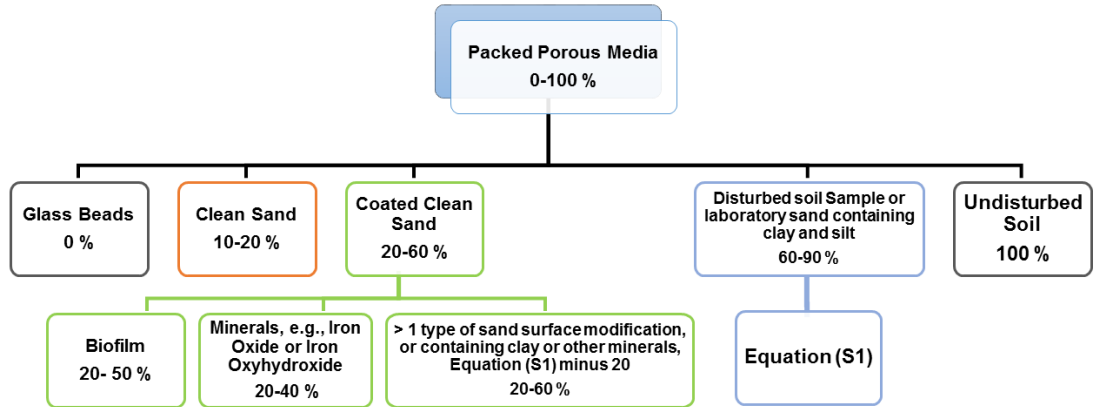


**Figure E1** Diagram of porous media heterogeneity ranges used in developing the heterogeneity parameter.

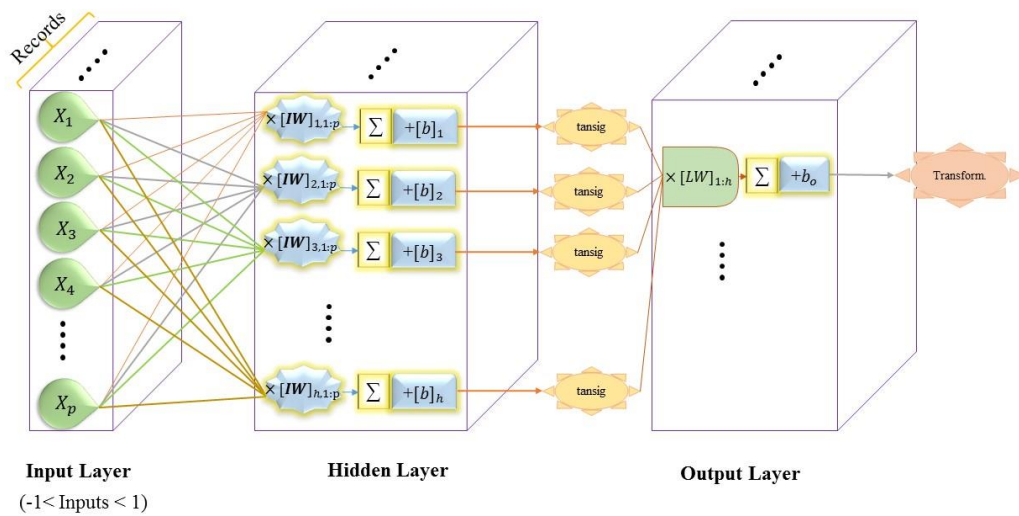


**Figure E2** Schematic of the three-layer perceptron ANN structure used in this study.

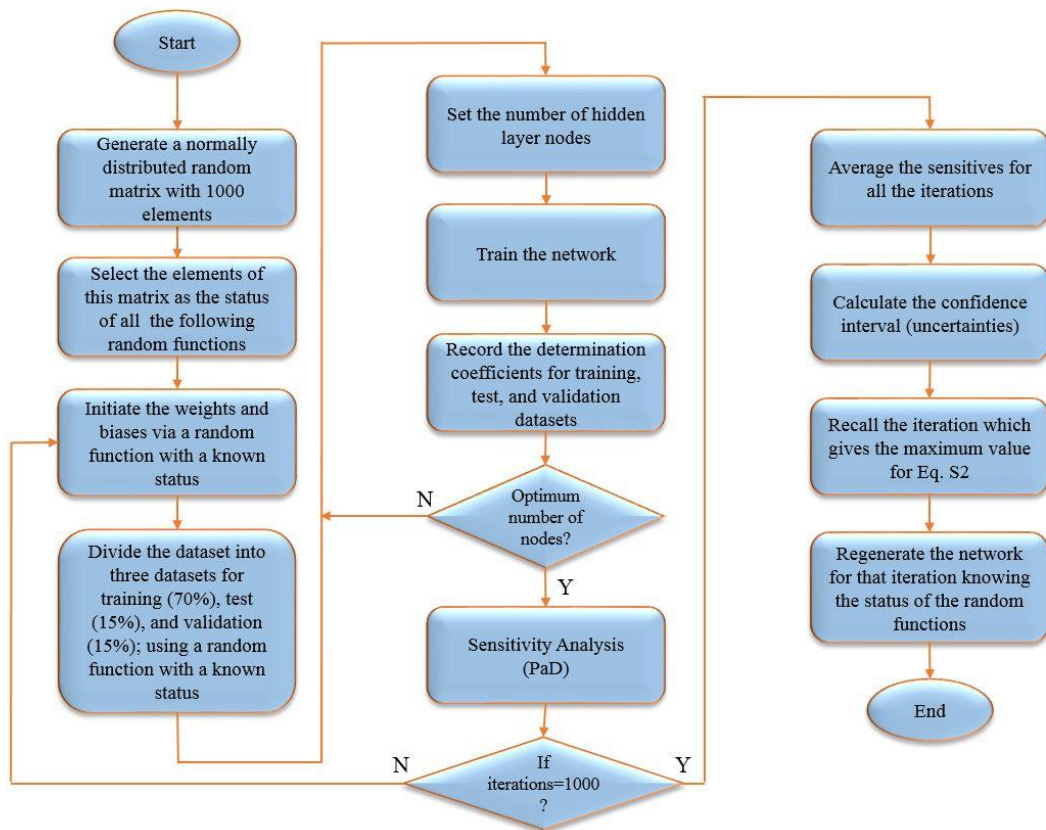


**Figure E3** The flow chart of code algorithm developed in MATLAB<sup>®</sup> for ANN modelling, analysis of sensitivity and uncertainties, as well as finding the best model for prediction. Equation S2 in the chart refers to Eq. (E1).

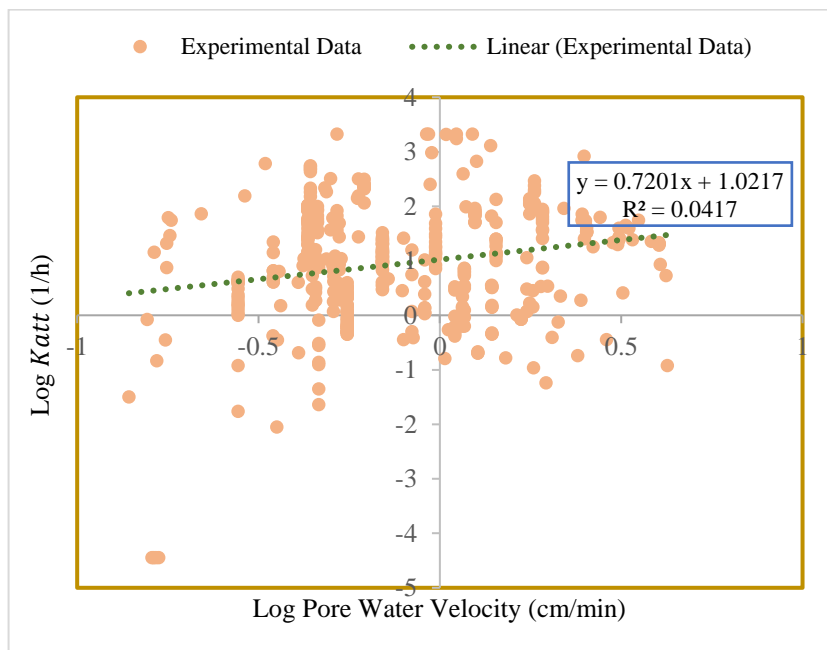


**Figure E124** Log linear regressions between the attachment rate and the pore water velocity for the raw experimental data.

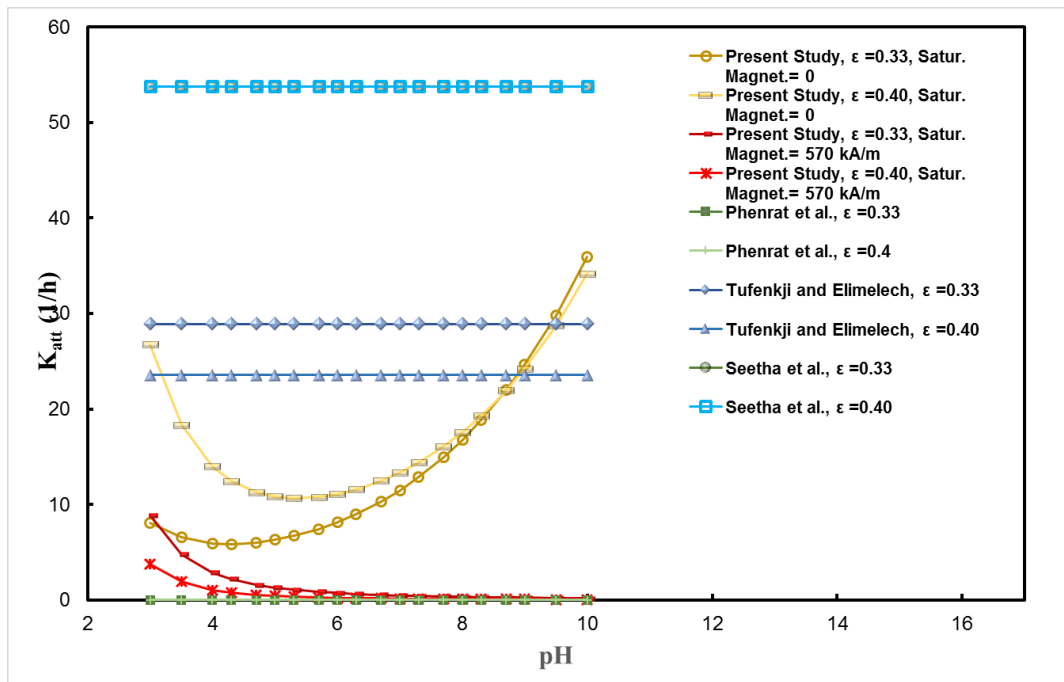


**Figure E125** Relationship between  $K_{att}$  and the pH obtained from the present study, and Seetha et al. [20], as well as CFT, the collector efficiencies of which were obtained based on the correlations of Phenrat et al. [21] and Tufenkji and Elimelech [22]. The data were selected in the ranges of simulated values in Seetha et al. [20]. Most of experimental conditions used resembled those of [23]. The parameter values used in the model are: a free-polymer concentration of zero mg/L, a particle zeta potential of -30 mV, and a grain zeta potential of -30 mV, a particle diameter of 150 nm, a grain diameter of 0.15 mm, a NP density of  $6.7 \text{ g/cm}^3$ , an input concentration of 200 mg/L, a column diameter (Inner) of 2.6 cm, a column length of 25.5 cm, a heterogeneity of 15 % (clean sand), porosities of 0.33 and 0.4, a dispersivity of 0.015 cm, a pore water velocity of 0.015 cm/min, an IS of 10 mM, an injection duration of 1 PVs, an aspect ratio of 1, an adsorbed coating concentration of 1 mg/L, saturation magnetizations of zero and 570 kA/m, an IEP pH at 6.3, and pH ranging from 3 to 10. Extra parameters assumed in the correlations of Seetha et al. [20] include a temperature of 298 °K, a dynamic viscosity of 0.89 mPa.S, and a cylindrical pore constriction radius of  $6.2 \times 10^{-5} \text{ m}$  calculated based on grain size following Phenrat et al. [21]. Single collector attachment efficiency in the equation of Tufenkji and Elimelech [22] was assumed equal to one.

## 12.6 Tables

**Table E1** The values of isoelectric point (IEP) or the point of zero charge (PZC) assumed for each NP type in the dataset.

NP type	Selected Ave IEP for the uncoated NP	PZC/IEP	Ref
AgNP	7	IEP	[24]
NZVI	6.3	IEP	[25]
Iron Oxide (Fe <sub>3</sub> O <sub>4</sub> )	6.4	IEP	
HAP	6.7	IEP	[26]
GO	4	PZC	[27, 28]
Graphene	5.7	PZC	[29, 30]
CeO <sub>2</sub>	3	PZC	[31]
TiO <sub>2</sub>	6	IEP	[32]
ZnO	9.3	PZC	[33]
QD, CdSe/CdZnS	2.5	IEP	[34]
CdTe QDs	1.7	IEP	[35]
Carboxylate-modified latex (CML)	2	IEP	[26, 36]
Aluminum oxide	9.38	PZC	[37]
Boehmite	9.1	IEP	[38]
Silica	1.9	IEP	[26]
MWNT	2.4	PZC	[39]

**Table E2** Linear correlations between  $K_{att}$  and ionic strength for the separated data of different ionic compositions.

	a (First Const.)	b (Second Const.)	Number of data	Correlation Coefficient	$r^2$	Fisher F statistics	F- critical*	F>F- critical Significant
NaCl	0.34	11.35	71	0.42	0.18	14.8	4.0	Passed
MgSo <sub>4</sub>	0.23	7.63	7	0.93	0.86	30.1	6.6	Passed
KNO <sub>3</sub>	16.39	-12.58	23	0.78	0.61	32.8	4.3	Passed
CaCl <sub>2</sub>	9.46	-7.35	66	0.89	0.79	234.4	4.0	Passed
NaHCO <sub>3</sub>	4.42	7.84	39	0.75	0.57	48.2	4.1	Passed

\*Values for 95 % confidence interval

**Table E3** Ranges of heterogeneity parameter ( $\Theta$ ) variation for different amounts of Clay, Silt, and Sand.

<b>Clay (%)</b>	<b>Silt (%)</b>	<b>Sand (%)</b>	<b><math>\Theta</math> (%)</b>
<b>33.3</b>	33.3	33.3	77.5
<b>99.9</b>	0	0.1	90.0
<b>99.9</b>	0.05	0.05	88.5
<b>99.9</b>	0.1	0	87.0
<b>0</b>	0.1	99.9	60.0
<b>0.05</b>	0.05	99.9	64.5
<b>0.1</b>	0	99.9	69.0
<b>0</b>	99.9	0.1	81.0
<b>0.05</b>	99.9	0.05	81.0
<b>0.1</b>	99.9	0	81.0
<b>50</b>	50	0	84.0
<b>50</b>	0	50	79.5
<b>0</b>	50	50	70.5
<b>5</b>	5	90	66.5
<b>5</b>	90	5	80.3
<b>90</b>	5	5	87.0
<b>10</b>	0	90	71.1
<b>5</b>	5	90	66.5
<b>0</b>	10	90	62.1
<b>90</b>	0	10	87.9
<b>90</b>	5	5	87.0
<b>90</b>	10	0	86.4
<b>0</b>	90	10	78.9
<b>5</b>	90	5	80.3
<b>10</b>	90	0	81.6

**Table E4** Sensitivity analysis outcomes, RS (%).

	$C/C_0$	$K_{att}$	$K_{det}$	$S_m$	$\beta$	$K_{att2}$
<b>Asp.Rati.</b>	2.7	-7.9	-4.5	5.2	-3.8	5.4
<b>C0</b>	3.3	4.6	3.6	7.2	12.0	-3.3
<b>Coat.Conc.</b>	3.0	-25.7	3.8	-4.5	3.2	5.2
<b>Colum.Diam.</b>	3.0	-3.1	-4.6	6.9	5.2	4.2
<b>Colum.Leng.</b>	-7.5	6.9	-4.0	9.3	3.4	5.9
<b>Dispersivity</b>	-3.6	1.7	5.1	3.9	-2.8	3.8
<b>Fre.Pol.Conc.</b>	-2.2	1.6	-3.6	2.5	2.2	2.1
<b>Grain-Diam.</b>	5.5	2.6	4.2	-3.1	2.6	-12.5
<b>Heterogen.</b>	3.0	2.4	6.2	3.8	4.9	3.7
<b>IEP</b>	-2.9	5.6	3.1	4.7	-8.6	5.8
<b>IS</b>	-3.5	2.9	-14.8	3.2	4.6	4.9
<b>Partic.Dens.</b>	-3.9	-4.9	-4.8	-4.2	-4.1	4.2
<b>Partic.Diam.</b>	-4.0	2.2	3.0	3.7	-8.7	4.6
<b>pH</b>	3.7	-2.2	4.5	4.2	-2.4	3.5
<b>Porosity</b>	4.9	3.0	8.8	4.9	-7.7	-3.2
<b>PV-No.</b>	4.5	2.7	-3.4	5.6	3.9	3.5
<b>Satur.Magnet.</b>	2.1	-3.6	-3.2	N.A.	3.9	-3.2
<b>Veloc.</b>	3.2	4.4	3.8	-4.3	-5.6	3.3
<b>Zeta-Grain.</b>	-28.7	8.3	-6.2	11.6	-6.3	-4.6
<b>Zeta-Partic.</b>	4.8	3.8	4.6	7.2	4.0	13.0

N.A.: not applicable.

## 12.7 References

1. Nourani, V. and M. Sayyah-Fard, *Sensitivity analysis of the artificial neural network outputs in simulation of the evaporation process at different climatologic regimes*. Advances in Engineering Software, 2012. **47**(1): p. 127-146.
2. Yu, L., S. Wang, and K.K. Lai, *Data Preparation in Neural Network Data Analysis*, in *Foreign-Exchange-Rate Forecasting With Artificial Neural Networks*. 2007, Springer: US. p. 39-62.
3. Aqil, M., et al., *Analysis and prediction of flow from local source in a river basin using a Neuro-fuzzy modeling tool*. Journal of environmental management, 2007. **85**(1): p. 215-223.
4. Beale, M.H., M.T. Hagan, and H.B. Demuth. *Neural network toolbox™ user's guide*. 2015. The MathWorks, Inc. 3 Apple Hill Drive Natick, MA 01760-2098 [www.mathworks.com](http://www.mathworks.com).
5. Bishop, C.M., *Regularization and complexity control in feed-forward networks*. 1995.
6. Coulibaly, P., F. Anctil, and B. Bobee, *Daily reservoir inflow forecasting using artificial neural networks with stopped training approach*. Journal of Hydrology, 2000. **230**(3): p. 244-257.
7. Dehghani, M., et al., *Uncertainty analysis of streamflow drought forecast using artificial neural networks and Monte-Carlo simulation*. International Journal of Climatology, 2014. **34**(4): p. 1169-1180.
8. Hosseini, S.M., M. Kholghi, and H. Vagharfard, *Numerical and meta-modeling of nitrate transport reduced by nano-Fe/Cu particles in packed sand column*. Transport in porous media, 2012. **94**(1): p. 149-174.
9. Nash, J.E. and J.V. Sutcliffe, *River flow forecasting through conceptual models part I — A discussion of principles*. Journal of Hydrology, 1970. **10**(3): p. 282-290.
10. Babakhani, P., et al., *Supplementary Material for "Modified MODFLOW-based model for simulating the agglomeration and transport of polymer-modified Fe nanoparticles in saturated porous media"*. Environ Sci Pollut Res, 1-20, doi:10.1007/s11356-015-5193-0, 2015.
11. Noori, R., et al., *Development and application of reduced-order neural network model based on proper orthogonal decomposition for BOD5 monitoring: Active and online prediction*. Environmental progress & sustainable energy, 2013. **32**(1): p. 120-127.
12. Yu, H., et al., *Prediction of the Particle Size Distribution Parameters in a High Shear Granulation Process Using a Key Parameter Definition Combined Artificial Neural Network Model*. Industrial & Engineering Chemistry Research, 2015. **54**(43): p. 10825-10834.
13. Castrup, S. *Comparison of methods for establishing confidence limits and expanded uncertainties*. 2010.
14. Couto, P.R.G., J.C. Damasceno, and S.P. de Oliveira, *Monte Carlo simulations applied to uncertainty in measurement*. 2013: INTECH Open Access Publisher.
15. Lu, M., S.M. AbouRizk, and U.H. Hermann, *Sensitivity analysis of neural networks in spool fabrication productivity studies*. Journal of Computing in Civil Engineering, 2001. **15**(4): p. 299-308.
16. Gevrey, M., I. Dimopoulos, and S. Lek, *Two-way interaction of input variables in the sensitivity analysis of neural network models*. Ecological modelling, 2006. **195**(1): p. 43-50.

17. Morshed, J. and J.J. Kaluarachchi, *Application of artificial neural network and genetic algorithm in flow and transport simulations*. Advances in Water Resources, 1998. **22**(2): p. 145-158.
18. Nourani, V., A.H. Baghanam, and M. Gebremichael, *Investigating the Ability of Artificial Neural Network (ANN) Models to Estimate Missing Rain-gauge Data*. Journal of Environmental Informatics, 2012. **19**(1).
19. Yerramareddy, S., S.C.Y. Lu, and K.F. Arnold, *Developing empirical models from observational data using artificial neural networks*. Journal of Intelligent Manufacturing, 1993. **4**(1): p. 33-41.
20. Seetha, N., et al., *Correlation equations for average deposition rate coefficients of nanoparticles in a cylindrical pore*. Water Resources Research, 2015. **51**(10): p. 8034-8059.
21. Phenrat, T., et al., *Empirical correlations to estimate agglomerate size and deposition during injection of a polyelectrolyte-modified FeO nanoparticle at high particle concentration in saturated sand*. Journal of Contaminant Hydrology, 2010. **118**(3-4): p. 152-164.
22. Tufenkji, N. and M. Elimelech, *Correlation equation for predicting single-collector efficiency in physicochemical filtration in saturated porous media*. Environmental Science & Technology, 2004. **38**(2): p. 529-536.
23. Phenrat, T., et al., *Particle size distribution, concentration, and magnetic attraction affect transport of polymer-modified FeO nanoparticles in sand columns*. Environ. Sci. Technol., 2009. **43**(13): p. 5079-5085.
24. Cornelis, G., et al., *Retention and dissolution of engineered silver nanoparticles in natural soils*. Soil Science Society of America Journal, 2012. **76**(3): p. 891-902.
25. Kim, H.-J., et al., *FeO nanoparticles remain mobile in porous media after aging due to slow desorption of polymeric surface modifiers*. Environmental Science & Technology, 2009. **43**(10): p. 3824-3830.
26. Kosmulski, M., *The pH-dependent surface charging and points of zero charge: V. Update*. Journal of colloid and interface science, 2011. **353**(1): p. 1-15.
27. Zhao, G., et al., *Preconcentration of U (VI) ions on few-layered graphene oxide nanosheets from aqueous solutions*. Dalton Transactions, 2012. **41**(20): p. 6182-6188.
28. Zhou, Y., *Adsorption of halogenated aliphatic contaminants by graphene nanomaterials: Comparison with carbon nanotubes and granular activated carbons*. 2014.
29. Mehrizad, A. and P. Gharbani, *Decontamination of 4-chloro-2-nitrophenol from aqueous solution by graphene adsorption: equilibrium, kinetic, and thermodynamic studies*. Polish Journal of Environmental Studies, 2014. **23**(6).
30. Lakshmi, J. and S. Vasudevan, *Graphene—a promising material for removal of perchlorate (ClO<sub>4</sub><sup>-</sup>) from water*. Environmental Science and Pollution Research, 2013. **20**(8): p. 5114-5124.
31. Li, Z., et al., *Transport and deposition of CeO<sub>2</sub> nanoparticles in water-saturated porous media*. Water research, 2011. **45**(15): p. 4409-4418.
32. Toloni, I., F. Lehmann, and P. Ackerer, *Modeling the effects of water velocity on TiO<sub>2</sub> nanoparticles transport in saturated porous media*. Journal of contaminant hydrology, 2014. **171**: p. 42-48.

33. Jones, E.H. and C. Su, *Transport and retention of zinc oxide nanoparticles in porous media: Effects of natural organic matter versus natural organic ligands at circumneutral pH*. Journal of hazardous materials, 2014. **275**: p. 79-88.
34. Won, Y.-H., et al., *Multifunctional calcium carbonate microparticles: Synthesis and biological applications*. Journal of Materials Chemistry, 2010. **20**(36): p. 7728-7733.
35. Rocha, T.L., et al., *Immunocytotoxicity, cytogenotoxicity and genotoxicity of cadmium-based quantum dots in the marine mussel Mytilus galloprovincialis*. Marine environmental research, 2014. **101**: p. 29-37.
36. Pontius, F.W., G.L. Amy, and M.T. Hernandez, *Fluorescent microspheres as virion surrogates in low-pressure membrane studies*. Journal of Membrane Science, 2009. **335**(1-2): p. 43-50.
37. Rahman, T., H. Millwater, and H.J. Shipley, *Modeling and sensitivity analysis on the transport of aluminum oxide nanoparticles in saturated sand: Effects of ionic strength, flow rate, and nanoparticle concentration*. Science of The Total Environment, 2014. **499**: p. 402-412.
38. Sakka, S., *Handbook of sol-gel science and technology. 1. Sol-gel processing*. Vol. 1. 2005: Springer Science & Business Media.
39. Tian, Y., et al., *Deposition and transport of functionalized carbon nanotubes in water-saturated sand columns*. Journal of hazardous materials, 2012. **213**: p. 265-272.

# Appendix F

## 13 Supporting information for Chapter 3

### 13.1 Drag coefficient correction factor and fluid collection efficiency

The drag coefficient correction factor [1-4] is given as:

$$\Omega_i = \frac{2\xi^2 \left(1 - \frac{\tanh(\xi)}{\xi}\right)}{2\xi^2 + 3 \left(1 - \frac{\tanh(\xi)}{\xi}\right)} \quad (\text{F1})$$

where  $\xi$  is the non-dimensional permeability of the porous aggregate for aggregates in size class  $i$  given as:

$$\xi = \frac{a_i}{\kappa^{1/2}} \quad (\text{F2})$$

where  $\kappa$  is permeability [ $L^2$ ] and  $a_i$  is the radius of aggregates in size class  $i$ .

The fluid collection efficiency,  $\eta_c$ , of each aggregate can be determined from the Brinkman equation [2, 5]:

$$\eta_c = 1 - \frac{d_c}{\xi} - \frac{c_c}{\xi^3} \quad (\text{F3})$$

where

$$d_c = \frac{3}{J} \xi^3 \left(1 - \frac{\tanh(\xi)}{\xi}\right) \quad (\text{F4})$$

$$c_c = -\frac{1}{J} \left( \xi^5 + 6\xi^3 - \frac{\tanh(\xi)}{\xi} (3\xi^5 + 6\xi^3) \right) \quad (\text{F5})$$

$$J = 2\xi^2 + 3 - 3 \frac{\tanh(\xi)}{\xi} \quad (\text{F6})$$

It should be noted that the collision frequencies calculated based only on fractal relationships and without permeability consideration [3, 6], was accomplished by assuming  $\eta_c$  and  $\Omega_i$  in Eqs. (F4-F6) equal to one. In Eqs. (F2-F4) and their subsequent equations, the subscript  $i$  has not been placed for parameters for the sake simplicity.

The calculation of permeability for collision frequencies is the same as that of settling velocities that are described next.

### 13.2 Various sedimentation velocity models

The settling velocity models used in the present study are as follows:

1. An empirical power law equation that is based on fractal dimension [7-9]:

$$\frac{U_k}{U_0} = \left(\frac{a_k}{a_0}\right)^{D_{sed}} \quad (\text{F7})$$

where  $a_0$  is the radius of the primary particles,  $a_k$  is the radius of aggregates in size class  $k$ , and  $D_{sed}$  is the sedimentation exponent which can be expressed in terms of fractal dimension of aggregates via various empirical relationships [8]. The most frequently-used expression is [9, 10]:

$$D_{sed} = D_f - 1 \quad (\text{F8})$$

$U_0$  is the settling velocity for primary particles [ $L T^{-1}$ ], and can be determined from the Stokes' equation [11]:

$$U_0 = \frac{2g}{9\mu}(\rho_0 - \rho_w)a_0^2 \quad (\text{F9})$$

where  $g$  is the gravitational acceleration,  $\rho_0$  is density of primary particles, [ $ML^{-3}$ ], and  $\rho_w$  is density of water [ $ML^{-3}$ ]. Combination of these equations yields [12]:

$$U_k = \frac{g}{18\mu}(\rho_0 - \rho_w)(d_0)^{3-D_f}(d_k)^{D_f-1} \quad (\text{F10})$$

where  $d_0$  is diameter of the primary particles and  $d_k$  is diameter of aggregate in size class  $k$ .

2. Permeability model [13]:

$$U_k = \frac{4g}{18\mu}(\rho_0 - \rho_w)a_k^2 \frac{\xi}{\xi - \tanh(\xi)} + \frac{3}{2\xi^2} \quad (\text{F11})$$

As mentioned before  $\xi$  is variable with size classes and the subscript has not been shown for brevity. Permeability of each aggregate,  $\kappa_k$ , can be calculated from the Davies correlation [14] as:

$$\frac{1}{\kappa_k} = \frac{16}{a_k^2} (1 - \varphi_k)^{1.5} [1 + 56 \times (1 - \varphi_k)^3] \quad (\text{F12})$$

where porosity of aggregate class  $k$ ,  $\varphi_k$ , is determined from [5, 12, 15]:

$$\varphi_k = 1 - \left(\frac{a_k}{a_0}\right)^{D_f-3} \quad (\text{F13})$$

3. In the same approach, permeability can be calculated from the Brinkman's model [5]:

$$\kappa_k = \frac{(a_0)^2}{18} \left( 3 + \frac{3}{(1 - \varphi_k)} - \left( \frac{8}{(1 - \varphi_k)} - 3 \right)^{\frac{1}{3}} \right) \quad (\text{F14})$$

It should be noted that considering  $\Omega_k$  from Eq. (F1), another form of Eq. (F11) is given as [1, 2]:

$$U_k = \frac{4g}{18\mu} (\rho_0 - \rho_w) a_k^2 \frac{\varphi_k}{\Omega_k} \quad (\text{F15})$$

4. Settling velocity considering particle size distribution (PSD) in each aggregate can be calculated as follows [16, 17]:

$$U_k = \frac{g}{18\mu} \theta (\rho_0 - \rho_w) (d_{50})^{3-D_f} \frac{(d_k)^{D_f-1}}{1 + 0.15Re_k^{0.687}} \varphi_{dist} \quad (\text{F16})$$

where  $\theta$  is a dimensionless particle-shape factor which is assumed to be one for spherical particles of this study.  $\varphi_{dist}$  represents the impact of size distribution in each aggregate via:

$$\varphi_{dist} = \frac{m_3}{m_F^{3/D_f}} \quad (\text{F17})$$

where

$$m_3 = \left( \sum_{i=1}^k d_i^3 \right) / k \quad (\text{F18})$$

$$m_F = \left( \sum_{i=1}^k d_i^{D_f} \right) / k \quad (\text{F19})$$

where  $k$  is the aggregate size class index. The median size of the component particles within each aggregate,  $d_{50}$ , is assumed here to be determined as follows:

$$d_{50} = 2 \times a_{\left(\frac{k}{2}\right)} \quad (\text{F20})$$

$Re$  is the Reynolds number for aggregate size class,  $k$ , given as:

$$Re_k = \frac{\rho_w U_k d_k}{\mu} \quad (\text{F21})$$

Since  $Re_k$  is dependent on the sedimentation velocity, we solved this equation along with Eq. (F16) iteratively to determine the sedimentation velocity.

### 13.3 Details of the MATLAB code for simulating the aggregation and sedimentation of nanoparticles

Consideration of the initial conditions might be challenging in the model. In this study, we considered two approaches to deal with this: first using the initial PSD observed in the beginning of every experimental case and second using an idealistic PSD taken from the PSD observed for HAp when there is no aggregation.

In first approach the PSD observed in the first measurement of each experimental case is used as the initial condition of the model. In doing so, one challenge is the consideration of primary particle size and volume of aggregates in the model. The primary particle size is used as the first bin size in the aggregation modelling process. Additionally, this primary particle radius,  $a_0$ , is used in the calculation of sedimentation velocity and collision rates. In this study, we assume this size as the minimum of the following two sizes:

- a. The minimum initial hydrodynamic diameter observed among different experimental cases. This size is 80 nm for HAp used in the present study.
- b. The minimum size of the PSD bins which has a non-zero concentration in the initial-measured PSD, i.e., PSD at time zero. This size varies among different cases with different initial PSD.

The primary particle sizes ( $a_0$ ) used in various modelling cases of this study are 6.8, 7.9, 35.5, 35.5, and 35.6 nm at 2.5, 3, 5, 7.5, and 10 mM CaCl<sub>2</sub> (pH 6), respectively, and 35.6, 25.4, and 12.2 nm at pH values 7, 10, 11, (pH 6) respectively.

The initial hydrodynamic radius,  $R_H$ , observed in the experimental data may be converted to the radius of gyration,  $R_g$ , following [18]:

$$\frac{R_H}{R_g} = \frac{1}{\Gamma(2 - D_f^{-1})} \quad (\text{F22})$$

where  $\Gamma$  is the gamma function. This conversion is performed, because the radius of gyration is believed to be more suitable for being considered as the size of primary particle size bin forming aggregates rather than the hydrodynamic radius, which is the size with which particles are moving. After determining the primary particle size, their volume is calculated based on the spherical assumption.

Another challenge is to calculate the average size of aggregates from the model outputs and to convert it to hydrodynamic size, so that they can be compared with experimental data of hydrodynamic size evolution. In this study, after examining a variety of averaging methods proposed for particle size measurements [19] we found a mass- or solid volume-weighted geometrical mean approach calculates the average diameter of PSD produced by the model best at any time. This geometric mean diameter,  $D_{geom}$ , is as follows [19]:

$$D_{geom} = \exp\left(\frac{\sum_{i=1}^{k_{max}} C_i d_i^3 \ln d_i}{\sum_{i=1}^{k_{max}} C_i d_i^3}\right) \quad (\text{F23})$$

where  $C_i$  is the mass concentration in bin  $i$  and  $d_i$  is aggregate diameter in size class  $i$ . To convert this average size to the hydrodynamic size, we determined the ratio of the initial experimental hydrodynamic size to the model-calculated geometric mean size ( $R_H/R_g$ ). Then this ratio is utilized to convert all the geometric mean sizes over the duration of simulation to the hydrodynamic size that can be used as model output for comparing with observed hydrodynamic size data. The conversion ratio used in this study was in the range of 0.008 to 0.96. It should be noted that in this process it is assumed that the ratio of  $R_H/R_g$  is constant over the duration of the simulation. Although no exact relation can be derived for this ratio, an available formula [20] suggested that the ratio of  $R_H/R_g$  drops rapidly from  $\sim 1$  for monomer with increasing the cluster mass. However, this trend asymptotes toward a constant value up to 1000 particles per cluster. Therefore, the assumption of constant  $R_H/R_g$  in the present study which deals with a bin size distribution in the range of  $1 - 4 \times 10^{12}$  should not cause considerable errors.

In the second approach, we used the first peak observed in the case of the HAp measurement under no added electrolyte and shifted in the way that the initial

hydrodynamic diameter ( $\sim 80$  nm) in the cases of low electrolyte concentration can be produced via  $D_{geom}$  calculated by the model without the need for any conversion. Then this initial PSD, which is shown in Fig. F11, was used for all other experimental cases. In this approach a pre-early stage is considered for aggregation before measurements start. In this stage, which averagely takes  $\sim 70$  s in our experiments, the sample is being shaken by vortex and pipette while being transferred into the DLS cuvette. Thus, we considered the shear rate in this short period estimated roughly at  $26.7$  1/s, and we also turned off the settling mechanism during this period since all the mass of the sample is transferred to the cuvette.

The solid volume of each bin is obtained from the size of each bin following [12]:

$$v_k = \frac{\pi}{6} (d_0)^{3-D_f} (d_k)^{D_f} \quad (\text{F24})$$

where  $v_k$  is the volume of solid fraction in each aggregate of size class  $k$ , and  $d_0$  is the diameter of primary particles forming the PSD. This should be equal to  $2a_0$ . However, since  $a_0$  can be considerably smaller than  $a_1$ , which is the smallest bin with non-zero concentration, this assumption can cause a high mass balance error when the smallest bin contains a significant concentration, e.g., when this bin is used for monodispersed initial PSD like the case used for comparison with the analytical solution. Therefore, for such cases we consider  $d_0$  equal to  $2a_1$ . It should be noted that the assumption of  $d_0 = 2a_0$  in simulation cases of this study with realistic initial PSD of the experimental data does not lead to any noticeable mass balance error (absolute error  $< 1.0\text{E-}05$  %).

The mass of aggregates in each size class,  $m_k$ , is determined from [12]:

$$m_k = \rho_0 v_k \quad (\text{F25})$$

The expanded form of fixed pivot (FP) governing equation (Eq. 3.1, Chapter 3) [21] may be shown as follows:

$$\begin{aligned} \frac{dn_k}{dt} = & \sum_{i=1}^{Kmax} \sum_{j=1}^i \left[ 1 - \frac{1}{2} \delta_{j,i} \right] \eta_k \alpha_{j,i} \beta_{j,i} n_j n_i \\ & - n_k \sum_{i=1}^{Kmax} \alpha_{k,i} \beta_{k,i} n_i - \frac{U_k}{Z_s} n_k \end{aligned} \quad (\text{F26})$$

Such an equation can be derived for the moving pivot (MP) equations in a similar way which is not shown here. One can refer to the source code available as electronic supporting information of the version of Chapter 3 published as a paper in *Environmental Science and Technology*. An explicit forward Euler scheme was used to solve this partial differential equations as follows [22]:

$$n_{k,t} = n_{k,t-\Delta t} + \Delta t \frac{dn_{k,t-\Delta t}}{dt} \quad (\text{F27})$$

where  $n_{k,t}$  is the population of aggregates in size class  $k$  at time  $t$ . In this study in order to improve the stability of the model while using an efficient adjustable time step, we derived an approximate stability criterion that may be used for population balance models:

Considering the two summations in Eq. (F26) as:

$$SS_1 = \sum_{i=1}^{Kmax} \sum_{j=1}^i \left[ 1 - \frac{1}{2} \delta_{j,i} \right] \eta_k \alpha_{j,i} \beta_{j,i} n_j n_i \quad (\text{F28})$$

and

$$SS_2 = \sum_{i=1}^{Kmax} \alpha_{k,i} \beta_{k,i} n_i \quad (\text{F29})$$

and substituting them in Eqs. (F26) and (F27) yields:

$$n_{k,t} = n_{k,t-\Delta t} + \Delta t \left[ SS_1 - SS_2 n_{k,t-\Delta t} - \frac{U_k}{Z_s} n_{k,t-\Delta t} \right] \quad (\text{F30})$$

This can be further rearranged as:

$$n_{k,t} = n_{k,t-\Delta t} \left[ 1 - \Delta t \left( SS_2 + \frac{U_k}{Z_s} \right) \right] + \Delta t SS_1 \quad (\text{F31})$$

In order to ensure the stability of the problem the slope of this equation, which represents a linear curve, should be less than one, i.e.:

$$\left| 1 - \Delta t \left( SS_2 + \frac{U_k}{Z_s} \right) \right| \leq 1 \quad (\text{F32})$$

Following rearrangement and substituting the max of velocities among various size classes, the following stability criteria is yielded:

$$\Delta t \leq \frac{2}{SS_2 + \frac{U_{max}}{Z_s}} \quad (F33)$$

where  $u_{max}$  is the maximum settling velocity among all classes of the aggregates. It should be noted that in this stability criteria the summations,  $SS_1$  and  $SS_2$ , are assumed to be constant in respect to the size classes, i.e., the maximum of  $SS_2$  across all size classes is selected in each time step to calculate  $\Delta t$  in for the next time step using Eq. F33. Thus, this stability criterion is only an approximation to improve the stability of the population balance models when being solved with the explicit forward Euler scheme. It should also be mentioned that still this criterion does not guarantee the stability of the explicit population balance model for all ranges of parameters. Yet, it was observed that using this criterion a better stability, especially in the case of MP approach, was achieved without the need for reducing initial time step. An increasing factor of time step, e.g., 1000 was used to increase the time step by the user when the above criteria led to long run times. This was especially useful for the FP method. Overall, the initial selected time step is controlled by the observation data intervals and can be still modified by the user using a multiplier. The model then reduces this time step based on the criteria described above. This can be enhanced by the user if the run time is long. Additionally, once the early stage of the process is passed the time steps can be increased from 50-2000 times to twice the initially selected time step since the numerical issue related to the start of simulation is passed in most of the models, especially when using FP method. The fraction of the simulation time after which the time step can be relaxed is selected by the user (commonly between 1/40 and 1/3 of simulation duration).

We also tried a positivity criteria following [23]. However, for the models of the present study this led to very small time steps and impractical run times. Thus, this positivity criterion was not used anymore.

The model by default considers the bin size distribution that is also used by the DLS instruments, Malvern ZetaSizer, Nano ZS model, UK. The code is designed so that this default particle size discretization can be refined linearly for further resolution of the discretization or for further accuracy of the modelling when a finer interval is required. This code is also capable of reading the data from MS Excel spreadsheets,

modelling batch experiment data, simulating the data in different depths, and producing various plots of results.

### 13.4 Variable attachment efficiency model with DLVO

The interaction energies between particles with radii of  $a_1$  and  $a_2$  can be calculated as follows [24]:

$$U_{wdw}(h) = -\frac{A_H}{6} \left[ \frac{8R_R^2}{h(8R_R + h)} + \frac{8R_R^2}{(4R_R + h)^2} + \ln\left(\frac{h(8R_R + h)}{(4R_R + h)^2}\right) \right] \quad (F34)$$

$$U_{EL}(h) = 4\pi\epsilon\epsilon_0R_R \left[ \varphi_1\varphi_2 \exp(-\kappa_{Deb}h) - \frac{1}{4}(\varphi_1^2 + \varphi_2^2) \exp(-2\kappa_{Deb}h) \right] \quad (F35)$$

$$U_{DLVO} = U_{wdw} + U_{EL} \quad (F36)$$

where  $U_{wdw}(h)$ ,  $U_{EL}(h)$ , and  $U_{DLVO}$  are the van der Waals, the electrostatic, and the total DLVO interaction energies as a function of interaction distance,  $h$ .  $A_H$  is the Hamaker constant in water.  $R_R$  is related to radii of two interacting particles:

$$R_R = \frac{a_1a_2}{a_1+a_2} \quad (F37)$$

$\epsilon_0$  is the dielectric permittivity of a vacuum ( $8.854 \times 10^{-12}$  C/(V · m)),  $\epsilon$  is the dielectric constant of water (78.5).  $\varphi_1$  and  $\varphi_2$  are the surface potentials (mV) for the two interacting particle surfaces, and can be determined from the following equation [25-27]:

$$\varphi = \zeta \left( 1 + \frac{h_s}{a} \right) \exp(\kappa_{Deb}h_s) \quad (F38)$$

where  $Z$  is the valence of electrolyte,  $\zeta$  is the zeta potential (V),  $h_s$  is the distance between the surface of the charged particles and the slipping plane— usually taken as 5 Å. Despite using this equation in this study,  $\varphi$  is commonly assumed approximately equal to the surface zeta potential [24].  $\kappa_{Deb}$  is the inverse of the Debye length (nm) given as:

$$\kappa_{Deb}^{-1} = \sqrt{\frac{\epsilon\epsilon_0k_bT}{2N_AIe^2}} \quad (F39)$$

where  $k_b$  is the Boltzmann constant ( $1.381 \times 10^{-23}$ ),  $T$  is the temperature ( $K$ ),  $N_A$  is Avogadro's number ( $6.02 \times 10^{23} \text{ mol}^{-1}$ ),  $e$  is unit charge,  $1.602 \times 10^{-19} \text{ C}$ , and  $I$  is the ionic strength (M), ( $I = 0.5 \sum c_i Z_i^2$ , where  $c_i$  is the molar concentration of each ionic species (i) in the solution, and  $Z_i$  is the valency of the that ion).

DLVO forces can be related to the attachment efficiency and thereby the population balance model via the reciprocal of the Fuchs stability ratio,  $W$ , that can be calculated as [24, 27, 28]:

$$\alpha = \frac{1}{W} = \left[ \int_0^\infty \lambda(u) \frac{\exp\left(\frac{U_{vdW}(h)}{k_B T}\right)}{(2+u)^2} du \right] \cdot \left[ \int_0^\infty \lambda(u) \frac{\exp\left(\frac{U_{DLVO}(h)}{k_B T}\right)}{(2+u)^2} du \right]^{-1} \quad (\text{F40})$$

where  $u = h/a_0$  and  $\lambda(u)$  is the correction factor for hydrodynamic interactions between particles and is related to the separation distance via [28, 29]:

$$\lambda(u) = \frac{6u^2 + 13u + 2}{6u^2 + 4u} \quad (\text{F41})$$

To incorporate this approach in the model, before the time loop starts,  $\alpha$  is calculated and saved for all size classes interacting with each other within a 2-D matrix.

### 13.5 Development of parameter estimation algorithm

To calibrate the parameters of the model, which comprise of attachment efficiency and fractal dimension, a heuristic optimization algorithm was developed in this study for two purposes. First, this was aimed to deal with potential stability problems of the numerical code, and second, to utilize parallel computational capabilities more efficiently in the calibration process. In brief, this algorithm consists of two major loops. In the first loop the Nash-Sutcliffe  $R^2$  [30] as an objective function, is elevated iteratively until the difference between  $R^2$  in two successive iterations is below 0.1. In the second loop, the similar procedure is pursued with more refined parameter increments until the difference between  $R^2$  in two successive iterations reaches below 0.01. In each loop, the parameter values are multiplied by a series of 5 factors, and the model is run for each value. The multiplication which results in the best  $R^2$  is exerted in the next iteration. It is important to note that in each iteration only one multiplication which results in the best  $R^2$  among all multiplications in the two parameters is selected for the next iteration. In other words, only one parameter can be changed in each

iteration. The stability issue of the explicit numerical code was mostly arisen when a combination range of the two parameters led to very high rate of aggregation and low rate of sedimentation which cannot occur in realistic experimental conditions, but could be encountered in the automatic parameter calibration process. For these cases the optimization algorithm, acting as a ‘master’ model, was designed to decrease the time step of the numerical code, acting as a ‘slave’ model, if this goes unstable. Additionally, the scheme considers if after three increments in the time step size the model was still unstable, the optimization algorithm skipped that multiplication of the parameter value.

Unlike the other automatic calibration schemes in which noise or instability issues can hinder the calculation of parameter gradients [31, 32], in the present approach, skipping the unstable runs could not prevent finding the final optimum parameter values. Similar to other optimization techniques [33], feeding the model with appropriate initial values of parameters was important, especially, the model should be stable in the initial values of parameters fed to the optimization model. This stable initial condition causes the optimization model goes ahead without being hindered by unstable runs. This is because a factor of one is among the five parameter value multiplications, and thus from the beginning to the end of the parameter calibration process always there is at least one set of parameter values for which the model produces correct outputs. If the increments in the first major loop meet the requirement of the loop or fail to find any stable solution, then the optimization procedure proceeds to the second loop. In this loop, more refined multiplications enhance the fit and a greater chance of finding a stable solution is offered since the parameters adopt closer values to the stable ranges. The ability of the parallel runs of the model for incremented parameter values is believed to enhance the total run time significantly. Parameter calibration was mostly conducted on the Chadwick high performance computational (HPC) system at the University of Liverpool, consisting of single, quad- and dual-core nodes (1.6-2.33 GHz), as well as the Condor high throughput computing (HTC) system consisting of ~300 dual-core nodes (2.33 GHz).

It should be noted that Nash-Sutcliffe  $R^2$  might not perform very well as an objective function. Especially, we noticed that when the distance of the data points with the horizontal axis is small, even though visually a good match is achieved between the two graphs of the observation and modelled data, in opposite to

expectation Nash-Sutcliff  $R^2$  is not showing a value close one. This can cause difficulty for the optimization code to find the best set of parameters in such cases. In future uses this objective function can be simply replaced with sum of squared errors (SSR).

### 13.6 Comparison between numerical and analytical solutions

Analytical solution of the Smoluchowski model of aggregation for simplified condition, i.e., pure aggregation and the initial condition in which the initial population of the particles,  $n_0$ , is located in the first bin, is given as follows [29]:

$$n_{k,t} = \frac{n_0 \left(\frac{t}{\tau}\right)^{k-1}}{\left(1 + \frac{t}{\tau}\right)^{k+1}} \quad (\text{F42})$$

where  $\tau$  is the characteristic aggregation time:

$$\tau = \frac{3\mu}{4k_B T n_0} \quad (\text{F43})$$

where  $\mu$  is the dynamic viscosity of the suspending fluid ( $\text{Kg m}^{-1} \text{S}^{-1}$ ).

Considering a log-normal distribution for the initial condition, the analytical solution for the total number of suspended aggregates at time  $t$ ,  $N_t$ , based on a Brownian collision frequency is given as [34, 35]:

$$N_t = \frac{n_0}{1 + A\beta_0 n_0 t} \quad (\text{F44})$$

where

$$A = 1 + \exp(Z_0) \quad (\text{F45})$$

$$Z_0 = \ln^2(\sigma_0) \quad (\text{F46})$$

$$\beta_0 = \frac{2k_B T}{3\mu} \quad (\text{F47})$$

where  $\sigma_0$  is the geometric standard deviation of the initial PSD. The result of the analytical solution was compared with that of numerical model for the same condition and with turning off the sedimentation mechanism by assuming identical density of

particles with that of water. The binning approach for solving the analytical solution with monodisperse initial condition includes an arithmetic series of aggregate volumes while for the numerical solution the binning approach remains a geometrical series ( $v_{i+1}/v_i = 2^{1/q}$ ).  $D_f$  was assumed equal to 3 and  $q$  was varied between 1.1 to 3. It should be noted that when  $D_f$  is 3,  $q=1.5$  yields a volume-based discretization close to that of DLS which is used in experimental data of this study.

The comparisons for monodisperse analytical solution, shown in Figs. F12 and F13, demonstrates that an excellent match between numerical and analytical results of averaged hydrodynamic size is achieved when using the FP method. Regarding the MP technique, producing the results compatible with the condition of the analytical solution faced with difficulty, because placing the initial population of particles in the first bin hindered the solution due to some unknown reason. Yet, the result could be normally achieved when the second bin was used for this purpose, although it necessitated matching the second bin size with the analytical solution condition and therefore a difference between the primary particle size and the bin containing the initial mass in the MP model. After this partial mitigation of the issue, the final results for the comparison (Fig. F13) showed a poorer match between the analytical solution results (MP outcomes) compared to that of the FP technique results. Moving pivot results start to underestimate averaged analytical hydrodynamic size with an increase in the discretization interval corresponding to a decrease in  $q$ . Overall, these results demonstrate comparisons of numerical models with analytical solution of the aggregation model is totally promising in an initial condition which keeps all the particles in the smallest bin that can cause sharp gradient of the solution and consequent numerical difficulties. In the experimental PSD used in this study, the smallest bins of PSDs were less involved (see Fig. F2, F3). Thus, minor deviation of the average size predicted by MP in certain  $q$  when using this specific initial condition could not occur in modelling the experimental data of this study which mostly exhibits a distributed initial PSD. This is confirmed by negligible mass balance errors occurred in simulation cases.

The results of comparison of FP and MP model output with the analytical solution based on log-normal initial PSD is given in Figs. F14 and F15, respectively. These results show that total number concentration of NP predicted by FP over various DF and  $q$  values agrees well with that predicted by the analytical solution. For MP method,

still a good match is achieved when  $q$  is one and with different  $D_F$  values. However, with the increase of  $q$  some minor deviations are observed between the two curves. After all, very accurate reproduction of PSD might not be expected from FP and MP methods since these methods only conserve two properties, mass and number [21, 36], whereas such accurate reproducing of PSD might need conserving other moments as well [37].

### **13.7 Further investigations of sedimentation models combined with the MP approach**

In finding the best settling velocity model when using the MP approach, we selected three cases of experimental data, namely, pH at 7, 10, and 11 and IS at 5 mM CaCl<sub>2</sub>. The three settling velocity models included here are power law correlation, Brinkman permeability, and size distribution and the results are shown in Table F4 and Figs. F5, F6. According to these results, the Brinkman permeability model is the best one in terms of fitting, with averaged  $R^2$  values 0.69 and 0.79 for  $D_H$  and DCR data, respectively, whereas these figures for size distribution-based model are 0.61 and 0.74, respectively, and for Power law model are 0.61 and 0.52, respectively (Table F4). Nevertheless, looking at the parameter values estimated in the calibration process, it is revealed that attachment efficiency,  $\alpha$ , resulted from the Brinkman permeability are up to three orders-of-magnitude higher than one—the maximum theoretical value expected for this parameter. Similarly, the calibrated parameter values obtained for the  $D_f$  (2.67-2.98) are close to the limit of Euclidian particles ( $D_f=3$ ), rather than fractal aggregates with  $D_f$  commonly in range of 1.8 to 2.2. These results are improved when power law sedimentation model is used with  $\alpha$  in the range of 2.2 to 35 and  $D_f$  in the range of 2.4 to 2.8. The use of the particle size distribution-based model yields even better results in terms of the rational of the parameters estimated in the calibration process with  $\alpha$  ranging from 0.6 to 1.35 and  $D_f$  ranging from 1.8 to 2.5 (Table F4). Thus, using the MP approach, the best sedimentation models appears to be the size distribution-based model for settling velocity. Here it should be also mentioned that the rationale of the parameter values might not be still a reliable criteria for selecting the best models since they depend widely on the model applied [38] and already scaling the parameters resulted from such models are common [5].

## 13.8 Assessing the impact of number of depth discretization intervals

It should be noted that in Eqs. 3.1 and 3.3 which have been used for producing sedimentation graphs (Fig. 3.3) and other aggregation modelling results (as the FP technique), the only derivative is in respect to time. Therefore, the model outcomes must be fully independent of the number of spatial discretization intervals ( $\Delta z$ ) [39, 40]. To provide evidence for this, we compared the model results for various number of  $\Delta z$  ranging from 3, which can be crucial if the numerical dispersion is an issue, to 100, which may alleviate the issue of numerical dispersion if it exists. The results for the case of 5 mM  $\text{CaCl}_2$  after 300 min aggregation, which is shown in Fig F16, demonstrate that all curves resulted from selection of different numbers for depth intervals match very well. Numerical dispersion is not an issue in the modelling of this study. In respect to the number of bins for the particle size dimension (size classes), we should note that this too cannot cause inaccuracy as the fixed pivot approach used in this study is already claimed to be independent of the number of size classes by Kumar and Ramkrishna [21].

## 13.9 Experimental versus modelling PSDs

Reproduced PSDs by the model matched to  $D_H$  evolution data, are shown in Fig. F2 for various IS and Fig. F3 for various pH. The models based on the case-specific initial PSD (without considering pre-early stage of the aggregation), significantly overestimate the PSD positions, though they might describe the width of PSDs (Fig. F2a,d,g, F3a,d,g). Their heights are also reproduced in cases where aggregation rate is moderate or low. It should be noted that experimental measurements of the hydrodynamic size might be biased by the larger size fraction in the dispersion [41]. Accordingly, matching the model to hydrodynamic size data and then using the model to predict PSD might overshoot the observation.

When the pre-early stage of the aggregation is taken into account by considering a fixed initial PSD in all cases, a much better estimation of the PSD peak positions are obtained (Fig. F2b,e,h, F3b,e,h). When this approach is combined with a variable attachment efficiency predicted using DLVO, PSD comparison show similar results

with the former approach though a slightly better match is obtained in some cases, e.g., at pH 11, while the model fails to predict the PSD at low IS, e.g., 2.5 and 3 mM CaCl<sub>2</sub>.

It should be noted that considering PSD as the model objective function in fitting is a better practice since calculation of geometric mean size for the PSD of the observation data over time shows large oscillations (results not shown), indicating higher reliability of  $D_H$  data for being used in the model than averaged PSD data. Studies which have attempted to match experimental and modelling PSDs in similar condition with that in the present study are not abundant. One recent report [35] attributed the reason for the discrepancy between modelled and experimental PSDs to the widening of experimental PSD and its shift toward smaller bins which must not be the case when there is no breakage in the system. Overall, although the modelling approach with fixed initial PSD fairly matches the experimental PSD in later times, the reason for the observed discrepancies might be related to the experimental deficiency in measuring PSD rather than the model inaccuracy.

## 13.10 Figures

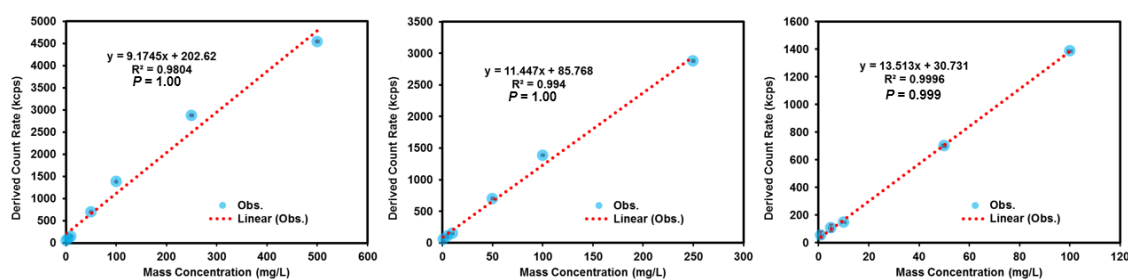


**Figure F1** The linear correlation between the derived count rate (kilo count per second) and the mass concentration (mg/L) of HAp NP for three different ranges of concentration: up to 500 mg/L (left panel), up to 250 mg/L (middle panel), and up to 100 mg/L (right panel). Standard deviations of duplicate experiments are shown as error bars which are barely visible.

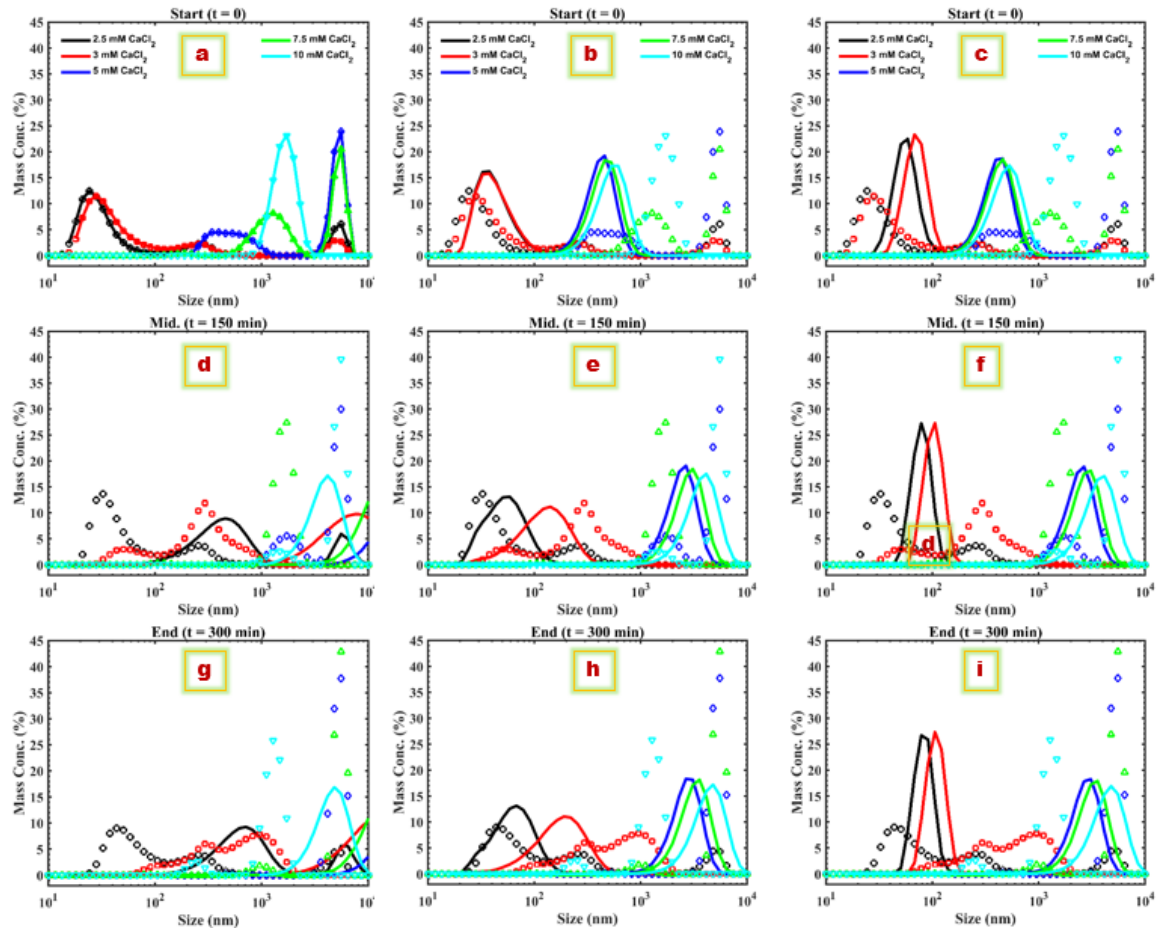


**Figure F2** Mass concentration-based particle size distribution in the beginning (a-c), middle (after 150 min, d-f), and the end of each aggregation experiment (300 min, g-i) at various IS and a fixed pH at 6. The model used here was FP approach with using power law velocity formulation and Brinkman collision model. The approaches are: case-specific initial PSD (a,d,g), fixed initial PSD in all cases (b,e,h), fixed initial PSD along with a variable attachment efficiency predicted b DLVO (c,f,i). It should be noted that size in the horizontal axis refers to diameters specified for bins.

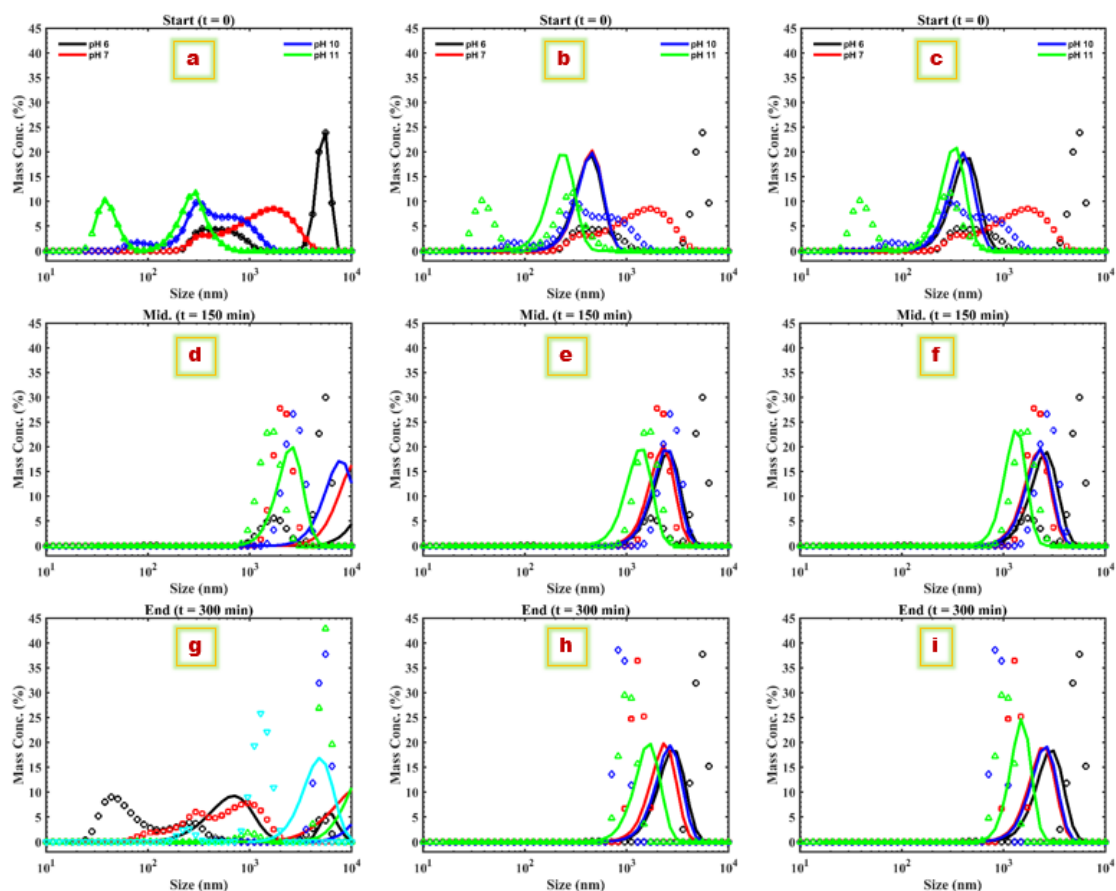


**Figure F3** Mass concentration-based particle size distribution in the beginning (a-c), middle (after 150 min, d-f), and the end of each aggregation experiment (300 min, g-i) at various pH and a fixed IS at 5 mM CaCl<sub>2</sub>. The model used here was FP approach with using power law velocity formulation and Brinkman collision model. The approaches are: case-specific initial PSD (a,d,g), fixed initial PSD in all cases (b,e,h), fixed initial PSD along with a variable attachment efficiency predicted b DLVO (c,f,i). It should be noted that size in the horizontal axis refers to diameters specified for bins.

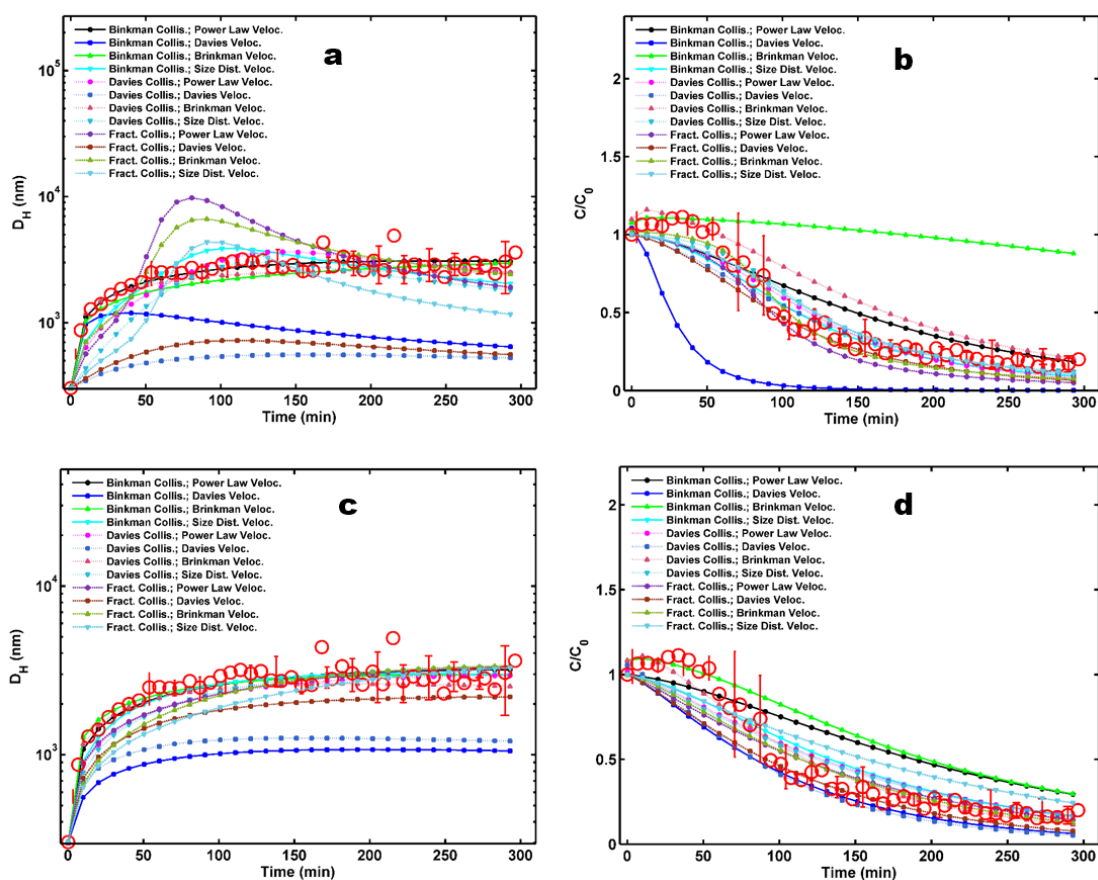


**Figure F4** Different modelling approaches to sedimentation velocity and collision frequency calculation using the FP (a,b) and MP (c,d) aggregation model. Hallow large red circles are the experimental data obtained at pH 10 and 5 mM  $\text{CaCl}_2$ .

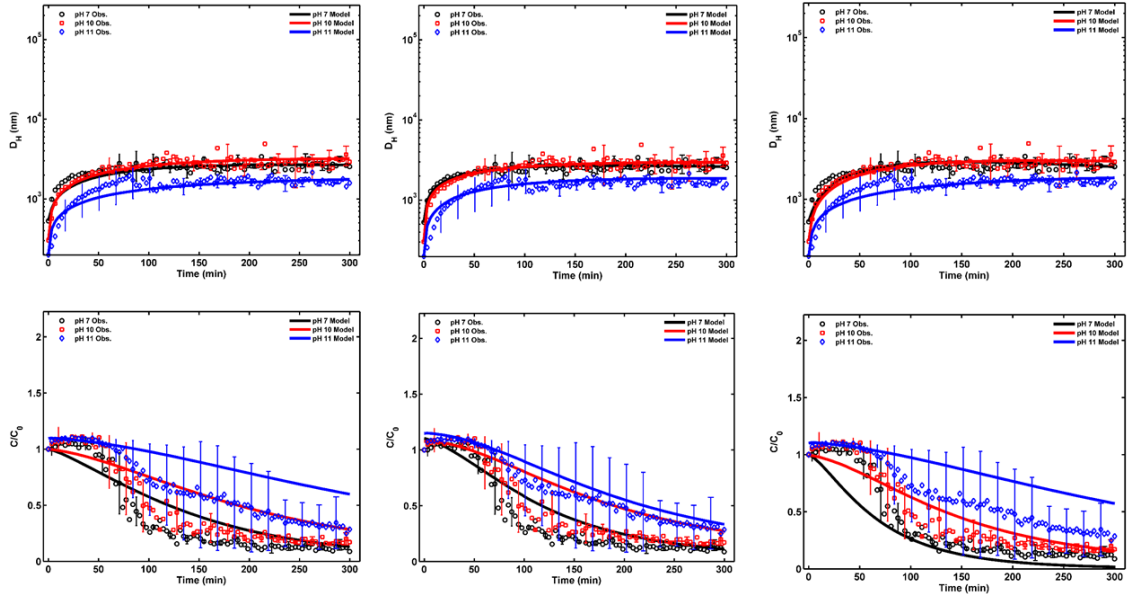


**Figure F5** Evolutions of  $D_H$  and DCR data modeled with MP models along with Brinkman permeability-based collision rates and different velocity models including: power Law (left), Brinkman permeability (middle), and size-distribution-based (right) models. The experimental data include three cases conducted under pH values of 7, 10, and 11, at 5 mM  $\text{CaCl}_2$ .

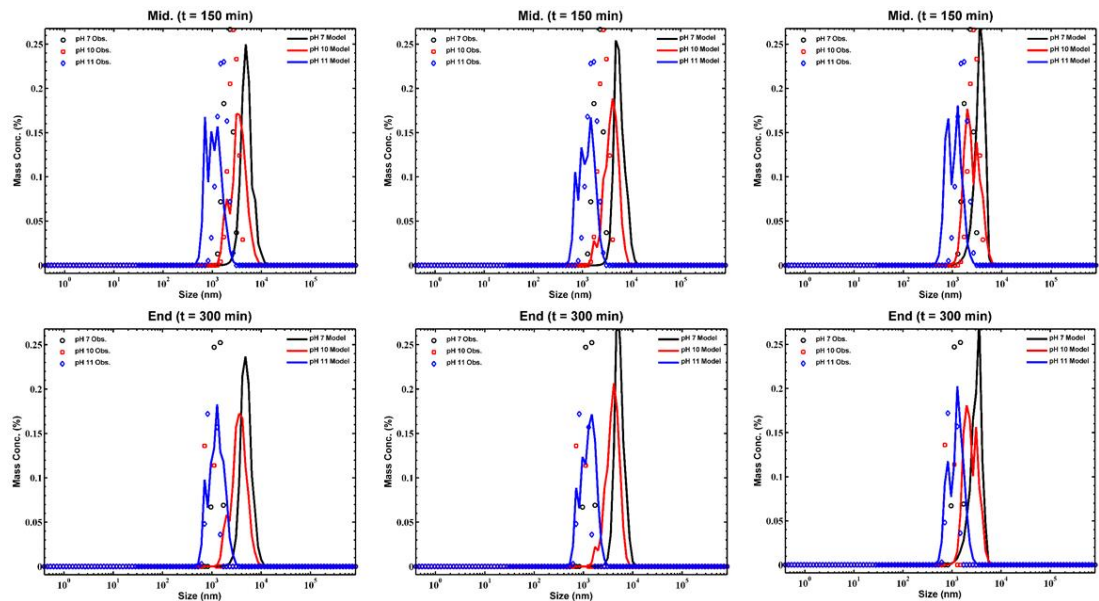


**Figure F6** Size distribution modeled with MP model along with Brinkman permeability-based collision rates and different velocity models including: power Law (left), Brinkman permeability (middle), and size-distribution-based (right) models. The experimental data include three cases conducted under pH values of 7, 10, and 11, at 5 mM  $\text{CaCl}_2$ .

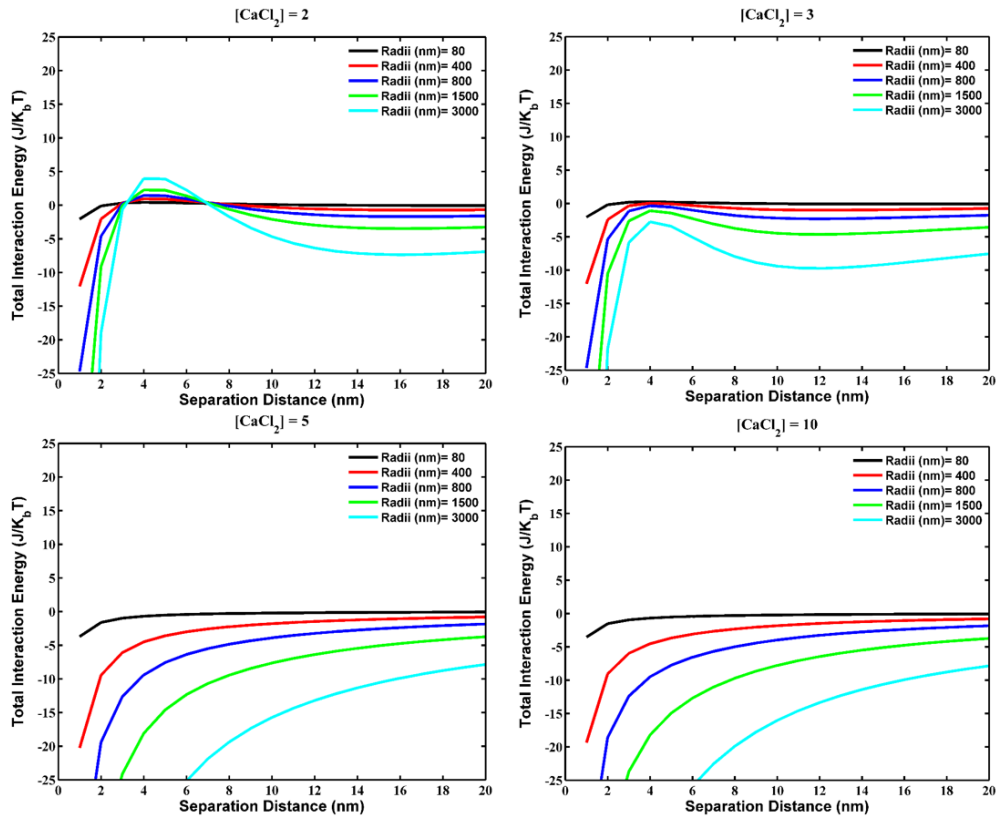


**Figure F7** DLVO profiles for various concentrations of  $\text{CaCl}_2$  and different particle radii.

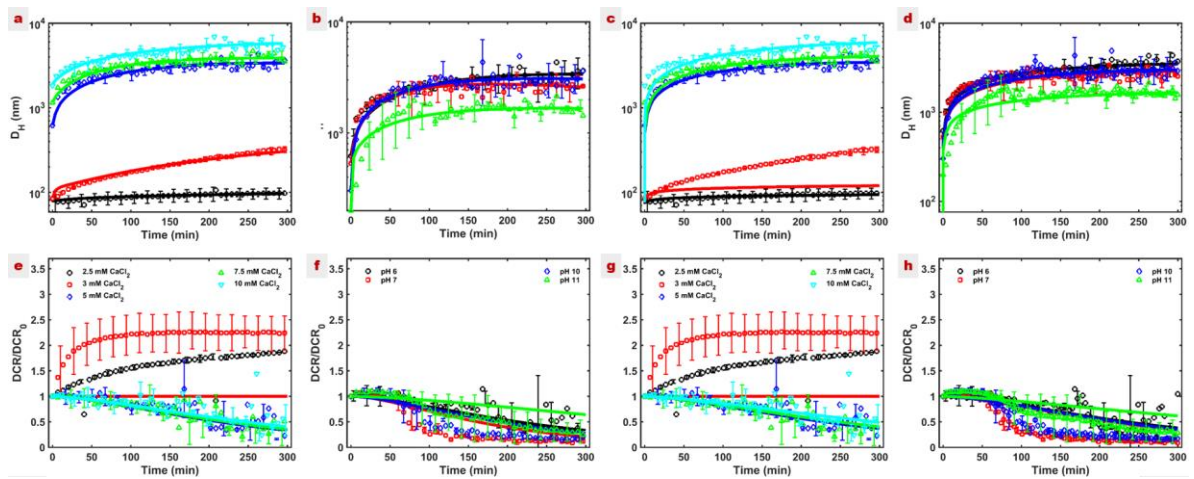


**Figure F8** Evolution of Size (a-d) and change in normalized derived count rate (e-h) for HAp NPs at the point of measurement at various IS with a fixed pH at 6 (a,c,e,g) and various pH with a fixed IS at 5 mM  $\text{CaCl}_2$  (b,d,f,h). The model set used here includes the FP approach with power law velocity formulation and Brinkman collision model. The modelling approaches include using case-specific observed initial PSDs (approach A) (a,b,e,f) and using a fixed initial PSD with considering the pre-early stage of aggregation combined with a variable attachment efficiency predicted by DLVO (approach C) (c,d,g,h).

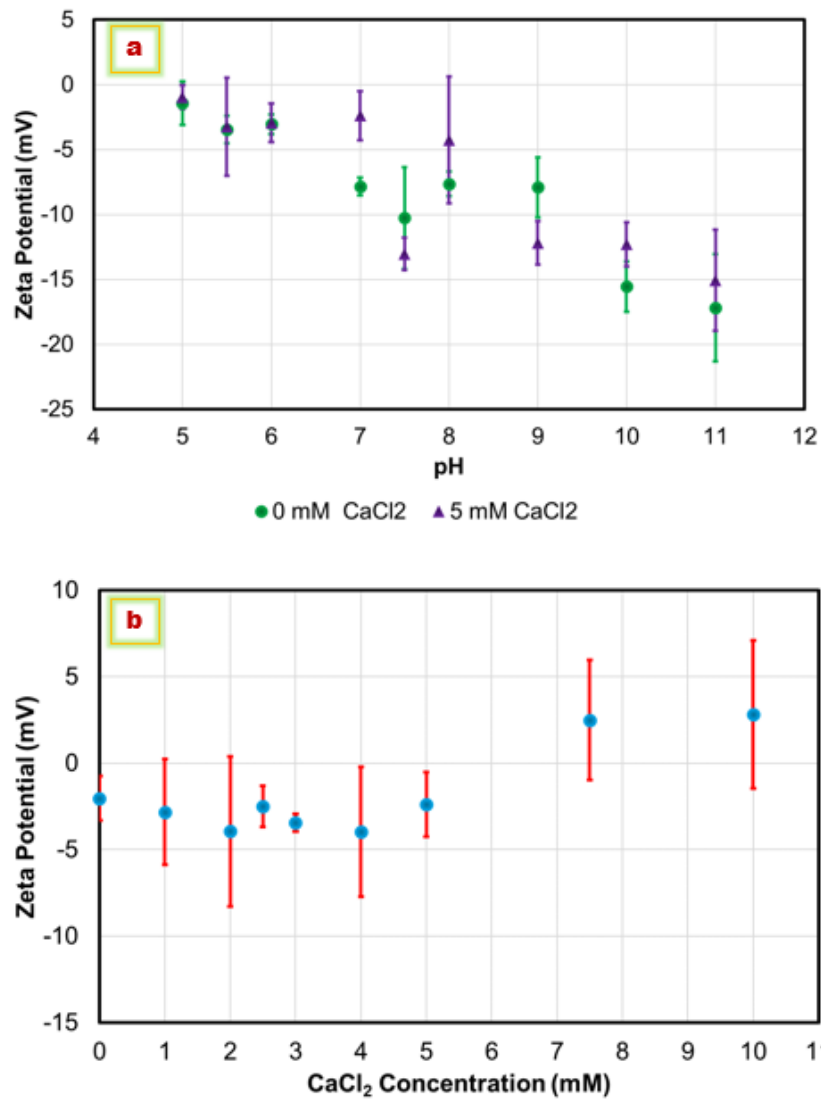


**Figure F9** Zeta potential versus pH at 0 and 5 mM CaCl<sub>2</sub> (a) and versus various electrolyte concentration at pH 6 (b).

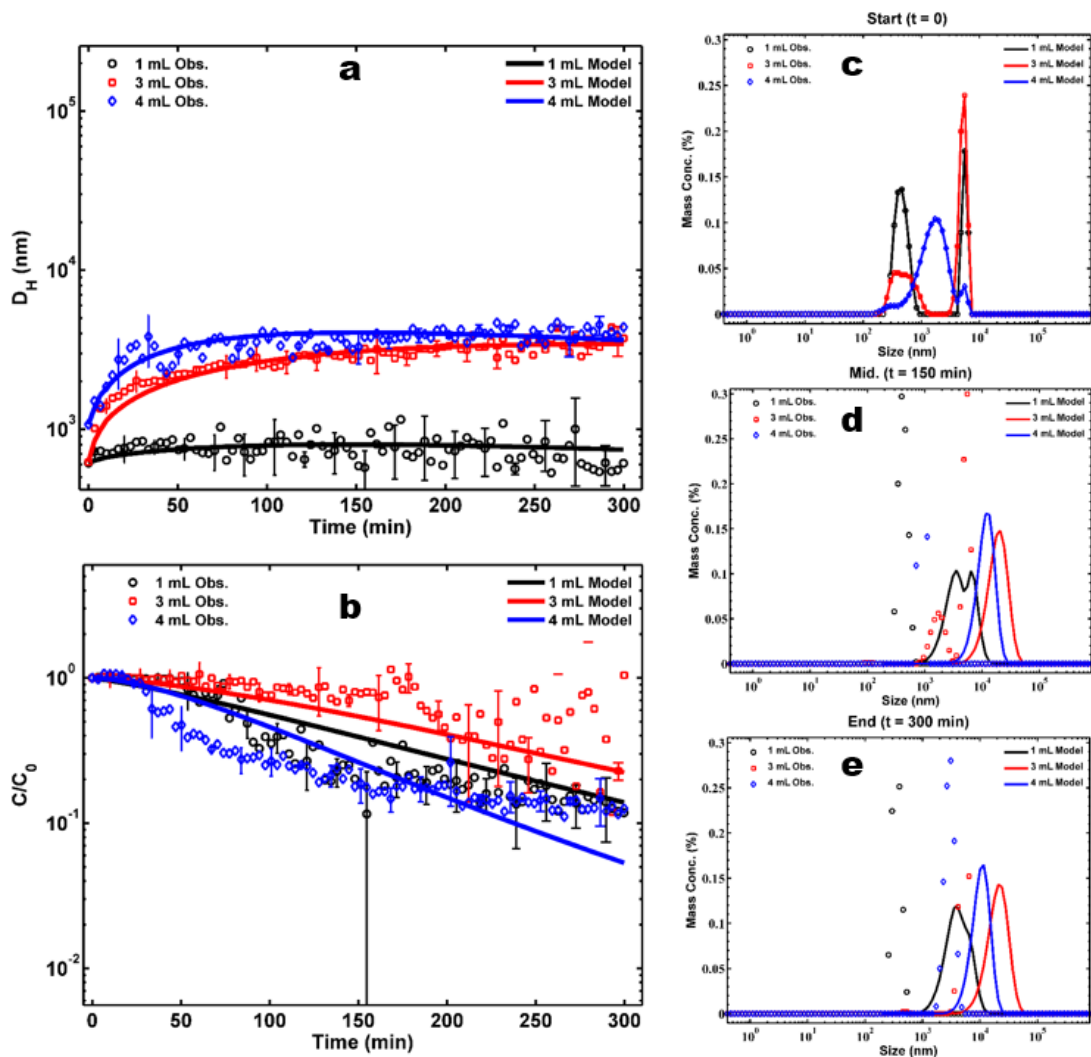


**Figure F10** Evolution of Size (a) and change in normalized derived count rate (shown as  $C/C_0$ ) (b) and PSDs at the start (c), the middle (d), and the end (e) of experiments for HAp NPs with different sample volumes, 1, 3, and 4 mL corresponding to different depths of measurements, 0.33, 2.33, and 3.33 cm, respectively. Experiments were conducted at pH=6 and an IS of 5 mM  $\text{CaCl}_2$ . The models used here comprise of FP approach, power law settling velocity formulation, and Brinkman collision rate model

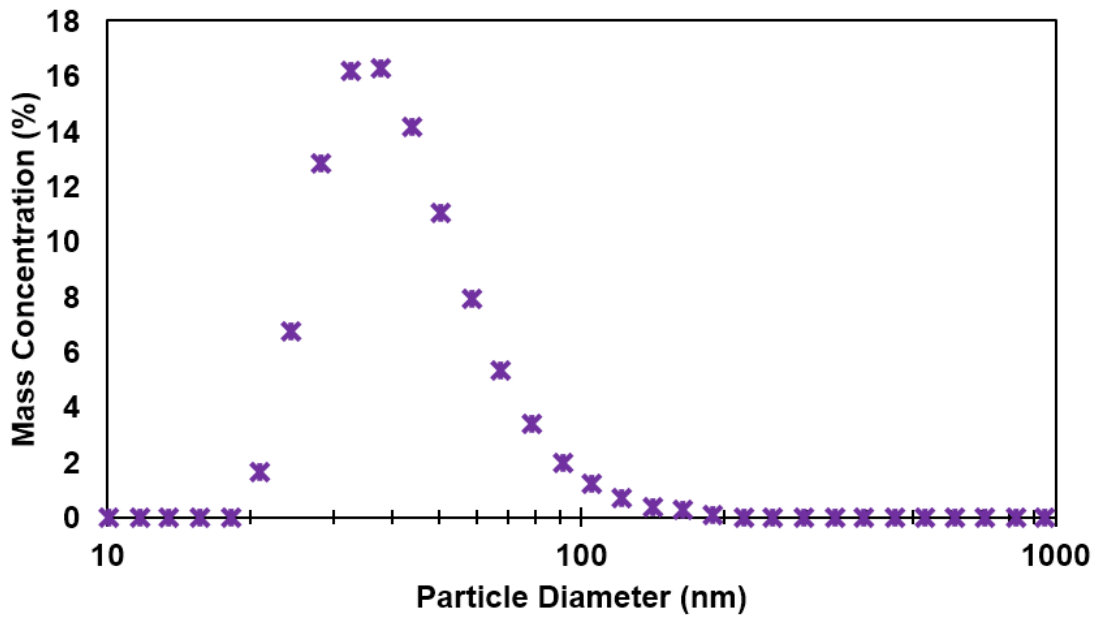


**Figure F11** Set initial particle size distribution used in the fixed-initial-condition approach.

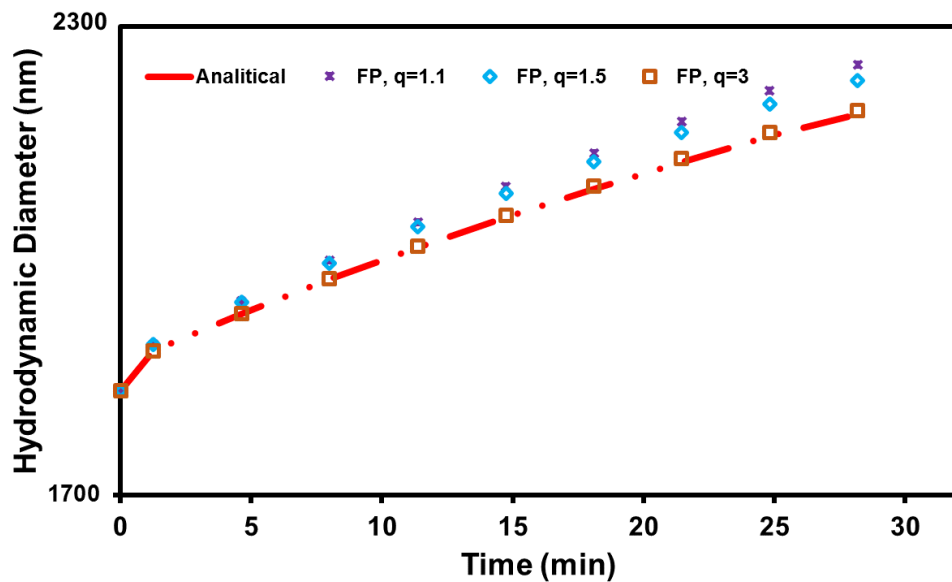


**Figure F12** The outputs of FP numerical model compared with the analytical solution for pure aggregation. All the initial population of particles is placed in the first bin. Similar to the condition of the case at pH 6 and IS of 10 mM CaCl<sub>2</sub>, the primary particle size was assumed 800 nm. Attachment efficiency was assumed one and  $D_f$  was assumed 3. The geometric discretization spacing factor,  $q$ , varied between 1.1 and 3.

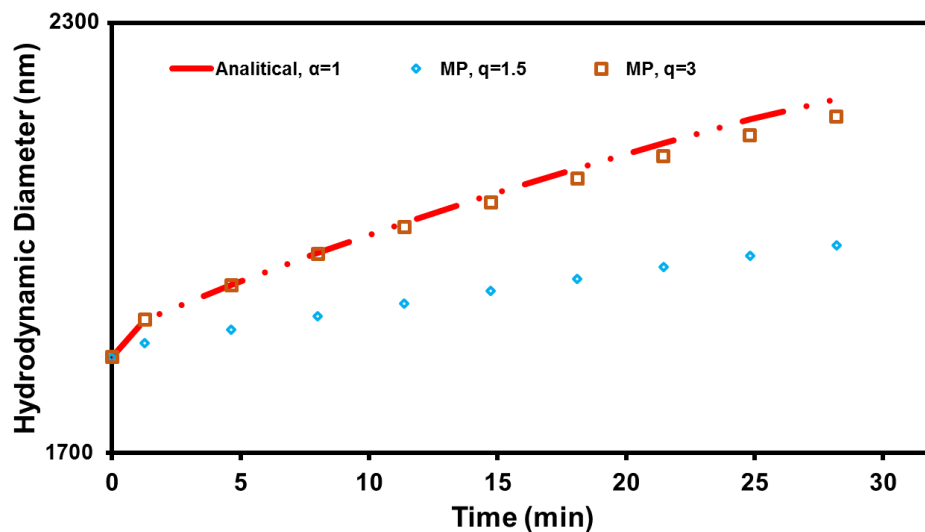


**Figure F13** The outputs of MP numerical model compared with the analytical solution for pure aggregation. All the initial population of particles is placed in one bin. The rest of the condition were selected similar to the case at pH 6 and IS of 10 mM  $\text{CaCl}_2$ . Attachment efficiency was assumed one and  $D_f$  was assumed 3. The geometric discretization spacing factor,  $q$ , varied between 1.1 and 3.

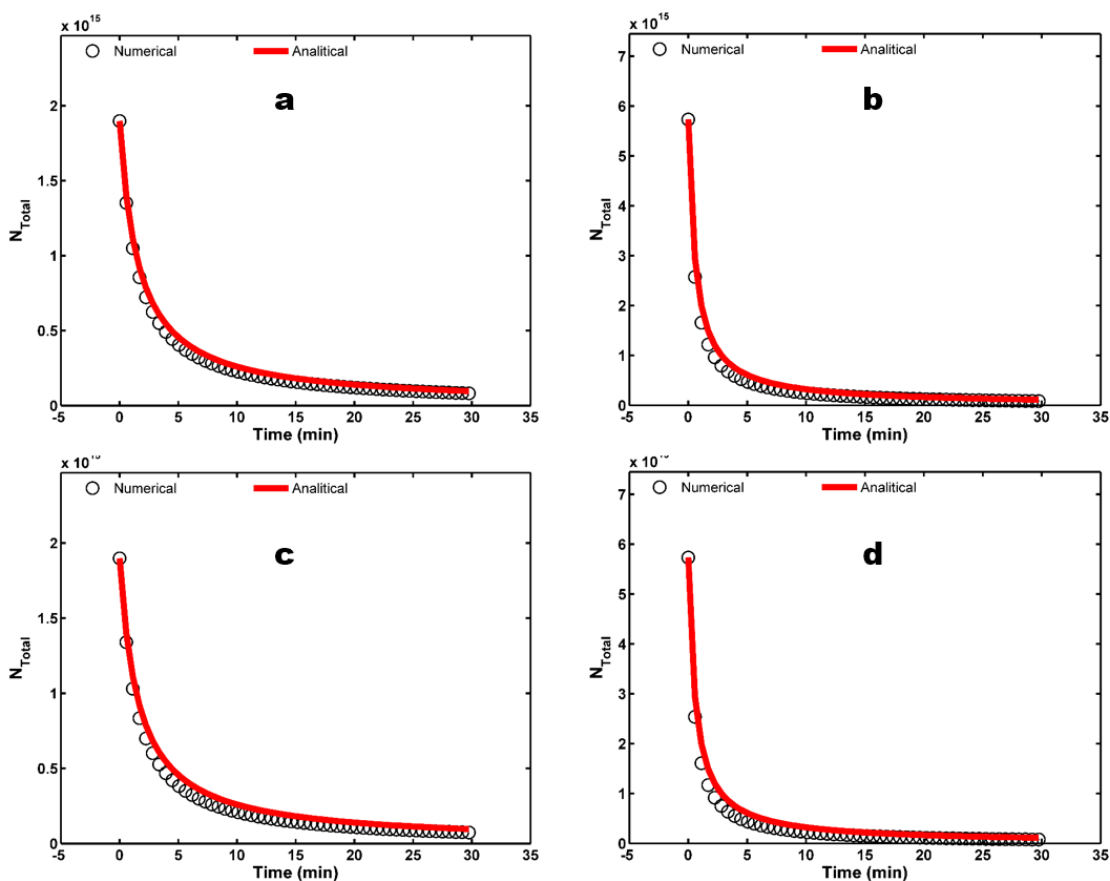


**Figure F14** The outputs of FP numerical model compared with the analytical solution for pure aggregation with log-normal initial PSD. The rest of the condition were selected similar to the case at pH 6 and IS of 10 mM CaCl<sub>2</sub>. Attachment efficiency was assumed to be one and  $D_f$  is 3 (a,b) or 1.8 (c,d). The geometric discretization spacing factor,  $q$ , is 1 (a,c) or 3 (b,d).

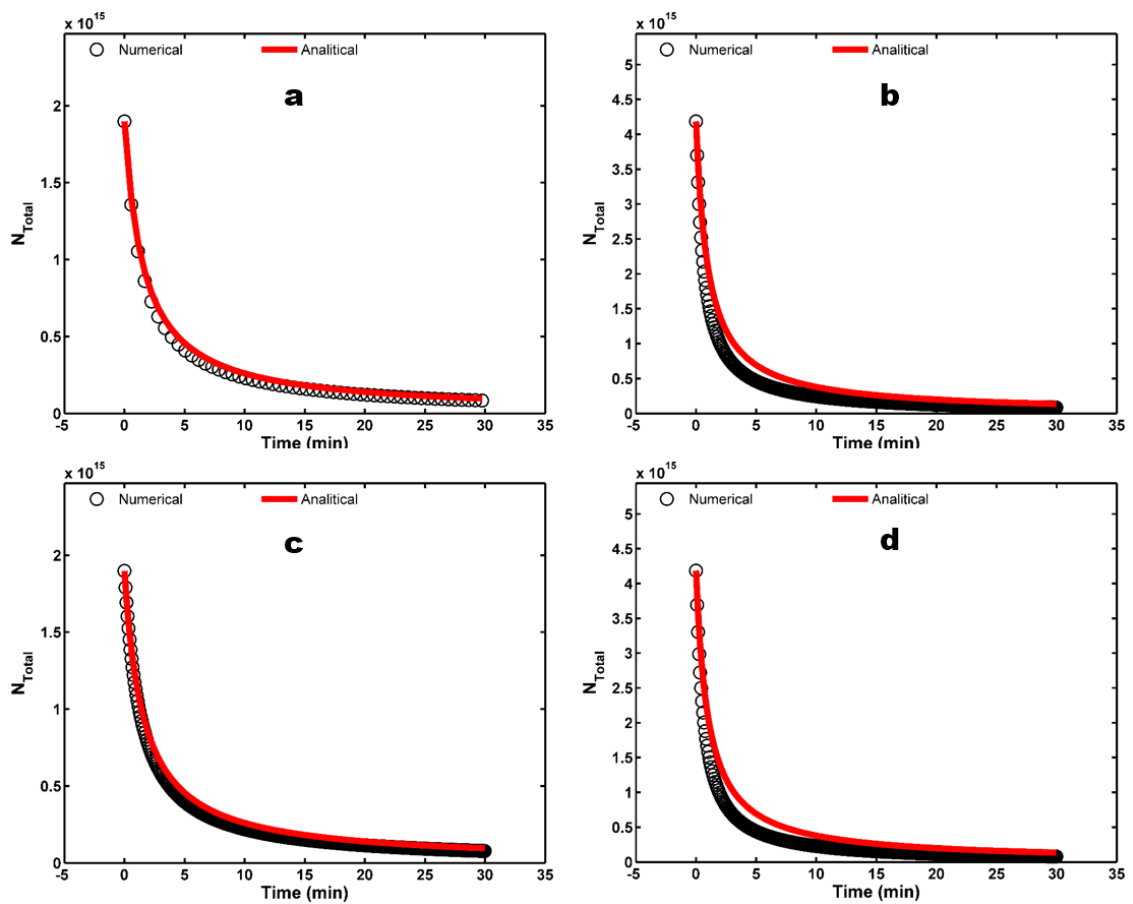


**Figure F15** The outputs of MP numerical model compared with the analytical solution for pure aggregation with log-normal initial PSD. The rest of the condition were selected similar to the case at pH 6 and IS of 10 mM CaCl<sub>2</sub>. Attachment efficiency was assumed to be one and  $D_f$  is 3 (a,b) or 1.8 (c,d). The geometric discretization spacing factor,  $q$  is 1 (a,c) or 2 (b,d).

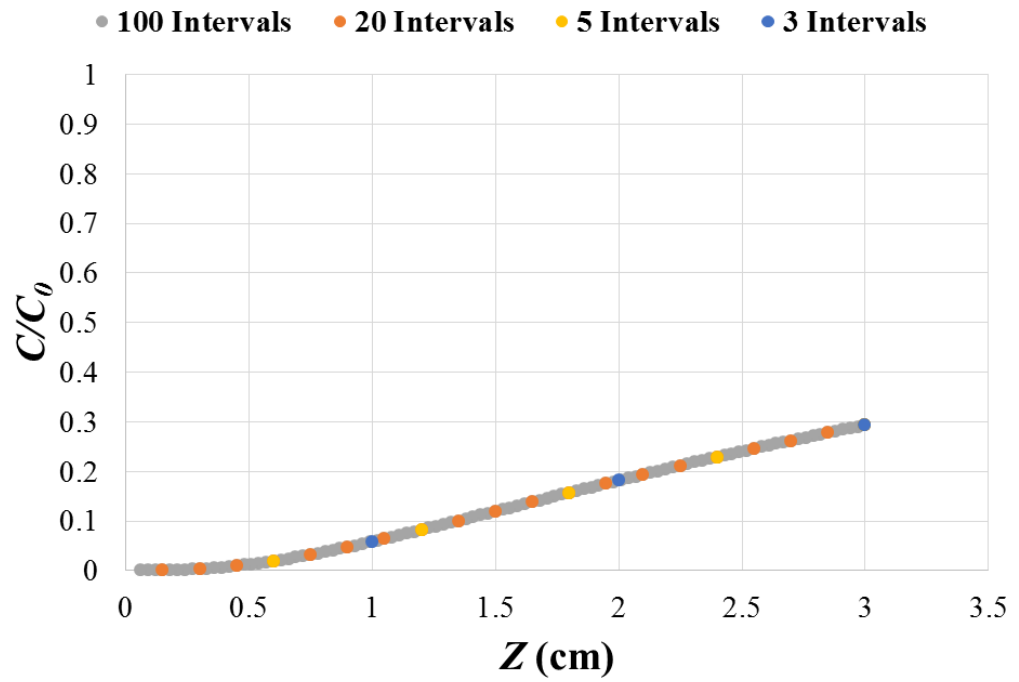


**Figure F16** Predicted mass concentration profiles with sedimentation depth,  $Z$ , confirming that selection of the number of depth intervals chosen is not significant in the prediction of mass loss rates using the models described in this work.

## 13.11 Tables

**Table F1** Fixed pivot fitting results with various sedimentation velocity and collision rate models.

<b>Collision model</b>	<b>Settling velocity model</b>	<b><math>\alpha</math></b>	<b><math>D_f</math></b>	<b><math>R^2</math> -Size</b>	<b><math>R^2</math> - DCR</b>	<b>Mass balance error (%)</b>
<b>Permeability with Brinkman model</b>	Power Law	6.33	2.317	0.714	0.835	9.5E-07
	Permeability, Davies	5.00	3.000	-8.581	0.759	1.6E-06
	Permeability, Brinkman	95.0	2.999	0.406	-2.103	-1.1E+01
	Size distribution	0.05	1.505	-0.017	0.924	6.0E-06
<b>Permeability with Davies correlation</b>	Power Law	0.80	2.473	0.356	0.922	6.1E-13
	Permeability, Davies	2.00	2.985	-9.336	0.902	5.4E-07
	Permeability, Brinkman	130	2.992	0.432	0.709	-1.7E+01
	Size distribution	0.002	1.830	-0.177	0.933	5.8E-13
<b>Simple fractal model</b>	Power Law	2.5	2.550	-16.412	0.870	1.9E-07
	Permeability, Davies	2.0	2.985	-8.432	0.866	1.6E-05
	Permeability, Brinkman	28.0	2.988	-5.323	0.941	-1.8E+00
	Size distribution	0.20	2.200	-2.285	0.926	3.6E-04

**Table F2** Moving pivot fitting results with various sedimentation velocity and collision rate models.

<b>Collision model</b>	<b>Settling velocity model</b>	<b><math>\alpha</math></b>	<b><math>D_f</math></b>	<b><math>R^2</math> -Size</b>	<b><math>R^2</math> - DCR</b>	<b>Mass balance error (%)</b>
<b>Permeability with Brinkman model</b>	Power Law	15.6	2.468	0.679	0.620	1.6E-01
	Permeability, Davies	15.0	2.990	-6.011	0.878	-1.2E+00
	Permeability, Brinkman	230	2.980	0.705	0.584	-8.2E+00
	Size distribution	1.35	2.020	0.695	0.872	4.2E-01
<b>Permeability with Davies correlation</b>	Power Law	280	2.765	0.506	0.874	-4.2E-02
	Permeability, Davies	40.0	3.000	-4.264	0.797	-5.0E+00
	Permeability, Brinkman	125	2.920	0.529	0.944	-1.3E+01
	Size distribution	3.60	2.542	0.482	0.875	2.8E-01
<b>Simple fractal model</b>	Power Law	39.0	2.893	0.484	0.871	5.6E-01
	Permeability, Davies	26.0	2.950	-0.672	0.828	6.3E-01
	Permeability, Brinkman	3.50	2.500	0.338	0.887	6.8E-02
	Size distribution	3.60	2.500	-0.010	0.773	8.9E-02

**Table F3** Goodness-of-fit results for FP model fittings to various experimental cases under different pH, IS, over 5 h with three approaches, to consider the initial condition: (1) PSD obtained at the initial measurement of each case; (2) an identical PSD for all cases; (3) an identical PSD for all cases and considering variable  $\alpha$  based on DLVO. The power-law model and Brinkman-based permeability model are used to calculate the sedimentation velocity and collision frequencies, respectively. Measured zeta potential are also compared with the adjusted zeta potential in fittings when approach 3 is used.

pH	[CaCl <sub>2</sub> ] (mM)	Case specific initial PSD		Identical PSD		Identical PSD, variable $\alpha$ with DLVO			
		R <sup>2</sup> Size data	R <sup>2</sup> -DCR data	R <sup>2</sup> Size data	R <sup>2</sup> -DCR data	Measured Zeta potential (mV)	Adjusted Zeta potential (mV)	R <sup>2</sup> Size data	R <sup>2</sup> -DCR data
6	5	0.829	0.201	0.852	0.578	-2.3	-2.3	0.852	0.607
7	5	0.633	0.879	0.624	0.474	-2.4	-4.5	0.484	0.013
10	5	0.714	0.835	0.692	0.581	-12.3	-5.0	0.608	0.378
11	5	0.740	0.922	0.606	0.091	-15.1	-7.3	0.640	0.262
6	0	0.433	-0.973	NC	NC	NC	NC	NC	NC
6	1	-0.058	-0.651	NC	NC	NC	NC	NC	NC
6	2.5	0.821	-5.238	0.742	-5.22	-2.5	-27.0	0.701	-5.22
6	3	0.973	-24.31	0.984	-24.24	-3.4	-23.5	-1.834	-24.2
6	7.5	0.825	0.507	0.851	0.566	2.5	2.5	0.765	0.760
6	10	0.839	0.499	0.793	0.790	2.8	2.8	0.774	0.555

**Table F4** The results of MP model in combination with three different sedimentation velocity models fit against experimental data of different pH. The Brinkman permeability model is used to calculate collision rates.

Settling velocity model	pH	$\alpha$	D <sub>f</sub>	R <sup>2</sup> -Size	R <sup>2</sup> - Concentration	Mass balance error (%)
Power law	7	35.0	2.410	0.562	0.800	1.3E-01
	10	15.6	2.468	0.679	0.620	1.6E-01
	11	2.20	2.800	0.596	0.139	-9.9E+00
Permeability, Brinkman	7	1000	2.98	0.678	0.909	-1.0E+01
	10	230	2.98	0.705	0.584	-8.2E+00
	11	1.99	2.67	0.695	0.877	-1.5E+01
Size distribution	7	1.20	1.79	0.476	0.759	7.6E-04
	10	1.35	2.02	0.695	0.872	4.2E-01
	11	0.99	2.59	0.673	0.582	-8.3E+00

**Table F5** Fixed pivot with the case-specific initial PSD approach fittings to early stage (the first 20 min) of various experimental cases under different cases of high pH, and IS. The power-law model and Brinkman-based permeability model are used to calculate the sedimentation velocity and collision frequencies, respectively.

<b>Approach</b>	<b>pH</b>	<b>CaCl<sub>2</sub></b>	<b><math>\alpha</math></b>	<b>D<sub>f</sub></b>	<b>R<sup>2</sup></b>	<b>R<sup>2</sup></b>	<b>-</b>
<b>to D<sub>f</sub></b>		<b>Concentration</b>			<b>Size</b>	<b>concentrat</b>	
		<b>(mM)</b>			<b>data</b>	<b>ion</b>	
						<b>data</b>	
Free in the	7	5	0.525	1.55	0.939	-2.180	
estimation	10	5	0.361	1.75	0.979	-4.543	
process	11	5	0.008	1.65	0.920	-5.651	
	6	5	0.926	1.52	0.931	-0.639	
	6	7.5	0.851	1.65	0.914	-0.412	
	6	10	0.059	1.58	0.913	-0.130	
Fixed in the	7	5	0.772	1.60	0.955	-2.255	
estimation	10	5	0.175	1.60	0.978	-4.440	
process	11	5	0.007	1.60	0.909	-5.647	
	6	5	1.550	1.60	0.947	-0.786	
	6	7.5	0.620	1.60	0.918	-0.383	
	6	10	0.059	1.60	0.900	-0.129	

**Table F6** Fixed pivot with the case-specific initial PSD approach fittings to early and late stages at pH 6 and 5 mM CaCl<sub>2</sub> at different measurement depths. The power-law model and Brinkman-based permeability model are used to calculate the sedimentation velocity and collision frequencies, respectively.

Measurement depth (cm)	$\alpha$	$D_f$	$R^2$ Size data	$R^2$ concentration data	Mass balance error (%)
0.3	0.53	1.98	0.050	0.876	1.8E-08
2.3	11.6	2.03	0.829	0.201	-2.8E-05
3.3	35.00	2.33	0.531	0.738	-1.0E-05

## 13.12 References

1. Vikesland, P.J., et al., *Aggregation and sedimentation of magnetite nanoparticle clusters*. Environmental Science: Nano, 2016. **3**(3): p. 567-577.
2. Thill, A., et al., *Flocs restructuring during aggregation: experimental evidence and numerical simulation*. Journal of Colloid and Interface Science, 2001. **243**(1): p. 171-182.
3. Aziz, J.J., C.A. Serra, and M.R. Wiesner, *Hydrodynamics of permeable aggregates in differential sedimentation*. Environmental engineering science, 2003. **20**(1): p. 21-31.
4. Neale, G., N. Epstein, and W. Nader, *Creeping flow relative to permeable spheres*. Chemical Engineering Science, 1973. **28**(10): p. 1865-1874.
5. Jeldres, R.I., F. Concha, and P.G. Toledo, *Population balance modelling of particle flocculation with attention to aggregate restructuring and permeability*. Advances in colloid and interface science, 2015. **224**: p. 62-71.
6. Therezien, M., A. Thill, and M.R. Wiesner, *Importance of heterogeneous aggregation for NP fate in natural and engineered systems*. Science of The Total Environment, 2014. **485**: p. 309-318.
7. Li, D.H. and J. Ganczarczyk, *Fractal geometry of particle aggregates generated in water and wastewater treatment processes*. Environmental Science & Technology, 1989. **23**(11): p. 1385-1389.
8. Dolgonosov, B.M., *Kinetics of sedimentation of a coagulating suspension*. Theoretical Foundations of Chemical Engineering, 2005. **39**(6): p. 635-642.
9. Allain, C., M. Cloitre, and F. Parisse, *Settling by cluster deposition in aggregating colloidal suspensions*. Journal of colloid and interface science, 1996. **178**(2): p. 411-416.
10. Tang, P. and J.A. Raper, *Modelling the settling behaviour of fractal aggregates—a review*. Powder technology, 2002. **123**(2): p. 114-125.
11. Gregory, J., *Particles in water: properties and processes*. 2005: CRC Press.
12. Sterling, M.C., et al., *Application of fractal flocculation and vertical transport model to aquatic sol–sediment systems*. Water research, 2005. **39**(9): p. 1818-1830.
13. Johnson, C.P., X. Li, and B.E. Logan, *Settling Velocities of Fractal Aggregates*. Environmental Science & Technology, 1996. **30**(6): p. 1911-1918.
14. Logan, B.E. and J.R. Hunt, *Advantages to microbes of growth in permeable aggregates in marine systems*. Limnol. Oceanogr, 1987. **32**(5): p. 1034-1048.
15. Lee, D.G., et al., *Modeling coagulation kinetics incorporating fractal theories: a fractal rectilinear approach*. Water Research, 2000. **34**(7): p. 1987-2000.
16. Vahedi, A. and B. Gorczyca, *Settling velocities of multifractal flocs formed in chemical coagulation process*. Water research, 2014. **53**: p. 322-328.
17. Khelifa, A. and P.S. Hill, *Models for effective density and settling velocity of flocs*. Journal of Hydraulic Research, 2006. **44**(3): p. 390-401.
18. Henry, C., et al., *A refined algorithm to simulate latex colloid agglomeration at high ionic strength*. Adsorption, 2016. **22**(4-6): p. 503-515.
19. Merkus, H.G., *Particle size measurements: fundamentals, practice, quality*. Vol. 17. 2009: Springer Science & Business Media.

20. Lattuada, M., et al., *Modelling of aggregation kinetics of colloidal systems and its validation by light scattering measurements*. Chemical engineering science, 2004. **59**(8): p. 1783-1798.
21. Kumar, S. and D. Ramkrishna, *On the solution of population balance equations by discretization—I. A fixed pivot technique*. Chemical Engineering Science, 1996. **51**(8): p. 1311-1332.
22. Jacobson, M.Z., *Fundamentals of atmospheric modeling*. 2005: Cambridge university press.
23. Singh, M., J. Kumar, and A. Bück, *A volume conserving discrete formulation of aggregation population balance equations on non-uniform meshes*. IFAC-PapersOnLine, 2015. **48**(1): p. 192-197.
24. Zhang, W., *Nanoparticle aggregation: principles and modeling*, in *Nanomaterial Impacts on Cell Biology and Medicine*, Y.C. David G. Capco, Editor. 2014, Springer. p. 19-43.
25. Inyang, M., et al., *Filtration of engineered nanoparticles in carbon-based fixed bed columns*. Chemical engineering journal, 2013. **220**: p. 221-227.
26. Tian, Y., et al., *Transport of engineered nanoparticles in saturated porous media*. Journal of Nanoparticle Research, 2010. **12**(7): p. 2371-2380.
27. Li, K. and Y. Chen, *Effect of natural organic matter on the aggregation kinetics of CeO<sub>2</sub> nanoparticles in KCl and CaCl<sub>2</sub> solutions: measurements and modeling*. Journal of hazardous materials, 2012. **209**: p. 264-270.
28. Zhang, W., et al., *Attachment efficiency of nanoparticle aggregation in aqueous dispersions: modeling and experimental validation*. Environmental science & technology, 2012. **46**(13): p. 7054-7062.
29. Elimelech, M., et al., *Particle deposition and aggregation: measurement, modelling and simulation*. 1998, Amsterdam: Elsevier.
30. Babakhani, P., et al., *Parameterization and prediction of nanoparticle transport in porous media: A reanalysis using artificial neural network*. Water Resources Research, 2017. **53**: p. 4564-4585.
31. Lo, B.P., A.J. Haslam, and C.S. Adjiman, *Parameter estimation for stochastic differential equations: algorithm and application to polymer melt rheology*. Computer Aided Chemical Engineering, 2006. **21**: p. 143-148.
32. Taghavy, A., et al., *Mathematical modeling of the transport and dissolution of citrate-stabilized silver nanoparticles in porous media*. Environmental Science & Technology, 2013. **47**(15): p. 8499-8507.
33. Doherty, J., *Pest, Model-Independent Parameter Estimation User Manual: 5th Edition*. 2004: Watermark Numerical Computing.
34. Lee, K.W., Y.J. Lee, and D.S. Han, *The log-normal size distribution theory for Brownian coagulation in the low Knudsen number regime*. Journal of Colloid and Interface Science, 1997. **188**(2): p. 486-492.
35. Tourbin, M. and C. Frances, *Experimental characterization and population balance modelling of the dense silica suspensions aggregation process*. Chemical Engineering Science, 2008. **63**(21): p. 5239-5251.
36. Kumar, S. and D. Ramkrishna, *On the solution of population balance equations by discretization—II. A moving pivot technique*. Chemical Engineering Science, 1996. **51**(8): p. 1333-1342.

37. Nopens, I., D. Beheydt, and P.A. Vanrolleghem, *Comparison and pitfalls of different discretised solution methods for population balance models: a simulation study*. Computers & chemical engineering, 2005. **29**(2): p. 367-377.
38. Lee, D.J., et al., *On the free-settling test for estimating activated sludge floc density*. Water Research, 1996. **30**(3): p. 541-550.
39. Zheng, C. and P.P. Wang, *A modular three-dimensional multi-species transport model for simulation of advection, dispersion and chemical reactions of contaminants in groundwater systems; documentation and user's guide*. US Army Engineer Research and Development Center Contract Report SERDP-99-1, Vicksburg, Mississippi, USA, 1999.
40. Schelde, K., et al., *Diffusion-limited mobilization and transport of natural colloids in macroporous soil*. Vadose Zone Journal, 2002. **1**(1): p. 125-136.
41. Tomaszewska, E., et al., *Detection limits of DLS and UV-Vis spectroscopy in characterization of polydisperse nanoparticles colloids*. Journal of Nanomaterials, 2013. **2013**: p. 60.

# Appendix G

## 14 Supporting information for Chapter 5

### 14.1 Figures

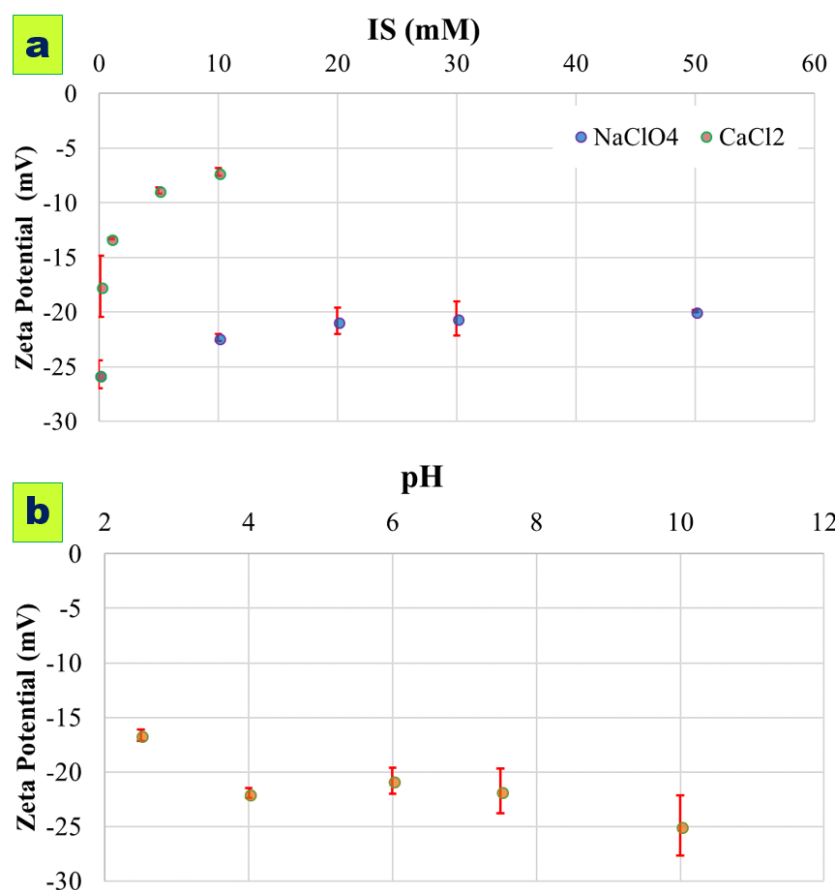


**Figure G1** Zeta potential of SGO nanoparticles at different electrolyte concentrations (mM) of NaClO<sub>4</sub> and CaCl<sub>2</sub> at pH 6 (a) and for different pH values at an electrolyte concentration of 20 mM NaClO<sub>4</sub> (b).

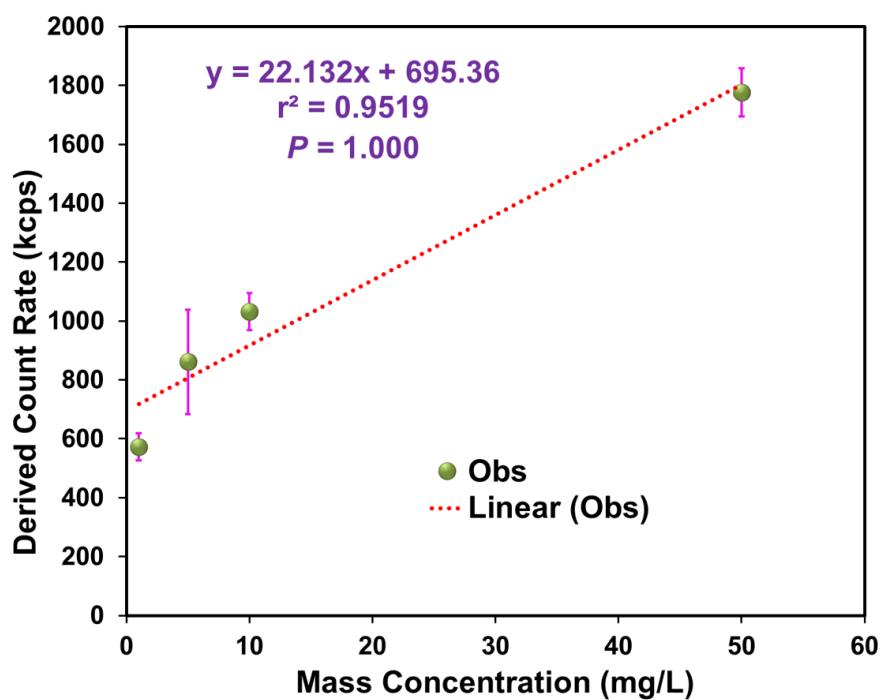


**Figure G2** The correlation between different concentrations and their equivalent derived count rate (DCR).

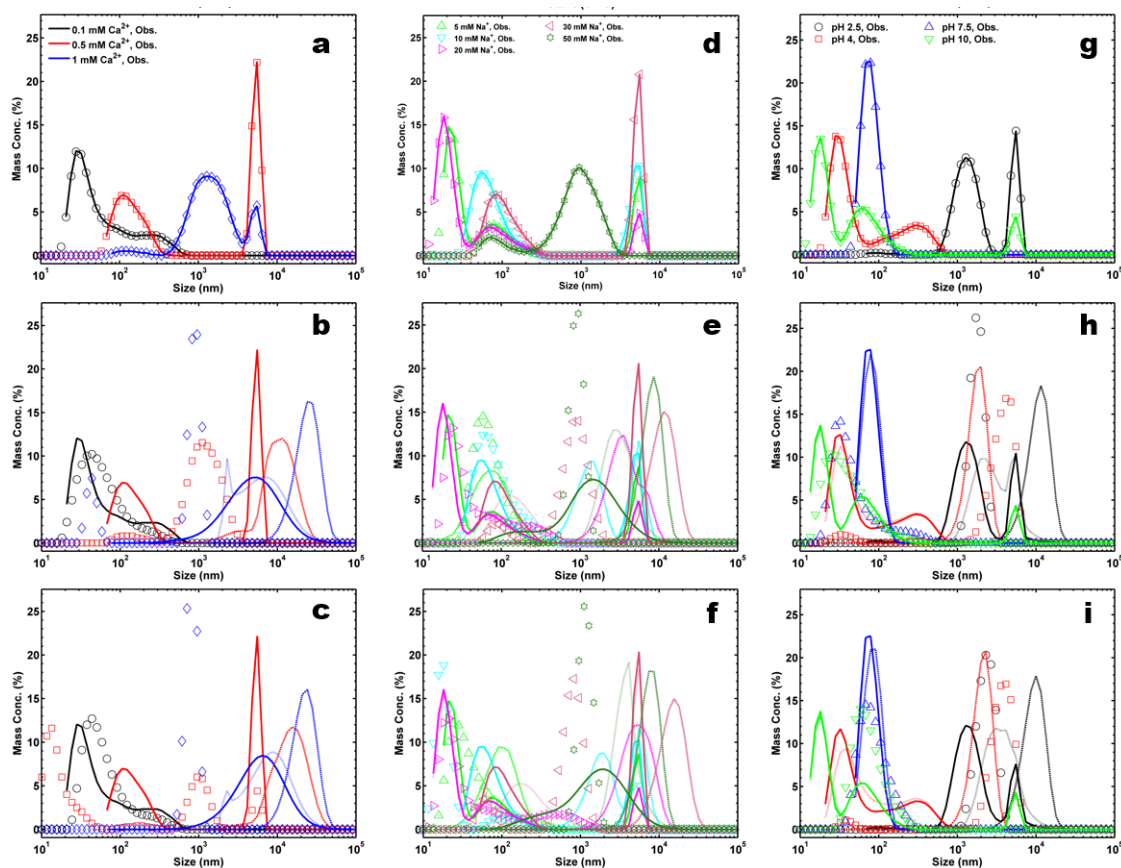


**Figure G3** Comparisons of PSD for SGO NPs at various  $\text{CaCl}_2$  (panels a-c) and  $\text{NaClO}_4$  (d-f) concentrations with a fixed pH at 6 and various pH (g-i) with a fixed IS at 20 mM  $\text{NaClO}_4$  at the beginning ( $t=0$ , a,d,g), middle ( $t=150$  min, b,e,h), and the end of experiments ( $t=300$  min, c,f,i). Continuous lines represent C-CRM; dot lines represent FP technique, and hash lines represent the S-CRM model outcomes.

## Appendix H

### 15 Supporting information for chapter 6

#### 15.1 Figures

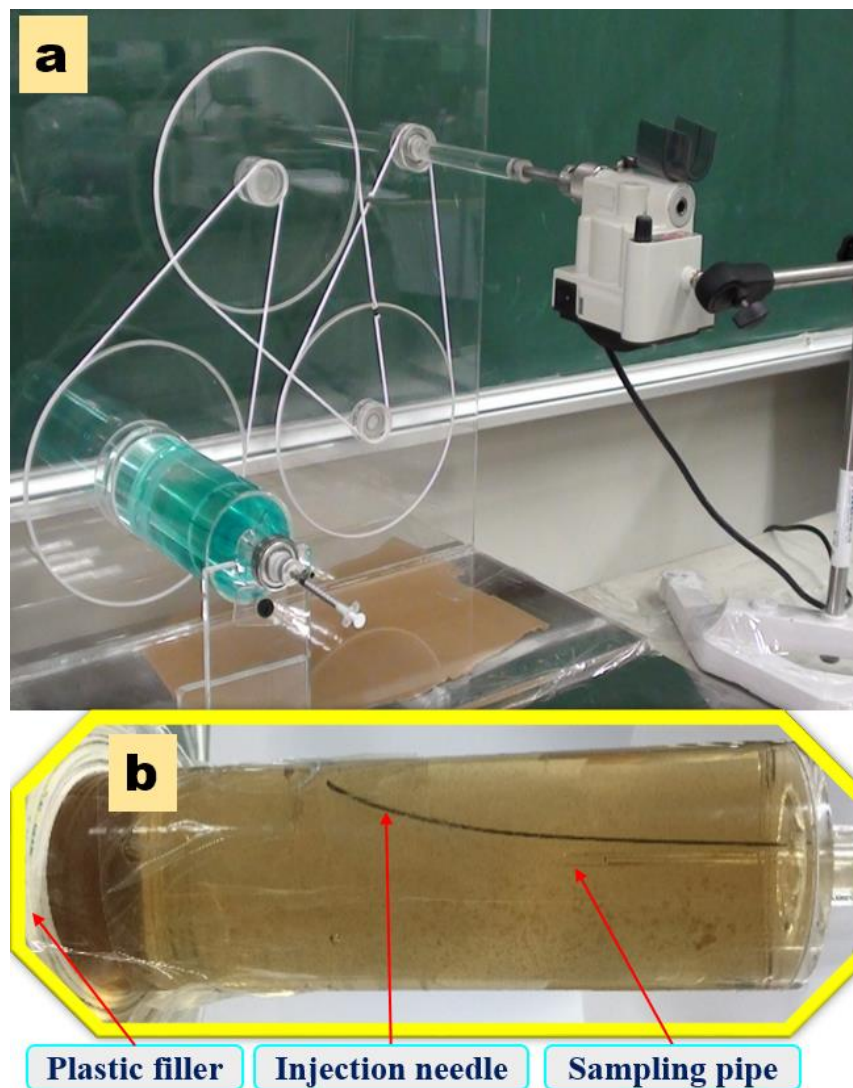


**Figure H1** The experimental setup used in this work (a) and an enlarged photograph of the cylinder (b). The diameter of the cylinder shown in panel (a) is 8.2 cm which was manufactured for initial trials while the diameter of the cylinder shown in panel (b) is 5 cm which was used for the main experiments.

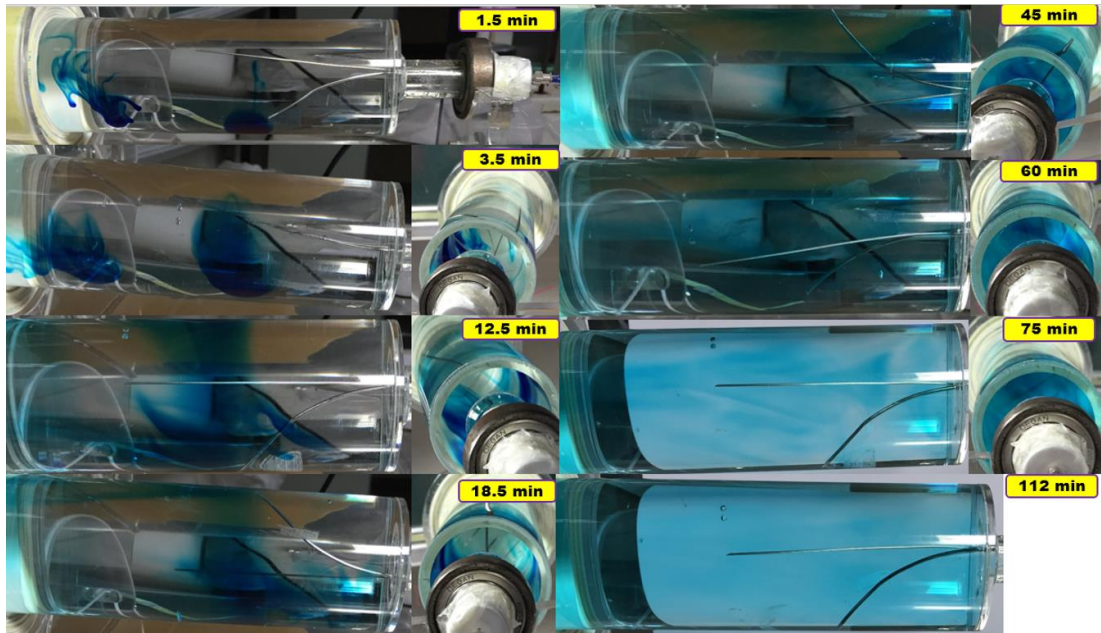


**Figure H2** Experimental photos of the cylinder ( $a_{cyl}=2.5$  cm) rotating at 4.71 rph corresponding to  $Re=0.91$  after Methylene Blue injection.

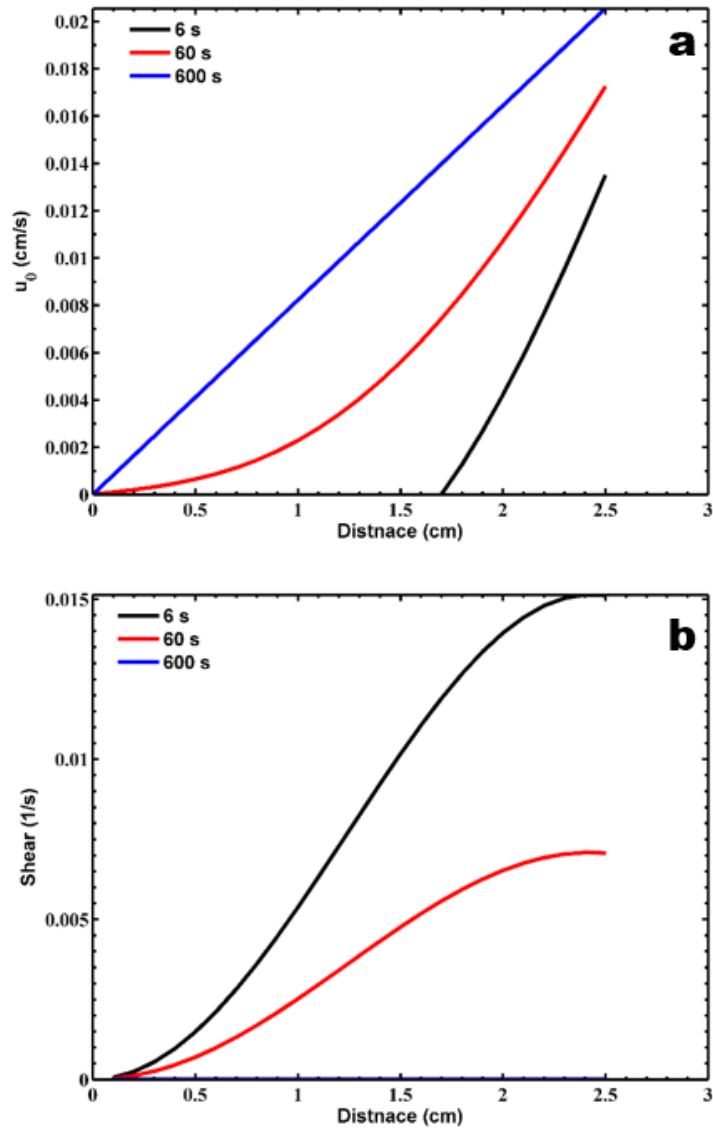


**Figure H3** (a) The rotational component of velocity and (b) shear rate vs distance from the centre of the cylinder for the cylinder at different times.

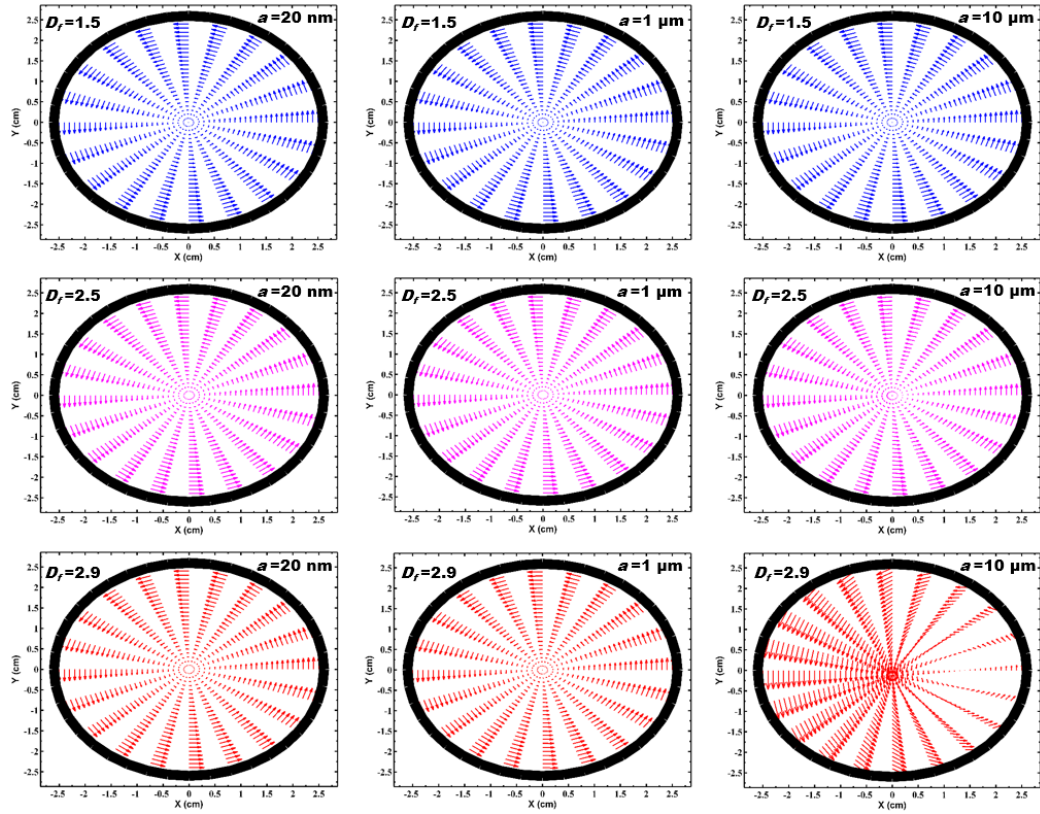


**Figure H4** Velocity vectors for various  $D_f$  and particle radii.

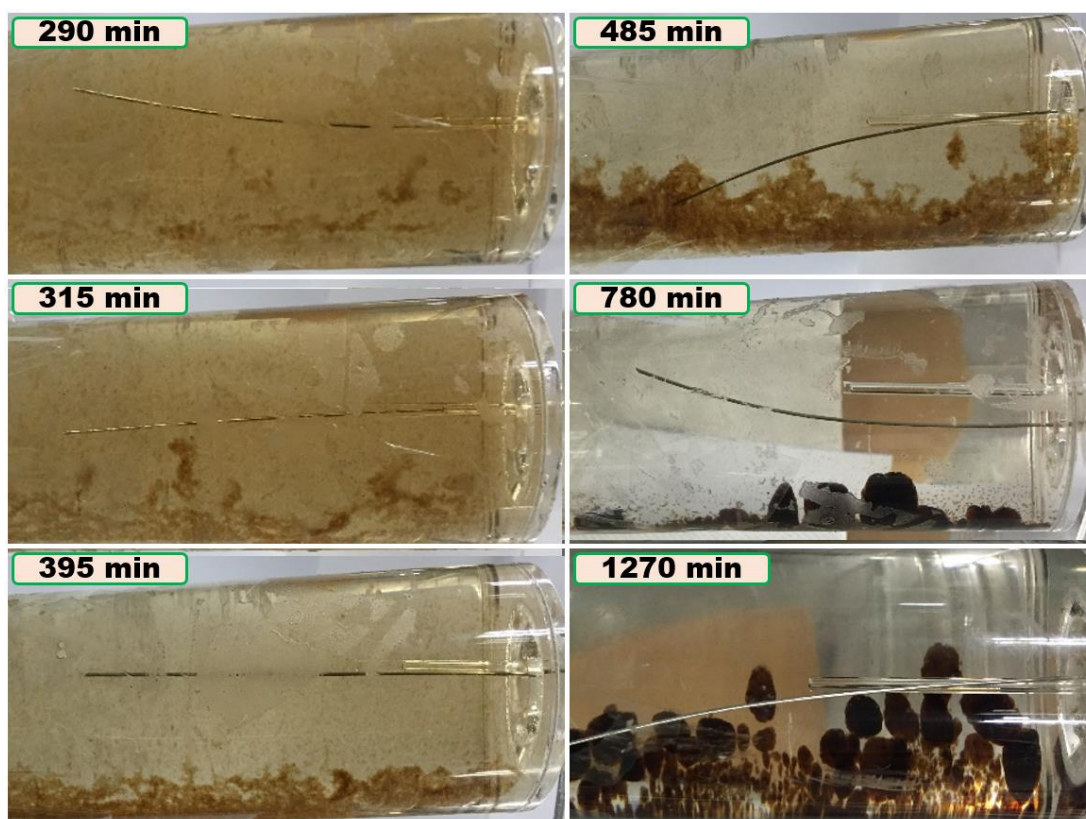


**Figure H5** Experimental photos of SGO aggregation over longer times for the case of rotating cylinder filled with SGO NP in 0.75 mM CaCl<sub>2</sub> solution and pH 6.

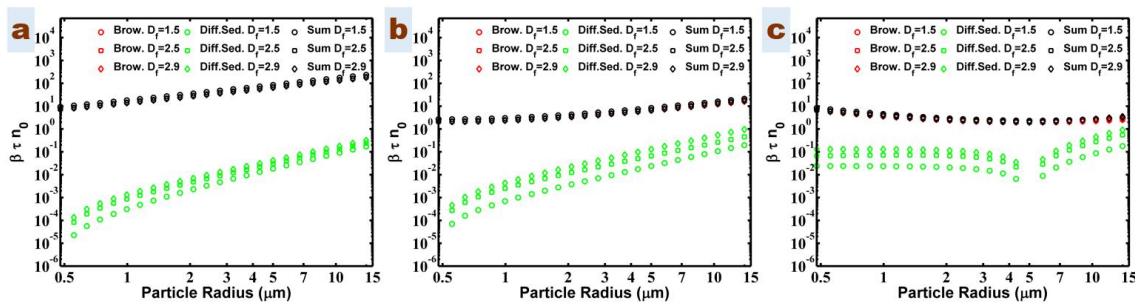


**Figure H6** Variation of nondimensionalized collision frequency calculated for collision between particles/aggregates with radii 50 (a), 500 (b), or 2000 (c) nm with all other particle size classes for different fractal dimensions. Other input parameters of the aggregation model assumed as: attachment efficiency  $\alpha=1$ , particle density 1800 Kg/m<sup>3</sup>, and shear rate  $G=0$ .  $\tau$  is the characteristic time of aggregation [1] and  $n_0$  is the initial population of particles.

## 15.2 Tables

**Table H1** Parameter values estimated in the fitting process together with Nash-Sutcliff goodness-of-fit criterion,  $R^2_{NS}$ .

<b>Ionic strength</b>	<b>Condition</b>	$\alpha$	$D_f$	$R^2_{NS}$
<b>0.5</b>	control	7.0E-06	1.36	0.709
	static	1.0E-05	1.38	0.433
	dynamic	4.9E-05	1.53	0.814
<b>0.75</b>	control	6.5E-04	1.34	0.870
	static	1.1E-03	1.82	0.776
	static	1.2E-04	1.40	0.960
	dynamic	1.4E-03	2.06	0.578
	dynamic	6.8E-03	2.63	0.921

## 15.3 References

1. Elimelech, M., J. Gregory, and X. Jia, *Particle deposition and aggregation: measurement, modelling and simulation*. 1998: Butterworth-Heinemann.